CWD 2025

CONFERENCE FOR
WIND POWER DRIVES

Eurogress, Aachen

March 11 - 12, 2025

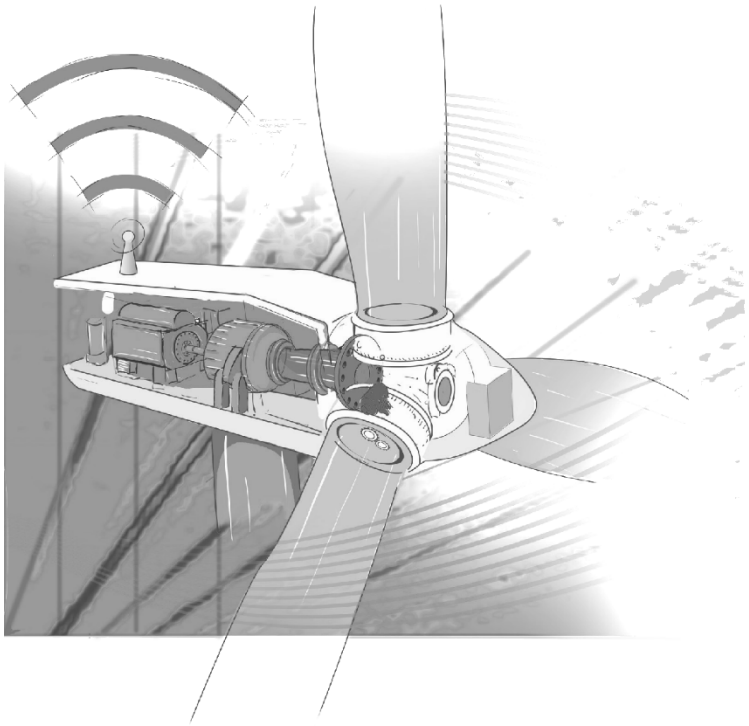

CONFERENCE PROCEEDINGS

sponsored by

DASSAULT SYSTEMES

WAUKESHA BEARINGS a DOVER company

Vestas

hosted & organized by

CENTER SYSTEMS ENGINEERING

CWD Center for Wind Power Drives

FVA Software & Service

Please note:

This is the collection of the conference proceedings.

If you are interested in the peer-reviewed journal publications, follow this link:

https://link.springer.com/collections/eehgdcbhda

Table of Contents

Planetary Plain Bearing I

Next Generation Plain Bearing Technology for Wind Turbine Gearboxes

H. van Lier

ZF Wind Power Antwerpen NV
Gerard Mercatorstraat 40, 3920 Lommel, Belgium

Keywords: Plain Bearing, Wind Turbine Gearbox

Abstract: Plain bearings in planet gears are becoming state-of-the art in wind turbine gearboxes. In recent years, ZF Wind Power successfully introduced a first generation of plain bearing technology in serial products. The continuously growing fleet demonstrates good performance in the field. In order to keep up with recent market developments, a next generation plain bearing technology is needed. This publication explains which new bearing solution ZF Wind Power selected for planetary gears and gives an insight into the systematic development approach that is being followed to introduce the new technology. Results from component and gearbox testing under challenging wind turbine specific operating conditions prove high operational robustness.

1 Introduction of Plain Bearings for Wind Turbine Gearboxes

The use of plain bearings in wind turbine gearboxes is widely established in the industry. Key opportunities of using plain bearings in this demanding application are:

- Increase of gearbox torque density due to the low radial space requirement
- Cost competitive
- Easy to assemble
- High operational robustness
- Good damping properties

As a leading gearbox supplier, ZF Wind Power launched early screening activities with respect to the use of plain bearing technology in 2011. The subsequent development trajectory [LEI15a], [LEI15b], [LEI16], [GOR17] resulted in introduction to serial products in 2019.

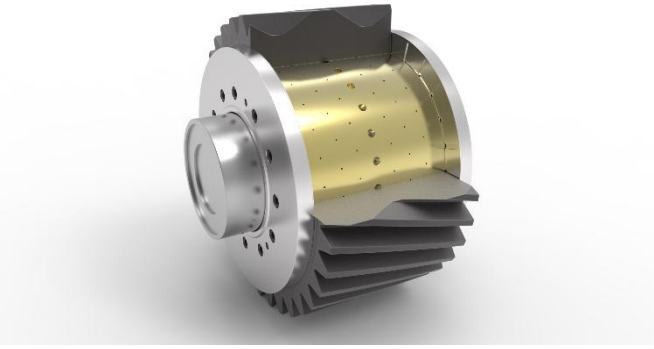

Figure 1: ZF Wind Power plain bearing solution for planet bearing application

ZF Wind Power uses a floating sleeve plain bearing solution for planet bearing application (see Figure 1). The concept consists of a bronze sleeve which is free floating between the planet shaft and the planet gear. Two thrust washers guide the planet gear as well as the floating sleeve axially. At nominal operating conditions, the sleeve rotates at a lower rotational speed with respect to the

planet shaft compared to the planet wheel. That enables a hydrodynamic oil film build-up in both lubrication gaps, meaning between the planet shaft and the sleeve, as well as between the sleeve and the planet gear. The sleeve speed is a result of the equilibrium of the friction moments induced by the two fluid films, because the speed influences the fluid friction in both films and vice versa (dual film bearing concept).

In general, plain bearings offer a high operational robustness when sufficient lubrication is ensured. However, some specific wind turbine operating conditions are more challenging for a plain bearing solution compared to a roller bearing design. These conditions are usually linked to turbine states where either the oil supply is limited, e.g. no grid idling, or where high loads combined with low speed occur, e.g. single blade installation. Such conditions require special attention as there will be no relevant hydrodynamic oil film build up and safe operation of the bearing is mainly dependent on the materials tribology [VLI23].

2 Experience using Plain Bearings in Wind Turbine Gearboxes

Figure 2 shows the cumulative number of delivered gearboxes equipped with plain bearings between 2018 and 2023. From the number of shipped units by end 2023 and taking into account a certain lag due to transport, storage and commissioning, it can be stated that at least 3000 gearboxes with plain bearings are running in the field today. In this fleet, more than 800 units are in operation for more than 3 years.

Until today no failures have been reported from the field, that can be related to the plain bearing concept or design itself. The few issues that have been observed are related to unintended conditions like insufficient oil supply or oil cleanliness. Inspections of bearings after one year of operation in the field show a rather smoothened surface topology, with only minor scratches. Although the surface roughness is reduced, ZF Wind power has never experienced measurable wear patterns.

Overall, the ZF Wind Power plain bearing solution demonstrates good field performance with no indication of slow progressing wear [VLI24].

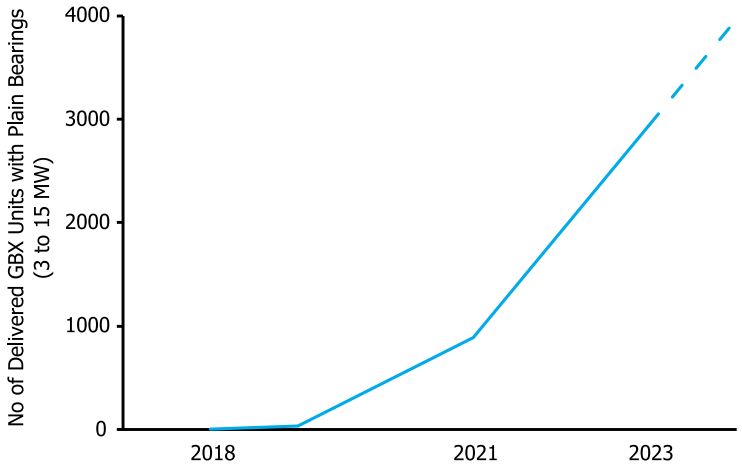

Figure 2: Cumulative deliveries of ZF Wind Power gearboxes equipped with plain bearings

3 Plain Bearing Technology Evolution

Recent market developments and continuous striving for cost reductions in wind industry initiated a further evolution of plain bearing technology. ZF Wind Powers objective is to reduce cost both on component as well as gearbox level. Reducing cost on component level can be achieved by using cheaper materials or simply use a smaller amount of bearing material. On the other side, enabling a reduction of cost on gearbox level by an evolution of bearing technology requires a reduction of component size, while maintaining or even increasing load carrying capacity. Using the reduced space requirement can lead to more torque dense gearbox designs which is linked to a cost reduction on product level.

3.1 Selected Concept

ZF Wind Power selected a bearing concept where the bearing material is fixedly connected to the shaft (single film) instead of using the well-established floating sleeve concept (dual film). The single film concept enables the usage of latest manufacturing technology. Laser cladding has been selected to deposit the bearing material directly on the planet pins outer diameter. Therefore, the bearing becomes a partially integrated function of the planet pin.

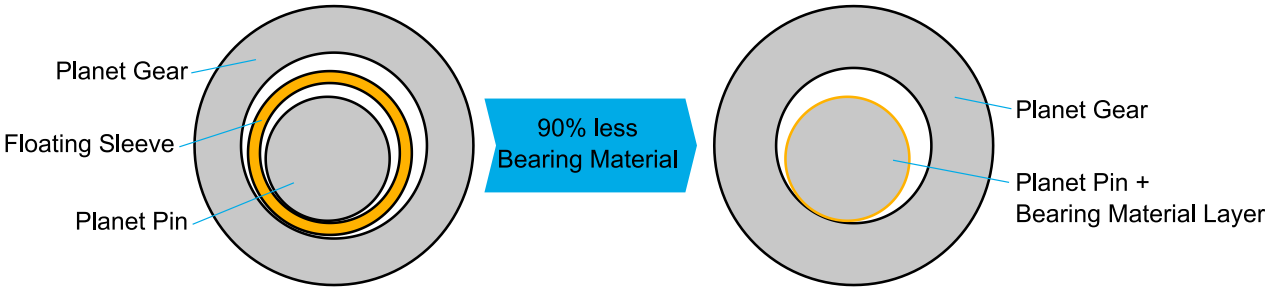

Figure 3: Plain bearing concept evolution

The combination of the single film concept with the laser cladding manufacturing process allows to significantly reduce the amount of rather expensive bearing material. This is because the layer thickness is mainly defined by the bearing functionality and not by structural requirements or manufacturing limitations – as it is the case for the dual film concept as well as the assembled single film concept. Reducing the amount of bearing material is a direct cost saving on component level but is also leading to a reduced radial space demand which is a contributor to more torque-dense gearbox designs.

3.2 Validation Trajectory

The next generation plain bearing technology is validated in a systematic way (see Figure 4). ZF Wind Power has successfully finalized the majority of component, subsystem and gearbox bench testing. A 4 MW gearbox has been modified for the validation. The existing plain bearings have been replaced by the new bearing concept, whereas the size of the bearings has been reduced in order to test closer the operational limits. The new plain bearing technology has demonstrated its capability during the gearbox robustness test including significant overload and single blade installation conditions.

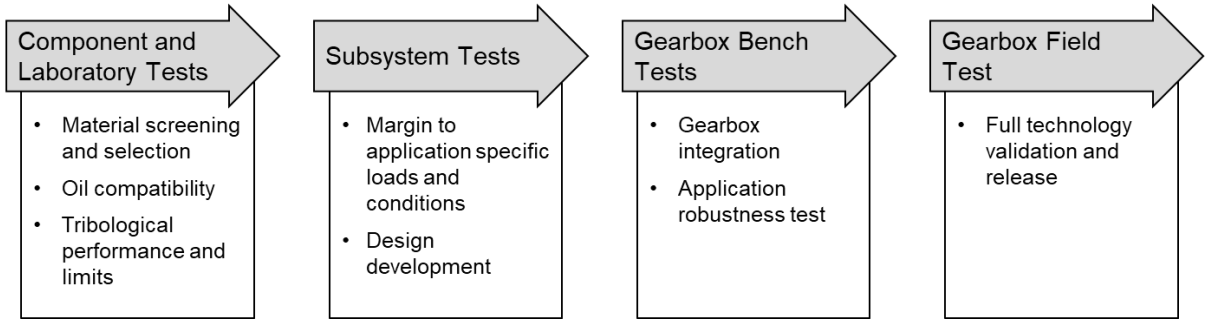

Figure 4: Validation Trajectory

A comprehensive validation and qualification of the laser cladding process is carried out beside the validation of the bearing technology itself.

3.3 Implementation

Start of serial production of gearboxes which use the next generation plain bearing technology is targeted within the next year. By then, a multi-source supply chain will be set up and qualified to ensure stable and high-quality supply to all global plants of ZF Wind Power. The next generation plain bearing technology will replace the current plain bearing technology in some of the existing gearboxes but will also be implemented in new gearbox designs where the additional opportunities on system design can be used.

4 Conclusion

ZF Wind Power has successfully introduced plain bearings in wind turbine gearboxes and is observing good field performance. In line with current market demands, a next evolution of plain bearing technology is needed with the main objective to further reduce cost of wind turbine gearboxes. The next generation plain bearing technology is a single film bearing concept where the bearing material is deposited directly onto the planet pin. The capability of this technology has been validated by component and gearbox bench tests. ZF Wind Power targets to implement the new bearing concept in serial products during the next year, after finalizing field validation and industrialisation.

5 Bibliography

[GOR17] Goris, Sonja; Ooms, Maarten; Goovaerts, Michel; Krieckemans, Koen; Bogaert, Roger: Plain bearings for wind turbine gearboxes - trajectory towards technology readiness

Conference for Wind Power Drives, Aachen, 2017

[LEI15a] Leimann, Dirk-Olaf: Berechnungs- und Test-Erfahrungen von gleitgelagerten Planetenrädern in einem 2 MW Windkraft Getriebe.

11. VDI-Fachtagung – Gleit- und Wälzlagerungen 2015

[LEI15b] Leimann, Dirk-Olaf: Case study and test observations on helical gearing with plain bearings in a 2 MW wind turbine gear unit

VDI International conference on gears, Munich, 2015

[LEI16] Leimann, Dirk-Olaf: Plain Bearing Lubrication in Wind Turbine Gearboxes

Technische Akademie Esslingen - 20th International Colloquium – Tribology – Industrial and Automotive Lubrication - Stuttgart

[VLI23] van Lier, Hermann; Verdyck, Bert; Ceustermans, Jo; Witter, Dennis: Validation of Plain Bearings on Planetary Stages for Single Blade Installation

Conference for Wind Power Drives, Aachen, 2023

[VLI24] van Lier, Hermann: Plain Bearing Technology for Wind Turbine Gearbox Application – Experiences and Trends

6. VDI-Fachkonferenz Schadenmechanismen an Lagern, Aachen, 2024

Simulation and application of hydrodynamic planet bearings for wind turbine gearboxes

M. Plogmann[1], M. Schubert[1], M. Indenbirken[1], M. Kittsteiner[1]

[1]Schaeffler Technologies AG & Co. KG, Industriestraße 1-3, 91074 Herzogenaurach, Michael.Plogmann@schaeffler.com

Keywords: Hydrodynamic plain bearing, planetary gearbox, simulation, mixed friction

Abstract:

Hydrodynamic plain bearings enable a significant increase of torque-density of wind turbine gearboxes. Schaeffler has developed a bronze coated pin solution based on additive manufacturing for this application.

The upcoming revision of IEC 61400-4 specifies requirements for the design of such bearings. For detailed analysis, Schaeffler has integrated the simulation of hydrodynamic plain bearings into Bearinx – Schaeffler's simulation tool for drivetrains.

The influence of the rim thickness of the planet on the performance are discussed as well as the influence of load offsets and profile. The investigations lead to the conclusion that a detailed analysis of the specific simulation case is essential for a reliable bearing design. An outlook is given on the simulation of electrical properties of hydrodynamic plain bearings for gearboxes.

1 Schaeffler plain bearing solution

For planets in wind turbine gearboxes, Schaeffler has developed and validated a bronze coated pin based on additive manufacturing as well as a Triondur© coating solution for high levels of mixed friction. Several gearbox and field tests have proven the robustness of the material solutions. Additionally, tribometer tests as well as plain bearing tests have been performed in the validation phase. Among others, the strength of the composite material has been investigated in 4-point bending tests as well as plain bearing tests (rotating coated shaft) and the coating has proven to withstand high stress levels.

Figure 5: Schaeffler portfolio for wind turbine gearboxes: bronze coated pin and Triondur© coated pin

2 Theoretical background

The plain bearing is modeled with flexible bodies for the pin and the planet. The deformations of the planet carrier and the planet are calculated based on stiffness matrices reduced to the nodes on the sliding surface and nodes for load application as well as other gearbox elements modeled in Bearinx. The Bearinx internal solver for multibody systems is used to solve the coupled problem.

The hydrodynamic fluid film and pressure between these components are simulated via the Reynolds equation using the finite volume method under consideration of the mass conserving Elrod cavitation model. Flow factors according to Patir and Cheng [PC78] and the asperity pressure model of Greenwood-Tripp [GT70] are used. The viscosity model is pressure- and temperature-dependent.

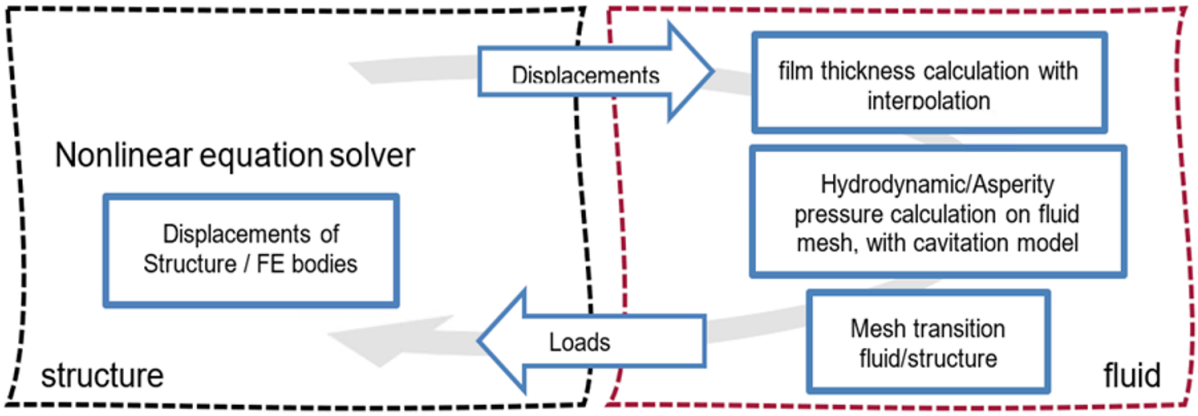

Figure 6: Calculation flow of the coupled fluid-structure problem

3 Simulation model

The investigations presented are based on the model of a first planetary stage planet bearing, see Figure 7. The planet is in this case approximated by a ring with a cylindrical outer surface. The outer diameter of the planet is approximated to match with the original planet concerning the deformation. The loads at the teeth and the relative speed are directly analyzed in Bearinx from the logical structure and the input torque and input speed of the gearbox.

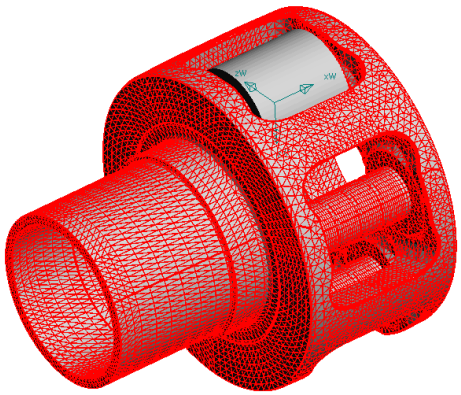

d_{pin} = 360mm (diameter of the pin)
D_{planet} = 554mm (diameter of the planet)
B = 505mm (total width of the bearing
c = 490µm = 1.36‰ (clearance)

η = 96mPas (ca. 62°C for ISO VG 320 PAO oil)
n_{rel} = 26.7rpm (100% rated speed, ca. 0.5m/s)

Figure 7: Hydrodynamic planet bearing model in Bearinx of first stage (low speed shaft) - planet carrier and boundary conditions

4 Influence of the profile

The influence of different profiles was investigated using Bearinx, see Figure 8. Without a profile the smallest gap is situated at the edge of the bearing and edge pressures occur. The film thickness increases by the use of a profile.

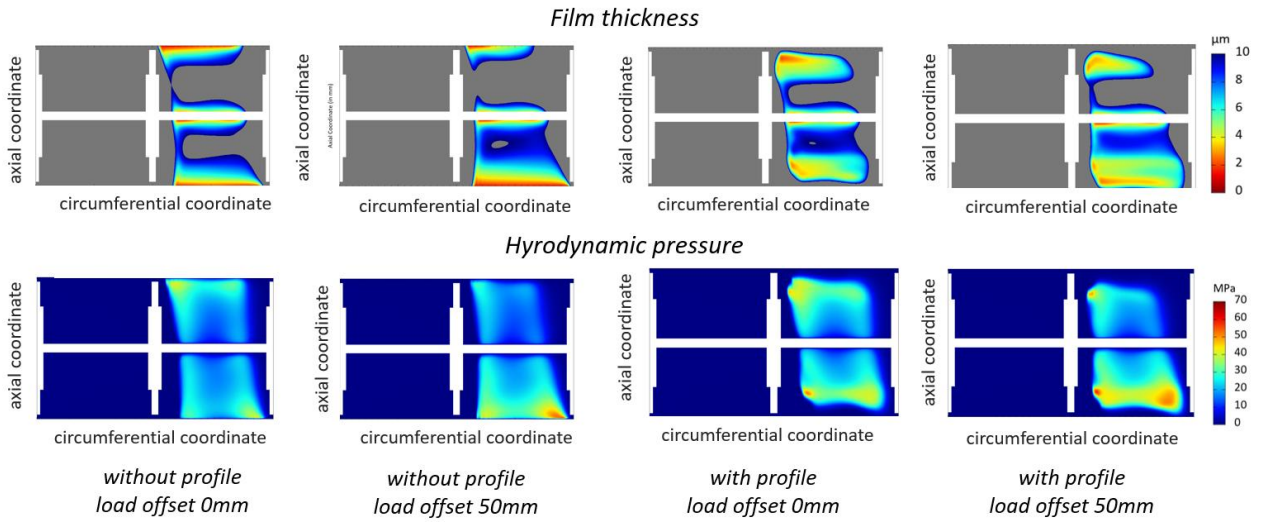

Figure 8: Investigation of profile and load offset in Bearinx

After the production of the gearbox usually a short-time test is made. After transport and installation, the single blade installation is made during which the bearing must take up high loads at low speeds.

This short-time gearbox test is most probable not sufficient for larger adaptions of the profile by running-in wear. Designing and manufacturing a profile has the advantage that these adaptions are not necessary and furthermore less particles are generated by wear. The bearing will have an optimized profile already when single blade installation is made. Also, it can run with lower friction torque from the beginning of the power production.

5 Influence of the rim thickness

Next, the influence of the rim thickness on the pressure distribution is analyzed in Bearinx. Here, only the planet outer diameter was changed and the pin diameter as well as the loads were kept constant. The load was applied by a central node at the planet. These simplifications have been made to get a clear interpretation of the results by only changing the rim thickness while all other boundary conditions (e.g. pin diameter) are kept the same.

Figure 9 shows the film thickness and pressure distribution for the different rim thickness of the planet. With the decrease of the rim thickness the area of hydrodynamic pressure build-up gets larger, and the maximum pressure is reduced (see Figure 10).

While there is a general trend for the pressure, the film thickness is largest at a medium rim thickness *th* 140mm and decreases for smaller and larger rim thickness investigated. Nevertheless, the film thickness is on a comparable level for all rim thicknesses. Most obvious is the different shape of the pressure distribution for the smallest rim thickness *th* of 70mm. Here two pressure peaks are visible at different circumferential positions - one at the beginning and one at the end of the hydrodynamic pressure distribution.

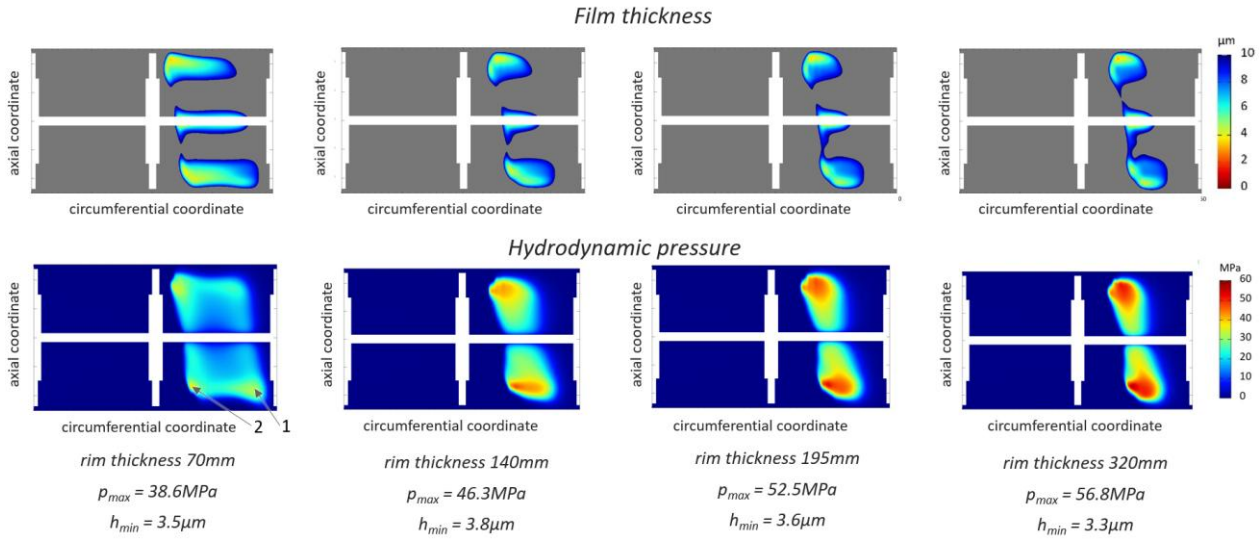

Figure 9: Results for different rim thickness of the planet (*th* = 70mm, *th* = 140mm, *th* = 195mm and *th* = 320mm, pin diameter 360mm)

For a better interpretation, Figure 10 shows the pressure and film thickness distribution over the circumferential direction for the different rim thickness in detail. For all cases examined, the pressure begins to increase already at a relatively high film thickness (>20µm) – despite the low sliding speed of 0.5m/s.

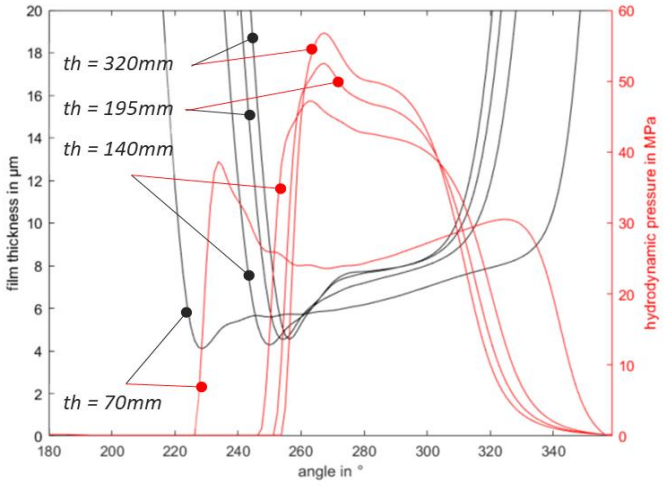

Figure 10: Pressure and film thickness for different rim thickness *th* at the position of the maximum pressure

Interestingly, even for the highest rim thickness *th* of 320mm (outer diameter / inner diameter = 2.78), the bearing shows an extended area of pressure build-up which can be attributed to local deformations. In the region between 240 and 300° the film thickness drops below 10µm. Here the lubricating gap is only slightly convergent in the sliding direction. This shape is different to what can be expected from rigid components. With the smallest rim thickness *th* of 70mm (outer diameter / inner diameter = 1.39), pressure is not constantly increasing but peaks occur at the beginning and the end of the pressure zone.

This investigation shows again that it is important to take the elasticity of the components into account – on a local and global level.

6 Influence of the pin-carrier connection

In gearbox applications different pin-carrier connections are used by gearbox manufacturers. For small overlaps of the interference fit between pin and carrier, larger torsional deformation of the carrier can be expected than for a very tight interference fit. An opening of the gap on one side of the pin-carrier connection is possible.

In order to investigate the influence of the pin-carrier connection on the pressure and film thickness distribution at the radial bearing, the pin-carrier connection was modelled with a tie-constraint over 25, 50 and 100% of the surface area of the pin-carrier contact.

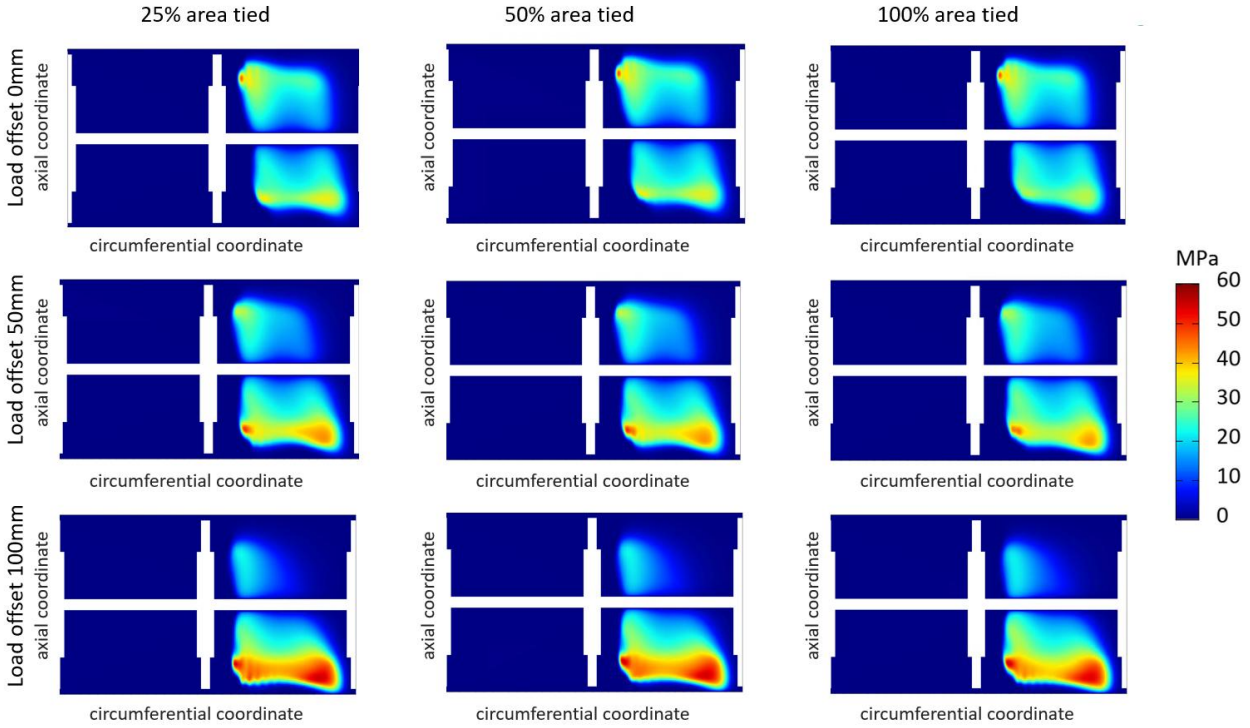

Figure 11: Hydrodynamic pressure for 25%, 50% and 100% of the pin-carrier contact area connected via a tie-constraint for different load offsets

As can be taken from Figure 11, there is only a small influence of the pin-carrier connection on the pressure distribution. Nevertheless, some differences occur between the results for 50% and 100% area tied. The same applies to the film thickness distribution.

Nevertheless, the pin-carrier connection has an influence on the load offset at the gear contact. This leads to changes of the pressure and film thickness distribution at the hydrodynamic plain bearing – as can be taken from Figure 11. The load offsets are typically provided by the gearbox manufacturer who has detailed information on the tooth corrections. Like shown, with Bearinx this effect can be considered.

7 Thrust bearing simulation

The thrust bearing design of Schaeffler consists of a flat disc without any grooves or tapers. A convergent gap automatically occurs between the planet and the thrust washer due to the tilting between these components. Relevant for the tilting are among others the torque resulting from the thrust forces at the gear contacts and the load offsets. The deformation of the planet and the planet

carrier will also contribute to the misalignment between these components. A tapered land design (fixed profile) is therefore not needed to reach a convergent gap.

The simulation in Bearinx takes into account the mechanical interaction between the radial and the thrust bearing. Figure 12 shows the simulation result of the radial and thrust bearing. Here the influence of the load offset for the same input torque / input speed is analyzed.

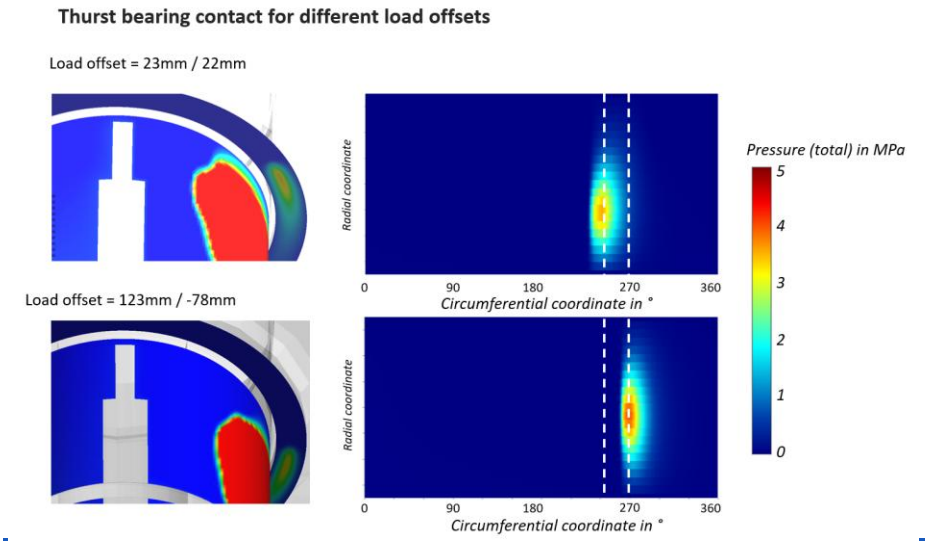

Figure 12: Pressure distribution at the thrust bearing for different load offsets

As can be taken from the figure, the position where hydrodynamic pressure is built up changes due to different tilting and different position of the minimum film thickness. The pin-carrier connection will also influence the inclination between planet and carrier flange. The investigation shows that the bearing design is made in such a way that the performance of the thrust bearing is insensitive for the influence of the load offset.

8 Simulation of electrical properties of hydrodynamic plain bearings

Electrical models for rolling element bearings and gear contacts are already available in Bearinx, see [MCJ22] and Schaeffler can provide helpful advice for complete mechanical systems. At the moment, the simulation of electrical properties of hydrodynamic plain bearing are integrated into Bearinx.

Figure 13 shows a comparison between simulations in Bearinx and measurements concerning the electrical capacity of a plain bearing from a test rig. The temperature-dependent permittivity of the ISO VG 320 gearbox oil has been determined in measurements and taken into account.

As can be taken from Figure 13 the simulated and measured capacities for the different rotational speeds match well. With reduced speed the capacity increases as the film thickness gets smaller. Relevant for the high values of electrical capacity is the large surface area with small film thickness which can also be taken from Figure 13, right side. Therefore, the deformation of the components is essential and differences in the rim thickness will therefore also lead to differences in the electrical capacity. Also tilting between the components will be important as shown by Furtmann [FUR17].

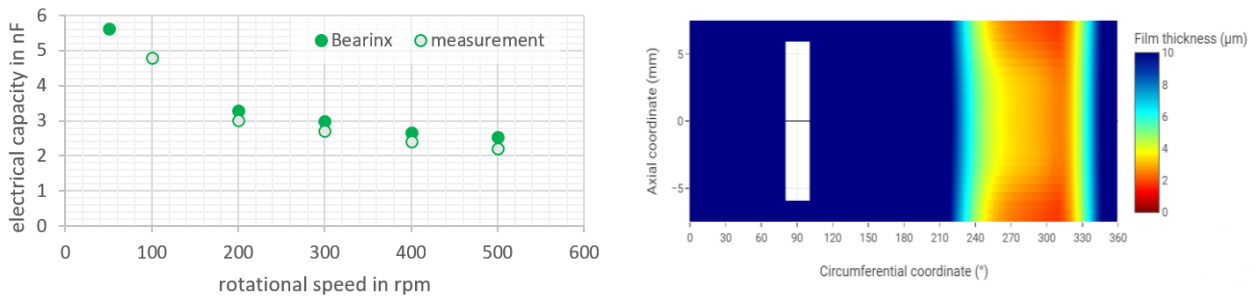

Figure 13: Electrical capacity for simulation and measurement of a bronze test bearing (32mm x 15mm, ISO VG 320 oil, 50°C, 10MPa) and simulated film thickness distribution at 100rpm

Further validation of the electrical model for the plain bearing in Bearinx will be made and investigations on the electrical network for the drivetrain of wind turbine gearboxes are a next step. The differences in the electrical properties of hydrodynamic plain bearings and rolling element bearings need to be taken into account when the drivetrain is evaluated.

9 Conclusion

Bearinx is a powerful analysis tool of Schaeffler that provides detailed insights for designing bearing solutions and enables a knowledge based customer support. Now also detailed hydrodynamic plain bearing simulations are possible, and a complete drivetrain supported by rolling element bearings and plain bearings can be investigated in Bearinx. A seamless workflow is ensured.

Several influencing factors are considered in the simulation of the hydrodynamic plain bearing, among them the deformation of the components and the load offset at the gear contact. The simulation possibilities available in Bearinx are an excellent basis for a reliable bearing design of hydrodynamic plain bearings in terms of film thickness, asperity and hydrodynamic pressures, friction as well as electrical properties of the bearing.

10 Bibliography

[FUR17] Furtmann, Alexander: Elektrisches Verhalten von Maschinenelementen im Antriebsstrang. Hannover: Gottfried Wilhelm Leibniz Universität Hannover, Diss., 2017, https://doi.org/10.15488/8972

[GT70] Greenwood J. A., Tripp J. H.: The Contact of Two Nominally Flat Rough Surfaces, Proceedings of the Institution of Mechanical Engineers, 185(1):625-633, 1970.

[MCJ22] Meinel, A.; Correns, M., Jakob, B.: Electric Properties of Gears and Bearings – From Component to Integrated System Simulation, BEARING WORLD – International Conference 2022

[PC78] Patir, N.; Cheng H. S.: An Average Flow Model for Determining Effects of Three-Dimensional Roughness on Partial Hydrodynamic Lubrication, Journal of Lubrication Tech., 100(1): 12-17, 1978.

Analysing and Predicting the Behaviour of Journal Bearings on the Gearbox Operational Behaviour

T. Marske[1], D. Piel[1], T. Schröder[1]

[1]Vestas Nacelles Deutschland GmbH, Henry-Koch-Straße 9-13, 23570 Lübeck-Travemünde

Keywords: Journal Bearings, Deflections, System Simulation, Noise-Vibration-Harshness

Abstract: Journal Bearings in wind turbine generator (WTG) main gearboxes are the key technology for enabling high power density in gearboxes. The needed volume of control for journal bearings, fulfilling the same load carrying requirements, is much smaller compared to roller bearings. Furthermore, the fatigue failure mode typically does not exist for properly designed journal bearings and the reduced number of single components increases the reliability of the application. For designing journal bearings, multiple tools are available. However, when it comes to the analysis of the operational behaviour of the powertrain system, those tools often lack proper and detailed journal bearing calculation methods, even though it is essential to consider the impact of journal bearings on the gear mesh misalignment and dynamical behaviour early in the design phase.

To close this gap, enable analysis of the behaviour of journal bearings and feed the parameters into the system analysis, Vestas works with Center for Wind Power Drives (CWD) at RWTH Aachen University and Winergy in a public funded project. Here, an approach is developed to extract the stiffnesses from a JB software, to process the data and to feed the information into a system simulation software. This paper describes the process of applying the extraction method developed by CWD and its integration in the tool chain for powertrain system analysis. This paper discusses the verification of the method through testing of a 3 MW planetary stage equipped with journal bearings. Sensors shall identify the running behaviour and condition of the bearings and thereby support the verification of the newly developed Vestas' tool chain.

1 Introduction and Motivation

The rising demand for wind power, driven by the global push for renewable energy, necessitates advancements in wind turbine technology to enhance efficiency and reduce costs. A critical area of focus is the increase in power density in wind turbine gearboxes, which allows for more compact and efficient designs capable of handling higher loads. [CAR22]

The importance of gearbox reliability can be highlighted by the fact that up to 20% of wind turbine downtime can be attributed to gearbox failures [RIB07]. Even though gearboxes do not have the highest failure rates among wind turbine components, their failures contribute disproportionally to turbine down time because size and mechanical complexity prolong repair time [SAN22]. While higher torque density is essential for improving power output and reliability, it also imposes greater mechanical stresses on gearbox components, making it more challenging to control the overall operational behaviour.

In general, noise, vibration, and harshness (NVH) behaviour significantly impact turbine performance and reliability as well as market compatibility, as noise emission regulations are becoming increasingly more stringent.

Therefore, understanding of the vibration behaviour of the structure and the generation of tonalities to accurately predict NVH behaviour of wind turbine gearboxes is crucial for ensuring their reliability,

efficiency, and longevity. Given that wind turbine gearboxes operate under varying and often harsh conditions, it is imperative to accurately predict their operational behavior for each significant operating condition. This understanding helps avoid non-optimal operation, which can lead to higher operational and maintenance costs [GIO19].

To address these challenges, the use of journal bearings is becoming increasingly important. While traditionally roller bearings have been the standard choice for wind turbine gearbox planetary bearings, journal bearings have emerged as a viable alternative due to their unique advantages including high load capacity, reduced noise and vibration, lower maintenance requirements, and cost-effectiveness. Vestas has been a frontrunner in adopting this technology, introducing a first prototype gearbox with journal bearings in a 2 MW V90 turbine in 2013. The use of journal bearings can reduce the risk of localized stress concentrations and spalling damage, common issues with traditional roller bearings. Consequently, integrating journal bearings into wind turbine gearboxes can enhance their performance and longevity, making them a vital component in the evolution of wind energy technology.

Despite these advantages, journal bearings are sensitive to specific operational requirements, particularly oil cleanliness, and cannot run without a sufficient lubrication regime, which is crucial for their safe operation, for a prolonged time. Understanding the behaviour of journal bearings under different operating conditions is also crucial, since wind turbines operate in a wide range of environmental conditions, from extreme cold to high winds, and undergo various load conditions, including start-up, shutdown, and emergency stops. Each of these scenarios can significantly impact the lubrication regime as well as the overall performance of journal bearings. Therefore, a thorough understanding of their behaviour under varying conditions is necessary to ensure reliability and efficiency and to fully leverage their benefits.

Additionally, including journal bearing stiffness in the system simulation will give an indication of the significance of the journal bearing stiffness on the overall system, allowing to assess the importance of the inclusion into the simulation tool chain.

2 Problem Statement

Despite the availability of various methods and tools for designing and analysing journal bearings, there is a notable knowledge gap in accurately predicting their stiffness behaviour and integrating these parameters into the overall flexible system analysis. This gap poses a challenge in the design phase, where understanding the impact of journal bearings on gear mesh misalignment and dynamic behaviour is essential. The knowledge and predictability of the mesh misalignment is key for designing the micro geometry and optimizing the excitation and operational behaviour of gear stages. This lack of knowledge is especially critical in the early design phases, when test results are not available but essential decisions in respect of design solutions must be made.

To address this challenge, Vestas has collaborated with CWD and Winergy in the publicly funded project Journal Bearings for Wind Turbines (JB4WT) to develop a method for extracting stiffness parameters from a journal bearing simulation software, post-processing the data, and integrating it into a system simulation software.

The aim is to extract reliable fluid stiffness parameters of the journal bearings from a high-fidelity multibody simulation, which also considers the flexible environment of the journal bearing, and to provide them as input for the system analysis software after postprocessing. It is important to put the focus solely on the fluid stiffness to avoid a double consideration of the flexible environment.

Furthermore, the post processing needs to be robust to cope with different definitions as for example the coordinate systems of the software solutions. By comparing the results to previous system simulations based on assumed stiffness values, the necessity for the need of a more detailed journal bearing simulation can be evaluated.

3 Methodology

The pursued methodology for predicting and analysing the behaviour of journal bearings in wind turbine gearboxes involves several consequential steps, see **Figure 14**. These steps ensure that the stiffness parameters of the journal bearings are accurately integrated into the system simulation, allowing for more precise NVH behaviour predictions.

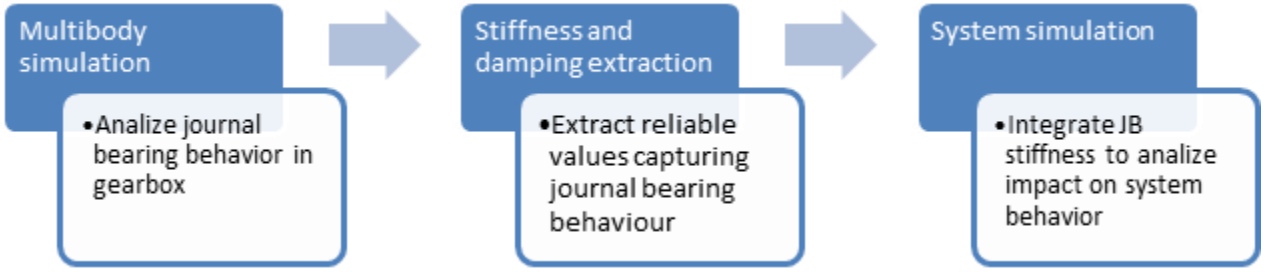

Figure 14: Workflow of Tool Chain

Initially a multibody simulation model of a gearbox equipped with journal bearings is implemented, relevant parameters are identified and defined, and a dynamic analysis of realistic operation points is performed. From this simulation model, in the second step the stiffness parameters of the journal bearings are extracted for the various load conditions. The third step is the system simulation. Depending on the level of detail, the system simulation can be done with a full powertrain environment or focus on the gearbox. The objective of the system simulation is to analyse and optimise the gear mesh performance, the excitation behaviour or to understand the overall deflection behaviour by considering parasitic wind loads on the powertrain system. SMT Masta uses a scripting interface to read the post processed fluid stiffness and writes it into the internal parameter list for the analysis steps.

4 Journal Bearing Modelling and Analysis using AVL Excite

In the initial step of the workflow, a comprehensive multibody simulation model of a planetary gearbox with planetary journal bearings is implemented and simulated using the simulation software AVL Excite. For this purpose, the geometry of all gearbox parts is initially transformed into condensed models in ANSYS Mechanical, reducing the number of degrees of freedom while retaining the essential model characteristics. Relevant nodes exposed to boundary conditions such as load, contacts and other interactions are retained.

After importing the reduced order bodies into AVL Excite, configuring the connecting joints between all interacting bodies and defining the operating conditions (torque and speed), dynamic analyses are performed to compute the load situation of the gearbox for a range of operational conditions and the joint results, see **Figure 15**:.

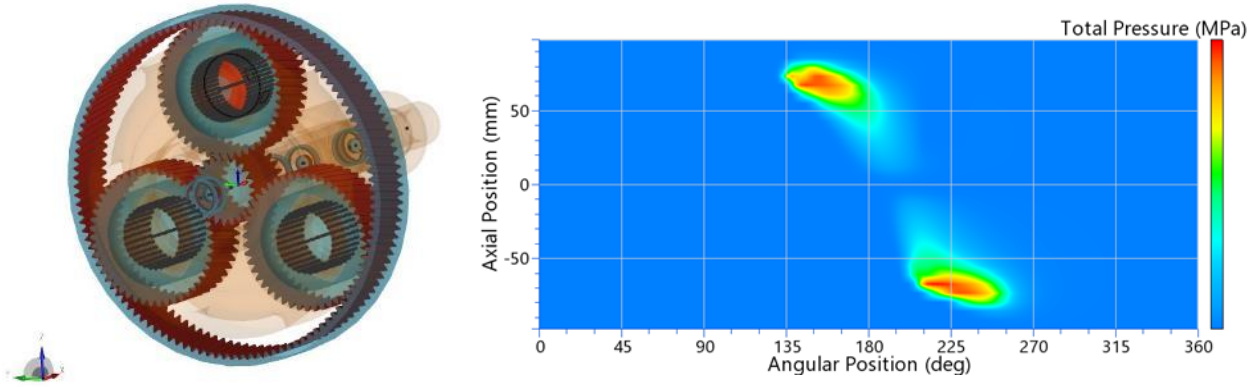

Figure 15: Multibody simulation model (left) and 2D result plot of total pressure in EHD joint

The simulation includes an elastohydrodynamic (EHD) simulation of the lubricated sliding contacts of the planetary bearings. The EHD contact considers the stiffness of the coupled structures involved, the profiles of the bearing surfaces, the oil properties and the oil supply boundary conditions such as shapes of the supply geometry and supply pressure. Based on these inputs, result parameters like asperity contact pressure and hydrodynamic pressure, oil film thickness, fill ratio, friction power loss, clearance and oil temperature are computed. To achieve this, the solver computes motion equations for bearing and journal structures resulting in a height input for the hydrodynamic simulation solving the Reynolds equation which in turn is then providing pressure information acting on the structures.

Having the EHD contact in the multi body simulation model provides detailed information about the dynamic loads, motions and structural deformations of the components involved, which is crucial for realistically capturing the coupled interactions and to compute reliable results. The simulation results can then be postprocessed to extract key performance metrics such as forces, stresses and system vibrations.

5 Stiffness parameter extraction with MATLAB

To extract the accurately computed stiffness parameters of the journal bearing from the multibody simulation and provide them as input for the system simulation, a MATLAB-based extraction routine was developed at RWTH Aachen University. The process involves setting up two separate simulation models in AVL Excite, see **Figure 16**:.

While the first model computes the journal bearing behaviour with the fully elastohydrodynamic joint (EHD2) to capture realistic bearing results, the second model simplifies the journal bearing by dividing it into several slices and modelling it using arbitrary tabular force/moment joints (FTAB). Using this approach, only the center nodes of the interacting bodies in each slice are connected, and a unique set of stiffness and damping values for each degree of freedom is assigned to each individual node pair as input.

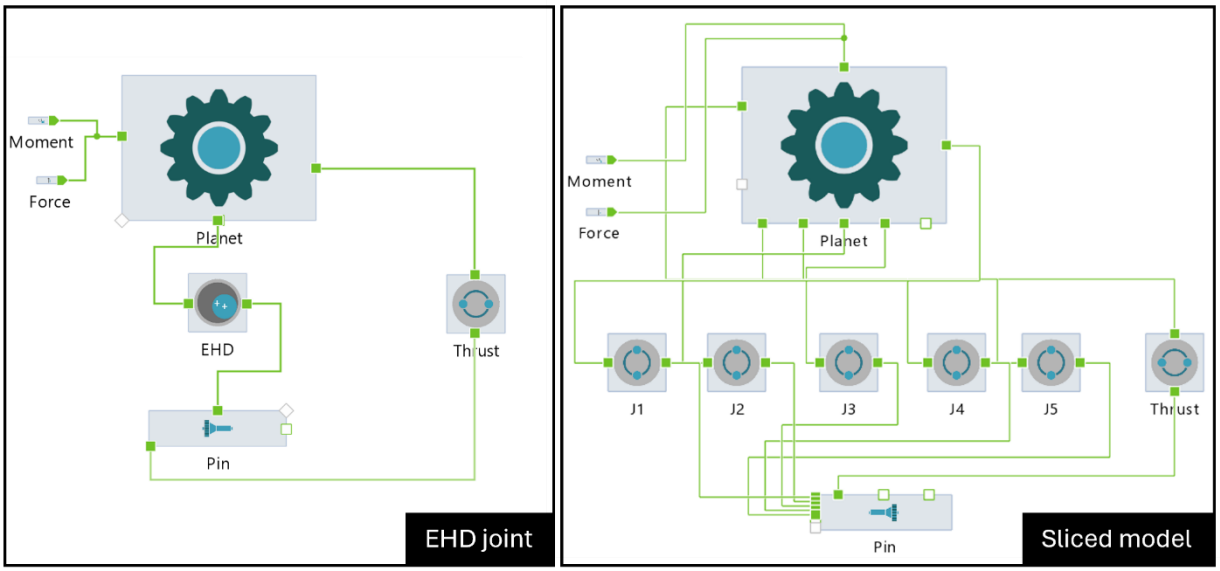

Figure 16: Comparison of model setup with EHD joint and sliced simplified model for stiffness extraction

After calculating the EHD results for each operating point of interest, an iterative process is started, connecting the two models. After computation, the results of the simplified sliced model are evaluated and compared to the EHD joint model, after which the stiffness and damping parameters are iteratively adjusted, and a new computation is initiated until the results of both models converge below a defined threshold. When the difference between the two models becomes negligible, it can be assumed that the stiffness and damping parameters of the EHD joint have been accurately determined, see **Figure 17**:.

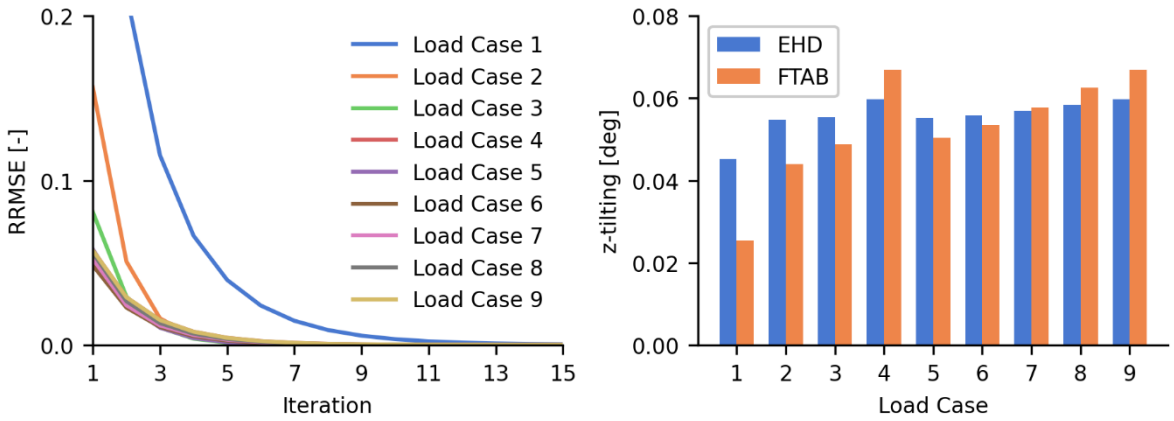

Figure 17: RRMSE error of simplified model for 9 load cases after 15 iterations (left) and tilting results of the final iteration compared to EHD model (right)

6 Gearbox Operational Analysis with SMT Masta

Vestas has qualified SMT Masta as systems simulation software to analyse the operational behaviour of powertrain systems, especially the gearbox behaviour. In previous papers presented at Conference for Wind Power Drives it has been shown how the system simulation of gearboxes can successfully be utilised to predict the excitation behaviour of gearboxes [PIE21]. Since the journal bearing module in SMT Masta is not sufficient for deflection analysis, there was the need for reading

fluid stiffnesses from an external software. SMT supported us in providing an interface for concept bearings which can be controlled by the scripting interface.

The first step in Masta is to build up the model. The previous chapter described that the journal bearing needs to be modelled in slices, this needs to be reflected in the Masta model as well. The journal bearing gets represented by five concept bearings in parallel. The analysis workflow in Masta starts with an external load file template which contains all relevant load case information like torque and speed level and if needed also non-torque loads from the rotor. The script reads the load file and creates the load cases in Masta. Afterwards the analysis in the deflection module starts and the script reads the file with the provided fluid stiffness and writes it into the parameter list. If more than one load case must be solved, this repeats for each load case. So, it can be guaranteed that the torque- and speed-dependent stiffness parameters are considered. Afterwards the results can be reviewed, and conclusions can be drawn.

A major challenge in the development was to match the stiffnesses with the correct deflection behaviour, see **Figure 18**. The actual journal bearing stiffness is not linear and does not cross the origin of the coordinate system. The stiffness provided by the journal bearing software is linearized in the operating point and can be the tangential or the secant stiffness. The pure information about the linearized stiffness will lead to a deviation in the resulting deflection as the offset is missing.

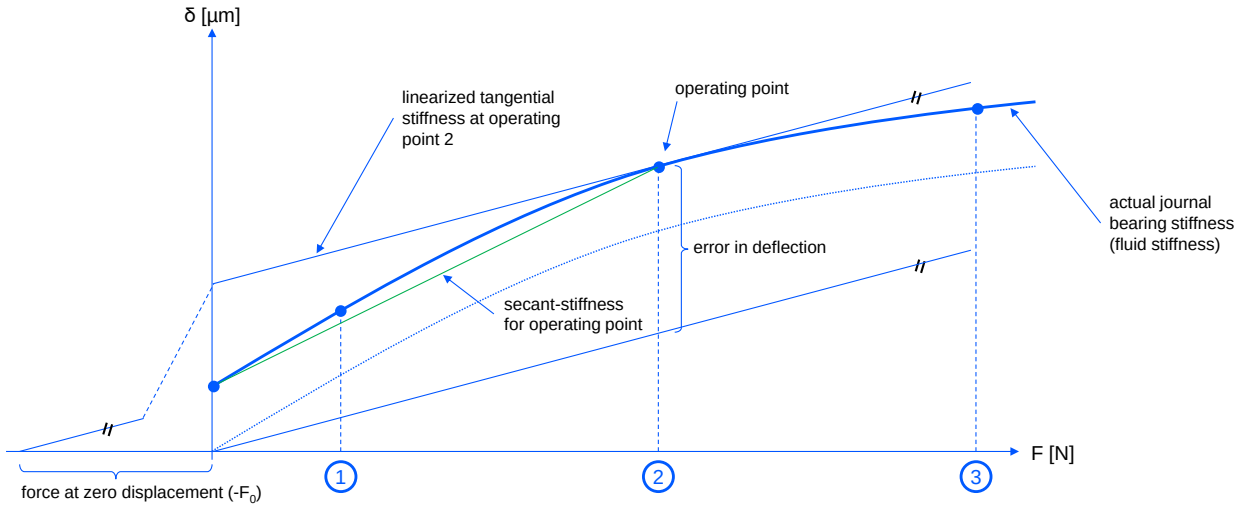

Figure 18: Definition of Stiffnesses

For this problem the user can specify a force at zero displacement. If this information is fed into Masta, the stiffness curve can be moved to reflect the proper deflection. This force at zero displacement has been added as additional parameter for extraction from the journal bearing software and is part of the input parameters for Masta.

With this workflow the linearized journal bearing stiffness can be considered in the system deflection analysis in Masta for different load cases. This supports in the prediction of the mesh misalignment and the resulting excitation and operational behaviour of gearboxes.

7 Test Setup for Planetary Gear Stage at Vestas Test Centre

The validation of the newly developed tool chain utilizes a test rig at Vestas Test Centre. The test rig is a back-to-back setup equipped with two 3 MW planetary gear stages, see also [PIE21]. The

device under test has been equipped with different sensors inside and outside to monitor the operational behaviour of the journal bearings. In this paper the focus is on the face load distribution and the transmission error between the planet carrier and the sun gear shaft. Those two parameters can be easily compared with outputs of the system simulation and linked to the operational behaviour. **Figure 19** shows the different validation steps, from gearbox preparation, over a short end of line test at the supplier towards the component test at Vestas and the final comparison between the test and simulation results.

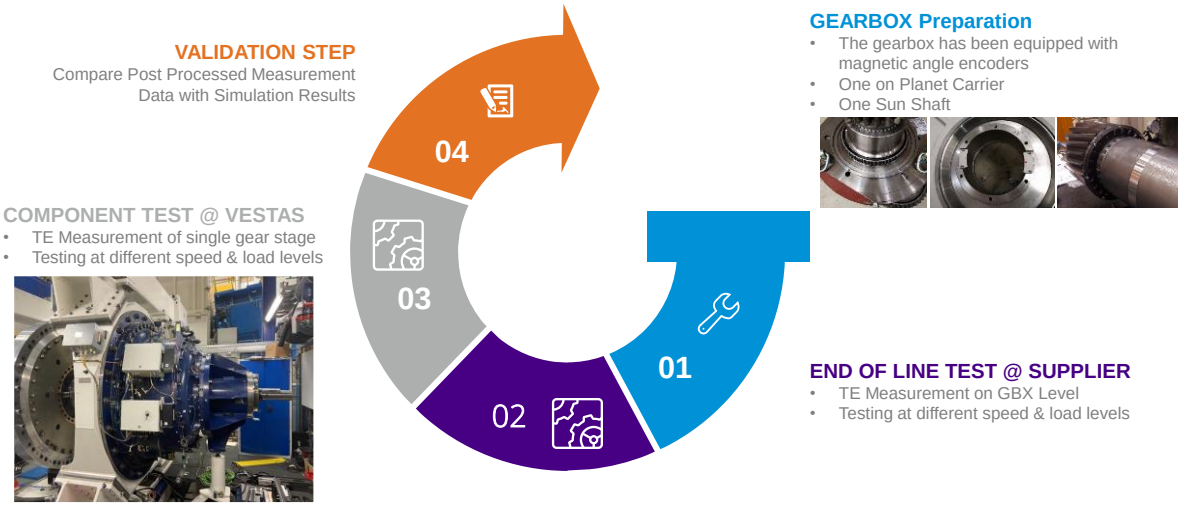

Figure 19: Validation Strategy for Gear Excitation [PIE21]

The test program foresees different steady state operation points along the operational range of the turbine. Additionally, speed run-ups at different torque levels were performed. For investigating the journal bearing and performing additional qualification steps in regards of condition monitoring, the test program also considers an artificial misalignment of the planet carrier. The change in operational behaviour is also part of the simulations performed in SMT Masta.

8 Discussion of Test Results

The test rig driveline has been fully built up in Masta. The device under test has been modelled in detail including gear micro geometries. Structural elements like planet carrier and gearbox housing have been represented by FE-substructures. The previously described workflow has been applied to consider the journal bearing stiffness. The investigated torque levels are in line with the torque levels tested on the test rig. The evaluation of the results is focussing on the load distribution at the ring gear and the transmission error of the planetary gear stage. Both parameters are affected by the journal bearing stiffness and driven by the mesh misalignment. The virtual encoders for the transmission error evaluation are at the same position as in the test rig and allow a direct comparison between the test and simulation environment.

At the stage of the paper creation the test result evaluation is not yet concluded but will be shown and discussed on the conference.

9 Summary and Conclusion

Journal bearings in WTG main gearboxes are state of the art and have major impact to the operational behaviour of gearboxes and gears. The prediction of the journal bearing impact is key to optimise and analyse excitation behaviour of gear stages as well as the load distribution of gear

meshes. This paper describes a toolchain which provides a robust approach for integrating journal bearing stiffness parameters into system simulations. By implementing a multibody simulation model with AVL Excite, extracting journal bearing stiffnesses, and conducting system simulations with SMT Masta, the impact of journal bearing stiffness on the overall system behaviour can be assessed. Furthermore, the paper describes the validation through test rig comparisons. The validation process, involving a 3 MW planetary gear stage test rig will confirm the accuracy and reliability of the developed method. The integration of journal bearing stiffness parameters into the system simulation is essential for capturing the correct parameters in the design phase, ensuring that the gearbox operates efficiently and reliably under various conditions. At the stage of the paper creation the test result evaluation is not yet concluded but will be shown and discussed on the conference.

For the audience, this paper highlights the critical role of system analysis in the early design phase and the importance of extending the range of influencing parameters to derive proper solutions. By understanding the impact of journal bearing stiffness on system behaviour, engineers can make informed decisions that enhance the reliability and performance of wind turbine gearboxes. This paper builds on previous research and presents new insights that contribute to the ongoing development of advanced gearbox technologies.

10 Acknowledgements

The authors gratefully acknowledge the financial support by the German Federal Ministry for Economic Affairs and Climate (BMWK). The presented results have been derived in the project Journal Bearings for Wind Turbines (JB4WT; FKZ03EE3054C).

11 Bibliography

[CAR22] Carranza Fernandez, R.; Tobie, T.; Collazo, J: Increase wind gearbox power density by means of IGS (Improved Gear Surface). In: International Journal of Fatigue, Volume 159, 2022

[RIB07] Ribrant, J., Bertling Tjernberg, L: Survey of failures in wind power systems with focus on Swedish wind power plants during 1997-2005. In: Proceedings of the 2007 IEEE Power Engineering Society General Meeting, Tampa, 2007

[SAN22] Santelo, T.N.; De Oliveira, C.M.R.; Maciel, C.D.; De A. Monteiro, J.R.B: Wind Turbine Failures Review and Trends. In: Journal of Control, Automation and Electrical Systems, Volume 33, 2022

[GIO19] Gioia, N; Peeters, C.; Guillaume, P; Helsen, J: Identification of Noise, Vibration and Harshness Behavior of Wind Turbine Drivetrain under Different Operating Conditions. In: Energies, Volume 12, 2019

[PIE21] Piel, D.; Klönne, M.; Nalliboyana, D.; Gupta, M.: Method for Predicting the Risk of Tonality on WTG Level. In: Conference for Wind Power Drives CWD 2021, Aachen, 2021

Planetary Plain Bearing II

Measurement of operational characteristics inside a planetary plain bearing under wind turbine operating conditions

D. Witter[1], H. van Lier[1], J. Ceustermans[1], S. Ahsani[1]

[1]ZF Wind Power Antwerpen NV, Gerard Mercatorstraat 40, 3920 Lommel (BE)

Keywords: Plain Bearings, Pressure and Gap Distribution, Measurement and Testing

Abstract:

Plain bearings in wind turbine gearboxes face unique challenges due to their highly flexible environment, gear tilting, high specific bearing loads, and low sliding speeds. These conditions can result in low film thicknesses and high local pressures. To design effective bearings, suitable calculation and simulation methods are essential.

Since the late 1960s, EHL (Elasto Hydrodynamic Lubrication) calculation methods have been developed and are now used to simulate planetary plain bearings in wind turbine gearboxes. Measuring operational characteristics within a plain bearing is crucial to validate simulations against test results. Key parameters for validation include pressure and gap distribution. However, these measurements are difficult due to space constraints and the exposure of sensors to high pressure and shear forces. Existing publications either focus on measurements at specific points within the plain bearing or fail to represent the unique conditions of a planetary plain bearing.

This study presents a method to measure key operational characteristics and their distribution within a planetary plain bearing. The measurements will be compared with simulation results obtained using standard EHD approaches.

1 Introduction and Motivation

Since 2013, ZF Wind Power has been continuously developing planetary plain bearings for wind turbine gearboxes. The first market solution, a floating sleeve concept (refs. [LEI15a], [LEI15b], [LEI16], [VLI23], [VLI24]), has demonstrated outstanding performance, particularly under high load and very low speed conditions such as Single Blade Installation (SBI).

Market demands for cost reduction and increased load density in wind turbine gearboxes necessitate ongoing improvements in gearbox components. ZF has introduced a new planetary plain bearing technology (ref. [VLI25]), featuring a single film bearing used as a radial planetary bearing with the bearing material cladded onto the shaft. This design allows for smaller bearing dimensions, potentially operating closer to physical limits.

Unlike many industrial plain bearing applications, wind turbine applications now require detailed numerical simulations to evaluate pressure and gap distribution. EHL simulation software is well-established (refs. [WIT11], [WIT17], [LAN23]), but validating this software is increasingly important to enhance the load capacity of ZF's new plain bearings.

A common validation method compares calculated temperatures with measured values, but this approach has limitations due to high latency and dependency on surrounding machine elements. Another method involves comparing contact patterns with pressure distributions from simulations, suitable only for mixed friction conditions.

Measuring gear displacement combined with global deformation is complex and prone to uncertainties from tolerances and measurement inaccuracies. Currently, there is no precise and direct validation method for wind turbine planetary plain bearings.

A new measurement technique has been developed and applied to a planetary plain bearing. The results will be compared to simulation outcomes after testing. The following chapters will detail the progress in both simulation and testing of plain bearing operating parameters.

2 Outline of History of Plain Bearing Research

The hydrodynamic effect of plain bearings was first discovered and investigated by BEAUCHAMP TOWER in 1883 and 1884. He observed that when two surfaces in an oil bath move relative to each other and are pressed together by a force, they create an oil film pressure. This pressure separates the surfaces and significantly reduces friction. In 1886, OSBORNE REYNOLDS published the first fluid mechanical formulation for this phenomenon.

$$\frac{\partial}{\partial x}\left(h^3\frac{\partial p}{\partial x}\right)+\frac{\partial}{\partial z}\left(h^3\frac{\partial p}{\partial z}\right)=12\cdot\eta\cdot\left(\frac{u_1+u_2}{2}\frac{\partial h}{\partial x}+\frac{w_1+w_2}{2}\frac{\partial h}{\partial z}+\frac{\partial h}{\partial t}\right) \qquad \textbf{Eq. 1}$$

The REYNOLDS DIFFERENTIAL EQUATION (RDE) describes the oil film pressure distribution in the presence of a viscous fluid, relative speed, and lubrication gap distribution over time. REYNOLDS solved this equation numerically for various problems. However, for low film thicknesses, the equation results in pressure singularities, affecting accuracy. In [BUS49], the authors presented initial pressure distribution measurements under lab conditions, observing that, unlike REYNOLDS' calculations, peak pressure does not tend towards infinity but approaches a limit gradually.

In the 1950s, the foundations for the now well-known Elasto Hydrodynamic Lubrication (EHL) Theory were established by ERTEL (refs. [GRU49], [MOH84], [CAM85]) and DOWSON-HIGGINSON [DOW54]. However, their solutions showed convergence issues under higher loads. KNOLL coupled the RDE with the elastic structural deformation problem of the surrounding components using a Finite-Element-Method (FEM) solution (ref. [KNO74]), an approach still used in common EHL simulation software.

In 1978, PATIR-CHENG published an extended solution for the RDE, incorporating rough surfaces through flow factors [PAT78], commonly used in micro hydrodynamics. In 1971, GREENWOOD-TRIPP enhanced the HERTZIAN Contact Model to a statistical, rough surface [GRE71], an approach now established for calculating contact pressure in planetary plain bearings in common software.

Despite continuous development, there is no generic validation available. The mathematical formulations and commonly measured parameters differ, as shown in the following Table 1. Typically, the commonly measured parameters are not perfectly suitable or accurate enough to correlate directly with the results from RDE solutions. However, the most direct comparison between test and simulation results involves the pressure and gap distribution. In addition to [BUS49], [LOH21] presents gap measurements within a planetary plain bearing. The gap sensors are fixed at four specific positions on the planetary pin, which disables observation of peak magnitudes and their locations. To improve software validation and enhance understanding of planetary plain bearings, ZF is conducting a comprehensive test campaign to measure the distribution of pressure, gap, and temperature.

Parameter	Simulation	Test
Gap distribution	Direct result of RDE	Not measured
Pressure Distribution	Direct result of RDE	Not measured
Temperature Distribution	Derived from friction energy	Available
Friction Coefficient	Available from friction models	LAB Conditions
Wear / Surface Topology	Available from wear model	Available
Component Displacements	Available from load-displacement equilibrium	Available

Table 1: Common plain bearing operation parameters in simulation and tests

3 Development of a Measurement System

To validate simulation models and test results, it is important to isolate the planetary system from parasitic effects such as

- planetary carrier deformation,
- deformation of the gearbox housing and ring gear,
- load sharing between multiple gears and
- undefined thermal environment influenced by neighboring machine components.

Therefore, ZF's planetary test rig has been selected.

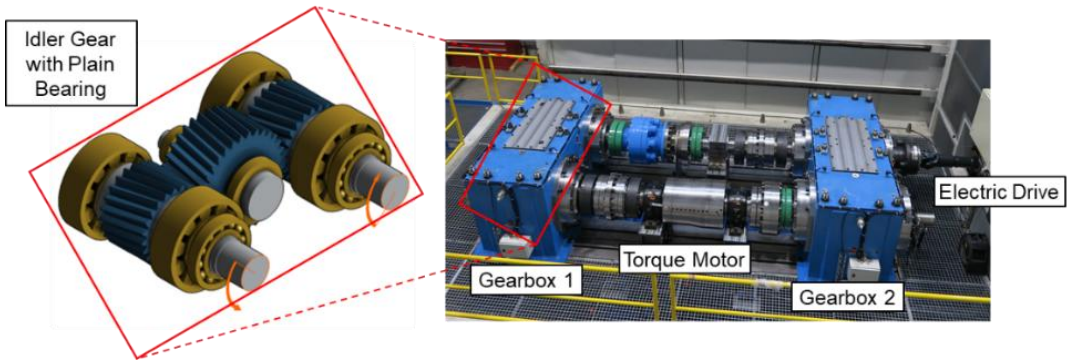

Figure 20: Planetary System Test Rig

It enables repeatable test conditions and allows for comparison of test results with a comprehensive test database. The test rig features a mechanical closed-loop system with two gearboxes, where speed is applied by an electric drive and test load by a torque motor. The gear mesh design accounts for the load distribution in a wind turbine gearbox. The helical gear mesh causes the gear to tilt during operation, resulting in a slanted pressure distribution, as shown in the following FEM contact simulation results.

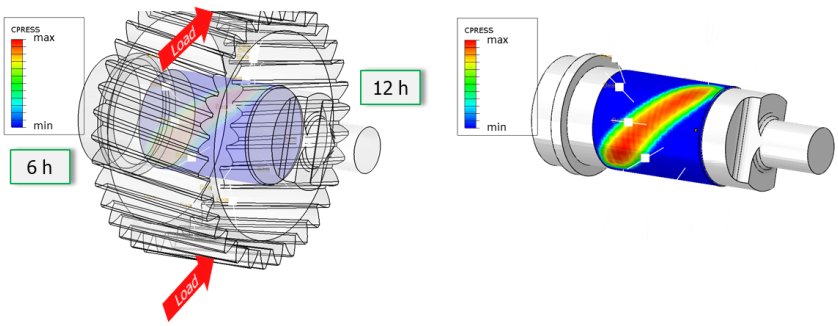

Figure 21: Pressure Distribution from FEM Contact analysis of BTR002 Test gear

To measure suitable results, the architecture of the instrumentation needs to be defined carefully.

3.1 Principle Instrumentation Architecture

To achieve accurate distribution measurements, it is essential to minimize the impact of instrumentation on the hydrodynamic fluid film. This means placing as few sensors as possible in the load area. Generally, there are two options for sensor placement:

a) Inside the planetary pin
b) Inside the planetary gear

Option a) is the simplest solution. However, achieving proper discretization would require a dense mesh of sensors in the load area. In contrast, option b) is more challenging in terms of measurement architecture but minimizes the sensors' impact on oil film pressure, as demonstrated in the following figure.

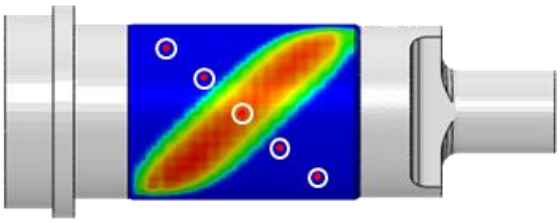

Figure 22: Pressure Distribution from FEM Contact analysis of BTR002 Test gear

Due to the sensor positioning, a maximum of two sensors cross the load area simultaneously. Considering a straight gear mesh, three sensors across the width provide sufficient resolution for the distribution.

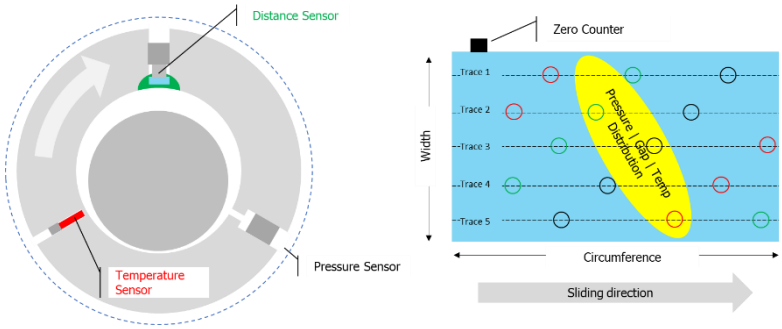

Figure 23: Example of the Sensor Location Setup for distribution measurements

When considering deformation effects, five or more sensors are required. A total of 15 sensors are needed to measure pressure, temperature, and gap height. To obtain results at the same axial location, sensors are arranged in traces across the width. Each trace includes all three sensor types, which pass through the load zone sequentially, as shown in Figure 4. To minimize the influence of neighboring sensors, the distance between them should be maximized.

Another challenge of this measurement architecture is designing the sensor seats. It is crucial to ensure they can be mounted, the gear can be produced, and the test rig can be operated safely.

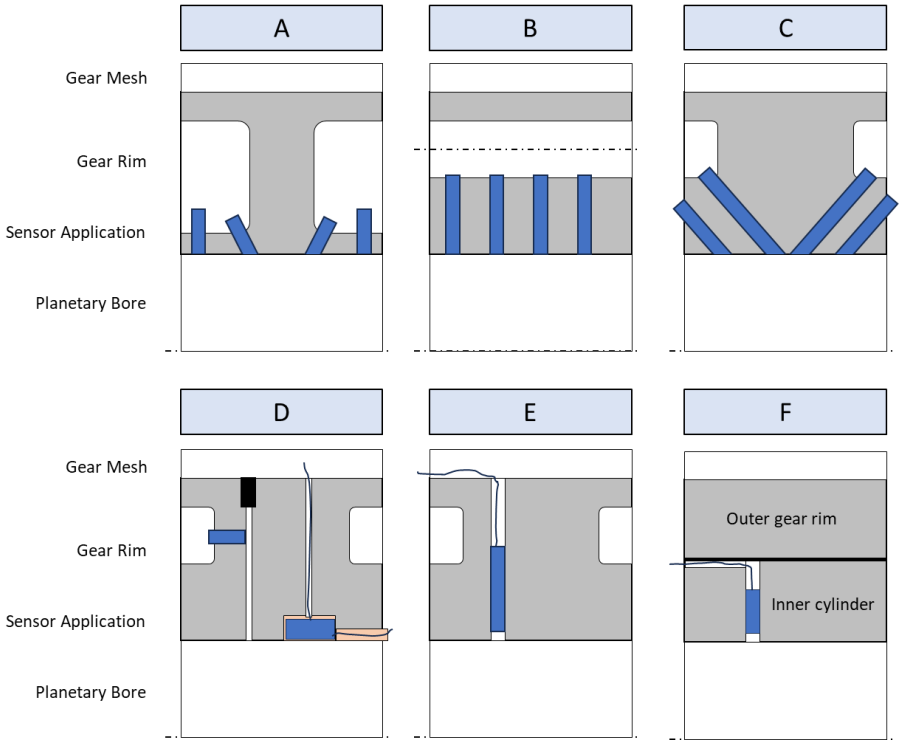

Figure 24: Principal solutions for sensor application into the planetary gear

Figure 24 shows different solutions for the sensor application into the gear which are discussed in the next table.

Option A	increased circumferential grooves	☹ change of stiffness
Option B	axial bores for sensor cables	☹ difficult machining of the radial bores
Option C	diagonal bores	☹ difficult machining of the bores
Option D	axial pressure sensor bore, cavity gap sensor hole	☹ high hydraulic latency on pressure sensor & difficult machining on gap sensor hole
Option E	radial bores	😊 best compromise
Option F	circum. splitted gear	☹ risk of gear damage due to ovalization

Table 2: Discussion of sensor application options

Option E has been selected: radial holes will be drilled into the gear to mount the sensors. The cables will be routed through the gear teeth roots, mitigating the risk of gear mesh damage due to the bores.

3.2 Instrumentation Setup

To select suitable sensors and finalize the complete setup, the boundaries for the measurement campaign need to be defined. Based on ZF's experience with both LSS and ISS operating conditions, the following requirements are listed:

- Acceptable pressure range: 0 – >2000 bar, high frequency, safety included
- Acceptable gap range: 0 – >50 µm, high resolution, high frequency
- Acceptable temperature range: 20 – 120 °C, low frequency

Additionally, the setup must function in a metallic and oily environment. The typical ambient temperature can exceed 80°C, and the sensors need to be supplied with electrical energy without limiting the gear's agility. Therefore, a suitable telemetry system and energy supply are required. The necessary sensors and telemetry solution have been provided by a supplier.

3.2.1 Temperature Measurement Setup

It is assumed that the temperature measurement reaction time is slow because a typical planetary gear has significant heat capacity and comparatively low heat generation. Thermocouples are selected and mounted at a safe distance from the high-pressure loaded plain bearing surface, as shown in the following figure.

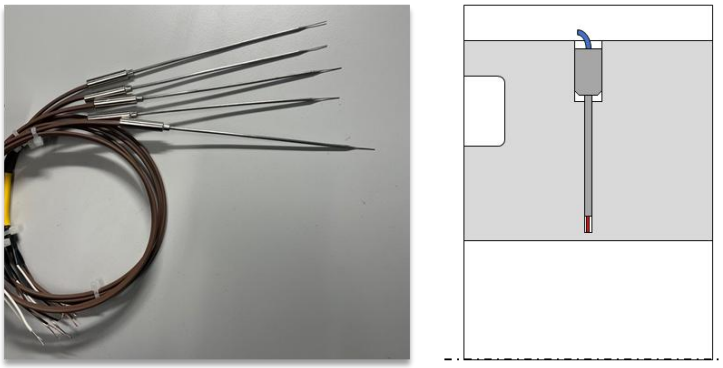

Figure 25: Example of the temperature sensor and its position

3.2.2 Pressure Measurement Setup

Different options are available to capture hydrodynamic pressure:

1. Measuring the direct hydrodynamic pressure
2. Measuring the direct hydrodynamic pressure using small Bernoulli resistance, as in [BUS49]
3. Placing a needle against a spring and capturing the needle's displacement

The following figure illustrates these working principles. Option 3 was discarded due to high assembly and calibration effort. Option 1 involves an open connection to the plain bearing, allowing oil to act directly on the sensor. However, the large cross-section might significantly reduce hydrodynamic pressure around the sensor. Ultimately, Option 2, using pressure transducers, was selected.

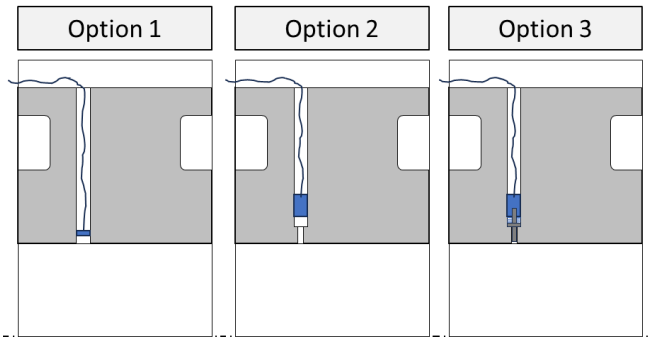

Figure 26: Options for pressure measurement

The capillary bore to the plain bearing bore minimizes pressure loss during measurement. The cavity between the sensor and the plain bearing bore is designed to be small, reducing latency as much as possible.

3.2.3 Gap measurement

To measure the gap within the planetary bore and the planetary pin, a distance sensor is necessary. Direct contact during measurement would damage the plain bearing, so contactless distance sensors are required. The following figure discusses the suitability of different sensor types.

Sensor Type	Pro	Contra
Ultra Sonic	▪ Contamination Resistance ▪ Contact less ▪ Broad material suitability (solids, fluids, …)	▪ Blind area close at the sensor ▪ Sensitive for temperature influence ▪ Sensitive for viscosity and density in oil
Capacitive	▪ High precision ▪ Contact less ▪ Broad material suitability (metals, fluids, …)	▪ Sensitive for temperature, humidity, … ▪ Vulnerable for external e-fields ▪ Regular calibration required
Inductive	▪ High precision ▪ Contact less ▪ High robustness, especially in oiled conditions	▪ Only for metal surfaces (no matter) ▪ Sensitive for magnetic fields ▪ High costs
Eddy Current	▪ Contact less ▪ High precision at high frequencies ▪ High robustness	▪ Material dependent ▪ Sensitive for temperature ▪ High energy consumption

Figure 27: Options for gap measurement

Inductive sensors are the most suitable due to their high accuracy, robustness, and low energy consumption. Figure 9 illustrates different options for gap sensor application. Option A was deemed infeasible for production reasons.

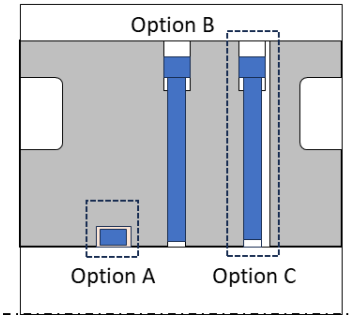

Figure 28: Options for Gap Measurement Design

Option B allows for a small distance from the bearing bore but requires a pressure release hole to protect the sensor from high hydrodynamic pressure. Therefore, Option C is selected. The expected pressure release around the sensor is deemed acceptable based on positive experiences with the floating sleeve bearing design.

3.2.4 Energy supply and Data transfer

Enabling high-frequency measurement resolution and providing energy for the electronics data requires special attention. A wireless telemetry system that provides sufficient energy was not feasible. A slip ring transmitter could supply both electrical energy and signals, but it affects gear displacements and, consequently, the measurement results. The most suitable solution is a battery power supply and telemetry capable of transmitting 16 channels. Both were supplied and installed by a supplier.

3.3 Practical Application

The resulting gear design includes 15 sensor bores and the necessary modifications for energy supply and telemetry. The solution is illustrated in the following figure.

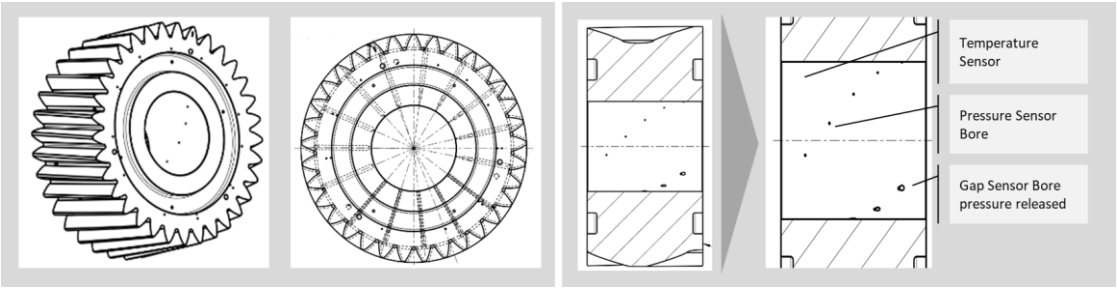

Figure 29: Modifications on the test gear

The sensor bores are minimized in diameter to manage the stress concentration effect in the gear mesh. For the gap sensors, a twin bore was designed to allow pressure release and protect the sensor. The final application of the instrumentation to the gear is shown in the following figure.

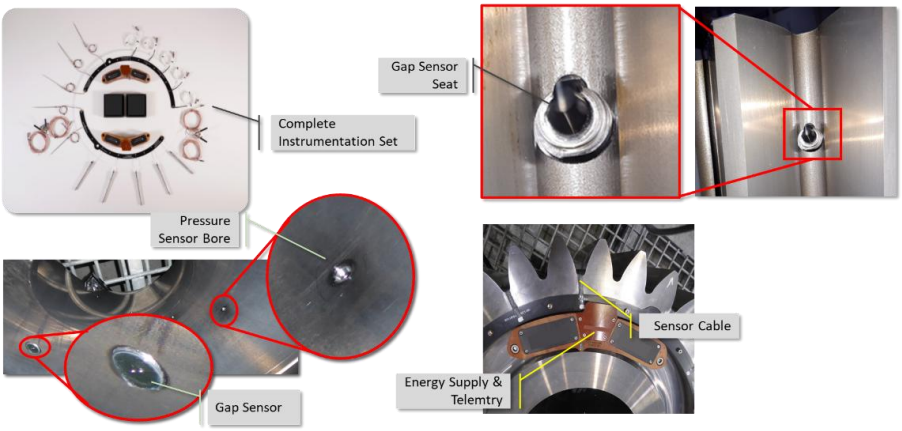

Figure 30: Instrumented test gear

The gap sensor seats do not touch the gear flanks. The entries of the bores into the plain bearing are clean, without any burrs. Both the telemetry system and the power supply are mounted in the axial groove without affecting the axial plain bearing or the gear's agility.

4 Simulation of a Wind Turbine Planetary Plain Bearing

The detailed simulation is conducted by solving the RDE for elastic environments (ref. [KNO74]) using the flow factor approach (ref. [PAT78]) and the roughness contact approach (ref. [GRE71]). The goal of the simulation is to provide pressure and gap distributions as an expectation horizon for the test. Initially, the effect of the radial sensor bores will be neglected, like the real application inside the gearbox. In subsequent simulation steps, the pressure release will be considered using appropriate pressure boundary conditions.

4.1 Operation Modes

To observe the effects discovered in [BUS49], at least three load steps are required. Additionally, to investigate the hydrodynamic characteristics of both LSS and ISS plain bearings, two speed conditions should be considered.

Operation Mode	Load	Speed
OM 1	60 % L_{nom}	n_{LSS}
OM 2	80 % L_{nom}	
OM 3	100 % L_{nom}	
OM 4	120 % L_{nom}	
OM 5	60 % L_{nom}	n_{ISS}
OM 6	80 % L_{nom}	
OM 7	100 % L_{nom}	

Table 3: Set of operation modes during simulation

The temperature for the simulation will be assumed to be isothermal, consistent with ZF's test experience. Therefore, the typical average temperature for each gearbox stage is considered as the ambient temperature. The final operation modes are listed in Table 3.

4.2 Model Setup

The simulation model is set up by experience in a simplified way.

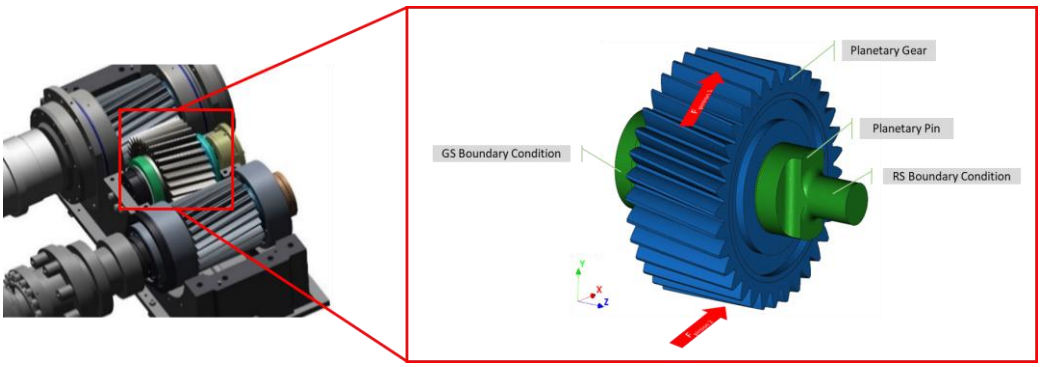

Figure 31: Setup of the simulation model

The housing, pinions, and support bearings were neglected due to their low influence on pressure and gap distribution. The pin and gear are the most critical components to consider [WIT17]. Boundary conditions are applied based on ZF’s experience. The planetary bearing is modeled as an EHL joint between the pin and gear (ref. [LAN23]). The roughness of the shaft and gear in their manufactured state is used to set up both the flow factor model and the contact pressure model. The

viscosity definition aligns with typical wind oils, and the oil supply conditions match the real test setup.

4.3 Simulation Results

The initial simulation results for OM 2 and OM 4, which neglect the pressure release, have been completed. Both the pressure and gap distributions have been post-processed.

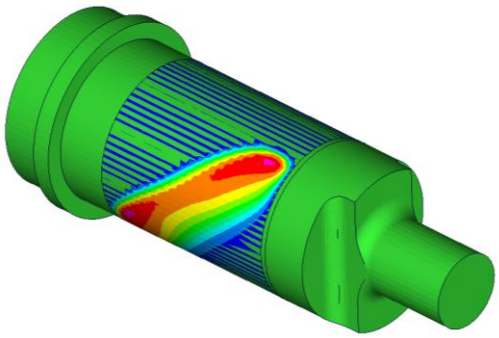

Figure 32: Pressure distribution from simulation of OM 4

The figure illustrates the simulated pressure distribution around the shaft. In this case, it is purely hydrodynamic, without any contact pressure. The gear tilts due to the clearance, the plain bearing profile, and the helical gear mesh forces, resulting in a slanted pressure distribution with a wrap angle of about 150°. The effect of a linear load increase on the EHL pressure is shown in the next figure.

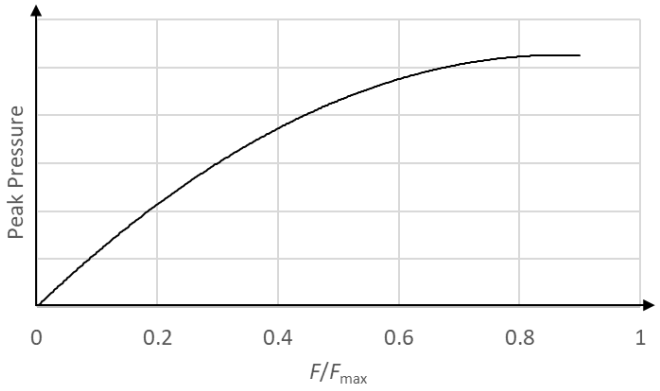

Figure 33: Peak pressure plotted over the relative load

As observed by [BUS49], the peak pressure behavior calculated by recent EHL software increases gradually rather than progressively, which would be expected from solely solving the RDE. Detailed simulation results, focusing on film thickness, have been post-processed for 80% and 120% of the design load.

Figure 15 shows the pressure and gap distribution for OM 2 (80% Load) and OM 4 (120% Load) at the same LSS speed. With higher load, the pressure buildup is slightly wider in the circumferential direction. Additionally, the area with a small gap height is also widened. The 40% load increase has only a slight effect on the decreasing film thickness. Finally, no mixed lubrication or contact is expected for the planned load cases. These simulations are suitable for exploring the upcoming tests.

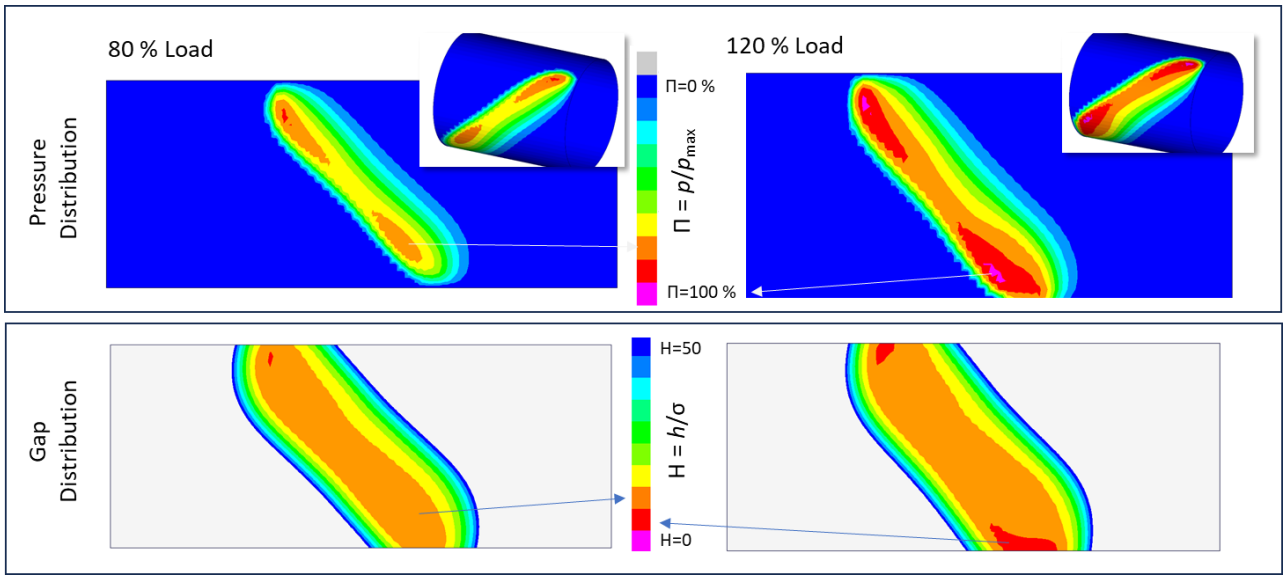

Figure 34: Pressure and gap distribution for OM 2 and OM 4

However, the impact of sensor application needs to be thoroughly investigated within the simulations. Therefore, the simulation model will be extended to include additional aspects and will be compared to the test results in the future.

5 Conclusion

After over 140 years of scientific research and industrial development of plain bearings, there is still no direct validation of key parameters applicable to wind turbine gearbox conditions. To gain confidence in simulation results and extend current design limits, ZF is preparing a comprehensive test campaign on BTR002. This campaign will investigate pressure, temperature, and film thickness distribution in planetary plain bearings under wind turbine conditions. This paper details the measurement setup and simulation results for the planned test conditions. Various architectures and sensor setups are presented, discussed, and evaluated to identify the most suitable solution.

6 Bibliography

[BUS49] Buske, A.; Rolli, W.: Measurement of oil-film pressures in Journal Bearings under constant and variable loads

National Advisory Committee for Aeronautics, Technical Memorandum, Vol. 1200, Washington, 1949

[CAM85] Cameron, A.: Righting a 40-year-old wrong: A.M. Ertel – the true author of Grubin's EHL-Solution

Tribology International, Vol. 18, No. 1, p. 92, 1985

[DOW54] Dowson, D., Higginson, R.: A Numerical Solution to the Elasto-Hydrodynamic Problem

Journal of Mechanical Engineering Science, Vol. 1, pp. 6-15, 1954

[GOR17] Goris, Sonja; Ooms, Maarten; Goovaerts, Michel; Krieckemans, Koen; Bogaert, Roger: Plain Bearings for wind turbine gearboxes - trajectory towards technology readiness

Conference for Wind Power Drives, Aachen, 2017

[GRE71] Greenwood, J.A.; Tripp, J.H.: The contact of two nominally flat rough surfaces

Proc. Instn. Mech. Engrs.; Vol. 185, pp. 625-633, 1971

[GRU49] Grubin, A.N.: Fundamentals of the Hydrodynamic Theory of Lubrication of heavily loaded cylindrical surfaces.

Investigation of the Contact of Machine Components, Vol. 2, 1949

[KNO74] Knoll, Gunther: Tragfähigkeit zylindrischer Gleitlager unter elastohydrodynamischen Bedingungen

Dissertation RWTH Aachen, 19974

[LAN23] Lang, Jochen; Knoll, Gunther: Efficient Elastohydrodynamic Gearbox Simulations,

Conference for Wind Power Drives, Aachen, 2023

[LEI15a] Leimann, Dirk-Olaf: Berechnungs- und Test-Erfahrungen von gleitgelagerten Planetenrädern in einem 2 MW Windkraft Getriebe.

11. VDI-Fachtagung – Gleit- und Wälzlagerungen 2015

[LEI15b] Leimann, Dirk-Olaf: Case study and test observations on helical gearing with plain bearings in a 2 MW wind turbine gear unit

VDI International conference on gears, Munich, 2015

[LEI16] Leimann, Dirk-Olaf: Plain Bearing Lubrication in Wind Turbine Gearboxes

Technische Akademie Esslingen - 20th International Colloquium – Tribology – Industrial and Automotive Lubrication - Stuttgart

[LOH21] Lohmann, Christoph; Wiersch, Petra; Bertels, Thomas: Planetengleitlager Prüfstand – Aufbau, Messung und Simulation relevanter Betriebsparameter

14.VDI-Fachtagung – Gleit- und Wälzlagerungen, VDI-Berichte Nr. 2378, 2021

[MOH84] Von Mohrenstein; Ertel, A.: Die Berechnung der hydrodynamischen Schmierung gekrümmter Oberflächen unter hoher Belastung und Relativbewegung

VDI-Fortschrittsbereichte Reihe 1, Düsseldorf, 1984

[PAT78] Patir, N.; Cheng, H.: An Average Flow Model for Determining Effects of Three-Dimensional Roughness on Partial Hydrodynamic Lubrication

Transaction of the ASME – Journal of Lubrication Technology, Vol. 100, pp. 12-17, 1978

[REY86] Reynolds, Osborne: On the Theory of Lubrication and its Application to Mr. Beauchamp Tower's Experiment, including and Experimental Determination of the viscosity of Olive Oil

Phil. Trans., Vol. 177, pp. 157-234, 1886

[VLI23] van Lier, Hermann; Verdyck, Bert; Ceustermans, Jo; Witter, Dennis: Validation of Plain Bearings on Planetary Stages for Single Blade Installation

Conference for Wind Power Drives, Aachen, 2023

[VLI24] van Lier, Hermann: Plain Bearing Technology for Wind Turbine Gearbox Application – Experiences and Trends

6. VDI-Fachkonferenz Schadenmechanismen an Lagern, Aachen, 2024

[VLI25] van Lier, Hermann: Next Generation Plain Bearing Technology for Wind Turbine Gearboxes

Conference for Wind Power Drives, Aachen, 2025

[WIT11] Witter, Dennis; Schelenz, Ralf; Jacobs, Georg: Simulation of highly stressed slow-rotating radial journal bearings in mixed friction area under consideration of elastic distortion and wear

VDI Tagung Gleit- und Wälzlagerungen, Schweinfurt, 2011

VDI-Berichte 2147

[WIT17] Witter, Dennis; Jacobs, Georg; Schelenz, Ralf; Weiser, Ingo: Hydrodynamic plain bearings in a main gearbox of a 6 MW wind turbine

Conference for Wind Power Drives, Aachen, 2017

Failure mechanisms of bronze-based plain bearings implemented in gearbox under presence of foreign particles

Akash Deo[1], Christian Böhm, Mario Witt, Nelly César, Athanassios Skiadas

Rheinmetall | Division Power Systems | BU Bearings, Am Bahnhof 14, 68789 Sankt Leon-Rot, DE

Keywords: *Plain bearing, Condition monitoring, Vibration sensors, particle detection, Machine Learning*

Abstract: Bronze-based plain bearings have long been preferred for high-torque, low-speed gearboxes due to their reliability and impressive load carrying capacity. However, they are susceptible to two types of failure when subjected to metallic particles: spontaneous failure or slow progressive wear, depending on size and number of particles.

Metallic particles inevitably find their way into gearboxes through assembly processes, component manufacturing, and operational wear. Detecting these particles typically requires specialized oil analysis equipment, which do not detect presence of particles in the tribological contact in real-time. In bearings, metallic particles can cause degradation of running surfaces, making their detection crucial for implementing preventive measures to prolong operational lifespan.

This study commences with the development of a risk map using advanced simulation tools to guide a comprehensive test campaign. Testing points are strategically placed to assess particle impact under varying load and speed conditions.

The study aims to achieve two primary objectives. Firstly, it delves into the failure modes of bronze-based materials, examining how they are affected by varying sizes and quantities of particles. Secondly, it explores the effectiveness of vibration measurements in detecting the presence of particles within plain bearings.

1 Introduction

The increasing utilization of plain bearings in wind turbines is driven by several technological advancements and operational requirements. Plain bearings, which reduce radial space and noise compared to traditional rolling contact bearings, have become a preferred choice in modern wind turbine gearboxes. This shift is primarily driven by the need for more compact designs capable of handling the torque outputs of wind turbines without increasing the overall size or weight of the turbine systems [Sid23], [LDG+23]. In addition to mechanical considerations, the integration of plain bearings aligns with broader trends in the wind energy sector aimed at reducing the levelized cost of energy (LCOE) [LDG+23].

Given the burdensome downtime and maintenance costs associated with wind turbines, emphasis should be placed on enhancing the reliability of plain bearings. Consequently, it is essential to address various failure mechanisms of plain bearings. The failure of plain bearings, due to the presence of particles, is a critical issue in various engineering applications. Particles can originate from manufacturing processes, external contamination or can be generated internally through wear processes. The presence of solid contaminants in lubricants significantly affects the performance and longevity of bearings. Furthermore, different bearing materials exhibit varying sensitivities to particulate contamination in oil [DSWS10]. The presence of particles in lubricants significantly contributes to the failure of plain bearings through various mechanisms, including increased wear rates,

changes in tribological behavior, and, in some cases, sudden failure due to seizure. Understanding these interactions is crucial for improving bearing design and maintenance practices, thereby enhancing reliability and performance in engineering applications.

When it comes to detecting particulate contamination studies have shown that solid contaminants can lead to increased acoustic emissions (AE) levels, which can be detected as precursor to failure. Poddar and Tandon show that [PT19] larger particles within plain bearings, generate higher level acoustic emissions. A higher concentration of particles in oil also leads to an increase in acoustic emission levels.

In the context of monitoring techniques, several studies corroborate the effectiveness of AE, thermoelectric voltage and vibration measurements in detecting various forms of contamination and wear in bearings. Mokhtari et al. [MPN+20], utilizes machine learning algorithms to analyze AE signals for monitoring friction and wear in plain bearings, indicating a trend towards more sophisticated diagnostic methods in tribology. F. König [KSOJ21] shows that using AE sensor data, higher accuracy and higher sensitivity can be achieved in the detection and classification of three-body abrasion due to particle contamination. Studies by Ates et al. [AHW+23] explore the use of a convolutional autoencoder on vibration sensor data to perform wear estimation. Recent studies have investigated the diagnosis of friction states using machine learning based on thermoelectric measurements. This was conducted on a test rig featuring three shafts with helical gears mounted, representing an abstraction of a planetary gearbox [WJB+24]. Works related to monitoring of plain bearing contamination using vibration data in gearbox applications could not be traced.

The paper is organized into several sections. In the second chapter, we present the experimental setup, along with detailed descriptions of the measurement parameters. Following this, it is explained how the test campaign was designed and refined using component test results and simulation tools. The results section is divided into two parts. The first part examines the failure modes of bronze-based plain bearing materials. The second part evaluates the effectiveness of vibration measurements in detecting the presence of particles within plain bearings.

2 Experimental and Simulations setup

2.1 Experimental setup

Two test-benches were used to understand failure mechanisms in bronze based plain bearings. Although, failure mechanisms can be observed and reproduced on component test-bench with less efforts, gearbox test bench was used for this paper. Main motivation for using gearbox test-bench is to check if vibration measurements can detect the presence of particles in a complex environment.

2.1.1 Component testbench

In component testbench various tests of plain bearings can be conducted (Figure 1). It enables testing plain bearings under dynamic load conditions. In a component testbench, full factorial experimentation can be conducted. Various quantities such as oil type, particles size, particle concentrations and bearing materials can be changed to understand effects of changes in details. Construction of this test rig is fairly simple; it has a shaft with supported ends. The test bearing is mounted in a housing, such that its rotational degree of freedom is locked. Test bearing housing is pushed against the shaft. Various quantities such as friction torque and temperature of bearing can be measured on this testbench. Radial forces and shaft speed are controlled inputs. This test bench

can also be equipped with vibration sensors to measure vibrations and collect data for machine learning (ML)-based condition monitoring. Additionally, the specifications of test bearings on the gearbox test bench can be easily replicated on the component test bench to facilitate comparisons.

After conducting various tests on this test bench, two key insights emerged: specific velocity plays a more critical role than specific pressure in particle-induced failures, and operating temperature is a pivotal factor in studies of such failures.

2.1.2 Gearbox testbench

The tests for this paper were primarily conducted using a gearbox test-bench (Figure 1). This test-bench comprises of a drive unit (synchronous motor), spring clutch, a modified planetary gearbox, and a hydraulic pump. The gearbox was modified by replacing the needle bearings between the planet gears and carrier with plain bearings. A hydraulic pump is connected to the planetary gear to simulate loading. Specifications used for the tests are given in the table below (refer Table 1).

Bearing Specification	
Material	CuSn12Ni2
Pin diameter	24.8 mm
B/D-ratio	1
Relative clearance	0.8‰
Roughness & Friction specification	
Roughness pin	Ra 0.12 µm
Roughness bearing	Ra 0.22 µm
Friction coefficient	0.09
Oil specification	
Lubricant	ISO VG 220
Kinematic viscosity	
At 28.5 °C	381.4 mPas
At 55 °C	79.1 mPas
Speed & Load specifications	
Speed range	0.07 to 0.68 m/s
Specific load	2.1 to 11.3 MPa

Table 1: Test and simulation specifications

The measuring chain includes several sensors that record accelerations in three Cartesian spatial directions. All data is collected in a measurement system, allowing real-time monitoring and storage as ASCII files. The tests are controlled using a LabView-based program.

2.2 Targeted testing using simulations

Tests using gearbox can be highly resource intensive. In order to focus on tests which, bring meaningful results, simulation was used to determine area of testing.

Simulation of gearbox test-bench were conducted using iST FIRST (Multi-body simulation software). In these simulations, all gear contacts were considered. In the actual gearbox, needle bearings between carrier and planet gears were replaced with plain bearings. These plain bearings were simulated using Elasto-hydrodynamic (EHD) simulations, with specifications outlined in the table above.

A profile optimization was performed, prioritizing high-load and high-speed operating conditions. The main goal of the optimization was to achieve an evenly distributed oil film thickness.

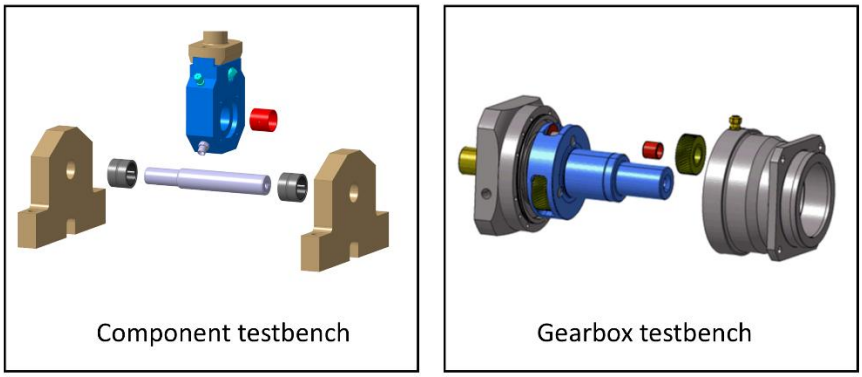

Figure 35: Testbenches

Dissipation energy was used as an indicator to identify critical operating conditions for the bearings. It was observed that unprofiled bearings exhibited critical operating conditions at high loads and high speeds. These issues were mitigated by implementing an optimized bearing profile. By integrating the results from simulations and key insights from component testing, the focus was directed toward the high-speed region.

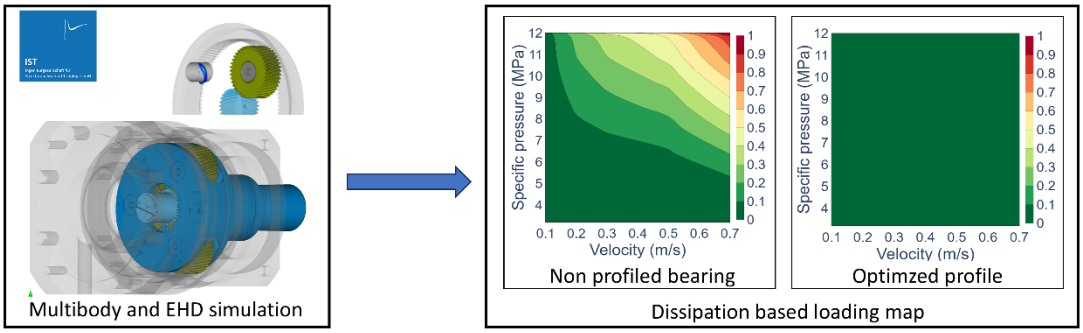

Figure 36: Dissipation based loading map

2.3 Test campaign

The aim of the tests was to investigate the effects of chips and particles in plain bearings. Additionally, the data collected was intended to train and test machine learning models for condition monitoring. A distinction was made between runs without chips or particles and runs with chips or particles.

For the tests involving chips, three metal chips were introduced into the plain bearing. For the tests with particles, three different concentrations were evaluated. Measurement data was recorded at a frequency of 100 kHz. Dimensions and details of the chips and particles are provided in Table 3.

Analysis revealed that the chips used during testing broke into smaller pieces over the course of the test. This observation prompted an increased focus on particle-based testing.

The speed ramp, shown in Figure 3, was used for the test procedure. The procedure began at a standstill, with the speed increased in increments of 10 rad/s up to a maximum of 100 rad/s. Each speed level was maintained for 30 seconds.

Various setup modifications, including assembly and disassembly, warm-up, and cold-run tests, were performed during this test campaign to evaluate the robustness of the generated features for machine learning.

Particle type	**42CrMo4 chips**		**Iron powder**		
Size	300x300x50 µm	700x300x50 µm	distribution 35 to 42 µm		
Quantity	3 chips	3 chips	0.1 g	0.5 g	1 g
Number tests	6	3	4	4	6

Table 2: Test campaign details

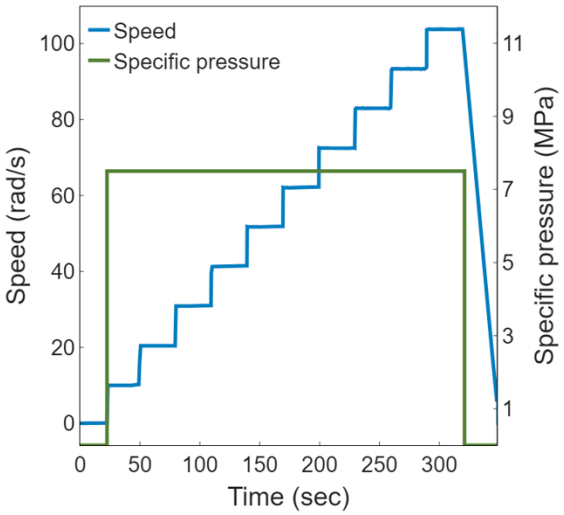

Figure 37: Testing conditions

3 Results

Results section is divided into two parts. First part discusses failure mechanisms in bearing observed during testing. Second part discusses about effectiveness of vibration sensors in condition monitoring systems.

3.1 Test results and failure mechanisms

In these tests, general roughing of running surfaces is seen. Analyzing *Sv* roughness revealed that the depth of the valleys increased when exposed to particles. However, since the runtime for tests with particles was not long enough, less wear volume was observed.

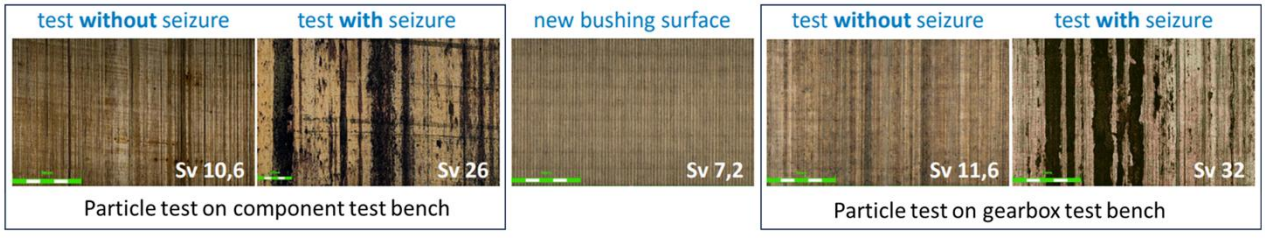

Figure 38: Particle test results

As expected from the component test bench results, seizure was first observed at the highest operating speed. The concentration of particles also plays a significant role in causing seizure in bearings. The particle concentration was gradually increased to determine the point at which seizure occurs. It was found that 1g of iron filings could generate seizure at the highest operating speeds. The bearing surface after seizure exhibited even deeper troughs, combined with microstructural changes.

3.2 Effectiveness of vibration sensors in condition monitoring

In following chapters, we discuss data distribution, feature engineering and results of condition monitoring.

3.2.1 Data distribution

Vibration data was collected for different operating points. For each test which include 10 ramps as shown in Figure 3 data packet for 1 second is used. Out of all data points 50% are data points with particles and rest without particles.

3.2.2 Feature engineering

A variety of time-based and frequency-based features were analyzed and tested. The features were evaluated to determine their effectiveness in detecting the presence of particles. Based on this analysis, custom frequency-based features were developed to enhance detection capabilities.

The goal was to extract a manageable number of features from the dataset while also considering the computation time required for feature generation, ensuring practicality for real-world applications.

3.2.3 Vibration sensor for particle detection

Based on vibration sensor data, various features were generated. Figure 5 demonstrates a clear separation between tests with and without particles.

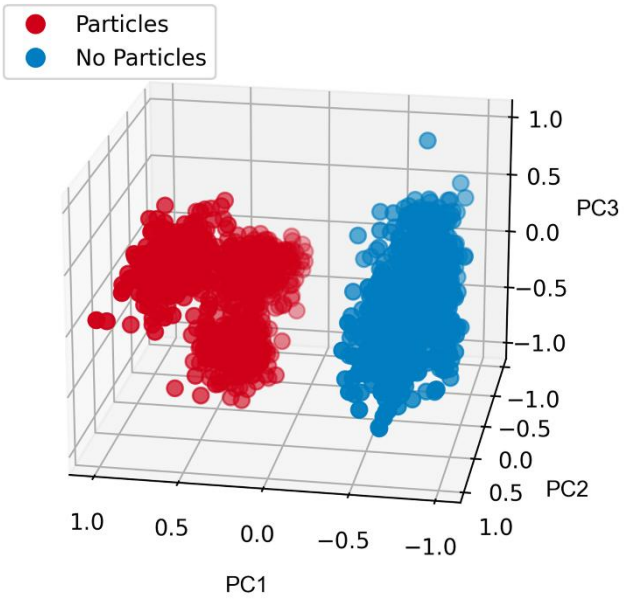

Figure 39: Classification of measurements with particles and without particles

Furthermore, an anomaly detection algorithm, utilizing the same features, was able to detect seizures in bearings. In Figure 6, anomalies are represented by red dots, the blue line indicates feature readings for tests with seizures, and the grey lines represent feature readings for tests without seizures. Using these features, anomalies were detected 10 seconds before the onset of a seizure.

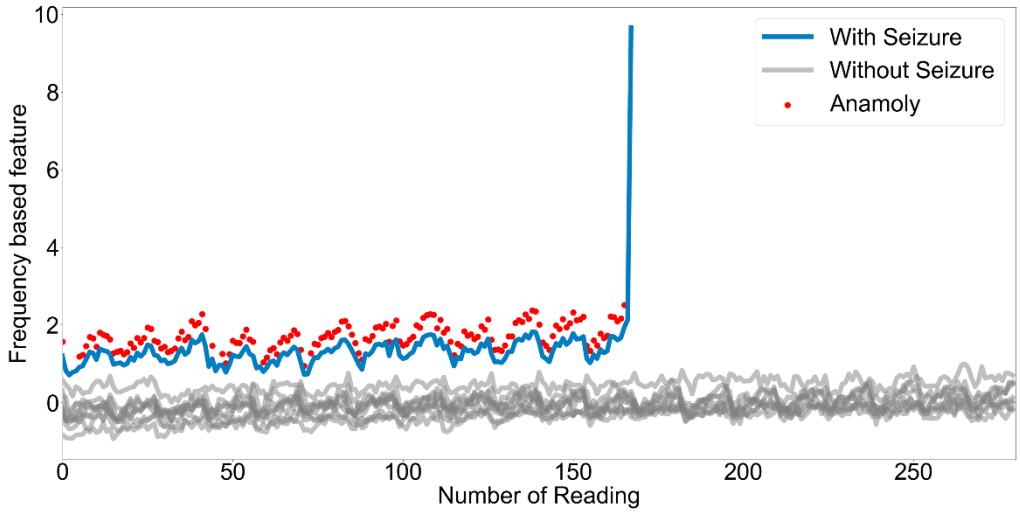

Figure 40: Seizure detection

4 Conclusion

The key conclusions derived from this study can be summarized as follows:

1) Critical Role of Speed: The study highlights that speed is the primary factor influencing seizure generation. While the load on the bearing does have a significant impact, it plays a comparatively secondary role.

2) Concentration of particles: This study indicates that a higher concentration of particles is necessary to induce a seizure caused by particles.

3) Surface Damage vs. Wear: Tests conducted during the study revealed that the presence of particles leads to greater surface damage than conventional wear mechanisms. This underscores the severe impact of particle contamination on component longevity.

4) Effectiveness of vibration sensors: By leveraging machine learning classification algorithms on data obtained from vibration sensors, the presence of particles can be detected with high accuracy and reliability. This approach demonstrates significant potential for predictive maintenance and fault detection.

5) Reproducibility on Test Rigs: All mechanisms of particle and bearing interactions observed in gearbox can be effectively reproduced using the component test-rig. This ensures controlled and repeatable testing for deeper insights into failure mechanisms.

5 Outlook

An investigation will be carried out to explore whether deep learning methods can be directly applied to time-series data for particle detection, while also reducing the time required for feature calculation.

Additionally, further tests will be conducted to assess the prediction of the remaining usable life of bearings using machine learning algorithms.

6 Bibliography

[AHW+23] Cihan Ates, Tobias Höfchen, Mario Witt, Rainer Koch, and Hans-Jörg Bauer. Vibration-based wear condition estimation of journal bearings using convolutional autoencoders. Sensors, 23(22), 2023.

[DSWS10] Klaus Damm, Athanassios Skiadas, Mario Witt, and Hubert Schwarze. Gleitlagererprobung anhand der forderungen des automobilmarkts. ATZextra, 15(1):54–63, Mar 2010.

[KSOJ21] F. König, C. Sous, A. Ouald Chaib, and G. Jacobs. Machine learning based anomaly detection and classification of acoustic emission events for wear monitoring in sliding bearing systems. Tribology International, 155:106811, 2021.

[LDG+23] Mattheüs Lucassen, Thomas Decker, Francisco Gutiérrez Guzmán, Benjamin Lehmann, Dennis Bosse, and Georg Jacobs. Simulation methodology for the identification of critical operating conditions of planetary journal bearings in wind turbines. Forschung Im Ingenieurwesen, 2023.

[MPN+20] Noushin Mokhtari, Jonathan G. Pelham, Sebastian Nowoisky, José-Luis Bote-Garcia, and Clemens Gühmann. Friction and wear monitoring methods for journal bearings of geared turbofans based on acoustic emission signals and machine learning. Lubricants, 2020.

[PT19] Surojit Poddar and N. Tandon. Detection of particle contamination in journal bearing using acoustic emission and vibration monitoring techniques. Tribology International, 134:154–164, 2019.

[Sid23] Muhammad Omer Siddiqui. The influence of journal bearings on the gearbox dynamics of a 5 MW wind turbine drivetrain. Journal of Physics Conference Series, 2023.

[WJB+24] Martin Winnertz, Georg Jacobs, Thao Baszenski, Mattheüs Lucassen, and Benjamin Lehmann. Detection of wear in sliding bearings with the use of machine learning techniques. Tribologie und Schmierungstechnik, 70:18–26, 01 2024.

Effect of adding hard particles to welded sliding material in plain bearings for planetary gears

Ryo Asaba[1], Eisaku Inoue [1], Yuki Kawashima [1]

[1] DAIDO METAL CO., LTD, Tendoh Shinden, Maehara, Inuyama, Aichi, Japan

Keywords: Plain bearing, Hard particle, Welding, Planetary gear, Wind turbine gearbox,

Abstract: There is a growing interest in transitioning wind turbine gearbox roller bearings to plain bearings, with a specific emphasis on directly coating the bearing material onto the shaft. Under planetary gear operating conditions, the sliding material coated on the shaft and the sliding counterpart (planetary gear inner surface) contact each other at locally high pressure due to deformation of the shaft, planetary gear, carrier, etc. In addition, as wind turbines start and stop, they are subjected to repeated contact and non-contact conditions. Therefore, as plain bearing materials, high wear resistance is particularly important among the generally required seizure, fatigue, and wear resistance. Therefore, we added hard particles to the bearing alloy to improve wear resistance.

We manufactured test pieces with shafts coated with a copper alloy containing hard particles and evaluated their wear resistance in a start-stop test. We report on the effect of hard particles addition on sliding performance.

1 Introduction

Wind turbine generators are becoming larger to increase power generation for the purpose of reducing levelized cost of energy (LCOE). In line with this trend, there is a demand for downsizing and weight reduction of components. In planetary gearboxes, as a countermeasure, the conversion from conventionally used rolling bearings to plain bearings is being promoted. For smooth rotation, conventional rolling bearings become integral parts of a circular structure consisting of an inner ring, outer ring, and rolling elements. In contrast, the planetary gearbox itself can be made smaller and lighter because the plain bearing is only a sliding material part. In addition, due to their simple configuration, plain bearings are expected to improve maintenance costs and equipment utilization rates by reducing maintenance work, and may contribute to LCOE reductions.

As a wind turbine planetary gearbox, a common plain bearing used is a solid bush that can be mounted on a planetary shaft or planetary gear (housing). However, when the solid bush is used, there is concern that creep may occur due to deformation caused by insufficient rigidity of the gear and insufficient interference. Coating the sliding material directly onto the shaft is attracting attention as a way to avoid this concern [TES23] [LIE23].

Under planetary gear operating conditions, the sliding material coated on the shaft and the sliding counterpart (the planetary gear inner surface) contact each other at locally high pressure due to deformation of the shaft, planetary gear, carrier, etc. In addition, as wind turbines start and stop, they are subjected to repeated contact and non-contact conditions. Therefore, as plain bearing materials, high wear resistance is particularly important among the generally required seizure resistance, fatigue resistance, and wear resistance. (“VDMA23903 2019-1” also states that sliding materials will be evaluated under conditions where wear is expected to occur to demonstrate performance.) Therefore, the bearing alloy, which is the sliding material, was coated by welding for

bonding strength, and hard particles were added to improve wear resistance. This paper reports on the effect of the addition of hard particles on the sliding performance.

2 Material concept

In casting plain bearings, it is common practice to precipitate compounds with higher hardness than the matrix in the alloy to increase strength and other properties (e.g., tin-based white metal). However, the aforementioned hard particles are not compounds formed within the molten alloy, which are affected by cooling and heat treatment conditions, etc., but rather harder compounds that are less reactive with the bearing alloy (e.g., silicon carbide). The addition of such hard particles is known for high wear resistance cemented carbides, such as nickel alloys and cobalt alloys, which are also applied to plain bearings for internal combustion engines in the car and truck sector [SAK01].

2.1 Sliding mechanism of hard particles

Two advantages of the presence of hard particles on sliding surfaces are as follows (Figure 1).

- Hard particles scrape off bearing alloys that have adhered to the sliding counterpart
- Hard particles smooth out the surface roughness of the sliding counterpart

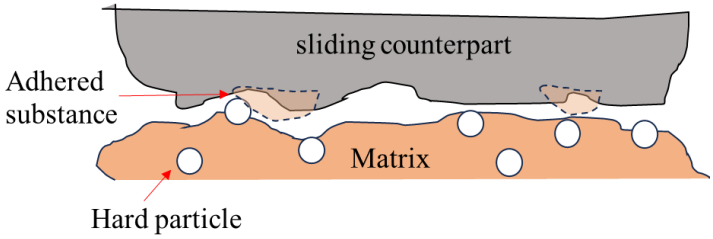

Figure 1: Sliding mechanism of hard particles

Under fluid lubrication, an oil film exists between the plain bearing and the sliding counterpart, and metal contact does not occur. However, due to a lack of lubricant or sudden changes in surface pressure, the oil film cannot exist at the sufficient thickness and metal contact often occurs between the sliding counterpart and the bearing alloy, causing the bearing alloy to adhere to the surface of the sliding counterpart. If sliding continues as it is, the bearing alloy of the plain bearing will come into metal contact with the adhered substance on the surface of the sliding counterpart. Since the adhered substance and the bearing alloy are of the same material, adhesion is more likely to occur, resulting in significant wear of the bearing alloy (adhesive wear) or, in the worst case, seizure. However, when hard particles are present in the bearing alloy, they scrape off the bearing alloy that has adhered to the sliding counterpart. This prevents metal contact between the adhered substance and the bearing alloy, leading to improved wear and seizure resistance.

Hard particles make metal contact with the surface of the sliding counterpart in addition to the adhered substance on the surface of the sliding counterpart. Since the bearing alloy is softer than the general sliding counterpart material (e.g., hardened steel), the alloy side wears during metal contact. However, hard particles are harder than the sliding counterpart material, so the sliding counterpart is polished. During sliding, the convex surface of the sliding counterpart makes metal contact with

the hard particles and is polished. The surface roughness of the sliding counterpart is then smoothed, and a sufficient oil film can be formed between the bearing sliding surface and the surface of the sliding counterpart, so that metal contact itself is less likely to occur. In addition, when the bearing alloy makes metal contact with the sliding counterpart, if the surface roughness of the sliding counterpart is low, adhesion is less likely to occur, leading to improved wear resistance and seizure resistance.

In addition, the number of hard particles present on the sliding surface gradually increases because the bearing alloy wears as it comes into metal contact with the sliding counterpart, but the hard particles hardly wear. Therefore, the addition effect improves with sliding up to a certain amount.

2.2 Test piece preparation

Since the operating conditions of planetary gears cause deformation of the shaft, planetary gear, carrier, etc. and low peripheral speeds, it is thought that contact between the bearing and the planetary gear inner surface will increase due to the inability to form a sufficient oil film. The addition of hard particles is expected to improve wear and seizure resistance, but the matrix itself must also have a certain level of wear and seizure resistance, and must be strong enough to withstand shaft deformation, so a copper alloy was selected as the sliding material. Welding was selected as the manufacturing method because of the need to directly join the sliding material to the shaft side and for high adhesion and alloy strength. The copper alloy with hard particles was welded onto a steel shaft, and the test piece was machined to a thickness of 1 mm (Figure 2).

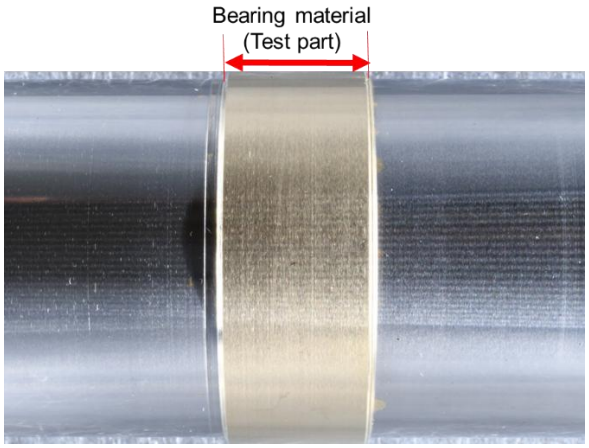

Figure 2: Photograph of experimental welding product

A copper alloy with hard particles added (test piece No.1) as described above was evaluated in a sliding test and compared with a copper alloy of the same material (test piece No.2) without hard particles and the DIN standard material Cu12Sn2Ni (test piece No.3) (Table 1).

No.	Material	Manufacturing method
1	Copper alloy + Hard particle	Welding
2	Copper alloy	Welding
3	Cu12Sn2Ni	Casting

Table 1: Test material

No.2: Coating on outer circumference of steel shaft as in (test piece No.1)

No.3: Made by interference fit of a cast bushing to a steel shaft

The above three materials were subjected to a reciprocating sliding test (ball on disk test) as a basic evaluation test in advance. The test conditions and results are shown in Table 2 and Figure 3.

Load	500 gf
Velocity	10 mm/s
Distance traveled	5 mm one way
Lubrication	Application
Oil	VG320
Oil inlet temperature	80 ℃
Number of round trips	200 cycles
Sliding counterpart	JIS SUJ2 (equivalent ISO 100Cr6) Φ 8 mm

Table 2: Reciprocating sliding test conditions

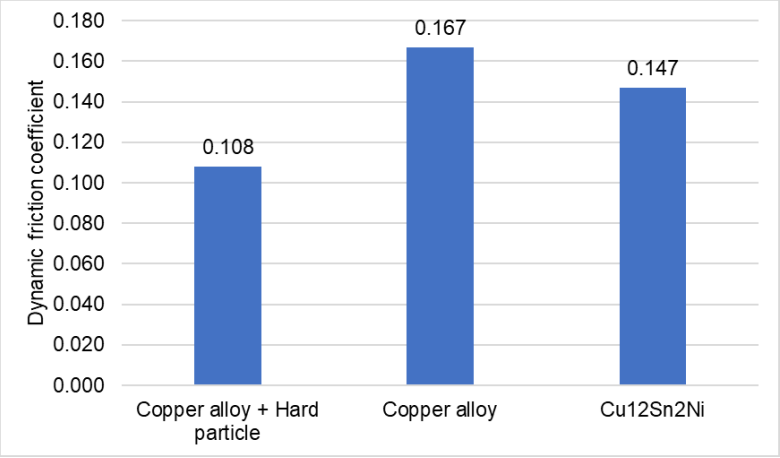

Figure 3: Reciprocating sliding test result

The addition of hard particles significantly reduced the dynamic friction coefficient. In addition, test piece No.1 shows a dynamic friction coefficient lower than that of Cu12Sn2Ni, which means that it has high sliding characteristics, at least in a simplified evaluation. To confirm whether the addition of hard particles is effective even in a sliding configuration more like that of the actual machine, a sliding test was conducted as described below.

3 Sliding test

3.1 Test rig configuration

Although the planetary gear orbits around the sun gear, the shaft does not rotate, but the planetary gear (housing) does. The test rig described in Figure 4, which simulates this sliding mechanism, was used for the evaluation.

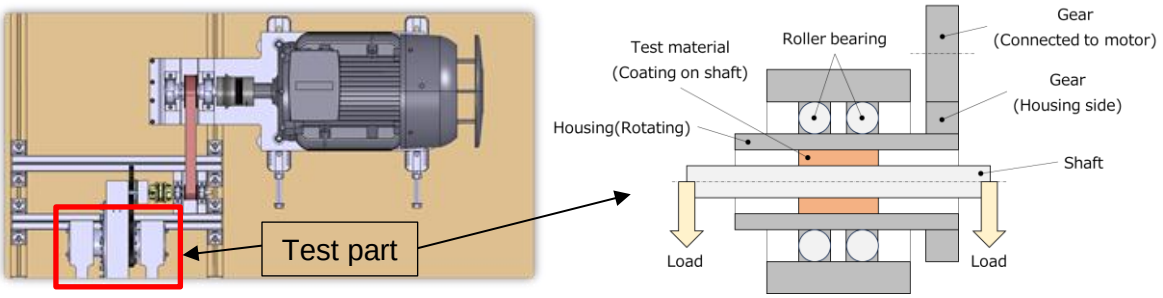

Figure 4: Schematic representation of the test rig

In this test rig, the housing side rotates as in the planetary gear operation mechanism. On the other hand, the shaft side does not rotate, and the load is applied in a constant direction (downward in Figure 4). There is an oil hole on the opposite side of the sliding surface of the shaft. Lubricant is supplied to the sliding part through the supply path in the shaft and its oil hole.

3.2 Test conditions

The test conditions are shown in Table 3. This test was conducted to evaluate the wear resistance of plain bearings under planetary gear operating conditions at startup and shutdown, when wear is expected. The test loads, speeds, etc., were matched to the steady-state operating conditions of the planetary gear. The load and speed for one cycle of the start-stop test are shown in Figure 5. A hardened steel bush was selected as the sliding counterpart material and mounted inside the housing.

Test pattern	Start-stop cycle
Specific load	5 to 35 MPa
Velocity	0 to 0.5 m/s
Lubricant	VG320
Amount of oil supply	0.5 L/min (constant value)
Oil inlet temperature	60 ℃ (constant value)
Test time	4,500 cycles (19 s/cycle)
Sliding counterpart	JIS SCM440 (equivalent DIN 42CrMo4) HRC50~60 Ra0.2~0.3

Table 3: Sliding test conditions

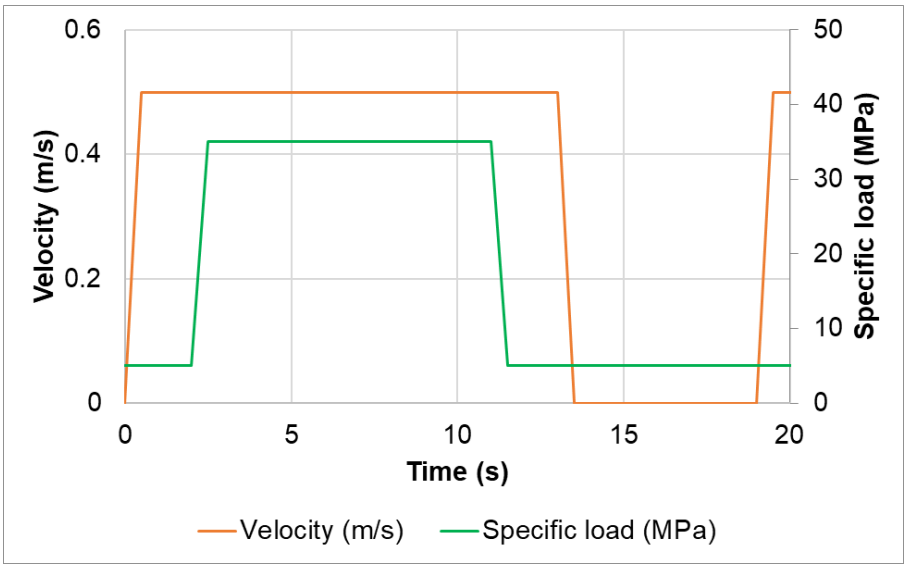

Figure 5: Load and velocity in one cycle

4 Test result

The appearance and shape of the test piece after the test are shown in Figure 6. The test piece with hard particles (test piece No.1) shows almost no wear, while the test piece without hard particles (test piece No.2) shows wear at the load portion. This suggests that the addition of hard particles improves wear resistance even in a sliding environment close to the operating mechanism of planetary gears. Data from the test results are elaborated in more detail within the presentation.

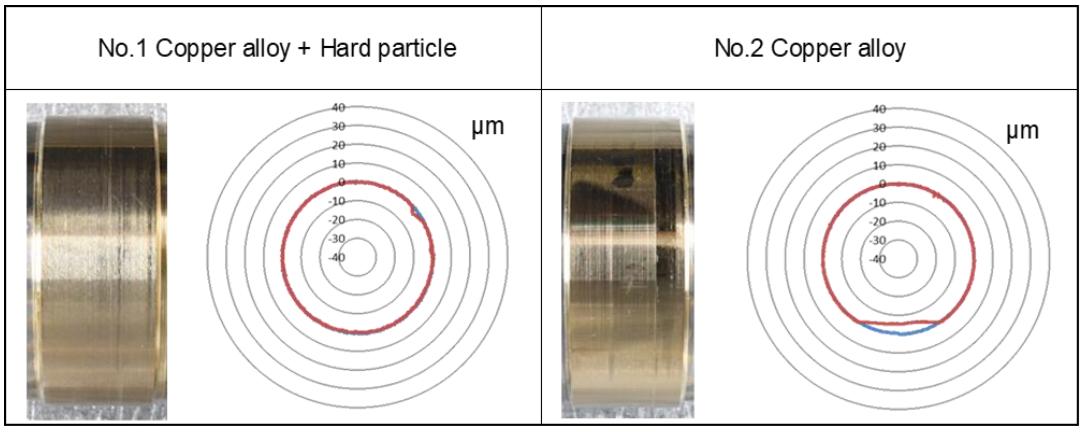

Figure 6: Photograph of shaft appearance and shape after test

Red line: shape after testing Blue line: shape before testing

5 Conclusion

Through this test result, the addition of hard particles to the matrix of the bearing material, which is a common technique for plain bearings for internal combustion engines, was shown to leads to improved wear resistance even in a sliding environment (start-stop) close to the operating mechanism of planetary gears. Since high wear resistance is more important for plain bearings in a wind turbine planetary gear operating environment, the improved wear resistance provided by this technology is beneficial for wind turbine planetary gear bearings. However, wind turbine planetary gear bearings are required to have sliding performance under oil-cut condition and single-blade mounting condition in addition to start-up and shutdown. In the future, we will conduct tests under these conditions to prove that the sliding materials with hard particles can be adapted to wind turbine planetary gear bearings.

6 Bibliography

[TES23] P. Tesini, J. Dzwonczyk-Mertzanis, R. Reynders: A new generation of hydrodynamic plain bearings, enabling the next step in gearbox torque density.

CWD2023 CONFERENCE PROCEEDINGS, 2-10, Eurogress Aachen, 2023

[LIE23] H. van Lier, B. Verdyck, J. Ceustermans, D. Witter: Validation of Plain Bearings on Planetary Stages for Single Blade Installation.

CWD2023 CONFERENCE PROCEEDINGS, 11-17, Eurogress Aachen, 2023

[SAK01] K. Sakai, S. Kurimoto, K. Yamamoto: Effect of WC or Mo_2C addition on tribological AND MECHANICAL PROPERTIES OF COPPER BASED BEARING ALLOY.

WTC Vienna, Austria, September 2001.

Main Bearing I: Plain Bearing

Miba's Segmented Journal Bearing (SJB™) - an innovative solution for wind turbine main bearings

Johannes Hölzl[1], Patrick Laubichler[1], Michael Mirza[1], Johannes Reisenberger[1], Christopher Zeh[2]

[1]Miba Gleitlager Austria GmbH, Dr.-Mitterbauer-Str.3, A-4663 Laakirchen

[2]Miba Industrial Bearings Germany GmbH & Co. KG, Rolandsweg 16-20 D-37520 Osterode

Keywords: Miba's SJB™, *main bearing, hydrodynamic journal bearing, segmented,*

Abstract: Starting from 2008, Miba has been involved with journal bearing solutions in wind turbine drivetrains. Miba, as an innovative component supplier, has proven journal bearings as a recognized technology for wind gearboxes.

Journal bearings provide significant advantages over existing main bearings in wind turbines. The power density of drivetrains can be increased. Journal bearings enable easy up tower inspection and service due to a segmented design. Potential wear parts of the main bearing can be replaced without rotor teardown. This reduces maintenance costs and increases turbine availability. The physics behind hydrodynamic journal bearings and the segmented design enables scalability for larger turbine classes.

Miba's SJB™ allows a "one-to-one" replacement for existing roller element bearings. Furthermore, the SJB™ comprises of a low number of components, low complexity, and potential for further simplification of the main bearing unit (MBU).

The focus for the first development starting from 2019 has been on the replacement of spherical roller element bearings (SRB) with the SJB™ in 3-point suspension drivetrains. Basic tests regarding tribology and component life, scaled system tests, and real-size tests on a 3.5 MW drivetrain were carried out. Principle feasibility towards replacing tapered roller bearings (TRB) with SJB™ in highly integrated drivetrains is also assessed.

In addition to this technical qualification, an economic evaluation regarding Levelized Cost of Energy (LCoE) was in focus. The demonstrator bearing will be subjected to a field test in year 2026 - 2027 and 0-series are aimed for 2028

1 Introduction

1.1 Wind turbine developments and trends

To compete with existing and other sources of energy, the Levelized Cost of Energy (LCoE) of wind turbines must be further brought down.

This can be done by lowering the CapEx and OpEx but also by increasing the AEP & reduction of downtime.

The AEP can be increased by high power density turbines. This trend has already started with China making fast progress on this.

However, this rapid power density increase in short time also brings in risk due to limits of existing bearings in terms of load carrying capacity, size, weight, failure probability, serviceability, etc.

1.2 Roller main bearing developments and limits

Up to 1.5 MW to 2 MW typically a combination of SRB with a cylindrical roller bearing (CRB) or a combination of double-tapered roller (DTRB) bearings with CRBs have been a standard solution for main shaft support.

For wind turbines from 1.5 MW to 7 MW the so-called 3-point suspension drivetrain was established as the most economical concept and became standard in this power class. In this drivetrain configuration the rotor-side main bearing is an SRB, and the generator-side support of the main shaft is integrated into the main gearbox. Currently SRBs are used as main bearings in dimensions up to 1250 mm shaft diameter. The roller elements become broad and heavy which results in insufficient roller contact situations leading to bearing failures. According to [EPR24] 1.5 MW to 2 MW main turbines have significant premature main bearing failure rates.

For wind turbines with power class above ~ 8 MW, pre-tensioned tapered roller element bearings (TRB) in an O-arrangement, became standard. Actual market reports [ELI24] confirm this trend to use mainly TRB in future. These bearings are smaller but need to be pretensioned, which is a complex and expensive process.

Although known failure modes from SRBs can be reduced, however, due to increasing ring diameters and reduced bearing width, ring-creep as failure mode becomes more relevant.

2 Journal bearings as main bearings

2.1 Benefits of journal bearings

Generally, journal bearings enable increasing power density due to non-Hertzian contact. Besides that, journal bearings can be designed in a segmented architecture. A segmented design allows an up-tower exchange of wearing segments without the need to disassemble the rotor. Therefore, the cost for heavy-duty cranes for maintenance operations can be avoided.

2.2 Journal bearing concepts and their differences

Miba started in 2010 with first concepts of a journal bearing as main bearing for a wind turbine and analyzed several solutions as explained below.

2.2.1 Double tapered segmented journal bearing

The first step was the development of a replacement solution for DTRB [MIB10].

The concept was proven by scaled sub-system tests during a cooperation project [SCH18] [LAN19] [ROL20]. The functional enabler was the introduction of structural adaptation (flexibility) of the segments to avoid excessive edge loading.

In an integration and concept study of the double conical bearing solution for a 3-point suspension drivetrain, initiated by a wind turbine manufacturer, a fatigue risk due to the flexibility was identified. The demanding segment substrate material requirements result in high direct material cost and finally to a Miba internal concept stop.

2.2.2 Industrial bearing solution(s)

Based on the learning from the integration study done with a wind turbine OEM, Miba initiated an extended analysis of bearing concepts.

DOME concept

This concept [KOC19] is a bearing arrangement with radial and axial thrust segments which are supported in a spherical compensating structure. The spherical compensating structure is required to allow tilting and thus avoiding edge loading on the bearing segments. Simulations showed that an additional compensation element for the thrust segments is needed. This led to a complex design expensive to manufacture. Furthermore, a critical risk for fretting on the spherical compensating structure due to dynamic loading was identified.

Tilt segment bearing

Tilt segments are traditionally used for high-speed applications. Due to a pivot element, the converging fluid film gap adjusts dependent on the sliding speed. When it comes to very slow sliding speeds the bearing load is concentrated on the segment-edges that leads to bearing damage. This can be avoided with additional elastic support elements but also this design becomes complex, prone to failures and expensive to produce.

3 Miba's SJB™

3.1 Spherical journal bearing

Besides traditional industrial bearing solutions, a new bearing concept, the spherical hydrodynamic journal bearing (see Figure 41) was developed as optimum solution for spherical roller element bearing replacement.

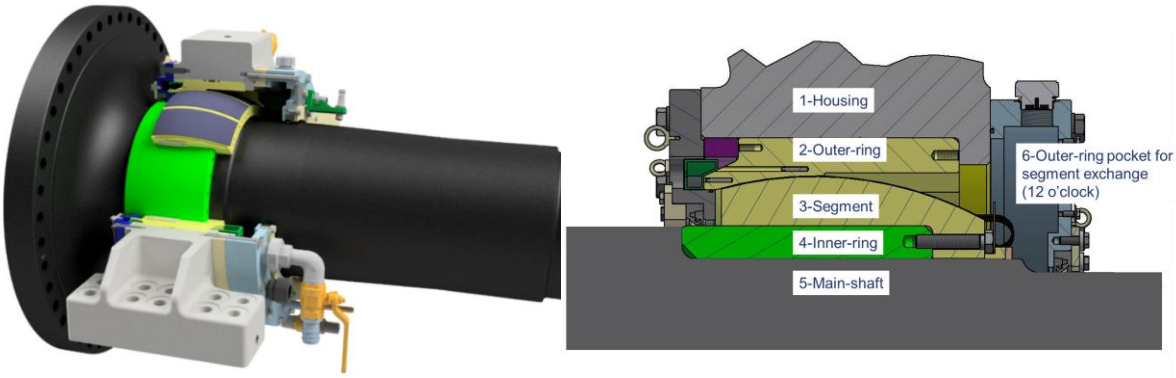

Figure 41: Spherical journal bearing design

The bearing segments (3) are bolted to an inner ring (4) that is fixed to the shaft (5). These segments slide relative to an outer ring (2) that is mounted in the main bearing housing (1). The shape of both contacting surfaces is spherical. Therefore, both axial thrust and radial loads can be supported while the bearing is designed to allow main shaft deformations and tilting. The rotating segments are dipping into an oil sump; thus, lubrication is given for all load situations without additional devices. For maintenance purposes each single segment can be rotated to the unloaded area (12 o'clock position) and replaced through a cut-out in the outer ring (6).

As described in section 2.1 the benefits of all segmented journal bearing solutions are:

- Higher load carrying capability than roller element bearings.
- Easy and fast up-tower inspection and exchange of wear parts.
- Scalability for higher power rating of turbines

The SJB™ solution specifically offers the following additional potentials:

- 1:1 replacement of roller element bearings using existing design space for technology introduction and therefore low risk & cost of change.
- Integration of bearing parts to housing and main shaft.
- Robustness and due to less components lowering the failure probabilities than roller element bearings.
- Reduced wear due to rotating bearing segments
- Easy segment exchange process as the segments can be easily rotated towards service window.

3.2 Toroidal journal bearing

As highly integrated drivetrains become increasingly relevant, Miba identified a journal bearing solution that fits their challenging requirements. This solution provides the benefits and potential as described above. For the main shaft support of such drivetrains a combination of two segmented bearings that are integrated into the main bearing unit are required. By specific combination of the sliding surface shape of each bearing the main shaft run-out requirements coming from the main gearbox can be met. The Miba segmented toroidal bearing solution offers the following capabilities and benefits:

- Adjustable axial, radial and bending load carrying capabilities (see Figure 42)
- Stiffest journal bearing solution that meets the challenging requirements of highly integrated drivetrains.

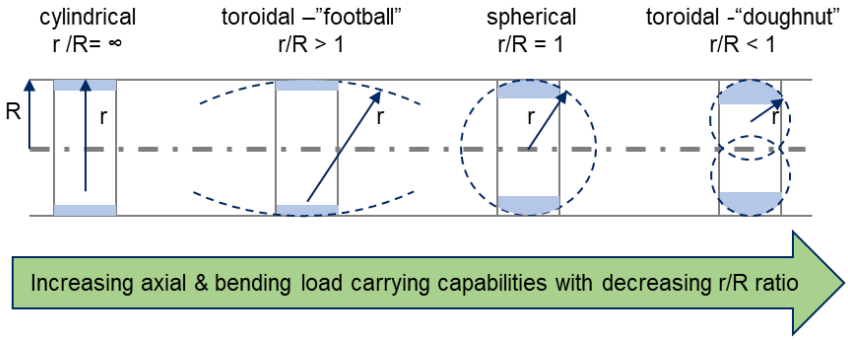

Figure 42: Surface geometry of sliding contact dependent on load carrying requirements

4 Journal bearing qualification

4.1 Test plan derivation

Miba's development process is based on the V-Model approach (see Figure 43). The wind turbine and main bearing requirements were provided by turbine manufacturers and further linked to the

physical structure of the main bearing. Risks to fail were identified and ranked by use of a D-FMEA method in loop. To mitigate the identified risks a verification plan including tests on different abstraction levels and scales was derived. Numerical methods were developed. These methods enable linking of the tests on different scales.

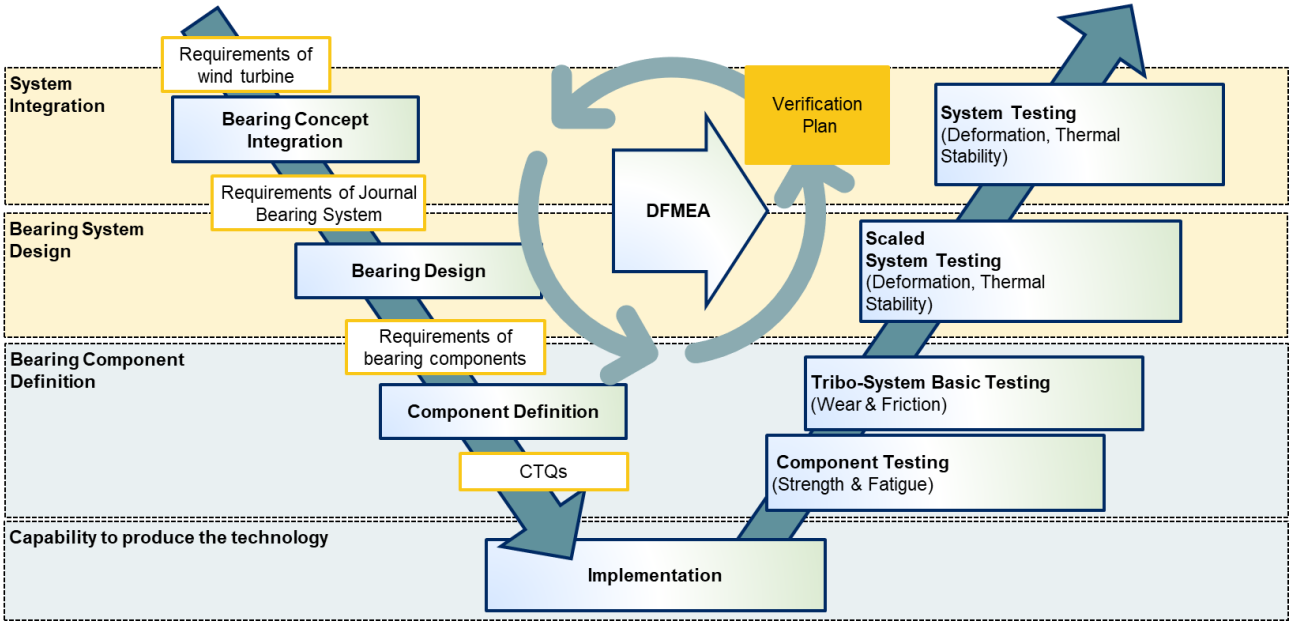

Figure 43: Development process based on V-Model

The tests on all scales and simulations were performed in a loop to improve the bearing design variants thereby establishing a virtually validated development process.

4.2 Journal bearing failure modes

The failure modes of journal bearings differ significantly from those of roller element bearings currently used in wind turbines (see Table 3).

Failure mode	Drivers
Short term seizure	Extreme loads
Thermal instability	All loads during turbine life
Wear	Turbine start & Idling
Static strength	Extreme loads
Fatigue	All loads during turbine life
Failure of surrounding components (e.g. gearbox)	Design incompatibility (e.g. shaft movements)

Table 3: Failure modes of a journal bearing as rotor main bearing of a wind turbine

4.3 Test results

Exemplary test results related to journal bearing development for a 3.5 MW turbine are explained below.

Thermal behavior

Several geometrically scaled system tests (scaling-ratio 1/3) and two real-size system tests per-

formed on a dynamometer provided valuable input for design-, material- & test procedure improvements. Scaled system testing considering all customer load/speed requirements are planned. This final confirmation on real size system test will be completed in April 2025.

Stable thermal system behavior and a strong correlation between bearing load and temperature has been confirmed by scaled system testing (see Figure 44).

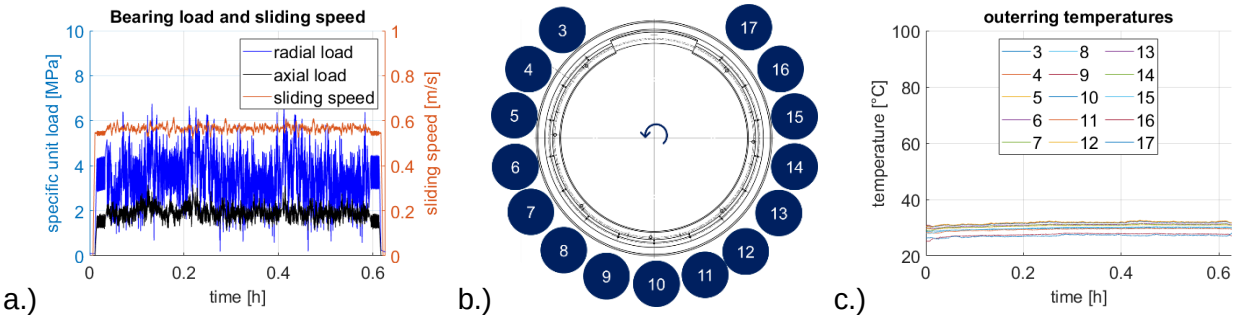

Figure 44: Stable temperature behavior (c.) for highly dynamic energy production load-case at 14m/s wind speed (a) during scaled testing measured at several outer-ring positions (b)

Start and Idling operation behavior

Wear, resulting from mixed friction operation, is one of the lifetimes limiting factors of low speed / high load journal bearings. Existing test results show that at very slow sliding speeds of ~0.03 m/s to ~0.05m/s hydrodynamic operation starts. The derived dynamic friction coefficient μ is ~0.003 (see Figure 45a). Another key aspect is the effect of stillstand time on the break-away behavior of the bearing. Test results show that after ~30 min the static friction coefficient μ_0 stabilizes at a value of ~0.14 (see Figure 45b).

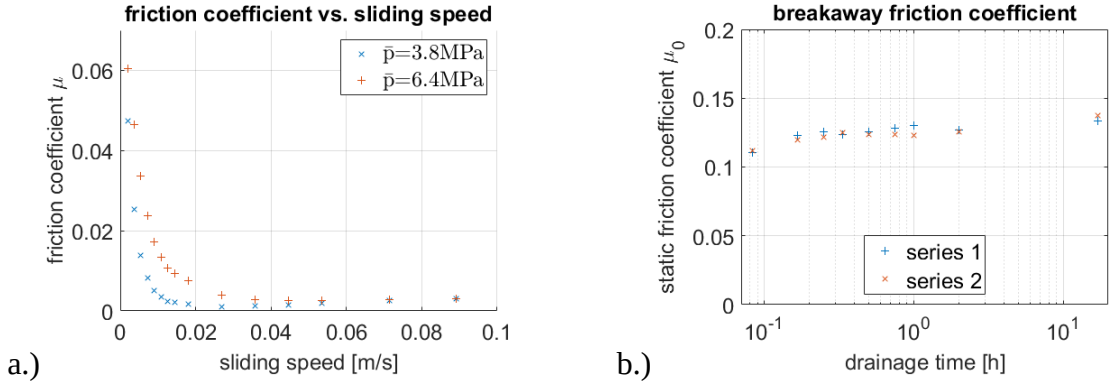

Figure 45: Friction behavior of the bearing identified by scaled system testing.

The local loading of the bearing is calculated using finite element (see Figure 46) and elasto-hydrodynamic multibody simulations. A specific unit load of ~6 MPa results in a local load of ~15MPa

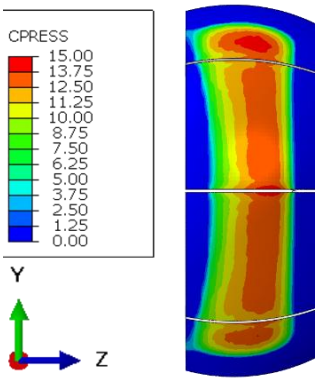

Figure 46: Example pressure distribution for an idling load-case

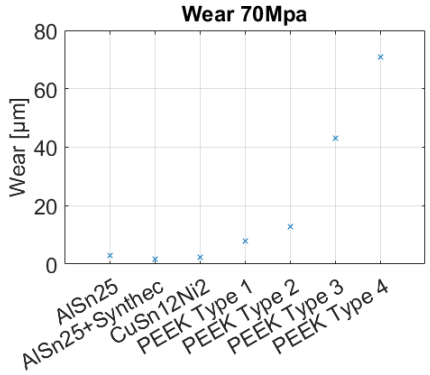

Figure 47: Identified idling wear for different bearing materials on ring on disk at a sliding speed of 0.02 m/s at 70 MPa for 3h.

The wear-stabilization behavior was tested on Miba internal test rigs for relevant idling loads-speeds using Miba standard test specimen. Test results are promising but varying. Therefore, a new test specimen is currently being developed for lifetime wear testing.

Next to that, a comparison of different potential bearing materials has been benchmarked on a ring on disk tribometer (see Figure 47). Combining planetary wind gearbox experience with this benchmark, AlSn25 and CuSn12Ni2 are the most promising bearing materials for the Miba SJB™ solution.

Shaft constraint study for "rotor-side integrated" drivetrains

A numerical investigation to figure out the fit of the toroidal bearing concept for a highly integrated drivetrain was performed. Main shaft runout constraints and relevant load-cases were provided by a turbine manufacturer.

Except for one extreme reverse thrust load case, the bearing met all runout requirements. Even the results for this load case were close to the given boundaries (see Figure 48). A detailed study and development will start in 2025.

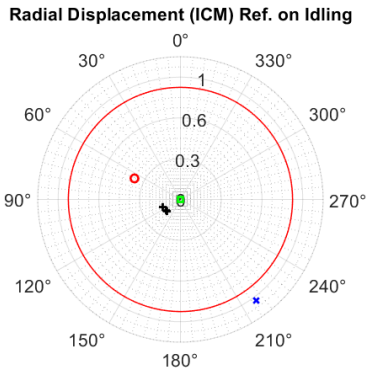

a.)

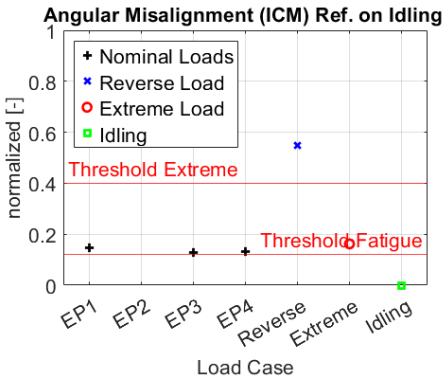

b.)

Figure 48: Normalized radial (a) and angular (b) displacement of generator side reference point relative to the idling position.

5 Conclusion and Outlook

Journal bearings are a promising technology as the main bearing in wind turbine drivetrains.

Investigations on different journal bearing concepts have been performed and the most promising solution identified. Miba's SJB™ is designed to consider current pains and provides benefits that are relevant not only for future drivetrains but also for current or retrofits and future drivetrains. Robustness, power density increase, scalability to higher turbine power classes, up-tower serviceability and lifecycle extension by minimal design changes in existing drivetrains are the main benefits of the solution.

Current qualification status is promising and after the final real size tests in April 2025, field validation tests are planned.

6 Literature references

[SCH18] Schröder, Tim, Hölzl, Johannes, & Rolink, Amadeus; "Innovative Lagerkonzepte und neue Gleitlagerwerkstoffe für den Antriebsstrang von Windenergieanlagen."; In: Schadensmechanismen an Lagern - VDI 2018; https://doi.org/10.18154/RWTH-2019-01707 (2018)

[LAN19] Lang, Jochen; Knoll, G.; Hölzl, Johannes; Schröder, Tim; Bosse, Dennis: "Innovative Bearing Concepts and New Journal Bearing Materials for the Drivetrain of Wind Turbines." In: Abel, Dirk; Brecher, Christian; De Doncker, Rik W.; Hameyer, Kay; Jacobs, Georg; Monti, Antonello; Schröder, Wolfgang; Hirt, Andreas (ed.): Conference for Wind Power Drives, CWD 2019: conference proceedings; Books on Demand, Norderstedt (2019), pages 483-494

[ROL20] Rolink, Amadeus., Schröder, Tim, Jacobs, Georg, Bosse, Dennis, Hölzl, Johannes, & Bergmann, Philipp; "Feasibility study for the use of hydrodynamic journal bearings with balancing support characteristics as main bearing in wind turbines."; In: Journal of Physics: Conference Series, volume 1618, page 052002; https://doi.org/10.1088/1742-6596/1618/5/052002 (2020)

[EPR24] EPRI; "Wind Turbine Main Bearing Reliability Analysis, Operations, and Maintenance Considerations", https://www.epri.com/research/products/000000003002029874 (2024)

[ELI24] Eliane Choquette, "Global Wind Supplier Forecast 2024 to 2034", Brinckmann (2024)

[KOC19] Koch, Thilo; Laabid, Abdelhakim; Hein, Andreas; EP4062078B1 "Lageranordnung und Verfahren zum Montieren einer Solchen" (2019)

[MIB10] Miba Gleitlager Austria GmbH; AT509625B1 „Lagerelement" (2010)

Fluid Film Main Bearings: An Alternative to Roller Bearings

Waukesha Bearings, 1780 Hughes Landing Blvd, Spring, TX 77380

Stefan Haverkamp, Dr. Shravan Janakiraman

Keywords: Fluid Film Bearing as Main Bearing, Uptower Exchangeability

Abstract

Attendees of this presentation will be introduced to fluid film bearing technology, based on tilting pad technology designed using advanced polymer materials, as an alternative solution to the roller main bearing in wind applications. Through basic evaluations and validations, including Stribeck curves, the speed range of mixed friction, and operational/failure modes, we will demonstrate how Waukesha Bearings' fluid film bearings allow uptower exchangeability, increased performance, and lower maintenance requirements.

1 Introduction

Fluid Film Bearings (FFBs) have been used for decades in many applications, typically high-speed turbomachinery. They are also applied in nearly 100% of large marine drivetrains. The larger the drivetrain, the more likely an FFB is integrated. This is mainly because FFBs are more robust, easier to exchange, and can handle a higher capacity.

FFBs are also an established technology in wind turbine gearboxes (GBs). It is almost standard for new GBs applications to have some FFBs, at least in the 1st planetary stage.

In another example, CWD applied an FFB concept (HydRoLa project) through BMWK (Bundesministerium fuer Wirtschaft und Klimaschutz) from 2015 to 2020. They also included a scaled test (1 MW and 3 MW) on the 4 MW test rig at CWD Aachen.

2 Technology

To create a hydrodynamic bearing, main characteristics are mandatory:

- differential speed to load (fixed housing and rotational shaft or rotational housing and fixed shaft)
- Lubricant (e.g. gearbox oil VG 320)
- conus (eccentrical shaft or/and tilting pads)

2.1 Movability of Tilting pads

The degrees of freedom due to the pivots make the pads less sensitive to shaft deflection and are shown in Figure 1.

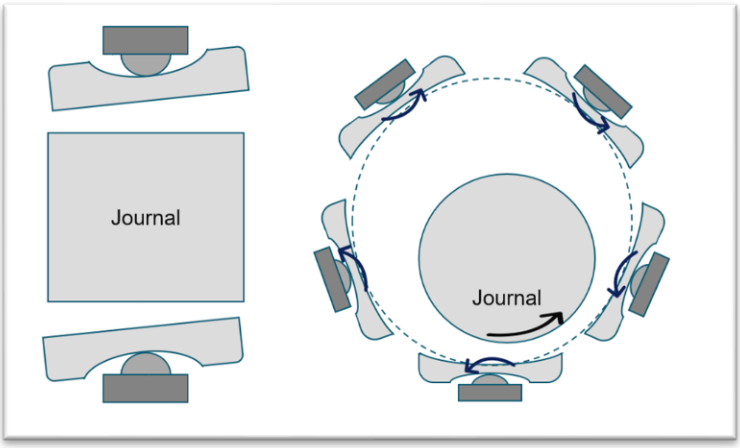

Figure 1: 3D movability of tilting pads due to the pivots

2.2 Design & evaluation

An initial design is developed based on a generic drivetrain concept and load spectra of a typical onshore turbine.

Using iterative loops via the plain bearing calculation, hydrodynamic pressure distribution in the pads, and structural analysis using FEM) and its deformation field, this design is optimized until convergence is achieved. The calculation iteration scheme to evaluate main bearing behavior is shown in Figure 2.

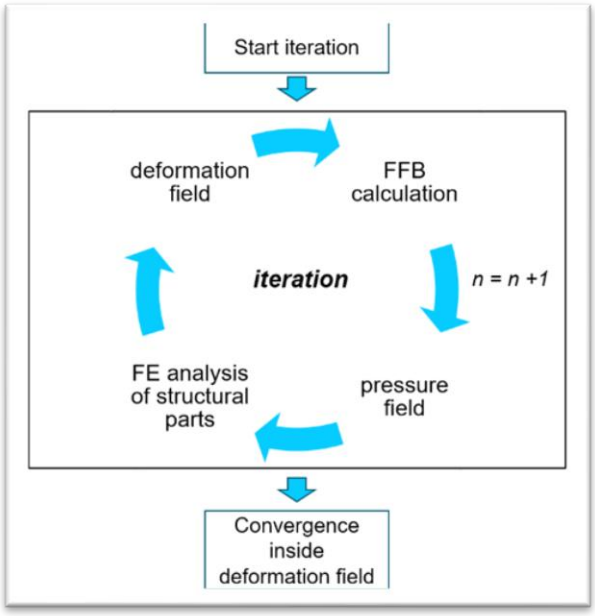

Figure 2: Design evaluation scheme for a FFB in a wind turbine application

2.3 Non-hydrodynamic operational modes

Ideally, the bearing should operate in the hydrodynamic lubrication regime. However, in the low-speed range, such as start-up and low-speed idling, hydrodynamic operation cannot be achieved

without hydrostatic pressure. Here, the bearing will operate in the mixed-friction range, illustrated by the Stribeck curve in Figure 3 [STR01]. It shows that friction in fluid-lubricated applications is a nonlinear function of the contact load, the lubricant viscosity, and the lubricant entrainment speed.

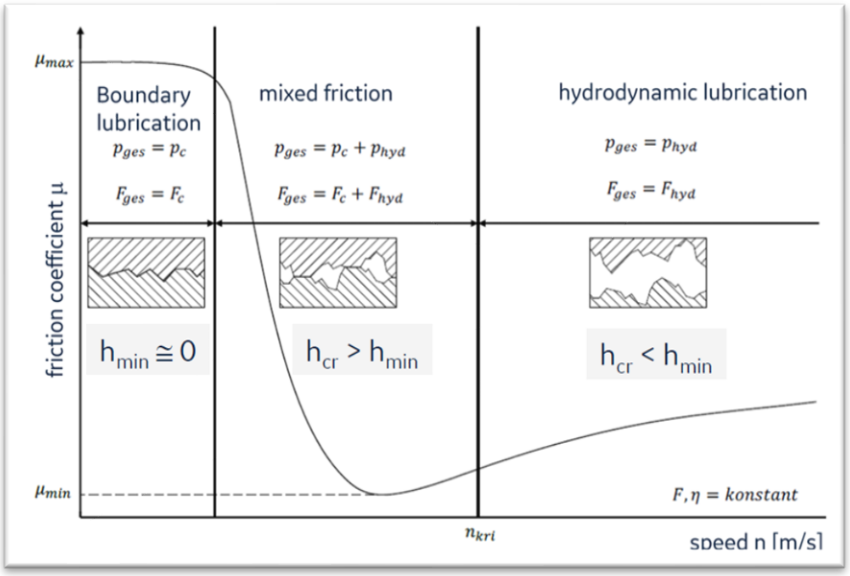

Figure 3: Typical Stribeck curve showing the different regions of operation

Using a specific polymer with high wear resistance and high specific loadi~~ng~~ capacity will minimize the risk of wear due to mixed friction.

2.4 Validation

The validation of the engineered design is performed through model checks, component testing, and subassembly testing. The first level of validation is a model check, where actions and reactions at various locations are checked to ensure model integrity and correct load flow paths.

Next, complete validation tests are performed on a specific wind component test rig “NORBERT”, shown in Figure 4, using representative sizes of pads. At this test rig, a deep dive into journal bearing perspective is performed by running different Stribeck curves, nominal operational modes, and installation modes such as SBI (Single Blade Installation) and other specific failure modes. Breakaway torques at the starting and stopping conditions are also tested by initiating approximately 20 k start-stop cycles and analyzing the wear behavior.

Subassembly testing is planned on the “NAUTILUS” test rig, to validate system level behavior. The NAUTILUS rig has been built and will be commissioned soon.

Figure 4: Waukesha wind component test rig “NORBERT”

2.5 Results

Coefficient of Friction (CoF) tests for varying loads and rotational speeds were performed on the NORBERT rig. The aim of these tests was to determine the impact of speed and load on the lubrication regime the bearing operates in. Based on these results, the transition point from mixed friction into hydrodynamic lubrication can be determined. Some selected results are presented below.

Figure 5 shows the measured CoF vs rotational speed at a constant load, corresponding to a nominal pressure of 16 MPa. The results follow typical Stribeck curve behavior, where an increase in speed leads to the bearing operating in a hydrodynamic regime (low CoF). This is an important indication of the suitability of polymer-lined tilting pads for wind turbine main bearing applications.

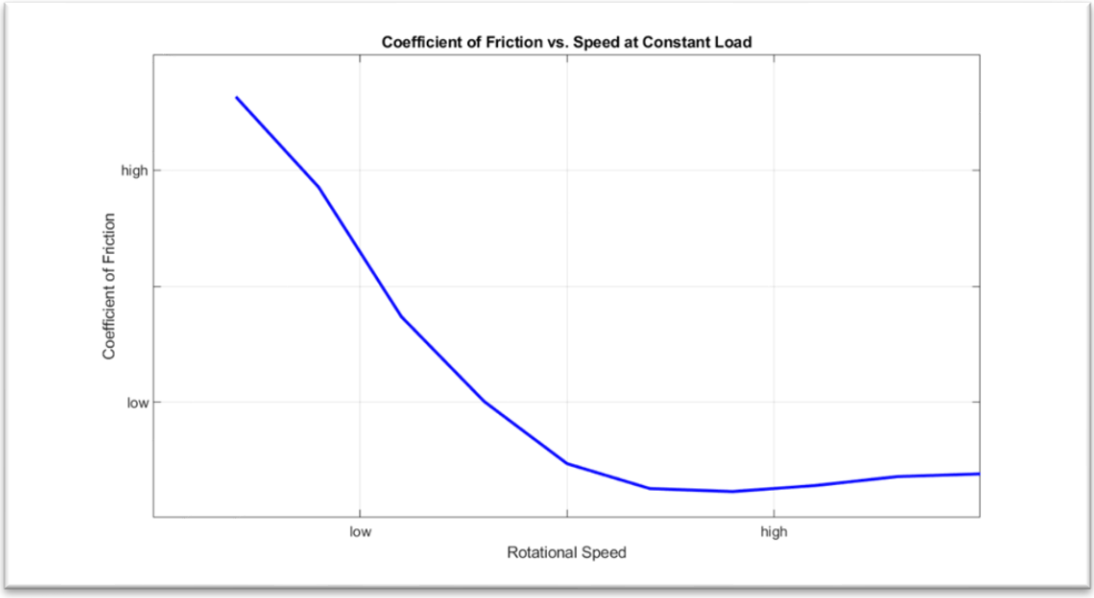

Figure 5: Measured CoF vs Rotational speed result obtained by NORBERT testing

In Figure 6, the shaft rotational speed is kept constant, and the load is varied. The result is as expected. At lower loads with a larger minimum film height, higher CoFs are observed than at higher

loads. This is due to the greater volume of oil being displaced through the bearing, creating greater internal friction within the oil.

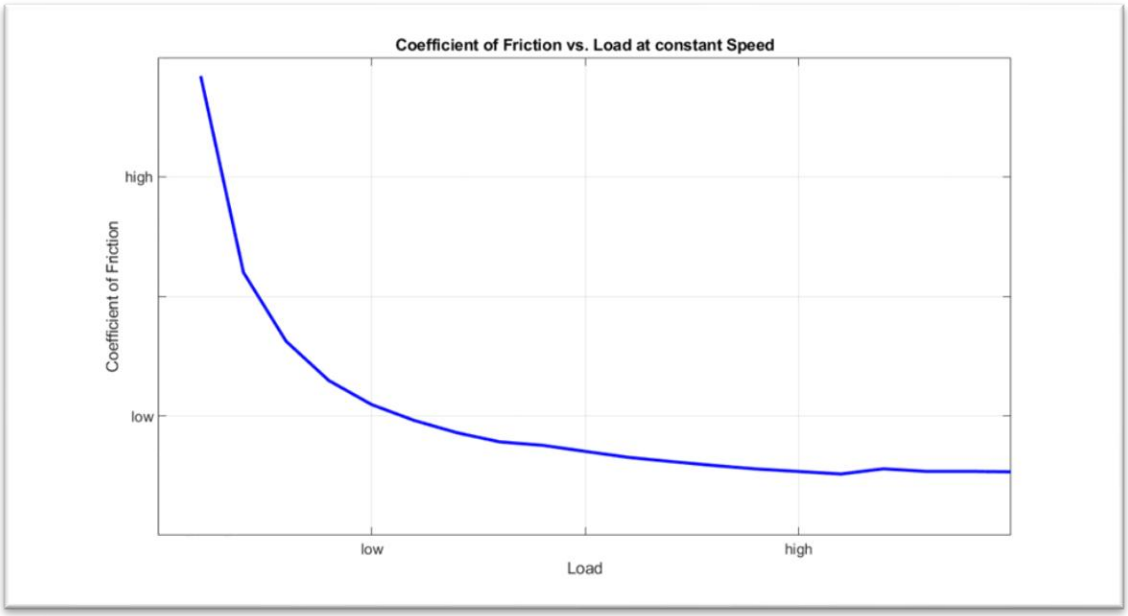

Figure 6: Measured CoF vs load result obtained by NORBERT testing

Figure 7 shows the measured breakaway torque obtained by conducting start-up tests on the NORBERT rig. On the horizontal axis the time is shown and on the vertical axis the measured torque. Once the system is set into motion, the torque values stabilize at lower values, demonstrating typical behavior.

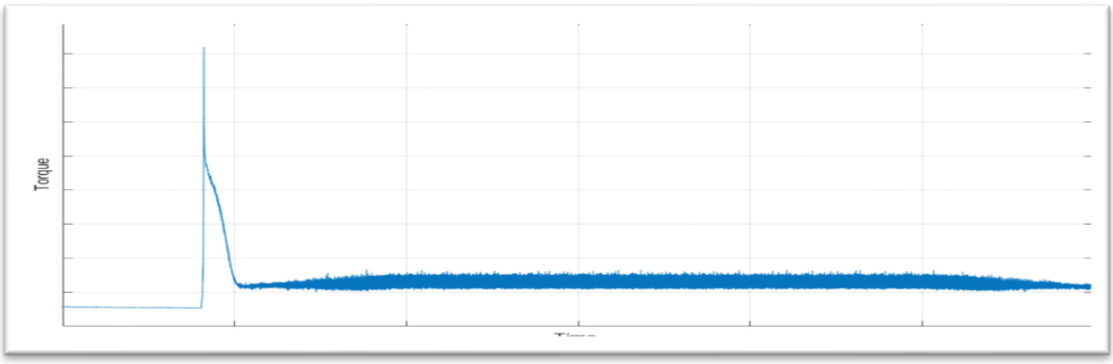

Figure 7: Breakaway torque obtained by NORBERT testing

Based on selected test results shown above, as well as tests conducted to simulate other wind turbine operating conditions, Waukesha Bearings has successfully demonstrated, at a component level, the capability of its polymer-lined tilting pads to function as load-carrying members in a wind turbine main bearing.

3 The Waukesha Bearing Concept for Main Bearing

Using the FFB tilting pad technology allows the bearing to be less sensitive to shaft movements and deflections. These modules, arranged for a specific bearing based on a given drivetrain concept, provide a high level of flexibility to meet any specific demand, including uptower exchangeability.

The combination of radial and axial pads with pivots leads to a complete bearing and is illustrated in Figure 8.

Figure 8: Waukesha Bearing's wind Main Bearing concept

Key Design Features:

- Radial tilting pad bearing – modular in design and exchangeable without a high crane.
- Axial tilting pad bearing – modular in design and exchangeable without a high crane.
- Journal surfaces = polymer-lined
- Full hydrodynamic at > 0.0x m/s rotational shaft speed
- Oil Lubricated – ISO VG 320 (Oil used in GBs)
- Shaft arithmetic average roughness Ra <= 1.6 µm

3.1 Uptower exchangeability - Example

A strong focus is placed on creating an uptower exchange without the demand for a large crane. This is one of the major advantages of using a tilting pad FFB compared to roller bearings.

Considering the environment around the bearing and using single pads as separate modules integrated into bearing housing, opens doors for various customer-specific solutions. An example of Waukesha Bearings' radial pad exchangeability solution is shown in Figure 9.

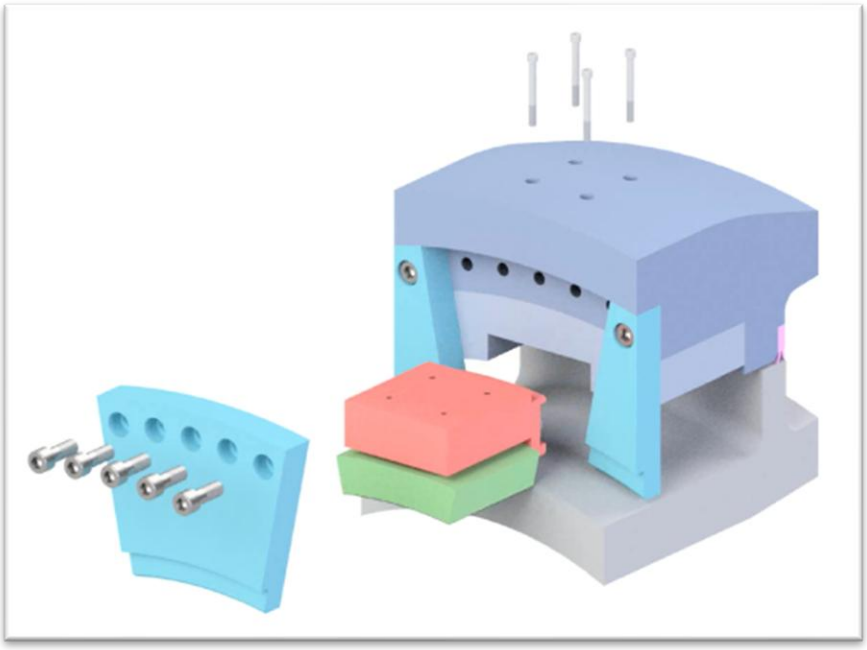

Figure 9: Example for Waukesha Bearing's wind radial pad exchangeability

The following table headlines the main benefits of FFBs over roller bearings.

Item	Roller Bearing	Plain Bearing	Benefit of Plain Bearing
Lifetime	Limited lifetime given by L_{10h}	Endless lifetime	Endless lifetime
Load Capacity	Line or dot contact (Hertzian pressure) limits loading	Area contact enlarged for higher load capacity	More robust at same diameter
Sensitivity to wear	Min. oil film thickness at 1µm or smaller. Small wear affects lifetime	Min oil film thickness at 5-10 µm. Small wear has no effect to lifetime	Less sensitive to wear
In case of damage	Main shaft to be disassembled – jack up vessel required	Easy exchangeability of single pads – No jack up vessel support needed	**No jack up vessel needed** to exchange a Main Bearing Uptower **Less downtime** ➔ less OPEX
Maintenance	Grease impact by wear to be replaced and bearing to be flushed	Known bypass filtration similar like gearbox lubrication	Improved oil lubrication

Table 1: Benefits of FFBs over roller bearings

Given the actual discussions about the main bearing failure rates with roller bearings, the opportunity for an uptower exchange is of high interest. For offshore turbines with high jack-up vessel costs, pad exchangeability would especially show a significant OPEX advantage.

Considering the latest report by NREL [NRL01] "Main Bearing Replacement and Damage – A Field Data Study on 15 GW of Wind Energy Capacity", failure rates of 10% or more are common.

3.2 Outlook

The FFB technology is feasible in keeping similar dimensions like a roller bearing. However, an axial thrust collar is needed at the shaft to cover axial loads.

There are two ways to accomplish this:

1. Directly Integrated in the structure (combined design with OEM)
2. A radial housing (additional split line) and a connected axial pad housing.

4 Summary and Conclusion

Fluid film bearings offer a variety of advantages for wind turbine main bearings, including reduced failure rates, unlimited bearing lifetime, low sensitivity to wear and limited maintenance required. Our modular design can scale up to fit larger wind turbines, resulting in cost savings. The optimized pad shape easily integrates into the nacelle and provides advanced bearing performance within a broad range of operating conditions, including assembly, low speed/idling and extreme events.

5 Bibliography

[NRL01] Edward Hart, Kaiya Raby, Jonathan Keller, Shawn Sheng, Hui Long, James Carrol, James Brasseur and Fraser Tough

Main Bearing Replacement and Damage – A Field Data Study on 15 Gigawatts of Wind Energy Capacity

Technical Report: NREL/TP-5000-86228

NREL, US, July 2023

[STR01] Stribeck Curve

Address of the website (Stribeck curve - Wikipedia)

(2025-01-06)

Main Bearing II: Roller Bearing

Wind Main Shaft Roller Bearing Release Test for 25 MW Turbines

Philipp Kirchner[1], Dominik Fritz[1], Jesko-Henning Tanke[1], Jürgen Reichert[1]

[1]SKF GmbH, Gunnar-Wester-Straße 12, 97421 Schweinfurt - Germany

Keywords: Release test, full-scale testing, validation, 25 MW wind turbine, large size bearing, tapered roller bearing, main shaft, sensor technology, advanced condition monitoring, segmented single pocket cage, ring creep

Abstract: The focus on cost efficiency in the wind industry leads to an additional increase in both size and power density of future turbines. SKF is already testing main shaft bearings for 25 MW turbines, which could require bearing diameters of 4 m. With increasing dimensions of bearing outer and inner geometry, new effects related to kinematics arise, strongly influenced by roller masses and inertia. A comprehensive validation of new bearing designs is an essential part of the product development process. Therefore, the new SKF test strategy employs unique monitoring technologies to gain unparalleled insights into cage loads and bearing kinematics. The commonly used validation process by “survival” is herewith supplemented by an extensive validation through direct measurements of key characteristics, that provides a strong contribution to make wind turbine design processes faster and more reliable. The evaluation of sensor data during the test accelerates the development phase and improves the accuracy of simulation models through a direct comparison of calculated and measured loads and deformations.

1 Introduction and market trends

The offshore wind energy sector has experienced remarkable growth over the past two decades, establishing itself as a critical component of the global renewable energy landscape. By the end of 2023, the global offshore wind capacity reached 75 GW with approximately 11 GW being added in 2023 [WIL24]. This growth is expected to continue exponentially, with projections indicating that the total offshore wind capacity could reach 486 GW by the end of 2033, driven by increasing installations and supportive political frameworks [WIL24]. One key factor, that has been influencing the historic market development of the offshore wind energy sector and that will continue to contribute to the future capacity expansion, is the strong focus on cost efficiency to reduce the levelized cost of electricity (LCOE) [SHI21]. Figure 49 illustrates the decrease of the global weighted average LCOE of offshore wind turbines from 2010 to 2023 and highlights the reduction of more than 50 % over the last decade [FER24]. This decline has been realized through increasing power densities, that allow the construction of bigger and more efficient turbines due to the overall optimization of nacelle masses [HAY18]. The trend of growing turbine size and power output can be observed in the size progression of installed prototype turbines and is expected to continue in the future [MCC24]. Figure 49 shows the development of the maximum power rating of the deployed wind turbine prototypes per year since 2002, covering also planned projects for 2025. Especially the last decade shows significant growth, as the power output of installed prototype turbines has more than doubled from 8 MW in 2014 to 20 MW in 2024 [MCC24, JEN24]. Recent publications regarding new size records of up to 26 MW also indicate the continuation of the turbine growth in the future [JEN24].

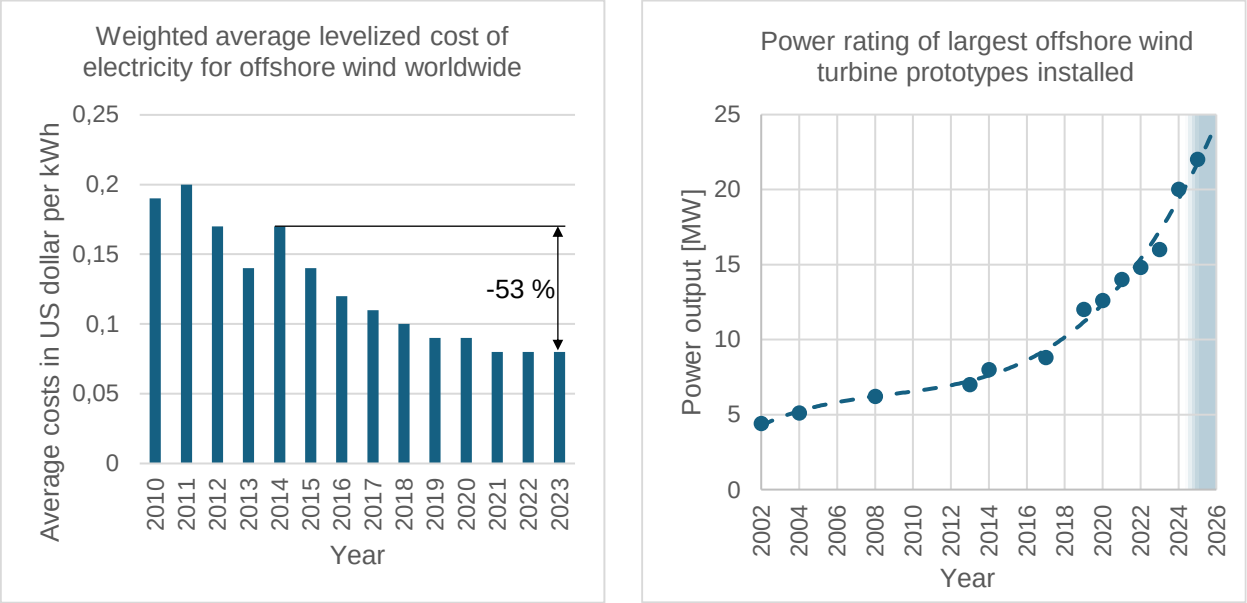

Figure 49: Left: LCOE decrease over time [FER24]; Right: Development of the power rating of offshore prototype turbines over time [MCC24, DUR23]

However, the development of turbines beyond 25 MW with increased power densities and lightweight drive trains results in higher loading of the components as well as the surrounding structures and introduces new challenges for the complete turbine system including the main shaft bearings. SKF internal studies show that cross-located tapered roller bearings (TRBs) are a successful solution to combine the lightweight design approach with the necessary load carrying capacity. To keep the outer bearing diameter in the 4 m range and to achieve the required load rating, the roller masses will disproportionally increase. Due to the larger roller sizes, new effects related to kinematics arise, that influence the cage design. Growing roller sizes and bearing loads combined with a reduced relative system stiffness of the drive train resulting from the lightweight design approach can also create significant ring creep.

SKF has performed a test campaign to address the mentioned topics, as these risks need to be evaluated, estimated and measured to ensure robust field performance of the bearings. Masses and inertia cannot be properly replicated in a scaled down test, because they increase at a cubic rate while length and diameters grow linearly. A full-scale test has been performed to obtain the realistic interaction between these effects. A comprehensive validation of new bearing designs is an essential part of the product development process. Therefore, the used test strategy employs specifically developed monitoring technologies to quantitatively measure cage loads and bearing kinematics as well as micro and macro movement of the components during ring creep. The commonly used validation process by “survival” is herewith supplemented by an extensive validation through direct measurements of key characteristics.

This paper presents the test setup, employed sensor systems and test strategy in chapter 2. Section 3 deals with the validation process for segmented single pocket cages and chapter 4 focuses on the investigation of ring creep. A summary and conclusion close the paper in section 5.

2 Test campaign

The test campaign has been performed in the SKF Sven Wingquist Test Centre in Schweinfurt, that contains several test rigs for different bearing sizes (up to 6 m outside diameter), applications (wind,

metals, pulp and paper, etc.) and test objectives (life-, functional-, failure mode-, lubrication testing, etc.).

2.1 Test setup

The left image in Figure 50 shows the main shaft test rig (MSTR) with the test setup highlighted in red. The MSTR is one of the world's most powerful test rigs for wind turbine main shaft bearings and can replicate realistic application loads from normal operating conditions up to extreme loads and dynamics. It can be used for the validation and development of single wind main shaft bearings and full wind main shaft arrangements. Radial and axial loads of up to 8 MN and bending moments of up to 40 MNm can be applied. The function of the MSTR can be described as a rotor simulator. By combining loads and moments, the hydraulic load unit can simulate all realistic stationary and dynamic load scenarios for the main shaft bearings.

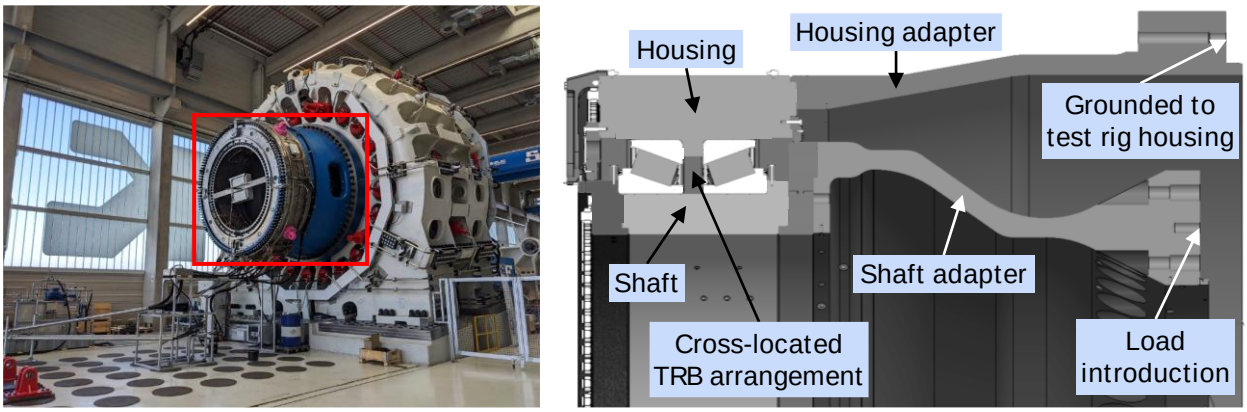

Figure 50: Main shaft test rig and cross section of the test setup

The right image in Figure 50 contains a cross-sectional view of the test setup highlighted in red. The hydraulic load unit is connected to the shaft via the shaft adapter and introduces the loads into the bearing arrangement. Housing and housing adapter subsequently transfer these loads back to the test rig housing. With this test setup, also highly accelerated life tests (HALT) can be performed, that would not be possible with series or prototype drive trains, as they are not designed to continuously operate at extreme load levels. The test specimen are two identical tapered roller bearings with segmented single pocket cages in a back-to-back arrangement. Their inner bearing geometry is based on an SKF internal study regarding main shaft bearings for 25 MW turbines and results in roller masses of 20 kg each, summing up to a total roller set mass of approximately 1500 kg. Oil lubrication has been selected to precisely regulate the lubrication conditions and to control the bearing temperature. Thus, the test bearings can be lubricated to the optimal level, but also varying conditions can be applied to analyse critical situations, e.g. starved lubrication. As the investigation of ring creep is a key objective of the test campaign, housing and shaft have been designed with specifically defined component stiffness, which allows the quantitative evaluation of the creep behaviour at different load levels. Shaft and housing are made from cast iron to resemble the materials used in real wind turbines and to replicate the identical tribological conditions in the bearing seats.

2.2 Sensor systems and test strategy

The test setup is equipped with an array of sensor systems designed to measure key parameters critical to the evaluation of bearing performance. Standard test rig sensors include, for example, the measurement of the temperature distribution, vibration measurement and bearing wear detection

through online lubricant investigation. Both bearings contain sensor rollers to monitor roller load and roller rotational speed as well as load zone size, orientation and shape. Additionally, special sensor systems are integrated into the setup to provide further insights into bearing kinematics, cage performance and ring creep. These comprise sensors for the measurement of the axial roller position and roller skew around the radial axis. Cage behaviour is quantified through the measurement of cage position and deformation. A calibration of the cage sensors allows to transform local cage strain to external cage loads, thereby enabling the real-time measurement of cage loads with high accuracy. The time-resolution of the measurement system is sufficient to observe a continuous load curve, not only for static load situations, but also during all dynamic loading events. Furthermore, ring creep is monitored by tracking the circumferential position of all four rings. Through the absolute encoding of the ring positions in relation to their seats down to 1 µm, micro and macro movements can be detected (see chapter 4).

A significant feature of this sensor setup is the live transmission of the measurement data, to continuously evaluate the response of the system to individual load scenarios. This enables the allocation of key parameters like cage loads or ring creep rate directly to specific load cases. Therefore, the planned test program can be adapted to focus on the most relevant aspects. By providing quantitative results, the validation of the bearing components is achieved not only through survival under test conditions but also through precise measurements of their behaviour. This approach ensures a thorough understanding of component performance. In addition to this, the real-time measurements can be compared with simulation results in parallel to the test campaign, to improve the simulation accuracy and reliability.

3 Segmented single pocket polymer cages

Segmented polymer cages have been used in double row TRBs (SKF Nautilus™ bearings) as well as in single row TRBs for over 20 years and offer advantages over one-piece cage solutions by decoupling the rolling elements. For one-piece cages, the varying kinematic behaviour of even single rolling elements, e.g. through the acceleration or deceleration during dynamic load changes, can lead to constraint forces and increased cage loads. The decoupling effect of the single pocket segments reduces the forces acting on the cage as only the neighbouring rollers are exerting compressive forces influencing the cage load and not the complete roller set. The presented test campaign is used to evaluate the performance of the design evolution of single pocket cage segments for roller masses up to 20 kg and to validate it by a combined approach of simulation methods, validation of relevant load levels in full-size bearing operation and static and fatigue load testing on cage components.

In a first step, dynamic multibody simulations of a bearing including the cage in operation are performed by an SKF internal bearing simulation tool (“BEAST”) to identify critical load cases for the cage (see Figure 51). It is important to note, that extreme load cases for the bearing, e.g. having maximum stresses in the roller-raceway contacts, are not necessarily extreme load cases for the cage. Cage loads must be observed especially during dynamic changes of load zones. One output from the BEAST simulations are relevant load levels on the cage, that happen in bearing operation. Through the comparison of simulation results and directly measured cage deformation, the load cases identified as critical by BEAST simulations, as well as the multibody simulation itself are validated. Herewith, realistic and relevant load scenarios for the segmented single pocket polymer cage are determined. In a second step, the strain measurements are used to validate a finite element model of the cage for determining the maximum cage stresses in operation.

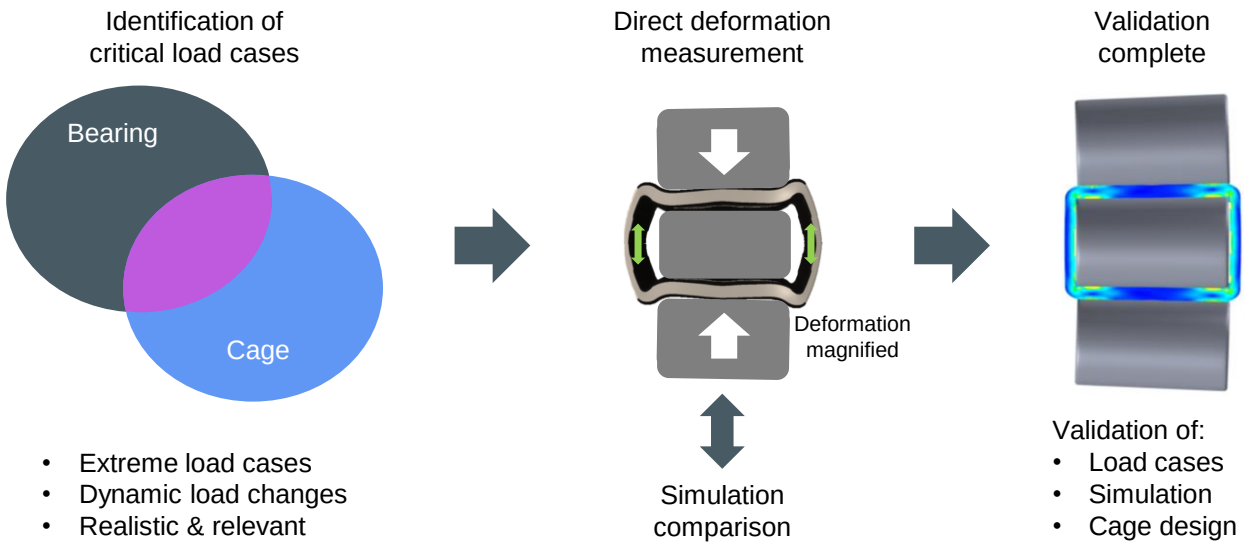

Figure 51: Validation process for the segmented single pocket cages

By additional component testing static and fatigue safety have been evaluated. The component test setup principle is replicated in the finite element model (see Figure 51). It contains a cage with encapsulated roller and neighbouring rollers above and below the investigated cage segment. With this setup the cage segment can be loaded by either a static force or by an oscillating load with defined frequency and maximum force amplitude. The maximum stress values respectively stress cycles are then used to determine safety against the static and fatigue loading. Fatigue testing has been performed at a load level approximately two times higher than the maximum measured cage load during extreme load situations. After more than 10^7 cycles, the component test has been stopped and no signs for crack initiation or loss of structural integrity have been found.

4 Ring creep investigation

Ring creep refers to the stepwise relative movements that occur in bearing seats. This phenomenon can be attributed to two primary mechanisms: rolling element-induced ring creep and structure-induced ring creep. Rolling element-induced ring creep arises from local strain patterns in the ring seating, which are caused by the loaded rolling elements. In contrast, structure-induced ring creep results from housing or shaft deformations due to external forces exerted by the adjacent constructions [LED25]. The extent of these deformations plays a crucial role in the severity of structure-induced ring creep, as larger deformations can increase the relative movements between inner ring and shaft respectively outer ring and housing [MAI17]. Therefore, future wind turbines are particularly sensitive to structure-induced ring creep, due to the relatively low system stiffness of lightweight drivetrains combined with higher bearing loads resulting from increasing power densities. The occurrence of ring creep can lead to significant issues such as fretting corrosion and abrasive wear. These effects can cause bearing damage and eventually system failures. Consequently, the investigation of ring creep in wind turbine applications is essential to ensure the design of robust systems.

As mentioned in section 2.1, the test setup has been designed to facilitate the generation of ring creep through a defined stiffness of shaft and housing. The dynamic capabilities of the test rig enable the investigation of structure-induced inner ring as well as outer ring creep. Figure 52 shows the ring creep measurement of an inner ring during an example load case with a stationary load zone. The left diagram illustrates the tangential macro movement of the ring in relation to the shaft of

1100 mm over the time span of five hours. The right graph in Figure 52 contains an enlarged view of the ring movement and spans approximately eight inner ring rotations. A repetitive pattern can be observed, that repeats itself after each rotation. The movement consists of forward and backward rotation components, resulting in a tangential displacement of 400 µm per revolution (observed at a fixed shaft position), defined in this study as creep rate.

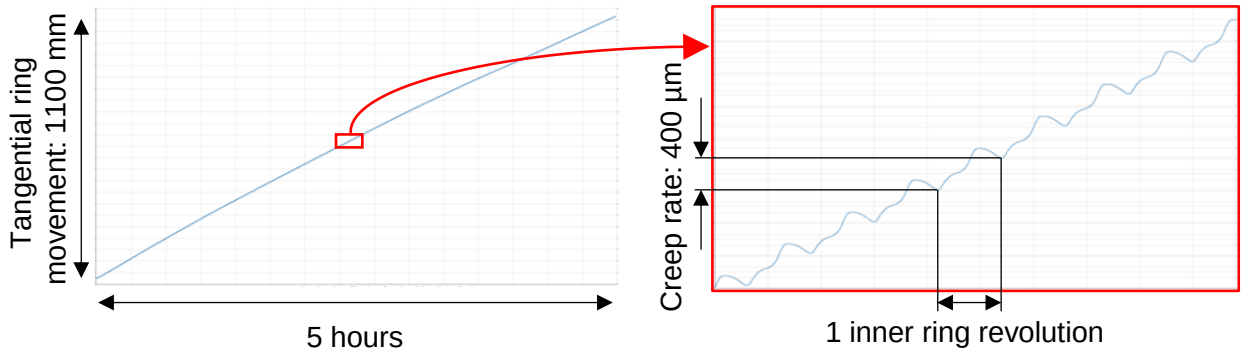

Figure 52: Tangential ring creep: Macro and micro movement of an inner ring

Over the five-hour time span covered by the left diagram in Figure 52, the load case has remained constant. Thus, the constant creep rate and slope of the curve suggest a stable creep behaviour. However, during testing of different load cases, variations in the ring creep behaviour could be detected. The left graph in Figure 53 covers the tangential inner ring movement during a different stationary load case, that also was unmodified for a duration of five hours. The slope of the curve of the ring position decreases over time, as the creep rate is reduced until it stops after approximately one hour. An oscillating movement of the inner ring with a cyclic range between 80 µm and 100 µm can still be measured and persists until the end of the load case. The observed phenomenon of increasing resistance to ring creep is caused by the so-called training effect in the frictional contacts [AUL08].

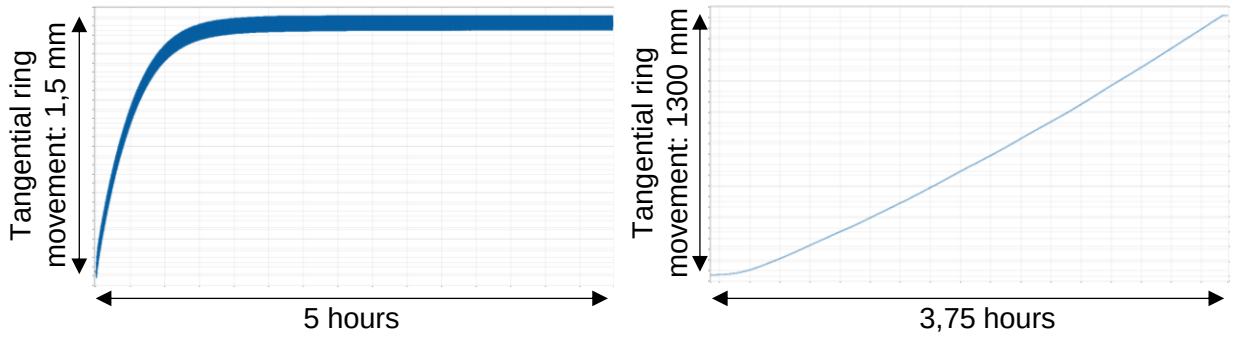

Figure 53: Training effect build up and reduction

The graph on the right in Figure 53 illustrates the influence of changing load scenarios on ring creep behaviour. The load case from the left diagram was modified to alter the load zone size while maintaining an almost identical load level. The maximum contact pressure in the roller raceway contact varies by approximately 80 MPa, from 1400 MPa to 1480 MPa. The graph displays a tangential movement of 1300 mm in less than four hours, compared to 1,5 mm in five hours. Throughout the testing of the altered load case, the creep rate increased from around 20 µm per inner ring revolution

to approximately 500 µm. The ring creep measurements during two example load cases demonstrate the existence of a training effect. However, they also show that this effect can be mitigated through load changes, resulting in a reset of the creep behaviour.

5 Summary and conclusion

The analysis of offshore wind turbine market trends shows a significant growth of turbine sizes and power ratings over the past two decades. To further reduce the LCOE of offshore wind power, this evolution will continue in the future. However, the development of turbines beyond 25 MW will introduce new challenges for the whole turbine system, including the main shaft bearings due to increased power densities and flexible surrounding structures. To address these challenges, SKF conducted a full-scale test campaign to validate new bearing designs with roller masses of around 20 kg. The test strategy employed specifically developed monitoring technologies to quantitatively measure cage loads, bearing kinematics and ring creep behaviour. A segmented single pocket polymer cage solution is validated through the measurement of cage loads in operation. Based on system tests, component tests and simulation results, static as well as fatigue safety factors have been calculated. The investigation of ring creep quantifies the micro movement behaviour on a micron resolution for various load situations. It was confirmed that under certain conditions, the training effect can reduce and stop ring creep, but load changes can again reset this effect, re-initiating creep behaviour.

In conclusion, the test campaign demonstrated the feasibility of cross-located TRBs as main shaft bearings for 25 MW turbines and beyond. The direct measurement of key characteristics like cage loads and ring creep behaviour supplements the traditional validation process by “survival" and provides a strong contribution to make wind turbine design processes faster and more reliable. The findings of the test underline the remarkable performance of segmented single pocket polymer cages in wind turbine main shaft bearings. Due to the decoupling of rolling elements, cage loads can be reduced in relation to a one-piece cage solution, especially with increasing roller masses and drive train deformations. Furthermore, the obtained understanding of ring creep mechanisms allows SKF to assess the risk of individual turbines towards ring creep and enables the optimization of the main shaft system together with wind OEMs. The evaluation of sensor data during the test accelerates the development phase and improves the accuracy of simulation models through a direct comparison of calculated and measured loads and deformations.

6 Bibliography

[AUL08] Aul, Eduard; Walther, Volkhard: Wandernde Wälzlager-Innen- und Außenringe unter verschiedenen Einsatzbedingungen (FVA 479 I; Heft Nr. 852)

Forschungsvereinigung Antriebstechnik e.V., Frankfurt a. M., 2008

[DUR23] Durakovic, Adnan: 22 MW Offshore Wind Turbine in the Works for 2024/25

https://www.offshorewind.biz/2023/10/23/22-mw-offshore-wind-turbine-in-the-works-for-2024-25/

10.01.2025

[FER24] Fernández, Lucía: Weighted average levelized cost of electricity for offshore wind worldwide from 2010 to 2023

https://www.statista.com/statistics/1027721/weighted-average-lcoe-of-offshore-wind-worldwide/

10.01.2025

[HAY18] Hayes, Austin; Sethuraman, Latha; Dykes, Katherine; Fingersh, Lee Jay: Structural Optimization of a Direct-Drive Wind Turbine Generator Inspired by Additive Manufacturing

In: Procedia Manufacturing, Volume 26, 740 – 752

Elsevier B. V., Amsterdam, 2018

[JEN24] Jenkinson, Orlando: Mingyang claims 'world's largest' for new offshore wind turbine prototype

https://www.windpowermonthly.com/article/1886646/mingyang-claims-worlds-largest-new-offshore-wind-turbine-prototype

10.01.2025

[JEN24] Jenkinson, Orlando: China's Dongfang unveils world-leading 26MW offshore wind turbine

https://www.windpowermonthly.com/article/1892065/chinas-dongfang-unveils-world-leading-26mw-offshore-wind-turbine

10.01.2025

[LED25] Le Duc, Loc; Zimmermann, Markus: Einfluss der Nachgiebigkeit von Lagergehäuse und deren Anschlusskonstruktion auf das Wanderverhalten von Wälzlagern (Vorläufiger Abschlussbericht FVA 479 IX)

Forschungsvereinigung Antriebstechnik e.V., Frankfurt a. M., 2025

[MAI17] Maiwald, Andreas: Besondere Wanderphänomene in Wälzlagersitzen von Planetengetrieben im Industrie- und Windkraftbereich – Untersuchungen zum Einfluss von Gehäuseverformungen auf irreversible Schlupfbewegungen im Lagersitz

In: Gleit- und Wälzlagerungen 2017, VDI-Berichte 2308, 273-282

VDI Verlag, Düsseldorf, 2017

[MCC24] McCoy, Angel; Musial, Walter; Hammond, Rob; Mulas Hernando, Daniel; Duffy, Patrick; Beiter, Philipp; Pérez, Paula; Baranowski, Ruth; Reber, Gage; Spitsen, Paul: Offshore Wind Market Report: 2024 Edition

National Renewable Energy Laboratory, Golden CO, 2024

[SHI21] Shields, Matt; Beiter, Philipp; Nunemaker, Jake; Cooperman, Aubryn; Duffy, Patrick: Impacts of turbine and plant upsizing on the levelized cost of energy for offshore wind

In: Applied Energy, Volume 298

Elsevier Ltd., Amsterdam, 2021

[WIL24] Williams, Rebecca; Zhao, Feng: Global Offshore Wind Report 2024

Global Wind Energy Council, Brussels, 2024

Simulation-based damage analysis of main bearings in wind energy application

Patrick Wingertszahn[1], Jonathan Müller[1], Oliver Koch[1]

[1] Chair of Machine Elements, Gears, and Tribology (MEGT), RPTU Kaiserslautern-Landau, Gottlieb-Daimler-Str., 67663 Kaiserslautern, Germany

Keywords: Wind application, Renewable energy, Rolling Bearings, Bearing Simulation, Damage Prediction, Dynamic Simulation, Damage Analysis

Abstract: In the global persuit for sustainable energy, wind energy is at the forefront as a key renewable resource. The quest for greater efficiency remains at the forefront of wind turbines. Innovations in drive technology have enabled higher energy capture rates and optimization of turbine performance. As a result, bearing requirements are also increasing. The main bearings in particular must support ever greater and, above all, dynamic loads as rotor diameters increase. This presentation will highlight the latest advances in the development of simulation tools at MEGT and their use in the design of rolling bearings in wind applications. A case study will demonstrate the incorporation of environmental factors. The influence of operational conditions on load distribution, and fatigue life of main bearings under varying wind conditions will be shown. The presentation will demonstrate how this advanced simulation tool empowers engineers to iteratively refine main bearing designs, leading to improved efficiency, reduced downtime, and extended operational lifespan of wind energy plants.

1 Introduction

Wind energy plays a crucial role in the transition toward renewable energy sources. As wind turbines increase in size to harness more energy, the mechanical components, particularly main bearings, are subjected to higher dynamic loads. These components must withstand complex loading conditions due to fluctuating wind speeds, operational variations, and environmental factors. The reliability of main bearings is essential for minimizing downtime, reducing maintenance costs, and improving turbine efficiency [She13].

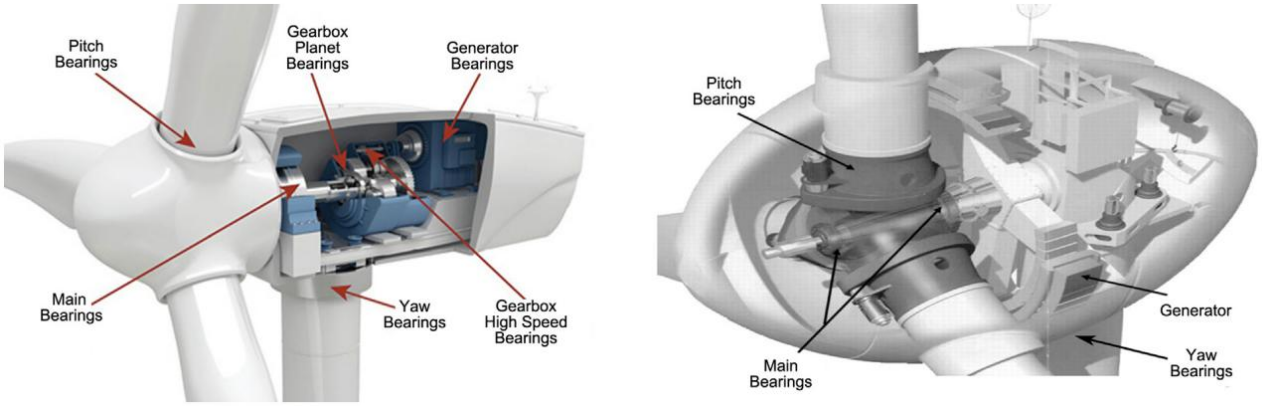

Figure 54: Wind turbine configuration (left) gearbox operated wind turbine [Fie16] and (richgt) direct-drive wind turbine [Oya09].

Due to increasing cost pressure, wind turbine manufacturers are increasingly demanding more extensive calculations in addition to the established standards IEC ISO/TS 16281 [ISO08], ISO 76 [ISO17] and ISO 281 [ISO07]. The standards require verification for a large number of load situations. The verifications must be provided for all components. This study demonstrates the benefits of dynamic models for advanced damage prediction and detection, using the example of the main bearing of a wind turbine with gearbox. A double-row tapered roller bearing such as that used in Figure 54 as the main bearing in gearbox operated configuration is examined. In a study by Hart et al., the failure rates of main bearings of wind turbines with an output of 1.5 to 2.5 MW were examined, and the results were presented as 20-year (i.e. lifetime) failure rates. The study found that the failure rate for turbines due to main bearing failure exceeded 15%. The underlying causes of these failures were found to be diverse and could not be attributed to a singular mechanism [HTF19]. Dynamic simulation can help to identify many of the causes of damage, or at least it can provide indications and input data for further analysis. In addition to the bearing manufacturers characteristic values for identifying surface-induced damage risks, characteristic values for predicting damage due to adhesive wear in particular have been published. Table 1 provides an overview of the most common parameters and the limit values determined in tests on rolling bearings. Similar parameters, which are primarily based on single contact analyses, have also been published in the English-speaking international area. For the sake of clarity, however, they are not mentioned here.

Damage value	Equation	Limit value	Reference
Specific power (Potthoff)	$p_{hertzian} \cdot v_{rel}$	$300\ \mathrm{MPa} \cdot \frac{m}{s}$	[Pot86]
Specific frictional power (Hansberg)	$p_{hertzian} \cdot v_{rel} \cdot \mu$	$344 \frac{mW}{mm^2}$ *	[Han91]
Local frictional energy (Wadewitz)	$\int_{t}^{t+t_{2b}} F_r \cdot v_{rel}\, dt$	$10 \ldots 15\ \mathrm{mJ}$	[Wad93]
Sum of frictional energy (Wadewitz)	$\int_{tba}^{tea} \int_{t}^{t+t_{2b}} F_r \cdot v_{rel}\, dt\, dt$	$150 \ldots 250\ \mathrm{mJ} \cdot \mathrm{ms}$	[Wad93]
Specific frictional energy (Eglinger)	$\int_{t}^{t+t_{2b}} \frac{F_r \cdot v_{rel}}{2 \cdot b}\, dt$	$0.35 \ldots 0.45\ \mathrm{J}/\mathrm{mm}$	[Egl95]

Table 4: Characteristic damage indicators

They all assume a relationship between slippage and risk of damage. In rolling bearings, this usually occurs in the contact between the rolling element and raceways when the rolling element enters the load zone, as the rolling elements are accelerated there. Depending on the design of the load zone and the speed of the rolling element, the acceleration is stronger or weaker. The structural deformation of large bearings in wind turbine main bearings especially that of the cages, has a significant influence on both. In order to include cage stiffness in a MBS model of roller bearings Hahn presented a method for deep groove ball bearings connecting rigid cage segments with calculated stiffness matrices from an FE model [Hah05]. This approach is successfully applied in [FKS13] to model a more complex brass cage and a three-part window cage for spherical roller bearings. For model verification the deformation of the segmented cage in MBS and a full FE cage model were compared. Büscher further implemented a segmented cage model in a commercial MBS software [BLS20] on the example of a pitch bearing and extended the model for detailed contact calculation between roller and raceways [BSS22]. Yuqing et al. used a lumped-mass flexible cage like the one developed by Hahn in their investigations on the Skidding dynamic performance of rolling bearing under acceleration [LCT21]. Detailed bearing models of deep groove ball bearings for specific applications have been developed by Sadeghi et al. to investigate grease lubricated ball bearings in

regard to their losses, damping characteristics of the cage pockets and grease distribution [PSW06, RSK24].

2 Main section

As indicated in the introduction (see chapter 1), this study examines an example of damage to a double-row tapered roller bearing with pin cage, which serves as the main bearing in a wind turbine. The simulation model set up for this purpose is briefly introduced in chapter 2.1. Further, a multi-stage process was employed to analyze smearing damage in an extended load zone and a parameter variation study was conducted, adjusting bearing preload to mitigate damage risks (see chapter 2.2). Finally, a summary is given and the long-term benefits of extending the design process of rolling bearings in wind turbines are shown (see chapter 3).

2.1 Simulation model

For this study a TRB Model from LaMBDA was utilized. LaMBDA is a combination of software components allowing to setup MBS models of Roller Bearings, simulating them in a commercial MBS software, Simpack, developed in [WGK24]. The TRB models have been validated against friction torque measurements and other calculation tools in several studies [WKM23]. It has also been utilized for the evaluation of smearing risks and damage analysis [WK24]. These investigations included small size TRBs with comparatively stiff cages. Therefore, the cages were modeled rigid and the influence of cage deformation was neglected.

Figure 55: MBS model of a double row tapered roller bearing used as a main bearing in a multiple MW wind turbine modeled using LaMBDA

To set up the MBS model of the bearing LaMBDA was utilized. It allows to easily create a single row tapered roller bearing with pocket window cage type from a graphical user interface. However, for this study the cage had to be modeled from scratch as it is a pin type cage, which is not available in LaMBDA. The contacts between the rolling element and the cage had to be included. In this case, there are two relevant points for modeling the cage type. The axial contact between the rolling element end-face and the cage rings and the contact between the rolling element and the pin. Axial contact is implemented via a friction-induced spring-damper element with the standard values for damping and friction from LaMBDA [WGK24]. For roller pin contact a slice model was employed.

The cage is thin compared to its total weight. In order to consider the cages macro-elasticity the approach developed by Hahn is applied. Thereby, the macro elasticity is described by discretizing the cage into 91 segments. - each segment supporting one roller. The segments are in serial connection using spring-damper elements connected by nodes. The force elements contain two 6x6 matrices - one containing the stiffness values and the second the damping values. The stiffness values are determined from an FE model of a cage segment. High-resolution contact models allow the calculation of the individual force components, the rheology model, the lubrication condition and the shear (examples of selected output variables can be seen in Figure 56), so that damage-critical characteristic values can be determined.

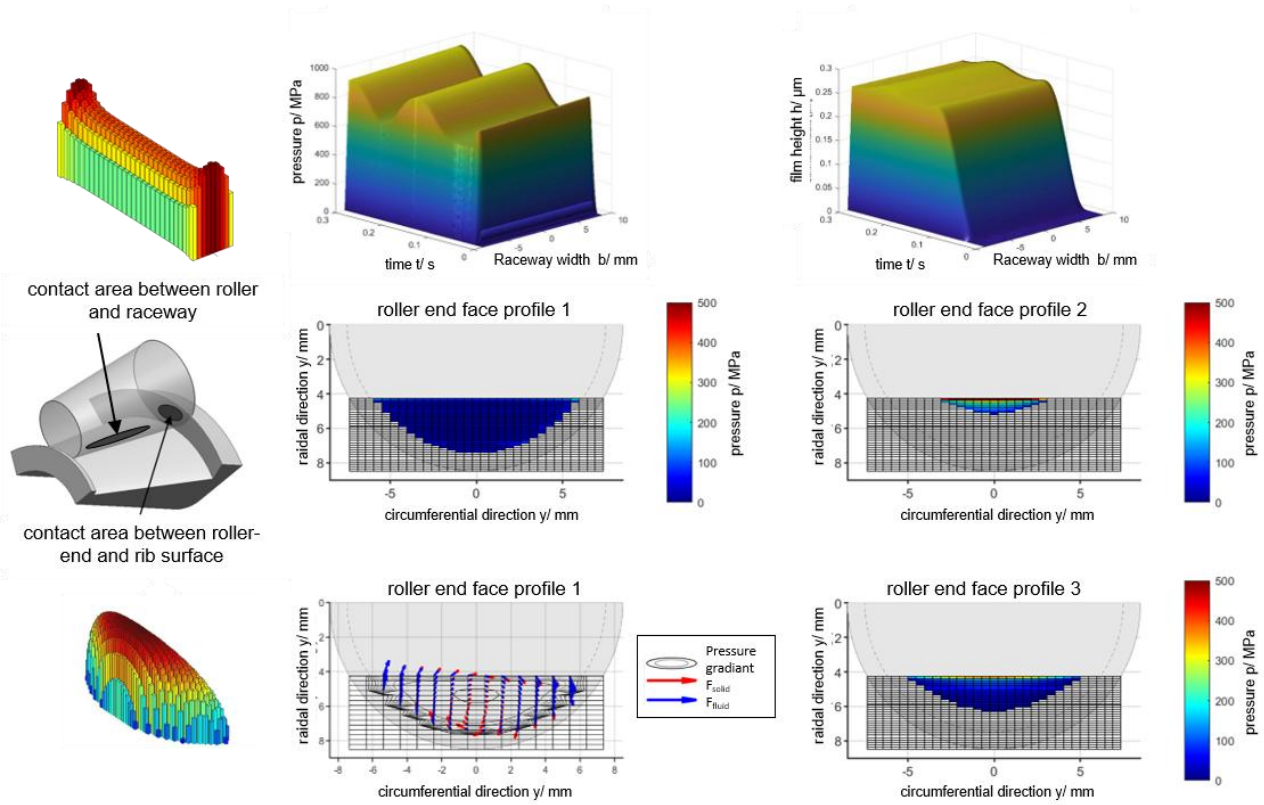

Figure 56: Evaluation of exemplary contact parameters at the two contacts - rolling element inner ring raceway and rolling element inner ring rib

2.2 Methodology

Based on a damage pattern that suggests smearing in the inlet area of an extended load zone as initial damage, a multi-stage analysis process was carried out. The process is shown in Figure 57. The first step was to define load scenarios. These can originate from measurements in the field or from simulations and take into account wind force and direction. The bearing loads are then derived from models of the entire drivetrain. These are specified directly as extreme events or minimum loads. Despite the numerous load cases, only a few of them result in critical conditions. A screening of the predefined load cases was therefore carried out in the second step. For each load case, the damage indicators listed in table 1 were determined locally and temporally resolved from the simulation. Based on the damage characteristics of all individual tribological contacts of the bearing, the critical load situations were identified. To determine why this load leads to critical conditions, the dynamics of the bearing were analyzed in the identified case. The results of this analysis will be discussed in detail in the presentation and are only shown here as an example in Figure 57. The

interaction between cage deformation under dead load and strong braking of the rolling elements outside the load zone is discussed.

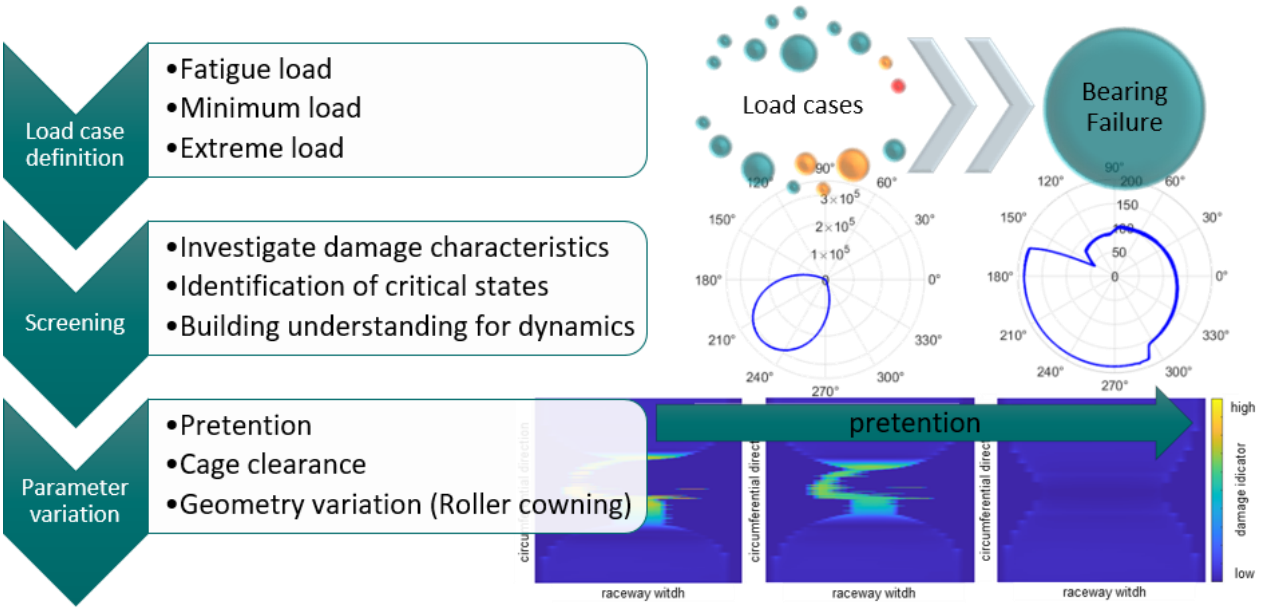

Figure 57: Schematic representation of the workflow for determining damage-critical load conditions and identifying solution approaches

In the final step, a parameter variation was carried out regarding the bearing preload in order to find a solution approach. Depending on the accessibility of the geometry or the design, the bearing and cage clearance, roller and raceway crowning can be varied. In this case, the focus was on the preload, as this is usually adjusted via the thickness of a middle ring between the two inner rings of the double-row bearing and is therefore easier to adjust than profiling. When varying the preload, the thickness of the middle ring was initially selected so that there is nominally no play in the axial direction in the bearing. Based on this, the thickness of the middle ring was then reduced by several 100 µm. The simulation was repeated for the load case in concern with preload and the characteristic damage values were evaluated. The objective was to minimize the characteristic values as far as possible in order to reduce the risk of damage. The influence of the preload is illustrated in Figure 57 using a damage indicator. While no increase in the risk of damage can be seen over the entire circumference of the bearing with a high preload (right), the diagrams in the middle and on the left show some areas with a strong yellow color. These are located outside the load zone or in the inlet of the load zone of the bearing and indicate an increased risk of smearing damage there.

3 Summary / Conclusion

Using an exemplary case of damage, a simulation process was presented that can further enable damage analysis. This simulation-based damage analysis was demonstrated on the example of a main bearing in wind energy application with a DRTRB bearing of a multi MW wind turbine. The model of the main bearing was generated on the basis of the LaMBDA calculation tool, which has already been validated several times and is widely used by FVA users. A preliminary study was carried out to identify critical load cases and the dynamics of rolling elements and cages were analyzed in the scenario concerned. Based on these results, a study on remedial measures was then carried out and the preload of the double-row bearing was varied. The results presented show that this methodology is very promising for research into the causes of damage and for determining

solutions. In addition, the method presented can make an important contribution to damage prediction in the long term and thus improve the design process.

4 Bibliography

[BLS20] Büscher, M., Leupold, S., Schelenz, R., Jacobs, G.: Cage loads of wind turbine blade bearing. Journal of Physics: Conference Series 1618(5), 052061 (2020)

[BSS22] Büscher, M., Schneider, V., Schelenz, R., Jacobs, G., Poll, G.: Contact analysis of wind turbine blade bearings by means of finite element method and alternative slicing technique. (2022)

[Egl95] Eglinger, M.: Einfluss des Schmierstoffes und der Rollenbeschaffenheit auf die Entstehung von Anschmierungen. PhD thesis, Universität Erlangen-Nürnberg, Abteilung für Maschinenelemente und fertigungsgerechtes Konstruieren, Erlangen, 1995

[Fie16] Fierro, Toni: Extending Bearing Life in Wind Turbine Mainshafts.

Power Engineering, 2016, https://www.power-eng.com/renewables/wind-energy/extending-bearing-life-in-wind-turbine-mainshafts/ (accessed 03.02.2025)

[FKS13] Fiedler, S., Kiekbusch, T., Sauer, B.: Untersuchungen zur Käfigdynamik an Pendelrollenlagern in experimentell validierten MKS-modellen. In: 54. Tribologie-Fachtagung, Gesellschaft Für Tribologie e.V. (GfT), Vol. 76. Göttingen, pp. 1–11, 2013

[Hah05] Hahn, K.: Dynamik - simulation von w¨alzlagern. PhD thesis, TU Kaiserlautern, Kauserslautern, 2005

[Han91] Hansberg, G.: Freßtragfähigkeit vollrolliger Planetenrad-Wälzlager. PhD thesis, Fakultät für Maschinenbau, Ruhr-Universität Bochum, Bochum, 1991

[HTF19] Hart, Edward; Turnbull, Alan; Feuchtwang, Julian; McMillan, David; Golysheva, Evgenia; Elliott, Robin: Wind turbine main-bearing loading and wind field characteristics, Wind Energy, Wiley, Vol. 22 (11), pp. 1421-1653, 2019

[ISO07] ISO 281:2008 Rolling bearings – dynamic load rating and rating life, 2007.

[ISO08] ISO TS 16281:2008 Rolling bearings – methods for calculating the modified reference rating life for universally loaded bearings, 2008.

[ISO17] ISO 76:2006+A1:2017 Rolling bearings – static load ratings, 2017

[LCT21] Liu, Y., Chen, Z., Tang, L., Zhai, W.: Skidding dynamic performance of rolling bearing with cage flexibility under accelerating conditions. Mechanical Systems and Signal Processing 150, 107257, 2021

[Oya09] Oyague, Francisco: Gearbox modeling and load simulation of a baseline 750-kW wind turbine using state-of-the-art simulation codes. No. NREL/41160. National Renewable Energy Lab.(NREL), Golden, CO (United States), 2009.

[Pot86] Potthoff, H.: Anwendungsgrenzen vollrolliger Planetenrad-Wälzlager. PhD thesis, Fakultät für Maschinenbau, Ruhr-Universität Bochum, Bochum, 1986

[PSW06] Pederson, B., Sadeghi, F., Wassgren, C.: The effects of cage flexibility on ball-to-cage pocket contact forces and cage instability in deep groove ball bearings. SAE Technical Paper 2006-01-0358, 2006

[RSK24] Russell, T., Sadeghi, F., Kang, Y.S., Mazzitelli, I.: The influence of cage pocket lubrication on the simulation of deep groove ball bearing cage motion. Journal of Tribology 146(2), 2024

[She13] Sheng, S.: Report on wind turbine subsystem reliability-a survey of various databases (presentation). No. NREL/PR-5000-59111. National Renewable Energy Lab.(NREL), Golden, CO (United States), 2013.

[Wad93] Wadewitz, M.: Anschmiererscheinungen - Ursachen der Anschmierung Im Wälz/ Gleitkontakt: Forschungsvorhaben Nr. 164 I: Abschlussbericht Heft 384. Forschungsvereinigung Antriebstechnik e.V., Frankfurt am Main, 1993

[WGK24] Wingertszahn, P., Graf, S., Koch, O.: Dynamiksimulation Verschiedener Wälzlagertypen - Betriebsverhalten Von Kegelrollenlagern in Abhängigkeit der Belastungssituation Im Antriebssystem: Abschlussbericht zum FVA Vorhaben: FVA-Nr. 625 III: Abschlussbericht, Heft 1598. Forschungsvereinigung Antriebstechnik e.V., Frankfurt am Main, 2024

[WK24] Wingertszahn, P., Koch, O.: Prediction of bearing damage beyond rolling contact fatigue. In: 78th Annual Meeting & Exhibition (STLE), Minneapolis (2024)

[WKM23] Wingertszahn, P., Koch, O., Maccioni, L., Concli, F., Sauer, B.: Predicting friction of tapered roller bearings with detailed multi-body simulation models. Lubricants 11, 369, 2023

Simulative and experimental investigations of roller and structural induced bearing ring creeping mechanisms considering design aspects for 2TRB rotor main bearings

D. Billenstein[1], C. Liewen[1], M. Neidnicht[1], N. Safieh[1], J. Rollmann[1], D. Becker[1], B. Lüneburg[1], A. Necker[1]

[1]thyssenkrupp rothe erde Germany GmbH, Beckumer Str. 87, 59555 Lippstadt

Keywords: Bearing ring creeping, shrinked bearing rings, micro contact sliding, trained coefficient of friction, ring creeping test rig, 2TRB rotor main bearings, multi-MW rotor main bearing arrangements

Abstract: The increasing power rating of multi-megawatt wind turbines and the simultaneously growing size of rotor main bearings pose challenges to ensure long-term reliability of the powertrain. One functional-critical failure mode for non-bolted 2TRB bearing applications is "bearing ring creeping", whereby a bearing ring incrementally rotates relative to its adjacent component during operation. This failure mode can lead in the very first stage to fretting corrosion and/or abrasive wear between the clamped bearing ring and the shaft or the housing. At a later stage, the functionality of the powertrain and here in particular the structural integrity of the bearing ring and/or the companion structure is subjected to a major functional risk. The underlying creeping mechanism occurs due to a local and temporary reduction or even an entire loss of the contact pressure within the interference fit caused either by the roller elements themselves (so-called *roller induced*) or by oscillating global deformations of the surrounding drivetrain components (so-called *structural induced*).

In order to investigate the failure mode on a component-scale level and to ultimately figure out potential risk mitigation measures at an early design stage, an advanced FE-based simulation approach and creeping test benches with component-like specimens have been developed at thyssenkrupp rothe erde (tkre). The main focus of the investigations is on (i) an in-deep understanding of the structural and roller induced creeping phenomena, (ii) the validation of the simulation results based on experimental measurements and (iii) the evaluation of e.g. bearing design-related countermeasures. The latter in particular is focusing on the influence of the so-called “trained” coefficient of friction (COF) and the interference fit. This kind of in-depth evaluation of the drivetrain-specific creeping behavior is facilitated by the so-called “*creeping scale*” indicator which exceeds the current state-of-the-art due to its quantifiable metric. Hence, this indicator as proposed within this framework contributes to assess the risk profile for different drivetrain designs as well as specifications (e.g. load cases, COFs, etc.) and provides targeted recommendations regarding both drivetrain design and assembly related countermeasures. In combination with the advanced and highly sophisticated FE-based simulation approach, the *creeping scale* indicator enables a detailed analysis of the creeping mechanism and at the same time reveals significant potential for the development of a simplified approach for project-related application. Finally, both experimental and numerical results are discussed in the context of an improved 2TRB bearing design process taking into account structural integrity of both bearing ring and bearing seat.

1 Ring creeping

Global wind turbine development trends towards increasing rotor diameter and power ratings are more and more setting higher requirements regarding the design and calculation process for both slewing bearings as applied for the blade and yaw system [BEC22, BEC24a, BEC24b] and rotor main bearings [LUE22, NEI24]. In particular the failure mode “ring creeping”, which can lead to fretting corrosion and/or abrasive wear (see Figure 58) between bearing ring and shaft (respectively housing), is design-critical for non-bolted large-sized diameter rotor main bearing applications [HEU22, RAU16].

Figure 58: Exemplary impact of creeping on the bearing seat of a large-sized diameter bearing (left: inner ring; right: shaft) [LIE22]

Ring creeping in general refers to a failure mode caused by a bearing ring rotating relatively to its adjacent component during operation. This ring movement as a result of the accumulated micro slip depends primarily on the coefficient of friction (COF) as well as on the local radial and shear stresses within the joint. These local stresses are caused by the contact pressure of the interference fit and additionally either by the rollers themselves (RIC: roller induced creeping; see Figure 59 left) or by the non-static deformation of the adjacent drivetrain components (SIC: structural induced creeping; see Figure 59 right) [BAB10, DUC25].

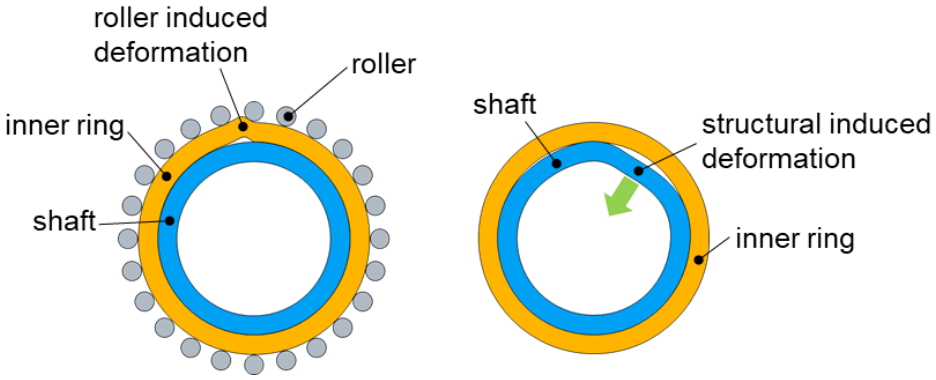

Figure 59: Schematic illustration of roller (left) and structural induced creeping (right) using the configuration of an inner ring (yellow) and a shaft (blue) as an example

In the case of roller induced creeping, the radial load of the roller forces (static bearing condition) causes a wave-like deformation of the bearing ring. Underneath the roller to raceway contact, this leads to an increase in the frictional shear stress and at the same time to a reduction of the contact pressure (or even in the worst case to a gap between the ring and the bearing seat) inbetween the circumferential positions of the rollers. If the frictional contact is exceeded, local slippage occurs. In combination with rotating rollers this can lead to a tangential displacement of the bearing ring by a

few µm (depending on load level). As this process takes place continuously, the resulting displacements add up to macroscopically visible, relative displacements between the bearing ring and the adjacent component. [BIL23b]

The same procedure is the underlying root cause of structural induced creeping movements, although here the decisive triggers are not the roller forces, but the deformation of the adjacent component (shaft or housing) [DUC25, MAI22]. Particular in this case, it is important that the creeping movement can only occur if the deformation of the adjacent component rotates at a different rotational speed than the adjacent component itself - analogous to roller induced creeping, which can also only occur because the rollers rotate at a different relative speed compared to the bearing ring. If the structural deformation rotates at the same speed as the adjacent construction, this purely causes an adapted load distribution, which can only (but does not have to) lead to roller induced creeping.

The prerequisite for creeping in both cases is therefore a deformation (either a deformed ring due to the roller forces or a deformation of the adjacent component), which affects the local stresses within the joint and rotates itself with a relative speed difference. In practice, it is possible that both creeping variants occur separately or simultaneously. In general, however, all kind of creeping movements (regardless of the underlying root cause) should be avoided, as both mechanisms can lead to the same aforementioned damage.

2 Developed procedure

In order to cope with the above-mentioned challenges regarding both creeping mechanisms of rotor main bearings, a structured procedure is shown to investigate creeping by experiments (chapter 3) and simulations (chapter 4).

To enable an isolated investigation of the ring creeping detached from the global system behavior, a test rig has been developed for roller induced creeping including the training effect [LIE22, BIL23a], see also chapter 3. In addition to that, as will be shown in this paper, an additional test rig has been developed to also investigate structural induced creeping. By doing that, important parameters such as e.g. the ring movement/creeping distance, creeping speed, creeping limit, the trained COF and ring/shaft deformation can be determined to develop an in-deep understanding of both creeping mechanisms and to purposefully address mechanism-specific countermeasures.

Afterwards a workflow for the evaluation of a creeping simulation is presented (see chapter 4). The advanced evaluation method and its quantifiable as well as normalized scale allows (in particular compared to the binary creeping statement of other calculation methods such as SimWag [DUC25, NUE15, VIE17, ZIM21]) the detailed investigation of creeping (see chapter 4.1). Both the simulation model and the creeping scale are validated using test bench results for the case of roller induced creeping (see chapter 4.2) and the practical application is demonstrated as part of a parameter study regarding countermeasures (see chapter 4.3).

3 Experimental investigations

The investigation of **roller induced creeping** was completed on a specialized creeping test rig (see Figure 60 left) developed by the authors [LIE22, BIL23a]. The test specimen consists of a cast iron stub shaft with a cylindrical roller bearing. The inner ring of the slewing bearing together with the stub shaft (interference fit) is rotating with $n_{joint\ fit}$; the outer ring of the bearing stands still. The radial

load is applied using a hydraulic cylinder, which is pressing onto the outer ring of the slewing bearing.

In a typical test run, the external load is gradually increased until a permanent relative movement between the inner ring and shaft is measured via an inductive displacement sensor. The resulting relative movements in the joint fit lead to an increased, so-called "**trained COF**" due to the accumulation of wear particles introduced by micro slip movements between the bearing ring and the shaft. The external radial load at which permanent creeping occurs is referred to as the "**creeping limit**" and is determined after the COF was trained to its maximum – a state in which permanent creeping occurs which cannot be counteracted by training and therefore describes the threshold from non-creeping to creeping state. Please explicitly note, that the creeping limit is a test bench-specific value which is only used to validate the simulation model, see chapter 4.

The COF in the joint fit of the specimen - representing run-in contact conditions or the trained conditions mentioned above - is determined on another test rig, see Figure 60 middle. For this purpose, the shaft is fixed at the base plate and the inner ring is moved in circumferential direction by hydraulic cylinders. By measuring the required force to initiate a defined relative movement and considering the nominal force due to the interference fit, the increased COF of the trained specimen is calculated and is later used as an input variable for the simulation.

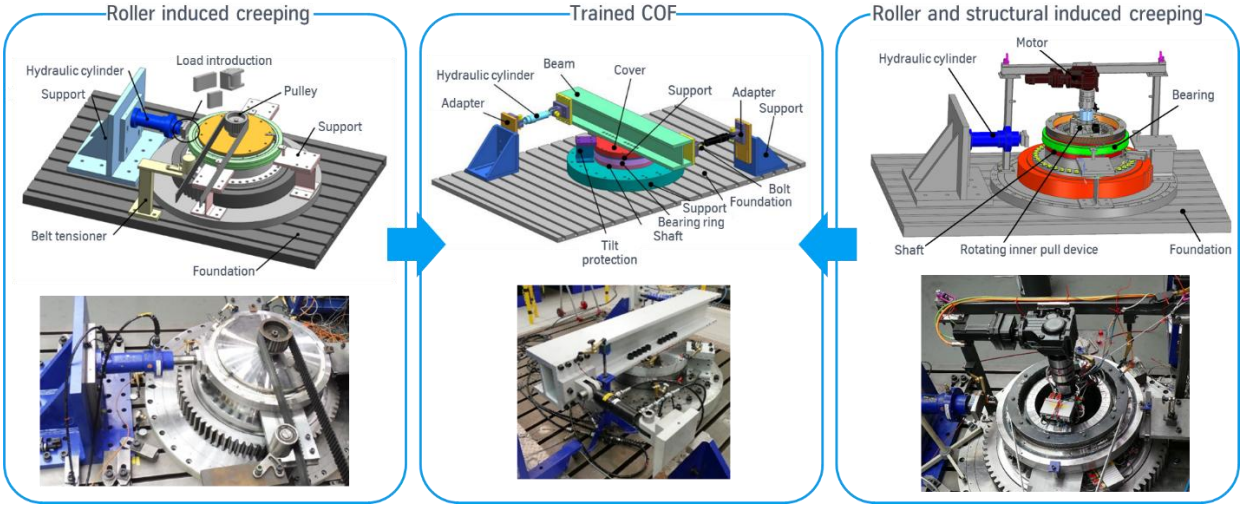

Figure 60: tkre creeping test benches

For the investigation of **structural induced creeping** a new test rig has been developed (see Figure 60 right). Compared to the test rig for roller induced creeping an additional rotating pull device has been added. This pull device induces a structural deformation (ovalization) of the hollow shaft which leads to a local reduction of the contact pressure in the joint fit. Due to a separate drive, the structural deformation can independently rotate (direction and speed) with n_{def} compared to the joint fit. This enables the determination of parameters such as the relative ring movement/creeping distance, creeping speed and creeping limit due to structural induced creeping. As it is possible that both creeping mechanisms occur simultaneously in practice, at the test rig, external loading (hydraulic cylinder) with rotating of the joint fit as well as internal loading (inner pull device) with rotating of the deformation can be triggered at the same time. This enables the investigation of and the interaction between roller and structural induced creeping on one test rig. The determination of the trained COF of the specimens joint fit is also performed on the test rig illustrated in Figure 60 middle.

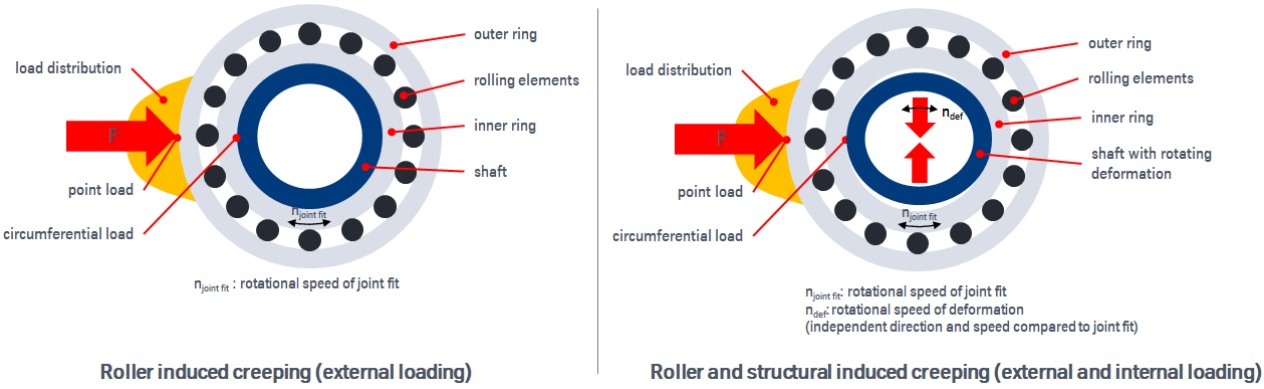

Figure 61: Operating principle of tkre creeping test benches

3.1 Experimental results – Roller induced creeping

To determine the creeping limit of a test specimen on the RIC test rig (later be used for comparison with simulative results, see chapter 4.2), at first, the COF of the interference fit is trained to its maximum by gradually increasing the load multiple times, from zero load up to a load level in which permanent creeping occurs. By analyzing the creeping behavior during these tests, this load level is estimated. For the exact determination of the creeping limit, several stepped load hysteresis, surrounding the estimated load level, are performed. One of these gradually increased load hysteresis can be seen in Figure 62. In the upper part of the figure, the applied force of the hydraulic cylinder is plotted over time (force has been normalized regarding the estimated load level). Below the creeping speed is illustrated. After the load has been raised to a normalized force of 0.96, the inner ring starts to creep. The creeping limit - the threshold from non-creeping to creeping – in this case is a normalized force of 0.96. At the highest load level, the creeping speed reaches its maximum. By decreasing the external load, the creeping slows down until it comes to a standstill at a normalized force of 0.89.

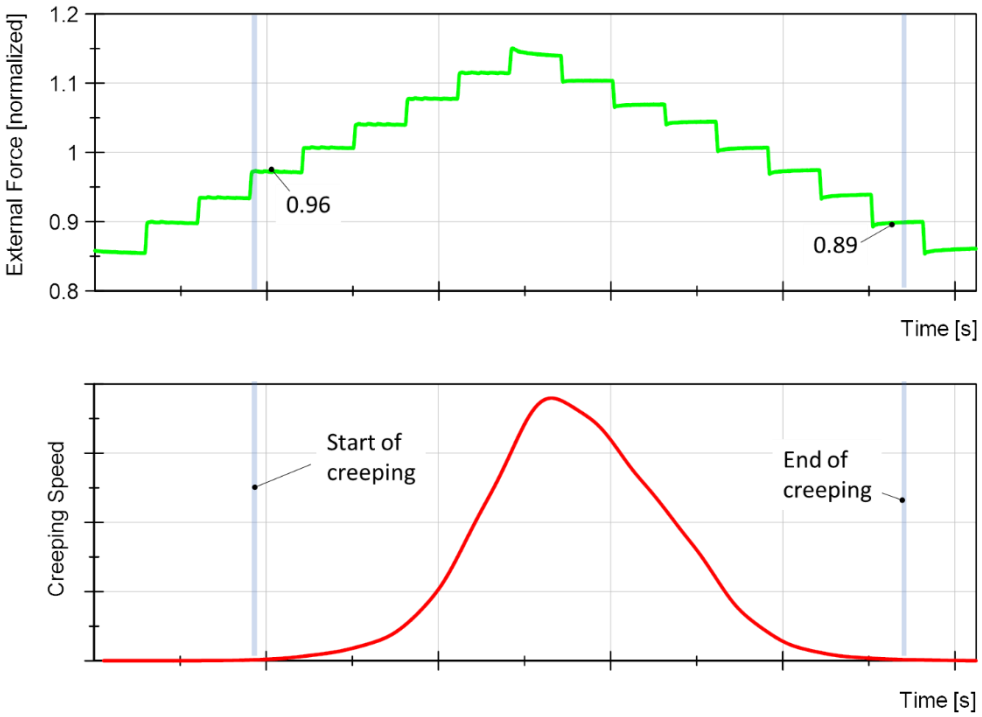

Figure 62: Determination of creeping limit at the RIC test rig

The new developed test rig (Figure 60 right) can be used to determine the creeping limit for structural induced creeping or a combination of roller and structural induced creeping. To determine the creeping limit after structural induced creeping one would follow the same procedure as described in this chapter, but with adapted loads induced by the rotating inner pull device.

3.2 Experimental results – Structural induced creeping

Figure 63 shows the measurement curves of a test run performed to investigate structural induced creeping behavior associated to different rotational speeds. This test has been performed at a constant load level of the inner pull device (in the range of the creeping limit) and no external radial load has been applied. This means that no roller forces are applied and any relative movement is structural induced creeping. As can be seen in the middle part of Figure 63, the different rotational speeds of the rotating deformation of the shaft (n_{def}) and the rotating joint fit ($n_{joint\ fit}$) lead to sectors with a positive relative rotational speed and also sectors with a relative rotational speed of 0 rpm, either for a complete standstill of all components or for the same rotational speed of joint fit and rotating deformation (all speeds normalized). The lower part of the illustration shows the emerging structural induced creeping distance. It can be stated that structural induced creeping only occurs for a relative rotational speed ≠0 rpm, so when the deformation of the shaft rotates at a different rotational speed than the joint fit. This corresponds well with the definition presented in chapter 1.

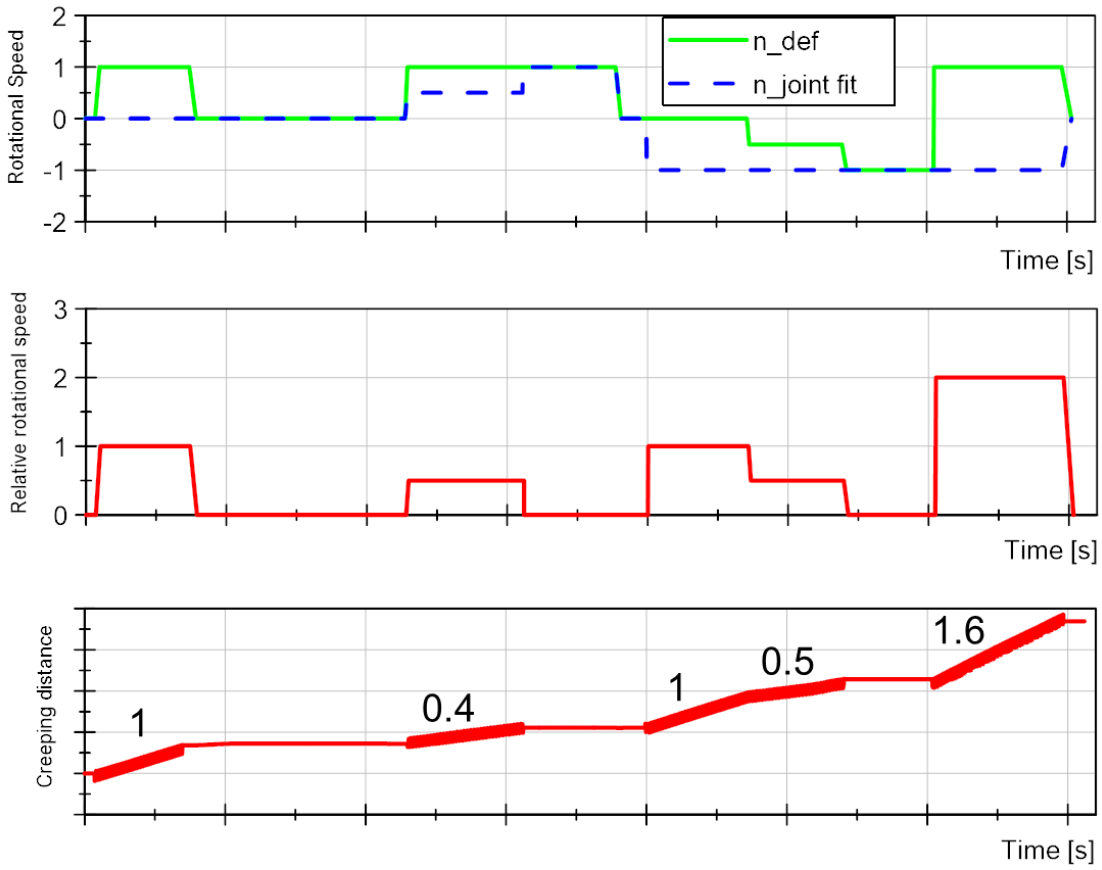

Figure 63: Structural induced creeping on the SIC test rig

The numbers in top of the creeping distance curve represent the normalized creeping speed for the specific sector. It can be seen, that the relationship between the relative rotational speed and the creeping speed is nonlinear, as a doubling of the relative rotational speed, does not lead to a doubling in creeping speed.

4 Validation of the numerical simulation method

The development of an advanced numerical simulation method is described by the authors in [BIL23a] and [BIL23b]. The obtained method addresses both creeping mechanisms - roller and structural induced creeping. The finite element model itself is based on a nonlinear, static transient structural analysis and it is designed to be inherently consistent without requiring experimental calibration, and thus the scope of application is not limited to any calibration range. In order to achieve this (and its robustness/efficiency for practical applications), the development was supervised by extensive convergence studies. It incorporates meshing, (solver) settings, contact mechanics and system-level interactions to provide a detailed understanding of creeping effects. A first qualitative comparison with test bench results confirmed the reliability of the simulation approach [BIL23a].

To confirm the validity of the model quantitatively, the numerical creeping evaluation will be introduced first and then the simulative results will be validated using test rig results.

4.1 Quantitative creeping scale

The numerical creeping assessment (see Figure 64) consists of two evaluation steps: Based on the results of the kinematic creeping simulation, a decision is made on whether creeping occurs or not.

If creeping is detected, the intensity, the so-called creeping activity, is determined in a second evaluation step. If creeping is not detected, the amount of buffer before creeping occurs, referred to as the creeping buffer, is evaluated.

Figure 64: Advanced evaluation method of a creeping simulation (left) and the quantifiable as well as normalized creeping scale (right)

Both scales together form the creeping scale, which is normalized and defined from -1 to +1. Values between -1 and 0 represent the creeping buffer, with a more negative value indicating greater resistance to creeping, while a negative value next to zero represent a non-creeping configuration which is on the verge of creeping. Values between 0 and +1 represent creeping activity, with higher positive values indicating more intense creeping. Accordingly, the value 0 is exactly the threshold between a non-creeping and creeping configuration.

By using this developed creeping scale, a numerical evaluation is provided, which not only enables the comparison of different calculated configurations. Thereby the creeping buffer helps to assess the risk profile for both different turbines and specifications (e.g. load cases, coefficient of friction, etc.), while the creeping activity provides guidance for recommending countermeasures, such as design adjustments or overlap.

4.2 Comparison of experimental and simulative results

The described creeping scale is used in the following to compare the experimentally determined creeping limit (roller induced creeping) of replicated specimen (same manufacturing parameters, surface finish, interference fit, material and hardening) with the simulation model in order to validate the FE model itself. A test bench run in which the external load is gradually increased until permanent creep occurs was repeated on the replicated test specimens. The measured test rig-specific creeping limits – expressed as average 0.81 and standard deviation 0.11 – are plotted in Figure 65 right.

The kinematic simulation was calculated using the trained COF for several load levels to determine the simulative creeping limit. For each calculated load level, the creeping scale was evaluated and the result is shown as a blue bar in Figure 65 left. Starting from 0.57 up to a load level of 0.96, no creeping occurs and the creeping buffer decreases continuously. At a load level of 0.96, there is almost no buffer left. If the load is increased to the load level 1.00, creeping occurs for the first time, which increases for higher loads - indicated by the increasing creeping activity. The change between non-creeping and creeping - and therefore the simulative creeping limit - is therefore between 0.96 and 1.00.

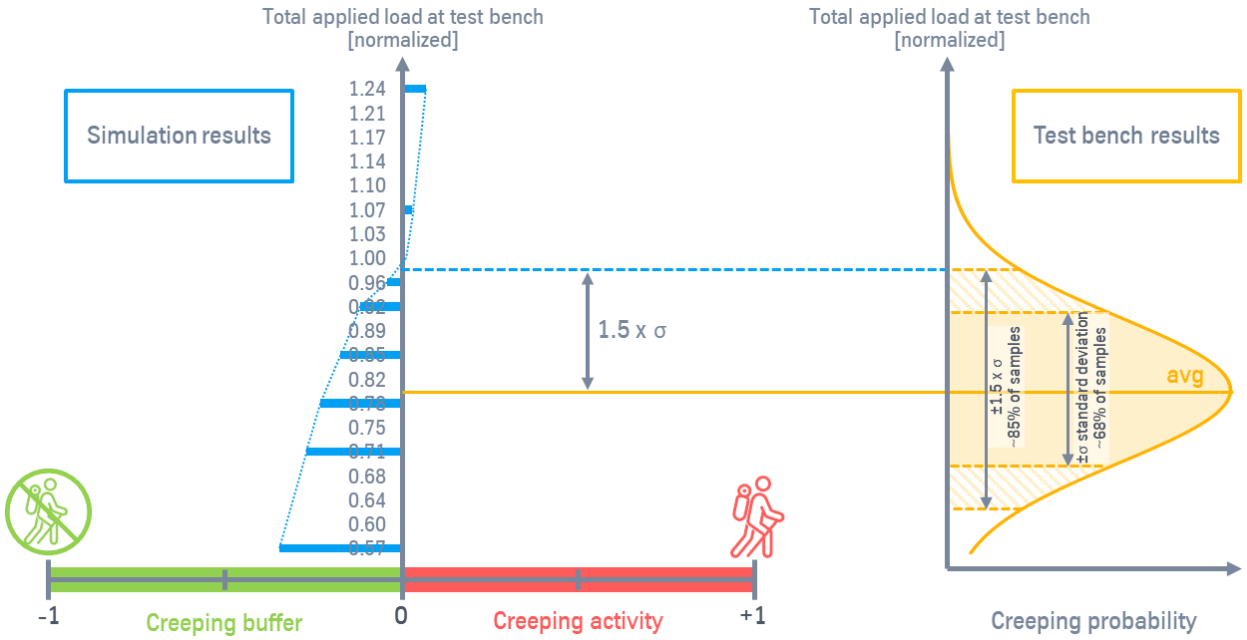

Figure 65: Successful comparison of the experimental and simulative creeping limits using the creeping scale

A comparison of the simulated with the experimental results shows that the simulative creeping limit corresponds to the measured creeping limit: In more detail, the simulation is within 1.5 times the standard deviation of the measured creeping limits.

As no calibration with test bench results was carried out during the development of the simulation model, the developed simulation method can therefore be classified as validated and generally applicable.

4.3 Evaluation of countermeasures: COF and overlap

General countermeasures for both types of creeping are, for example, a high coefficient of friction and also a large overlap. For more specific countermeasures, however, it is essential to strictly distinguish between the two creeping mechanisms, as in the worst case the creeping movements can otherwise be intensified instead of reduced (or completely eliminated): for example, enlarging the ring cross-section can reduce the creeping tendency in the case of roller induced creeping and is therefore a recommended countermeasure - in contrast, the same countermeasure would favor the creeping tendency in the case of structural induced creeping, wherefore a thinner ring cross-section would actually be appropriate.

The developed and validated simulation method (as well as the creeping scale) can be used, among other things, to evaluate different countermeasures. This is exemplified in the following using the trained coefficient of friction and the overlap. Based on the simulated configuration at a load level of 0.96, both parameters are varied in a range of ± 20%. Thereby, not only the individual parameters are varied (and the other kept constant), but both are also varied simultaneously so that cross-influences can also be analyzed. The resulting configurations are summarized in Figure 66, where a red dot indicates that creeping occurred with this parameter combination, whereas a green dot means no creeping.

Figure 66: Simulated creeping configurations by varying the overlap and the trained coefficient of friction in a range of ± 20% (green dot: no creeping occurred; red dot: creeping occurred)

However, the diagram in Figure 66 only contains a binary creeping evaluation - in Figure 67 left, the creeping scale value (consisting of the creeping buffer and creeping activity) is therefore added to the z-axis so that a quantitative comparison is possible.

The configuration in which both the coefficient of friction and the overlap were reduced by 20 % therefore indicates the highest activity, while the configuration in which both parameters were increased by 20 % shows the largest buffer. With the other configurations analyzed, this results in a surface that contains the individual and cross-influences of both parameters on the creeping tendency. A closer look at the individual influences (see Figure 67 right) shows that the scale is strictly monotonically decreasing, thus confirming the validity of the creeping scale for individual calculations. The graphs also confirm that the trained coefficient of friction is the main influencing factor. At the same time, however, the diagram shows that an increasing overlap has also a considerable influence on the creeping tendency: This beneficial effect should always be utilized, as only geometrical parameters need to be adjusted and no additional manufacturing steps - and consequently no additional costs - are required. On doing so, the maximum possible overlap is limited by the tolerable inner ring strength (respectively the housing), which is why a precise stress evaluation is essential for the dimensioning [BEC24b].

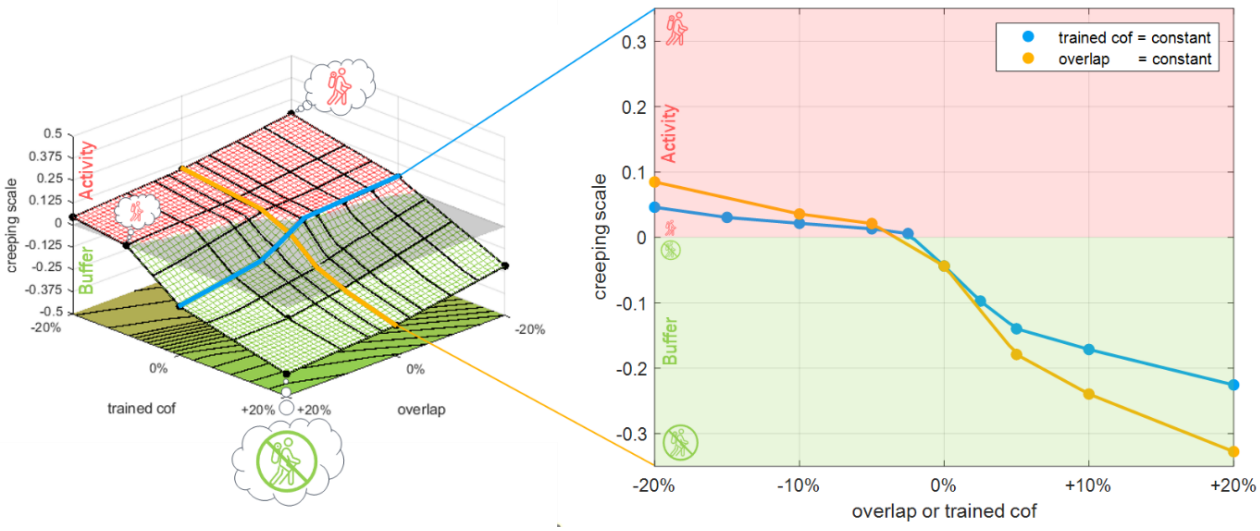

Figure 67: Quantified exemplary influence of the overlap and coefficient of friction on the creeping tendency measured with the help of the creeping scale

The shown validity and quantifiability of simulated creeping results not only enables a reliable approval calculation in order to evaluate the creeping tendency, but also enables the targeted weighting of creeping against other competing damage mechanisms.

5 Summary / Conclusion

In this investigation, an advanced simulation approach for the ring creeping of 2TRB rotor main bearings has been compared with experimental results of a creeping test bench with component-like specimens. The new developed test rig is able to trigger structural induced creeping. It has been shown that a creeping movement can only occur if the deformation of the adjacent component rotates at a different rotational speed than the adjacent component itself. Structural and roller induced creeping can be triggered simultaneously at the test rig. This also enables the investigation of the interaction between both creeping mechanisms. As shown, the developed simulation method can be classified as validated for roller induced creeping. The same validation procedure is intended for structural induced creeping: The simulation model itself does not need to be adapted as the underlying simulation approach is not restricted in its scope and is therefore able to address both creeping mechanisms for large-sized diameter bearing applications such as 2TRB rotor main bearings. Moreover, an evaluation of influencing factors such as the trained COF and the overlap between bearing ring and shaft has been shown. This kind of in-depth evaluation of creeping results is facilitated by the quantifiable *creeping scale* indicator. This *new* indicator contributes to assess the risk profile for different drivetrain designs and assembly conditions as well as specifications (e.g. load cases, coefficient of friction, etc.) much more in deep than on a simplified binary level (that means occurrence of ring creeping: yes/no) according to current state-of-the-art like SimWag. In combination with the validated FE-based simulation model, this new approach as developed by thyssenkrupp rothe erde enables a detailed analysis of the creeping mechanisms and at the same time forms the base for the development and validation of a simplified approach to be applied in the upfront design phase.

6 Bibliography

[BAB10] Babbick, Till; Maiwald, Andreas; Vidner, Jakub; Sauer, Bernd; Leidich, Erhard: Beanspruchungsgerechte Auslegung von Wälzlagersitzen unter Berücksichtigung von Schlupf- und Wandereffekten (FVA479II; Heft Nr. 956).

Forschungsvereinigung Antriebstechnik e.V., Frankfurt a. M., 2010

[BIL23a] Billenstein, Daniel; Neidnicht, Martin; Becker, Daniel; Liewen, Christian; Rollmann, Jörg; Lüneburg, Bernd: Advanced, numerical simulation of the bearing ring creeping failure mode and comparison with experimental test results for rotor main bearing applications.

In: Conference proceedings, 110-120

Conference for Wind Power Drives, Aachen, 2023

[BIL23b] Billenstein, Daniel; Neidnicht, Martin; Becker, Daniel; Liewen, Christian; Rollmann, Jörg; Lüneburg, Bernd: Simulative and Experimental Investigation of the Ring Creeping Damage Mechanism Considering the Training Effect in Large-Sized Bearings.

In: Machines, 11, no. 5, 543

MDPI, Basel, 2023

[BEC22] Becker, Daniel; Lüneburg, Bernd; Billenstein, Daniel; Handreck, Thomas; Müller, Patrick; Neidnicht, Martin; Volmer, Gilles; Schlüter, David; Netz, Torben; Rollmann, Jörg: Design and calculation process for large-sized multi-MW blade bearing applications based on advanced multi-bearing FE-analyses.

In: Bearing World, 4th, 282-287

International FVA-Conference, Würzburg, 2022

[BEC24a] Becker, Daniel; Burtchen, Marco; Handreck, Thomas; Lüneburg, Bernd; Müller, Patrick; Neidnicht, Martin; Rollmann, Jörg; Schlüter, David; Stellmach, Sebastian; Volmer, Gilles; Necker, Armin: Pitch bearings for multi-MW wind turbine applications – advanced multi-blade bearing calculation process and product development trends regarding pitch system modularization and hub standardization.

In: Bearing World, 5th, 178-183

International FVA-Conference, Würzburg, 2024

[BEC24b] Becker, Daniel; Esderts, Alfons; Liewen, Christian; Masendorf, Rainer; Müller, Patrick; Stellmach, Sebastian; Rollmann, Jörg; Schlüter,

David; Volmer, Gilles; Wächter, Michael; Necker, Armin; Maier, Oliver: Zertifizierungskonformer Strukturnachweis von zyklisch hoch beanspruchten Großwälzlagerringen auf Basis der FKM Richtlinie.

In: 50. Jahrestagung, 71, DOI: 10.48447/BF-2024-BB

DVM-Arbeitskreis Betriebsfestigkeit, Clausthal-Zellerfeld, 2024

[DUC25] Le Duc, Loc; Zimmermann, Markus; Hasse, Alexander; Tremmel, Stephan: Einfluss der Nachgiebigkeit von Lagergehäuse und dessen Anschlusskonstruktion auf das Wanderverhalten von Wälzlagern (FVA479IX; Heft Nr. tbd).

Forschungsvereinigung Antriebstechnik e.V., Frankfurt a. M., 2025

[HEU22] Heuser, Lutz; Bager, Christian: Preload Adjustment and Creeping Prevention of large size Tapered Roller Bearings.

In: Bearing World, 4th, 254-263

International FVA-Conference, Würzburg, 2022

[LIE22] Liewen, Christian; Neidnicht, Martin; Billenstein, Daniel: Untersuchung zum Ringwandern an Großwälzlagern.

In: Schadensmechanismen an Lagern, 5th

VDI-Fachkonferenz, Aachen, 2022

[LUE22] Lüneburg, Bernd; Becker, Daniel; Rollmann, Jörg; Terwey, Torben; Michalek, Ivan; Mevius, Lars; Neidnicht, Martin: Advanced design and qualification of dual taper roller main bearing arrangements for multi-MW wind turbines.

In: Bearing World, 4th, 244-252

International FVA-Conference, Würzburg, 2022

[MAI22] Maiwald, Andreas: Specific creeping phenomena of roller bearings used in lightweight constructions.

In: Bearing World, 4th, 264-272

International FVA-Conference, Würzburg, 2022

[NEI24] Neidnicht, Martin; Becker, Daniel; Necker, Armin; Billenstein, Daniel; Liewen, Christian; Lüneburg, Bernd; Müller, Patrick; Netz, Torben; Rollmann, Jörg; Safieh, Nabil; Stellmach, Sebastian; Volmer, Gilles: Aufgelöste 2TRB Rotorhauptlagerungen (Sichere Auslegung bei konkurrierenden Schadensmechanismen).

In: Schadensmechanismen an Lagern, 6th

VDI-Fachkonferenz, Aachen, 2024

[NUE15] Nützel, Florian; Rieg, Frank: Erweiterung des FEA-Solvers im FVA-Programm SimWag (FVA479V; Heft Nr. 1155).

Forschungsvereinigung Antriebstechnik e.V., Frankfurt a. M., 2015

[RAU16] Rauert, Thes; Herrmann, Jenni; Dalhoff, Peter; Sander, Manuela: Fretting fatigue induced surface cracks under shrink fitted main bearings in wind turbine rotor shafts.

In: Procedia Structural Integrity, Bd. 2, 3601-3609

Elsevier, Catania, 2016

[VIE17] Viebahn, Felix; Schiemann, Tom; Rieg, Frank; Leidich, Erhard: Auslegung von Abhilfemaßnahmen mit SimWag2.1 (FVA479VII; Heft Nr. 1249).

Forschungsvereinigung Antriebstechnik e.V., Frankfurt a. M., 2017

[ZIM21] Zimmermann, Markus; Viebahn, Felix; Schiemann, Tom; Rieg, Frank; Leidich, Erhard: Erweiterung des Gültigkeitsbereichs zur Berechnung von Wälzlagerwandern mit Spielpassungen in SimWag2.2 (FVA479VIII; Heft Nr. 1448).

Forschungsvereinigung Antriebstechnik e.V., Frankfurt a. M., 2021

Roller Bearing

Development of a method to consider surface morphology into the calculation of fatigue life for rolling bearings in wind power applications

L. Rüth[1], M. Harich[1], F. Adler[1], J. Nitzpon[1], P. Wingertszahn[2], O. Koch[2]

[1]Nordex Energy SE & Co. KG, Langenhorner Chaussee 600, 22419 Hamburg, Germany

[2]Chair of Machine Elements, Gears, and Tribology (MEGT), Rheinland-Pfälzische Technische Universität Kaiserslautern-Landau, Gottlieb-Daimler-Str. 42, 67663 Kaiserslautern, Germany

Keywords: Rolling bearings, Fatigue Life, Surface Roughness, Wind Power, Rotor bearing

Abstract: In increasingly larger wind turbines, the rotor bearings are becoming more and more utilized. Spherical roller bearings have kinematically significant sliding components and in combination with higher pressures and mixed lubrication conditions, the risk of surface-induced damage increases. The surface roughness in combination with lubricant plays an important role here.

The ISO/TS 16281 standard for calculating fatigue life is specifically designed for conventionally manufactured rolling bearings made of 100Cr6 (AISI 52100) with grinding and honing as the finishing process and blank (uncoated) surfaces. Although there have been many studies on their effects, the fatigue life calculation does not yet fully account for topographies and microstructural properties that deviate from conventional manufacturing processes.

The following contribution consists of two content blocks. Firstly, a study at the Chair of Machine Elements and Gear Technology and Tribology (MEGT) aimed to investigate the impact of surface topography resulting from the finishing process on the fatigue life of rolling bearings operating under mixed lubrication conditions. To achieve this, three different variants (fine grinding, rough grinding, and hard turning) were used to manufacture rolling bearing inner rings made of 100Cr6 (AISI 52100). Experimentally investigations were performed to determine the fatigue life and the surface topographies resulting from the machining were analyzed. Secondly, various measures for robustness increase at Nordex are presented, which have a positive effect on friction and wear behavior because of optimized geometries and surfaces. With these knowledge and results, calculation methods can be optimized and improved in the next step.

1 Introduction

Rolling bearings are important components of rotating drive systems in almost all industrial sectors. Of the approximately 10 billion rolling bearings produced annually, about 50 million (0.5%) are replaced due to failure [ISO/TS 16281]. About half of all failures are directly or indirectly related to surface and lubrication. According to ISO 15243, the sub-failure modes of plastic deformation due to particle overrolling, surface-induced fatigue, and abrasive wear can be counted.

This means that insufficient lubrication or contamination, rather than fatigue caused by inclusions in the material, are the main causes of failure [HaKo07], [ISO15243], [FAG04], [SKF17]. This is related to the trend towards high power densities, reliability, and compact designs. As a result, rolling bearings are subjected to higher loads, speeds, and temperatures, which are associated with lower lubricant film thicknesses [ROK17], [MGV15]. With the aim of using lower viscosity lubricants to optimize friction performance [WGH19], surface topography is increasingly coming into focus in lifetime

considerations. When a rolling bearing is operated under mixed lubrication conditions, a lubrication state similar to that of insufficient lubrication occurs in the contact area. Partial solid contact occurs there, resulting in increased pressures and stress peaks directly below the surface, which can lead to premature bearing failure [LWH19].

For this reason, high requirements must be met in the production of the rolling surfaces, which involve time- and cost-intensive processes such as grinding or honing. The lifetime calculation standard according to ISO/TS 16281 applies to conventionally manufactured rolling bearings made of 100Cr6 (AISI 52100) with grinding and honing as the final machining process [ISO/TS 16281]. Deviating surface topographies and microstructural properties resulting from new manufacturing technologies or for special applications such as in aviation cannot yet be adequately taken into account in lifetime calculations despite numerous studies on their influences.

This work focuses on the challenges of increasingly loaded rotor bearings in mechanical drive trains of wind turbines. It shows how surface roughness affects the fatigue life of rolling bearings, using cylindrical roller bearings under mixed lubrication conditions as an example. Various Nordex measures for increasing the robustness of rotor bearings to reducing friction and wear are then presented. The behavior of surface roughness over time plays a crucial role here. From this, input boundary conditions for the computational determination of fatigue life can be obtained to identify the influence of surface topography on fatigue life.

2 Main Section

2.1 Spherical roller bearing as rotor bearing in a wind turbine

The drive train is supported on the machine frame by a so-called three point rotor support. The three point rotor support consists of a rotor bearing located on the hub side and two lateral torque arms. Axial forces as well as partial horizontal and vertical radial forces are transmitted from the rotor bearing into the machine frame. Horizontal and vertical radial forces at the two gearbox supports are also transmitted into the machine frame. The torque arm of the gearbox is supported by decoupling elements (elastomer bushings), which are part of the gearbox supports. The rotor bearing should be able to compensate manufacturing tolerances and relative movements of the drive train and support structure, especially by angular movement. The relative movements are caused by elastic deformation due to the loads on structural components and of the elastic gearbox suspension.

From the first generation Alpha turbines to the current Delta4000 generation, the maximum rotor diameter has more than doubled from 80 m to 175 m. With the development of new turbine generations, the structural design of the mechanical powertrain has also been improved, resulting in the rotor bearing replacing the rotor shaft as the dimensioning component. This means that the rotor bearing no longer needs to automatically expand with the rotor shaft, allowing for better utilization of the bearing's load capacity.

Due to kinematic reasons, spherical roller bearings have two points where perfect rolling occurs along the contact length. From these points with theoretically no wear, the sliding velocities increase towards the edge. In combination with high pressures and the present mixed lubrication conditions with a specific lubricant film height of Lambda < 1, the probability of surface-induced damage increases. Bending moments and axial thrust lead to a one-sided load on the gear-side roller row. The surface roughness, which interacts with the lubricant, is of crucial importance.

2.2 Test setup at MEGT

For the rolling bearing tests at MEGT, inner rings with three different surface morphologies were manufactured using three different production methods by Interprecise Donath GmbH. All of them came from a raw material batch to avoid the influence of material quality and heat treatment. The variants are referred to as fine ground, hard-turned, and rough ground in the following.

The sudden-death method was used to determine the experimental fatigue life. The tests were run until one of the four installed bearings failed. The rotational speed was 2500 rpm and the measured outer ring temperature was 70°C. The maximum pressure in the contact was 2.2 GPa in the contact between the rolling elements and the inner ring. In addition to determining the fatigue life under mixed lubrication conditions, intermittent tests were also carried out. These were intended to investigate the changes in surface morphology due to cyclic overrolling in the rolling contact.

2.3 Experimental results at MEGT

In summary, considering the confidence intervals, large overlaps could be observed between the results at both load levels. This is mainly due to the small number of failed inner rings, which is why the differences between the variants could only be evaluated qualitatively. For a quantitative, statistically validated statement, a broader database than the existing data obtained with high experimental effort would be required. It is noticeable that the hard-turned variant tended to have the lowest scatter of failure times and the highest lifetime [RWK24], [FRK23].

To evaluate the achieved fatigue lifetimes, surface topographies were characterized using tactile measurements. In the initial state, the rough ground variant had the highest roughness, followed by the hard-turned and fine ground variants. Over time, the fine ground variant did not change significantly. In contrast, the other two variants were smoothed, which occurred primarily after 0.5 million revolutions and thus in a very early phase of operation. After 10 million revolutions, the surface roughness levels were comparable, indicating a comparable functional behavior. The running-in process could be considered complete after 10 million revolutions, as the roughness did not show any further changes after the tests have ended [RWK24], [FRK23].

A look at the different material contact ratio ranges of the Abbot-Firestone curves is shown in Figure 68. In the unloaded state, the rough ground variant has the highest profile heights in both the positive and negative profile height ranges at the same material contact ratio, followed by the hard-turned and fine ground variants. With increasing stress duration, the profile heights from both directions decrease for both the rough ground and hard-turned variants. After the running-in process is completed, in the positive profile height range, the hard-turned variant has lower values than the fine ground variant up to the inflection point of the load-carrying capacity curve at a profile height of 0 µm and a material contact ratio of 40%. Despite the lower profile heights of the fine ground variant in parts of the core and valley areas, the two surfaces can be considered tribologically comparable.

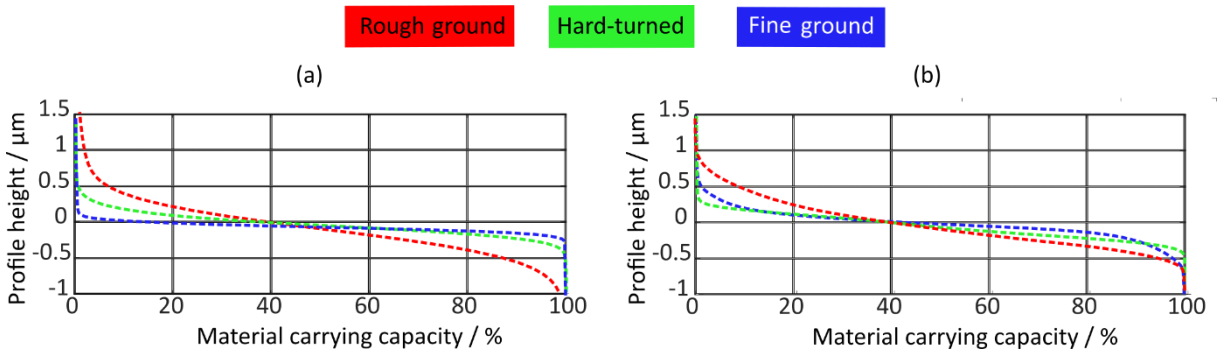

Figure 68: Abbot-Firestone curves of the confocal measured surfaces of the inner rings in the manufactured state (a) and after 10 million revolutions (b).

The surface roughness of the contact partners and the running-in behavior therefore also play a decisive role in determining the risk of surface-induced damage. The measures taken at Nordex in recent years to make the rotor bearings more robust also include the optimization of roughness peak smoothing.

2.4 Actions at Nordex to increase the robustness

Since 2021, geometrically optimized spherical roller bearings have been used to reduce pressures, friction and axial thrust. Depending on the manufacturer, this can mean, for example, that there is a rib permanently integrated into the inner ring instead of a loose rib in the form of a sleeve. Other optimization features include a cast iron cage instead of a brass cage to increase stiffness and add an additional roller. The material and heat treatment of the rollers can also differ from the catalog variants.

In the same year, Nordex installed black oxided rings or rolling elements of rotor bearings in wind turbines for the first time. A 0.5 - 2 µm thick layer of iron oxide (e.g. Fe_2O_4) is applied by immersing the part to be coated in a hot aqueous alkaline nitrate bath. Due to the low thickness, there are no fitting problems. The coating is corrosion-resistant and has a barrier against hydrogen. Sliding movements are reduced to minimize the probability of smearing damage [EBH13] and the risk of surface-induced damage can also be minimized. The most important advantage is the reduction of friction coefficient, a shortening of the running-in time and thus a delay in the start of adhesive wear [MSP10], especially under “severe” mixed lubrication conditions with lambda < 0.4. The improved smoothing of the roughness peaks can be related either to the increased running-in wear or the shearing of the black oxidized surface [HaGe15]. A disadvantage is that the surface is worn after a certain time, which is significantly lower than the fatigue life. However, this does not have consequently a negative effect on the fatigue life of the rolling surface [HaGE15].

The advantage of a durable coating to prevent adhesive wear and surface-induced fatigue is provided by the nanocomposite coating DLC (diamond like carbon). The 0.5 - 4 µm thick layer contains carbon in the diamond crystal structure for high hardness, carbon in the graphite crystal structure for low friction properties and is also doped with metal. The coating is applied using the PVD (physical vapor deposition) process. In this process, ionized metal vapour is deposited as a layer on the relatively cold substrate under high vacuum conditions at a temperature between 250°C and 450°C.

Compared to uncoated contact partners, H-DLC-coated contact partners show less wear and a significant improvement in the reduction of surface fatigue at 1.8 GPa load, lambda = 0.36 [SRE16] and less friction [HER23]. It has been shown that coating only the roller is sufficient and that a transfer of DLC (aC:H) coating to an uncoated contact partner can also take place [SRE16]. The field validation has been very successful so far.

3 Summary and Conclusion

As rotor diameters increase during new wind turbine developments, the rotor bearing is utilized more heavily as a dimensioning component. To increase the bearing service life, the focus is increasingly shifting to the surfaces of the contact partners under mixed lubrication conditions. The running-in wear can be specifically optimized through the manufacturing process or a surface coating. Several measures have been taken to increase the robustness of the rotor bearing and to minimize the risk of adhesive wear and subsequent surface-induced fatigue caused by micropitting. This shows that surface roughness must be considered for an accurate estimation of service life, which will be part of future investigations.

4 Bibliography

[EBH13] Evans, R.; Barr, T.; Houpert, L.; Boyd, S.: “Prevention of smearing damage in cylindrical roller bearings”. In: Tribology Transactions, Bd. 56 (2013), S. 703-716.

[FAG04] FAG, Hrsg.: Wälzlagerschäden: Schadenserkennung und Begutachtung gelaufener Wälzlager. 2004.

[FRK23] Foko Foko, F.; Rüth, L.; Koch, O.; Sauer, B.: „Study of the Plastic Behavior of Rough Bearing Surfaces Using a Half-Space Contact Model and the Fatigue Life Estimation According to the Fatemi–Socie Model“. In: Lubricants – Tribological Studies of Roller Bearings, Bd. 11(3) (2023).

[HaGe15] Hager, C.H.; Evans, R.D.: “Friction and wear properties of black oxide surfaces in rolling/sliding contacts. In: Wear, (2015).

[HaKo07] Harris, T. A.; Kotzalas, M. N.: Rolling Bearing Analysis. Advanced Concepts of Bearing Technology. 5. Aufl. Boca Raton, Florida und U.S.A.: CRC / Taylor & Francis, 2007.

[HER23] Humphrey, E.; Elisaus, V.; Rahmani, R.; Mohammadpour, M.; Theodossiades, S.; Morris, Nj.: “Diamond like-carbon coatings for electric vehicle transmission efficiency”. In: Tribology International, Bd. 189 (2023).

[ISO15243] Rolling bearings – Damage and failures –Terms, characteristics and causes, 2017.

[ISO/TS 16281] ISO/TS 16281: Rolling bearings – Methods for calculating the modified reference rating life for universally loaded bearings, 2008.

[LWH19] El Laithy, M.; Wang, L.; Harvey, T. J.; Vierneusel, B.; Correns, M.; Blass, T.: „Further understanding of rolling contact fatigue in rolling element bearings – A review“. In: Tribology International, Bd. 140 (2019), S. 105849.

[MGV15] Morales Espejel, G. E.; Gabelli, A.; Vries, A.: „A Model for Rolling Bearing Life with Surface and Subsurface – Tribological Effects“. In: Tribology Transactions, Bd. 58(5) (2015), S. 894-906.

[MSP10] Mihailidis, C.; Salpistis, K.; Panagiotidis, K.; Sachanas, C.; Gatsios, S.; Hoffinger, C.; Bakolas, V.: “Wear and smearing resistance of black iron mixed oxide coated steels”. In: Int. J. Surf. Sci. Eng., Bd. 4 (2010), S. 337-359.

[ROK17] Rycerz, P.; Olver, A.; Kadiric, A.: „Propagation of surface initiated rolling contact fatigue cracks in bearing steel“. In: International Journal of Fatigue, Bd. 97 (2017), S. 29-38.

[RWK24] Rüth, L.; Wingertszahn, P.; Koch, O.; Sauer, B.: „Method development for the consideration of surface morphology in rolling bearing fatigue life calculation”. In: Bearing World – 5th International FVA-Conference, (2024).

[SKF17] SKF, Hrsg.: Bearing damage and failure analysis. 2017.

[SRE16] Singh, H.; Ramirez, G.; Eryilmaz, O.; Greco, A.; Doll, G.; Erdemir, A.: “Fatigue resistant carbon coatings for rolling/sliding contacts”. In: Tribology International, (2016).

[WGH19] Woydt, M.; Gradt, T.; Hosenfeldt, T.; Luther, R.; Rienäcker, A.; Wetzel, F.-J.; Wincierz, C.: „Tribology in Germany – Interdisciplinary technology for the reduction of C02-emissions and the conservation of resources“. Tribology in Germany – Study of the German Society for Tribology, (2019).

High-Load-Capacity Tapered Roller Bearings for Wind Turbines

Etsuro Irie[1] , Yutaka Kanda[1], Dr. Brice Tchemtchoua[2], Ralf Petersen[2]

[1]NSK Ltd., 1-5-50, Kugenuma Shinmei, Fujisawa-shi, Kanagawa 251-8501, Japan

[2]NSK Deutschland GmbH, Harkortstrasse 15, Ratingen, 40880, Germany

Keywords: *High-Load-Capacity, bearing life, Tapered Roller Bearing, logarithmic crowning, edge loading.*

Abstract: The wind energy sector has consistently demanded smaller and lighter bearings which nevertheless offer higher load capacity and longer life. NSK's optimised logarithmic crowning profile for rollers results in reduced stress levels and increased bearing life under a range of different loading conditions. In this paper, the optimised roller profile of a tapered roller bearing is presented in comparison to a conventional and logarithmic profile. The calculated contact pressure and the life calculations are used to select the required design parameters. Then, in order to validate the profile parameters of the optimised logarithmic crowning, a lifetime test is carried out, which delivers excellent results.

1 Introduction

Across the wind industry we are seeing demands for a reduction in the cost of electricity generation (LCOE), as well as for lower CAPEX and OPEX costs. These demands are, in turn, driving trends towards ever larger wind turbines.

NSK is helping to accelerate the development of cost-effective larger wind turbines, introducing a special crowning design for tapered rollers bearings (TRB) specifically for use in this sector. This new design leads to longer life through higher load-carrying capacity (approximately 23% higher than the conventional model). This improvement increases wind turbine efficiency and contributes to lower OPEX costs, as does the resulting weight reduction of around 30% compared to conventional bearings.

NSK has optimised the roller crowning profile in order to reduce and equalise the contact surface pressure between the rollers and the inner and outer rings, and to prevent edge loading at the roller ends even under extreme loads. This paper will introduce the design of the NSK optimised logarithmic crowning and show comparisons with conventional and theoretical logarithmic crowning. Calculation and life test results will be presented.

2 Tapered roller bearing crowning design

Tapered roller bearings are used in a preloaded state for the planetary bearings and planet carrier bearings used in wind turbine gearboxes. They are also found in the rotor shaft, increasing rigidity and stabilising the operation of the rotating parts.

When the roller of a tapered roller bearing with conventional crowning is pressed against the outer ring, the contact pressure distribution along the roller length tends to be excessive at the contact end and is called edge load (Figure 1). This unwanted condition is made worse if the rollers are misaligned. To avoid edge loading, rolling bearings are typically crowned on either the rolling surface or the raceway surface or both.

Lundberg proposed a crowning expressed by a logarithmic function (hereafter referred to as logarithmic crowning) [LUN39] which makes the contact pressure uniform across the axial direction. However, in certain conditions this solution can shows edge loading with load increase at certain levels. Many researchers have modified the Lundberg profile to meet different needs and find an improvement solution to these issues [JOH81], [FUJ10], [LÖS87], [TUD16].

The NSK solution is an optimised crowning profile based on Lundberg's logarithmic function. It can be applied to cylindrical and conical rollers used in cylindrical and tapered roller bearings. NSK´s optimised logarithmic crowning profile reduces the contact pressure and ensures uniform distribution over the length of the roller whilst suppressing edge loading in all load cases, even under extreme loads.

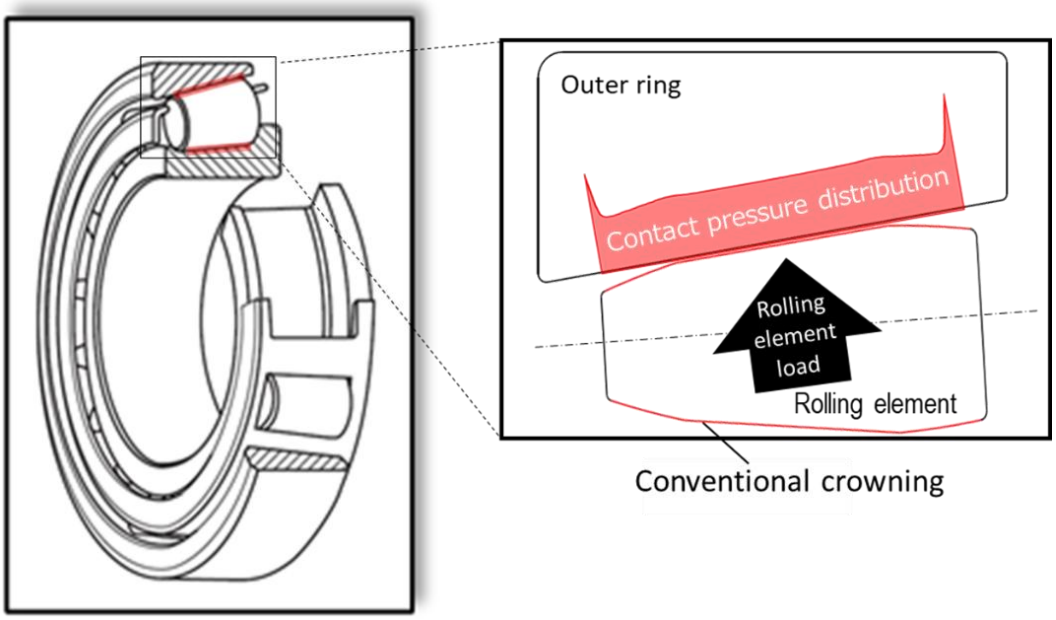

Figure 69: Contact pressure distribution in a tapered roller bearing along the roller with conventional crowning profile

In order to optimise the profile you need to know several things, including the bearing’s geometry and the operating conditions it is destined for. Specifics include operating loads, misalignment, bearing clearance or preload, roller diameter, effective roller length and raceway diameter. The process of optimsing the design profile whilst keeping the manufacturing process cost-effective is, unsurprisingly, quite challenging. To find the parameter variables for the optimal logarithmic crowning profile, NSK used a computer program for the analysis of non-Hertzian contact in rolling bearings using multi-level multi-integration (MLMI). Using MLMI allows for a detailed analysis to be performed on a personal computer in less than a minute [NAT99].

Figure 2 shows a comparison of the shapes of conventional crowning, theoretical logarithmic crowning, and NSK optimised logarithmic crowning.

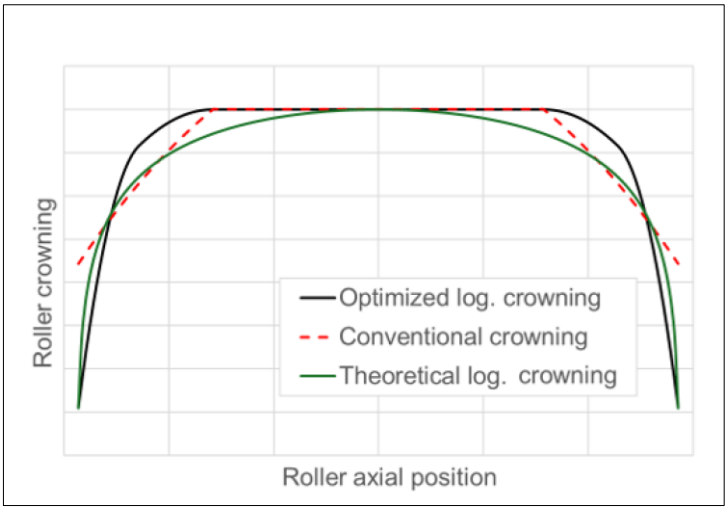

Figure 70: Comparison of the shape of roller crowning profile considered in this study

- The conventional crowning is a linear profile with one crowning radius.
- The theoretical logarithmic crowning is a single log profile.
- The optimised logarithmic profile is a combination of multiple profiles including linear, logarithmic and radius.

In the following chapters the effects of the three-roller crowning applied on the TRB used in the wind turbine gearboxes will be presented by describing the result of the contact pressure and their effect on the bearing life.

3 Effect of roller crowning on contact pressure

Three different load cases were used for the study, which we dubbed light load, medium load and heavy load. We then analysed the effect of the roller crowning on the contact pressure distribution, with P/Cr = 0.19, 0.32, and 0.615 respectively. (P: Dynamic equivalent load, Cr: Basic dynamic load capacity).

Figure 71 shows the contact pressure distribution of conventional crowning under each loading condition. The results show an uneven distribution of contact pressure under all load conditions. At low loads, the contact pressure increases at the boundary between the centre and the convex section, where the shape changes. At medium loads, edge loads occur, which increase significantly at high loads.

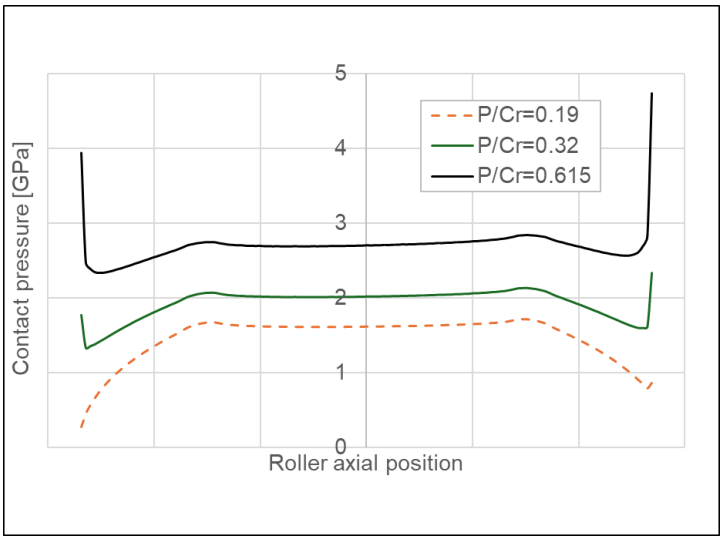

Figure 71: Contact pressure distribution of a conventional crowning profile under light, medium and high loading conditions.

Theoretical logarithmic crowning has a relatively uniform distribution of contact pressure (Figure 72). However, since the crowning shape begins to drop from the centre of the roller, the load is mainly borne by that centre, which therefore deals with the highest contact pressure from all the load cases (Figure 74). At medium loads the edge loading begins to build up slowly and becomes significant at high loads.

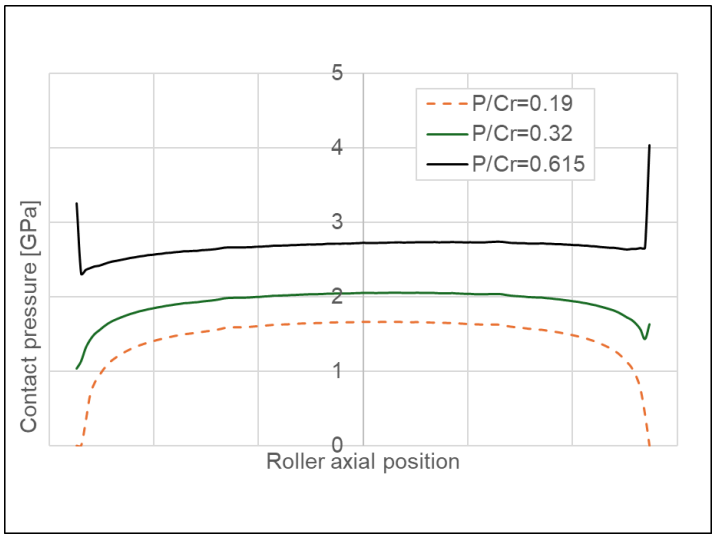

Figure 72: Contact pressure distribution of a theoretical logarithmic crowning profile under light, medium and high loading conditions.

The optimised logarithmic crowning has a shape that reduces contact pressures near the centre compared to theoretical logarithmic and conventional crowning (Figure 74). This ensures that the contact pressure is evenly distributed along the roller length under all loading conditions. While the crowning drop at the roller edge is the same in across the optimised logarithmic crowning and the theoretical logarithmic crowning, the edge load is very significantly suppressed when it comes to the optimised logarithmic crowning, which is a clear indication of the quality of the design NSK has developed.

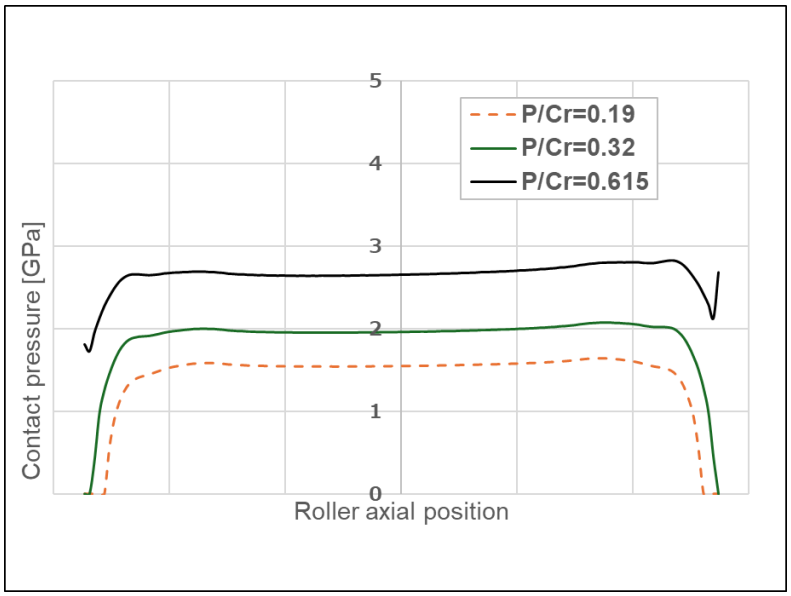

Figure 73: Contact pressure distribution of an optimised logarithmic crowning profile under light, medium and high loading conditions.

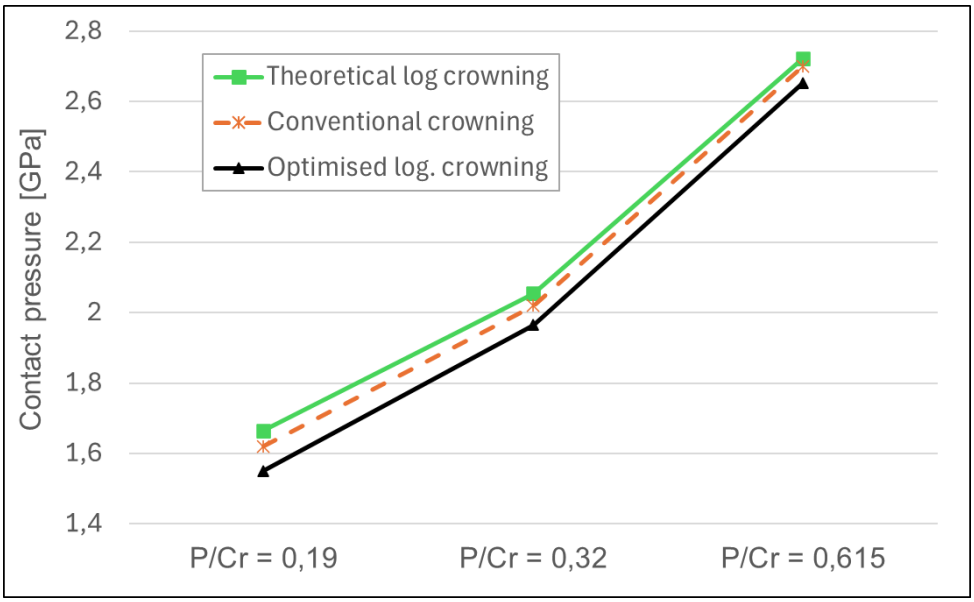

Figure 74: Comparison of contact pressure on the crowning at the centre of the roller under light, medium and high loading conditions.

4 Effect of roller crowning on bearing life calculations:

Tapered roller bearings were originally designed with the three-roller crowning profile considered in this paper. Life calculations were performed according to basic reference rating life L10r [ISO08] and the result presented in the life ratio L10r/L10, where L10 is the basic rating life [ISO07]. L10r considers the contact pressure distribution due to the actual crowning shape and is suitable for this evaluation. Bearing life calculations without misalignment were performed for the TRB HR30318J.

The calculation parameters considered in the calculation were: Outer diameter Φ190mm, inner diameter Φ90mm, assembled width 46.5mm. The basic dynamic load capacity Cr = 345kN and the basic static load rating capacity Cor = 425kN). 0 preload and 0 misalignment.

The calculation results are presented in comparison in Figure 75.

- The optimised logarithmic crowning has the longest life under all loading conditions.
- The conventional crowning has a shorter life under all loading conditions, and the life is particularly short under heavy loads due to high edge loads.
- The theoretical logarithmic crowning has a short life under light loads because of the high contact pressure in the centre of the roller (Figure 74), and under heavy loads the life is shortened due to edge loading.

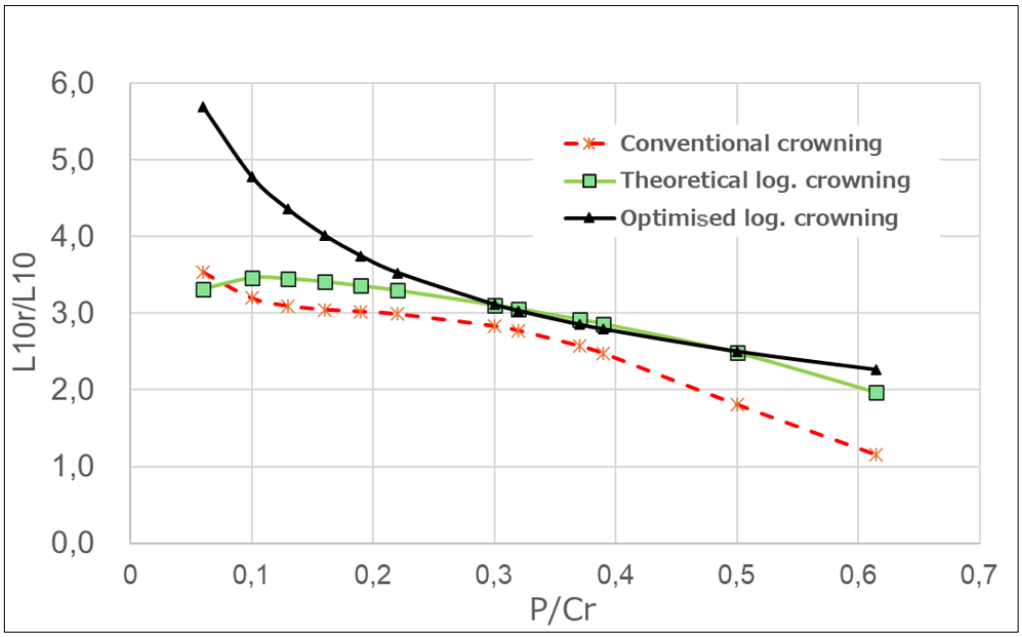

Figure 75: Calculation result of the tapered roller bearing HR30318J with the three crowning profiles in comparison

In addition, misalignment between the inner and outer rings of bearings used in wind turbines can contribute to a significant reduction in bearing life. We have performed calculations to show the impact misalignment can have on the life ratio of the optimised crowning profile in comparison to the conventional crowning.

The bearing considered for the calculation is the TRB HR32036XJ with following specification: Outer diameter Φ280mm, inner diameter Φ180mm, assembled width 64mm, Cr = 640kN, Cor = 1130kN. The calculation was carried out at high load P/Cr = 0.615 with misalignment from 0 rad to 0,0015 rad between inner and outer rings.

Figure 8 shows the results of the life ratio of the optimised and conventional crowning. The life ratio of the former is significantly higher over the misalignment range and is more than two times higher with the misalignment up to 0.0009 rad.

The maximum contact pressure of the conventional crowning increases by approximately 63% higher at 0.0009 rad, while the optimised crowning is approximately 23% higher.

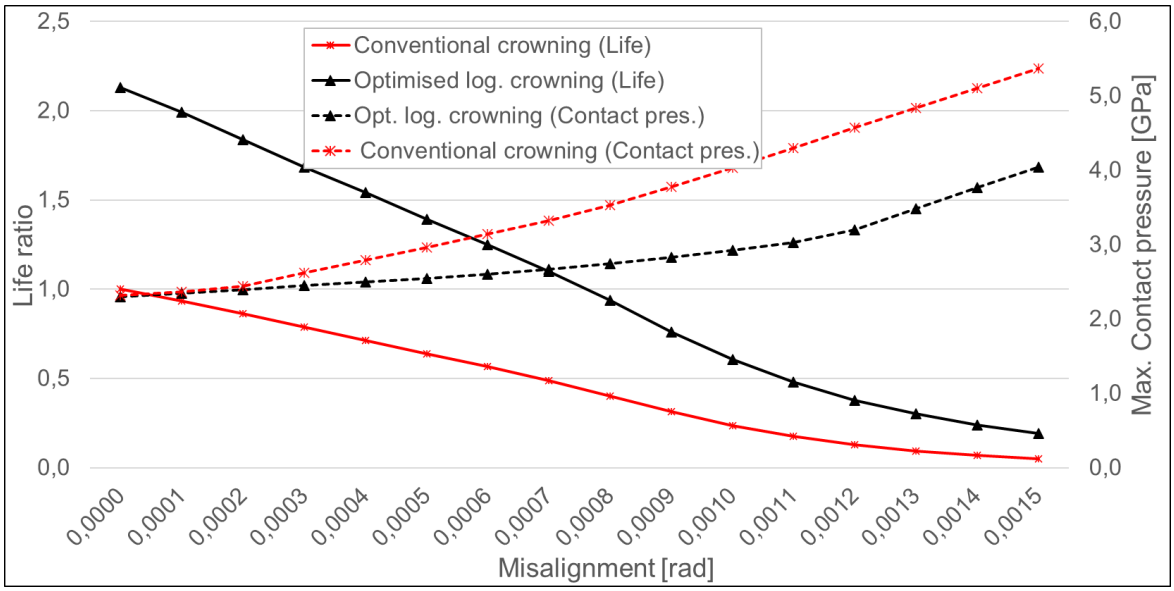

Figure 76: Effect of misalignment on the life ratio and maximal contact pressure of the TRB, comparing conventional crowning with optimised logarithmic crowning

5 Bearing life test

5.1 Test rig

For the study a test was carried out on a test rig under the following test conditions (Figure 77).

- The load conditions were
  - P/Cr = 0.5 for conventional crowning and
  - P/Cr = 0.615 optimised logarithmic crowning
- The rotation speed was 1300 min^{-1} under the lubricant oil with VG68
- The test bearing used was HR30318J tapered roller bearing with the conventional and optimised logarithmic crowning profile
- Operational preload was 0

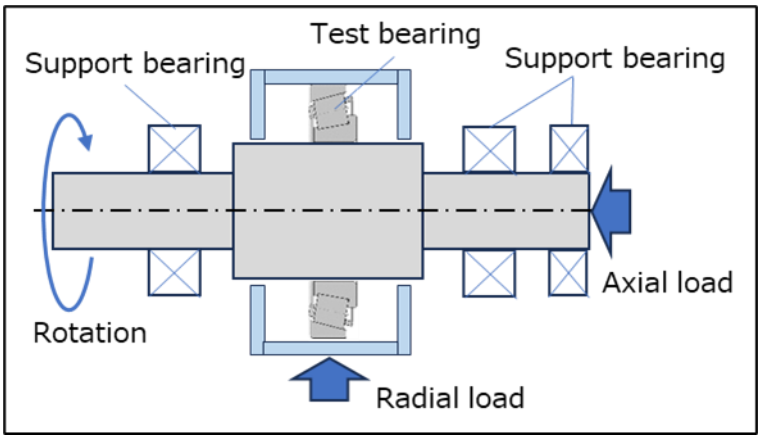

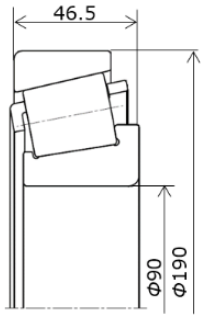

- Temperature = 38°C
- Speed = 1300 min^{-1}
- Oil lubrication
- Misalignmnent = 0 rad
- For optimised logarithmic profile P/Cr = 0,615
- For convetional crowning profile P/Cr = 0,5
- Cr = 345 kN
- Cor = 425 kN
- Roller with conventional and roller with optimised logarithmic profile
- Ring raceways without profile

Figure 77: Test rig and test bearing specification

5.2 Test result

Figure 78 shows the results of life testing for conventional crowning and optimised logarithmic crowning. Although the test load for optimised logarithmic crowning is larger than that for conventional crowning, the former has a longer life. In addition, the life test results of optimised logarithmic crowning at P/Cr = 0.615 are corrected to the life of P/Cr = 0.5 so that the life of conventional crowning can be compared under the same load condition.

Since the life of a roller bearing is proportional to the 10/3 power of the reciprocal of the bearing load, the life of optimised logarithmic crowning at P/Cr = 0.5 is corrected to twice the life at P/Cr = 0.615 $((0.615/0.5)^{10/3})$. The corrected life is shown by the black dash-dot line and is about 15 times longer than that of conventional crowning at 10% failed (806hrs vs 52hrs). The black triangle for optimised logarithmic crowning indicates the bearing life predicted by X-ray fatigue analysis after the test was terminated midway.

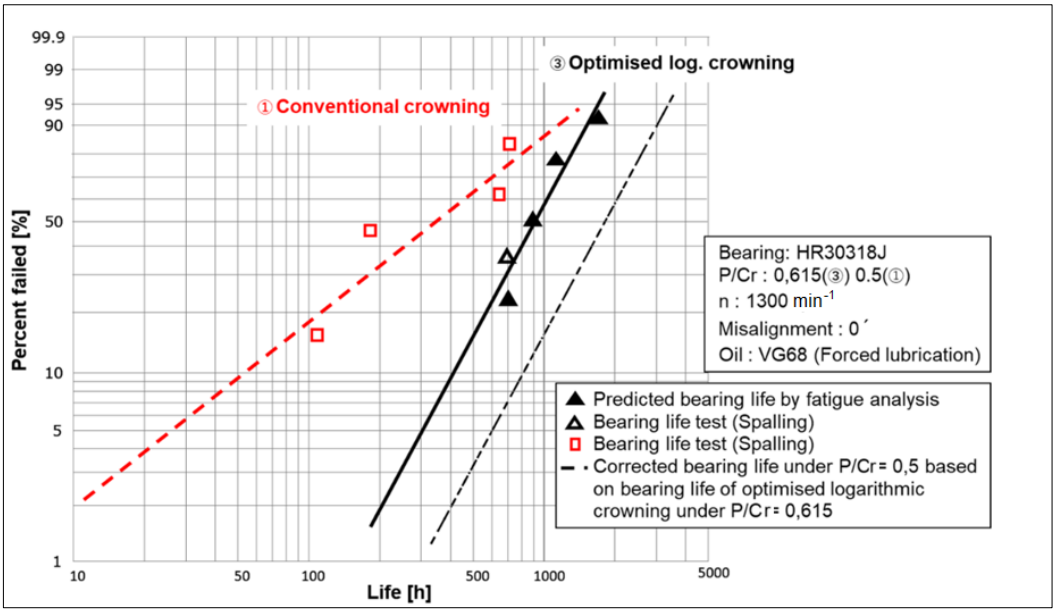

Figure 78: Life test result comparison of the TRB with conventional crowning and optimised logarithmic crowning

5.2.1 Load capacity increased and weight reduction from the optimised logarithmic crowning

As shown in Figure 7, the calculated life L10r of the optimised logarithmic crowning is more than twice the calculated life L10 under all loading conditions. Furthermore, the test result shows a bearing life result significantly longer (806 hrs) than the calculated life (L10r = 322 hrs of the optimised logarithmic crowning at P/Cr = 0.5). This is about 2.5 times longer than the calculated life L10r. Therefore, the dynamic load rating of optimised logarithmic crowning can be said to be at least 1.23 times higher than that of the conventional crowning. This equated to a dynamic load increase of approximately 23% for the optimised logarithmic crowning.

The general solution used to mitigate the excessive edge loading which occurs with the conventional crowning profile, is to increase the size of the bearing. The main reason for this drastic solution is to be able to fulfill the specification for contact pressure and lifetime defined by wind turbine guidelines [IEC12]. The increase in bearing weight, which is equivalent to 23% dynamic load rating, is estimated at about 30%. Hence a weight reduction due to the optimised logarithmic crowning profile.

6 Summary

By designing the optimised logarithmic crowning profile to handle a variety of unexpected loads that generate contact pressure as uniformly as possible, and largely avoiding undesirable edge loading, NSK was able to supply tapered roller bearings in a design that delivered the best possible results in terms of performance and weight reduction for wind turbine gearboxes. Bearings with optimised logarithmic crowning rollers and rings made from Super-TF [MUR03] material are successfully in operation in large size wind gearboxes and the optimised logarithmic crowning profile can also be applied to tapered roller bearings for the main shaft.

7 Bibliography

[FUJ10] Fujiwara H, Kobayashi T, Kawase T and Yamauchi K 2010 Optimized Logarithmic Roller Crowning Design of Cylindrical Roller Bearings and Its Experimental Demonstration, Tribology Transactions 53(6) 909-916

[IEC12] IEC 61400-4:2012 Wind turbines - Part 4: Design requirements for wind turbine gearboxes

[ISO07] ISO 281:2007 Rolling bearings — Dynamic load ratings and rating life

[ISO08] ISO/TS16281:2008 Rolling bearings — Methods for calculating the modified reference rating life for universally loaded bearings

[JOH81] Johns P M and Gohar R 1981 Roller Bearings Under Radial and Eccentric Loads, Tribology International 14 31-136

[LÖS87] Lösche T 1987 Capacity Increase Due to Modified Line Contact in Cylindrical and Tapered Roller Bearing, Ball and Roller Bearings Engineering 1 4-9

[LUN39] Lundberg,G .,E lastic Contact Between Two Semi-Infinit Beo dies, Forschunga uf den Gebiete deIsn genieurwesen5, (1939)p, p.201-211. (in German)

[MUR03] Y.Murakami: Long Life Bearing Technology by Carbonitriding Motion & Control No. 15(December 2003) p.10-14

[NAT99] S.Natsumeda: Application of multi-level multi-integration to contact problems Proc Instn Meech Engrs Vol 213 Part 3(1999) p.63-80

[TUD16] Tudose L, Ursache C, Tudose C and Rusu F 2016 Optimal 2ZB approximation of Optimal Profile of Rolling Bearings Cylindrical Rollers, 5th International Conference on Power Transmissions

BAPT, Ohrid, Macedonia, October 5-8, pp. 99-113

Bearing Creep in Wind Turbines

Jean-René KOCH

TIMKEN Europe, 2 rue Timken, 68002 Colmar, FRANCE

Keywords: bearing, creep, model, wind turbine

Abstract: The prevalent creep mechanism for wind bearing main shaft and gearbox positions is creep by runout (also known as “housing-induced” creep). Creep by strain (roller-induced) is usually prevented by the bearing design because of the large number of small rollers. Only rings rotating relative to the load are at risk of creep by runout.

The theory presented in this paper is that creep by runout is caused by differences of circumferential elongation between the bearing ring and its counterpart, combined with high contact pressure, typically in the load zone. The model developed to assess the risk of creep is a post-processing of a standard finite element calculation in the static condition. It captures the relative elongation and contact pressure at every point of the contact surface and quantifies the balance between cumulated tangential forces in the areas of negative versus positive relative elongation.

The model was successfully validated against test rig experimental results and against wind turbine configurations where creep had occurred.

1 Introduction

The purpose of this paper is to describe bearing creep, with a particular focus on wind applications. Creep is the rotation of a bearing ring relative to its counterpart (shaft or housing). Creep can generate wear and lead to catastrophic failures with very high repair costs.

The scientific community has not agreed on a common terminology for different creep mechanisms. We refer to [ISH17] to describe the two most common types of creep:

- Creep by strain, also known as “traveling-wave type” or “roller-induced” creep.
- Creep by runout, also known as “housing-induced” or “structure-induced” creep.

2 Bearing creep by strain – traveling-wave type

Creep by strain involves a deformation of the ring. Under the load caused by the rolling elements, the ring surface in contact with its counterpart (the housing in the figure below) becomes wavy. Because of the bearing’s rotation, these surface waves travel in the same direction as the rollers.

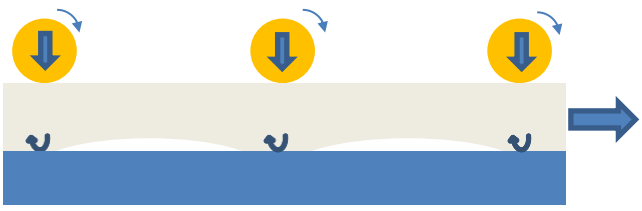

Figure 79: Sketch of creep by strain (traveling-wave type)

Influential parameters can be found in the literature [ISH17, NIW13, ZHA07, MAI13]. The bearing design – more specifically, the ratio between ring thickness t and the pitch interval (distance between

rollers) w – plays a significant role in the occurrence of creep by strain. A numerical model demonstrates that no creep can be generated for a t/w ratio above 0.6, as the amplitude of the micro-movements, which generate the waves shown in Figure 79, decreases with the depth below the roller-race contact point until it reaches zero for t/w=0.6 [NIW13].

As almost all bearing positions in a wind turbine have a design with a large number of small rollers, and therefore a t/w ratio above 0.6, creep by strain is not the prevalent creep mechanism for wind bearing positions. This paper focuses primarily on creep by runout.

3 Bearing creep by runout

3.1 Description

In its basic form, creep caused by runout occurs under two conditions:

- Loose fit.
- A rotating load relative to the ring.

Note: The loose fit value (difference in diameter between the ring and its fitting surface) is also known as "clearance" in some papers.

When the rotational load acts on the bearings, the ring rotates on the fitting surface based on the change of the load direction. If the clearance between the fitting surface and ring is c, the ring delays by π.c (the difference between the housing inner diameter and the outer ring outer diameter) per rotation of the bearing. This response causes creep – in this case, in the opposite direction of the bearing's rotation.

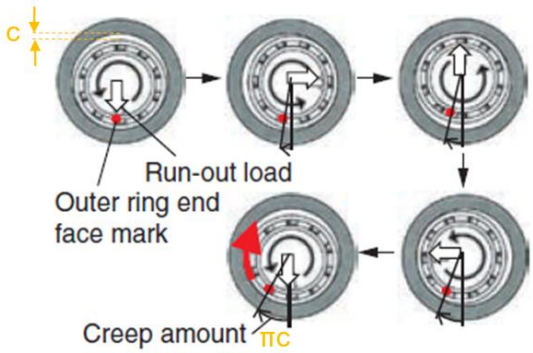

Figure 80: Creep caused by runout (from [ISH17])

The creep speed is proportional to the rotation speed and the clearance, a relationship that has been validated experimentally on our test rig (see below). This creep mechanism can generally be avoided if the following design rule is observed: **Tight fit is mandatory for rings subject to a rotating load**.

Note 1: Loads are most commonly fixed (e.g., weight), and therefore the tight fit must be applied on the rotating ring. If the load is rotating (e.g., vibrating screen), the tight fit is mandatory on the fixed ring.

Note 2: Fits are not only driven by the risk of creep. Tight fits may also be used on rings not subject to a rotating load.

However, a tight fit is not always sufficient to prevent creep caused by runout. When the housing or shaft stiffness is low and/or when the application is subjected to extreme loads, favorable conditions for creep can result.

3.2 Experiments

The Timken Company carried out a number of experiments to evaluate the effect of several parameters on creep by runout. The experimental setup is as follows, with two tapered roller bearings (TRBs) in an indirect arrangement:

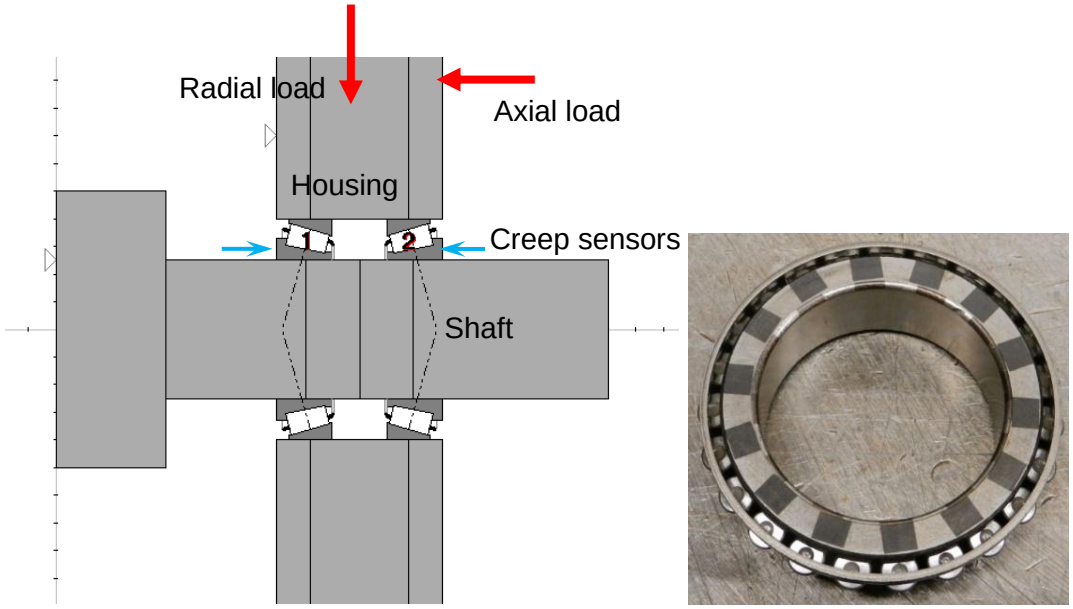

Figure 81: Creep by runout – experimental setup; cone back face is laser-marked

In this setup, the shaft rotates and the housing is fixed. Fixed loads in the radial and axial directions were applied on the housing. The creep between the inner rings (cones) and the shaft was evaluated, as they were the rings under the rotating load. The cone back faces were marked with dark and light angular sectors so the sensors could capture the amount of creep rotation.

A parametric variation was performed on the following parameters:

- Fits (difference between shaft outer diameter and cones' inner diameter)
- Loads
- Shaft stiffness (several hollow shafts with various inner diameters were used)

3.2.1 Experimental results with full shaft

With *loose fits* (clearance) between the cones and shaft, the experiments confirmed the creep distance of π times the clearance value per bearing rotation. Without an axial load, both cones experience creep. The addition of the axial load tends to prevent creep.

With *transition fits* (cone inner diameter equal to shaft diameter), some radial load is needed to generate creep. In most cases, only one bearing creeps. The creep speed increases as the radial load gets higher. An axial load tends to eliminate creep.

No creep is obtained with *tight fits*.

3.2.2 Experimental results with hollow shafts

The hollow shafts tested in this experiment have less radial stiffness than the full shaft. Similar trends are observed as with the full shaft: Favorable conditions for creep occurrence are transition fits or very light tight fits combined with high radial loads. Creep also tends to be prevented by the application of an axial load.

Compared to the full shaft, creep occurs at lower loads and with tighter fits. Creep was obtained with tight fits on all hollow shafts, whereas it was absent on the full shaft.

Generally, more favorable conditions for creep occurrence tend to generate a higher creep speed. No significant influence of the shaft rotation speed is expected on creep occurrence. When creep is obtained, the creep speed tends to be proportional to the shaft speed.

4 Creep by runout model

4.1 Overview

The creep by runout assessment is made through a post-processing of standard static finite element calculations. The Timken Company typically runs these calculations to model bearing behavior with roller load distribution as primary objective. Rings are modeled with their geometry and material, whereas rollers are modeled with non-linear springs that account for the roller, the Hertzian contact stiffness, and the roller-race profiles.

The first step of the calculation consists of solving for the mounted equilibrium, considering fits between the rings and shaft or housing and setting (for tapered roller bearings). External loads are applied in a second step.

4.2 Principle of the creep assessment

The theory underlying the model and creep assessment is based on the following assumptions:

- Only rings submitted to a rotating load are at risk for creep by runout: i.e., either rotating rings submitted to a fixed load or fixed rings submitted to a rotating load.
- When only fits (necessarily tight for rings submitted to a rotating load) are applied, diameters are equal at the interface between the ring and its counterpart: The inner ring bore diameter equals the shaft outer diameter; the outer ring outer diameter equals the housing inner diameter. The relative circumferential elongation is defined as equal to zero at every point of the contact surface between the ring and its counterpart.
- External loads locally modify the relative circumferential elongation. We define the relative elongation as **positive** if the larger component elongates less (or contracts more) than the smaller component. We define the relative elongation as **negative** if the larger component elongates more (or contracts less) than the smaller component. Note: Areas of negative relative elongation are normally in the majority, as the diameter of the larger component must remain greater than the diameter of the smaller component.
- Tangential forces at the contact surface are driven by the relative circumferential elongation and the contact pressure. These forces tend to create a difference in both components' rotation speeds. Typically, under radial loads, the load zone is an area of negative relative elongation and high contact pressure, causing the small component to rotate at a higher speed relative to the large component.

The next figure illustrates the theory in the case of a rotating inner ring submitted to a fixed load:

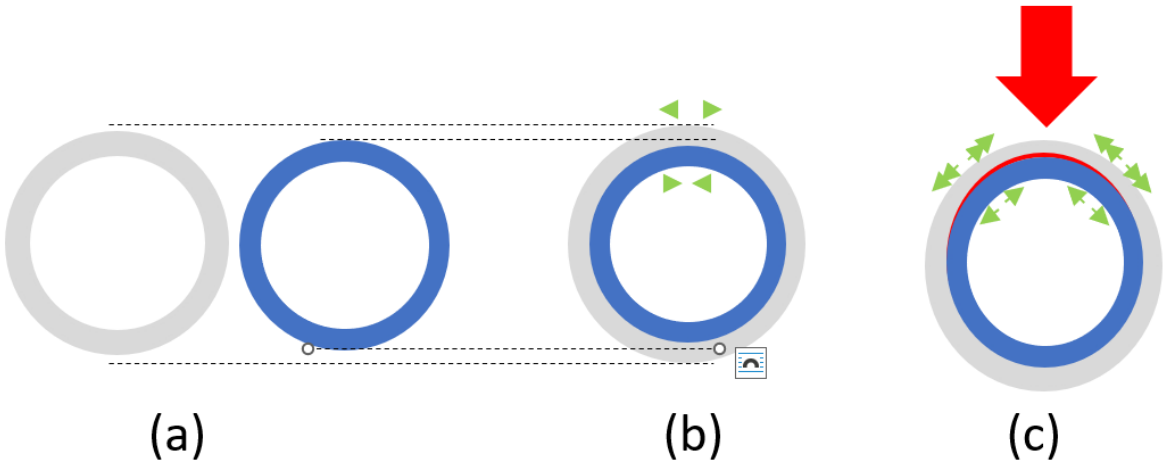

Figure 82: Relative elongation under radial load

- **(a)** Ring (gray) and hollow shaft (blue) before tight fit assembly
- **(b)** Assembled ring and shaft; the shaft contracts and the ring expands circumferentially
- **(c)** After the load is applied, an area of high contact pressure (red) is created in which the ring generally elongates more than the shaft compared to the reference state (b)

4.3 Post-processing practice

The creep by runout assessment is a post-processing of the finite element calculation results for rings under a rotating load.

The input data are the relative circumferential strain of the ring and its counterpart, shaft or housing, and the contact pressure between them at every node of their contact surface (bore or outer diameter; back faces are excluded). The relative circumferential strain is the difference between strain values in the circumferential direction at the final state (after loads are applied) and at the reference state (solved for the fits and setting).

Nodes are sorted in bins depending on their relative circumferential strain. In each bin, the contact pressure is cumulated for all nodes and multiplied by a nodal surface, resulting in a total contact force.

The following diagram is generated:

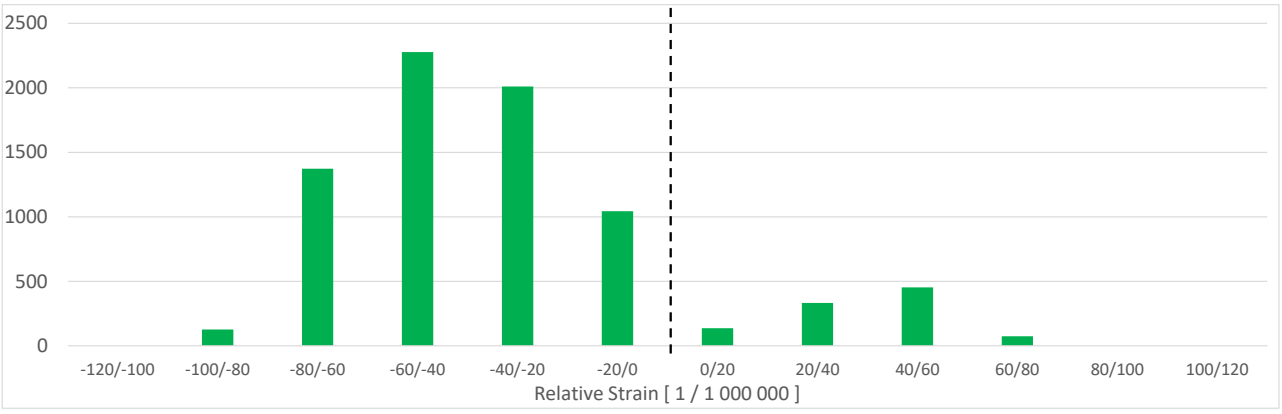

Figure 83: Post-processing results: Balance of forces in areas of negative relative elongation (left)

and positive relative elongation (right)

Ultimately, creep is generated when the cumulated forces in the area of negative relative elongation exceed the cumulated forces in the area of positive relative elongation.

4.4 Creep assessment

An indicator (not shared in the present paper) was defined to quantify the balance between both types of forces. Some limit value of this indicator must be found to materialize the limit of creep occurrence. Above this limit, the higher the indicator, the more severe the creep.

5 Experimental validation

5.1 Method

The model and the post-processing for creep assessment described in the previous section were implemented and compared with experimental results:

- Of the test rig (see paragraph 3.2).
- Of various configurations of wind turbine applications (main shaft and planet carrier positions).

On the horizontal axis, the indicator mentioned in paragraph 4.4 to predict the occurrence and severity of creep is used. On the vertical axis, the experimental result is mentioned: Creep or no creep, and for configurations with creep, the point is plotted higher for higher creep severity. The severity is measured by the creep speed (relative circumferential displacement between the ring and its counterpart in a given number of bearing revolutions).

5.2 Results of the experimental validation

Ideally, if the model predicting creep works well, all points should be aligned on a diagonal from the lower left corner to the upper right corner.

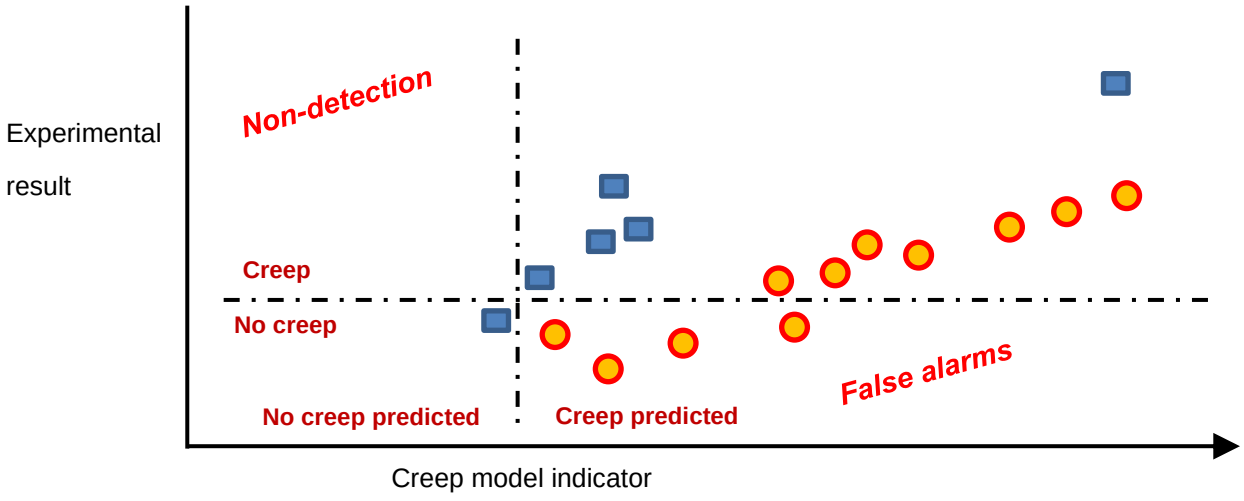

Legend:
Test rig configurations
Wind turbine applications

Figure 84: Experimental validation results

Comments:

- For wind turbine applications, the points are more or less aligned on the expected diagonal, and there is no false alarm (lower-right quadrant) or non-detection (upper-left quadrant).
- Test rig configurations are also positioned on a diagonal, but with the same creep occurrence limit; a few false alarms were observed.
- Moving the limit to the right for test rig configurations could solve the problem of false alarms; these could be attributed to a size effect, but different friction coefficients could also be the reason.

Note: The test rig explored steel-on-steel contacts between the bearing and shaft, whereas wind turbine applications are made of cast iron shafts or housings.

5.3 Influential parameters

The model can be used to carry out parametric variations. In this paper, the predicted effect of a change of the bearing tight fits is presented.

The following diagram helps to compare test rig configurations with different fits:

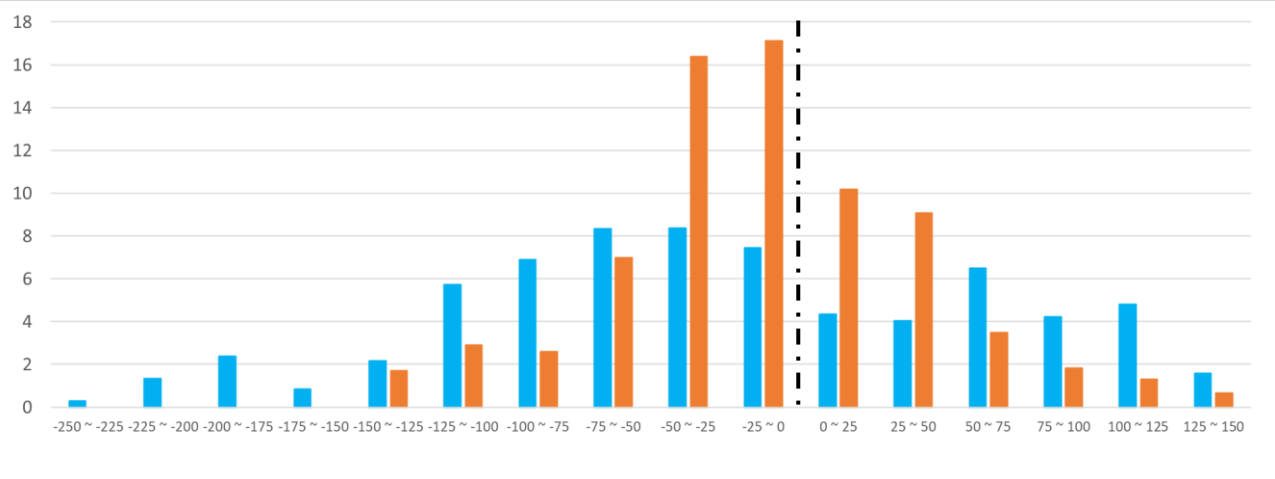

Legend:
Moderate tight fit
Higher tight fit

Figure 85: Balance of forces in areas of negative relative elongation (left) and positive relative elongation (right) - Prediction of fits effect

The distribution of contact forces with the tighter fit (orange) is more concentrated close to areas with zero relative elongation and is, on average, more centered than those with the less tight fit (blue). The indicator predicts less likelihood of creep with a tighter fit, which conforms with real-world test results.

According to this model, the primary reason tighter fits prevent creep by runout is not the increased contact pressure, but the reduction of circumferential relative elongation.

Other simulations can be performed. For example, the model predicts that a higher coefficient of friction tends to concentrate the distribution of forces close to areas with zero relative elongation, reducing the risk of creep.

Finding the exact limit between creep and no creep is certainly difficult, but this model will be useful for capturing the major trends and identifying design applications that have a reduced risk of creep.

6 Conclusion

Creep by runout (housing-induced) is the prevalent creep mechanism for wind turbine bearing positions. Creep by strain (roller-induced) is usually not possible because these bearings have a large number of small rollers, hence a high t/w ratio.

Only rings submitted to a rotating load are subject to creep by runout. A tight fit is not always sufficient to prevent it, especially for compliant structures submitted to high loads. A parametric variation on fits, loads and shaft stiffness carried out on a small test rig confirmed these trends.

A theory explaining creep by runout was suggested: Creep by runout is generated by a combination of high contact forces and differences of circumferential elongation between components, typically in the load zone. The creep assessment is performed via post-processing of a static finite element calculation; it quantifies the balance between cumulated forces in the areas of negative versus positive relative elongation.

The model was successfully validated against test rig experimental results and against wind turbine configurations where creep had occurred.

7 Bibliography

[ISH17] Y. Ishii and T. Jinbo, *Development of Anti-Creep Ball Bearing for Outer Ring*, JTEKT technical report, JTEKT Engineering Journal English Edition No. 1014E (2017)

[MAI13] A. Maiwald and E. Leidich, *FE Simulations of Irreversible Relative Movements (Creeping) in Rolling Bearing Seats – Influential Parameters and Remedies*, Proceedings of the World Congress of Engineering and Computer Science 2013 Vol. II, WCECS 2013, 23-25 October 2013, San Fransisco, USA

[NAG15] Yayoi Nagasoe, Shigeharu Wakui, Yuta Maeyoshi, *Technology for Prediction of Housing Wear due to Outer Ring Creep under Bearing Load*, technical paper, Honda R&D Technical Review (October 2015)

[NIW13] Tsuyoshi Niwa, *A Creep Mechanism of Rolling Bearings*, technical paper, NTN Technical Review No. 81 (2013)

[SCH19] Felix M. Schlüter, Georg Jacobs, Dennis Bosse, Thilo Brügge, Felix Schlegel, *Correlation of Planetary Bearing Outer Ring Creep and Gear Load Distribution in a Full-Size Wind Turbine*, NAWEA WindTech 2019, Journal of Physics: Conference Series 1452 (2020) 012062

[ZHA07] Jianjun Zhan, Hiromichi Takemura, Kinji Yukawa, *A Study on Bearing Creep Mechanism with FEM Simulation*, Proceedings of IMECE2007, 2007 ASME International Mechanical Engineering Congress and Exposition, November 11-15, 2007, Seattle, Washington, USA

Gearbox I

Probabilistic Modelling of the Tooth Root Strength of Wind Gears

Jonas Finken[1], Jean-André Meis[2]

[1]Flender GmbH (Winergy), Am Industriepark 2, 46562 Voerde

[2]Flender GmbH, Alfred-Flender-Straße 77, 46395 Bocholt

Keywords: tooth root, load capacity, probabilistic design, reliability, torque density

Abstract: Tooth root strength is one of the main design criteria for wind gearboxes, often being a major bottleneck for torque density potential. In contrast to this, the field experience of most gearbox manufacturers shows next to no tooth root failures. This is due to the conservative requirements of the IEC 61400-4 and the ISO standard 6336-3 [ISO06], especially the high minimum safety factor $S_{F,min}$ = 1.56. This leads to the question of how far the margin can be decreased without yielding to a significant increase of the failure probability. A possible way to answer this question is the use of probabilistic design. At Winergy, a method based on the framework of ISO 6336-3 and -5 was developed to calculate the tooth root failure risk under consideration of all relevant input data including scatter. This includes the statistical distribution of the material strength, the scatter of the CHD, deviations in the surface roughness as well as the effect of tolerances of supporting structures (e.g. positions of planet pins in the carrier) that effect the load sharing and the load distribution along the gear width. In this paper, the basic methodology will be shown as well as its implementation into an industrial framework. This includes the handling of data from production processes and suppliers as well as the calculation software. The newly developed method will be compared to the classical approach on a real-life application.

1 Introduction

The state-of-the-art calculation of gear tooth root load capacity according to ISO 6336-3:2006 [ISO06] involves empirical-analytical methods for determining tooth bending strength in spur, helical, and internal gears. This standard incorporates various geometry, material and load influences and provides a comprehensive method for evaluating tooth root stress, ensuring safety against tooth bending fatigue. One of the key features of this approach is its high safety margins, which are designed to account for uncertainties and ensure reliable performance under a wide range of conditions.

In contrast, probabilistic design considers the uncertainties of input parameters by treating them as random variables with specific probability distributions. This method allows for a more realistic assessment of gear performance under varying conditions, including influences from material properties, geometric variations, and load deviations. The advantages of probabilistic design include better material utilization, as it optimizes the design to account for a quantified variability, leading to more efficient use of resources. This optimization not only enhances economic benefits by reducing material costs but also has a positive ecological impact by minimizing waste and promoting sustainable practices.

In the wind gearbox industry, there is a continuous drive to improve torque density, which is crucial for enhancing the efficiency and performance of wind turbines. Achieving higher torque density means that gearboxes can transmit more power without increasing their size or weight, which is

essential for reducing costs and improving the overall sustainability of wind energy systems. A probabilistic approach is best suited to maximize torque density because it allows for a more precise optimization of gear designs. By accounting for the variability in material properties, geometric tolerances, and load conditions, probabilistic design ensures that gearboxes are both robust and efficient, pushing the boundaries of performance while maintaining reliability. This leads to better material utilization, reduced manufacturing costs, and a lower environmental footprint, aligning with the industry's goals of economic and ecological sustainability.

2 State of the Art

2.1 Tooth Root Load Capacity acc. to ISO 6336-3

The ISO 6336-3 standard for calculating the load capacity of spur and helical gears [ISO06] involves determining the nominal bending stress σ_{F0} at the root of the gear tooth and applying various correction factors to account for different influencing parameters. The base stress calculation typically involves using the tangential load on the gear tooth F_T, the face width of the gear (b), and the normal module of the gear (m_n). Important factors such as the form factor Y_F, which accounts for the shape and geometry of the gear tooth, and the stress correction factor Y_S, which corrects for the non-uniform distribution of stress at the tooth root due to the root shape, are critical in this calculation. Additionally, for helical gears, the helix angle factor Y_β adjusts the stress calculation to consider the inclination of the gear teeth. Finally, the rim thickness factor Y_B accounts for thin gear rims and the deep tooth factor Y_{DT} accounts for high transverse contact ratios. This leads to the nominal tooth root stress formula:

$$\sigma_{F0} = \frac{F_t}{b \cdot m_n} \cdot Y_F \cdot Y_S \cdot Y_\beta \cdot Y_B \cdot Y_{DT.} \qquad \textbf{Eq. 2}$$

To adjust for real-world conditions, several correction factors, or K-factors, are applied. The application factor K_A considers additional loads due to the operating environment, such as shocks and vibrations. The load distribution factor $K_{F\beta}$ corrects for the uneven distribution of load across the gear face width, which can be influenced by misalignment and deflection. The dynamic factor K_V accounts for dynamic effects, including the impact of gear tooth engagement and disengagement. [ISO06]

The final bending stress σ_F is then calculated by combining the base stress σ_{F0} with these correction factors. To ensure the gear design meets the required performance, the resulting stress is compared with the permissible stress σ_{FP}, which will be described in the following paragraph.

The permissible stress σ_{FP} defines the maximum allowable stress the gear teeth can withstand without failure for a failure probability of 1%. This value is determined by considering several influencing factors, including material properties, heat treatment processes, and various safety and reliability factors. The material's allowable bending stress limit, denoted as σ_{Flim}, is derived from its tensile strength, yield strength, and fatigue strength, which dictate how well the material can endure repeated loading and resist failure over time. Heat treatment processes such as carburizing, nitriding, and induction hardening significantly enhance the material's surface hardness and fatigue strength by modifying its microstructure, thus improving its wear resistance and ability to withstand high stress levels.

Several correction factors are applied to account for different aspects of gear performance and reliability: the stress correction factor Y_{ST} adjusts for the stress concentration at the gear tooth root,

accounting for the gear tooth geometry and profile of the standard reference test gear; the life factor Y_{NT} accounts for the anticipated number of load cycles the gear will experience during its service life, adjusting the permissible stress to ensure durability over the expected lifespan; the relative surface factor Y_{RrelT} adjusts the permissible stress considering surface roughness in the tooth root; the relative notch sensitivity factor $Y_{\delta relT}$ accounts for the material's sensitivity to notches and other stress concentrators, adjusting the permissible stress to reflect how the material's fatigue strength is affected by notches and surface imperfections; and the size factor Y_X corrects for the size effect, as larger gears may experience different statistical damage behaviour compared to smaller gears.

The permissible stress σ_{FP} is calculated by incorporating these factors into the base allowable bending stress limit σ_{Flim} using the formula [ISO06]:

$$\sigma_{FP} = \frac{\sigma_{Flim} \cdot Y_{ST} \cdot Y_{NT}}{S_{Fmin}} \cdot Y_{RrelT} \cdot Y_{\delta relT} \cdot \ Y_X \qquad \textbf{Eq. 3}$$

where S_{Fmin} is the minimum demanded safety factor. To ensure the gear design meets the required performance, the resulting stress σ_F is compared with the permissible stress σ_{FP}. If the resulting stress is within the permissible limits, the gear is deemed to be safe and suitable for the intended application.

2.2 Probabilistic design methods

Probabilistic design methods are essential in some fields of engineering such as civil engineering for assessing the reliability and safety of structures such as bridges, buildings, and dams. These methods incorporate the inherent uncertainties in material properties, loads, environmental conditions, and construction processes to predict the likelihood of failure or survival of a technical system. The central concept in probabilistic design is the use of limit state functions, which define the boundaries between safe and failure states of a structure.

A limit state function, g(X), is formulated to represent the difference between the capacity of a structure and the stresses it is subjected to. Here, X is a vector of random variables that influence the performance of the structure, such as material strengths, loads, and dimensions. The function is defined such that g(X) > 0 indicates a safe state, g(X) = 0 represents the limit state or the boundary of failure, and g(X) < 0 signifies failure. By modeling these variables probabilistically, engineers can account for the variability and uncertainty inherent in each component of the system.

To predict the probability of failure, probabilistic design methods utilize statistical techniques to evaluate the probability distribution of the limit state function. One common approach is the Monte Carlo simulation, which involves generating a large number of random samples of the input variables, computing the corresponding g(X) values, and estimating the probability of failure as the proportion of samples for which g(X) < 0..

Probabilistic design methods are especially critical for components of wind turbines where failure can have severe consequences, such as environmental hazards or risks to human safety. For instance, the collapse of a wind turbine tower or the failure of its foundation can lead to significant environmental damage, including the release of hazardous materials or disruption of local ecosystems. Additionally, such failures pose serious risks to maintenance personnel and nearby communities. Furthermore, these probabilistic approaches are gradually being integrated into the load capacity evaluation of machine elements, including housings, shafts, and gears. In mechanical engineering, these components often operate under fluctuating loads and varying operating conditions,

which can introduce uncertainties in their performance and longevity. For the tooth root load capacity of gears, a summary of selected primary influences can be found in Figure 86.

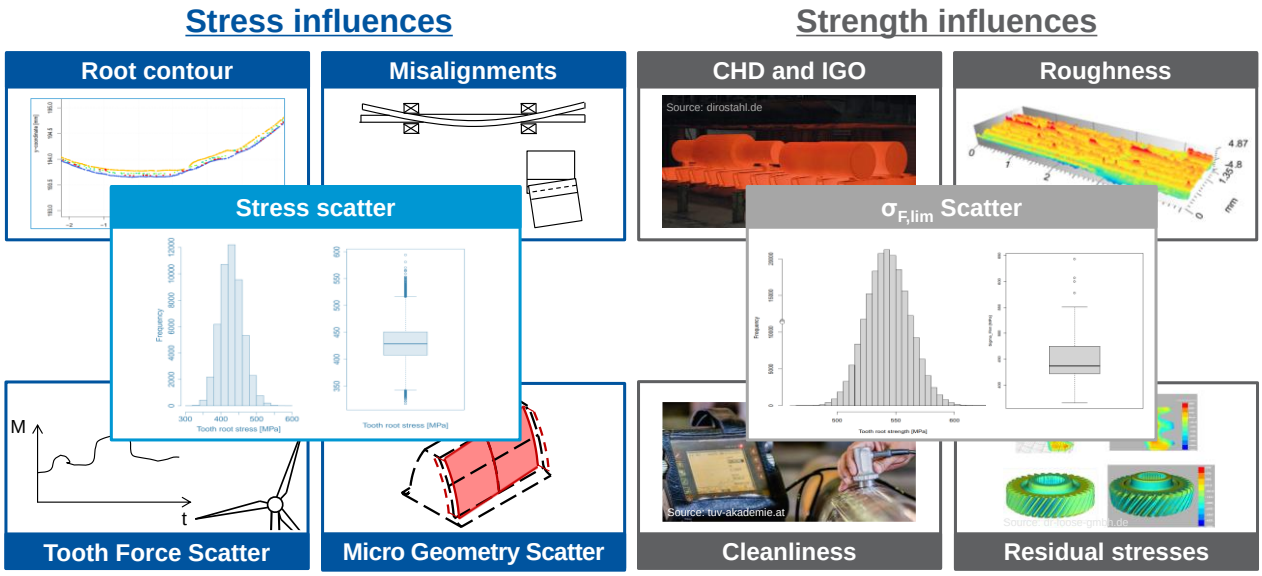

Figure 86: Selected influences on gear tooth root load capacity

3 Probabilistic Design Framework

At Flender, a probabilistic design framework for gearbox components has been developed to enhance reliability and performance. This sophisticated framework integrates both material-side strength factors, such as case hardening depth (CHD), grain structure, and inclusions, along with the geometric intricacies of the components, including tolerances. By adopting a probabilistic approach, the framework allows for a comprehensive modelling of the forces acting on the parts, factoring in the variability and tolerances of surrounding structures like planet carrier bores, bearing seats, and bearing tolerances, see Figure 87.

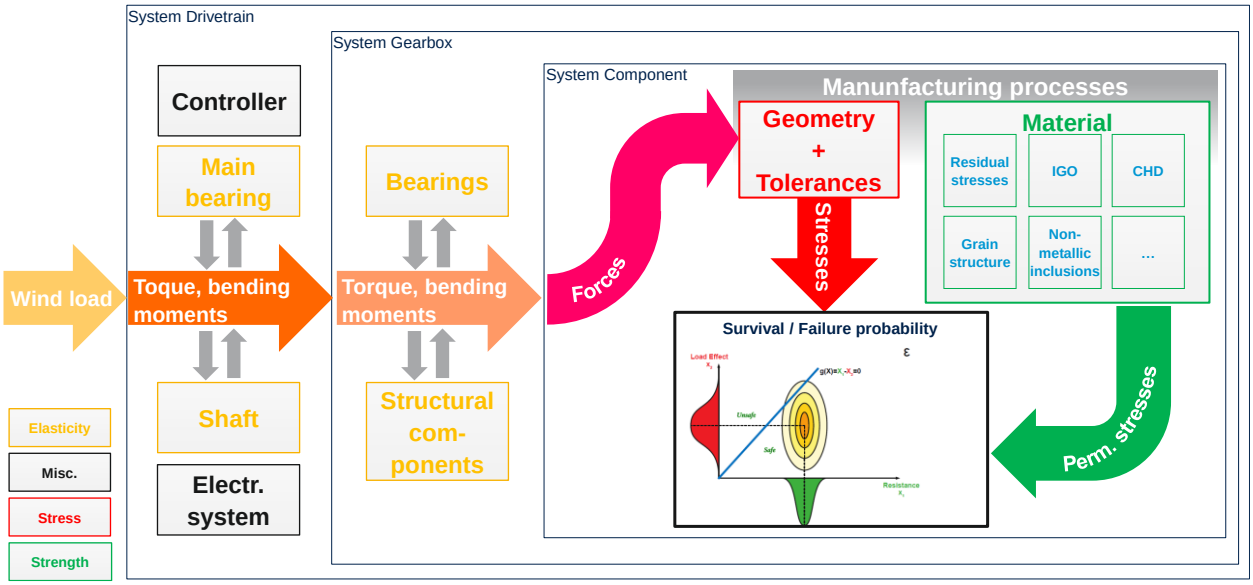

Figure 87: Modular probabilistic design environment for machine elements of a wind gearbox

In the pursuit of a more accurate probabilistic gear load capacity evaluation, Flender has adapted the basic formulae of ISO 6336-3 to better fit their advanced design framework. By modifying these standard calculations, the new approach incorporates the variability and statistical distribution of material properties, geometric tolerances, and operational forces.

4 Exemplary Application

An exemplary application of Flender's probabilistic design framework can be observed in the tooth root load capacity evaluation of the planet gear in a second stage of a series wind turbine gearbox with a three planetary stage layout. For the purpose of this paper, the following main influencing factors on tooth root reliability have been taken into account beyond the scope of the ISO 6336–3:

- Scatter of σ_{Flim} values as a result of varying material qualities and compositions
- Scatter of load sharing of the planets by varying K_γ
- Scatter of mesh misalignment expressed by varying $K_{F\beta}$ values
- Scatter of heat treatment distortion and grinding stock removal and subsequent variations in Y_S and Y_F

These main influences will be described in the following subchapters.

4.1 Statistical Modelling of Material Strength (σ_{Flim})

The distribution of the pitting and tooth root strength capacity was determined at Flender through intensive data evaluation of a large amount of test data and targeted material tests. As these distribution functions are strictly confidential, a simplification based on the information in ISO-6336-5 and Stahl's dissertation is used here.

The characteristic values σ_{Flim} and σ_{Hlim} apply to a survival probability of 99%. Stahl determined that the conversion factor from 50% to 99% survival probability assumes the value 0.92. With these two pieces of information, the mean value and the standard deviation of the strengths can be determined. This results in a mean value of 543.5 MPa and a standard deviation of 18.7 MPa for the

tooth root strength of case-hardened gears. Since a normal distribution can theoretically have negative strengths, it is not well suited for modeling gear strength capacity. Therefore, the two parameters are modified so that they describe a logarithmic normal distribution. The shape parameter σ then results as follows: $\sigma = \sqrt{\ln\left(\frac{Var}{\bar{x}^2} + 1\right)}$ while the position parameter μ can be determined according to the following relationship: $\mu = \ln(\bar{x}) - \frac{\sigma^2}{2}$. Var in both equations is the variance of the strength, $\bar{x}$ is the mean value. These distribution parameters can then be used to generate random numbers for the Monte Carlo simulation of tooth root safety. Figure 88 shows exemplary histograms for the root and pitting load capacity of case-hardened gears.

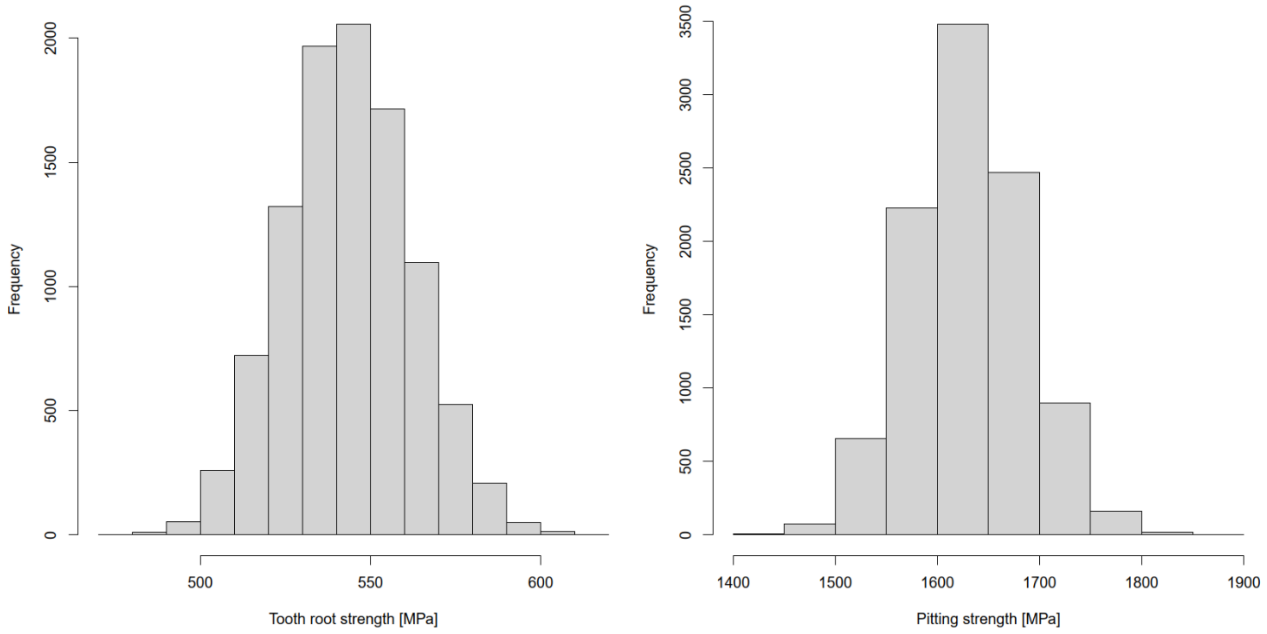

Figure 88: Random values for tooth root strength (left) and pitting strength (right) according to the distribution parameters for case hardened gears.

4.2 Statistical Modelling of Load Sharing (K_γ)

In order to quantify the influence of the manufacturing tolerances on the load distribution between the 6 planets, the parametric FE model was used, which has already been presented in [MEIS23]. Figure 89 shows the basic structure of the model on the left side. The load is applied to the rotor of the wind turbine, but only a torsional moment is taken into account. The load is then distributed to the 6 planets via the planet carrier, the ring gear is connected to the torque arm, to which the supporting torque is transferred, while the torque is transferred to the next stage at the sun gear.

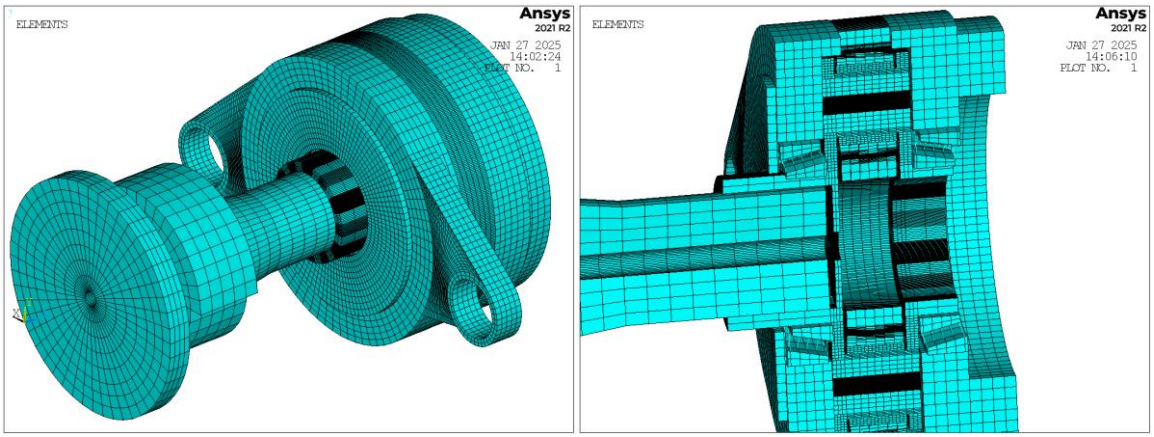

Figure 89: General layout of the parametric FE-model (left) and cut section of the planetary stage in the parametric FE-model (right)

The model considers the main bearing of the turbine as well as the two tapered roller bearings which are supporting the planet carrier, see Figure 89 right.

From the measurement data for the manufacturing accuracy of the planet carrier, the position deviation of each planet axle bore was evaluated for 23 real components and an FE model with the respective actual geometry was created. An offset of the generator and rotor-side bores or a radial or tangential shift of the entire position of an axis results in deviations in the load distribution between the planets. It should be noted here that the 6 planets together transmit the entire torsional moment, so there are individual planets with increased loads, while others are less loaded.

The individual load sharing factor Kγ can therefore be greater or less than one. Figure 6 shows this as an example using a box plot for 10,000 random variants of all 6 planets. The majority of the load sharing factors lie in the interval 0.9 to 1.1, but there are also rare outliers in the range 0.6 to 1.4. On average, however, the load sharing factor is 1.0, as the total load must be transferred across all planets. In addition, Figure 90 shows the combination of the individual load distribution factors for an exemplary stage using a red line. The first planet has the value 1.18, the second the value 0.9, the third 0.85, the fourth 1.025, the fifth 0.975 and the sixth 1.1. With these values, the tooth root safeties can now be scaled accordingly in the Monte Carlo simulation.

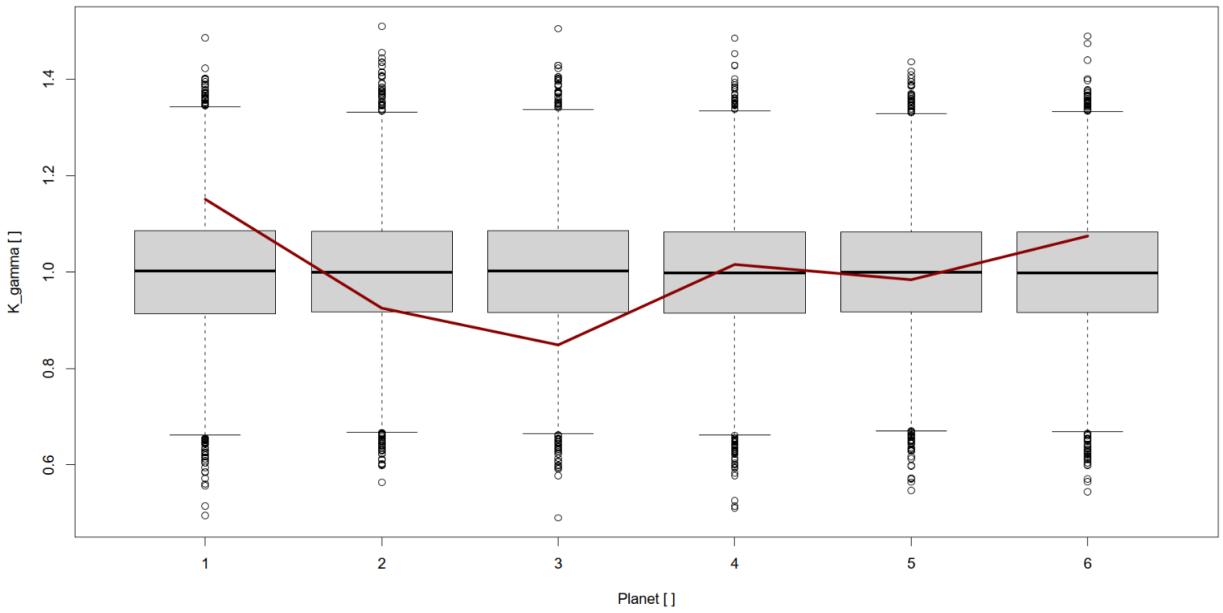

Figure 90: Boxplot of individual Kγ of the planets and one exemplary combinations of planets of one stage

4.3 Statistical Modelling of Load Distribution ($K_{F\beta}$)

In the context of this paper, the second stage of a three-stage planetary wind turbine gearbox has been analyzed as an example to demonstrate the process and importance of accurate positioning of planet axle bores in the planet carriers. Approximately 30 planet carriers, each with 12 bores (two for every planet axle), have been evaluated, resulting in around 360 measurements in total. The precise locations of these bores directly influence the alignment of the gear meshes.

To accurately derive the mesh misalignment values ($f_{H\beta}$), the positions of the centers of the bores have been converted using trigonometry and the transverse working pressure angle α_{wt}. The measured bore positions are first mapped onto a coordinate system, and trigonometric functions are applied to determine the effective displacement in the direction of the plane of engagement. Specifically, the sine and cosine of the transverse working pressure angle α_{wt} have been used to obtain the mesh misalignment $f_{H\beta}$ as a result of inclination and skew of the planet axles. By incorporating these trigonometric conversions, the effective mesh misalignment values ($f_{H\beta}$) are obtained, see left diagram in Figure 91.

Any deviations from the ideal positions can lead to mesh misalignment, which adversely affects the load distribution across the gear teeth. This misalignment is then used to determine the load distribution factor, $K_{F\beta}$, in accordance with ISO 6336-1, see right diagram in Figure 91. To model the $f_{H\beta}$ distribution, a normal distribution approach has been used. To model the $K_{F\beta}$ distribution, a generalized extreme value distribution (GEV) has been used.

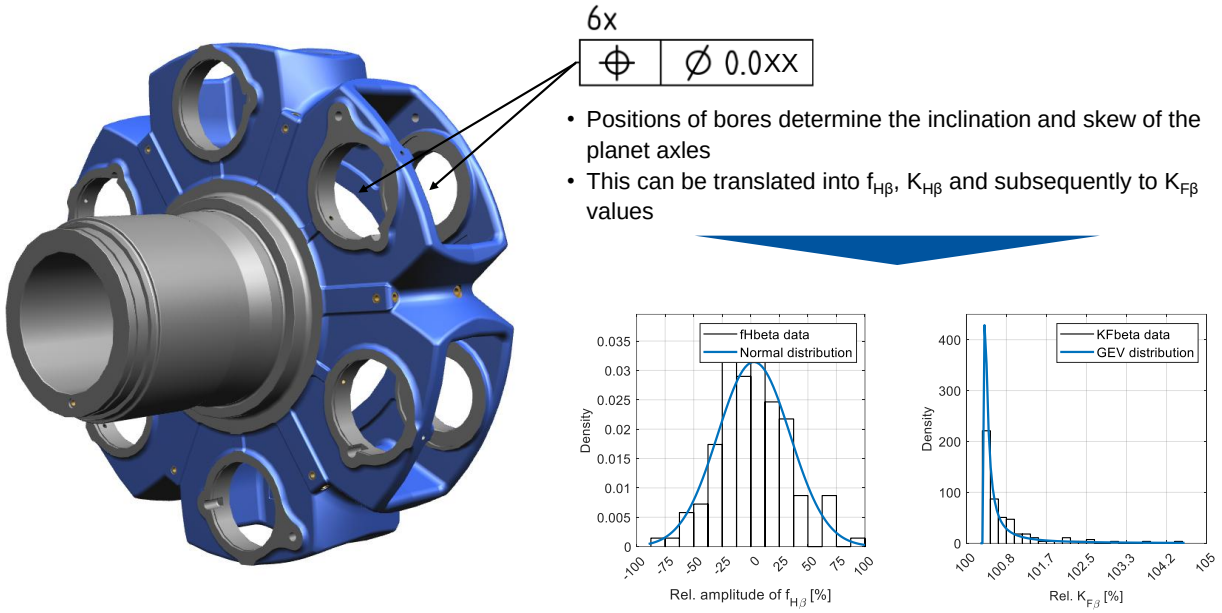

Figure 91: Influence of planet bore positions on $f_{H\beta}$ and $K_{F\beta}$

4.4 Statistical Modelling of Tooth Root Shape Influences (Y_S and Y_F)

Heat treatment is a critical process in gear manufacturing that enhances material properties but can also induce dimensional distortions. When gears undergo heat treatment, the thermal cycles of heating and cooling cause uneven expansion and contraction of the material, leading to warping or distortion of the gear's dimensions. This results in non-uniformities specifically in the geometry of the gear teeth flanks. Consequently, during the subsequent grinding process, the stock removal on the flanks of the individual teeth becomes non-uniform, which can affect the shape of the tooth root at the intersection of the grinding tool with the part.

Separately, the root diameter of the gears can also vary due to distortions from the heat treatment process. The uneven thermal expansion and contraction can cause inconsistencies in the overall shape and size of the gear, including the root diameter, which determines the lever arm geometry of the tooth when it comes to bending.

Such variations in the root diameter and tooth root shape can lead to a distribution of form factors (Y_F) and stress correction factors (Y_S) as defined by ISO 6336-3, which are essential for determining the gear's load-carrying capacity and fatigue performance. Since the amount of grinding removal and the shrinking or growing of the tooth root diameter are connected via the thermal expansion and contraction behavior of the individual gear, both effects can be expressed via the removed grinding stock since the nominal sooth shape before heat treatment and the shape of the grinding tools do not vary to any significant degree. This analysis has been conducted for the exemplary planet gear, see Figure 92. The resulting $Y_F \cdot Y_S$ values were then used to fit a GEV distribution comparable to the procedure in chapter 4.3.

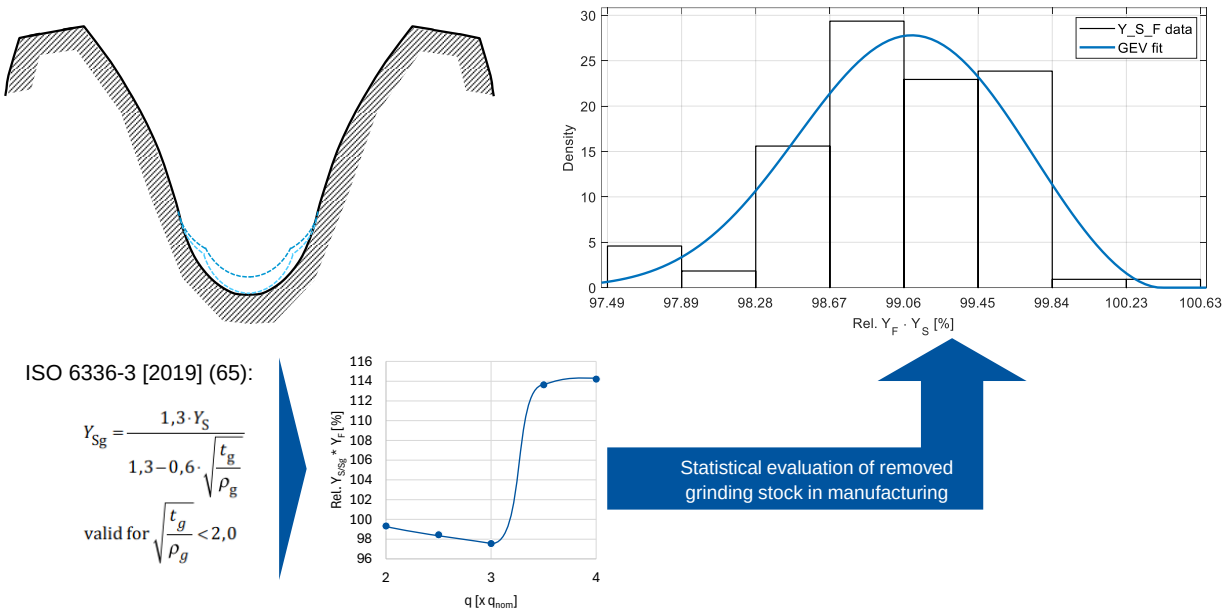

Figure 92: Influence of distortion and grinding stock removal on Y_S and Y_F

4.5 Results

For the exemplary planet stage, 10,000 individual random designs were generated using the distributions for the strength, the load sharing, the load distribution and the stress factors YF and YS as described in the previous sections. In the first step, the original tooth root safety factor of 1.689 was scaled with the random values for the influence factors. This led to a distribution of safety factors as show in the left side histogram in Figure 93. The red vertical line in the histogram represents the original tooth root safety factor. It can be seen, that due to the probabilistic influences, a few gears of the sample have even lower safety than the original value, but most of the random samples reach much higher tooth root safety, some even up to values between 3 to 3.5.

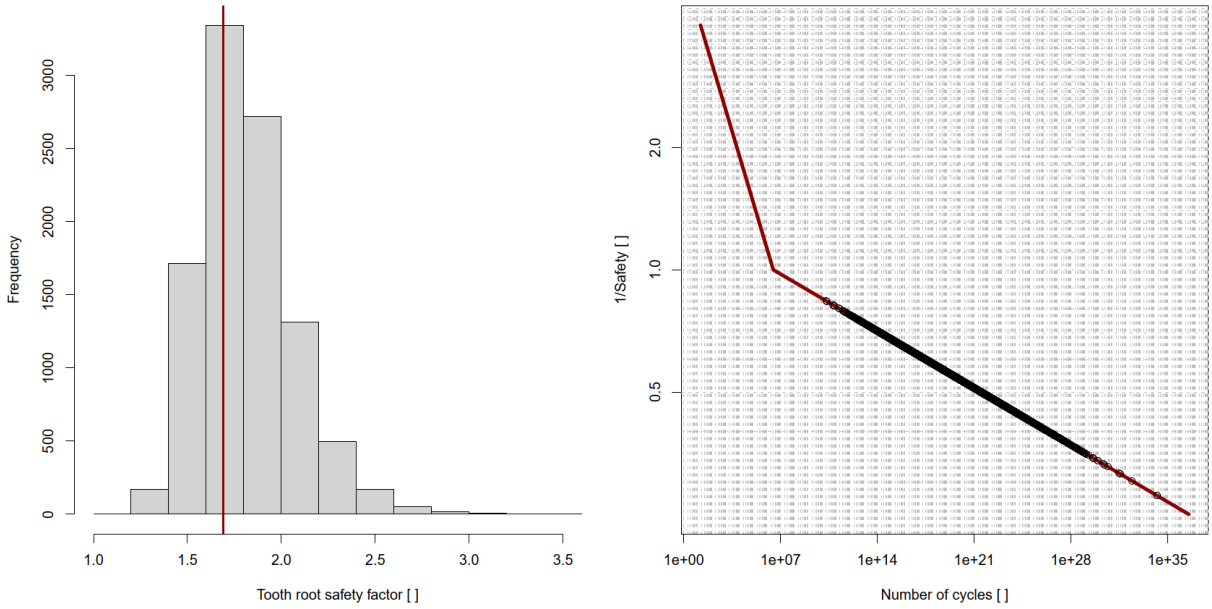

Figure 93: Histogram of tooth root safety factors of 10.000 planet wheels (left) and number of cycles until failure according S-N curve of ISO 6336 (right)

The diagram on the right side of Figure 94 shows the corresponding number of load cycles until fatigue failure for the calculated safety factors. It is obvious that all gears of the sample are in the ultra-high cycle fatigue region, most of them are even way above the value 10^{10}, for which the ISO 6336 normally assumes no further reduction of fatigue strength. In this study, a horizontal cut off of the S-N curve was not considered to ensure that the calculated failure rates are on the conservative side.

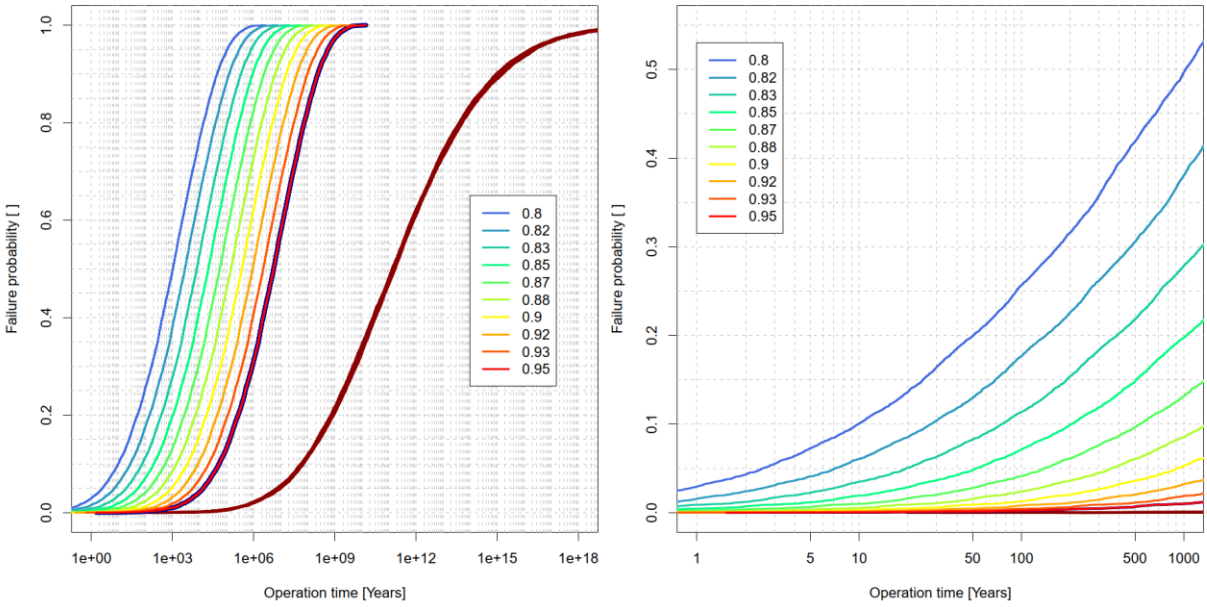

Figure 94: Failure rate curve for the six planets of the stage. Left: complete curves, right: detailed view on the technical relevant lifetime

Under the assumption that the turbine runs 24 hours a day, 365 days a year, the failure rate curves can be derived, using the operation time on the x-axis. Figure 94 shows the resulting diagrams. On the right in Figure 94, the thick red curve shows the failure rate of all 6 planets individually. The thick blue curve (below the thin red one) characterizes the combined failure rate of the planets in one stage (weakest link approach). Even the combined failure rate of all 6 planets leads to theoretical operation times that are not relevant for practical use anymore. The reason for these high operation times until failure is a combination of the high minimum safety factor of 1.56 for wind gearboxes and the conservative approach in classical gearbox design, where all influence factors are set individually on a conservative level. This leads to the question how much the minimum safety for this stage could be reduced to reach relevant operation times for a wind gearbox. To get a first indication of the torque density potential, the safety factor was scaled down step by step by a factor, starting with 0.95 and ending at 0.8. The resulting failure rate curves are also added in both diagrams of Figure 94. The plot on the right side of figure 9 shows a detailed view on the technically relevant time of operation. The reduction of the safety factor by 0.8 yields in a failure rate of 14% after 20 years of operation, which is definitely too high for a wind gearbox. For a reduction factor of 0.87, the failure rate in 20 years is below 2%, which can be deemed suitable. The initial tooth root safety factor of the planet gear was 1.689, therefor with a safety of 1.47, according to the probabilistic study, it still would have maintained sufficient reliability. Compared to the value of 1.56, this would lead to a torque density increase by 6%. This value makes sure that the combined 6 planets reliability is above 98%. If we stick to ISO 6336, we only have the information that σ_{Flim} has an assumed reliability of 99%, the effective reliability of the gear in the conditions of the gear stage is not stated in any standard or guideline. Therefor there is no clear advice for the settings of the needed reliability of a

gear or the overall gear stage. If we want to achieve a reliability of 99% for a single planet tooth root for 20 years of operation, the minimum safety factor could be scaled down to 1.4, which results in a torque density increase of 11.5%.

5 Conclusion

It has been shown that the probabilistic modelling of relevant influences on tooth root load capacity of gears can lead to much better predictions of calculated lifetime and safety reserves. The results show that with modern manufacturing methods, extensive simulation studies and knowledge of material quality, a probabilistic design of gears is possible and reasonable. One main finding is that the current minimum safety factor of 1.56 for the tooth root strength of wind turbine gearboxes is very conservative. From the probabilistic parameter study, it can be concluded that even a minimum safety of 1.47 only gives a failure rate of 2% after 20 years of operation for all 6 planets of this stage. This would lead to a potential torque density increase of approximately 6% for the gears in the turbine. If we want to achieve 99% reliability for the tooth root of one individual planet, a safety factor of 1.4 is sufficient, yielding in a torque density potential of 11.5%. Because only 4 influence factors were modelled in the probabilistic approach, the torque density increase should still be conservative. If further influences, especially the variation in the wind loads and the interaction between K_{γ} and $K_{F\beta}$ are considered, a higher decrease in the minimum safety factor could be achieved. It is important to note, that the proposed reduction of the minimum safety factor is only valid for the production and supplier quality at Flender / Winergy. Even with application of the same methodology, different gearbox manufactures will end up with different results due to their individual quality fingerprint.

6 Summary and Outlook

In this paper, a tooth root load capacity evaluation of the planet gear in a second stage of a three-stage planetary gearbox for wind turbines has been extended by statistical influences from material and manufacturing deviations. Four key influences have been modelled as distributions as an input for the tooth root strength assessment acc. to ISO 6336–3: σ_{Flim}, K_{γ}, $K_{F\beta}$ and $Y_F \cdot Y_S$. It was shown that the approach can result in a torque density increase by systematically lowering the minimum safety factor for the tooth root for wind applications.

A consideration of further statistical influences on tooth root load capacity will yield an even better estimation of failure probability in the future. Possible significant influences may be surface roughness, microgeometry, CHD and load fluctuations.

7 Bibliography

[ISO06] Calculation of load capacity of spur and helical gears — Parts 1-3
Standard ISO 6336
International Standardization Office (ISO), Geneva, 2006

[MEIS23] Meis, Jean-André: Parametric System Simulation of Load Sharing in Planetary Gearboxes
International Conference on Gears
VDI, München, 2023

Gearbox II

Elastic Interaction in Planetary Stages with Increased Torque Density

Sebastian Reisch[1], Andreas Klein[1], Alfons Böing[1], Pascal Weecke

[1]Winergy - Flender GmbH, Am Industriepark 2, 46562 Voerde, Germany

Keywords: gearbox, technology, interaction, stiffness, load sharing, load distribution, journal bearings

Abstract: As there is a continuous market demand for wind gearboxes with increased torque density, new potential technologies are identified and will be integrated into future gearboxes. The necessary light weight design of structures combined with increased utilization of machine elements lead to interaction effects which can only be covered on component test benches with great effort. By designing and testing a full-size technology demonstrator gearbox, Winergy has investigated specific combinations of future relevant technologies already now and demonstrate the technical feasibility and the potential on gearbox level. By measuring relevant interaction effects, simulation models can be validated and optimization potential in design and calculation can be uncovered. In the used example of a lightweight planetary stage, it can be shown how the gear meshes, the gear bodies, the journal bearings and the structure interact and therefore require a holistic calculation and testing approach.

1 Introduction

To remain competitive in the energy market in comparison with other generation technologies, wind turbine manufacturers (OEMs) and their suppliers continuously optimize their powertrain concepts and designs [DAN21]. The global objective is to reduce the levelized cost of electricity (LCOE) via maximizing the annual energy output and minimizing capital and operation costs. Further growing rotor diameters and a high power density of sub systems contribute to this objective, but also service and logistics concepts, the regional market requirements, the time to market and the risk management affect the selection and design of a powertrain concept [HAM25]. Turbine manufacturers weight these criteria differently based on their target markets.

The gearbox, one of the most essential powertrain components, must be tailored to the overall turbine concept and the strategy of the OEM. To contribute to the economic feasibility of the complete turbine, tighter design space and weight limits must be fulfilled while transferring higher input torque which represents one of the most relevant design parameters for the gearbox. In addition to an increased torque density a need for modularization and standardization is becoming more relevant to address the challenges of shortened development times and cost pressure. The gearbox can therefore not be designed and optimized independently from other powertrain components to reach an optimum from system perspective for new turbine generations. An increased torque density does not only reduce capital and operation costs, but also contributes to the sustainability because tons of material, mostly steel, can be saved which reduce the CO_2 emissions.

To fulfill the market and customer needs and to remain innovation leader in the international development race, Winergy has continuously increased the gearbox torque density by optimizing the gearbox design and introducing new technologies into their products. Figure 95 shows the development of the torque density over time. In the last 10 years a doubling has been achieved.

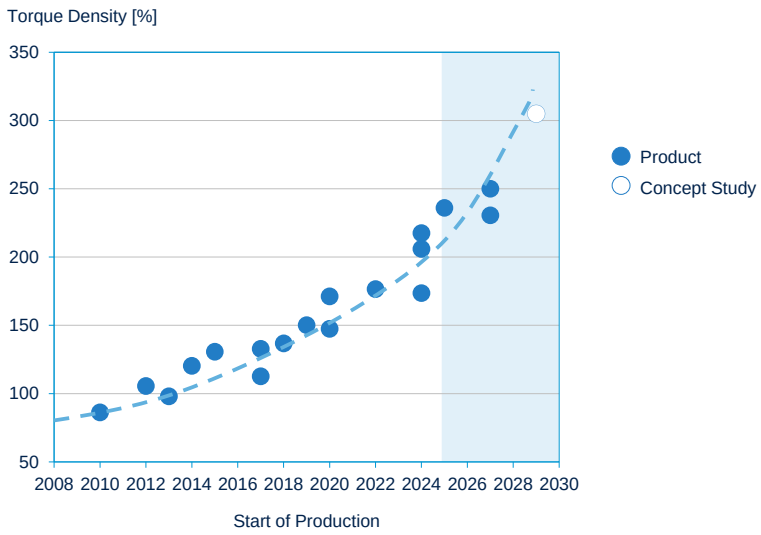

Figure 95: Torque density of Winergy gearboxes over time

Concept studies show that already in a few years a factor of three will be exceeded. This further increase is necessary to generate benefits for the customers, thereby secure Winergy`s market position and to ensure competitiveness of wind energy compared to conventional energy sources. In parallel the reliability of the complete powertrain has to be ensured. In the following sections some selected measures for increasing the torque density as well as resulting technical challenges are addressed.

2 Measures to Increase Torque Density

According to the widely used V-model the gearbox measures for increasing torque density can be derived on every level of the turbine structure, i.e. from material level over machine elements up to system level, Figure 96. The combination of measures on each level affects the design on the next higher level. The requirements for each measure can be derived from the higher level.

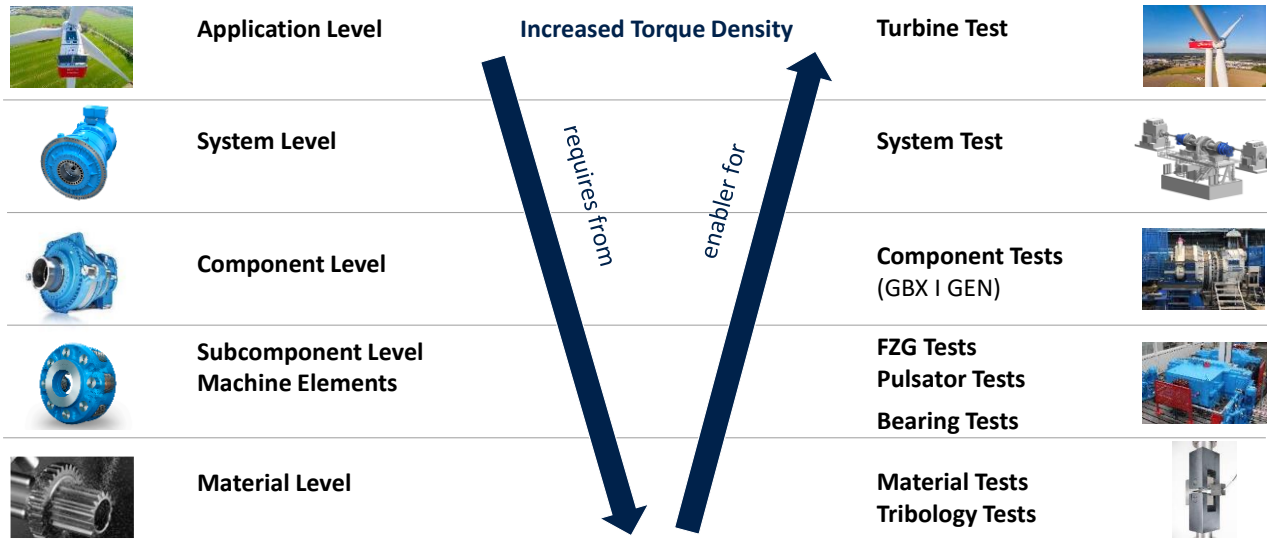

Figure 96: V-Model for the development of wind gearboxes

The basis of all mechanical gearboxes is formed by materials. Improvements in, for instance, material composition/quality, heat and surface treatment processes lead to optimized material properties. Also improved lubricant properties can be assigned to this level.

On the subcomponent level the use of journal bearings in planetary stages represents an important enabler for more compact designs. Optimized structural components enable an even material utilization. New probabilistic calculation methods for gears, considering real-world statistical distributions of input data, increase the utilization without a significant increase of failure probability [FIN25]. Improvements in manufacturing technology and accuracy also contribute to a higher capacity of the machine elements.

On component (gearbox) level the choice of the ratio distribution between the stages, the design of the internal interfaces and an optimized internal arrangement of the machine elements play an important role when influencing the torque density.

When the gearbox is examined with surrounding powertrain components, like the rotor suspension or the generator, the principle of function sharing can lead to an improved torque/power density. The gearbox ratio and the generator design can be balanced to achieve a compact and reliable overall system. Advanced simulation models help to quantify and consider the interaction effects [GEU23] [REI21].

On turbine level advanced control and operating strategies can for example lead to a load reduction of the powertrain components.

On each level specific test types (e.g. component test, gearbox test, field test) with an associated abstraction grade are available for verification and validation. A low abstraction grade enables operation closer to reality, but often requires more effort to carry out the test [REU25]. Measurement results can help to optimize calculation and design methods on all levels by using more realistic design parameters and load assumptions.

The examples mentioned above show that measures for increasing the torque density exist on every level of the V-model. However, the evaluation of the measures is not based exclusively on their technical potential. Also other criteria like costs, experience and maturity level need to be considered.

3 Combination of Future Relevant Technologies for Increased Torque Density

To fulfil the market needs and push innovations Winergy is continuously identifying and evaluating suitable technologies on different levels of the gearbox structure. With the help of scenario calculations, requirements for single technologies can be derived. In general, the aim is to achieve a uniform utilization of all gearbox components (e.g. gears, bearings, flange connections). Depending on the potential, risk and the availability, the technologies are further developed and optimized within the framework of technology roadmaps. The roadmaps ensure that the technologies reach a certain maturity level as soon as they are implemented in a gearbox design (technology package), Figure 97. Each technology package is characterized by a risk profile, a reliability estimation and a potential (torque density & costs).

With this procedure Winergy has derived and evaluated suitable technology packages which are needed to go the next step in torque density, as described in the introduction. The necessary technologies have been developed and tested extensively on material and subcomponent level to reach

a required technology readiness level (TRL) and derive design parameters [LOH21] [MEY23]. Nevertheless, there are some technical challenges when combining these technologies in a gearbox design on component level. This is discussed more in detail in the following section.

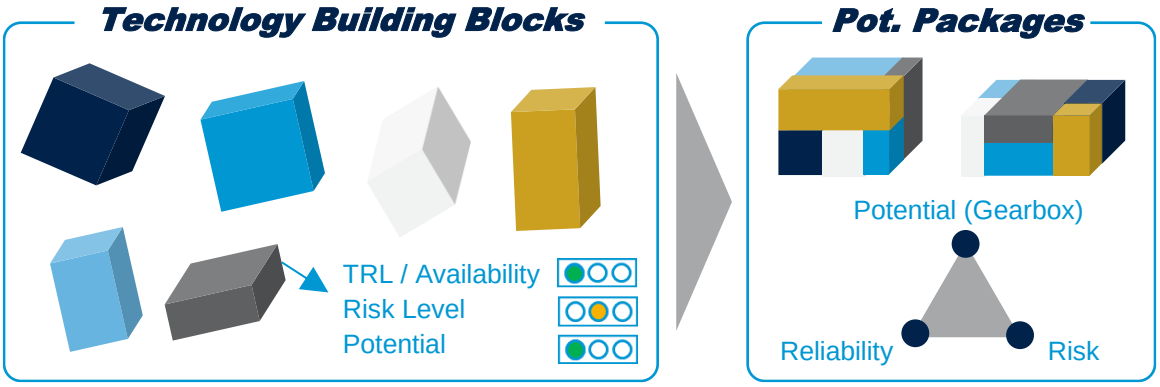

Figure 97: Selection of feasible technology packages (principal process)

3.1 Technical Challenges

When combining single technologies which have been successfully developed and tested on subcomponent or material level into a full-size gearbox, the boundary conditions and operating conditions can change. The necessary light weight design of structures combined with increased utilization of machine elements lead to higher component deflections and displacements. This results in complex interaction effects, which affect local stresses and contact conditions (e.g. pressure, oil film thickness, micro movement). The challenge is to understand and quantify these effects in such a way that they can be considered in the calculation of the subcomponent.

By using elastic gearbox models, for example on finite element basis, some interaction effects can be analyzed in detail. The stiffness of components can be tuned to adapt load transfer paths and avoid local overload of machine elements. But every simulation or calculation model is based on assumptions, e.g. regarding tolerances, friction value or surface roughness. This leads to a certain uncertainty in the results. To ensure that the combination of future relevant technologies leads to a robust gearbox design, a prototype test is essential, especially if experience with a similar design is limited. This will also be implemented in the next revision of the IEC 61400-4. The prototype test provides valuable verification data which can be used to improve simulation parameters or to adapt the subcomponent design [REU25].

3.2 Demonstrator Gearbox

To test the identified combination of future relevant and highly potential technology building blocks, Winergy developed, built and operated an internal demonstrator gearbox in 2024. The valuable test results provide evidence for the functionality of the technologies on gearbox level and thereby increase the TRL. The generated knowledge, principles and concepts reduce drastically the technical risk of future serial gearboxes.

For the development of the demonstrator gearbox, the requirements of a current serial gearbox in the 4 MW class, like interfaces, nominal torque and speed, have been used as a reference. The helical stage has been taken over. Under these boundary conditions the three planetary stages have been designed from scratch, while making use of the selected technologies. These include, among others, optimized journal bearings, gears and flange connections with higher utilization,

lower rim thicknesses, light weight structural components, several completely new design solutions and advanced calculation methods. Special attention was paid to the transferability and scalability to future drivetrain concepts and power ranges. The size comparison between the reference and the demonstrator gearbox in Figure 98 shows that the ring gear outer diameter could be reduced significantly while transmitting the same torque.

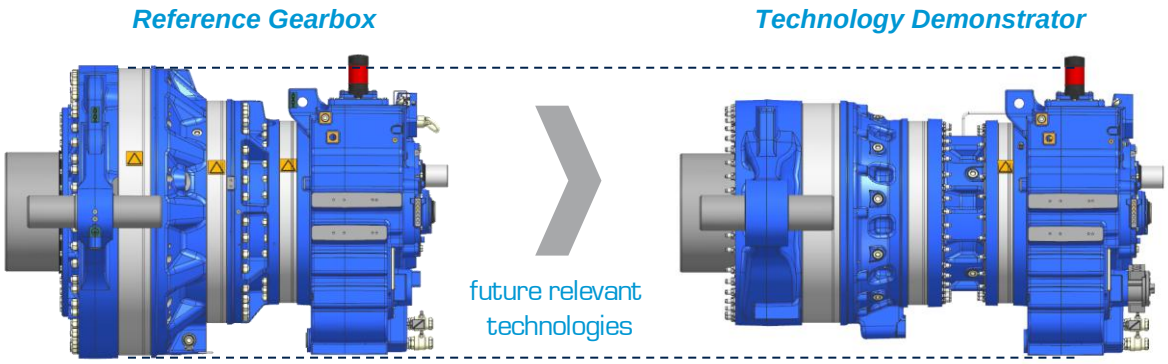

Figure 98: Reference Gearbox & Technology Demonstrator

Derived from a risk assessment, the demonstrator gearbox is equipped with over 240 sensors (without NVH sensors). The extensive test campaigns were done on a back-to-back gearbox testbench. As described in section 3.1, the investigation of the elastic interaction of gearbox components is one of the main objectives when increasing torque density. Therefore, this topic will be discussed in more detail in the next section using selected measurement results.

4 Experimental Investigation of Elastic Interaction Effects

The internal loads and operating conditions of journal bearings in planetary stages highly depend on the interaction with surrounding components, as the gears, the planet carrier and the carrier bearings [MEY23]. By testing the complete elastic gearbox system, more realistic boundary conditions can be ensured compared to component test benches. The influence of a reduced rim thickness, the rotation and deformation of the carrier, the real gear meshes and the lubrication concept can be analyzed. Using the example of the first stage of the demonstrator gearbox, selected effects will be investigated.

4.1 Measurement Setup

The focus in this contribution is on the interaction between the gear mesh of sun and ring gear and the journal bearing. Effects that affect the required convergent lubrication gap of the hydrodynamic journal bearing should be quantified. Among other, the following measurement setup has been implemented, Figure 99.

In one planet axle 12 radial inductive displacement sensors have been integrated in two sections (rotor and generator side). In each section six sensors are regularly distributed over the circumference to measure the local distance and shape of the planet wheel. The sensors are positioned in the edge area of journal bearing to ensure that they are not destroyed by the high pressure. An influence on the pressure build-up can be excluded. The sensor signals do not provide quantitative oil film thickness values, but can be used to evaluate planet deformation, position & orientation relative to the axle.

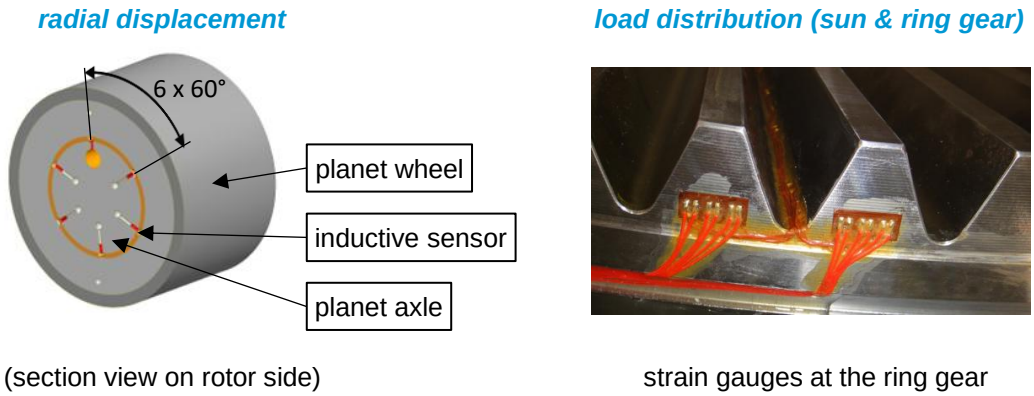

Figure 99: Qualitative Measurement Setup

The load distribution of the ring wheel mesh and the sun mesh is measured at 10 teeth with several strain gauges in the tooth root. Inductive proximity switches are used to record the angular position of the planet carrier and the sun.

4.2 Result Analysis

A suitable starting point for analyzing the interaction between the planet journal bearing and the gear meshes are the measured, mean radial displacements in the two sections. Figure 100 contains polar plots for 5 % and 120 % of nominal torque.

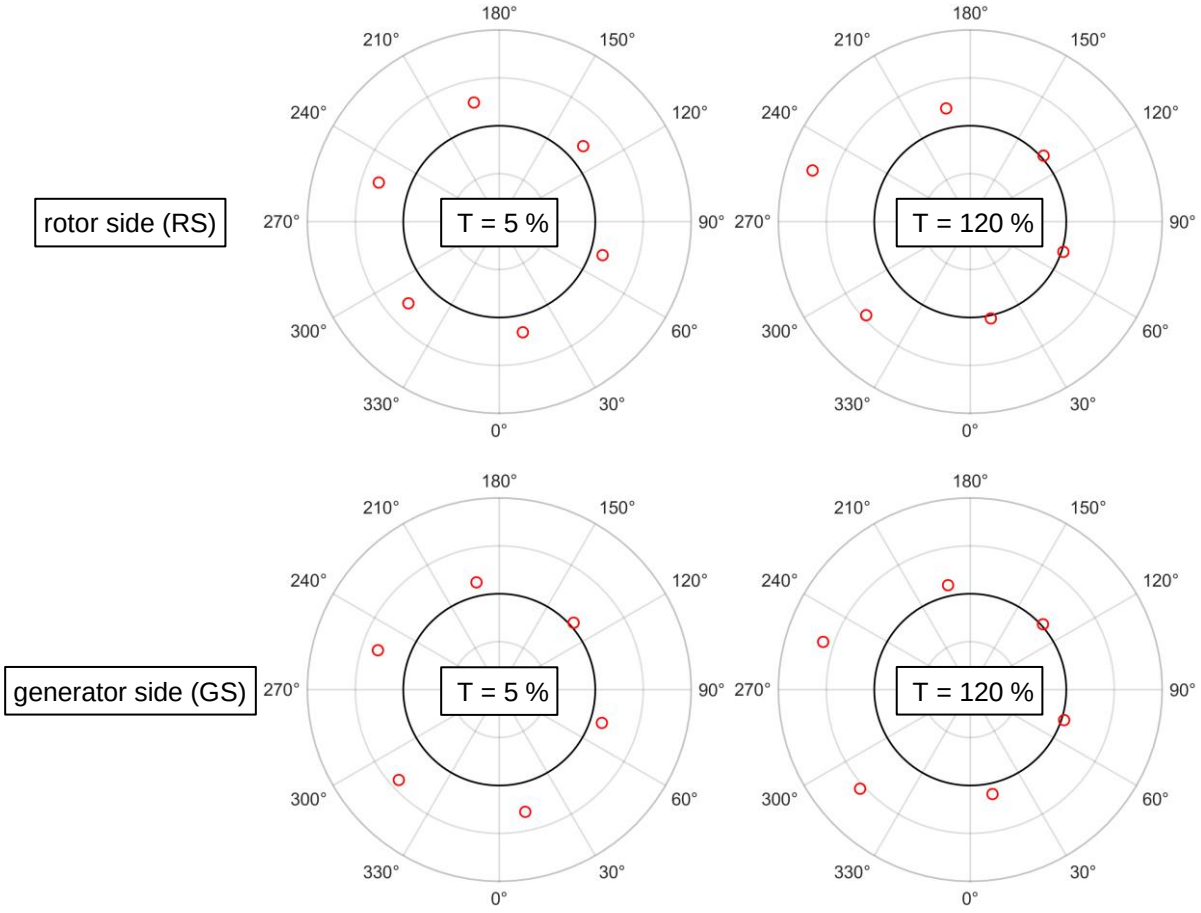

Figure 100: Mean Radial Displacements at 5 % and 120 % Torque

Zero degree corresponds to the sun mesh and 180° is pointing towards the ring gear. The direction of view is downwind. The discrete points allow an estimation of the planet shape. The minimal measured gap and its angular position are determined via interpolation and represent an indication for the location of the pressure zone.

It can be observed that the planet clings to the axle shape, forming a convergent gap for pressure buildup. Due to the low rim thickness of the planet wheel, rising torque leads to significant ovalization and to a larger pressure zone. Even under high deformations the convergent gap must be ensured for a reliable hydrodynamic operation.

Typically, elasto-hydrodynamic simulation models are used to find optimal journal bearing parameters during the design phase. The comparison of the mean measured and simulated gap for nominal load is shown in Figure 101. The used model predicts the deformation of the planet quite well, especially in the transition regions to the pressure zone.

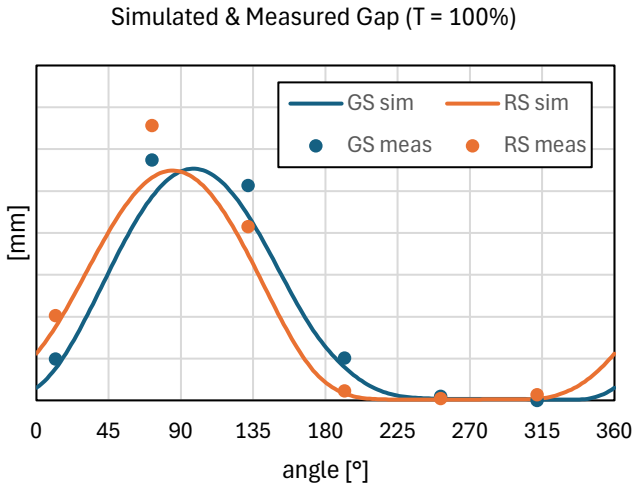

Figure 101: Comparison of Simulated and Measured Gap

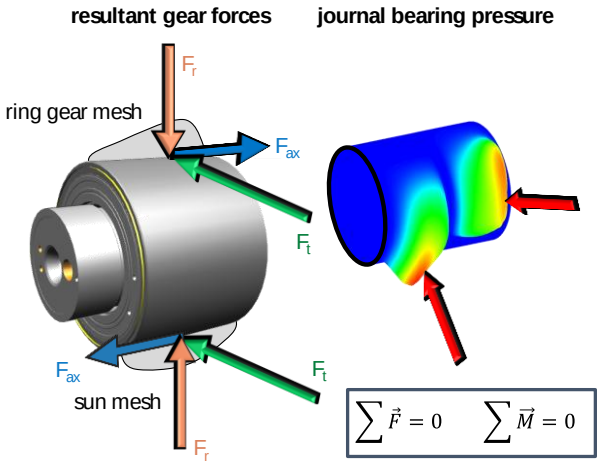

Figure 102: Balance of Forces at the Planet Wheel (qualitative)

To support the tilting moment of the planet (due to the axial gear mesh forces), the pressure zones of the two bearing halves (and thus also the gap) show an angular offset. Figure 102 shows qualitatively how the equivalent forces of the two gear meshes are supported by the journal bearing to fulfill quasi-static equilibrium conditions.

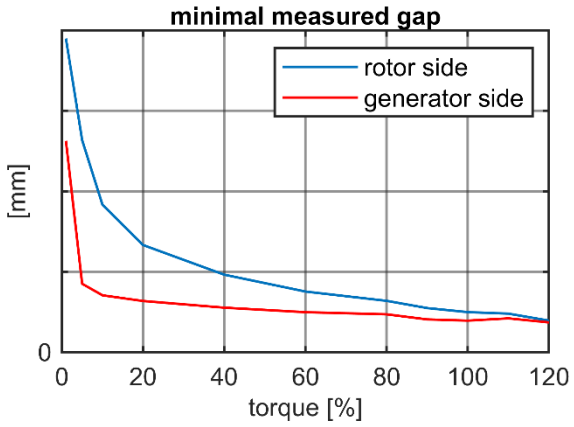

Figure 103: Min. Measured Gap over Torque

The load distribution of the gear meshes along the tooth width affect the axial position of the equivalent force vectors (load center) and thus the pressure and gap distribution inside the journal bearing. Figure 103 contains the minimal measured gap over the input torque. While the minimal gap on generator side only decreases slightly over 10 % torque, the rotor side gap starts at a higher value and shows a continuous constriction. This can be explained with the moving load center of the ring gear and sun mesh with rising torque. Figure 104 shows the load center of the sun and ring gear mesh over the circumference for 5 % and 120 % torque.

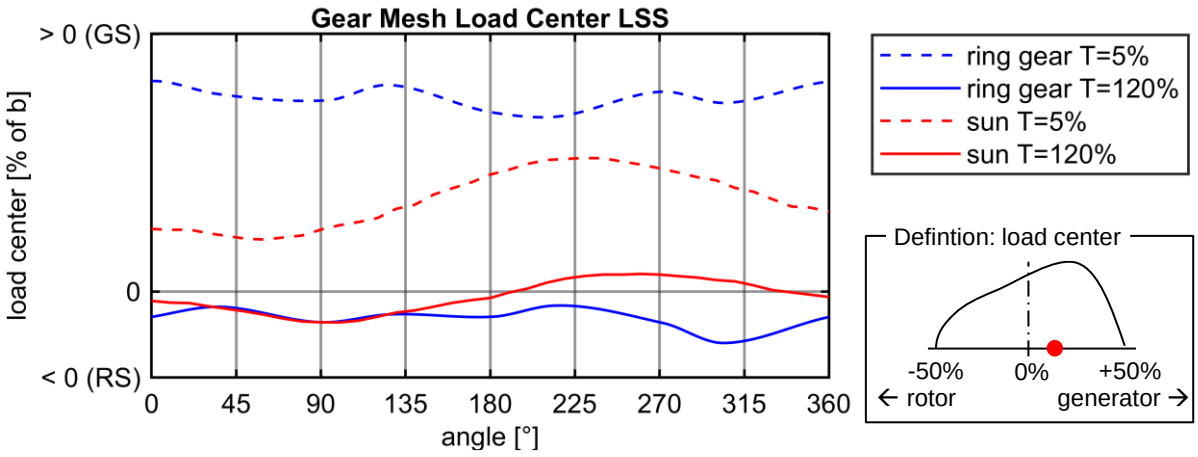

Figure 104: Gear Mesh Load Centers at 5 % and 120 % Torque

As the torque increases, the load centers move towards the rotor depending on the torsional stiffness ratio of the loaded components. As the total load on the journal bearing halves becomes more and more equal, the measured gaps also become more equal, too. This explains the curves in Figure 103 and can also be seen in Figure 100.

Furthermore, the gear mesh load centers of the sun and the ring gear show a dependence on the angular position of the mesh event. This effect mainly occurs due to gravity and tolerance effects and is considered in the design of the gearbox. It means that that the location of the equivalent forces in Figure 102 is slightly varying with the angular position of the sun and the planet carrier. When plotting the measured minimal gap at the journal bearing over the carrier angular position, the impact of this effect can be visualized, Figure 105.

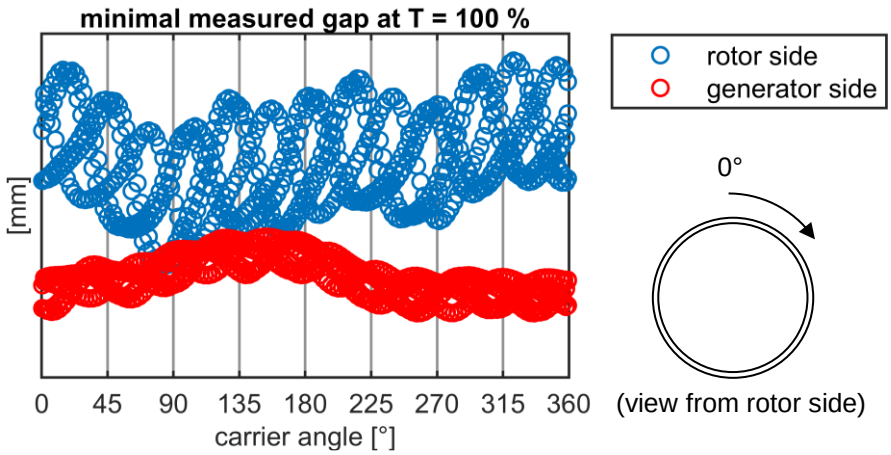

Figure 105: Min. Measured Gap at 100% Torque over Carrier Angle

The opposite periodic mean curves of first order indicate that the journal bearing tolerates small tilting movements of the planet and acts as a compensating element. The higher orders match the rotation frequency of the planet.

The exemplary results show how the elastic interaction between gears, journal bearings and structure inside planetary stages with increased torque density can be investigated and quantified. The generated data is also used to validate and optimize elastic system models which are needed to design future gearboxes.

5 Conclusion

In this contribution it has been addressed how Winergy has combined future relevant technologies in a demonstrator gearbox to investigate their performance and interaction on wind turbine component level. Using the example of the first planetary stage it became clear how gears, bearings and structure interact and that a holistic approach is needed in the design phase by using suitable simulation and testing methods. Only the combination of all parts in the load transfer path determines the gearbox behavior as well as local machine element loads.

By the specific alignment and successful implementation of future relevant technologies on gearbox level, Winergy is ready to go the next step in torque density and transfer the proven knowledge into customer benefits. Combined with the unique testing capability for complete drivetrains [HAM25], optimal conditions for providing reliable and robust drivetrain solutions are ensured.

6 Bibliography

[DAN21] Daners, Dominik et al.: More torque is better than torque - Higher Torque Density for Gearboxes

CWD2021 proceedings, Aachen, 2021

[FIN25] Finken, Jonas et al.: Probabilistic modelling of the tooth root strength of wind gears.

CWD2025 proceedings, Aachen, 2025

[GEU23] Geukes, Lars et al.: Key Applications of FEA and MBS in Wind Turbine Gearboxes.

CWD2023 proceedings, Aachen, 2023

[HAM25] Hambrecht, Ralf: Trends and Technology in Wind Turbine Powertrain Systems.

CWD2025 proceedings, Aachen, 2025

[LOH21] Lohmann, Christoph et al.: Planetengleitlager Prüfstand:

Aufbau, Messung und Simulation relevanter Betriebsparameter

VDI-Fachtagung Gleit- und Wälzlagerungen 2021, online, 2021

[MEY23] Meyer, Thomas: Journal Bearings in Wind turbine gear units: Performance – future aspects

CWD2023 proceedings, Aachen, 2023

[REI21] Reisch, Sebastian et al.: Elastic Interaction of the Gearbox in Powertrain Concepts with In-creased Integration Level.

CWD2021 proceedings, Aachen, 2021

[REU25] Reuter, Martin et al: Prototype testing of wind gearboxes on test bench and turbine.

CWD2025 proceedings, Aachen, 2025

High Detail System Level CFD-Lubrication Analysis of Wind Turbine Gearboxes

Dr.-Ing. Moritz Gebhardt [1], Martin Cardaun[1]

[1] NGC Transmission Europe GmbH, Duisburg

Keywords: Gearbox, SPH, system simulation, V-model

Abstract: Classical, mesh-based, computational fluid dynamics (CFD) methods make it difficult to include moving bodies into the physical domain. Their applicability to gearboxes with their inherent multitude of moving and interacting parts is limited. This has changed with the dawn of modern meshless CFD software based, e.g., on the smooth particle hydrodynamic (SPH) method. It is now feasible to analyze lubrication, oil flow, power losses and convective heat transport in the working environment, granting access to benefits like front-loading via virtual prototyping, substitution of experiments or test support via virtual sensors and the opportunity to investigate situations that are inaccessible experimentally. The reward is an increased security against errors that reveal themselves late in a project, with potential months of delay and costs in the M€ range.

“System simulation” is often associated with comprehensive low detailed models. In contrast, the models discussed here are highly detailed and include e.g. all rollers in the gearbox. A wind turbine gearbox, however, often contains more than 500 moving bodies. Targeted efforts and methods are necessary to secure the quality of model generation.

The process that was used to build up the models is inspired by the V-Model and has a strict approach to reduce complexity as well as inherent fidelity checks. Intense use of automation further reduces the complexity and as a side effect the CAD preparation effort. The simple GUI allows reused model parts and quick model changes. In the end it is possible to generate a failure tested, highly detailed, full gearbox model within less than a day once CAD preparation and data gathering are finished. Variants and parameter studies can be generated in minutes.

Sample CFD analysis cases show how the method can effectively be used to improve gearboxes.

1 Introduction

In order to decarbonize the generation of electrical power, which is one of the main contributors to manmade carbon emission, the installed capacity of renewable energy plants is increasing globally. Wind power is, next to solar photovoltaic, a main contributor here due to its lowest levelized costs of energy (LCOE) and comparably high-capacity factor. Due to scaling effects manufacturers globally are increasing wind turbine (WT) size regularly setting new records each year. This scaling is initially driven by rotor sizes. To make this possible, however, reliable drive trains must be developed to efficiently absorb and transmit the resulting power and loads. A critical part of the drivetrain is the main gearbox. In the main gearbox, a large number of components perform relative movements under contact and high loads e.g. at the gear meshing points and in the bearings. This can lead to failures in the absence of proper lubrication. While the failure rate of main gearboxes is generally lower than that of other drivetrain components, gearbox failures lead to significant downtimes und high costs for repair or replacement [1], [2], [3]. In order to keep pace with the constant growth in size and shorter development cycles, gearbox engineers have to adapt the design methods for dimensioning lubrication systems to these increased requirements.

Analyzing the performance of lubrication systems has traditionally relied on experimental methods that involve running extensive test rig trials. These trials demand prototypes and access to specialized facilities, making them expensive and time intensive. Additionally, the large size of the components complicates modifications to geometries during testing as well as design changes to the prototype. Perhaps the most significant limitation of experimental approaches is their inability to provide clear insights into fluid flow dynamics during operation. Even with transparent covers like Plexiglas, the environment remains obscured by oil residues, restricting detailed analysis.

To address these challenges, Computational Fluid Dynamics (CFD) has emerged as a powerful support to testing. By using CFD, engineers can evaluate designs virtually, eliminating the need for physical prototypes. CFD offers access to detailed flow properties across the entire fluid domain at any point in the simulated time, providing a level of insight impossible to achieve with traditional methods.

The Finite Volume Method (FVM) is one of the most widely used CFD techniques. This method divides the fluid domain into a grid, or mesh, to simulate flow behavior. However, in systems with moving and contacting components, such as meshing gear teeth, the constant changes in geometry necessitate frequent and dynamic remeshing of the grid. While solutions exist to manage this process [4], [5], they involve substantial preprocessing and computational effort, making the approach less efficient.

Smooth Particle Hydrodynamics (SPH), a more recent CFD method, takes a different approach. Instead of discretizing the environment, SPH models the fluid itself using particles in a Lagrangian framework. These particles interact with each other and with solid boundaries of arbitrary shape using the Navier-Stokes equations, with their interactions governed by distance-based weighted interpolation. This particle-based representation eliminates the need for remeshing when simulating moving components, reducing the time needed in the preprocessing stage significantly. A comprehensive explanation of the SPH methodology is available in [6].

The reduced complexity of SPH modeling makes it particularly suitable for simulating systems with moving parts. For example, SPH has been successfully applied to simulate parts of or even entire planetary gearboxes in WT, with each roller modeled as an independently moving element [7], [8]. This capability was a key factor in choosing SPH for the investigation of WT gearbox lubrication. However, even though the need for time consuming meshing procedures is eliminated, the number of individual parts that move on different trajectories and with different speeds is relatively high. For a standard gearbox this can easily be around 500 parts.

The process that was developed to build up such models is inspired by the V-Model and has a strict approach to reduce complexity as well as inherent fidelity checks. Intense use of automation further reduces the complexity and as a side effect the CAD preparation effort. As described in [9] the design process of a WT can be illustrated by a V-shape (Figure 106). In the initial phase, the process progresses from a less detailed definition to increasingly detailed concepts. The first step is to define the top system level and the requirements for it. The system is then broken down into sub-systems and sub-sub-systems, and here too the requirements are defined and concepts are developed. Once the design has been defined, the test phase begins. These range from material tests to field tests of the entire system. Due to the rapid pace of development, simulation is also playing an increasingly important role here.

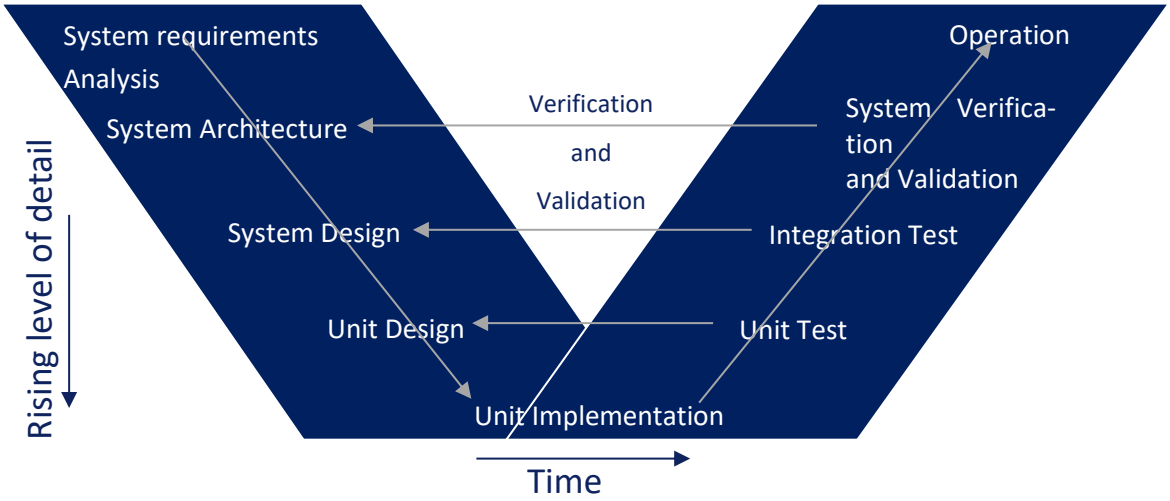

Figure 106: Conceptual representation of the V-model

2 Main section

2.1 Modeling approach

As stated in Chapter 1, models of multi-MW gearboxes can have more than 500 moving bodies. This leads to a high demand for a workflow that reduces complexity and the possibility to create errors e.g. when importing geometries and attributing movement definitions on each of them. For this reason, a modeling approach was developed that is inspired by the V-Model. A modified diagram can be seen in Figure 107. In a first step the scope of the investigation needs to be defined. From there, the requirements to the simulation can directly be derived. After the preparation of the CAD model and storing the component geometries in the component database (Chapter 2.1.1) as *.stl geometry files, the system arrangement will be defined. The analysis of the requirements for the simulation leads to the definition of the system model, which is then systematically broken down into subsystems. At the system level, global simulation parameters are established according to the overall scope of the simulation. These parameters provide the foundational context for the subsequent stages. At the subsystem level, the focus shifts to a more localized design, where specific details such as gearbox geometries, gear and bearing movements, and the positioning of fresh oil injection points from the lubrication system are determined. This structured approach ensures clarity and a logical progression from system-level considerations to detailed subsystem-level specifications.

After the definition phase, the model generation is carried out. A more detailed description of this process can be found in chapter 2.1.2. A key feature is the flexibility of the workflow. At any point, the design can be arbitrarily changed and new system and sub-system models are generated in a few minutes of processing time. Additionally, once stored in the component database, every geometry can be reused in subsequent investigations. A clearly defined nomenclature was used here to guarantee this. After the initial run of the sub-system models, the results can be checked for plausibility. If the sub-system results are satisfactory, the system model can be generated by assembling the sub-systems. This is handled by the automated workflow and comes with no loss regarding the level of detail of the model. Naturally this results in a model with high complexity. However, the inherent proneness to modeling errors in highly complex models is mitigated by the analysis on subsystem level. Without any delay or further preprocessing, the system model simulation can be started. Finally, the results can be compared with the defined scope of the simulation in order to

check if the simulation project brought the desired outcome and led to an increased understanding of the respective problem.

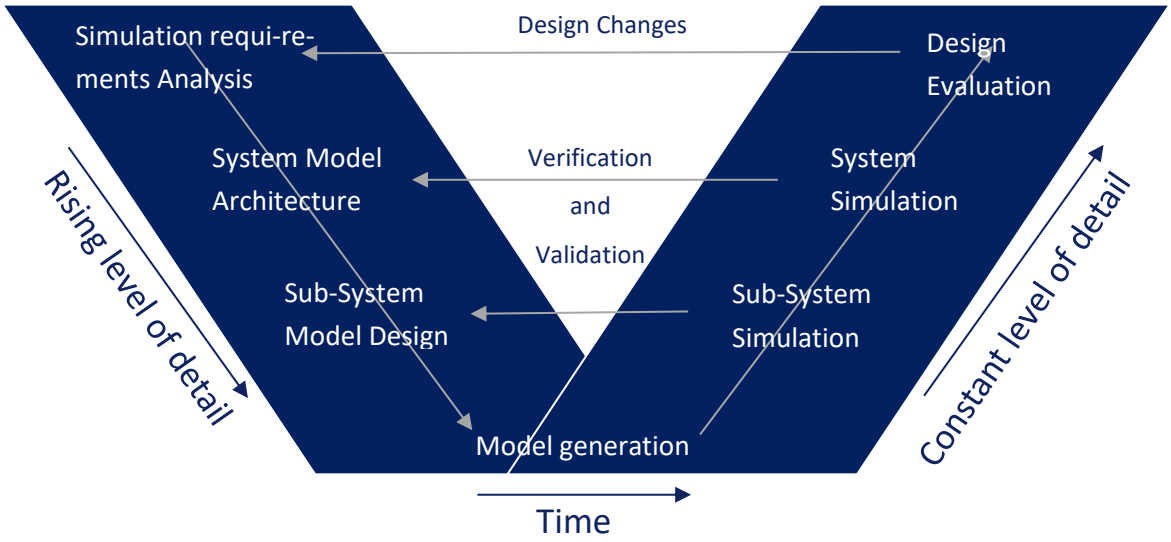

Figure 107: Modified representation of the V-model

2.1.1 CAD Preparation

As described in chapter 2.1 the initially available CAD model needs to be prepared in order to be used for high detail system level CFD-lubrication analysis of WT Gearboxes. The amount of effort highly depends on the setup of this model. A common first step is the definition of assemblies of parts that move on the same trajectory, e.g. the high speed stage (HSS) shaft and the HSS gear. Subsequently, the oil injection and extraction surfaces (open boundaries) need to be defined. Here, channel geometries must be created that are large enough so that a distinct Hagen-Poiseuille flow can form. Also, it needs to bring about the desired flow velocities at the nozzle. At the same time, undesirable interactions of the particles with the side and rear walls of the channel geometry must be avoided. The minimum channel dimensions are given in Figure 108 as a function of the particle diameter D. After the CAD preparation, the parts and assemblies need to be stored in the CAD database. Here a standard geometry format (*.stl) is used.

A final but optional preparation step before the automated workflow will take over the subsequent modeling is the definition of scaling parameters to the geometries. Scaling can be a powerful tool for controlling the simulation time. Surfaces of bodies that move in and out of contact zones will, dependent on local geometry and speeds, lead to particles being accelerated to high velocities. For a correct representation of such high velocities, the artificial speed of sound needs to be high enough. The formula for calculating the minimal artificial speed of sound v_{aSoS} in a SPH simulation is given in Equation 1.

$$v_{aSoS} \geq 13 \cdot v_{system,max} \qquad \text{Equation 1}$$

This parameter is linearly connected to the simulation runtime. If these contact zones are not a subject of interest in a given simulation setup, the gear or bearing bodies can be scaled down in order to create larger gaps between these bodies. This will have a negligible effect on the global fluid flows but will reduce high local velocities und thus the simulation runtime and costs.

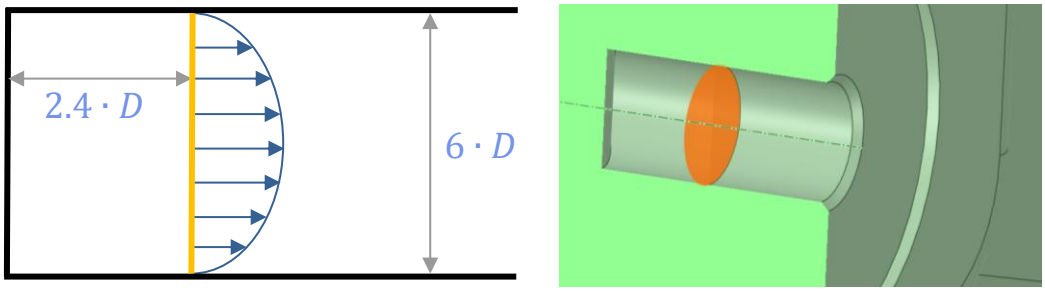

Figure 108: Schematic (left) and actual (right) representation of open boundaries

2.1.2 Automated modeling toolchain

After the system and the scope of the investigation are defined and the CAD database contains all necessary components, the developed automated workflow can be used to perform the modeling tasks. A schematic workflow diagram can be found in Figure 109. The simulation setup is defined by a clearly arranged Excel graphical user interface (GUI) where all parameters can be set in a well-structured manner. Excel is a widely used Engineering tool and the user-friendly GUI allows the workflow to be used even by engineers who are not specialized in CFD. Global parameters, such as particle size or operation point are set as well as the local setup of the individual bodies, their position and scaling. Also, the open boundaries are completely defined via the GUI. Now the developed scripts that run in a python environment can be activated. First the information given in the GUI is read. Only the geometry files needed are stored in the separate model database. The corresponding files are directly subjected to translation, rotation and scaling. This set of files can be read by any CAD viewer in order to inspect the geometric setup before uploading it to the cloud based CFD environment.

In the second phase, the python script will take the geometries from the model database and connect them with the movements that result from the selected operation point and the gear meshing parameters which are put into the GUI by the user. Using an application programming interface (API), the python script will build up the CFD model by defining the modeling elements, uploading the geometries and assigning attributes to them. Every aspect of the simulation setup is defined in the GUI and can be changed directly.

2.2 Sample analysis

In this publication a state-of-the-art gearbox with a rated power of around 6 MW will be used as a demonstrator. First, the simulation requirements are defined. In this case study, one of the high speed stage bearings will be investigated regarding lubrication of the roller surface. The investigation is planned on system level, meaning the whole gearbox is considered and the cross flow between the individual stages is taken into account. The gearbox has a design with two planetary stages, followed by a helical stage (PPH). For the fidelity checks with reduced complexity, the three housing sections are chosen as sub-systems. Namely the low speed stage (LSS), the intermediate speed stage (ISS) and the high speed stage (HSS). An illustration of these systems can be found in Figure 110.

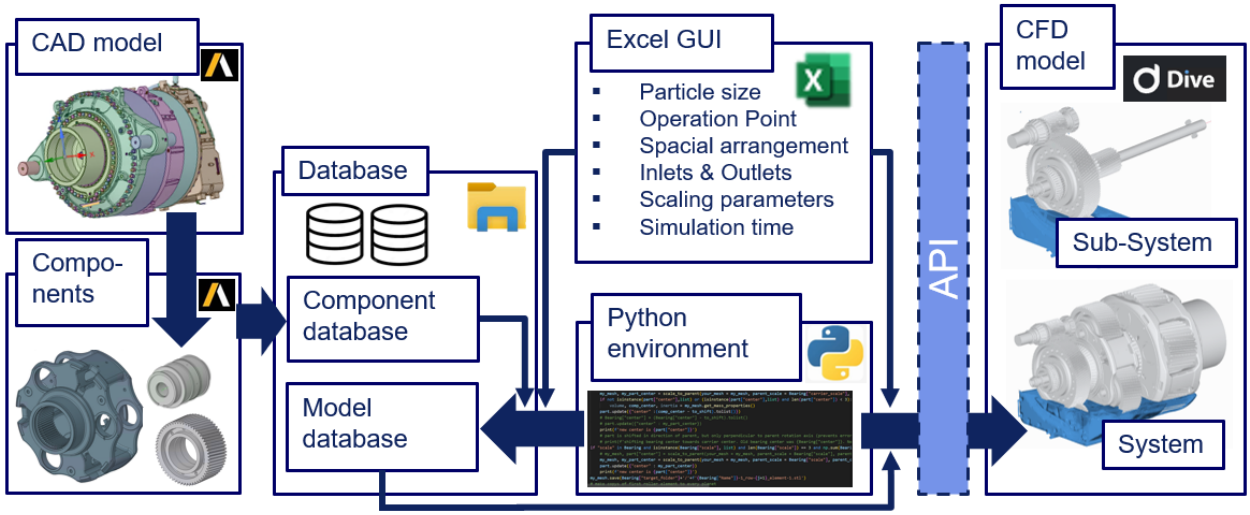

Figure 109: Modeling workflow

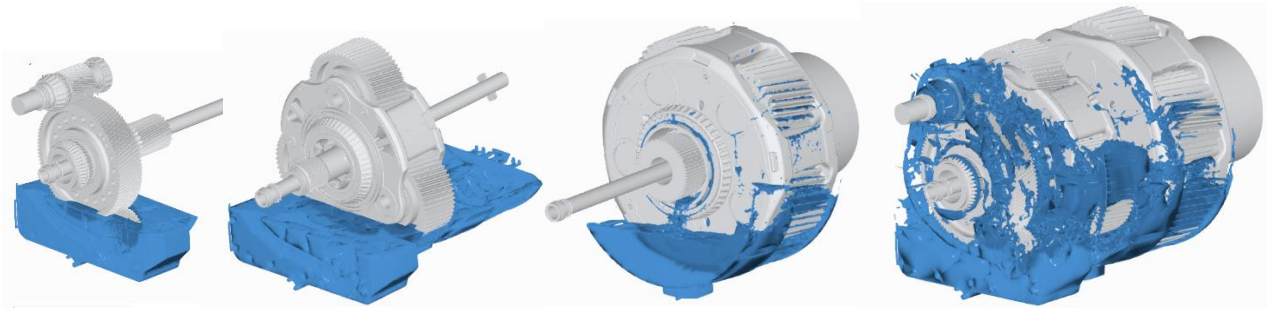

Figure 110: Sub-system geometries for the fidelity checks

After the preparation of the geometry files (Chapter 2.1.1) and entering the simulation parameter into the GUI, the automated modeling workflow generates the simulation models of each sub-system in the CFD environment. Here, the movement of the bodies can be checked. Gravity acts at 5° towards the downwind side in order to account for a drivetrain tilt that the gearbox is mounted in on the tower. The open boundaries on the moving parts, e.g. the planetary carriers, rotate with their corresponding bodies. The speed of sound is set globally for all models as well as the oil parameters. Surface tension is considered. All bearing rollers as well as the cage are modeled and move with the correct rotational speed between inner and outer raceways.

Table 4: Preparation effort and runtime comparison of the system- and sub-system models

Model	Preparation Effort	Simulation Time	Calculation Time	Oil Injection Points
LSS	4 h	10 s	24.49 h	44
IMS	3 h	8 s	31.66 h	27
HSS	1 h	6 s	19.72 h	6
Full Gearbox	5 min	10 s	66.89 h	77

After the buildup of the sub-system models is completed, the simulations are started. Table 4 gives an overview of the preparation effort (after CAD preparation) and simulations times of the different models.

Once the sub-system simulations are carried out, the results can be checked for validity or unexpected behavior. A sample investigation on the HSS-downwind (DW) bearing, a critical component for Wind Turbine down times [2], was conducted. Figure 111 shows the geometric location of the bearing rollers in the system and the results of the lubrication analysis for 3 different model setups. In addition to sub-system and system models an alternative system model was set up that does not have sump oil. This could be done by deactivating the pre-filling of the gearbox with sump oil via the GUI, which takes only seconds. The results show that the sump oil that is being accelerated through the HSS wheel and pushed into the bearing housing plays a larger role, whether directly or indirectly, in the overall lubrication than the fresh oil supply to this bearing via the nozzles. Also, a sub-system model of only the HSS stage would underpredict the fraction of lubricated surface by around 5% due to the cross flow between the GB stages. From this insight concerns regarding oil quality could be raised. Using advanced post processing tools, individual particles could be tracked and the oil composition at the bearing could be investigated. Following that, an improved design could be developed where the oil flow is directed in a more beneficial way.

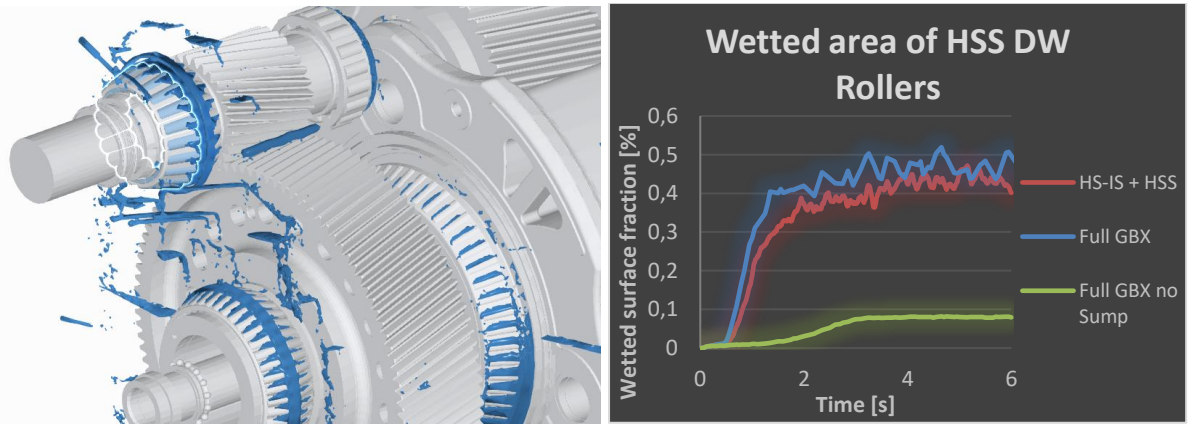

Figure 111: Evaluation of the lubrication of the HSS DW Bearing (highlighted left) rollers for different model setups

3 Summary and Conclusions

The continual growth of wind turbines, driven by increased rotor and tower sizes, necessitates the development of robust drivetrain components, particularly the main gearbox, which must efficiently handle increased power and loads while mitigating failures linked to lubrication issues. Although traditional experimental methods have been crucial in analyzing lubrication system performance, they are limited by high costs, lengthy development times, and inadequate fluid flow insights. The development of SPH models as presented in this work follows a structured, iterative process inspired by the V-Model framework, balancing complexity with fidelity through systematic automation and rigorous checks. This approach facilitates the efficient modeling and simulation of lubrication systems, supporting the rapid innovation cycles demanded by the wind energy sector.

Key steps include defining the investigation's scope, preparing CAD models, and organizing components into a reusable database. System and sub-system models are then iteratively developed and refined, with automated processes enabling rapid updates and assembly without sacrificing detail. Sub-system analysis ensures accuracy before progressing to the full system model, which can be simulated immediately. This approach enhances efficiency, reduces error-prone tasks, and ensures alignment with the simulation's objectives.

In this work an automated workflow for gearbox modeling was presented, integrating a user-friendly Excel-based GUI to define global and local simulation parameters. Python scripts process the input, prepare geometries, and configure movement patterns based on user-defined settings. The setup is then uploaded to a cloud-based CFD environment via an API, ensuring flexibility, accuracy, and efficiency in the modeling process. With this approach system level CFD investigations are possible as a standard tool in the design process.

In order to demonstrate the process, a sample CFD analysis using the SPH method in combination with the new modeling approach is presented. An exemplary investigation regarding bearing lubrication was conducted.

4 Bibliography

[1] C. Dao, B. Kazemtabrizi und C. Crabtree, „Wind turbine reliability data review and impacts on levelised costs of energy," *Wind Energy 22,* pp. 1848-1871, 2019.

[2] S. Sheng, „Report on WInd Turbine Reliability - A Survey of Various Databases," NREL, 2013.

[3] J. Igba, K. Alemzadeh, C. Durugbo und K. Henningsen, „Performance assessment of wind turbine gearboxes using in-service data: Current approaches and future trends," *Renewable and Sustainable Energy Reviews 50,* pp. 144-159, 2015.

[4] F. Concli, A. Della Torre, C. Gorla und G. Montenegro, „A New Approach for the Prediction of the Load Independant Power Losses of Gears: Development of a Mesh-Handling Algorithm to Reduce the CFD Simulation Time," *Advances in Tribology,* pp. 1-8, 2016.

[5] F. Concli und C. Gorla, „Windage, churning and pocketing power losses of gears: different modeling approaches for different goals," *Forschung im Ingenieurwesen 80,* pp. 85-99, 2016.

[6] B. Legrady, M. Taesch, G. Tschirschnitz und C. Mieth, „Prediction of churning losses in an industrial gear box with spiral bevel gears using the smoothed particle hydrodynamic method," *Forschung im Ingenieurwesen 86,* pp. 379-388, 2022.

[7] J. Gutekunst und I. Köse, „Beyond Plexiglas Covers," dive solutions GmbH, Berlin, 2021.

[8] M. Gebhardt, A. Rhode und B. Legrady, „Lubrication improvement at the HS-IS spline shaft interface of a wind turbine gearbox using the smooth particle hydrodynamic method," in *International Conference on Gears*, Munich, 2023.

[9] K. Forsberg und H. Mooz, „The Relationship of System Engineering to the Project Cycle," *Engineering Management Journal,* 1992.

Noise, Vibration, Harshness

Synergies of Parametric Optimisation and Topology Optimisation for Tonality Free Wind Turbines

Philip Becht[1], Emre Kanpolat[1], Sebastian Schmidt[1]

1ZF Wind Power, Gerard Mercatorstraat 40, 3920 Lommel, Belgium

Keywords: Wind Turbine Powertrain, optimisation, Frequency Based Sub-structuring

Abstract: This paper explores various optimisation techniques aimed at reducing the propagation and radiation of gearbox- or generator-induced vibrations through large surfaces of wind turbines. Two examples are presented to illustrate this. The first example involves optimising powertrain parameters by directly minimizing the predicted tonality at a field microphone. To enable a sufficiently fast solution for the powertrain, wind turbine, and surrounding acoustics model in the optimisation process, Frequency Based Sub-structuring is employed. The second example focuses on the topology optimisation of a main bearing unit. The novelty here lies in incorporating constraints that ensure the proposed design meets both structural requirements and NVH (Noise, Vibration, and Harshness) demands. Both examples demonstrate the potential of using optimisation techniques to enhance the NVH performance of wind turbine drivetrains while simultaneously reducing the design's mass and volume.

1 Introduction

The continuously increasing need for sustainable energy sources almost inevitably leads to the installation of wind turbines closer to inhabited areas. Among other factors, tonality—meaning a dominant, narrow-frequency-band noise—can cause increased annoyance or potential health issues for nearby residents. To mitigate the resulting conflict between wind turbine operators and the local population, many countries have implemented legislation setting limits on tonality, often based on IEC61400-11. This standard defines tonality as a narrow band noise that exceeds the wind turbine's masking noise. Consequently, the ongoing trend to reduce emitted rotor sound, and hence masking noise, makes narrow band sounds, such as those excited by meshing gears, relatively more significant. Additionally, increasing cost pressures, new powertrain concepts, and wind turbine control strategies reduce the degrees of freedom in the design of a wind turbine powertrain or gearbox. Therefore, new methodologies are needed to find optimal powertrain and/or gearbox designs within the remaining design space.

Traditionally, a gearbox or powertrain is designed and optimised based on experience. From an NVH (Noise, Vibration, and Harshness) perspective, this means creating an initial design, building a simulation model, assessing the tonality risk, and proposing improvements if needed. This process is repeated until a design that meets all requirements is found. It is important to note that in this classical process, the quality of the proposed improvements largely depends on the experience, imagination, and collaboration of the simulation and design engineers [CHR08].

In contrast to the experience-based approach, computer-based optimisation approaches can be employed, which automatically alter the design to minimize an objective function. This paper applies and compares two computer-based optimisation methods: parameter optimisation and topology optimisation. For the purposes of this paper, parameter optimisation refers to the optimisation of a set

of discrete parameters, which can be found in multi-body models, optionally including flexible bodies. Topology optimisation, on the other hand, is defined as a process that can handle topological changes, such as creating, removing, or merging voids in a three-dimensional structure [ALE20]. Finite element models are used as the basis for topology optimisation. The specific properties of experience-based, parameter, and topology optimisation are listed in the following table:

	Experience-based optimisation	Parameter optimisation	Topology optimisation
Requirements for optimisation (Pre-processing)	Experienced engineers, least formal description of the problem at hand	Parameters for optimisation must be discretised	Representative boundary conditions
Time for optimisation (Optimisation)	slowest, only few iterations possible, unlikely that optimal design is found	fast, many iterations possible	slow, many iterations needed, but model with many Dofs to solve
Applicability of output (Post-processing)	directly applicable	parameter values must be translated into a design	3d shape as output, but typically needs re-work to comply e.g. with manufacturing constraints
Including non-NVH conditions (e.g. strength, fatigue, …)	possible for few boundary conditions, if too many, problem too complex to be solved by human	very limited possibility, relevant components are typically lumped to masses and stiffnesses	possible, increases simulation time

Table 5: Properties of experience-based, parameter and topology optimisation.

As shown in the table, each method has specific advantages and disadvantages. Therefore, based on today's technology, none of them can be completely neglected. However, in many cases, the classic experience-based process can be replaced by parameter or topology optimisation, saving time and leading to new, previously undiscovered options.

This paper describes two application examples. In the first example, parameter optimisation is used to optimise a set of gearbox parameters. In the second example, topology optimisation is applied to a main bearing housing of an integrated powertrain. Both examples highlight the advantages of the respective computer-based optimisation approach over classical experience-based optimisation.

2 Application of optimisation to an integrated powertrain

2.1 Parameter optimisation on full system level

This example assumes the availability of an initial model of a 3-stage integrated powertrain and a wind turbine model, including radiation to potential IEC microphone positions in the field. One order in the second stage was found to be problematic with respect to tonality. Therefore, the objective of this optimisation example is to minimize the tonality in this order by altering parameters. Since ZF Wind Power can only make decisions on the design of their own products, parameter changes are limited to the powertrain model. Unlike previously published parameter optimisations [KAN23], the objective in this example is to directly optimise tonality at a microphone instead of optimising one or

multiple vibration signals on powertrain components, which are assumed to correlate with tonality. This allows for much more accurate tuning of these parameters.

The nature of optimisation involves solving the model many times, each with different combinations of the parameters to be optimised. The challenge is that a model containing the powertrain, wind turbine, and acoustics requires several days, if not weeks, to calculate the tonality along an order for just one parameter setting. A parameter optimisation based on such a model would take years. Therefore, ZF Wind Power proposed the use of Frequency Based Sub-structuring (FBS), which slices the full model into independent sub-structures, such as the acoustic domain, wind turbine, and powertrain. FBS uses Frequency Response Functions calculated for each sub-structure independently and assembles them so that the sound pressure at the IEC microphones is identical to the solution of the full model [DEK08]. The major advantage of this approach is that each sub-structure is solved independently. Since the wind turbine and acoustics remain unchanged in this example, only the powertrain model needs to be solved for new parameter sets. Merging the results of sub-structures using FBS is a fast process, resulting in a massive reduction of simulation time per parameter set. More details on the implementation of FBS used in this example can be found in [BEC24].

In this example, the powertrain model contains lumped parameters wherever possible and flexible bodies where necessary. In total, there are 108 Degrees of Freedom between the sub-structures. Solving the powertrain model, calculating the sound pressure at IEC microphones using FBS, and converting this into tonality is possible in only 11 seconds for one parameter set. The order-cut of the critical mode optimised in this section is depicted in Figure 2.1 by a red line in the initial situation. It can be seen that it clearly exceeds 0dB tonality at two points.

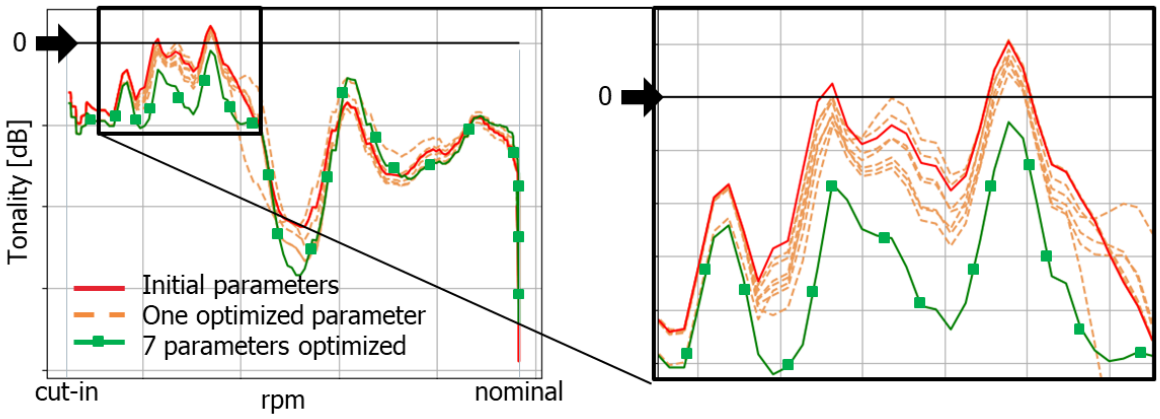

Figure 2-1: Tonality along critical order in initial condition (red, solid), with one optimised parameter (orange, dashed), and with 7 optimised parameters (green, boxes). Left: Full order cut from cut-in until nominal operation. Right: Zoom into most critical area.

For the optimisation, seven parameters in the powertrain model were identified as likely to influence tonality. These parameters were optimised within a realistic range (e.g., +/- 15% of the initial value) using the BFGS method provided by the Python package scipy. After 11 iterations and less than 20 minutes of total simulation time, the optimiser converged to the green curve in Figure 2.1, successfully lowering the tonality, particularly in the most critical areas.

The expected tonality when only one of the seven parameters is set to the optimised value, while all other parameters remain at their initial values, is shown by the dashed orange lines in Figure 2.1. Clearly, changing only one parameter individually is insufficient to lower the tonality along the complete order-cut below 0dB. Moreover, some parameters changed individually create additional operational conditions where the tonality increases to approximately 0dB. In contrast, with all seven parameters optimised, a distance between the 0dB line and the predicted tonality is maintained across the entire operational range.

In a subsequent step, these desired parameter changes need to be translated into actual designs. To this end, topology optimisation or design experience can be applied, demonstrating that using one of the three optimisation methods listed in Table 1 does not preclude using another to overcome specific disadvantages.

However, in some scenarios, optimising the design of a component itself, rather than its lumped representation in simplified parameters, is desired or even required. Such a scenario is presented in the following section.

2.2 Topology optimisation of a main bearing unit

The main bearing unit is one of the most important components of an integrated wind turbine design. Structurally, it supports the main bearings, gearbox housing, and yaw system. Dynamically, it plays a crucial role in transferring structure-borne noise induced by the gearbox and generator into the tower.

A conventional design process primarily focuses on the structural functionality of the main bearing unit and often overlooks its role in wind turbine noise. ZF Wind Power aims to address this issue with two approaches:

1. Topology optimisation with additional constraints and objectives:

- This approach includes constraints and objectives that account for tonality behavior, derived from parameter optimisation and engineering experience.

2. Multi-objective topology optimisation:

- This approach involves performing topology optimisation by directly optimising the predicted tonality at an IEC microphone (similar to the parameter optimisation example in section 2.1 – currently under development).

In both cases, the goal is to develop a lightweight main bearing unit design that ensures the wind turbine’s tonality compliance.

The following section demonstrates the application of the first approach to design a main bearing unit for a turbine with an integrated powertrain and a 3-planetary-stage gearbox.

2.2.1 FE model and boundary conditions

An FE model consisting of the gearbox housing, design space, yaw bearing, and tower is prepared (Figure 2.2), taking into account the following considerations:

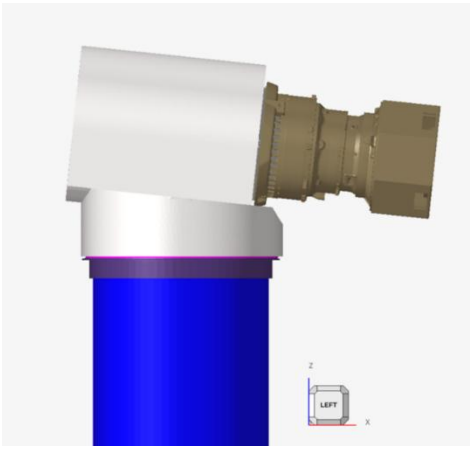

Figure 2-2: Design space for topology optimisation in FE model.

The **design space** is defined as large as possible within the given geometrical limits, primarily imposed by transportation constraints (white bodies in Figure 2.2). This design space connects the tower top, gearbox interface, and main shaft. Only one material is assigned to the design space, so no rubber bushing elements are foreseen.

Static loads are derived from extreme load cases and operational data, and these loads are applied to the respective interfaces. For example, Figure 2.3 shows loads applied to the main bearings in one load case. Multiple load cases and additional loads are considered for optimisation runs.

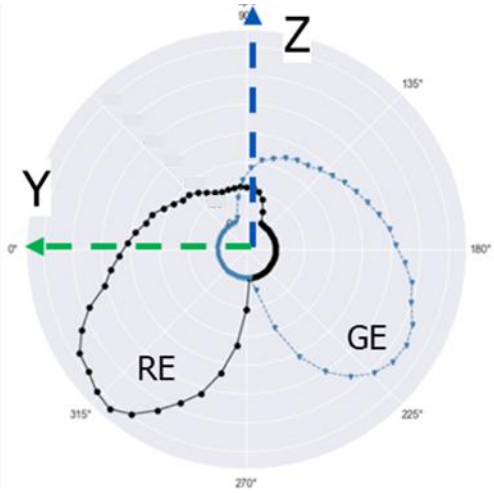

Figure 2-3: Static load case example.

Static responses are used to evaluate the structural functionality of the design. Maximum stresses and bearing seat deformations are examples of features tracked during optimisation runs.

Constraints can be applied to ensure the optimiser converges to a design that meets all relevant "binary" requirements. These are requirements that must be fulfilled to ensure the proper operation of the wind turbine, but there is no added value in reducing them significantly below the necessary threshold. Examples include tonality-defining constraints or constraints on maximum stresses in the material. If the turbine is tonality-free, there is no benefit in further reducing the tonality. Similarly, if maximum stress is not exceeded, it can be assumed that the gearbox will withstand the occurring loads. Reducing the stresses further (apart from a safety factor) does not add value.

Objectives can include the minimization of design volume and/or mass.

It is important to note that different definitions of constraints and objectives result in different final designs. Due to confidentiality, the results presented in the following section are obtained with an incomplete set of constraints.

2.2.2 Topology optimisation results of a Main Bearing Unit

Figure 2-4 illustrates the development of the optimisation run, which converged after 55 iterations. The left graph shows the continuous decrease of the objective function with each iteration. The right side of the graph provides a global metric measuring constraint violations. With a few minor exceptions, the optimised design (iteration 55) satisfies all the constraints.

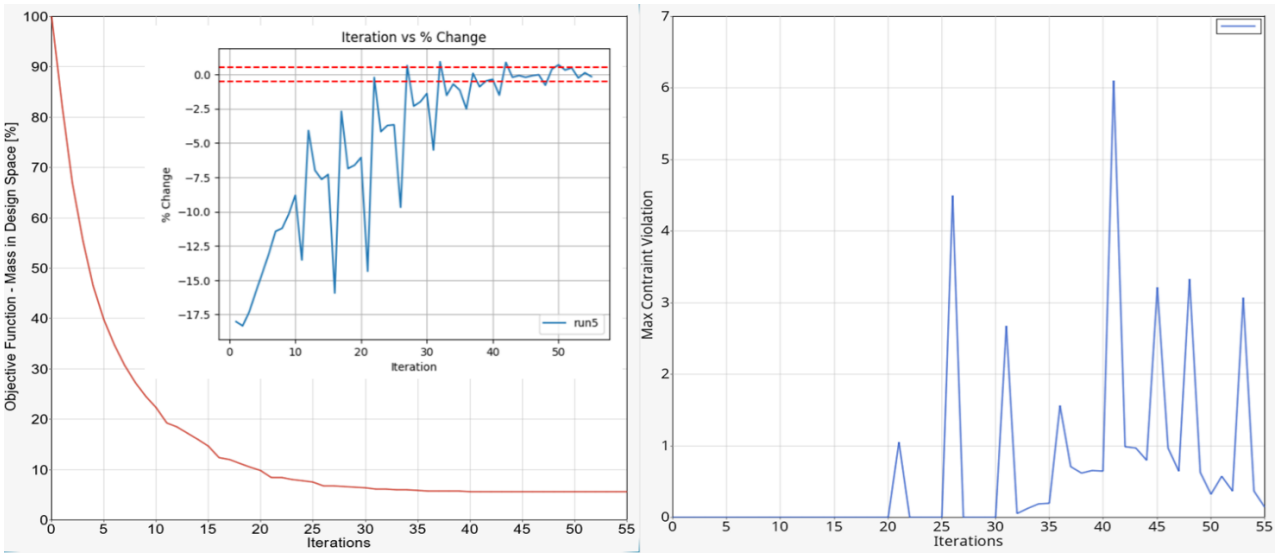

Figure 2-4: Optimisation run history.

Typical for topology optimisations, the proposed design (Figure 2-5) takes on a very organic shape. It features three arms connecting the generator and rotor side bearing seats, which are highlighted in blue. Additionally, the connection to the yaw bearing is ensured through two rather solid structures, one at the rotor end and one at the generator end. This design can fulfill the set constraints as well as a manually designed main bearing unit with the same constraints, but with approximately three times less weight. This example demonstrates a weight reduction of 67% without the use of rubber bushing elements, highlighting the potential of incorporating topology optimisation into the design process.

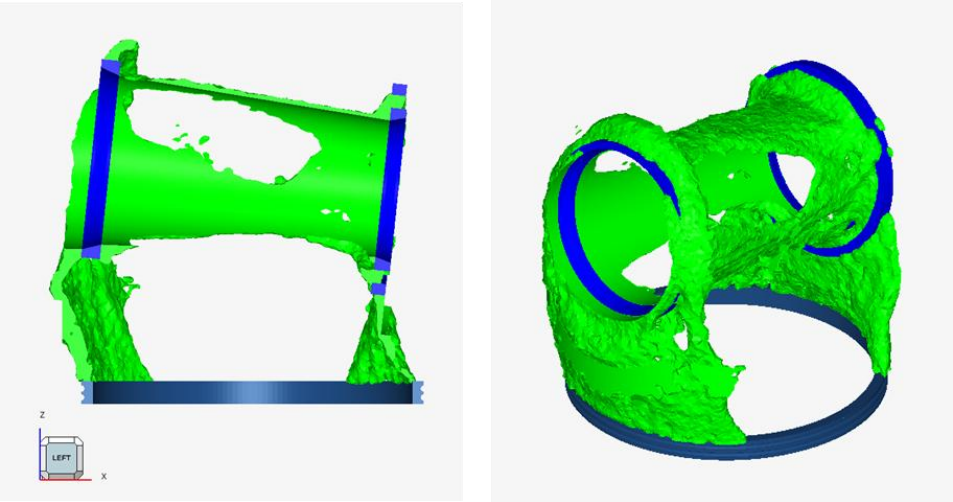

Figure 2-5: Topology optimisation result illustrative example (not all relevant constraints are switched on for confidentiality).

3 Conclusions

The increasing demand for sustainable energy necessitates the installation of wind turbines closer to rural areas. One consequence of this shift is an increased focus on wind turbine noise to protect the inhabitants of nearby settlements. In this context, avoiding tonalities (narrow band noise exceeding the broadband noise of the wind turbine) is particularly important when developing a wind turbine drivetrain.

To address these challenges, this paper proposes the use of computer-based optimisation techniques. The added value of these techniques is demonstrated through two key examples:

1. Optimisation of drivetrain parameters:

- Focus: Minimizing predicted tonality at the field microphone rather than vibrations at locations on the drivetrain, which are assumed to correlate with tonality.
- Method: Utilization of Frequency-Based Substructuring (FBS) to significantly reduce the simulation time for each parameter set.
- Outcome: The optimisation of an initially tonal design converged in less than 20 minutes within realistic limits implemented for each optimised parameter. The result was a tonality-free design over the full operation range considered in the optimisation.

2. Topology optimisation of main bearing unit:

- Focus: Minimizing mass and volume while considering both structural and NVH constraints.
- Outcome: Without implementing rubber bushing elements, the resulting design was two-thirds lighter than a manually designed counterpart with comparable constraints.

These examples underscore the potential of computer-based optimisation techniques in enhancing the NVH performance of wind turbines, while reducing volume, material, and cost, thereby contributing to the broader goal of sustainable energy development.

4 Bibliography

[ALE20] Alexandersen, Joe, and Casper Schousboe Andreasen. "A review of topology optimisation for fluid-based problems." Fluids 5, no. 1 (2020): 29.

[BEC24] Becht, Philip, De Smet, Bart, Schmidt, Sebastian and Blockmans, Bart. "Tonality spread of wind turbines due to production and measurement tolerances." In proceedings of ISMA 2024 Conference on Noise and Vibration Engineering, Leuven, 2024.

[CHR08] Christensen, Peter W., and Anders Klarbring. An introduction to structural optimization. Vol. 153. Springer Science & Business Media, 2008.

[DEK08] De Klerk, Dennis, Daniel J. Rixen, and S. N. Voormeeren. "General framework for dynamic substructuring: history, review and classification of techniques." AIAA journal 46, no. 5 (2008): 1169-1181.

[KAN23] Kanpolat, Emre. “Wind turbine tonality – A holistic approach to its prediction and mitigation.” In proceedings of 10th International Conference on Wind Turbine Noise, Dublin, 2023.

Deep learning approach to efficiently solve wind turbine acoustic tonalities

K. Schulze-Forster[1], P. Zech[1], M. Eckstein[1]

[1]Wölfel Wind Systems GmbH + Co. KG

Keywords: tonalities, vibration control, machine learning

Abstract: Tonalities in airborne sound radiated by wind turbines can lead to noncompliance with noise regulations. In this case, restricted turbine modes may be enforced which lead to reduced efficiency and loss of revenue. Tonalities are caused, for example, by harmonic gearbox vibrations and there are several methods to reduce such vibrations. However, it is not obvious which vibration mode they must target in order to achieve a strong reduction of tonalities. Therefore, extensive testing is usually required to find an effective vibration control strategy. The relation between gearbox vibrations and tones in radiated sound is frequency-dependent and highly complex. Corresponding measurement data may not describe this relation without ambiguity.

Hence, conventional methods such as correlation analysis fail at detecting the most relevant vibration components for tonality reduction. Experimental transfer path analysis may be an alternative but comes with extremely high efforts.

This presentation introduces a novel analysis method of this complex relation using deep neural networks. It shows how gearbox vibration components causing tonalities are found from simultaneous acceleration and sound measurements. The analysis helps deploying vibration control methods well-targeted for tonality reduction. As a result, costly testing time on prototype turbines is cut down.

1 Introduction

The sound generated by wind turbines is composed of broadband noise and narrowband components with tonal character. The broadband noise, produced by airflow blade interaction, is more and more reduced by optimized blade designs in modern turbines [DES19]. This results in lower overall noise levels but also reduces the masking effect for tonal components which then become more dominant. Tonal components whose levels are significantly higher than the masking noise are called tonalities according to standard IEC 61400-11 [IEC12]. They are perceived as particularly unpleasant. Therefore, in noise-sensitive markets like Europe and North America there are regulations which enforce reduced operating modes or downtime if tonalities exceed certain levels. This leads to yield losses for operators.

Tonalities are caused by harmonic vibrations which are, for example, excited by periodic gear mesh contacts in the gearbox [GER19] or by other machinery. These vibrations propagate through the drivetrain to large radiating surfaces such as tower and blades. Therefore, both the gearbox design and the design of transfer paths through the turbine have a strong impact on tonality levels. However, multiple conflicting design goals regarding loads, weight, efficiency, cost, time-to-market, etc. have to be considered. In this multi-criteria optimization the vibroacoustic performance usually is one of the less important goals.

To mitigate resulting tonality problems, add-on solutions such as passive or active dampers are applied on the drivetrain. The goal is to damp certain vibration modes in order to minimize the propagation of structure-borne sound which ultimately leads to tonalities. However, the relation between

drive train vibration modes and tonalities is highly complex and usually unknown. Therefore, it is not obvious which mode has the strongest impact on tonalities and should thus be damped.

The most important mode may be found experimentally by testing various damper setups or through experimental transfer path analysis [SCH21]. However, both approaches come with extremely high efforts and several practical challenges. Alternatively, data analysis methods such as correlation analysis may be applied to measurement data. Yet, they are not well-suited for non-linearities, high variance, and measurement inaccuracies to be expected from the problem at hand. Furthermore, no existing data analysis method is able to predict the importance of individual vibration modes upon the tonality without the aforementioned high-effort transfer path analysis. Therefore, there is a need for more advanced analysis methods to solve tonality problems efficiently. In this work, a new analysis method based on deep neural networks, which can cope with the above challenges, is introduced.

2 Method

The goal is to obtain a frequency-dependent evaluation of different drivetrain vibration modes with respect to their impact on tonality levels based on measurement data. The proposed method performs this evaluation in three steps: data preparation, model training, model analysis.

2.1 Data preparation

As a first step, a vibroacoustic measurement is performed while the turbine is in operation. Drive train vibrations and the rotor speed are recorded simultaneously with the sound pressure at one or multiple locations outside the turbine. Then, short-term vibration levels of relevant drive train modes and short-term sound pressure levels are extracted at the dominant tonality frequencies which usually correspond to some gear mesh frequency order of some gear box stage. An example of a point cloud of tonal sound pressure levels thus obtained is shown in Figure 4. Finally, the data points are divided into a training, validation, and test set.

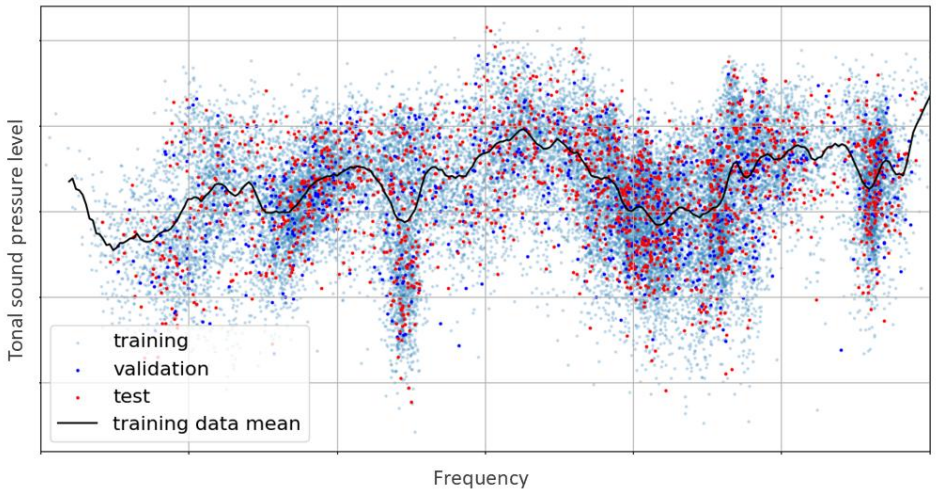

Figure 4: Example data set of tonal sound pressure levels

2.2 Model training

A Deep Neural Network (DNN) is trained to predict the tonal sound pressure level from the drive train vibration levels and the corresponding frequency as inputs. Figure 5 shows a schematic diagram of the inputs and output of the DNN. The training is performed using the training data, while the validation data is used to evaluate the learning progress and to decide when to stop training. Finally, the DNN is evaluated using the testing data. Not only the absolute prediction error but also the ability to predict data points that strongly deviate from the training data mean are of interest. If the DNN has only learned to predict the training data mean for all test data points, the training was not successful. In this case, the DNN size or training parameters must be adapted.

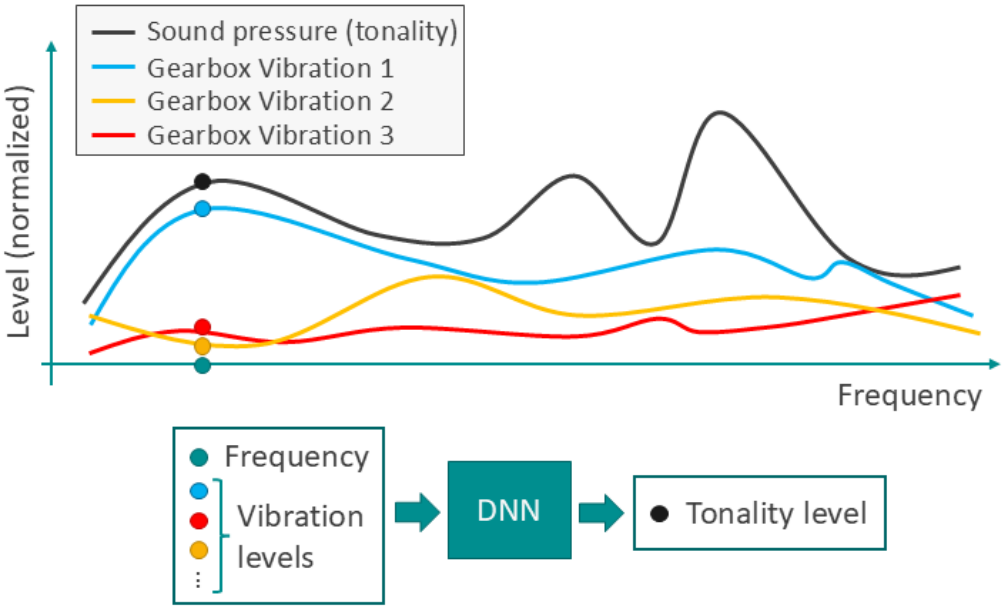

Figure 5: The upper diagram shows example order cuts of vibrations and tonalities (arbitrary curves). The lower diagram shows how such data are processed by the DNN.

2.3 Model analysis

After the DNN has been trained successfully, the prediction process of the DNN is analyzed. The aim is to find out which input features, i.e. drive train vibration modes, are most important to make the prediction of the tonality level. The underlying assumption is that the vibration mode with the strongest contribution to the prediction has the highest impact on the tonality level. Training and analysis of the DNN serve as an advanced correlation analysis which can handle challenging data with non-linearities, high variance, and noise. There are a number of methods from the field of explainable artificial intelligence to make such analyses [LIN20]. Figure 6 shows a schematic diagram of a result of such an analysis. One advantage of the proposed method is that it allows a frequency-dependent evaluation of the relation between vibrations and tonalities.

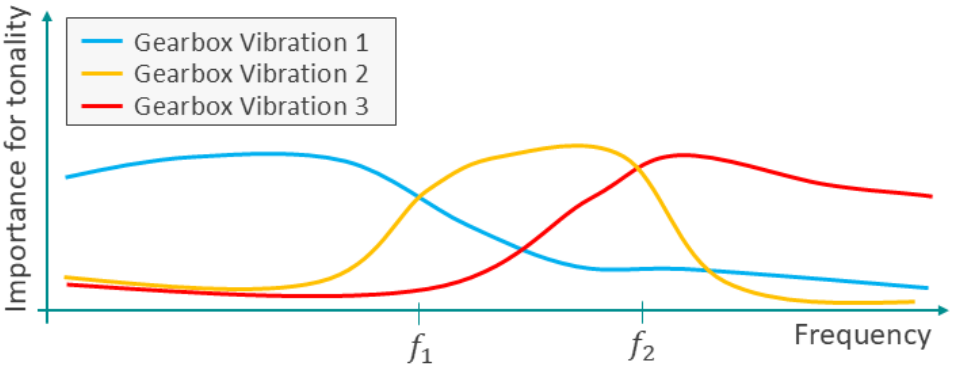

Figure 6: Example result of the analysis of the importance of gearbox vibrations

3 Evaluation

The proposed method was evaluated regarding consistency and validity of the results. In this context, consistency means that the analysis results are reproducible on different data sets recorded at the same turbine. Validity means that the estimated importance of gearbox modes for tonality levels can be confirmed experimentally.

3.1 Consistency

Two vibroacoustic measurements performed on one wind turbine on different dates may produce data with different information content. The drive train vibration data usually show neglectable differences. The sound pressure recorded outside of the turbine, though, is influenced by environmental factors such as temperature, wind speed, or wind direction as well as the yaw-angle of the nacelle relative to the microphone position. The resulting differences may be small, however, DNNs may be sensitive to such nuances. Therefore, it is important to evaluate the consistency of the proposed method.

For that purpose, two measurements were performed on one wind turbine on two different days and two different data sets were obtained according to Section 2.1. For each data set, a DNN was trained and analyzed as described in Sections 2.2 and 2.3. The results are shown in Figure 7.

Each data point represents the importance of a gearbox vibration mode estimated based on the corresponding data pair of vibration and sound pressure for the given frequency. The results show a good consistency with Vibration 2 being estimated the most important on both data sets. Also, the variation of importance over frequency is consistent for all vibration modes. Nevertheless, the results are not fully identical. A certain degree of variance is expected from stochastic machine learning mechanisms like deep learning. Overall, it can thus be concluded that the method is able to yield consistent results across different data sets.

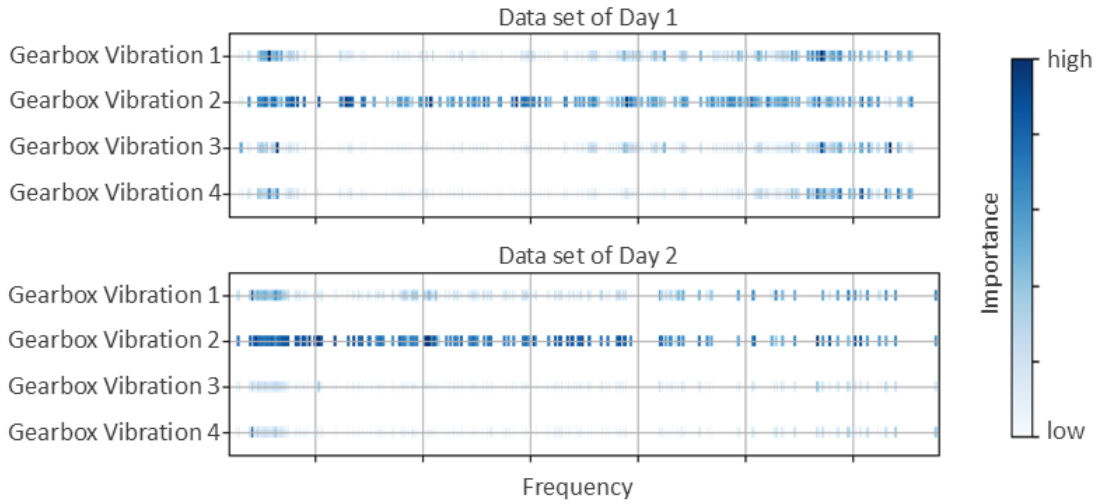

Figure 7: Analysis results of the importance of gearbox vibrations for tonality levels for two data sets recorded on different days on the same turbine.

3.2 Validity

In order to evaluate the validity of the results, an Active Vibration Control (AVC) system was installed on the gearbox of the same turbine on which the vibroacoustic measurements described in Section 3.1 were done. Two more measurements were then performed. In the first one, Gearbox Vibration 1, which had a low importance assigned to it by the method (cf. Figure 7), was reduced by the AVC system. In the second one, Gearbox Vibration 2, which had a high estimated importance (cf. Figure 7), was reduced by the AVC system. For each measurement, a baseline was recorded while the AVC system was switched off. The corresponding tonality sound pressure levels are shown in Figure 8.

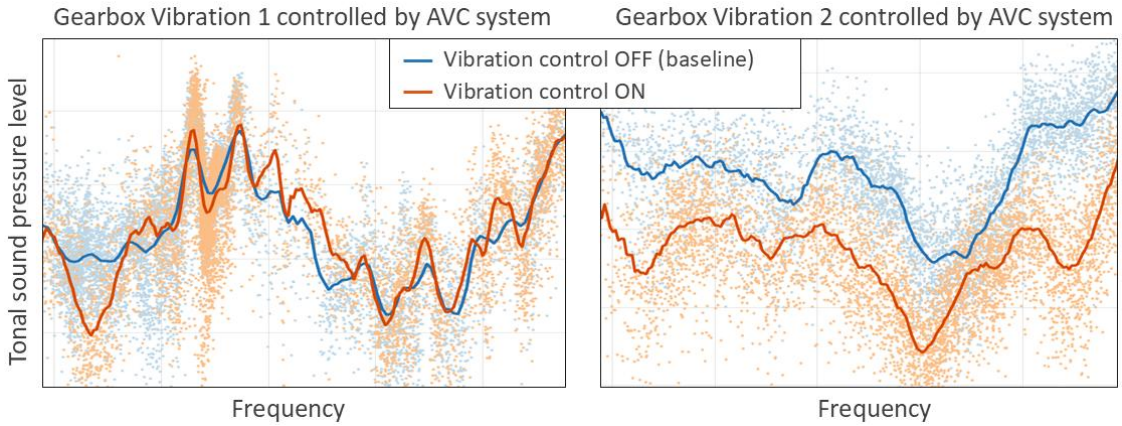

Figure 8: Analysis results of the importance of gearbox vibrations for tonality levels for two data sets recorded on different days on the same turbine.

The graphs show that the tonal sound pressure level was not significantly changed when Gearbox Vibration 1 was reduced. Only at low frequencies the tonality was reduced for a small frequency range. This is consistent with the prediction in Figure 7. On the other hand, when Gearbox Vibration 2 was reduced, the tonal sound pressure was reduced over the whole frequency range. This

behavior is also in line with the prediction. This means that the method was able to predict which vibration mode has a strong influence on the tonality level.

4 Summary

Tonalities in wind turbine noise may be penalized by noise regulations with restricted operation modes or even downtime. Therefore, they must be kept at low levels. This may be done by applying active or passive dampers on the drive train in order to reduce harmonic vibrations, which are caused by the gearbox, for instance. However, it is often unclear which vibration mode has the strongest influence on tonality levels and should thus be reduced.

In this work, a new method to analyze the relation between drive train vibrations and tonal sound pressure based on vibroacoustic measurement data was introduced. It is based on deep learning and can handle challenges such as nonlinearities, high variance and measurement noise.

The method was evaluated regarding both prediction consistency across measurement data from different days of one turbine and validity of the prediction. The evaluation showed that the results are indeed consistent for different data sets of the same turbine and that the predictions can be confirmed experimentally.

The proposed method allows deploying vibration control methods well-targeted for tonality reduction. As a result, costly testing time on prototype turbines may be cut down and tonality problems can be solved efficiently.

5 Bibliography

[DES19] Deshmukh, Shubham, et al.: Wind turbine noise and its mitigation techniques: A review.

In: 2nd International Conference on Energy and Power, 160, 633-640, 2019

[GER19] Geradts, Peter, et al.: Reduction of the tonality of gear noise by application of topography scattering.

In: Applied Acoustics 148, 344-359, 2019

[IEC12] International Electrotechnical Commission: IEC 61400-11, Wind turbines – Part 11: Acoustic noise measurement technique, Edition 3.0, 2012

[LIN20] Linardatos, Pantelis, et al.: Explainable ai: A review of machine learning interpretability methods.

In: Entropy, 23(1), 18, MDPI 2020

[SCH21] Schünemann, W. et al.: Identification of relevant acoustic transfer paths for WT drivetrains with an operational transfer path analysis.

In: Forschung im Ingenieurwesen, 85(2), 345-351, 2021

Powertrain I

Prototype testing of wind gearboxes on test bench and turbine

Martin Reuter, Gabriel Aydin, Timo Zundel

Flender GmbH - Winergy, Am Industriepark 2, 46562 Voerde, Germany

Keywords: gearbox, testing, test bench, field measurements

Abstract:

Prototype gearboxes are equipped with a high number of different measurements – load related strain based signals like torque, bending or forces, temperatures, pressures and displacements in and outside the gearbox.

Testing on serial test benches allows only pure torque testing conditions. Depending on the high integration and the increased torque density the elastic effects in a gearbox cannot be completely simulated without the simulation of bending and force from the rotor system.

For prototype testing with wind loads in the last years several WLUs were commissioned all over the world. They allow the implementation of rotor bending and forces into the drivetrain – they are suitable for dynamic load conditions like in a wind turbine as well as for static load conditions to establish constant tilt and yaw moments to find out correlations between outer loads and inner reactions.

Measurements on a wind turbine are the most realistic test environment. Short time measurements only deliver a short view on the behavior of the drivetrain – long term field measurements deliver a more complete overview on the operating behavior. A longterm field measurement is a complex enterprise and to deliver a complete picture of the behavior of the wind turbine.

On a test benches the load situation is defined by the setpoint settings. The real operation in a wind turbine depends on the wind condition and is random. Therefore, signals from the turbine controller are needed for a complete picture which is the foundation for further analysis of the measured data.

1 Introduction

The prototype tests of wind turbine main gearboxes are conducted according to IEC 61400-4. The upcoming new release will bring in new tasks which are already part of the Winergy validation philosophy.

The component prototype tests are conducted under pure torque conditions on serial test benches. Field validations are also already implemented in the IEC 61400-4 and field measurements in wind turbines are usual. But new turbine designs with different drivetrain layouts and higher torque density lead to more interactive effects, so that testing on Wind Load Units (WLU) and measurements in wind turbines become much more important in the future.

2 Functional test

The functional tests are conducted on the serial test benches under pure torque conditions. The aim is to show the functionality and prove the performance of the gearbox.

At the very beginning of every test, the gearboxes are statically flushed until a certain oil cleanliness is reached. This removes all particles that can damage the components in the gearbox. Afterwards is repeated during dynamic flushing with turning gearboxes and low torque applied.

The gearboxes are equipped with a high number of different sensors to be able to fulfill the required measurements. Torque and speed sensors are needed for efficiency measurements and the documentation of the driven loads during the complete test. In combination with an encoder the stiffness measurements are taken out. Up to 45 triaxial accelerometers in- and outside the gearbox deliver a good view on the dynamic behavior of the gearbox.

Further measurements depending on new designs are continuously developed and realized in our prototype gearboxes. Sebastian Reisch [REI25] gives an interesting insight in our possibilities during prototype testing.

2.1 Robustness test

The robustness test will be implemented in the new release of IEC 61400-4 but is already part of the Winergy testing philosophy. The robustness test can either be conducted on component level for the gearbox or it can be done on different system levels, for example gearbox with main bearing unit (MBU). This is depending on the general design of the drivetrain – for example we need to test the MBU with our gearbox in the so-called 2-PRS semi-integrated concepts, where the planet carrier of the first stage of the gearbox is supported by the bearings of the MBU. Dr. Ralf Hambrecht gives a good overview in the different Trends and Technology in Wind Turbine Powertrain Systems [HAM25]. It is also common that the serial shrink disk is also validated during a robustness test.

Intention of the robustness test is to provide indications related to risks which cannot be calculated in the design process. Even if high loads are implemented in the robustness test – the robustness test is not an accelerated lifetime test. The maximum torque should be comparable to the maximum torque in the design load cases (DLCs). The duration of a robustness test is defined to 300 h and is divided up into different parts which shall evoke different failure modes in components of the gearbox or drivetrain. Possible failures are categorized in different failure modes A1, A2, B and C. The focus of the robustness test failure modes A2 and B:

A2: deterministic failures where validated models for calculating the failure are (not yet) available – best example tooth flank fracture (TFF) or white edging cracks (WEC)

B: stochastic failures, mainly caused by friction, abrasion or extreme temperatures, a non-cumulative failure like scuffing

Failures of the mode C are random failures e.g. caused by debris in the gearbox or loose parts due to bad assembly. These failures are stochastic and cannot be systemically detected by testing. Failures of the mode A2 will change to failures mode A1, when the reliable simulation models are accepted in design and calculation process. Dr. Jonas Finken shows his probabilistic approach for the prediction of TFF [FIN25].

Micropittings on gears or roller bearings shall be checked for example by high loads up to 130% nominal torque at 80% nominal speed combined with high oil temperatures.

Extreme high loads during a limited duration can generate scuffing.

Journal bearings are stressed with high speed idling situations or highly dynamic procedures like start/stop cycles with a high number of repetitions. To rise the challenge for the plain bearings these tests can be conducted with emergency lubrication or no-grid lubrication.

Overspeed is a challenge for the high speed shaft roller bearings and can cause smearing and skidding effects.

Single blade installations (SBI) can cause plastic deformation due to possible extreme high loads during the time when the unbalanced rotor is partly installed. A SBI test may be part of a prototype test in the factory – but depends always on external support for the tools to bring in the high torque at standstill.

At the beginning and the end of the robustness test control slices are driven to check the influence of the treatments during the robustness test on the performance of the gearbox. After the robustness test the test specimens are completely disassembled, and all the parts are visually inspected.

2.2 Climate test

The test is intended to verify the oil distribution, the gearbox tightness and the gearbox operation in extreme climate conditions.

The gearbox is tested in a non-load setup and driven by an electrical motor connected to the generator shaft. The gearbox is turned in the original direction to prove the correct distribution of the oil during the test slices. It can be neglected, that the non-working flank of the tooth is loaded, as there are no high loads applied. The gearbox is set up with a tilt-angle which corresponds to the turbine installation. The gearbox shall be connected to the original oil supply system (OSS) to test the lubrication system under realistic conditions. To protect the gearbox against oxidation in the humid climate chamber, it shall be primed in advance.

Depending on the customer specification the gearbox is cooled down to the lowest possible ambient temperature of -40°C. If the desired temperature is reached, the cooling of the climate chamber is kept switched on to keep the ambient temperature.

The complete start-up procedure shall follow the specification of the customer in terms of:

- Gearbox speed depending on the oil temperature
- Switching point(s) of the oil supply system depending on the oil temperature
- Switching points of heating elements (if available) depending on the oil temperature
- Oil flow depending on the oil temperature
- Switching points dry/wet mode depending on the oil temperature

The oil fill test aims at measuring the exact amount of oil, which is needed to fill the gearbox to minimum and maximum at different planet carrier positions.

The cold start-up procedure aims at testing the oil supply system capability to heat up the oil and start the gearbox from low ambient temperatures. Additionally, it shall prove, that the oil supply to the different gear mesh and bearing positions at all operation temperatures is sufficient. Therefore, oil pressures, oil flow and temperatures are recorded continuously.

Supporting task can be the qualification of oil supply systems – here it is possible to measure the startup current of the electrical oil pump motor.

The purpose of the leakage test is to prove the oil tightness of all flange and housing joints as well as all gap sealings. Therefore, additionally to the leakage check during cold start up procedure, a dedicated test at different gearbox speeds and oil temperatures is conducted.

3 Integrated system test

In integrated system tests more than one component of a wind turbine drivetrain are tested together. This can be done under load conditions or in non-load conditions and especially with non-torque loads and at the end as a complete test in the wind turbine during field measurements.

On wind load units (WLUs) we are able to investigate the influence of the non torque loads on displacements and the load distribution by driving at constant speed and loads within a few hours. Load Distribution Measurements (LDMs) can be taken out in short time in a wind turbine, too. Here the turbine torque can be limited to different values and we measure 10 min time series at constant load to be able to get a quick impression on the general LDM in the wind turbine. Noise emissions, transient effects and full system dynamics can only be measured in a wind turbine itself.

A clear shortterm measurement on a wind turbine is the measurement of torques during single blade installation on the wind turbine: In this case the turbine is in construction mode and the surrounding conditions are very different from the normal turbine operations – an inclinometer and an anemometer are installed on our own temporarily to get information on the rotor position and to check the wind speed during installation. A torque measurement point on the main shaft can be installed in cooperation with the turbine manufacturer. A Winergy Torque Sensor (wTS) already implemented during the prototype test in the factory gives a well validated signal on the torques during the assembly.

3.1 Winergy field measurement system and data acquisition strategy

The actual version of Winergy field measuring systems have different components to guarantee a long running measurement system. The main components are:

- Computer and measurement amplifiers for data acquisition
- Receiver for the slow telemetry systems like temperature and pressure in the rotating gearbox components and fast telemetry e.g. for the load distribution on the suns
- Devices for remote access and remote control of different hardware components of measuring system
- Power supply including an uninterruptable power supply

The configuration of amplifiers is open and can be adapted to the purpose of the required measurements. It is possible to measure a longterm LDM in a wind turbine. The installations in the ringgears are measured directly hard wired and permanently, for the signals of the sun pinions we have a solution for a remote controlled activation of battery powered telemetry systems to save battery lifetime during not interesting turbine states.

The DAQ works with 3 different sampling rates. The slow one is use for e.g. temperatures and pressures in lubrication system. The medium speed sampling rate is defined to 100 Hz and is used for the 10 min@100 Hz time series and turbine controller signals, the load related signals around the rotor system. The fastest sampling rate will be used for torque highspeed shaft or a longterm LDM on the wind turbine. Sampling rates of signals like displacements of different planet carriers are defined corresponding to rotational speed of the investigated component.

During a longterm measurement we store the measured values in mainly 3 different groups:

- 10 min@100 Hz
- Statistic journal

- Events

The 10 min@100 Hz time series are the base for the longterm evaluations. In a post-evaluation for each dataset the 10 min mean windspeed value and turbulence intensity are added to a capture matrix according to DIN EN 61400-13. A certain number of valid 10 min time series for each windbin is mandatory to fill up the capture matrix. A defined number of needed time series is mandatory to declare the measurement as completed.

The statistic journal gives a good overview on the operation on the turbine – even month wise. With min/max and mean values of 10s intervals we still get an impression on the dynamics in the signal

Event measurements are triggered measurements with higher sampling rates during interesting turbine operations like emergency stops. To detect these situations different signals from the turbine controller are extremely helpful.

3.2 Important input: turbine controller signals

During longterm measurements signals from the turbine controller are very helpful for investigating the behavior of the gearbox in real turbine life. Best practice is sharing the data stream via CAN-Bus, proved in several measurements on different turbines with different customers.

Windspeed is the most important signal during a longterm measurement. Wind is the input to the turbine and to be able to fill the capture matrix we need a good wind speed signal in our measurement system.

Electrical power delivers the output on the electrical side of the turbine. The signal is used to validate the measured torque values and gives a good information on the operation grade of the turbine.

Turbine status and pitch are very good signals to see the actual operation mode of the wind turbine and its influence on the actual performance of the gearbox in operation.

Azimuth angle / the nacelle position combined with wind speed can give an impression on the wind situation, too. If we have unsteady wind conditions the nacelle will follow the wind direction as good as possible. In this case an influence of non-torque loads is visible.

If available, the non-torque loads tilt and yaw moment deliver a valuable input on the operating behavior. Modern wind turbines with blade sensors can deliver these values via turbine controller. In prototype turbines often strain gages and inductive powered telemetry systems are installed on the main shaft to measure the bending on the main shaft. This can be supported in cooperation with the turbine manufacturer by Winergy as well. With higher torque density and a higher degree of integration into the drivetrain non-torque loads are becoming more and more interesting. Bending moments in yaw and tilt direction can have an influence on internal displacements, on the load distribution in gears and cause strains in the torque arm which can be measured by strain gage installations. This can be evaluated in regard to internal displacement or the effect on the load distribution during operation under real wind conditions. As well ring creeping effects can be investigated regarding wind loads.

A supportive measurement during the installation of a wind turbine can be torque measurements during a SBI or checking measurements of strain during the alignment of the drivetrain. A short term LDM gives a good picture on the performance of the microgeometry of the gears in turbine operation and can be realized within 1 or 2 days on the wind turbine.

4 Conclusion

Testing is an important part of the development process of wind turbines. Higher torque densities and a higher degree of integration of different components lead to new challenges, which need to be tested in a system environment. All tests which are conducted inhouse at Winergy are proven and new challenges due to new designs are in scope of Winergy. Testing in wind turbines require a good cooperation between the different teams to be able to deliver good results and a complete view on the performance of the wind turbine with its single components. From gearbox side we can support these activities by supporting a well-equipped measurement gearbox and proven measurement systems with a complex data acquisition strategy.

5 Bibliography

[FIN25] Dr. Finken, Jonas: Probabilistic modelling of the tooth root strength of wind gears

CWD2025 proceedings, Aachen, 2025

[HAM25] Dr. Ralf Hambrecht Trends and Technology in Wind Turbine Powertrain Systems

CWD2025 proceedings, Aachen, 2025 Circulation

[REI25] Dr. Reisch, Sebastian: Elastic Interaction in Planetary Stages with increased Torque Density

CWD2025 proceedings, Aachen, 2025

Optical Fiber Sensing to measure the gear load distribution in a planetary stage of a wind turbine gearbox

Jelle Bosmans[1], Florin Tatar[1], Luk Geens[1], Laveen Prabhu Selvaraj[1], Georgo Angelis[2], Mats Kolsteeg[2]

[1]ZF Wind Power Antwerpen B.V., Gerard Mercatorstraat 40, Lommel, Belgium

[2]Sensing360 Development, Oss, The Netherlands

Keywords: Optical fiber sensing, Gearbox condition monitoring, Gearbox lifetime.

Abstract: An important target for the wind industry is to reduce the LCoE. Avoiding unplanned downtime using early anomaly detection methods (1) and enabling lifetime extensions using remaining useful life (RUL) calculations (2) are important contributors to achieve this target. A significant parameter, which can serve as an indicator of (1) and (2) for a wind turbine gearbox, is the load distribution in the planetary stage.

Measuring and understanding the direct effect of e.g., extreme loads, unfavorable load conditions or unbalance in the load distribution of the gears can both enable to detect anomalies in the gearbox as well as to predict the expected RUL.

Today, there are no industrial market solutions to physically measure the load distribution in a planetary stage in a gearbox. The expected minimum service life of 20 years, the sensor system costs and the high number of sensors to be installed over a circumference of 360 degree are factors limiting the implementation of such kind of measurement solution in serial applications.

This paper summarizes a new technical solution using fiber optic strain sensors to solve this problem. A validation test with 35 sensing elements around the gearbox circumference will give a measurement position at every 10°: the positions are centered near the middle of the ring gear of the first planetary stage which has seven planets. The torque, speed and planet load share are calculated and further processed to be integrated in the RUL calculation as well as for application to detect anomalies in the gearbox. In ongoing developments, the reliability for a 20-year service life, the optimal sensor configuration (number and positions) and a lab on chip development for the interrogator integration (to lower the cost of the system) are being investigated.

1 Introduction

This paper describes a ZF development on a novel technology using optical fiber sensing elements to measure the load distribution in the planetary stage. The main objective is to use this technology to further detect gearbox failures and to determine gearbox remaining useful life (RUL). Several optical fiber sensor configurations are analyzed with the main scope of enabling the industrial implementation and cost reduction.

The paper is structured as follows: Section 2 will introduce the tested gearbox and the back-to-back test rig on which it was running during the measurements. Section 3 elaborates on the measurement principle of the Fiber Optic Sensor (FOS) as well as the sensor layout. Section 4 continues by describing the algorithms that are used to calculate speed, torque, and load share from the raw FOS measurements. Section 0 then discusses the results of these algorithms. Section 6 closes the paper with some conclusions and an outlook to future development of this technology.

2 Test setup and campaign

During the test campaign, a gearbox from the ZF 7k family with rated power of 7.2 MW was tested. This gearbox family is part of ZF's SHIFT product line of modular gearboxes for the wind market. Testing was carried out on a back-to-back test rig which is shown in Figure 120. On the test rig, two gearboxes are connected at the low-speed shaft side. One gearbox is operated in motor-mode by driving its high-speed shaft with an electric motor while the other gearbox operates in its normal generator mode. In the results shown in this paper, the gearbox instrumented with fiber optic sensors (FOS) was operating in generator mode.

The gearbox itself is a four-stage gearbox with three planetary stages and a single helical stage, achieving a total ratio close to 200. The first planetary stage, of which the ring gear is instrumented with fiber optic sensors, contains 7 planet gears.

Next to the FOS which will be discussed in Section 3 several reference sensors are available as part of the setup. The torque is measured by HBM transducers at the high-speed shafts of both gearboxes. These transducers also contain a 1024 pulse encoder to measure angular velocity. A single pulse per revolution sensor that tracks the position of the low-speed planet carrier of the instrumented gearbox is also available.

The gearbox was tested under speed run-ups at various torque levels. This variation of torque and speed allows for testing the FOS and the algorithms under various conditions.

Figure 120: Back-to-back gearbox test rig at ZF Lommel. Installed gearboxes are illustrative and do not represent the gearbox instrumented in this paper.

3 Fiber optic sensing system

3.1 Sensing principle

An array of 35 fiber optic strain sensors was installed around the outer surface of the ring gear of the first planetary stage. The sensors used are so-called Fiber Bragg Gratings (FBGs). An FBG

sensor is a section of the optical fiber with a periodic variation of its refractive index. This section acts like a mirror, reflecting specific wavelength while transmitting others. The reflected wavelength of the FBG is sensitive to both variations in strain and temperature, and by tracking this variation in reflected wavelength a measurement is realized. Benefits of FBGs compared to traditional strain gauges are that they offer a higher signal-to-noise ratio, are immune to electromagnetic interference and that a single optical fiber can accommodate multiple sensors. All of these together lead to a simplified and more time-effective installation process. The optical fiber was bonded using a cyanoacrylate glue to the outer surface of the gearbox at the midpoint of the first planetary stage, as shown in Figure 121.

Figure 121: Installation of FBGs. Photo by Sensing 360 B.V.

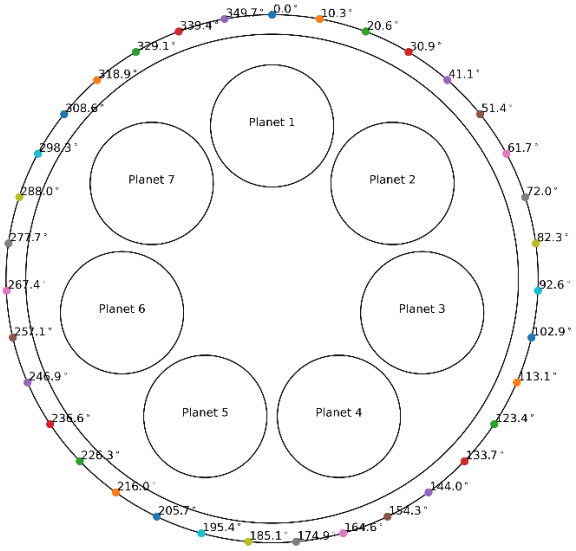

Figure 122: Angular location of the 35 FBGs on the outer surface of the ring gear.

3.2 Sensor layout

All 35 FBGs are equally spaced around the circumference of the gearbox to allow for a continuous calculation of the torque output. Figure 122 shows the angular location of FBG sensors. The sensor numbering starts at the sensor at 0.0º on top of the gearbox later referenced as sensor 1 and continuous in a clockwise fashion until the sensor at 349.7º referenced as sensor 35.

The measurement principle is that during operation of the gearbox, when a planet passes the location of a sensor, the mesh forces between the planet and the teeth of the ring gear cause a deformation of the outer surface of the ring gear proportional to the rotor torque. This deformation of the surface strains the FBG sensor in the optical fiber. This is then picked up by a fiber optic interrogator, which analyzes the wavelengths reflected by the sensors. The interrogator and data acquisition system can continuously log the strain up to 24 kHz. For practical reasons, the sample rate used for this study was limited to 317 Hz. Sensing360 B.V. provided the fiber optic sensors and data acquisition system.

4 Algorithms for speed, torque, and load distribution calculation

4.1 Initial data processing

The data acquisition system logged the strain data from each of the 35 FBG sensors. These strain signals were then detrended to remove the effect of temperature changes during the measurements. The remaining strain signal is assumed to be caused solely by the deformation of the ring gear following the mesh events between the planet and ring gear. Figure 12 shows the strain signal for a single sensor during a full revolution of the gearbox input shaft. Each peak corresponds to one of the seven planets passing the sensor. This strain signal from each of the 35 sensors was then used as the input for the torque, rpm and load sharing estimations.

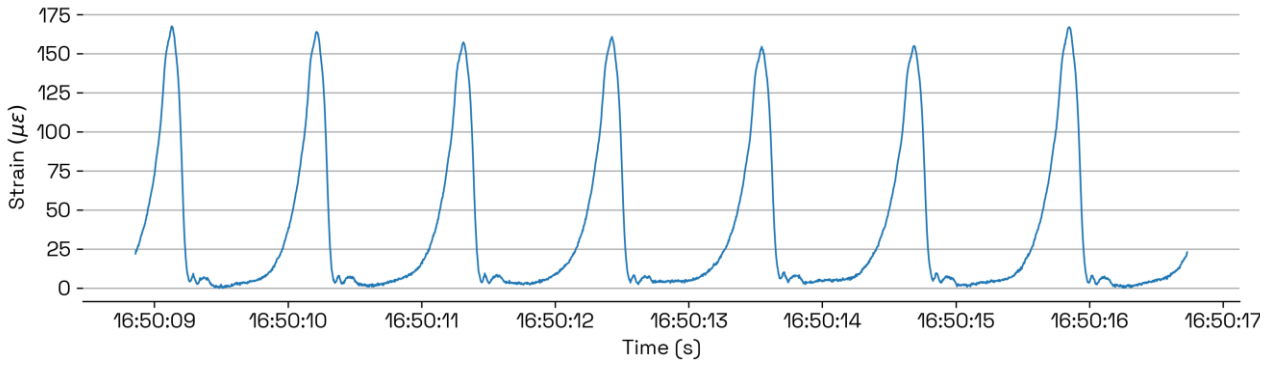

Figure 12: Strain signal for a single sensor during a full revolution of the shaft.

4.1.1 Torque and Speed Estimation

The strain measured by the FBGs on the outer surface of the ring gear of a planetary stage was found by Sensing360 to be proportional to the rotor torque, as described in [GUT22]. Using a Sensing360 proprietary signature-based algorithm [ANG19], the strain data was decomposed to recover the main shaft torque. Furthermore, using the same signature-based algorithm, the speed of the low-speed shaft was estimated as well.

4.1.2 Load Distribution

The mesh load factor K_γ accounts for deviations in load splitting e.g. in gearboxes with planetary stages [NEN13]. The values of K_γ used during design should be verified by detailed simulations and measurements. If data from simulations and measurements is not available, standardized values of the mesh load factor apply, as given in Table 6. The ISO 6336-1 [ISO19] standard defines the mesh load factor as the load carried by the planet gear carrying the higher load divided by the average load of all planets.

The following expression can be derived for the mesh load factor K_γ of a single planet from the measured peak-to-peak strain values:

$$K_{\gamma,p} = \frac{\overline{\Delta\varepsilon_p}}{\overline{\Delta\varepsilon_{all}}} \qquad \textbf{Eq. 2}$$

Where $\overline{\Delta\varepsilon_p}$ is the average peak-to-peak value of the single planet and $\overline{\Delta\varepsilon_{all}}$ is the average peak-to peak value for all planets. The mesh load factor for all planets then follows as:

$$K_{\gamma,all} = \frac{\max\left(\overline{\Delta\varepsilon_{p1}}, \overline{\Delta\varepsilon_{p2}}, \overline{\Delta\varepsilon_{p3}}, \overline{\Delta\varepsilon_{p3}}, \overline{\Delta\varepsilon_{p4}}, \overline{\Delta\varepsilon_{p5}}, \overline{\Delta\varepsilon_{p6}}, \overline{\Delta\varepsilon_{p7}}\right)}{\overline{\Delta\varepsilon_{all}}} \quad \textbf{Eq. 3}$$

In Figure 12, each peak in the strain signal corresponds to the passing of a single planet. Each time that a planet passes under a strain sensor, the mesh load factor K_γ can be calculated.

Number of planets	3	4	5	6	7
Mesh load factor K_γ	1.10	1.25	1.35	1.44	1.47

Table 6: Default mesh load factors for number of planets [NEN13]

5 Results

5.1 Torque and speed

Figure 124 shows the torque and speed estimated with the aforementioned algorithms using all 35 FBG sensors, together with the torque and speed from the reference sensors described in Section 185. The shaded regions indicate segments with constant torque and speed that are used for more detailed reporting of the results in the next sections. These segments represent torque levels equal to 35%, 51%, 72%, and 98% of the nominal torque (in order of occurrence). During each segment the speed was constant and equal to 50% of the nominal value.

It was found that the maximum deviation for the torque and speed estimation from the FOS sensors during these constant torque and speed levels is 0.2% of nominal torque and 0.1% of nominal speed. Both the torque and speed estimations from the FOS sensors show a good match with the reference data for the whole range of torque conditions, both transient and stationary.

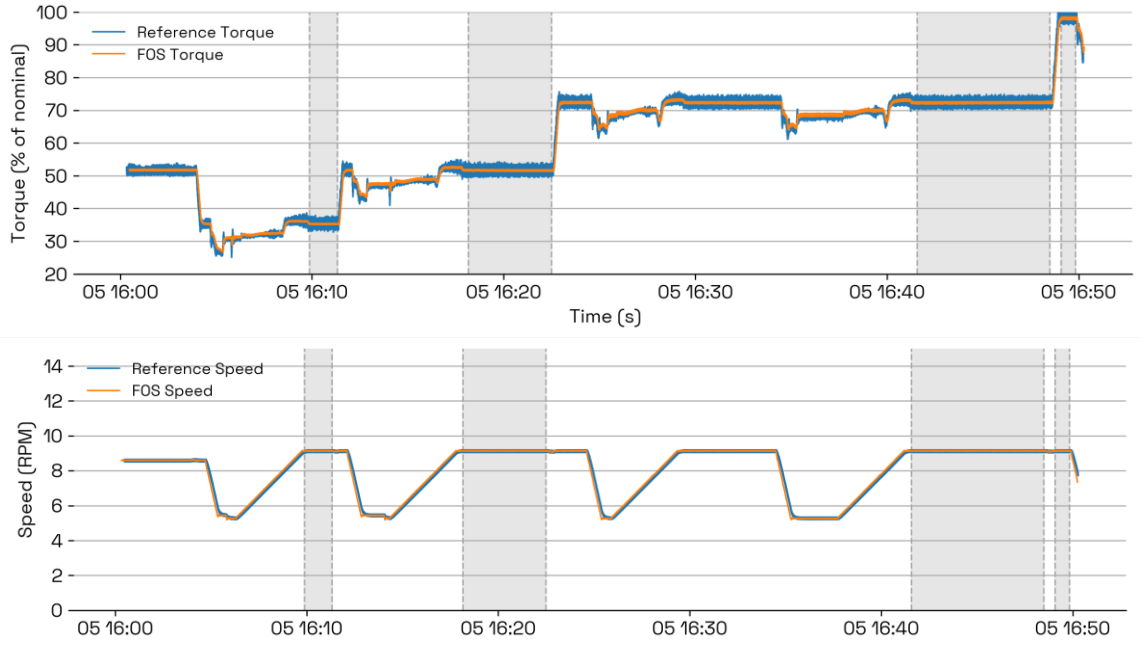

Figure 124: Torque and speed factor from reference and Fiber Optic Sensing (FOS) data using all 35 sensors.

5.2 Load distribution

Figure 125 shows the mesh load factor K_γ calculated using all 35 FBGs following Eq. 3. The same highlighting is used to indicate segments of constant torque and speed. The factor decreases when higher torque is applied (the latter part of the sequence). This reflects a more equal sharing of load at high torque, for which the design is optimized.

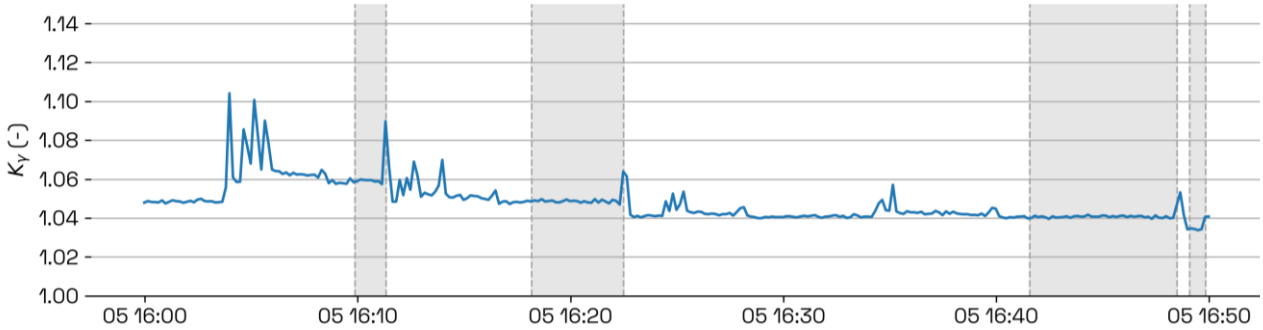

Figure 125: Load distribution calculated from FOS data using all 35 sensors.

5.3 Sensor set reduction

To study the effect of fewer sensors, the torque, speed, and load distribution were calculated for two different groups of subsets with 5-7 sensors.

The first group of subsets consists of a range of adjacent sensors around a section of the ring gear. Five of such subsets have been defined, each consisting of seven sensors covering 72º of the circumference of the ring gear. The second group of subsets consists of evenly distributed sensors around the ring gear. Four of these subsets have been defined, each consisting of five sensors, evenly distributed around the full circumference of the ring gear.

For each subset, the mean and standard deviation of the torque and mesh load factor were calculated over four segments of constant torque and speed. These segments were indicated as the shaded areas in Figure 124 and Figure 125. The results of this study can be found in Tables Table 7: through Table 10:.

Table 7 shows that for the first group of subsets the maximum torque difference versus the reference increases from 0.2% to 0.9% and the standard deviation increases from 0.2-0.3% to 0.4-0.7%. In Table 8 shows the result of the second group of subsets. The maximum torque difference with the reference increases from 0.2% to 1.8% and the standard deviation increases from 0.2-0.3% to 0.5-1.0%.

Table 9 shows that the first group of subsets has a maximum difference in the load sharing (with respect to the full set) of 0.005 and that the standard deviation increases from 0.001-0.002 to 0.001-0.007. Similarly, Table 10 shows that for the second group of subsets, the maximum difference in load sharing with respect to the full set is 0.009 and that the standard deviation increases from 0.001-0.002 to 0.001-0.008.

Reducing the sensor set from the original 35 sensors to a subset of 7 sensors, placed either in a sector of 72 degrees or placed equidistantly around the circumference, still leads to satisfactory results of the estimated torque, speed, and load distribution, while reducing the production and installation effort.

Reference data	All 35 sensors	Sensors 1,8,15,22,29	Sensors 2,9,16,23,30	Sensors 3,10,17,24,31	Sensors 7,14,21,28,35
Torque [% of nominal value] (mean ± SD)					
35.2 ± 1.0	35.1 ± 0.2	35.2 ± 0.4	35.2 ± 0.4	34.9 ± 0.4	36.1 ± 0.5
51.4 ± 1.0	51.5 ± 0.2	51.5 ± 0.5	51.5 ± 0.5	51.1 ± 0.5	52.6 ± 0.5
72.0 ± 1.0	72.2 ± 0.3	72.2 ± 0.5	72.2 ± 0.6	72.0 ± 0.5	72.6 ± 0.6
98.0 ± 1.0	98.0 ± 0.3	98.0 ± 0.5	98.0 ± 0.6	98.0 ± 0.6	98.0 ± 0.7

Table 7: Torque estimation based on subsets of sensors consisting of five sensors evenly distributed around the full 360º of the circumference of the ring gear.

Reference data	All 35 sensors	Sensors 1-7	Sensors 8-14	Sensors 15-21	Sensors 22-28	Sensors 29-35
Torque [% of nominal value] (mean ± SD)						
35.2 ± 1.0	35.2 ± 0.2	33.0 ± 0.6	34.8 ± 0.6	35.9 ± 0.5	36.2 ± 0.6	35.2 ± 0.6
51.4 ± 1.0	51.5 ± 0.2	49.7 ± 0.8	51.2 ± 0.7	52.0 ± 0.6	52.3 ± 0.7	51.5 ± 0.7
72.0 ± 1.0	72.2 ± 0.3	71.3 ± 0.9	72.0 ± 0.8	72.5 ± 0.7	72.5 ± 0.7	72.2 ± 0.8
98.0 ± 1.0	98.0 ± 0.3	98.0 ± 1.0	98.0 ± 0.9	98.0 ± 0.8	98.0 ± 0.8	98.0 ± 0.9

Table 8: Torque estimation based on subsets of sensors consisting of seven adjacent sensors covering 72º of the circumference of the ring gear.

All 35 sensors	Sensors 1,8,15,22,29	Sensors 2,9,16,23,30	Sensors 3,10,17,24,31	Sensors 7,14,21,28,35
Mesh load factor K_γ (mean ± SD)				
1.064 ± 0.002	1.065 ± 0.006	1.061 ± 0.006	1.059 ± 0.006	1.065 ± 0.007
1.053 ± 0.002	1.049 ± 0.006	1.053 ± 0.006	1.055 ± 0.007	1.054 ± 0.006
1.043 ± 0.002	1.042 ± 0.005	1.043 ± 0.005	1.045 ± 0.005	1.046 ± 0.005
1.037 ± 0.001	1.036 ± 0.004	1.035 ± 0.003	1.034 ± 0.003	1.039 ± 0.003

Table 9: Mesh load factor estimation based on subsets of sensors consisting of five sensors evenly distributed around the full 360º of the circumference of the ring gear.

All 35 sensors	Sensors 1-7	Sensors 8-14	Sensors 15-21	Sensors 22-28	Sensors 29-35
Mesh load factor K_γ (mean ± SD)					
1.064 ± 0.002	1.073 ± 0.008	1.065 ± 0.007	1.061 ± 0.006	1.061 ± 0.007	1.068 ± 0.007
1.053 ± 0.002	1.058 ± 0.006	1.053 ± 0.006	1.052 ± 0.005	1.051 ± 0.005	1.055 ± 0.005
1.043 ± 0.002	1.047 ± 0.005	1.045 ± 0.005	1.044 ± 0.005	1.043 ± 0.004	1.046 ± 0.004
1.037 ± 0.001	1.038 ± 0.003	1.039 ± 0.004	1.034 ± 0.003	1.036 ± 0.003	1.039 ± 0.003

Table 10: Mesh load factor estimation based on subsets of sensors consisting of seven adjacent sensors covering 72º of the circumference of the ring gear

6 Conclusions

This article has described a study on several configurations of fiber optic strain sensors for measurements on a wind turbine gearbox. An extensive setup consisting of 35 fiber optic strain sensors was used to measure the torque, speed, and load distribution. A good correspondence was found between the estimated torque and speed signals from the fiber optic sensors and the reference data.

Furthermore, the effect of selecting subsets of sensors on the torque, speed, and load sharing estimation was presented. It was found that reducing the sensor set from the original 35 sensors to a subset of 7 sensors, placed either in a sector of 72 degrees or placed equidistantly around the circumference, still leads to satisfactory results of the estimated torque, speed, and load distribution.

For future work, the effect of the sensor configurations in actual wind turbines during a wider variety of operating conditions should be studied. It is suggested to initially use a setup with a large number of fiber optic sensors, similar to the setup used for this study. Eventually, this will lead to a proposed sensor configuration for a product with fewer sensors.

The fiber optic sensing system for wind turbine gearboxes as described in this article will make direct measurement of the torque, speed and load sharing cost-effective. These signals are key in improving the reliability and avoiding unplanned downtime using early anomaly detection methods. Furthermore, they enable lifespan extensions using remaining useful life calculations.

7 Bibliography

[GUT22] Gutierrez Santiago, Unai: Input torque measurements for wind turbine gearboxes using fiber-optic strain sensors.
In: Wind Energ. Sci., 7, 505-521,
Copernicus Publications on behalf of the European Academy of Wind Energy e.V., -, 2022

[NEN13] NEN-EN-IEC 61400-4:2013 Wind turbines - Part 4: Design requirements for wind turbine gearboxes

[ISO19] ISO 6336-1 : Calculation of load capacity of spur and helical gears - Part 1: Basic principles, introduction and general influence factors

[ANG21] Angelis, Georgo: GB201904221D0 Method of decomposing a load of interest associated with bearing-supported equipment
European Patent Office, United Kingdom, 2021

Powertrain II

Trends and Technology in Wind Turbine Powertrain Systems

Dr. Ralf Hambrecht

Flender GmbH - Winergy, Am Industriepark 2, 46562 Voerde, Germany

Keywords: drive train concepts, modularization, FlexibleFit, wind load unit

Abstract: This paper is providing an overview on the recent and future powertrain concepts for wind turbines. Derived from the market development and influenced by technical and logistic limitations the influencing criteria are explained that lead to different drive train architectures. Torque density increase, modularization and standardization in wind turbine powertrains are requirements in combination with reduced product lifecycle times, shortened development times and cost pressure. Next to these challenges there is a high focus on the drive train reliability and the need to consider system behavior impacting the major components like gear or main bearing units. Therefor intensive system validation with wind load testing on test benches and in the field is an important part of the development process.

1 Introduction

With the move of two large OEM's to medium speed for onshore wind turbines in the years 2020 and 2022 the question about the best powertrain concepts was raised again. This discussion was not just about the generator concept like direct drive, medium speed or highspeed, it was even more about the best suited mechanical drive train concept.

Reduced product lifecycle times, shortened development times, and the cost pressure create a need for modularization, standardization and torque density increase in wind turbine powertrains.

In combination with a higher integration level and the further increasing sizes and weights of the onshore powertrain components, new challenges need to be considered.

2 Market trend

A trend from the past years which is still ongoing is the continuous increase of turbine power ratings in new developments and installations. Most relevant for gearbox dimensioning is the wind turbine rotor toque. In the global volume forecast from 2022 the average turbine rotor torque for 50% market volume was expected to double from below 5.000+ kNm to 10.000 kNm in 9 years by 2030, see figure 1. Recent market figures from 2024 show that the torque level for 50% market volume split already reached 8.000 kNm and will still reach 10.000-12.000 kNm from 2030 on. This faster increase was also influenced by the rapid grow of turbine power ratings in China with realization of up to 12 MW onshore turbines. [WOM24], [BRM24], [WIN24]

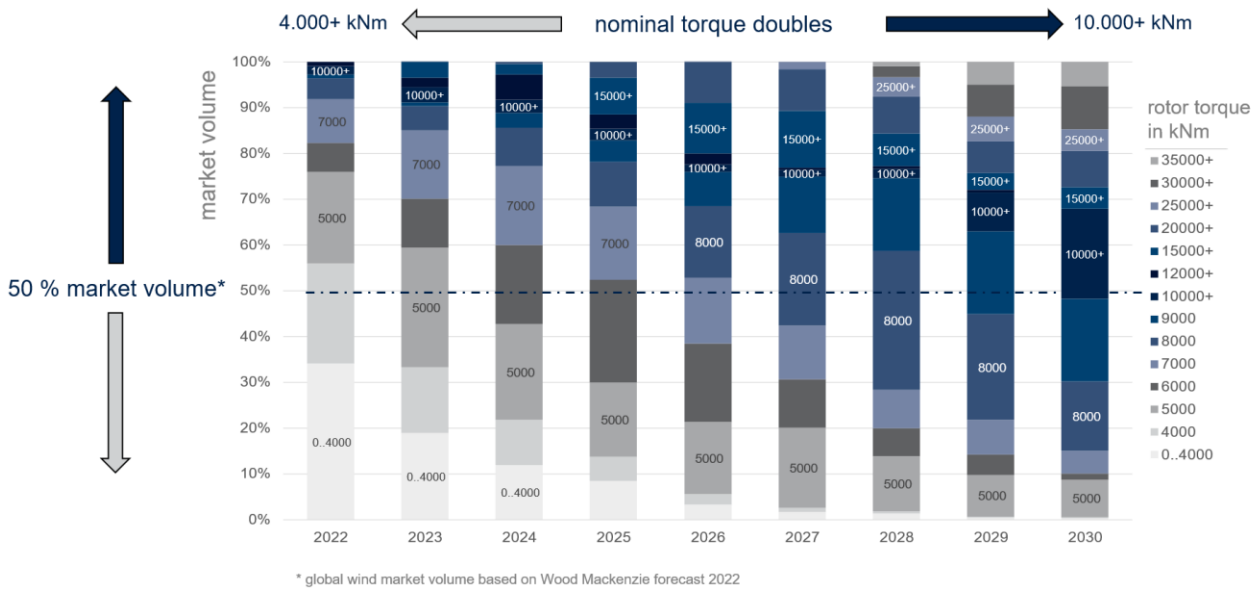

Figure 126: Wind market trend in 2022 [WIN24]

In the offshore segment mainly direct drive turbines and geared medium speed drives are entering the next power level ratings above 15 to 21 MW plus. Especially Chinese OEMs are the front runners in targeting the highest power rating wind turbines. [WOM23], [BRM24]

The onshore market is more and more dominated by geared drives. Most of the onshore DD turbine manufacturers have phased out the DD technology for new turbines. [BRM24]

The trend to medium speed powertrains initiated from Vestas and Goldwind for onshore turbines slowed down a bit as especially in China the highspeed DFIG technology was pushed to higher power ratings of up to 12 MW plus and were installed in the strongly CAPEX driven Chinese market.

For the mechanical drive train in the onshore segment up to 6 MW the 3-point rotor support (3-PRS) with a spherical roller bearing (SRB) as main bearing is dominating the market. For turbines with higher power ratings a trend to pretensioned tapper roller bearings in a main bearing unit can be seen. Technical and economical drawbacks of SRBs with increasing size and thrust loaded reinforce the trend. 4-point rotor support (4-PRS) arrangement and especially in China 2-PRS are taking over as dominating drive train concept.

3 Drive train concepts

The geared drives are usually classified in mid-speed and high-speed concepts dependent on the generator speed.

The major difference in mechanical drive train concepts can be seen in the way how the wind loads are supported by the drive train. This is usually categorized by the number of supporting points and the way the connection to the turbine structure is done – elastic with flexible elements or rigid via a metal-to-metal contact, see figure 2.

Very often in use is the 3 Point Rotor Support (3-PRS) which means that there is a first main bearing support and two supports from the torque arms of the gearbox taking the rotor loads. Also very common is the 4-PRS where two main bearings and the two torque arm points take the rotor loads.

If the reaction torque is directly transferred to the main bearing housing and not to the base frame via a torque arm this is called a 2-PRS. Inside such a main bearing unit there are usually two pre-tensioned tapper roller bearings in O-arrangement.

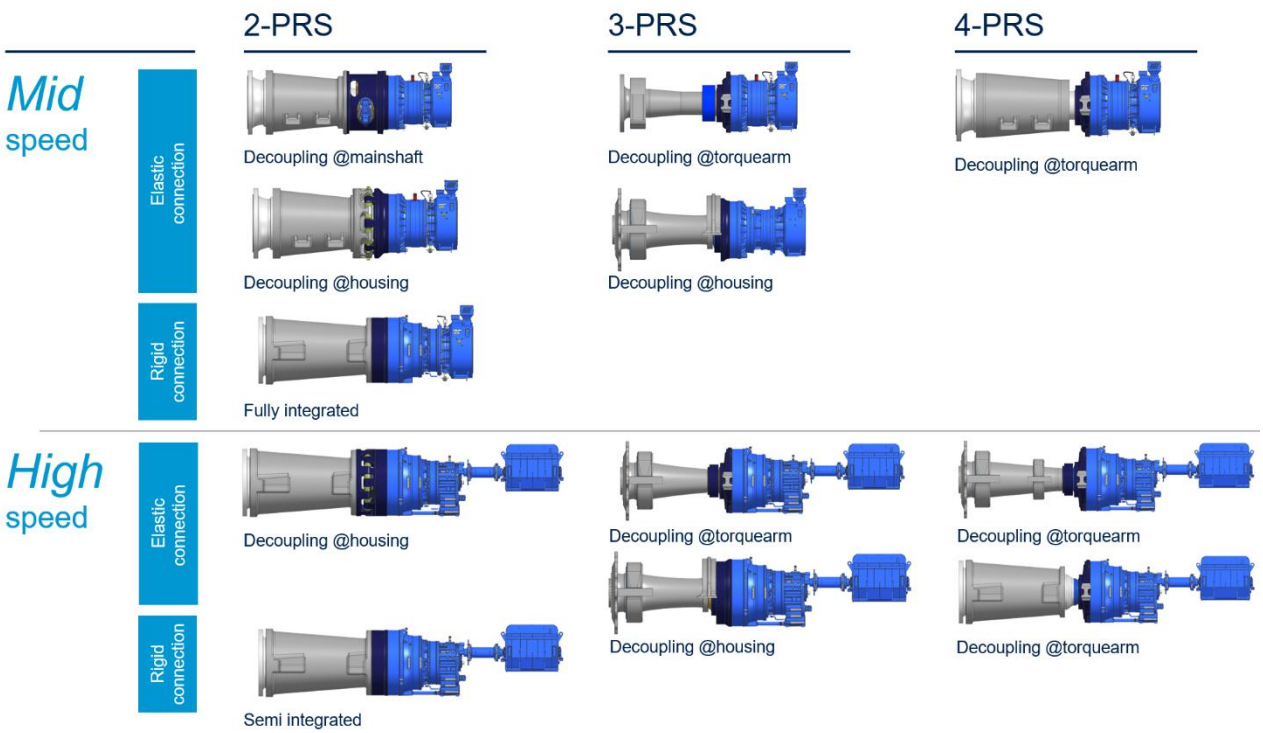

Figure 127: Geared drive train concepts overview

The conventional 3-point and 4-point rotor support have long track records with spherical roller bearings (SRB) as main bearings and allowing an elastic deformation of the main shaft. The powertrains can be easily dismantled into transport or service modules. The gear unit is elastically decoupled from the turbine base frame via torque arms with elastomer bushings. For larger turbines from power ranges of 6 to 7 MW the SRB bearing type is mainly replaced by pretensioned tapper roller bearing arrangement in a main bearing unit that provides a stiff rotor support.

For even bigger turbines where the weight of the gear unit and generator should not rest on the planet carrier bearings the 2-PRS decoupling@mainshaft solution transfers the weight loads to the main bearing housing. This solution also omits a large torque arm that would hinder transportation. Due to the torsional stiff but bending flexible coupling, the deflection on the main bearing unit from the massive wind loads does not affect the gearbox. So undefined wind load effects are reduced to a minimum.

The 2-PRS decoupling@housing concept benefits from elasto-hydraulic bushings at the stationary housing interface between the main bearing unit (MBU) and the gear unit (GU).

It is designed as if you had several torque arms on the gear unit and they are tilted to the front in rotor direction to transfer the reaction torque directly to the main bearing housing. The reaction torque will be transmitted via multiple pins more equally to the turbine structure.

This is done on a smaller diameter than the typical span of the torque arm and without a direct connection between the gear unit and the main frame. This more compact design is advantageous

for gear unit transport and allows for easy division into transport or service modules of the powertrain.

Tolerances and deformation of the main bearing unit can be compensated with the elasto-hydraulic bushings. This solution enables passive and active vibration degeneration and is an option for low noise operation.

The 2-PRS fully integrated medium speed drive train concept with rigid connection is the most compact, standard drive train concept. In this case the main bearings also serve as planet carrier bearings for the low-speed stage of the gear unit and the generator rotor is supported by gearbox bearings.

This concept dispenses with elastic elements and rigidly connects the well-defined and accurate designed and manufactured interfaces.

For regions where the powertrain can be transported and craned in one piece this concept is a very good choice. A fully assembled and tested powertrain can be sent from the production facility directly to site for turbine installation. A thoroughly developed and validated integrated system can secure that no unforeseen extra loads are transferred to the gearbox and provides high reliability.

A concept that is most popular in China is the so-called 2-PRS semi-integrated concept. It combines the features of the fully integrated concept on the low-speed side with an independent generator on the high-speed side.

The wind load impact and interactions of the different drive train concepts on the gear tooth contact has been investigated at Winergy via simulation, field and test bench validation.

The specific impact of elastic interaction in planetary stages with increased torque density is presented by Dr. Sebastian Reisch at CWD 2025 [REI25].

4 Influencing factors for concept decision

The development of new wind turbine powertrains is driven by lowering CAPEX costs, torque density increase and regional market needs. The focus is changing from a pure component optimization to a system consideration and a need to fulfill best the upcoming use cases in the field with the ability to provide tailored solutions with modular concepts.

In the past 10 years the torque density in gear units of wind turbines has doubled and played a major role in the cost and space reduction of power trains and cost of energy.

Not always is the highest achievable toque density the most favorable option from a system perspective. Especially in the case of functional integration, e.g. with an integrated oil supply system, integrated vibration degeneration elements or an increase in ratio for higher generator speeds can lead to an optimized system solution. Figure 3 shows that the torque density of a gear unit is not independent from the powertrain concept even if the gears set is in the same way torque density optimized.

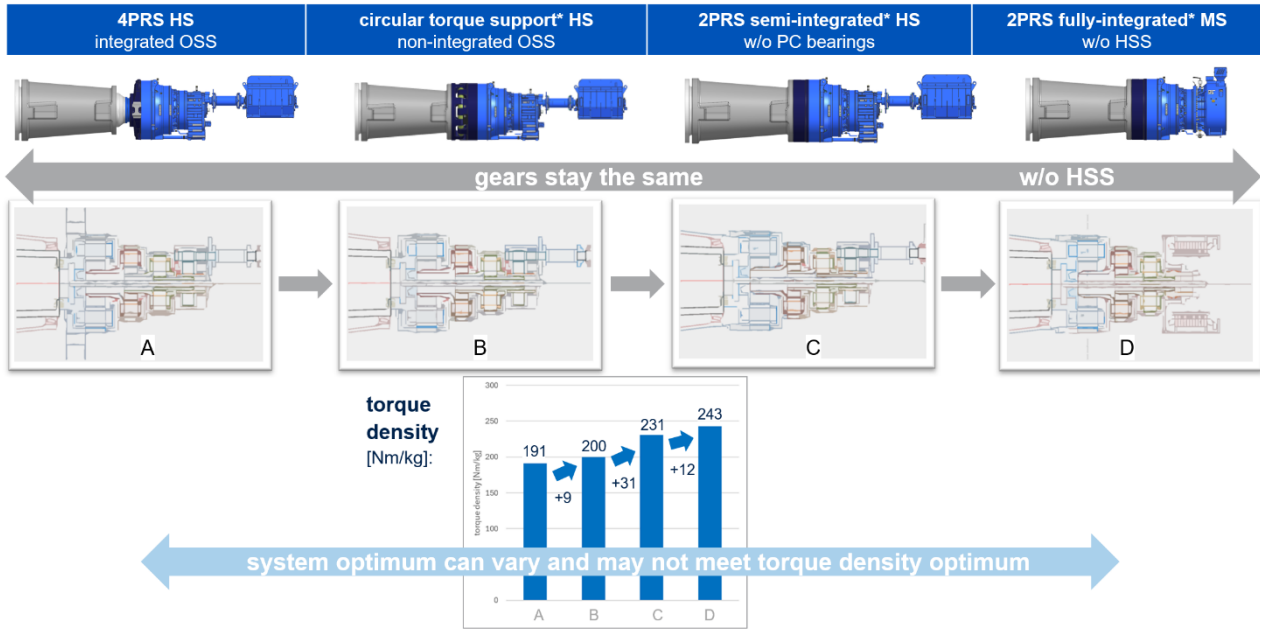

Figure 128: System optimization versus highest torque density

For further improvements on the torque density Dr. Jonas Finken from Winergy is showing a pathway to higher torque density of wind gearboxes without making concessions to system reliability with a probabilistic modelling approach of the tooth root strength [FIN25].

Along with the steady turbine power increase the powertrain size and weight in combination with a higher integration level can be limiting for onshore standard logistic use. New challenges with handling, transportation, servicing and site accessibility need to be considered. Therefore, splitability in modules for standard transportation in combination with easy and robust assembly possibilities on turbine will be major part of decision criteria for drive train concepts.

For inhabited areas low noise and vibration operation is becoming a key success factor. Possibilities to elastic decouple the main components from each other and the turbine structure with a contribution for vibration degeneration is a common practice.

In the strong CAPEX driven Chinese onshore market the semi-integrated concept is very popular. By the integration of main bearing and gear unit the planet carrier bearings on the low-speed gearbox stage can be omitted. This cost saving in combination with a partial converter and a high speed DFIG generator shows potential for the lowest CAPEX costs.

Large drive train weight and size as well as rigid connection between major drive train components are not an issue for the huge wind farms that are built in the Chinese deserts. There is no need for sound improved operation or extra elastic decoupling to minimize vibration. Even the largest onshore turbines will be able to be installed there as production facilities are built close to the wind farms so that transportation and logistics are not limiting the turbine size.

Which drive train concept fits best is dependent on the turbine size, the regional market requirements, the service and logistic concepts of the OEM, but also risk management in combination with time to market, engineering capability & capacity and LCOE impact. That is the reason why there is not the one perfect powertrain concept that fits all.

In the light of industrialization for wind turbines the call for standardization of powertrain components as high valuable parts is clearly noticeable.

Modularization and standardization in the powertrain of wind turbines works if dependencies can be reduced to a minimum and if a standardized module can be used in a cost-efficient way for several turbine configurations.

One possibility to achieve more freedom for modularization is the Winergy FlexibleFit approach, see figure 4. The FlexibleFit module is placed in-between a cost optimized gear unit and the customer specific turbine rotor support. It enables the gear unit to be dimensioned mainly by speed and torque. These are the fundamental gear unit features for its dimensioning.

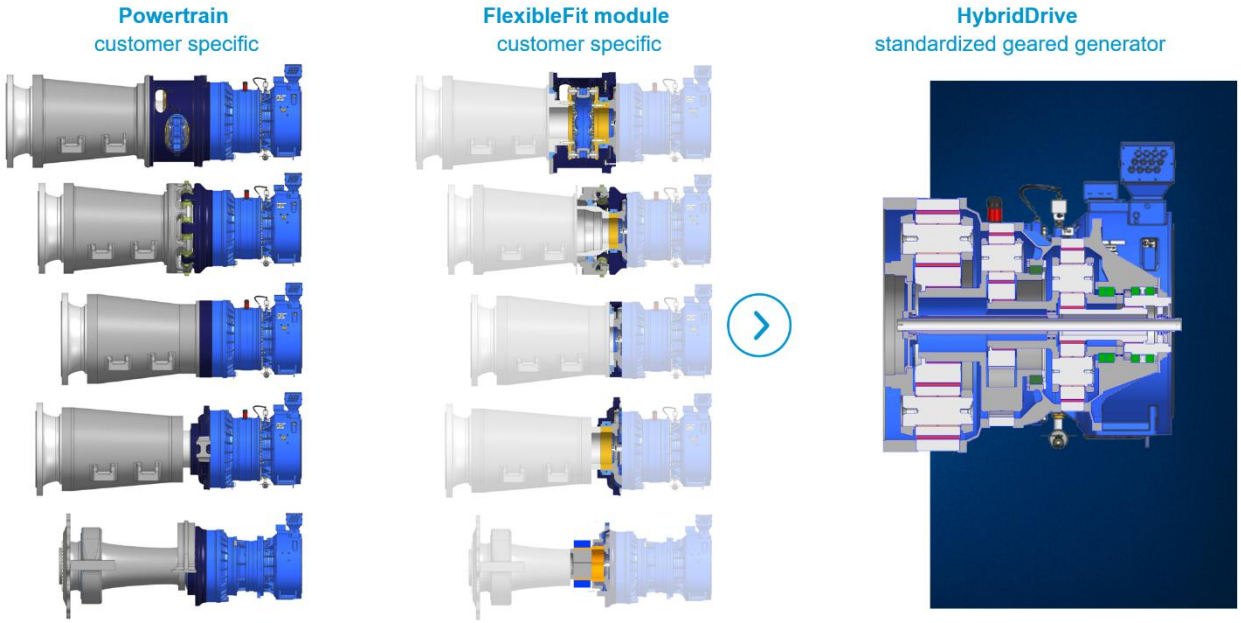

Figure 129: FlexibleFit approach for modularization and standardization

Wind loads other than torque or gravity weights of blades and hub resulting as bending moments on the drive train, are taken from the FlexibleFit module and are transferred to the turbine structure. No need not to be carried by the gear unit.

Additional to standardization activities, Winergy is also driving forward research and pre-development activities like a superconducting mid-speed generator. Dr. Roland Zeichfüßl is presenting about design and benefits of superconducting generators with oil-cooled stators at the CWD conference [ZEI25].

Especially in western markets, where long service contracts with the OEM or service provider are common, a high focus is put on test bench and field validation, track record or high technology readiness level and high reliability to achieve low OPEX costs.

Validation needs derived from the above-mentioned challenges as well as from component- and System-FMEA play a major role to achieve highly reliable powertrains. For highly utilized components and more integrated concepts it is necessary to consider the system behavior and how it is impacting the major components like gear or main bearing units. Therefore, intensive validation including wind load testing is an important part of the development process.

5 Drive train system validation

In the year 2018 Winergy built up a system test bench where two wind turbine drive trains can be tested at the same time with wind loads. The power of the driving motors is 17 MW on each side.

With a unique concept where the devices under test (DUT) are mounted on two moveable platforms that are supported by 14 hydraulic cylinders the wind loads can be applied at both DUT's in the same magnitude with 6 degrees of freedom, see figure 5.

In the beginning the wind load tests were done exclusively for one western OEM in a close cooperation for validation on a system level. In the following years the test bench is going to be used for different drive train architectures in further cooperations with OEM's and supply chain.

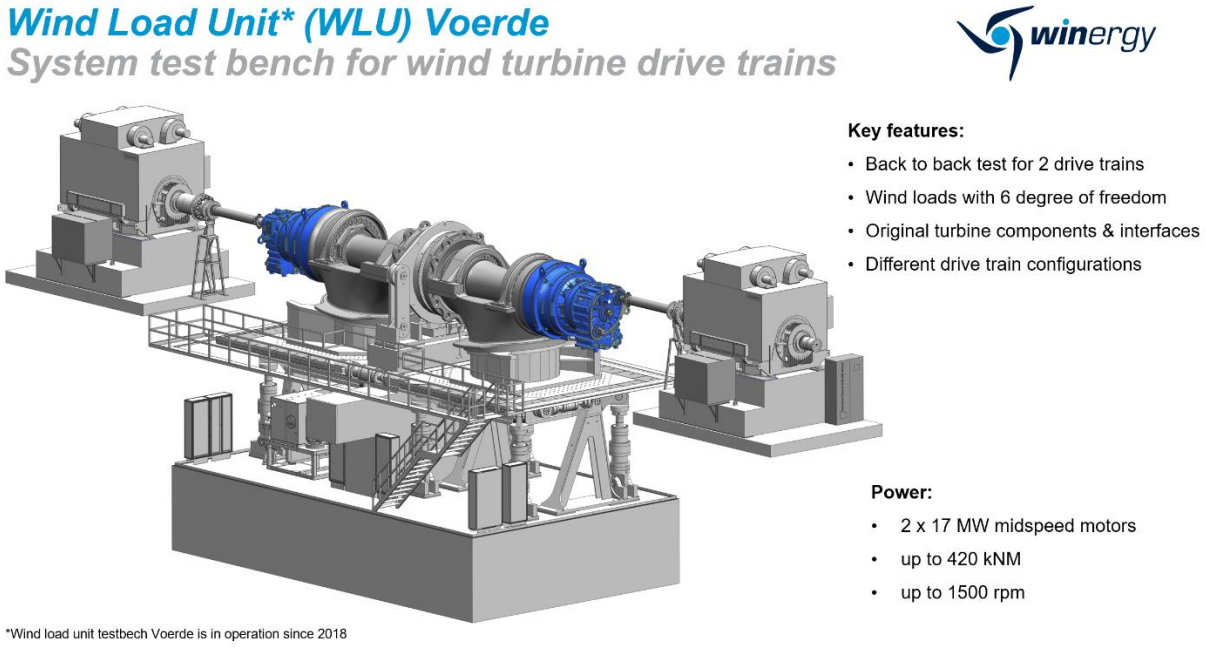

Figure 130: Drive train system testing with wind loads

A detailed description of the Winergy testing philosophy is presented by Dr. Martin Reuter at CWD 2025 "Prototype testing of wind gearboxes on test bench and turbine" [REU25].

Validation focus on the WLU Voerde will be the interactions of the main components in an original system environment. The measurement results are going to be compared with the simulation results for a doublecheck and to continuously improve the modelling.

Typical testing types are functional tests, endurance tests and extreme tests.

6 Conclusion

In future onshore wind turbine platforms of 8 MW and bigger will not narrow down the diversity of powertrain concepts to one best suited concept that fits all.

The best fitting drive train concept is dependent on the turbine size, the regional market requirements and the service and logistic concepts of the OEM. Additional influence on the concept decision is created by the combination of risk management with time to market, engineering capability & capacity and off-course the LCOE impact.

As these decision criteria are weighted differently at the turbine OEM's with a clear focus on their target markets the powertrain concepts will further vary.

Nevertheless, there are ongoing efforts and promising approaches for modularization and standardization on wind turbine drive trains.

Torque density in gear units played a major role in the past and will do so in the future with new approaches and technologies. Nevertheless, the system optimum does not necessarily need to meet the torque density optimum.

With new introduced drive train concepts, higher integration level and more dependencies between the main components at ever growing turbine power rating a need for system validation was triggered. With a system test rig of 17 MW, different drive train architectures can be validated with consideration of the wind load impact with 6 degrees of freedom at Winergy in Voerde.

7 Bibliography

[WOM24] Wood Mackenzie: "Global Wind Power Market Outlook Update - Q4 2024"

[BRM24] Brinckmann: "Global wind turbine technology forecasts", June 2024

[WOM23] Wood Mackenzie: "Global Wind Supply Chain Trends - Article 4 Drivetrains and Nacelle Components"

[WIN24] Winergy: Market intelligence database Q1/2022 - Q4/2024

[FIN25] Dr. Finken, Jonas: Probabilistic modelling of the tooth root strength of wind gears.

CWD2025 proceedings, Aachen, 2025

[REI25] Dr. Reisch, Sebastian: Elastic Interaction in Planetary Stages with Increased Torque Density.

CWD2025 proceedings, Aachen, 2025

[REU25] Dr. Reuter, Martin: Prototype testing of wind gearboxes on test bench and turbine.

CWD2025 proceedings, Aachen, 2025

[ZEI25] Dr. Zeichfüßl, Roland: Speedy_HTS: Design and Benefits of Medium-Speed Superconducting Generators with Oil-Cooled Stators.

CWD2025 proceedings, Aachen, 2025

System integration in an advanced 3-point suspension wind turbine drive train

Alf Trede

bewind GmbH, Hollesenstraße 27, 24768 Rendsburg, Germany

Keywords: *WEC, drivetrain, System integration*

Abstract: The aim of this work is to transfer the advantages of a self-aligning drivetrain (with 3-point suspension) into a new multi-MW class while keeping all logistical and installation advantages, still meeting all common limits and thresholds in the 7MW+ onshore turbine class. The presented conceptual arrangement is a technologically and commercially viable alternative to the prevailing stiff-drivetrain concepts with their specific disadvantages. A new drivetrain and bearing design, based on proven components and known designs, is proposed that allows better utilization of the main shaft bearing and simplifies the drivetrain components. The paper includes a literature review and an assessment of the technical and economic advantages of the new design. The results show that the new design offers better modularization, easier maintenance and lower noise level compared to stiff- drivetrain designs, as well as higher power density and better economic viability compared to conventional 3-point suspension drivetrain with a spherical roller bearing. This work thus represents an innovative contribution to the development of an advanced 3-point suspension drivetrain technology for larger wind turbines both on- and offshore.

1 Introduction:

The trend towards ever larger, more powerful wind turbines both onshore and offshore is challenging for some established drive train concepts. Scaling these is often not possible from a technological and economic point of view.

This particularly affects the flexible rotor bearing concepts based on spherical roller bearings. In particular, the 3-point suspension concept, which dominates onshore to this day.

The increasing rotor bending- and torques loads require a larger shaft diameter.

Spherical roller bearings used in flexible drive trains, especially when they have to absorb axial thrust forces in addition to radial ones, grow disproportionately with the increase in shaft diameter.

This is due to the functional geometry of this type of bearing, which requires the spherical rings to be positioned steeply relative to one another due to the relatively high axial to radial load ratio of a wind turbine.

Through this increases the width and the bearing cross-section for larger shaft diameters, which leads to a disproportionate increase in the bearing weight.

Double-row spherical roller bearings of the 240 series have proven themselves as fixed rotor bearings and can only be adapted to the radial and axial load components that occur to a limited extent, for example in an asymmetrical design.

In an asymmetrical design, the upwind-side raceway is narrower, as it only has to absorb thrust loads in exceptional cases “negative thrust”, as can occur during emergency stops, for example. During normal operation of a wind turbine, the thrust is positive and loads the downwind-side raceway.

Two bearing sizes used in the 4 to 6 MW power class are used here as an example of the increase in mass in relation to the shaft diameter.

SRB 240/900, d = 900 "100 %", m = 1570 kg "100 %"

SRB 240/1120, d = 1120 "124 %", m = 2925 kg "186 %" [SKF08]

This makes it clear that the costs increase disproportionately. Bewind field experience shows in addition that technical problems can arise in large spherical roller bearings with play due to smearing effects due to the disproportionately increasing rolling element masses.

By using proven components in a new arrangement, bewind has transformed the undeniable advantages of flexible rotor bearing concepts into a new size and performance class that is suitable for the largest onshore and offshore wind turbines.

This concept represents an interesting alternative to the prevailing rigid rotor bearing concepts with tapered roller bearings in the multi MW class.

The first 7MW onshore prototype based on this powertrain technology was successfully erected by WEG Energy in northeastern Brazil at the end of 2024 after an extensive test program and is currently in field validation.

2 bewind flexible, advanced, self-aligning rotor bearing concept:

When developing the new bewind drive train concept, the following requirements were at the forefront in order to achieve a robust, competitive and future-proof design.

- Scalability for the 10 MW+ power class
- Compact and lightweight
- Good load flow of the rotor loads to the tower head
- Insensitive to elastic structural deformations
- Good load-bearing behavior of the gear teeth
- Functional, production- friendly modularization of the nacelle systems
- Modules suitable for transport and installation in terms of dimensions and masses, specially onshore
- Interchangeability of the main components without dismantling the rotor, including the rotor bearings
- Structure-borne noise decoupling of the gearbox
- Use of proven components

In order to meet all of these requirements and the limitations of spherical roller bearings described in the introduction, the toroidal roller bearing (1) was selected as the rotor-side angle-adjustable bearing.

This type of bearing has already proven itself in hundreds of offshore wind turbines from the former manufacturer REpower / Senvion.

Due to the non-locating bearing function of the toroidal bearing (1), the width and cross-section of this bearing type is not directly dependent on the shaft diameter, but can be adapted according to the radial loads.

In the bewind drive train, the rotor thrust is absorbed by preloaded tapered roller bearings (4) in the gearbox (5), which simultaneously support the planet carrier of the first gear stage and function as a second rotor bearing.

These preloaded tapered roller bearings (4) absorb the rotor thrust, the bending moments of the rotor acting as radial loads and the weight of the gearbox- (5) generator (6) unit.

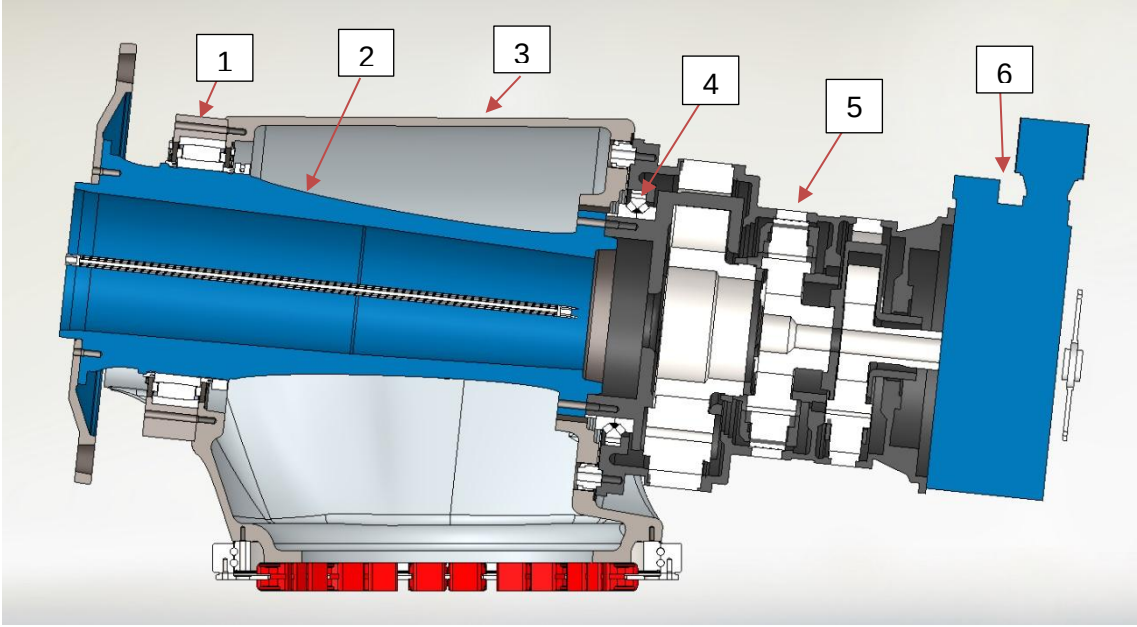

Figure 1: bewind drivetrain as midspeed version, toroidal roller bearing on rotor site (1) ,rotor shaft (2), main-frame (3), preloaded tapered roller bearing integrated in gearbox in O- arrangement (4), 3 stage coaxial plan-etary gearbox (5), MS Generator (6) Source bewind

To avoid additional bending constraints on the rigid second rotor bearing (4) caused by elastic de-formation of the rotor shaft (2) and the machine carrier (3) under rotor- bending loads, it is necessary to make the torque and radial support of the gearbox axially soft.

In addition, it must be ensured that the dominant loads from the rotor are diverted directly into the machine support structure in order to enable a "pure" torque load on the gearbox components.

Due to the arrangement of the rigid double-row tapered roller bearing (4) in front of the gearbox toothing parts, the dominant rotor loads consisting of rotor thrust and radial loads are transferred directly into the front end bearing shield of the gearbox (5) and from there into the machine support structure via the elastomer bushings.

The pre-loaded elastomer bushings arranged radially on the circumference of the gearbox bearing shield, which have a high radial, progressive and low, linear axial spring characteristic, prevent/re-duce any constraining forces from angular displacements of the rotor shaft and machine support structure due to elastic deformation.

To absorb the rotor thrust, two additional pairs of elastomer hydraulic layer springs are used, which are arranged in the 9 and 3 o'clock positions. At the same time, this advantageous arrangement of the elastomer spring elements used ensures that the structure-borne noise frequencies excited by the drivetrain are dampened both radially and axially.

Figure 2: Exploded view of the bewind rotor- bearing concept, Source bewind

2.1 Gearbox suspension:

The gearbox suspension consists of a combination of radially arranged, pre-stressed elastomer bushings (1) in combination with 2 pairs of elastomer hydraulic elements (2).

The elastomer bushings (1) are used to absorb the radial loads resulting from the yaw "Mz" and pitch loads "My" of the rotor and the rotor torque support "Mx". The rotor thrust "Fx" is absorbed by the elastomer hydraulic elements (2).

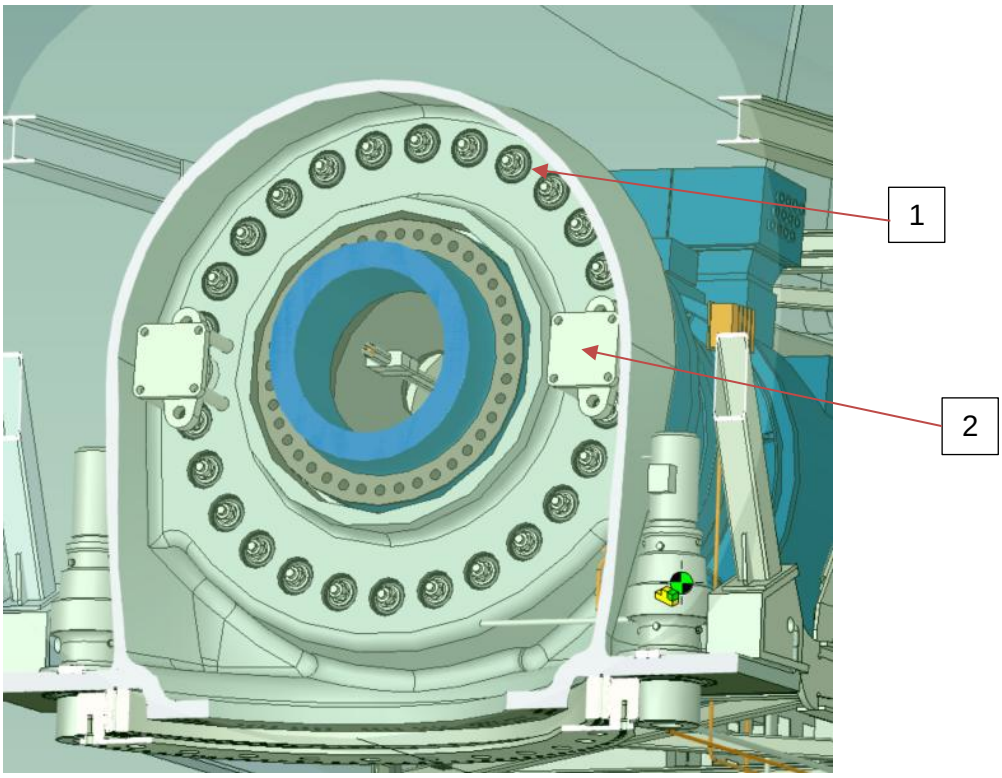

Figure 3: arrangement example of elastomer elements, elastomer bushing (1), elastomer hydraulic element (2) Source bewind

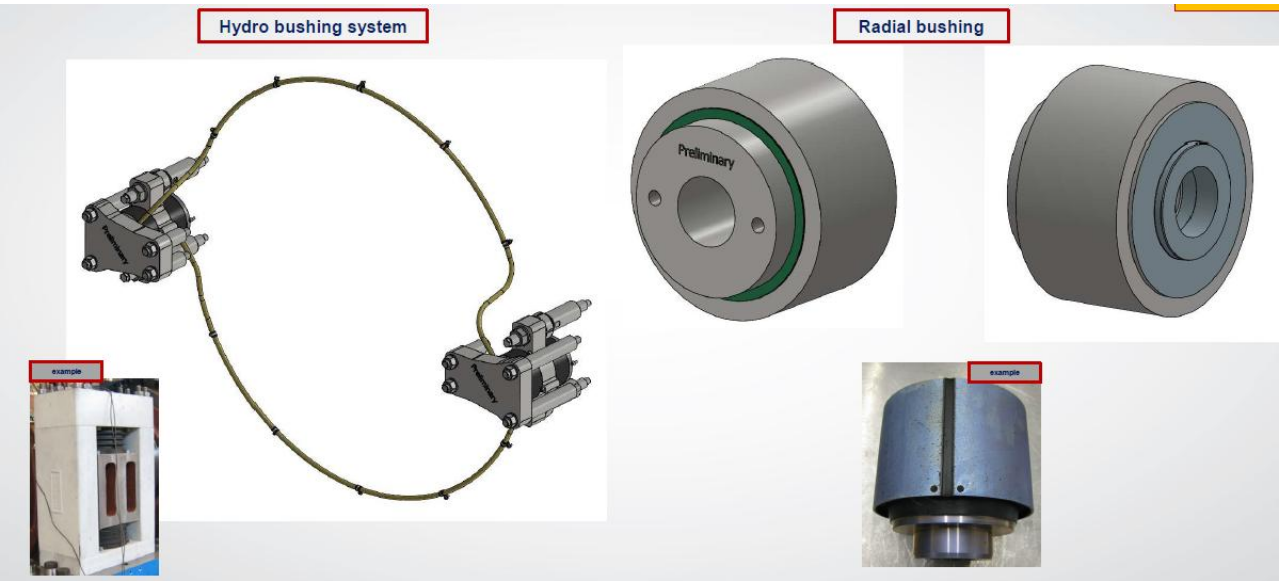

Figure 4: Elastomer hydraulic system, Source ESM **Figure 5:** Axial pre- stressable bushings, Source ESM

The axially soft bushings (1) prevent the second rotor fixed bearing and the gearbox from being constrained in the event of angular displacement of the gear unit caused by shaft deflection and elastic deformation of the support structure.

The hydraulic elastomer elements (2) arranged at the 3 and 9 o'clock positions serve to simultaneously transmit the rotor thrust forces. These are hydraulically connected in such a way that they have a high degree of rigidity when the 3 and 9 o'clock elements are loaded evenly "without angular displacement". If the elements are loaded unevenly (rotor thrust Fx and yaw load Mz), one element compresses and the second extends, as the hydraulic medium of the compressing element flows into the rebounding element. This works without major restoring forces while maintaining the overall rigidity of both elements.

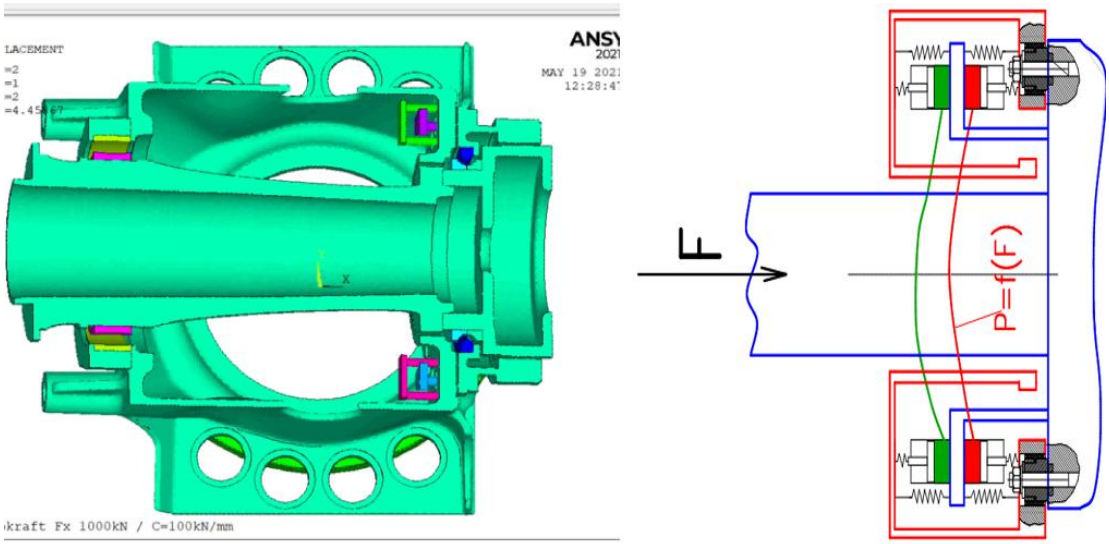

Figure 6: Behavior of the elastomer hydraulic elements under pure thrust load "Fx", Source bewind / ESM

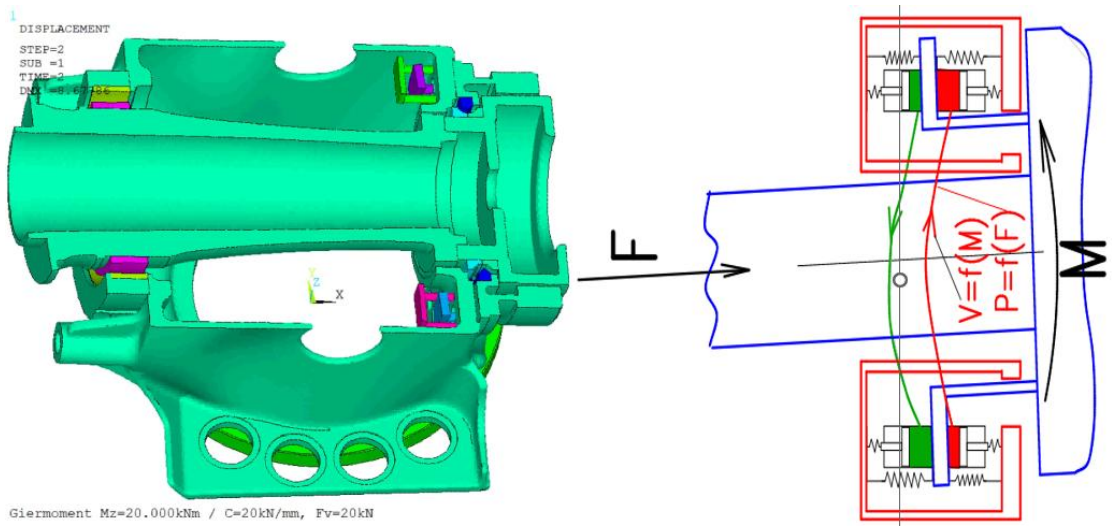

Figure 7: Behavior under combined yaw “Mz” and thrust load “Fx”, Source bewind / ESM

2.2 TCI, modular architecture, installation:

Another important aspect of a modern multi MW WEC is that the nacelle is divided into modules that must not exceed certain transport dimensions and weights.

These modules must be designed in such a way that they can be easily transported and erected in the field after pre-testing. This can be achieved with the bewind drive train concept, as the subsystems have clear, simple interfaces. This enables small individual lift and transport masses that can be mounted individually up tower.

Figure 8: Example of TCI Modules, Source bewind

The bewind drive train concept enables the following TCI requirements:

- Flexible Logistic concepts
- Use of easily available vehicle for road transport
- On site pre-assembly with small crane
- Reduced installation time
- Low ground space consumption
- Modular installation procedure
- Use of standard crane variants

2.3 O&M, Main Component Exchange without main crane:

The bewind drive train concept enables the most important main components to be replaced without the use of a large crane. The gearbox, including the second rotor bearing and the generator, can be replaced using a winch system. For this purpose, the rotor shaft flange on the gearbox side is positively supported against the bushing plate with the aid of compact clamping tools that can be handled by one person. The rotor lock is able to support the entire rotor weight instead of the rotor

bearing. The ring-shaped rotor bearing housing can be pulled forward so that a defective rotor bearing can be replaced with a new, split one without having to dismantle the rotor or the nacelle.

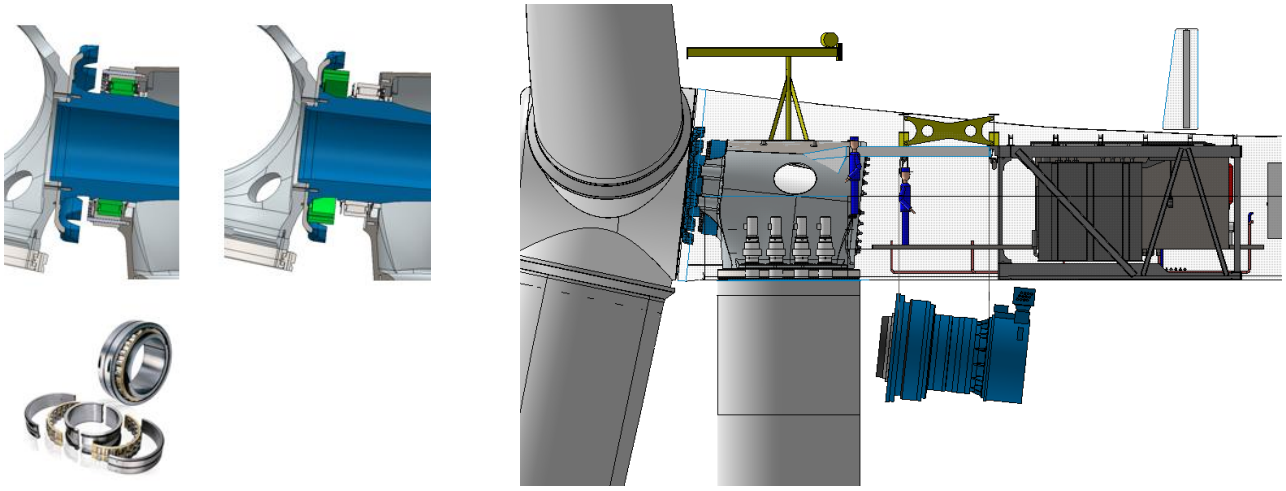

Figure 9: Main component exchange Example, Source bewind

3 Summary / Conclusion:

The flexible, advantageous, self-adjusting rotor bearing concept represents an interesting alternative to the rigid rotor bearing concepts prevalent in the 7MW+ power class. It transfers the advantages of a flexible rotor bearing to a new power class. The requirements placed on a drive train concept in this power class can be met with it.

In addition, there are further advantages such as the replacement of main components without a large crane and the dismantling of the rotor, which cannot be met or is very difficult with conventional rigid concepts. Further potential for optimizing these advantages lies in replacing the toroidal rotor bearing with a plain bearing.

Since the toroidal bearing is a loose bearing, it is much easier to replace it with a plain bearing than is the case with a fixed bearing.

The experience gained by bewind and the its partner WEG Energy through the successful development, construction, installation and commissioning of the AGW 172/7.0 shows the potential of this new rotor bearing concept in practice.

Figure 10: WEG AGW 172/7.0 Prototype with bewind drivetrain concept, Source private

4 Bibliography:

[SKF08] SKF: Hauptkatalog. Druckschrift 6000/I DE
SKF Gruppe, Hungary, 2008

Speedy_HTS: Design and Benefits of Medium-Speed Superconducting Generators with Oil-Cooled Stators

Roland Zeichfüßl[1], Andreas Jöckel[1], Robin Köster[2], Andreas Binder[2], Tabea Arndt[3]

[1]Flender GmbH, Hans-Loher-Str. 32, 94099 Ruhstorf a.d.Rott, Germany

[2]Technical University of Darmstadt, Department of Electrical Engineering and Information Technology, Electrical Drive Systems, Landgraf-Georg-Str. 4, 64283 Darmstadt, Germany

[3]Karlsruhe Institute of Technology, Institute for Technical Physics, Hermann-von-Helmholtz-Platz 1, 76344 Eggenstein-Leopoldshafen, Germany

Keywords: Speedy_HTS, midspeed, superconducting rotor, oil-cooled stator, power density, efficiency

Abstract: Wind energy is currently the crucial component of our transition to sustainable power sources. As wind turbines grow in size and capacity, the need for efficient and lightweight generators becomes paramount. In this context, superconducting generators offer promising solutions. Especially geared medium-speed generators with oil-cooled stator and superconducting rotor can minimize material consumption and weight. This paper explores the specification, the electromagnetic, and the mechanical design aspects of a full-sized demonstrator, along with its anticipated benefits.

The generator stator under consideration is taken from a series production turbine having 6 MW nominal power output with a conventional permanent magnet rotor at a rotational speed of 600 rpm. With a superconducting rotor the rotor field is considerably increased and acc. to calculations the same generator stator can produce even 13 MW.

The stator houses the oil-cooled and highly utilized AC copper winding, while the rotor pole winding is made of second generation high-temperature superconductors (HTS). These coils are cooled using stationary cryocoolers connected to a tailored rotating cooling concept, maintaining the coils at cryogenic temperatures.

Superconducting generators achieve higher power density compared to conventional permanent magnet generators. The reduction in weight and volume allows for more compact designs or higher efficiency at the same size. Further advantages are detailed out.

1 Superconductivity Enables a New Dimension of Utilization

To enhance cost and energy efficiency in the generation of renewable energy, the project Speedy_HTS was started. It contains the development and test of a gearbox-generator-unit for wind turbines with a superconducting rotor and an oil-cooled high-current stator. In addition to minimal material usage, the high power density will enable larger wind turbines without increasing the physical dimensions or exceeding transport limitations. This design eliminates the need for permanent magnets, which are predominantly sourced from China. Furthermore, this generator concept allows for higher system efficiencies and connection to both AC and DC grids via simple rectifiers.

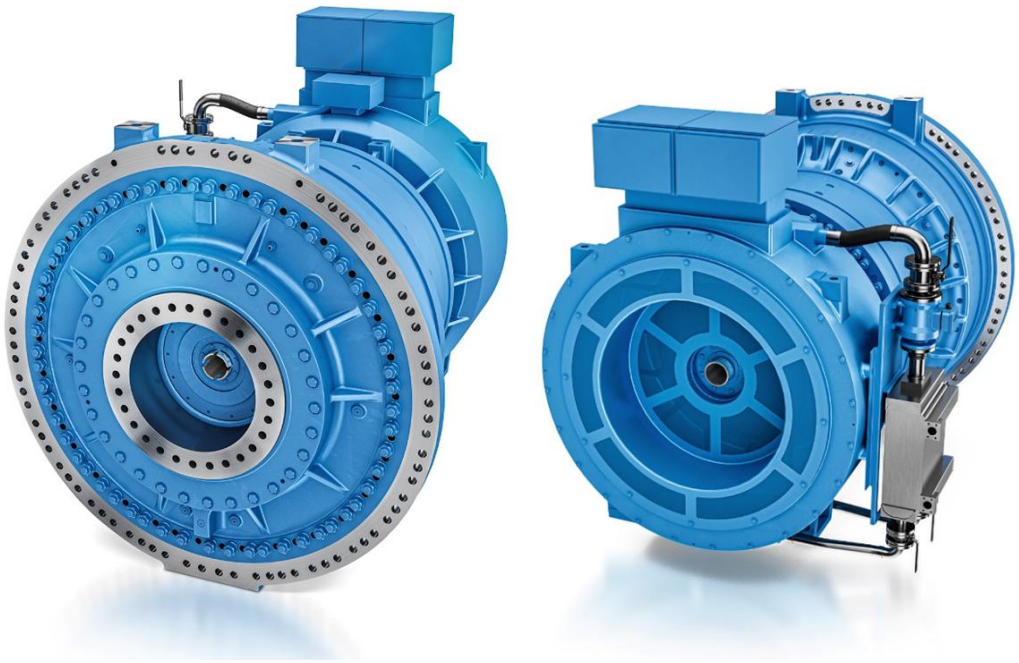

Figure 131: Winergy's HybridDrive with oil-cooled generator stator and conventional permanent magnet rotor

2 Usage of Superconductivity in Other Applications

Superconductivity has evolved from research to an industry standard in the last decades. In the field of medicine, superconducting materials are essential components of Magnetic Resonance Imaging (MRI) machines. These materials allow for the creation of powerful and stable magnetic fields, which are crucial for producing high-resolution images of the human body's internal structures.

2.1 Superconductivity in Stationary Energy Applications

In the realm of power transmission, superconductors offer significant advantages for transmitting electricity with high power density and minimal energy loss. Traditional power lines encounter resistance, which leads to energy dissipation in the form of heat. Superconductors, on the other hand, can carry electric current without resistance when cooled below their critical temperature. This property makes them ideal for creating efficient and high-capacity power transmission systems in urban areas. The 15-kilometer long SuperLink power transmission in Munich, Germany, with 500 MVA currently being under development [PRI24] could mark the successful commercialization in this area of application.

2.2 Superconductivity in Rotating Electrical Machines

Superconducting rotating electrical machines are being developed and tested for industrial applications where high power and efficiency are required. These motors can significantly reduce energy consumption and operational costs. Superconducting motors are also being explored for use in ship propulsion systems. These motors are more efficient and compact than traditional motors, making them ideal for large vessels where space and weight are critical factors [HAR17]. Back in 2008 Northrop Grumman already noticed the advantages of combining a superconducting rotor with an

oil-cooled stator. A 36,5 MW marine propulsion system has been developed and tested successfully [GAM11].

2.3 Superconductivity in Wind Energy Generation

Within the field of superconductivity for wind power, there was the EU-funded project 'EcoSwing' with the Chinese manufacturer Envision [BER19], as well as the project 'High Efficiency Ultra-Light Superconducting Generator (SCG) for Offshore Wind' by the U.S. company General Electric, which is funded by the U.S. Department of Energy [CRA24]. Both approaches share a common goal of pursuing a direct-drive approach using superconductivity. However, superconducting direct-drive generators might not become economically feasible due to the large surface area that needs to be cooled and the significant amount of superconducting material required.

3 Combination of Oil-Cooled Stator with Superconducting Rotor

Different drive trains are used in wind power. The spectrum ranges from high-speed generators to gearless generators (direct-drive). Midspeed generators with a low gear ratio are increasingly playing a role. An overview of various concepts is provided by [ZEI15]. Especially for wind turbines with higher power outputs, midspeed generators integrated into the gearbox are important because they are lighter and more compact than other drive trains. This allows for a higher power density of the electrical machine with lower material requirements and reduced costs.

In wind power, cooling concepts are almost exclusively limited to air or water cooling. High-current stators with oil cooling are currently only common in the automotive industry for machines of smaller sizes. In 2020 Winergy developed the first wind turbine drive-train with oil cooled stator, see also Figure 1 and Figure 2 [Zei21].

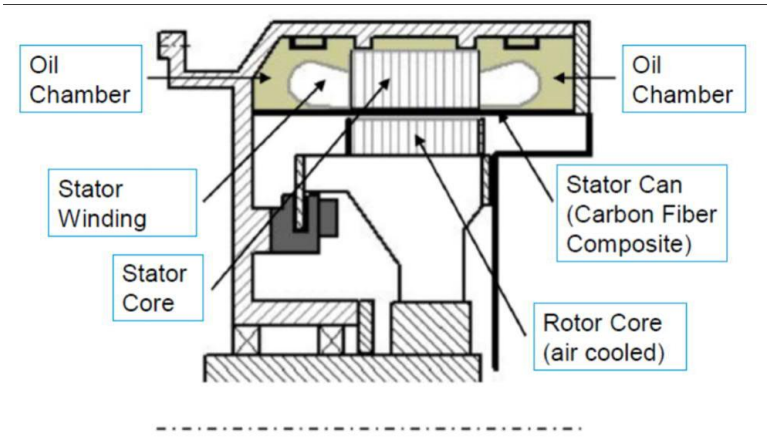

Figure 132: Half cross-section through the stator and conventional permanent magnet rotor of a midspeed generator

The use of oil-cooled high-current technology in the stator enables very high power densities, but the conventional rotor limits the machine's performance. This performance limitation is noticeable in efficiency, but even more so in the power factor of the machine – the limited excitation provided by the permanent magnet rotor significantly restricts the achievable power density, see Figure 3.

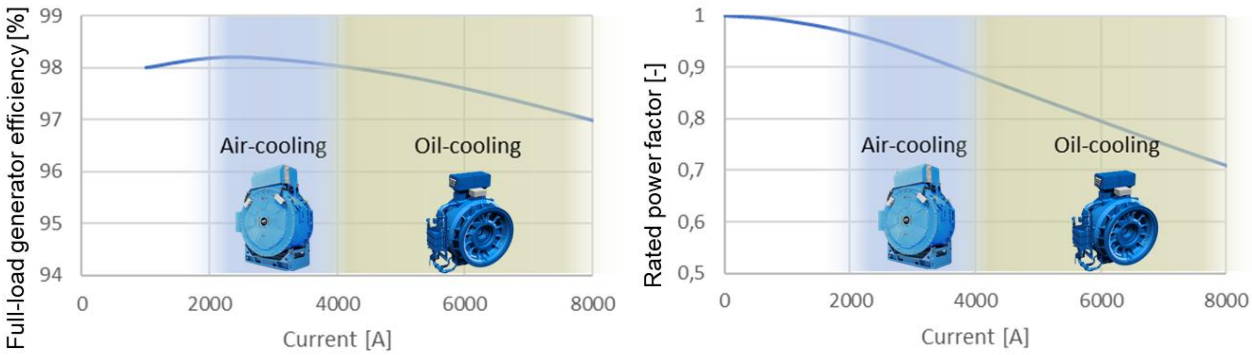

Figure 133: Efficiency and power factor in dependence of the stator current for a specific electromagnetic design with permanent magnet excitation and two different cooling methods

The use of HTS significantly expands the power range through the higher current density in the stator and higher air-gap fields produced by the rotor. Besides that, the compact high-current stator requires lower magnetization in general. Air gap flux densities above 2,0 T are feasible. Unlike permanent magnet generators, superconducting generators may generate solely active power, leading to minimum converter size.

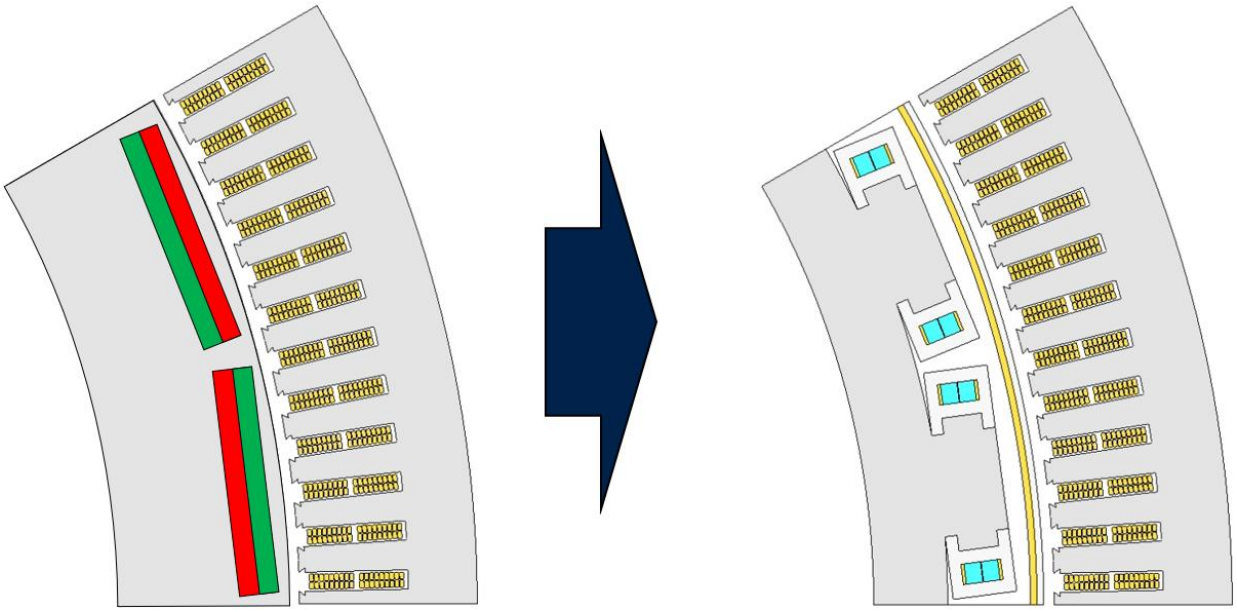

Figure 134: Pole pair of conventional permanent magnet excited generator (left) and generator with HTS rotor (right)

Anyhow HTS must be operated at cryogenic temperatures, which leads to other challenges. First, the losses inside the rotors and the heat transfer must be minimized. Thus, the rotor is encapsulated by a rotating cryostat, which provides vacuum around the rotor core without touching it, see Figure 5. Only a warm-cold coupling transfers torque from the cryostat to the rotor.

Second, the HTS rotor itself must withstand the centrifugal forces at cryogenic temperatures and the rotor core must provide high magnetic permeability. Only a few cold-tough steels are suitable for this. Third, the remaining losses in conductors and magnetic cores must be dissipated. A cold bus with copper bars collects the heat and guides it to a central cold reservoir. The reservoir is kept

at cryogenic temperatures by a continuous coolant flow from a stationary cooling system. Figure 5 shows the basic rotor concept.

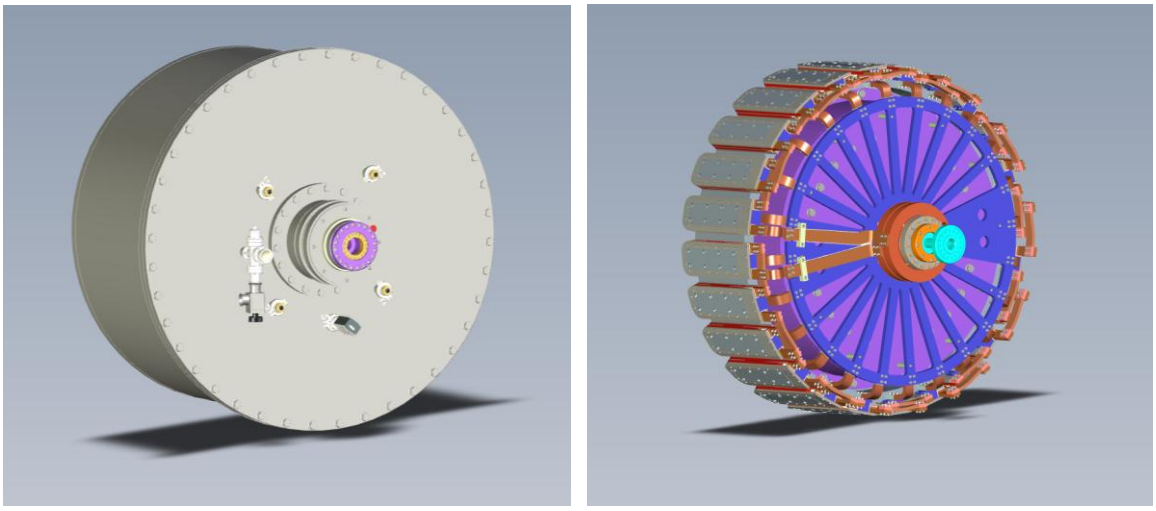

Figure 135: Left: Design of the rotor cryostat. Right: Design of the HTS rotor with coils (red), electrical connections and slip ring (orange) and cold bus (blue).

4 Calculated Performance Data

Oil-cooled permanent magnet generators are superior compared to conventional drive-trains. With a superconducting rotor the performance can be pushed even further. Based on electromagnetic FEM calculations the rated power of a specific 6 MW HybridDrive can be increased to 13 MW. This is even more than twice the original power rating while maintaining almost the same weight, see Table 1. Besides similar efficiency, the power factor can be set to 1. This reduces significantly size and cost of the inverter, as there is no reactive power circulating on machine side.

Winergy's HybridDrive permanent magnet / oil-cooled	
Rated power	6 MW
Rated speed	600 rpm
Generator Weight	9600 kg (incl. gear flange)
Efficiency	97 %
Power factor	0,80

Winergy's HybridDrive Speedy_HTS *	
Rated power	13 MW
Rated speed	600 rpm
Generator Weight	10600 kg (incl. gear flange)
Efficiency	97 %
Power factor	1,0

* calculated on the basis of the data available so far

Table 5: Expected performance data of a midspeed generator with superconducting rotor

5 Design for Optimized Efficiency

Superconducting rotor coils also offer ground-braking advantages in efficiency. High magnetic flux density allows more space for copper in the stator winding. Furthermore, high magnetic flux is available independently from the rotational speed. Hence superconducting rotors are enabling power

factor 1 over the whole speed range, which eliminates losses by reactive currents in the stator winding. Full-load efficiency as well as part-load efficiency can increase drastically.

		Conventional permanent magnet generator	Speedy_HTS optimized for efficiency
Power	[MW]	13,7	13,7
Speed	[rpm]	600	600
Torque	[kNm]	221	221
Weight	[t]	18,5	25,0
Cooling		Air-water	Air-water
Efficiency 100% P_n	[%]	98,4	98,7
Efficiency 80% P_n	[%]	98,3	98,7
Efficiency 60% P_n	[%]	98,2	98,6
Efficiency 40% P_n	[%]	98,1	98,6
Efficiency 20% P_n	[%]	97,6	98,4

Table 6: Calculated efficiency of a permanent magnet generator and an efficiency optimized generator with superconducting rotor with the same outer dimensions

6 New Ways for Grid Connection

The very high possible HTS excitation of the machine and the adjustability of the excitation enable operation with a power factor of 1, thus allowing rectification of the generator output voltage using an efficient and cost-effective diode rectifier. Figure 6 shows the electrical schematic. A cost reduction of almost 50% is expected compared to a conventional AC/AC converter. Even more, the switching and conduction losses are being reduced significantly, when changing from an actively controlled IGBT rectifier to an uncontrolled diode rectifier. An efficiency gain of more than 1,0 % is expected with a diode rectifier, assuming a typical wind turbine load curve and power distribution.

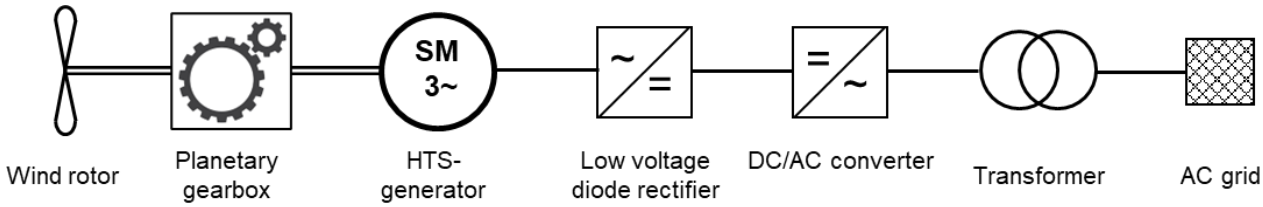

Figure 136: Wind turbine drive-train with passive diode rectifier on machine side

In the future, HTS excitation will also enable highly innovative grid integration topologies with a significantly reduced number of energy conversion stages. In contrast to controlled rectifiers, uncontrolled diode rectifiers are cost-effective at high voltage levels, too. So, using a medium-frequency transformer directly connected to the generator in combination with a high voltage rectifier, the wind turbine can be connected to a DC grid, resulting in very high savings potential and efficiency

increase. In island networks, as is the case with offshore grids, it may be useful to implement the network with a DC back-bone.

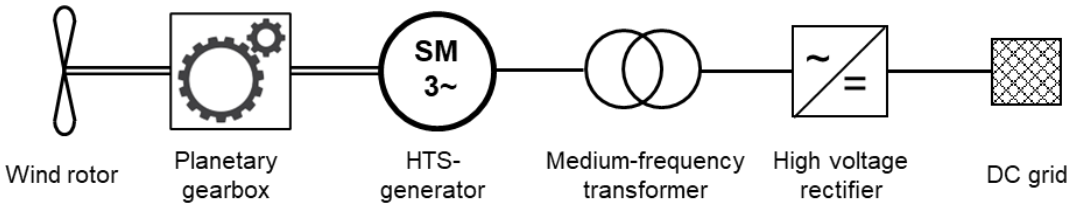

Figure 137: "Inverterless" wind turbine design with medium-frequency transformer for direct coupling to DC grids

7 Independence from Rare Earth Materials

The construction of a conventional direct-drive turbine with a capacity of 15 megawatts requires approximately 5 to 10 tons of magnets. These neodymium-iron-boron magnets are composed of 29 to 32 percent rare earth elements, primarily neodymium and praseodymium. So, such a turbine contains at least 1500 kg pure rare earth. Even fast-rotating drive-trains with permanent magnet generators contain a significant amount of rare earth. Assuming ten times less magnet weight for a medium-speed generator, still 150 kg pure rare earth are needed for the same output power.

The most promising HTS is rare earth barium copper oxide (ReBCO), which also contains a certain amount of rare earth elements, such as Gadolinium, Yttrium, and Europium. But the amount is really crucial. With an estimated 25 g for a 15 MW generator the amount is significantly less. Assuming a production of 500 turbines a year, it would still be easy to secure the 10-year demand of 125 kg. This is not more than the amount of rare earth in a single conventional generator.

8 Disruptive Innovation: The Novel Potential of Superconductivity

The Speedy_HTS project aims to enhance cost and energy efficiency in renewable energy generation by developing a gearbox-generator unit for wind turbines featuring a superconducting rotor and an oil-cooled high-current stator. In wind energy, superconductivity has been explored through projects like EcoSwing and the U.S. Department of Energy-funded High Efficiency Ultra-Light Superconducting Generator. However, the economic feasibility of superconducting direct-drive generators remains uncertain due to cooling and material requirements. By combining a geared generator with oil-cooled stator and a superconducting rotor, the project aims to achieve higher power density and efficiency at an attractive cost level.

The project also explores innovative grid connection methods, including cost-effective diode rectifiers and direct DC grid coupling, offering significant cost and efficiency benefits. Additionally, superconducting technology eliminates the need for permanent magnets, predominantly sourced from China.

Gefördert durch:

Bundesministerium
für Wirtschaft
und Klimaschutz

aufgrund eines Beschlusses
des Deutschen Bundestages

9 Bibliography

[BER19] Bergen, Anne et. al.: Design and in-field testing of the world's first ReBCO rotor for a 3.6 MW wind generator.

Superconductor Science and Technology, Vol. 32, 2019

[CRA24] Craig, Richard: GE Eyes Offshore Wind Turbines With Superconducting Generator.

https://www.windpowermonthly.com/article/1749355/ge-eyes-offshore-wind-turbines-superconducting-generator

(accessed on 17 December 2024)

[GAM11] Gamble, Bruce; Snitchler, Greg; MacDonald, Tim: Full Power Test of a 36.5 MW HTS Propulsion Motor.

IEEE Transactions on Applied Superconductivity, Vol. 21, No. 3, June 2011

[HAR17] Haran, Kiruba S. et. al.: High power density superconducting rotating machines—development status and technology roadmap.

Superconductor Science and Technology, Vol. 30, 2017

[PRI24] Prinz, Robert: Forschungsprojekt SuperLink 110kV HTS-Kabel für die Energieversorgung von München.

https://ivsupra.de/wp-content/uploads/2024/04/ZIEHL-IX-1-3-Prinz.pdf

(accessed on 17 December 2024)

[ZEI15] Zeichfüßl, Roland: Comparison of Concepts for Generators in the 3 MW Class.

Proceedings of Conference for Wind Power Drives 2015, Aachen

[ZEI21] Zeichfüßl, Roland; Jöckel, Andreas; Deicke, Matthias; Daners, Dominik; Fox, Christopher: Integrated 3-Stage Planetary Gearbox With Oil-Cooled Generator.

Proceedings of Conference for Wind Power Drives 2021, Aachen

Reliability and Wind (Gearbox) Industry

C. Sous[1], A. Klein-Hitpaß[1]

[1] ZF Wind Power Antwerpen NV
Gerard Mercatorstraat 40, 3920 Lommel, Belgium

Keywords: wind turbine, powertrain, reliability, availability, maintainability

Abstract: In recent years, the installed capacity for wind energy has increased due to a combination of more turbines and higher capacity per turbine. However, market profitability has decreased, while operation and maintenance costs have increased. Improving profitability is essential. With larger fleet sizes and higher investments per turbine, reliability and availability are crucial. The process of calculating wind turbine gearbox reliability and including it into the design phase is ongoing. This document first addresses the need for further improvements and definitions of key terminology, followed by an outline of how next steps to enhance profitability.

1 Introduction

Profitability remains a crucial aspect of the wind industry (cf. Figure 138), particularly given the overall emphasis on prices and costs (cf. Figure 139).

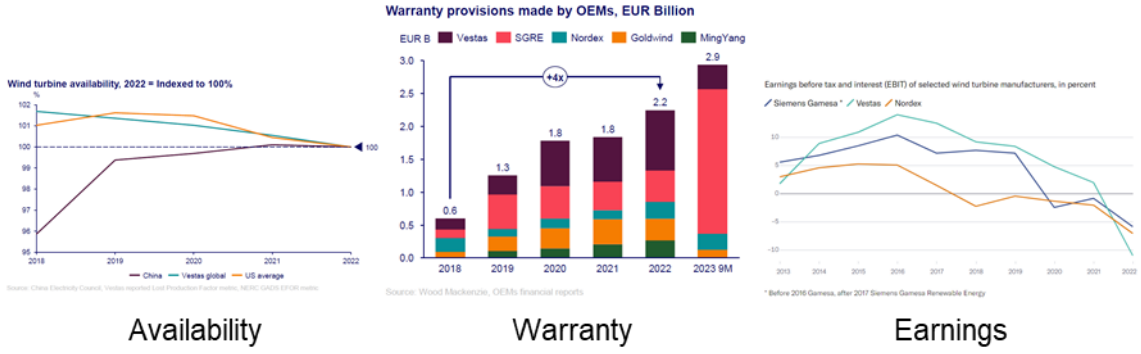

Figure 138: Impacted profitability of WT OEMs [LIC23]

Since the selling price of a wind turbine (WT) includes warranty provisions, the dependencies between availability, reliability, warranty costs and earnings are obvious. Therefore, improving availability and reliability is essential to enhance profitability.

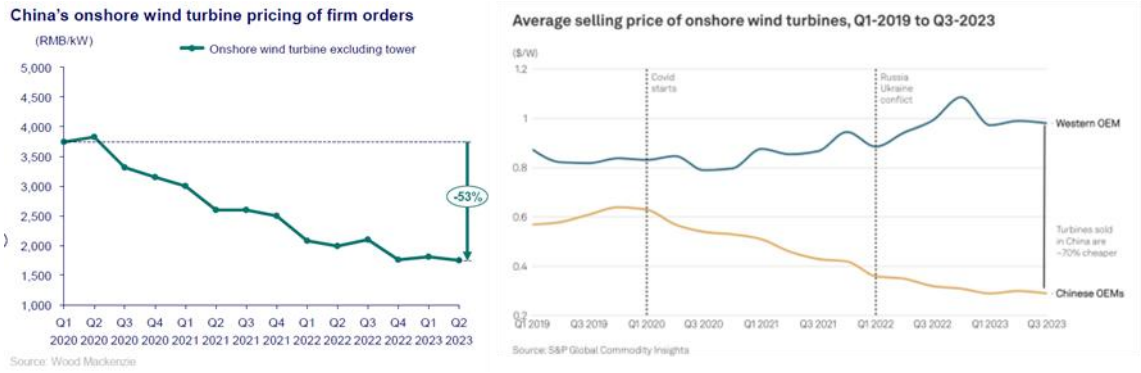

Figure 139: Pricing of onshore wind turbines; left: [LIC23], right: [S&P24]

2 Re-cap on reliability journey in wind industries

This summary does not claim to provide a complete overview or include every major step in the journey to the current state of reliability and its calculation in the wind industry. Important groundwork was laid with ANSI/AGMA/AWEA 6006-A03 [AGM04] and later ISO 81400-4 [ISO05]. Further works, such as [HOV15] discussed the use of reliability models, system elements, and the differentiation of failure modes in A1, A2, B, and C categories. [STR15] demonstrated viable approaches to reliability calculations, including references such as [BER08], supporting the next steps. IEC 61400-4:2012 [IEC12] was one such step, along with the evolution from ANSI/AGMA/AWEA 6006-A03 [AGM04] to ANSI/AGMA 6006-B20 [AGM20], and VDMA 23904 [VDM19]. [STR23] reiterated the motivation for reliability calculations in the wind industry engineering context and drafted a roadmap, including full probabilistic design (FPD) as a means for further improvements. The expected release of IEC/TS 61400-4-1, enabling the industry to gather experience by using commonly agreed approaches to quantify the reliability of a WT gearbox (GBX) is the next milestone.

The IEC/TS 61400-4-1 will link back to [HOV15] and emphasize that the calculated reliability of a WT GBX will differ from the apparent reliability. Current reliability approaches can only consider A1 failure modes (cf. chapter 3), while apparent reliability also includes A2, B, C category failure modes, as well as quality cases or failures resulting from process deviations.

3 Definitions

The previously mentioned categories of failure modes are listed in Table 7, reproduced from [VDM19]. The combination of a machine element and a failure mode is referred to as a system element. Considering category A2, which includes tooth flank fracture (TFF) or tooth interior flank fracture (TIFF), respectively, and white etching cracks (WEC) it becomes clear why calculated reliability would be more optimistic than the apparent reliability. This is because two of the most relevant failure modes cannot currently be included in its quantification.

Category		**A1**	**A2**	**B**	**C**
Life calculation		Recognized codes available	Recognized codes not available		Irrelevant
Load profile		Deterministic		Stochastic	
Typical Weibull shape		$\beta > 1$	$\beta > 1$	$0.8 \leq \beta \leq 1.2$	$0 \leq \beta \leq 1$
Examples	Gears	Tooth root bending fatigue	Tooth flank fracture	Scuffing	Overload fracture
	Rolling bearings	Rolling contact fatigue	Subsurface initiated fatigue (White etching cracks)	Fretting corrosion	Current leakage

Table 7: Typical system elements for wind turbine gearboxes [VDM19]

Before progressing, it is important to define relevant terminology.

Dependability is defined as the “ability to perform as and when needed” and encompasses the “core attributes of reliability, maintainability, and supportability and the resulting availability” [IEC15].

Availability is more specific than dependability and defined as “ability to be in an [up] state to perform as required under given conditions” [IEC15].

Reliability is the “ability [and as a measure the probability] to perform as required, without failure, for a given time interval, under given conditions” [IEC15]. A common assumption is that the reliability can be described by an exponential distribution, cf. Eq. 4, often assuming a constant failure rate λ, cf. Eq. 5 [IEC16]. For some system elements, a Weibull distribution (cf. e.g., Eq. 6: 2-parametric Weibull distribution) provides a more accurate depiction [VDA19]. The system reliability for serial structures, such as WT GBX i.e., without parallel redundancies, follows Eq. 7 [OCO12]. In case of a constant failure rate, it follows $\lambda = 1/MTTFF$, where MTTF is the **mean time to first failure**.

$$R(t) = e^{-\int_0^t \lambda(\tau) d\tau} \quad \textbf{Eq. 4}$$

$$R(t) = e^{-\lambda \cdot t} \quad \textbf{Eq. 5}$$

$$R(t) = e^{-\left(\frac{t}{\eta}\right)^{\beta}} \quad \textbf{Eq. 6}$$

$$R_{sys}(t) = \prod_{i}^{n} R_{SE,i}(t) \quad \textbf{Eq. 7}$$

Maintainability is the “ability to be retained in, or restored to, a state to perform as required, under given conditions” [IEC15]. Thus, maintainability is closely linked to reliability. It is switching from a down state (e.g., after failure) to an up state, thereby enhancing availability.

A **process** is understood as a “set if interrelated or interacting activities that use inputs to deliver an intended result” [ISO15]. This includes production processes (e.g., steel making or tooth grinding) as well as quality control and assembly.

The definition of availability refers to the two states up state and down state. IEC 61703:2016 [IEC16] provides an overview of the constitutes of up time and down time. While mean up time (MUT) comprises operating time, idle time and standby time, mean down time includes various constitutes such as fault detection time, fault localization time, and logistic delay [IEC16]. Mean down time can also be equated to **mean time to restoration** (MTTR).

When calculating asymptotic or inherent availability, cf. Eq. 8, it is important to differentiate between repairable and non-repairable items, as well as continuously operating items (COI) and intermittently operating items (IOI). An **item** can be an “individual part, component, material, device, functional unit, equipment, product, subsystem, system, service or process” [IEC15]. For COI, Eq. 8 can be expressed as Eq. 9 with MOTBF representing the **mean operating time between failures**. For simplicity, the items considered here are assumed to be repairable and COI.

$$\bar{A} = \frac{MUT}{MUT + MTTR}$$ **Eq. 8**

$$\bar{A} = \frac{MOTBF}{MOTBF + MTTR} = \frac{\lambda}{\lambda + \mu}, with\ MOTBF = \frac{1}{\lambda}\ and\ MTTR = \frac{1}{\mu}$$

$$\bar{A} = \prod_{i}^{n} \frac{\mu_i}{\lambda_i + \mu_i}$$ **Eq. 9**

4 How next steps can contribute to more profitability

In the wind industry, it's key to (1) reduce warranty costs, (2) increase availability, and (3) reduce product costs, cf. Figure 138 and Figure 139.

4.1 Reduce warranty costs

Reducing warranty costs hinges on improving reliability. Although a WT or a GBX is considered a repairable item, the definition of reliability includes the aspect of performing without failure. Therefore, public research to evolve A2 to A1 failure modes is crucial for enabling more accurate reliability predictions. However, as outlined above and mentioned in [HOV15] and [OCO12], calculated reliability differs from the apparent reliability due to factors such as process deviations. Actions to address this will be influenced by the balance of costs versus gains. Thus, a methodical approach that visualizes the gains versus costs could support decisions on the most relevant and preferrable actions.

4.2 Increase availability

Increasing the availability of WT, specifically the GBX for WT, is often a key point in economic discussions. Availability can be improved by increasing the reliability. However, for a fixed level of reliability, represented by a constant system degradation rate λ_{sys}, the mean availability $\bar{A}$ depends on the MTTR. Original Equipment Manufacturers (OEM) and GBX supplier should cooperate to consider maintainability during the design phase and tailor service contracts accordingly.

An important sidenote is that performance requirements in many markets include tonality. Therefore, a repaired system considered as good as new should also comply with tonality requirements, which is partially an overlooked aspect.

Future optimization of availability could be tailored for specific windfarms or regions. A suitable tool for this could be a Markov graph. First, the Reliability Block Diagram (RBD) of the system is depicted. Figure 140 shows an exemplary and simplified RBD of a planetary stage, considering A1 failure modes for the gears and bearings of the planetary gear.

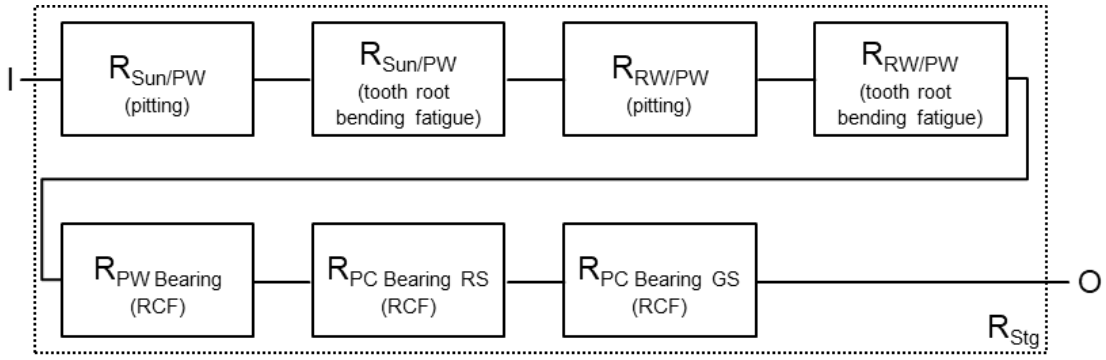

Figure 140: Exemplary and simplified Reliability Block Diagram of a planetary stage

The resulting reliability for this subsystem can be calculated separately with Eq. 7. VDMA 23904 [VDM19] and in the upcoming IEC/TS 61400-4-1 provide guidance on the details. These subsystems can then be combined into a RBD as in Figure 141.

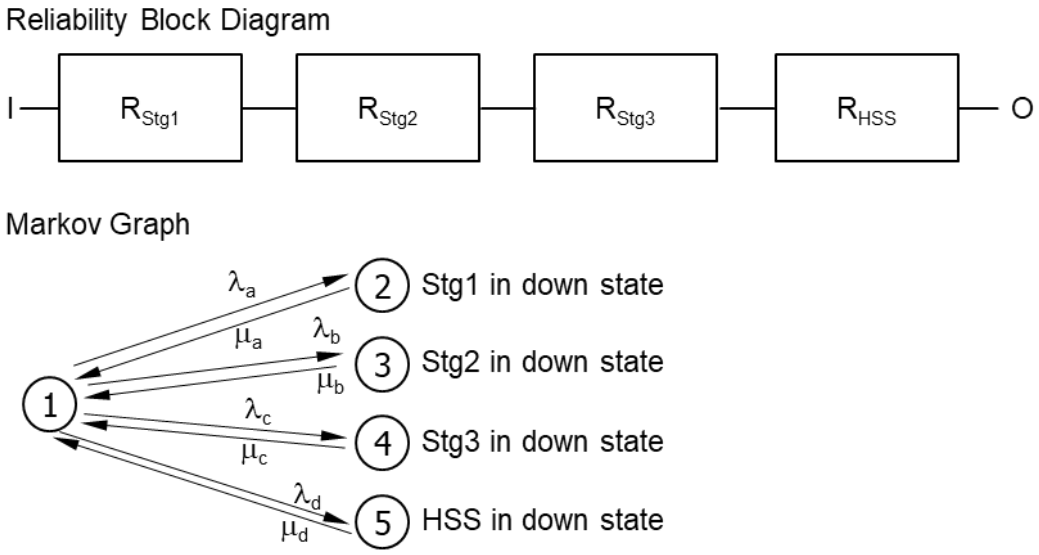

Figure 141: RBD and Markov graph (simplified) for a GBX with three planetary and one parallel stage

Results for such an RBD based on a dummy GBX are provided in Table 8. Based on calculated reliability, this GBX would be outstanding. Assuming the planetary bearings would be rolling bearings, further improvements could be achieved by using journal bearings.

While MTTR (ranging from 60 days in Var A to 15 days in Var C) might seem to have little influence on availability, the shift to “four nines” (99.99x %), as availability levels are sometimes nominated, is significant.

		Stg1	Stg2	Stg3	HSS	System
Dummy Design	*R*(**30** y) / %	98.227	99.479	98.639	99.398	**95.805**
	λ / year^{-1}	0.000596	0.000174	0.000457	0.000201	0.001428
Var A	μ / year^{-1}	6.0875	6.0875	6.0875	6.0875	6.088437
	A / %	99.990	99.997	99.992	99.997	**99.977**
Var B	μ / year^{-1}	12.175	12.175	12.175	12.175	12.17594
	A / %	99.995	99.999	99.996	99.998	**99.988**
Var C	μ / year^{-1}	24.35	24.35	24.35	24.35	24.35094
	A / %	99.998	99.999	99.998	99.999	**99.994**

$$\mu = \frac{\mathbf{6.0875}}{\boldsymbol{year}} = \frac{\mathbf{1}}{\mathbf{60}\,\boldsymbol{days}}, \boldsymbol{\mu} = \frac{\mathbf{12.175}}{\boldsymbol{year}} = \frac{\mathbf{1}}{\mathbf{30}\,\boldsymbol{days}}, \boldsymbol{\mu} = \frac{\mathbf{24.35}}{\boldsymbol{year}} = \frac{\mathbf{1}}{\mathbf{15}\,\boldsymbol{days}}$$

Table 8: Example of possible reliability *R* and availability *A* for a dummy GBX and failure rates satisfying on subsystem level (for sake of simplicity) the relation $R(t) = e^{-\lambda \cdot t}$ (cf. Eq. 5)

To address the difference between calculated and apparent reliability, failure rate and repair time data for offshore wind turbines and their GBX are taken from [CAR15] in the comparison below, cf. Table 9. It is noteworthy that these numbers are from 2015 and based on WT grouped as 3-5 years and > 5years in operation making them more than 13 years old from today's perspective. Additionally, in the study, the repair time likely does not follow the same definition as MTTR. Furthermore, a major replacement in [CAR15] was defined as a repair action consuming more than 10 k€ in material costs (excluding logistics, transportation etc.) which is assumed to be closest to the understanding of a failure impairing the ability to perform as required, without failure, for a given time interval, under given conditions.

		Stg1	Stg2	Stg3	HSS	System
System alone	*R*(**10** y) / %					**21.438**
	λ / year^{-1} [CAR15]					0.154
	μ / year^{-1} [CAR15]					0.026351814
	A / %					**99.596%**
I	μ / year^{-1}	12.175	12.175	12.175	12.175	12.32538
	A / -	0.999853	0.999957	0.999887	0.987804	**98.751**
II	μ / year^{-1}	12.175	12.175	12.175	24.35	23.928464
	A / -	0.999853	0.999957	0.999887	0.993865	**99.356**
III	μ / year^{-1}	12.175	12.175	12.175	∞	509.33897
	A / -	0.999853	0.999957	0.999887	1	**99.970**

$\mu = \frac{\mathbf{0.026}}{\boldsymbol{year}} = \frac{\mathbf{1}}{\mathbf{9.625}\ \boldsymbol{days}}, \boldsymbol{\mu} = \frac{\mathbf{12.175}}{\boldsymbol{year}} = \frac{\mathbf{1}}{\mathbf{30}\ \boldsymbol{days}}, \boldsymbol{\mu} = \frac{\mathbf{24.35}}{\boldsymbol{year}} = \frac{\mathbf{1}}{\mathbf{15}\ \boldsymbol{days}},$

Table 9: Comparison of the impact of increased failure rates (i.e., MTTFF = MOTBF) compared to Table 8 based on [CAR15] and varied MTTR, assuming to represent ten-year operation

Table 9 illustrates that, assuming the numbers in [Car15] accurately depict the state after 10 years, reliability would be subpar at approximately 21.4 %. For this exercise, it was assumed that the increased failure rate would be linked to the parallel stage, keeping the planetary stages same as in Table 8. The availability of ~**99**.596 % with an MTTR of 9.625 days is likely too optimistic due to omission of logistics etc. which are part of the MTTR definition. In scenarios I, II and III, an MTTR of 30 days for the planetary stages is assumed, comparable to Var B in Table 8. The MTTR for the HSS was varied: 30 days in scenario I, 15 days in scenario II, and instantaneous in scenario III.

Considering the impact of the shift between availability levels measured in “nines”, the comparison of Var B at **99.9**88 % (30 years) (cf. Table 8) with scenario I at **9**8.751 % (10 years) (cf. Table 9) emphasizes the significance of high failure rates on availability. Even with instantaneous repair (scenario III), “only” an asymptotic availability of **99.9**7 % can be achieved. Maintaining high availability for WT or WT GBX under these circumstances will come with high costs, underscoring the importance of maintainability (minimal costs in case of necessary repair) and a high initial reliability clear.

4.3 Reduce product costs

Not only are the total cost of ownership (TCO) and annual energy production (AEP) decisive factors, but product costs themselves are also crucial. Building on the aspects from chapters 4.1 and 4.2, one way to further reduce product costs is to employ designs that meet a target reliability. This falls

within the field of full probabilistic design. As outlined in chapter 4.2, it is essential to account for all relevant failure modes in the reliability calculation, such as TFF and WEC, but also failures from stray current (currently listed as category C in VDMA 23904 [VDM19]). Additionally, processes and process control that minimize quality cases or any process deviations are of utmost importance. Even though the bar for employing full probabilistic design is high, it may become a decisive factor in further reducing product costs in the future.

5 Conclusions

Profitability in the wind industry needs to improve with key aspects being availability, reliability and maintainability. It is important to emphasize that calculable reliability is expected to differ from apparent reliability due to certain failure modes and/or process deviations that cannot be considered. Therefore, public research and industry consensus on how to incorporate these factors are crucial. Additionally, maintainability should be integrated into the design process between OEMs and GBX supplies. ZF offers strong partnerships with “System Co*operation” [ZF25A] and Thrive [ZF25B]. The former aims to advance partnerships for increased profitability, while the latter aims to achieve availability levels of “four nines”.

Without compromising on availability and target reliability, full probabilistic design has the potential to further reduce product costs by squeezing out safety margins based on standards from past decades but local stress calculations, manufacturing processes and quality control have improved since. However, the necessary building blocks of improved failure models and reliability calculations need to be in place first.

6 Bibliography

[AGM04] AMERICAN GEAR MANUFACTURERS ASSOCIATION, ANSI/AGMA/AWEA 6006-A03, 2004

[AGM20] AMERICAN GEAR MANUFACTURERS ASSOCIATION, ANSI/AGMA 6006-B20, 2020

[BER08] Bernd Bertsche: Reliability in Automotive and Mechanical Engineering, Springer, 2008

[CAR15] James Carroll, Alasdair McDonald, David McMillan: Failure Rate, Repair Time and Unscheduled O&M Cost Analysis of Offshore Wind Turbines, Wind Energy, 2015, DOI: 10.1002/we.1887

[HOV15] Anja Hovgaard, Adriana Verde Rios, Douglas Guthrie, Antonio Correia: Harmonized Assessment of the Design Reliability of Wind Turbine Gearboxes, Conference for Wind Power Drives, 2015

[IEC12] International Electrotechnical Commission: IEC 61400-4:2012, Wind turbines - Part 4: Design requirements for wind turbine gearboxes, 2012

[IEC15] International Electrotechnical Commission: IEC 60050-192:2015, International Electrotechnical Vocabulary (IEV) - Part 192: Dependability, 2015

[IEC16] International Electrotechnical Commission: IEC 61703:2016, Mathematical expressions for reliability, availability, maintainability and maintenance support terms, 2016

[ISO05] International Organization for Standardization: ISO 81400-4, Wind turbines, Part 4: Design and specification of gearboxes (withdrawn), 2005

[ISO15] International Organization for Standardization: ISO 9001:2015, Quality management systems — Requirements, 2015

[LIC23] Endri Lico: Global wind turbine technology trends 2023, Wood Mackenzie, 2023

[OCO12] Patrick O'Connor, Andre Kleyner: Practical Reliability Engineering, Wiley, 5th edition, 2012

[S&P24] S&P Global Commodity Insights, 2024

[STR15] Dirk Strasser, Falko Thoma, Salih Yüksek, Philipp Schmaltz: From a Safety Factor driven Concept to Reliability Engineering: Development of an Multi-Mega-Watt Wind Energy Gearbox, Conference for Wind Power Drives, 2015

[STR23] Dirk Strasser, Joris Peeters, Bert Verdyck: Design for Reliability: Full Probabilistic approaches for the Wind Industry, Conference for Wind Power Drives, 2023

[VDM19] Verband Deutscher Maschinen- und Anlagenbau e.V.: VDMA 23904, Reliability Assessment for Wind Energy Gearboxes, 2019

[ZF25A] ZF Wind Power Antwerpen NV: Next Level of System Co*operation in Wind Power, 2025

System Cooperation - ZF

[ZF25B] ZF Wind Power Antwerpen NV: Thrive – For continuous availability, 2025

ZF Gearbox for Wind Turbines - Thrive - ZF

Power Electronics and Stray Current

Comparative, Experimental Analysis of Parasitic Currents in DFIG and SCIG based Wind Turbine Drives

Amandus Bach[1], Maximilian Zweiffel[2], Fabian Herzog[1], Julian Röder[2], Georg Jacobs[2], Rik W. De Doncker[1]

[1]Institute for Power Generation and Storage Systems, RWTH Aachen University, Aachen, Germany

[2]Chair for Wind Power Drives, RWTH Aachen University, Aachen, Germany

Keywords: bearing currents, high-frequency modeling, bearing current measurement, WRIG, DFIG, SCIG

Abstract: In this work, the measurement of parasitic currents within the drivetrain of a wind turbine with a wound-rotor induction generator operated as doubly-fed induction generator (DFIG) and squirrel-cage induction generator (SCIG) is presented. From the measured currents flowing through the high-speed-shaft, the bearing currents at bearing locations in the generator and the gearbox are calculated. Differences between DFIG and SCIG in terms of parasitic capacitances and the resulting bearing voltage ratio are discussed. The inductance in the common-mode (CM) path via ground is analyzed to compare the two drive systems regarding their susceptibility to high-frequency rotor-to-ground currents.

1 Introduction

Drivetrain failures in Wind turbines (WTs) have a significant impact on the plants' levelized-cost of energy (LCOE) due to costly repairs and downtimes. High-speed shaft (HSS) bearings show the highest failure rate among all gearbox components and, hence, contribute largely to the maintenance costs [SHE2016].

Electrical current passage through bearings can alter the metallic bearing surfaces and the lubricant provoking the bearings to fail often even early in the service time of WTs. Certain damages, e.g., white etching crack (WEC), correlate strongly with the occurrence and severeness of bearing currents [STE22, LOO16]. Moreover, electrical bearing loads are an underrepresented factor in bearing design standards as these are currently mainly based on fatigue. The origin of bearing currents lies in the voltage drop across the bearings caused by the CM voltage of the power electronic inverter [MUE14]. It can be distinguished between displacement currents due to charging and discharging of the bearing capacitance that are considered less harmful to bearings, electrical-discharge machining currents that occur when the breakdown voltage of the lubricant is exceeded and rotor-to-ground currents.

Injecting defined currents into the current path of the bearings on small component test benches allowed researchers in the past to gain understanding of bearing damages in presence of electrical currents from a material science point of view [STE22, LOO16]. In addition, many works have investigated and measured bearing currents on system level test benches or in the field for inverter-driven motors of small frame sizes [MUE14]. However, only a few works present the measurement of bearing currents on a system level in WT drives [ZIE05, KEL09] while it is often pointed out in literature that large frame-size electrical machines are prone to the existence of circulating

currents in addition to the different bearing current types previously mentioned [MUE14]. A systematic study of bearing currents together with bearing voltages and the CM voltage as their root cause has not been performed yet taking into account all bearing locations related to the HSS.

To fill this gap, this study presents the measurement of bearing currents and voltages in a WT drivetrain on a testbench. More specifically, a wound-rotor induction generator (WRIG) is deployed to investigate electrical bearing loads in the DFIG and SCIG drives. Figure 142 shows the schematic of the investigated drive systems. The converter is connected to a grid emulator with a transformer in between, while the main shaft of the gearbox is driven by a large 4 MW motor to emulate the rotation due to incoming wind.

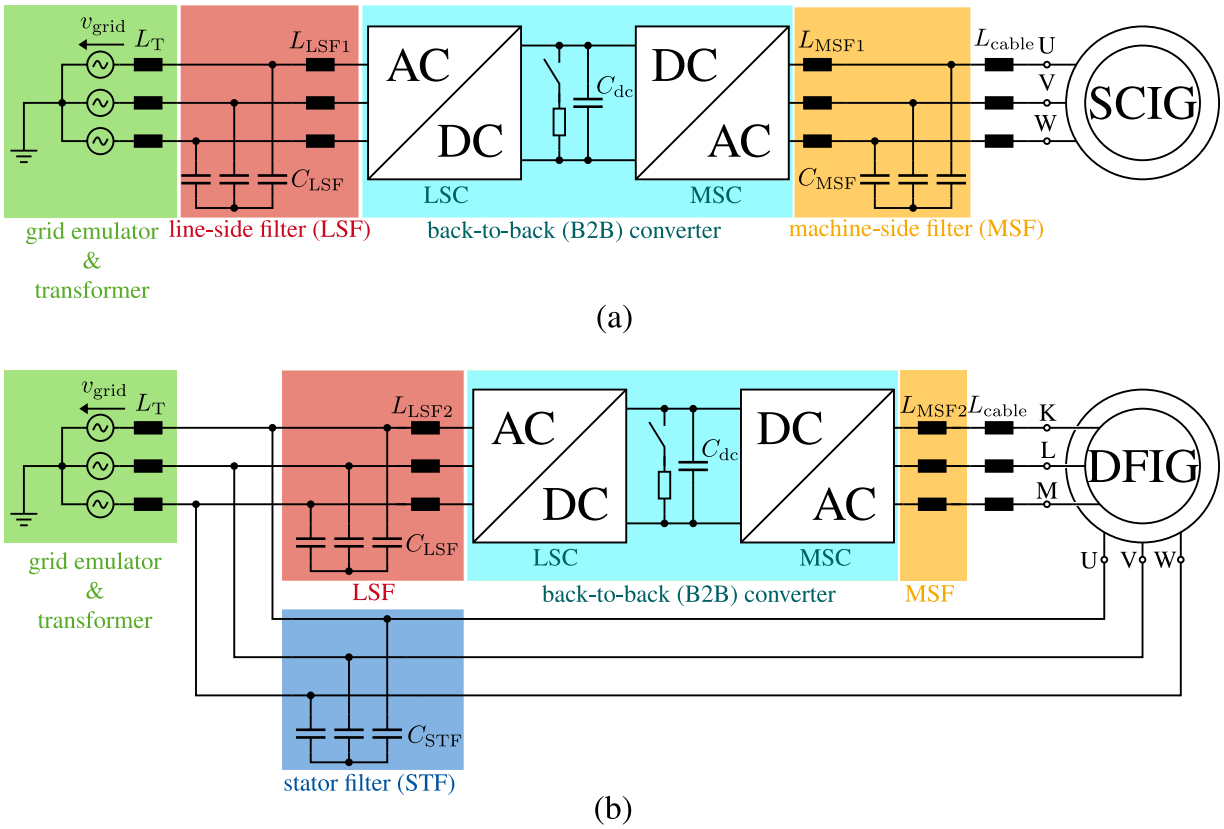

Figure 142: Schematics of the investigated drive trains – (a) SCIG, (b) DFIG.

Capacitive equivalent circuits of WRIG have been presented in [SCH15] for rotor-fed doubly-fed induction motors and in [ADA2009] for DFIG applications. However, in both presented models, only the electrical machine is considered and the electrical interaction with gearbox components is neglected. The complex interaction of electrical and mechanical domains in the bearing make it impossible to obtain an exact model of a wind turbine drivetrain to predict occurring electrical bearing loads. Especially, the further upwind the investigated gearbox part is located in the drive, the harder that prediction gets because more and more junctions need to be considered.

this work presents measurement results to quantify the electrical loads in gearbox parts connected to the high-speed shaft. In the future, these measurements can serve as an indicator for occurring loads in similar drivetrains, for model validation and for the parametrization of electrical loads applied on gearbox component testbenches.

The remainder of the paper is structured as follows: In chapter 2, the measurement techniques applied and the measurement equipment used in this measurement campaign are presented. Chap-

ter 3 reviews the capacitive high-frequency equivalent circuit of the WRIG to point at key differences in the CM path of the DFIG and SCIG drivetrain and anticipate certain expectations for the measurements carried out. Chapter 4 presents the measurement results for the SCIG drivetrain during maximum power-point operation across different rotational speeds. A qualitative comparison of the currents in the gearbox for both drivetrain concepts is given as well. Finally, the work is concluded in chapter 5.

2 Measurement Setup

For the measurement of bearing currents, the utilization of two rogowski coils per bearing presents a solution that does not require mechanical changes in machine components [QUA21]. The bearing current can be obtained by the difference of the currents measured in front of and behind the bearing. In this work, commercial rogowski coils of Power Electronics Measurements have been deployed [PEM24] that show a peak di/dt of 40 kA/µs. From previous measurements [ZWE24], the base frequency of the high-frequency currents after breakdown events are expected to be about 20 MHz. Due to the large required diameter of the rogowski coils because of the large shaft sizes, the coils' high-frequency bandwidth could not be matched to reach this frequency. Therefore, the measurements are damped in the high-frequency range. All rogowski coils for the determination of bearing currents have the same circumference, i.e., positions a, c, d, e, f in Figure 143. In addition, the sample width of the oscilloscope was set to 52.1 MS/s.

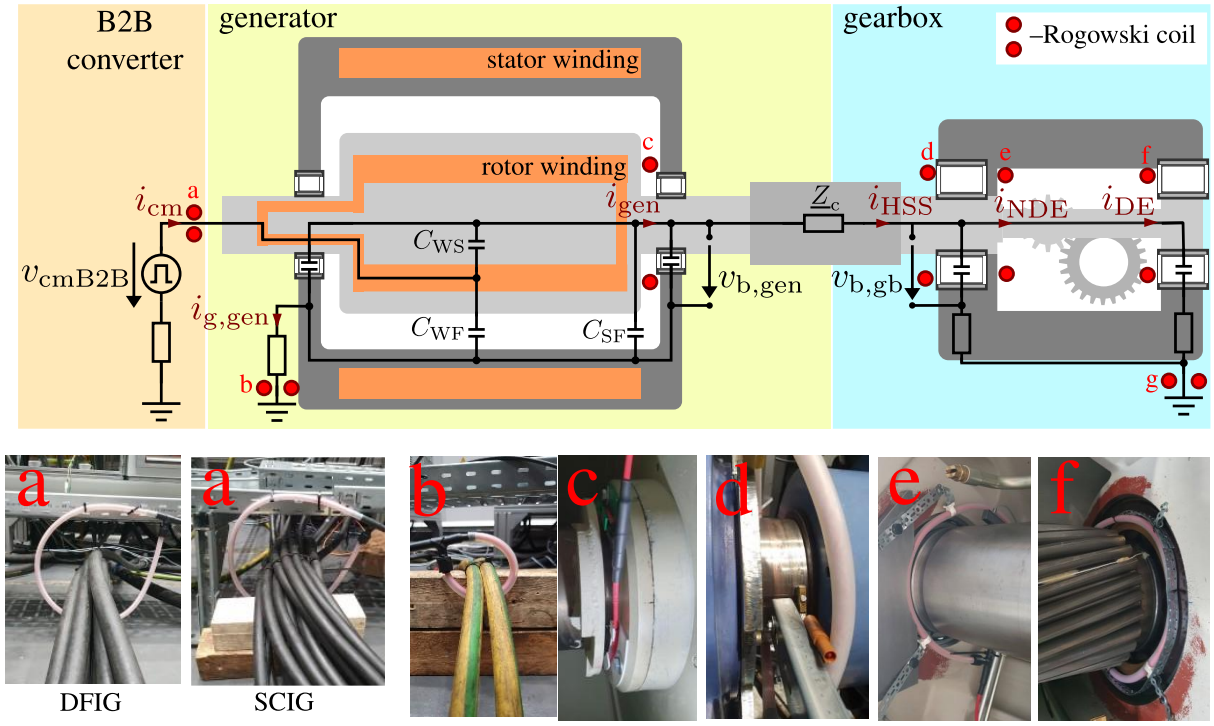

Figure 143: Positions of rogowski coils placed across the drivetrains.

In the SCIG configuration, a rogowski coil is put around all stator cables, whereas in the DFIG configuration it is connected around the rotor cables, to measure the total CM input current [GEM21]. Accordingly, to determine the CM voltage at the generator input, the three phase voltages v_U, v_V, v_W at the stator terminals or the rotor terminals v_K, v_L, v_M are measured for the with reference to the machine housing for SCIG and DFIG, respectively. The CM voltages are calculated by the sum of the three voltages divided by three.

3 High-Frequency Equivalent Circuit Models

Some elements of the high-frequency equivalent circuit of the WRIG are sketched already in the cross section of the generator in Figure 143. From this figure in can be deduced, how parasitic currents pave their way through the drive train: The high-frequency circuit is excited by a CM voltage v_{cm}. In case of the DFIG, as sketched in Figure 143, the shaft and the frame are capacitively coupled via the winding-to-shaft capacitance C_{WS} and the winding-to-frame capacitance C_{WF}, respectively. However, the shaft and the frame potentials are also capacitively coupled via the shaft-to-frame capacitance C_{SF}. The current loop closes via the shaft through different gearbox parts and ground. The representation of lumped capacitances neglects the voltage drop across the windings and it is assumed that shaft and rotor package, as well as the complete rotor winding and stator winding, are on a single potential, respectively. Therefore, it is referred to this approach as equipotential analysis. More complex equivalent circuits are elaborated in [BUB21]. Purely capacitive equivalent circuits, nevertheless, are easier to analyze and allow a convenient linkage between the excitation voltage v_{cm} and the generators bearing voltage $v_{\mathrm{b,gen}}$ via the bearing voltage ratio [MUE04]

$$BVR = \frac{V_{\mathrm{b,gen}}}{V_{\mathrm{cm}}}. \qquad \textbf{Eq. 4}$$

The capacitive high-frequency circuit of the doubly-fed induction generator proposed in [ADA09] is adopted in this work and is shown in Figure 144.

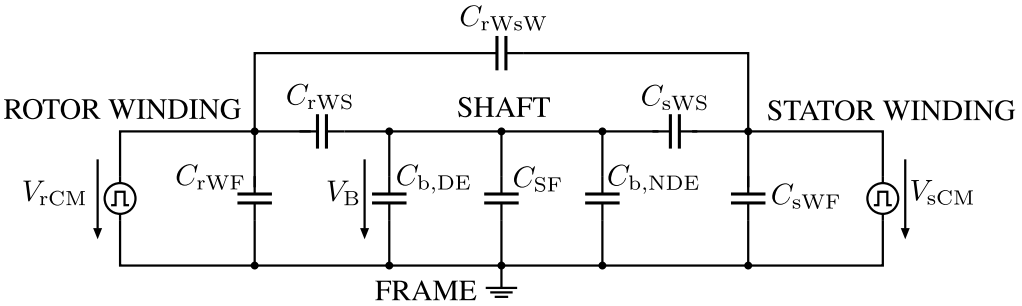

Figure 144: Capacitive high-frequency equivalent circuit of the WRIG based on [ADA09].

The values of the parasitic capacitances depicted in Figure 144 have been determined following the described equipotential analysis via 2D finite-element simulations. The bearing voltages for DFIG and SCIG can be calculated to 99.7 % and 9.5 %, respectively. These results are in the order of magnitude well in line with values obtained in other works for rotor- and stator-excited machine types [Liu18]. Hence, the DFIG configuration shows a higher capacitive coupling between the excitation winding and the shaft, i.e., the bearing. Therefore, only looking at the generator, it can be anticipated that the bearing currents in the DFIG configuration are higher compared to the SCIG configuration of the same WRIG.

To evaluate the susceptibility of the respective drivetrains to the occurrence of high rotor-to-ground currents, the impedance in the whole CM current path via ground has to be taken into account. Therefore, the single components of the electrical drivetrain can be transferred into their CM equivalent circuit [BRO15]. The CM equivalent circuit for the considered drivetrains present the same structure depicted in Figure 145 but exhibit different values. Large unknowns are the impedances to ground $\underline{Z}_{\mathrm{g,gen}}$ and $\underline{Z}_{\mathrm{g,gb}}$. All bearings are depicted as lumped capacitances, although their impedance varies depending on the lubrication regime [MUE04].

Besides the differences in machine parasitics C_{WS}, C_{WF} and C_{SF}, the filter elements are different as well. The sum of the transformer and filter inductances in the DFIG drive is 76.7 µH compared to 29.7 µH in the SCIG drive. Hence, the additional inductance causes a decrease in cut-off-frequency and, therefore, can lead to a lower susceptibility to high-frequency rotor-to-ground currents in the DFIG drivetrain.

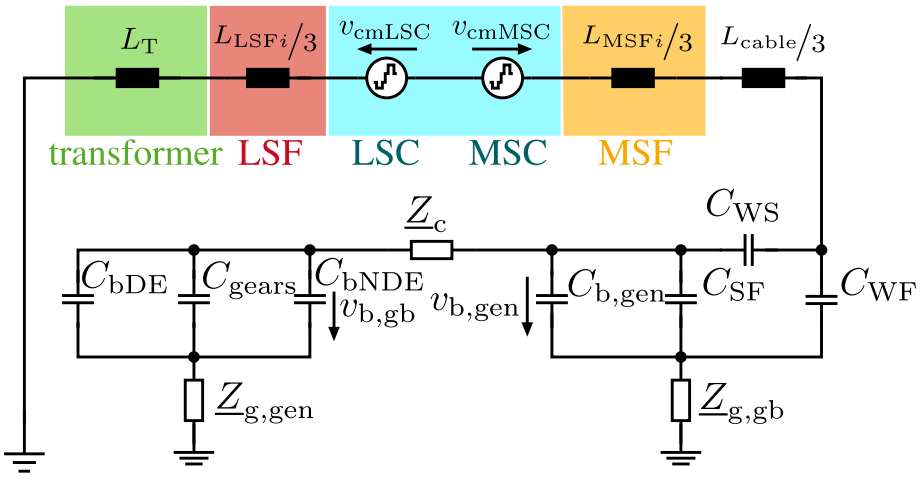

Figure 145: Simplified high-frequency equivalent circuit of the SCIG and DFIG Drive system.

4 Measurement Results

The measurements presented in this chapter were obtained under maximum power point tracking of the systems. The data of the deployed generator is given in Table 11.

nominal power	2750 kW
rated torque	24.7 kNm
rated speed	1100 rpm
frequency at rated power	54.5 Hz
number of poles	6
rated voltage	720 V (Y connection)
rated current	2564 A

Table 11: Data of the generator

Figure 146 shows the measured CM voltage v_{cm} at the generator input as well as the generator-side bearing voltage $v_{\mathrm{b,gen}}$, i.e., the voltage between downwind HSS and generator housing for a generator speed of 1114 rpm. The CM current i_{cm} and the ground current from generator to ground $i_{\mathrm{g,gen}}$ are shown as well.

The CM voltage measured in the DFIG drive shows the expected seven-level voltage profile typical for back-to-back converters [ADA09], whereas, in the SCIG configuration only some levels of $V_{\mathrm{dc}}/3$ can be made out, e.g., during the time between $1.2\ \mu s$ and $1.5\ \mu s$. Oscillations with decaying amplitude can be observed at the switching transitions.

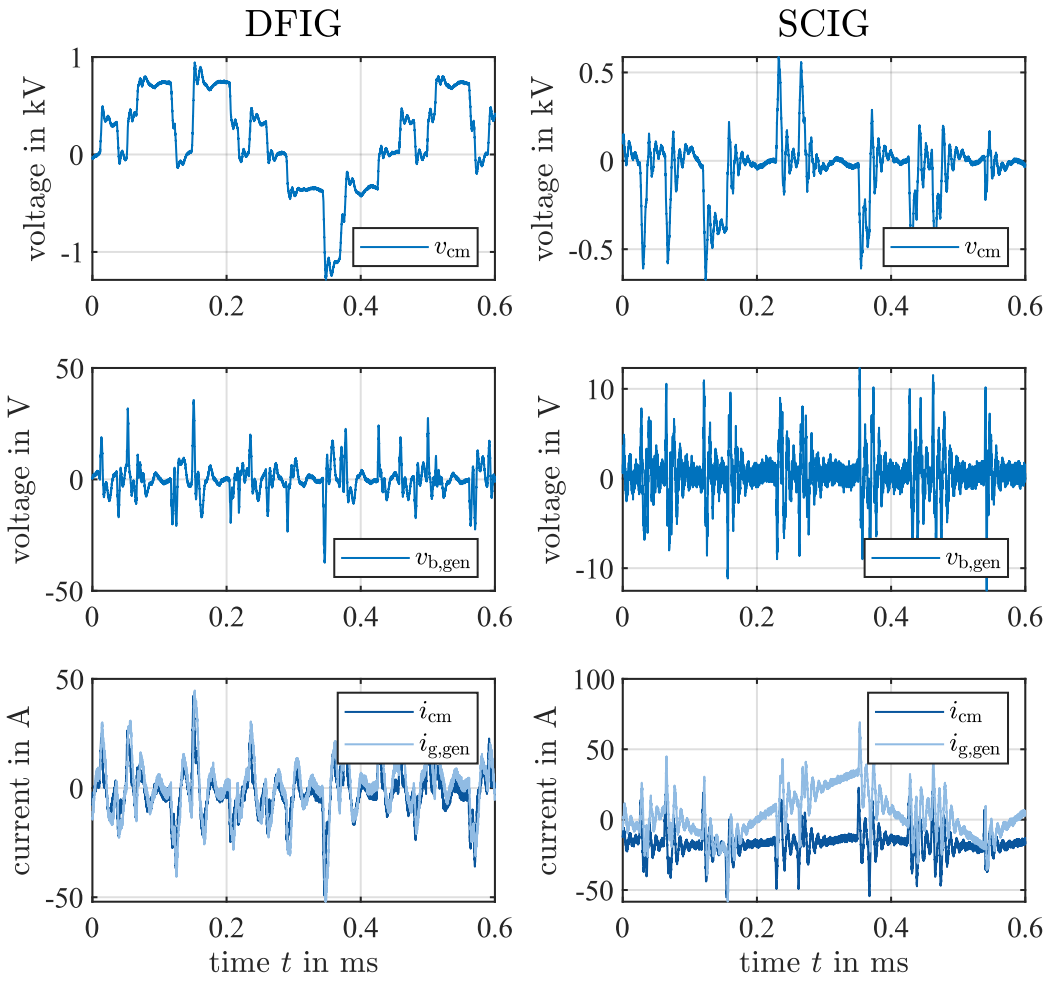

Figure 146: Measured CM and bearing voltages and CM and ground currents.

Comparing the bearing voltage measured on the generator side with the exciting CM voltage for both drives, it can be observed, that in the SCIG drive, the frequency at which the oscillations occur at the switching state transitions are the same. In the DFIG drive, a steep pulse is observed at the switching state transition. In both cases, the bearing voltage is not linked proportional to the measured CM voltage with the BVR as suggested by Eq. 4. Moreover, from the analysis presented in chapter 3, it has been anticipated that the DFIG shows a higher CM voltage than the SCIG. Investigating the peak values of the generator-side bearing voltage, this statement can be verified. However, the ratio between the RMS values of the bearing voltages of DFIG and SCIG is in a range between 1.92 and 2.89, as can be seen in Table 12.

	BVR	generator speed (rpm)						
		780	845	908	970	1033	1114	1195
		RMS($v_{b,gen}$)						
DFIG	99.7 %	7.92 V	7.12 V	7.2 V	6.58 V	6.59 V	6.77 V	7.39 V
SCIG	9.5 %	2.74 V	2.80 V	2.88 V	3.12 V	3.32 V	3.51 V	3.60 V
ratio	10.4	2.89	2.54	2.50	2.11	1.99	1.92	2.05

Table 12: RMS values of the generator-side bearing voltage for different generator speeds for DFIG and SCIG and their ratio

The values given in Table 12 are obtained from measurements over a duration of 10 s, i.e. 25000 switching periods for the SCIG and above 11250 switching periods for the DFIG, and for different generator speeds. These ratios are far below the ratio of calculated BVRs for both drivetrains with a value of 10.4.

Comparing the CM input current i_{cm} to the ground current from the generator grounding lug to ground $i_{\mathrm{g,gen}}$, it can be observed that they show similar oscillations, except for a superimposed disturbance on the generator ground current measurement of the SCIG. Hence, a large part of the CM input current flows to ground, either via the grounding brush or via machine elements in form of rotor-to-ground currents. The DFIG ground and CM currents present less high-frequent content than the currents measured in the SCIG. A potential explanation lies in the previously mentioned lower susceptibility to high-frequency rotor-to-ground currents due to higher inductance in the CM path of the DFIG.

In Figure 147, the measured currents within the drivetrain are shown together with the calculated bearing currents.

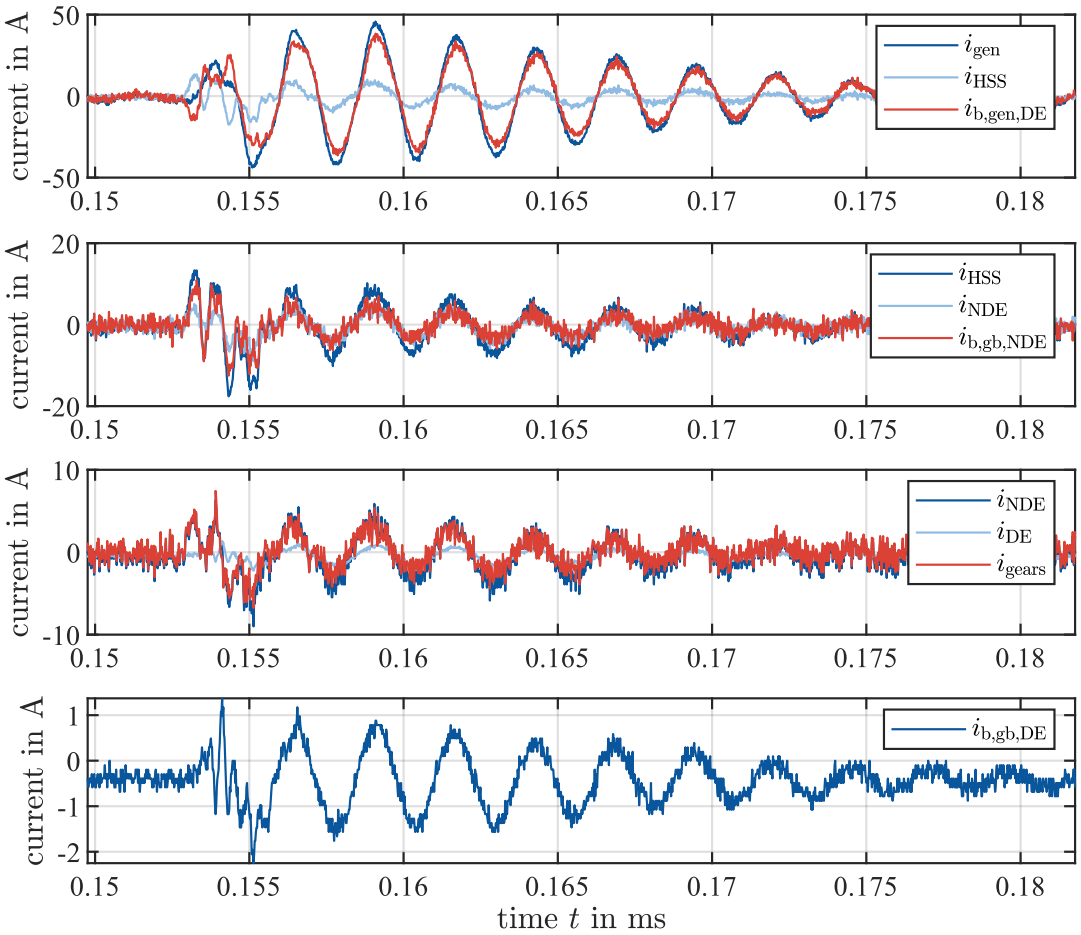

Figure 147: Measured currents within the drivetrain and the derived bearing current waveforms.

The measured currents i_{gen}, i_{HSS}, i_{NDE} and i_{DE} are shown in blue colors. The locations of the measurements within the drivetrain can be seen in Figure 143. The calculated bearing currents are: the current through the drive end (DE) generator bearing

$$i_{\mathrm{b,gen,DE}} = i_{\mathrm{gen}} - i_{\mathrm{HSS}}, \quad \textbf{Eq. 5}$$

the current through the non-drive end (NDE) gearbox bearing

$$i_{\mathrm{b,gb,DE}} = i_{\mathrm{NDE}} - i_{\mathrm{HSS}}, \quad \textbf{Eq. 6}$$

and the current through the gears

$$i_{\mathrm{gears}} = i_{\mathrm{DE}} - i_{\mathrm{NDE}}. \quad \textbf{Eq. 7}$$

The DE gearbox bearing current $i_{\mathrm{b,gb,DE}}$ is equal to the current i_{DE} through the HSS measured on the DE side of the gearbox. Therefore, it is plotted in blue as well.

It can be seen, that the amplitude of the bearing currents decays the further upwind the bearing is located, i.e., the further away the location is from the converter. Moreover, oscillations with a frequency of 389 kHz in this operating point are visible in all currents.

5 Conclusion

In this work, measurements conducted in a DFIG and SCIG drivetrain to analyze CM voltages and currents as well as bearing voltages and currents have been presented. The CM impedances in the investigated drivetrains have been analyzed. The BVR and the inductance in the CM path have been selected as theoretical criteria to compare the susceptibility to bearing current phenomena in in both drivetrains. It has been shown that even though the DFIG BVR is 10 times larger than the SCIG BVR, the observed RMS bearing voltages do not differ by the same ratio but are in a range between 1.92 and 2.89 across different operating points. Finally, Results for bearing current measurements using two rogowski coils per bearing to calculate the bearing current by the difference of both measured currents have been presented validating this approach for future analyses of current passage through machine elements in wind turbine gearboxes.

6 Bibliography

[ADA09] Adabi, Jafar: Analysis of Shaft Voltage in a Doubly-Fed Induction Generator.

IEEE, Valencia, Spain, 2009.

[BRO15] Brovont, Aaron D.: Equivalent Circuits for Common-Mode Analysis of Naval Power Systems.

IEEE, Old Town Alexandria, Virginia, USA, 2015.

[BUB21] Bubert, Andreas: Optimization of Electric Vehicle Drive Trains with Consideration of Parasitic Currents inside the Electrical Machine.

ISEA, Aachen, Germany, 2021

[GEM21] Gemeinder, Yves: Application Guide Bearing Currents.

Technische Universität Darmstadt, Darmstadt, Deutschland, 2021.

[KEL19] Keller, Jonathan: Uptower Investigation of Main and High-Speed-Shaft Bearing Reliability.

NREL, 2019.
https://research-hub.nrel.gov/en/publications/uptower-investigation-of-main-and-high-speed-shaft-bearing-reliab

(Jan 28th, 2024)

[LIU18] Liu, Ruifang: Comparative Analysis of Bearing Current in Wind Turbine Generators.

Energies, 11(5), 1605.

MDPI, 2018.

[LOO16] Loos, Jörg: Influence of High Electrical Currents on WEC Formation in Rolling Bearings.

In: Tribology Transactions, 59(5), 865-875, 2016.

Taylor & Francis, 2016.

[MUE04] Mütze, Annette: Bearing Currents in Inverter Fed AC-Motors.

Technische Universität Darmstadt, Darmstadt, Germany, 2004.

[MUE14] Mütze, Annette: On radio-frequency based detection of high-frequency circulating bearing current flow.

IEEE, Chicago, Illinois, USA, 2013.

[PEM24] Power Electronics Measurements Ltd: CWT (Original), CWTHF.

https://www.pemuk.com/uploads/files/datasheets/CWT-CWTHF-datasheet.pdf?v=1731411801

(Jan 28th, 2024)

[QUA21] Quabeck, Stefan: A Machine Integrated Rogowski Coil for Bearing Current Measurement

IEEE, Dallas, Texas, USA, 2021.

[SCH15] Schuster, Martin: Comparison of Different Inverter-Fed AC Motor Types Regarding Common-Mode Bearing Currents.

IEEE, Montreal, Quebec, Canada, 2015

[SHE16] Sheng, Shuangweng: Wind Turbine Reliability Database, Condition Monitoring, and Operation and Maintenance Research Update.

NREL, Golden, Colorado, United States, 2016

[STE22] Steinweg, Florian: Formation of White Etching Cracks under electrical current flow - Influence of load, slip and polarity.

In: Wear, 504/505, 204394, 2022.

Elsevier Science, Amsterdam, 2022

[ZIE05] Zitzelsberger, Johann, Bearing Currents in Doubly-Fed Induction Generators.

IEEE, Dresden, Germany, 2005.

[ZWE24] Zweiffel, Maximilian: Experimental Characterization of Common-Mode Voltages and Currents in Gearbox Bearings of a Doubly-Fed Induction Generator Wind Turbine on a Test Bench.

Journal of Physics: Conference Seriees, 2767, 042034.

IOP Science, Florence, Italy, 2024.

Digitalization and Artificial Intelligence

Wind Turbine Gearbox Digitalization Trends and Case Studies to Lower the Cost of Energy

D. Guthrie[1], K. Pelka[1], T. Theis[1], A. Silva[1], C. Keerthisinghe[1], P. Tardaguila[1], M. Ivanovl[2], D. Bijnens[2], J. Peeters[2]

[1]Vestas Wind Systems [2]ZF Wind Power

Keywords: Digitalization, Data Science

Abstract:

With a growing installed base and an ageing fleet, the wind industry will be confronted with increased challenges in optimizing the value of wind turbines throughout their entire lifecycle, including higher demands in Operations & Maintenance. It is the ambition to meet these challenges in future with full value chain optimisations towards high reliability, low OPEX, increased energy output and extended lifetime. Digitalization, which is about connecting, aggregating and analyzing data into actionable insights, will play a crucial role in this future.

Vestas and ZF present in this paper jointly the opportunities & challenges of adopting digitalization across the full value chain based on two exemplary case studies. Opportunities to lower the cost of energy are identified in design parameters and operation & maintenance actions. Challenges are related to demonstrating business value, data availability, quality and standardization, and merging subject matter expertise with data analytics.

Two concrete case studies are thoroughly worked out and successfully demonstrate the added value of digitalization across the value chain:

- Case Study #1 demonstrates how the use of actual tooth flank roughness values after gear grinding combined with actual kinematic oil viscosity values from operational wind turbines in a probabilistic evaluation method identifies a higher reliability potential in the gear pitting failure mode.
- Case Study #2 demonstrates how the combination of gearbox manufacturing data and wind turbine operational data for an operating fleet of more than 2000 wind turbines significantly improves the forecasted failure probability related to high-speed shaft (HSS) bearing spalling. To this end, methods from survival analysis are used.

Both case studies demonstrate how the combined utilization of data across the value chain contributes to improve reliability, which provides the basis to derive actionable insights for the full wind turbine lifecycle.

1 Introduction and Motivation

Main gearboxes in wind turbine generators are a significant factor in turbine design and economic performance of wind power plants. Using digital technologies to improve gearbox designs or predictability of gearbox behaviors can improve the OPEX modelling throughout the turbine operational lifetime. Vestas and ZF are adopting digital initiatives, at an enterprise level, to enable optimizations across the full wind turbine value chain. However, challenges exist to deploy digitalization into normal business processes for wind turbine gearboxes.

Vestas and ZF together investigated two case studies to evaluate the potential value and impacts of digitalization in the full value chain of wind turbine gearboxes.

2 Problem Statement

Despite the availability of various digitalization solutions at an enterprise level, there exist challenges to adopting digitalization techniques into daily business, as shown in Figure 2-1. As organizations are committing to digitalization initiatives the various business departments might be responsible to create roadmaps to integrate digitalization into technical and business processes. Utilizing smaller digitalization case studies can support roadmap creating by quantifying uncertainties and identifying potential constraints.

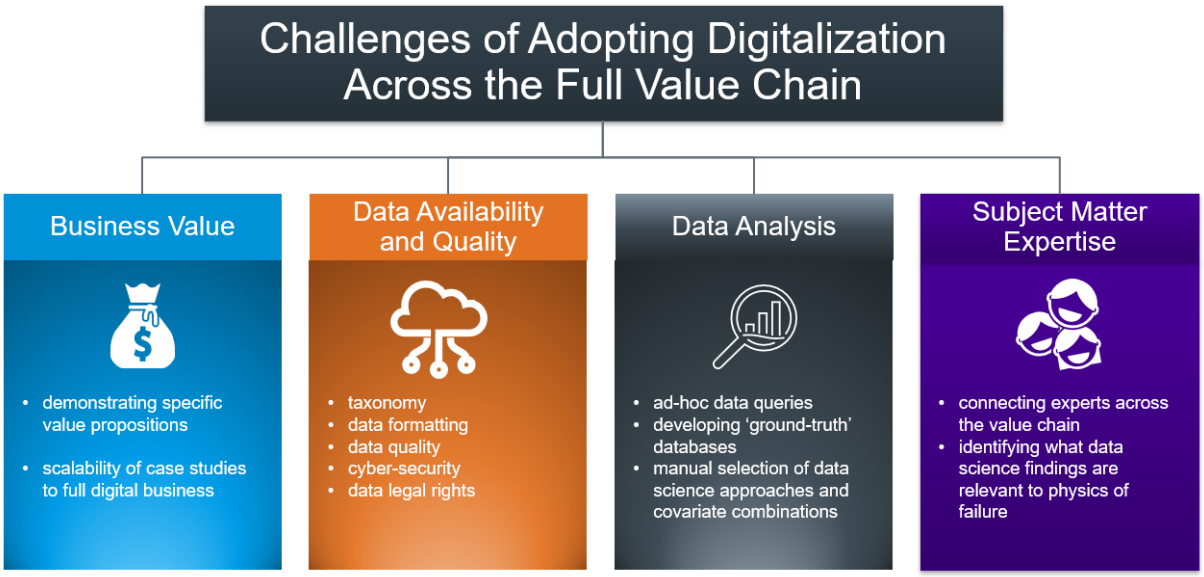

Figure 2-1: Digitalization challenges

3 Methodology

Vestas and ZF have collaborated to identify and investigate case studies from which the benefits and challenges related to integrating digitalization might be quantified. In general, the case studies were selected using several criteria, including:

- Substantial data sets including turbine population, operating gage, manufacturing data
- Stability in turbine population (limiting sub-populations due to changes in design, manufacturing, operating environment, etc.)
- Presence of manufacturing and operational data typically not shared between organizations

- Utilization of common data science techniques and methods (data science model validations are not included in the scope of this project)

After selection of case study topics, the method for investigation typically followed these steps.

1. Identify objectives and scope for the investigation
2. Evaluate data availability and quality
3. Define data analysis techniques
4. Involve relevant subject matter experts across the value chain to measure results.

Additionally, some definitions related to digitalization were adopted for use in the business cases as described in Figure 3-1.

CASE STUDIES

Digitisation	The process of converting information into digital signals, enabling digitalisation (Rachinger et al., 2019).
Digitalisation	The organisational and industry-wide use of data and digital technologies to improve efficiency, create insights, and develop products and services.
Digital transformation	The holistic process which integrates and adopts digitalisation on societal levels (Mergel et al., 2019).
Digital businesses	Businesses that incorporate digitalisation into their activities and derive a significant part of their turnover from digital products and services.

https://doi.org/10.5194/wes-8-947-2023

Figure 3-1: Selected definitions adopted for the case studies

4 Case Study #1 – Probabilistic Methods

4.1 Scope and Objectives

This case study compares two methods for estimating gearbox component reliability related to an individual component failure mode. The methods considered are a deterministic method based on calculation of lifetime safety factors and a probabilistic method sampling from representative distributions of calculation factors. The scope includes development of a framework for probabilistic analysis and selection of a gearbox failure mode for which sufficient data exists to approximate the probability distributions of calculation factors. For this case study the gear pitting failure mode was selected and the relationship of the available calculation factors to the component reliability are described in the ISO 6336-2 gear rating calculation standard.

4.2 Evaluate Data Availability and Quality

ZF has digital records of the as-manufactured gear flank roughness and provided data representing approximately 2000 gears. Vestas collects periodic gear oil samples from operating turbines which are analyzed in a laboratory and provided the measured kinematic viscosity from several thousand turbines. Both sample sets were extracted from internally managed databases. Oil sample data required some effort to eliminate outliers caused by known sources of error, for example mislabeling of hydraulic oil samples as gear oil.

4.3 Data Analysis Techniques and Results

A Monte-Carlo approach was used to sample values of flank roughness and oil viscosity from the probability distributions and a gear pitting safety factor was calculated for each simulation iteration. The mean simulated safety factor was 4.6% percent higher than the calculated design value, related to a 36% reduction in failure rate at design life (when calculated using an approach similar to the reliability calculation method in AGMA 6006-B20). Furthermore, 96% of the simulation results had safety factors equal to or greater than the design value. These results indicate a reliability margin in the operating gearboxes from which commercial value could be extracted, for example by increasing the power output or extending the lifetime.

5 Case Study #2 – Digitalization Pilot

5.1 Scope and Objectives

The objective of this case study, a digitalization pilot project, is to evaluate the potential benefits of applying data science and/or machine learning techniques to a gearbox failure with an inconclusive failure initiation. The scope is to apply established and validated data science and machine learning techniques to the large data set and consider the findings beyond a typical root cause analysis currently performed in the industry.

5.2 Evaluate Data Availability and Quality

The gearbox model for this pilot project was chosen based on the selection criteria mentioned in Chapter 3. The selected gearbox is a model found in the Vestas 2MW global turbine fleet. Vestas installed approximately 3400 gearboxes of this model in many variants of the 2MW turbine fleet (see Figure 5-1) featuring various rotor diameters, generator and converter technologies, turbine control strategies, and geographical regions. The quantity of turbines considered in the investigation was significantly lower than the operating fleet due to data access and quality issues.

Underlying Basis

Data streams
▪ Configuration / master data ▪ Failure data (referred to as CIM) ▪ Operating data (SCADA 10min averages, events, accumulation) ▪ Manufacturing / assembly data

Investigated assets	
Turbine types	V80-V100 1.8/2.0 MW
Mk versions	Mk2- Mk7
Gearbox type	Bosch Rexroth GPV 442
Total number of investigated GBX	2088
Operating sites (SBU Region)	AME, APC, LAT, MED, NCE

Underlying Failure Basis

Investigated failure type	**Total number of failures**
Spalling of unknown origin but suspect links to Fatigue +/o WEC +/o Smearing	150
Operating Fleet of ~3000 GBXs	

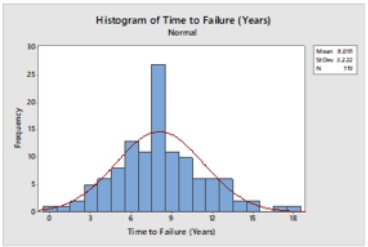

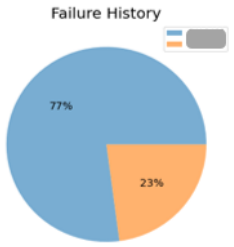

Figure 5-1: Data sets

Vestas maintains a database of high-speed bearing failures in operating turbines. The failure mode considered is raceway spalling and, while the failure initiation is inconclusive (e.g. fatigue, white etch cracking, smearing), it is suspected that bearing clearance could be a contributing factor. ZF had access to the as-assembled bearing installation and clearance data for a majority of the delivered gearboxes, including some of the older records being handwritten.

5.3 Data Analysis Techniques

A series of data analysis approaches were used in order of increasing complexity (see Figure 5-2), such as log rank test, Kaplan-Meier estimators, Cox proportional hazards, and a classification model. The investigations and multi-variate combination were manually guided based on findings from univariate analyses and based on the subject matter expertise. A future opportunity exists to automate the analyses, particularly if a parameter is identified around which to optimize.

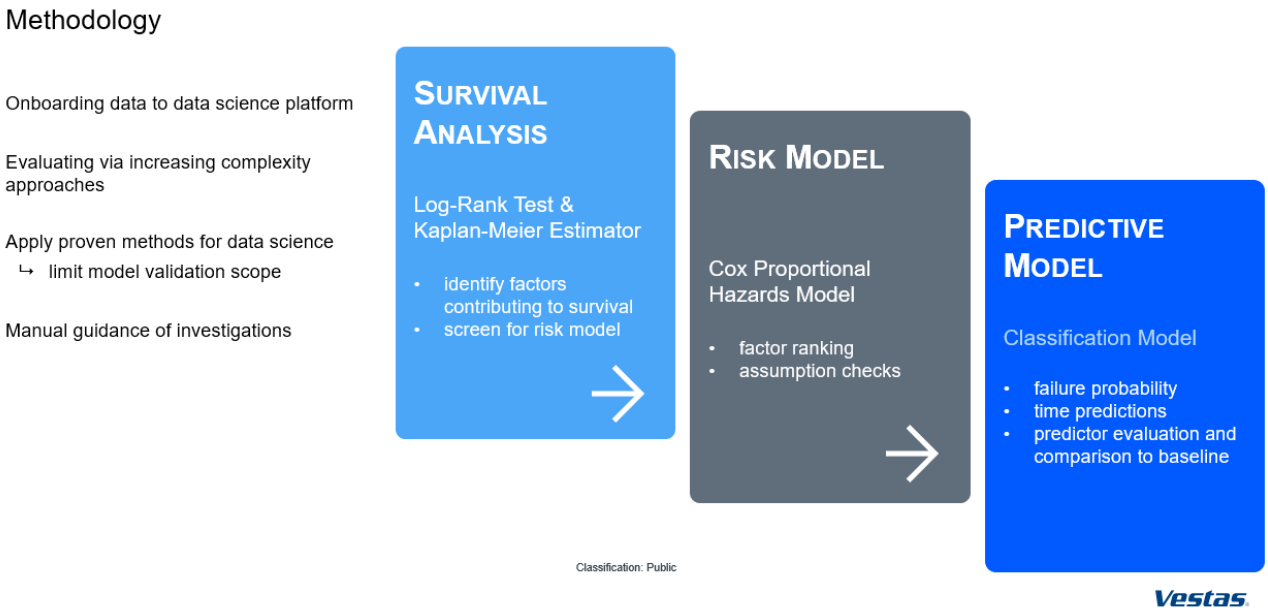

Figure 5-2: Data set analysis methodology

5.4 Data Analysis Results

Kaplan-Meier estimators with log-rank test p-values identified contributing factors which had statistically significant influence on the survival probability of the gearbox. Univariate investigations were typically split by category or by percentiles when numerical data was available; 20^{th}, 50^{th} and 80^{th} percentiles were typically used without attempting to optimize for log-rank test p-value (see Figure 5-3). Findings from the univariate investigations guided multivariate combinations, several of which resulted in statistically significant relationships to survival probability. Furthermore, those combinations could maintain statistical significance while identifying focused risk populations, thus increasing the potential for deploying mitigations in the latter portions of the value chain (e.g., Service upgrade). In one specific combination, considering the spacer width and bearing operating temperature, a risk population of 59 operating turbines was identified from the study population of 2088 turbines (see Figure 5-4).

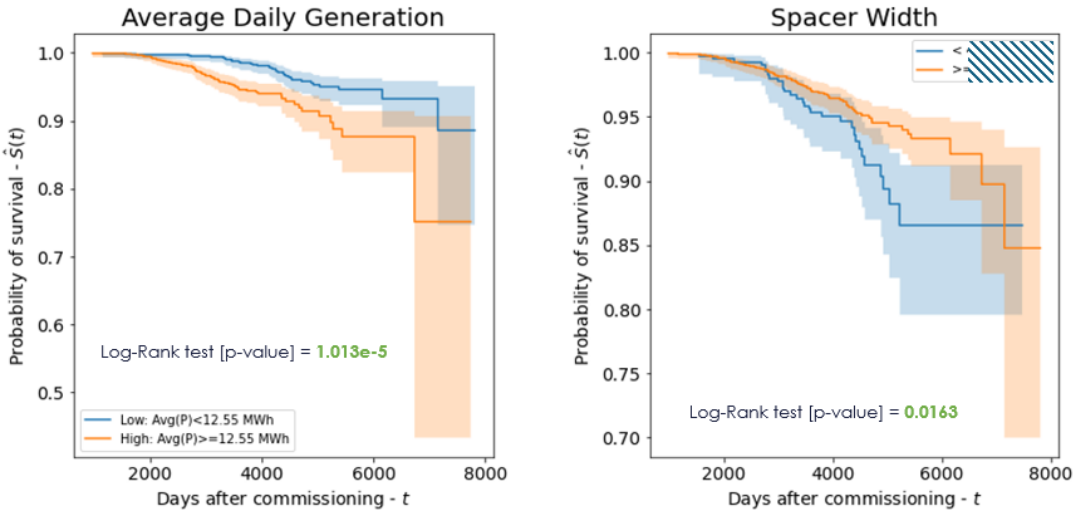

Figure 5-3: Kaplan-Meier estimator – univariate factors from operation and manufacturing

Combination of spacer width and bearing temperature is very statistically significant

High Risk populations (orange curve)

Spacer Width	0 - 20th percentile
Bearing Temperature	80th - 100th percentile

High-Risk population still operating:

59 of 2088 total WTG

Focused risk population improves feasibility of various mitigation options (in progress)

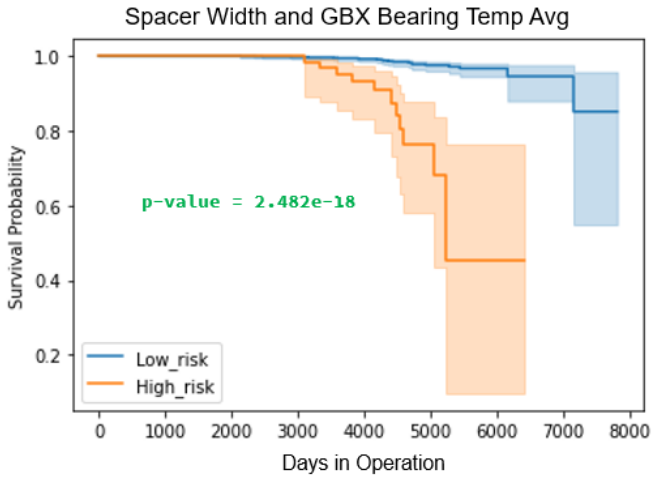

Figure 5-4: Kaplan-Meier estimator – bivariate factors

The Cox Proportional Hazards model provided insight about the relative importance of various factors considered in the analysis (see Figure 5-5). Results of the model indicated some anticipated findings but also revealed some influencing factors which were previously not considered. Of particular interest is the complement of data sources represented in the top-5 covariates rankings; there is a factor from each major area of the value chain (manufacturing, configuration, and operation) which demonstrates the importance of an open and collaborative data set. This point is further emphasized by comparing the model's performance when it is informed with the manufacturing data. Several model performance metrics are reported, demonstrating that access to the manufacturing data improves the ability to predict the risk of failure in the operating population (see Table 13).

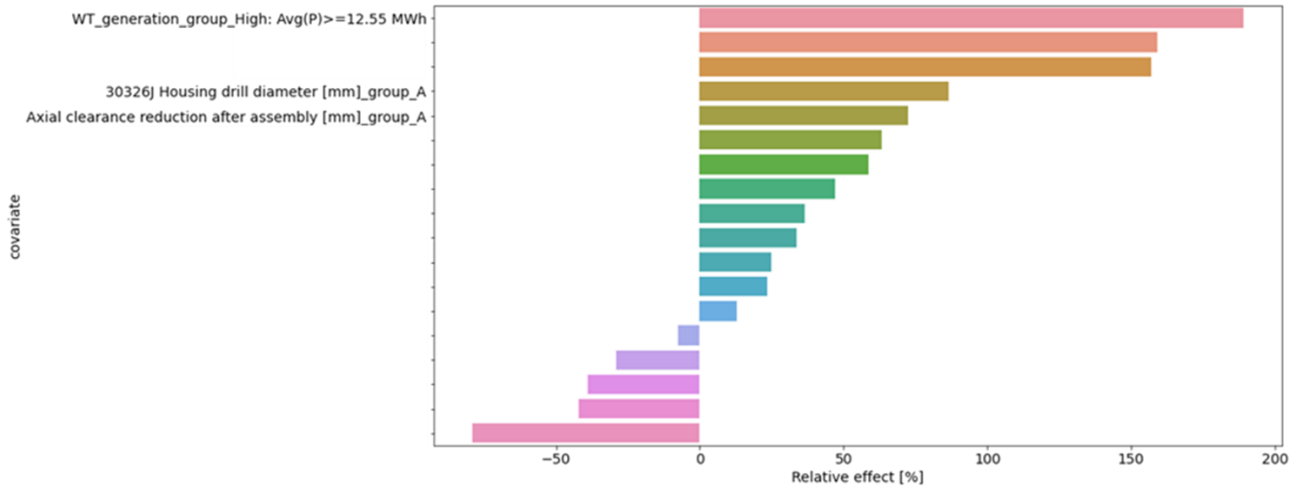

Figure 5-5: Covariate relative effects on survival probability

	Model 1	Model 2
Operational / Configuration covariates	**YES**	**YES**
Manufacturing covariates:	NO	YES
Performance metrics:		
Partial log-likelihood [Obj -> Maximize]	-643.94	-635.35
Concordance index [Obj -> Maximize]	0.74	0.76
Partial AIC [Obj -> Minimize]	1333.87	1326.69

Table 13: Model performance comparing the inclusion of manufacturing covariates

The investigations demonstrate the value of combining manufacturing, configuration, and operational data to build more effective models for failure prediction and to provide new information about failure modes.

The number of unique gearbox failures in the subject population was sufficient to identify several important risk factors which improve the ability to identify small gearbox populations at elevated risk of failure and significantly improve the ability of a binary failure model to discriminate between false positives and true positives across the entire gearbox population. These capabilities are of potential value in reducing service costs.

The identified manufacturing risk factors are involved in setting bearing clearance. It was further found that these risk factors are correlated with elevated operating temperature of the bearing prior to failure. Elevated operating temperature is a well-known signal of pending bearing failure, but the strong correlation with certain manufacturing parameters was not known prior to this study. This and other findings demonstrate the ability to improve the understanding of failure in our subject gearboxes and other gearboxes of similar design.

6 Summary and Conclusion

The case studies presented herein identify quantifiable commercial and technical value that is directly related to the use of digitalization approaches on wind turbine gearboxes. Large data sets, particularly from across the gearbox value chain, highlighting the benefit of collaboration between and within organizations. Solving data access and quality issues can be a substantial task and must be considered when planning a digitalization project. Industry standardization of data taxonomy and data science analysis methods will improve scalability of digitalization. Adoption of digitalization approaches into daily business and across the gearbox value chain can improve important techno-commercial metrics like decision time and decision accuracy.

7 Bibliography

[COX72] Cox, David R:"Regression Models and Life-Tables".
In:Journal of the Royal Statistical Society, Series B. 34 (2): 187–220
JSTOR 2985181, MR 0341758, 1972

[KAP58] Kaplan, E. L.; Meier, P. (1958). "Nonparametric estimation from incomplete observations".
In: J.Amer. Statist. Assoc. 53 (282): 457–481
doi:10.2307/2281868, 1958

[MAN66] Mantel, Nathan: "Evaluation of survival data and two new rank order statistics arising in its consideration"
In: Cancer Chemotherapy Reports. 50 (3): 163–70
PMID 5910392, 1966

[POL20] Pölsterl, S: “scikit-survival: A Library for Time-to-Event Analysis Built on Top of scikit-learn,”.
In: Journal of Machine Learning Research, vol. 21, no. 212, pp. 1–6
2020

[CLI23] Clifton, Andrew, et al: Grand challenges in the digitalization of wind engery.
https://doi.org/10.5194/wes-8-947-2023
2023

DIGIT-BENCH Digital Twin: Advancing the Large-Scale Testing Facilities for the Wind Industry

Elif Ecem Bas[1], Giuseppe Abbiati[2], Claudio Gomes[3], Uwe Jassmann[1], Sebastian Engelsgaard[4]

[1]R&D Test Systems A/S, Sigma 3, 8382 Hinnerup, DK

[2]Aarhus University Department of Civil and Architectural Engineering, Navitas – Inge Lehmanns Gade 10, 8000 Aarhus C, DK

[3]Aarhus University Department of Electrical and Computer Engineering, Finlandsgade 22, 8200 Aarhus N, DK

[4]Lindø Offshore Renewables Center (LORC), Lindø Sydvej 30, 5330, Munkebo, DK

Keywords: tight coupling, digitalization, digital twins, co-simulation

Abstract: The wind industry heavily relies on experimental testing to ensure reliable and cost-effective technology. However, for large components, these tests become lengthy and expensive. For example, fatigue testing of a wind turbine blade can take 12-14 months, and a highly accelerated lifetime test of a nacelle can take 6-8 months. It is estimated that a considerable amount of testing time could be saved by simulating test sequences using digital twins before testing. As obvious as this may seem, creating a suitable simulation, which includes high-fidelity Device Under Test (DUT) and test bench models, is a technical and organizational challenge.

A major barrier preventing the adoption of digital twins is that OEMs and test facilities are hesitant to share their digital models with each other. Especially when it comes to the drive train test benches, where the components are tightly coupled. To overcome this barrier, a digital twin framework that allows for coupling models in an industrial-secret-friendly environment is being developed in the DIGIT-BENCH project funded by the Energy Technology Development and Demonstration Program (EUDP). The DIGIT-BENCH digital twin is based on co-simulation, as described in the functional mock-up interface (FMI) standard. The current development focuses on dynamically simulating the test bench and the DUT models represented by two functional mock-up units (FMUs). A tight coupling scheme enforces the two-way interaction of these models. This contribution showcases the DIGIT-BENCH digital twin through a demonstrator based on the 16 MW nacelle testing facility of the Lindø Offshore Research Center, Denmark, and anticipates the direction of future developments.

1 Introduction

Wind turbines (WTs) are increasingly being designed in larger sizes to reduce the Levelized Cost of Energy (LCOE). To ensure the reliability and cost-effectiveness of this technology, full-scale testing of wind turbine components is crucial for both manufacturers and suppliers. While these tests are essential for advancing the wind energy sector, they are often time-consuming and costly. To improve quality while reducing costs and time-to-market, it is essential to enhance testing methods and ensure the cost-effectiveness of test campaigns. This can be done by utilizing both simulation models and incorporating data from experiments and simulations. In addition, training personnel and conducting test rehearsals often hide significant risks that could potentially harm the test bench.

To address some of these challenges and enhance the functionality of the Nacelle test benches, Clemson University implemented system-level simulations at their Wind Turbine Drivetrain Testing Facility [SCH13], where similarly, the system-level virtual models of the Dynamic Nacelle Testing Laboratory (DyNaLab) have been developed at Fraunhofer IWES [SID24].

Digital Twin (DT) technology connects physical assets with digital counterparts by creating digital mock-ups using Internet of Things (IoT) technology. By incorporating DT technology into test benches in the wind industry, we can develop a virtual representation of these physical systems. This provides several advantages that a physical asset alone cannot provide. Such as real-time monitoring and analysis for predicting anomalies, simulations of various scenarios for safer operations, and the identification of the most relevant and effective experimental conditions. These cases define the purpose of the DTs, meaning a DT can be developed based on its specific use case. These use cases are often referred to as applications. As a result, the DT improves the test bench's operation and maintenance (O&M) with different applications. Moreover, integrating the test bench with digital models from a DT facilitates hybrid numerical-experimental testing methods, such as virtual testing [SID24] and hardware-in-the-loop testing [JAS18], in addition to supporting O&M activities.

One of the main challenges in implementing DTs for large-scale test benches in the wind industry is the involvement of several stakeholders. For instance, a DT framework that supports planning an experimental campaign requires exchanging simulation models and data between Original Equipment Manufacturers (OEMs) and the testing facility. Such a DT framework will use simulation models for more valuable, higher quality, and cost-effective testing. However, this potential is not pursued efficiently due to intellectual property (IP) rights. To address this challenge, R&D Test Systems and Aarhus University are developing a DT framework called DIGIT-BENCH DT for LORC’s 16 MW Nacelle Test Bench. The DIGIT-BENCH DT utilizes co-simulation, as defined by the FMI standard [FMI25] to enable physical/digital substructure couplings.

Co-simulation is a simulation approach that involves the simulation of two or more subsystems. FMI-based co-simulation, on the other hand, provides a standardized and efficient method for coupling these subsystems. The FMI standard outlines the guidelines for encapsulating these simulation models in standardized containers called FMUs and specifies the process for exchanging signals between them. An FMU is a ZIP file containing either the binaries of a simulation model or the Application Programming Interface (API) required to interact with a physical system, such as a control system. Additionally, it includes an *.XML file that describes the input and output variables of the FMU. An FMU can be created using the FMU exporter from specific simulation software or programmed directly with existing software libraries such as UniFMU [LEG21].

FMI-based co-simulation enables industrial-secret-friendly simulations at either the FMU level or at the co-simulation level. FMUs can be exported as compiled model binaries, concealing the source code and preventing reverse engineering, while allowing for local co-simulation. Co-simulation can also occur online, enabling stakeholders to participate without physical access to all FMUs. These solutions protect models from disclosure among stakeholders, which is essential for safeguarding IP, especially for the DUT. Co-simulation is managed by an *orchestrator*, a middleware tool that initializes all the FMUs and coordinates their execution and data exchange according to the specific co-simulation *scenario*. In practice, MATLAB/Simulink is usually used as an orchestrator. This work implements co-simulation in FMPy [FMP25], a free Python library to simulate FMUs, and enables users to control the simulation execution, which is crucial in our use case.

This proceeding introduces the DIGIT-BENCH DT and presents the testing simulation tool that combines the test bench dynamic model with the DUT. This tool enables simulations of experimental campaigns before their execution. The large-scale demonstrator being developed is the LORC 16MW Nacelle Test Bench. Section 2 introduces the DIGIT-BENCH's DT architecture, Section 3 presents and showcases the case study and the Test Simulation application, and Section 4 draws conclusions and future perspectives.

2 DIGIT-BENCH DT

The block diagram of the DIGIT-BENCH DT is illustrated in Figure 6. The DT comprises three primary components: digital space, physical space, and the database. Physical space is a collection of physical assets, such as the drive motors, the Test Loading Unit (TLU), and the DUT. The digital space includes computational models that simulate or visualize the physical world, such as Finite Element Models (FEM) and Multi-Body Dynamics (MBD) for behavior prediction, along with Computer-Aided Design (CAD) and Building Information Modelling (BIM) for visualization. The database is utilized to store information from both physical and digital spaces. The DT is supported by the application toolchain, where the user interacts with the DT. It is important to note that the development stage of the DIGIT-BENC DT is currently a simulation DT based on the classification in [WAG20]. However, the aim is to reach the intelligent level by monitoring the physical space and updating the digital space accordingly.

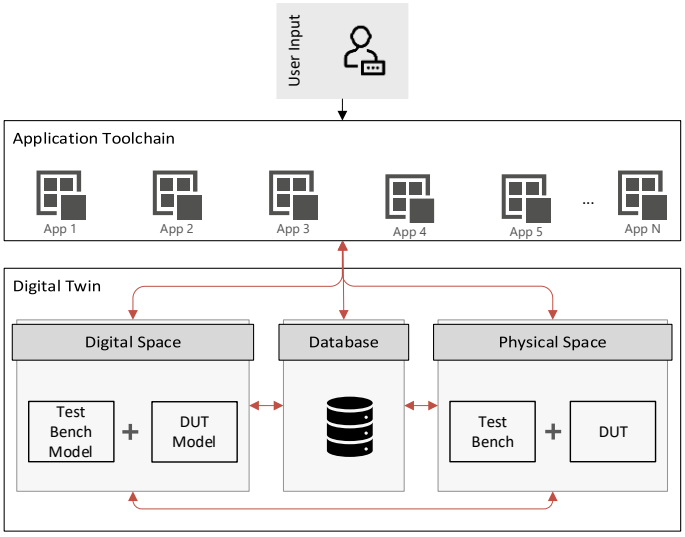

Figure 6: DIGIT-BENCH DT architecture.

The 16 MW Test Facility at LORC acts as the large-scale demonstrator for the DIGIT-BENCH project. R&D Test Systems designed and constructed the test bench, which LORC operates. The overview of the test bench is shown in Figure 7. The test facility is utilized for design verification and Highly Accelerated Lifetime Testing (HALT) of nacelles and drivetrain components, including gearboxes and main bearings. The drive motor system can deliver up to 15 MNm of torque, while the TLU can apply tilt and yaw moments of up to 25 MNm. This facility can conduct design verification for the most powerful onshore nacelles and drivetrain components in the 10 MW range.

The main components of the test bench are shown in Figure 7. The Test Bench's Drive Motors apply the torque signal to the coupled DUT generator. The non-torque loads, including tilt and yaw moments, thrust force, vertical force, and horizontal force, are applied to the DUT via the TLU, which the hexapod cylinders activate. In this physical asset, several stakeholders are involved. The OEM

provides the DUT and is reluctant to share their numerical models or testing results. Moreover, the test bench operator does not necessarily have the dynamic models of the test bench substructures. As a result, securely sharing data and integrating models are crucial when implementing the proposed DT architecture that is shown in Figure 6.

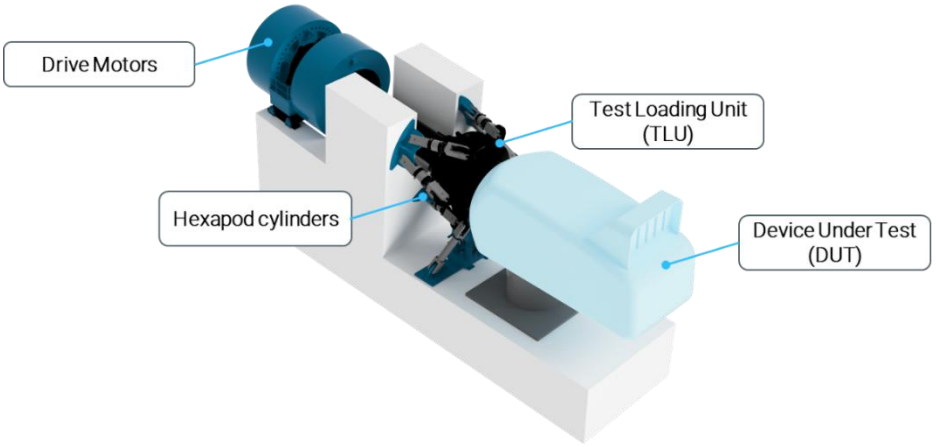

Figure 7: Overview of the LORC 16MW Test Facility.

3 Case Study: Test Simulation Application

This proceeding's focus application is the *Test Simulation Application*, which simulates a coupled test bench and DUT response for selected variables. This application enables users to simulate test sequences before the experiments, ensuring secure and effective testing. Understanding the desired test sequence's dynamic response helps the test bench operator and the OEM better plan and execute the experimental campaign. As a result, this can decrease the chances of conducting experiments that do not provide useful information.

A system-level dynamic simulation of the test bench and the DUT is essential for predicting performance capabilities. If the simulation models of these substructures are available to all parties involved, all components can be integrated into a *Monolithic System*. The Test Simulation Application facilitates the creation of a *Coupled System* through FMI-based co-simulation, enabling two or more substructures to interact and influence each other through their connections. Both systems are illustrated in Figure 8.

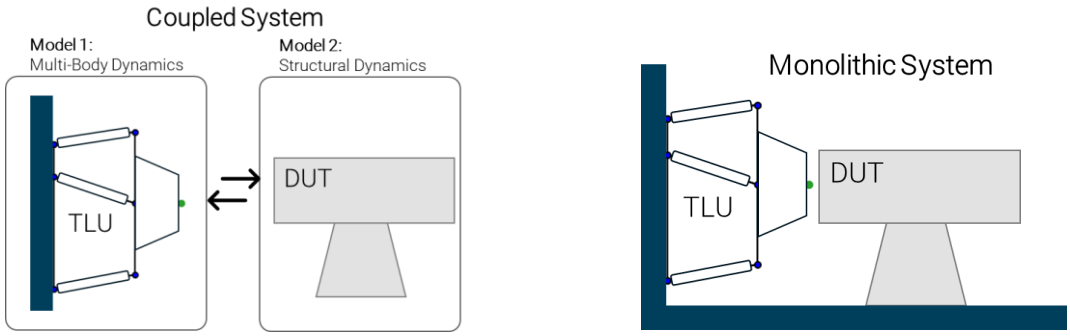

Figure 8: Monolithic and coupled system overview for the case study.

This case study focuses on the mechanical coupling between the TLU and the DUT, utilizing FMUs created for both subsystems: FMU-TLU and FMU-DUT. The two-way coupling demands displacement compatibility and force balance. A tight coupling algorithm has been developed and packaged

into the FMU-Coupling. In this section, we first introduce the MBD model of the TLU and the structural dynamics model of the DUT, followed by an explanation of the tight coupling algorithm for co-simulation. Finally, we compare the co-simulation results with those from the monolithic simulation model for validation.

3.1 TLU Model

The MBD model of the TLU was developed using SymPy [SYM25], a Python library for symbolic mathematics with a Mechanics module that simplifies deriving equations of motion for MBD systems using Kane's method. This method, utilized in commercial software like OpenFAST, minimizes symbolic complexity and facilitates the inclusion of nonlinearities through a focus on forces and torques. Consequently, we employed Kane's method for the MBD simulation model of the TLU.

The geometry of the TLU and the summary of the modeling steps are shown in Figure 9. As shown in the figure, the system consists of two main frames necessary for observing the motion of the TLU. The Inertia Reference Frame {B}, is a fixed frame that doesn't move with the TLU and where the actuator base joints are located. The Body Reference Frame {L} is the moving frame, where the Load Application Center (LAC) is. The model consists of 6 Degrees of Freedom (DOFs) located at the LAC and includes three translational and three rotational coordinates around x, y, and z.

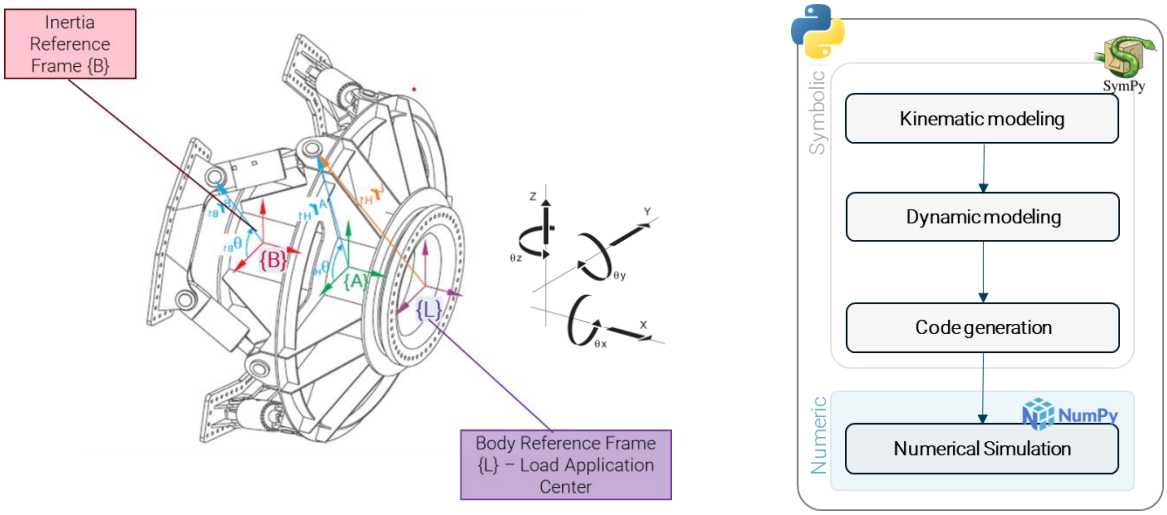

Figure 9: TLU geometry and summary of modeling steps in SymPy.

3.2 DUT Model

The DUT is simulated with a lumped parameter model implemented in Python. For simplicity, only the stiffness and mass matrix of the DUT is used to represent its structural dynamics response. A simplified linear elastic model for the DUT can be implemented, assuming a vertical cantilever beam. A simplified sketch in Figure 10 shows both undeformed and deformed TLU and DUT. The interface of TLU and DUT is shown in the green dot in the figure. The coordinate system of {L} is fixed to and moves with the TLU. The coordinate system {D} is colinear with the coordinate system {L} due to the rigid coupling between the TLU and DUT.

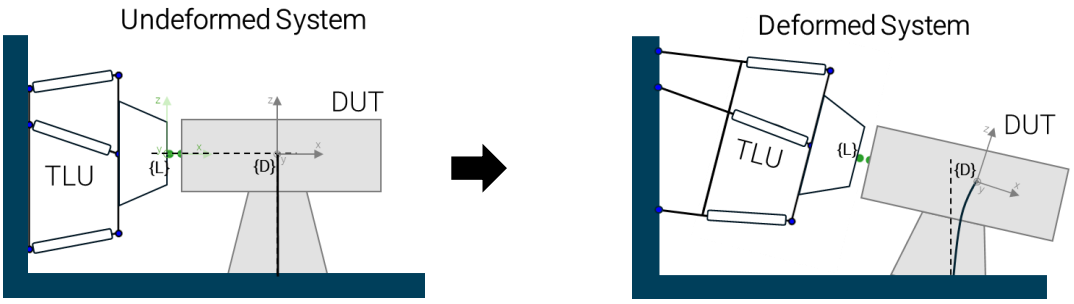

Figure 10: Deformation of the DUT when subjected to loading from the TLU.

3.3 Co-simulation with Tight Coupling

After implementing the models described in the previous sections, their FMUs are created using UniFMU [LEG21]. In this application, the FMUs have two-way coupling, in other words tight coupling. When FMUs are tightly coupled, kinematic quantities (displacement/rotation) are compatible, and corresponding forces are in equilibrium. This requires an orchestrator to accommodate iterations. This feature is not yet commonly available in orchestrators. Therefore, we implemented one in Python and controlled the FMUs via the FMPy [FMP25] module. Specifically, the orchestration algorithm adopts a partitioned FETI (Finite Element Tearing and Interconnecting) time integration algorithm. This method is particularly effective as it solves the coupling problem by only exchanging interface quantities [BUR17].

The following equations describe the dynamic response of TLU and DTU as nonlinear state-space models subjected to one-step-ahead time integration,

$$\boldsymbol{x}_{T,i} = h_T\left(\boldsymbol{x}_{T,i-1}, \boldsymbol{u}_{T,i}, \boldsymbol{f}_{T,i}\right) \qquad \textbf{Eq. 10}$$

$$\boldsymbol{y}_{T,i} = g_T(\boldsymbol{x}_{T,i})$$

$$\boldsymbol{x}_{D,i} = h_D\left(\boldsymbol{x}_{D,i-1}, \boldsymbol{u}_{D,i}\right) \qquad \textbf{Eq. 11}$$

$$\boldsymbol{y}_{D,i} = g_D(\boldsymbol{x}_{D,i})$$

where $\boldsymbol{x}_T, \boldsymbol{u}_T, \boldsymbol{f}_T$ are state vector, coupling force vector, and external load vector applied to the TLU, while $\boldsymbol{x}_D, \boldsymbol{u}_D$ are state vectors and coupling force vectors applied to the DUT; $h_T(\ \ )$ $h_D(\ \ )$ are state transition functions, $g_T(\ \ )$ $g_D(\ \ )$ are generic nonlinear vector functions that map state vectors into output response quantities y_T and y_D respectively. The coupling FMU solves one iteration of the interface problem as,

$$\begin{bmatrix} \mathbf{u}_{T,i} \\ \mathbf{u}_{D,i} \\ \mathbf{y}_{g,i} \end{bmatrix} = \begin{bmatrix} \mathbf{u}_{T,i} \\ \mathbf{u}_{D,i} \\ \mathbf{y}_{g,i} \end{bmatrix} - \begin{bmatrix} \frac{\partial \mathbf{y}_T}{\partial \mathbf{u}_T} & \mathbf{0} & -\mathbf{I} \\ \mathbf{0} & \frac{\partial \mathbf{y}_D}{\partial \mathbf{u}_D} & -\mathbf{I} \\ \mathbf{I} & \mathbf{I} & \mathbf{0} \end{bmatrix}^{-1} \begin{bmatrix} \mathbf{y}_{T,i} - \mathbf{y}_{g,i} \\ \mathbf{y}_{D,i} - \mathbf{y}_{g,i} \\ \mathbf{u}_{T,i} + \mathbf{u}_{D,i} \end{bmatrix} \qquad \textbf{Eq. 12}$$

where $\mathbf{y}_{g,k}$ is a vector of generalized interface displacement, $\frac{\partial \mathbf{y}_T}{\partial \mathbf{u}_T}$ and $\frac{\partial \mathbf{y}_D}{\partial \mathbf{u}_D}$ are the interface Jacobians of TLU and DUT, respectively.

The co-simulation block diagram is summarized in Figure 11. In this application, the test sequence, which is the input forces and moments time histories, should be applied to the DUT through TLU. The external forces, which is the actuator input in this case are calculated by using the TLU kinematics and packed together with the FMU-TLU. At each time step, both FMU-TLU and FMU-DUT

should be solved synchronously, and the outputs need to be inputted into the FMU-Coupling. The FMU coupling algorithm iterates the solutions until the of the system is reached. Once the iteration converges, the output of the coupling algorithm is sent to both FMU-TLU and FMU-DUT as inputs.

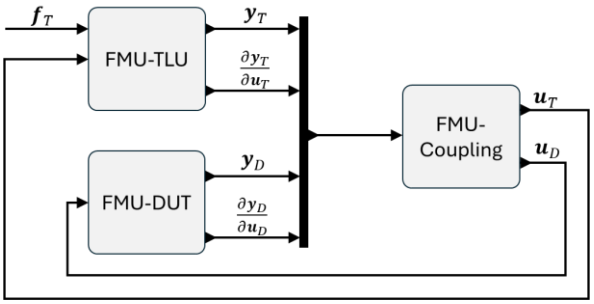

Figure 11: Block diagram of the co-simulation.

Figure 12 shows the verification of the coupled system simulation by comparing it with the monolithic DUT-TLU model. Coupling is solved with a fixed number of iterations (3). It should be noted that, for simplicity, only the translational DOFs are coupled. The coupled system's dynamic response agrees with the monolithic simulation models as seen from the displacement and velocity time histories.

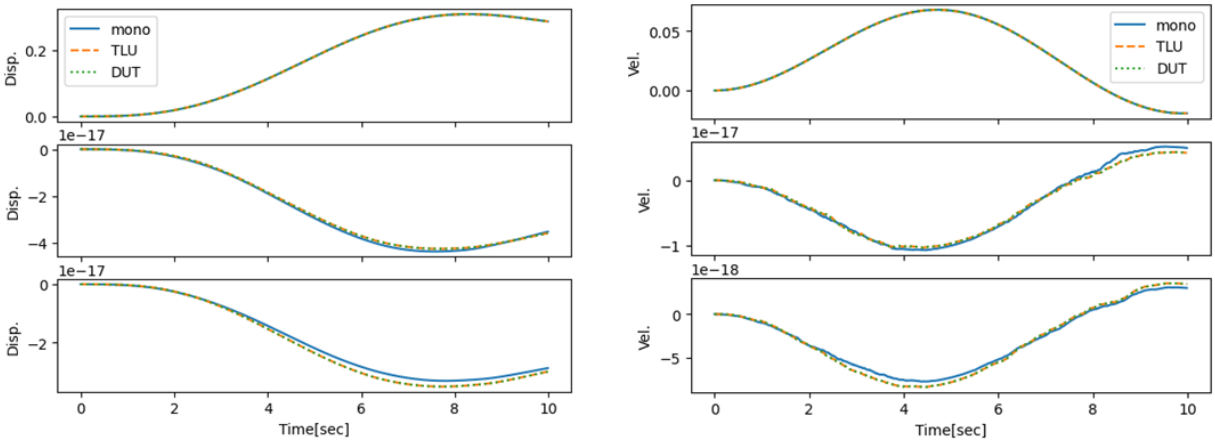

Figure 12: Verification of the coupling (monolithic vs. coupled)

4 Summary and Concluding Remarks

The development status of DIGIT-BENCH DT's Test Simulation Application is successfully developed and demonstrated using the 16MW LORC HALT Test Bench as a large-scale demonstrator. FMI-based co-simulation utilizes the DT as a collection of FMUs. A tight coupling algorithm is implemented and verified against the monolithic simulation. Python is used both in the model and orchestration level of this co-simulation.

The advantage of the proposed approach is that the inner state of each FMU is not shared but only the coupled response quantities, in line with the philosophy of exposing the least information. Moreover, stability and accuracy are ensured with few iterations. The downside is that interface Jacobian is needed, which might not be defined (e.g., in case of discontinuities in the state transition equations) or accessible. One drawback of using Python is computational speed. The development team believes that the stability and accuracy properties of the solution strategy based on FETI are worth investing in the computational optimization of the implementation by switching from Python to a compiled code (e.g., C++).

5 Bibliography

[SCH13] Schkoda, R.; Bulgakov, K.; Addepalli, K. C.; Haque, I.: System Level Dynamic Modeling Framework Being Developed at Clemson University's Wind Turbine Drivetrain Testing Facility.

Proceedings of the ASME 2013 Dynamic Systems and Control Conference. ASME, Palo Alto, California (USA), October 21-23, 2013.

[BUR17] Bursi, O.; Abbiati, G.; Cazzador, E.; Pegon, P.; Molina, F. J.: Nonlinear Heterogeneous Dynamic Substructuring and Partitioned FETI Time Integrations for the Development of Low-Discrepancy Simulation Models.

International Journal for Numerical Methods in Engineering. Volume 112, Issue 9. Pages 1253-1291. Doi: https://doi.org/10.1002/nme.5556. April 2017.

[SID24] Siddiqui, M. O.; Nejad, A. R., Pedersen E.: Virtual Model Application System of a Wind Turbine Nacelle Test Bench for Hybrid Test Applications.

ASME Journal of Dynamic System, Measurement and Control, Vol. 146(2): 021002 (9 pages). Doi: https://doi.org/10.1115/1.4063846. March 2024.

[JAS18] Jassmann, Uwe: Hardware-in-the-Loop Wind Turbine System Test Benches and Their Usage for Controller Validation.

PhD Dissertation. RWTH Aachen University, Aachen, 2018.

[WAG20] Wagg, D. J.; Worden, K.; Barthorpe, R.J.; Gardner, P.: Digital Twins: State-of-the-Art and Future Directions for Modeling and Simulation in Engineering Dynamics Applications.

ASME Journal of Risk and Uncertainty in Engineering Systems, Part B: Mechanical Engineering. Doi: https://doi.org/10.1115/1.4046739. May 2020.

[FMI25] Modelica Association. Address of the website (https://fmi-standard.org/)

(Date of Access: 26-01-2025)

[LEG21] Legaard, C. M.; Tola, D., Schranz, T., Macedo, H. D., and P. G. Larsen: A Universal Mechanism for Implementing Functional Mock-up Units. to appear.

SIMULTECH 2021. Virtual Event, 2021

[FMP25] FMPy. Address of the website (https://fmpy.readthedocs.io/en/latest/)

(Date of Access: 26-01-2025)

[SYM25] SymPy. Address of the website https://docs.sympy.org/latest/index.html

(Date of Access: 26-01-2025)

New AI approaches enabling Advanced Condition Monitoring of Wind Turbine Gearboxes

Sebastian Ortmann[1], Dr. Florin Tatar[2]

[1]ZF Friedrichshafen AG, Heinz-Paulisch-Straße 5, 97816 Lohr am Main, Deutschland

[2]ZF Wind Power Antwerpen B.V., Gerard Mercatorstraat 40, Lommel, Belgium

Keywords: Artificial Intelligence, CMS, Plain Bearing

Abstract: ZF Wind Power offers with Thrive a global service concept enabling continuous availability of wind turbines. Key in assuring availability is to avoid unplanned downtime and to proactively act for reducing consequential damage and high emergency repair costs. Therefore, it is crucial to have a reliable health assessment of wind turbine gearboxes which is done with monitoring their condition. The challenge is to combine many different condition parameters (vibrations, temperatures, speed, power, oil condition) into an algorithm, which should be highly sensitive to detect anomalies in a very early stage, without false positives. In special for plain bearing anomaly detection the challenge is even higher due to the lack of the condition monitoring technologies customized in the market. Therefore, ZF Wind Power is applying new AI supported algorithms in which expert product knowledge is combined with interpretation of data measured on test rigs as well as in the field. The plain bearing monitoring is one of the main focuses in the scope of the new AI tools.

The algorithm uses vibrations, temperature, speed and power as input. An AI model is trained with healthy data only. This model predicts normal behavior using the recent history of the mentioned signals. The deviation of this prediction to the measured signals is used as an anomaly indicator. Artificial synthetic failures and real test rig failure data were used to validate the model and to increase its sensitivity. Initially, the AI model used vibration time waveforms as input. To improve its performance and, especially, reduce false positives an alternative using data from the order domain was developed.

1 Introduction

As was highlighted in the abstract, the focus of the paper is to present a new Artificial Intelligence (AI) technology used for gearbox condition monitoring and with high applicability for the plain bearing failure detection. In 2023, within the same scope, during the CWD conference an analytical approach was introduced by ZF [ORT23]. The analytical approach is identified as a promising tool, but it still has some limitations, especially related to the speed of detecting an anomaly and the goal to eliminate false positive cases. Therefore, ZF has invested in the development of alternative condition monitoring tools using AI, with the objective to achieve a better accuracy for detecting a failure, but also to eliminate false positive alarms. Specific focus is on the detection of eventual failures of a plain bearing, which could progress faster compared to typical failures of other components.

This paper starts with a short summary of the analytical approach, continues with a detailed description of the AI approach and concludes with a comparison of both technologies.

2 Analytical Approach for anomaly detection using vibration measurements

In the CWD 2023 paper “Intelligent Powertrain for reducing LCoE in Wind Business” [ORT23] it was proposed to monitor plain bearings indirectly by tracking gear mesh frequency amplitudes.

Crucial for a reliable operation of a plain bearing is to have an adequate lubrication film. This oil gap defines the relative position of the planet in respect to the planet carrier in a planetary stage of a gearbox. During an eventual plain bearing anomaly, the oil gap could change, which will affect also the gear meshing. This slight change in the meshing will impact the vibration excitation and become visible in vibration measurements, particularly near the gear mesh frequencies. Therefore, it was proposed to track the gear mesh frequency amplitudes from vibration signals.

In this approach, the operating conditions, such as speed, torque (or power) and potentially temperature need to be considered as well, since they influence the gear mesh frequency amplitudes during normal operation. The analytical approach is used here as the benchmark for the AI approach introduced in Section 3.

The first step in the analytical approach is to calculate a Fast Fourier Transformation (FFT) in the angular domain, to get an order spectrum, i.e. a frequency spectrum of speed dependent frequencies. This is achieved by resampling the time equidistantly sampled acceleration to angular equidistant samples and calculating an FFT.

In the resulting order spectrum, local maxima are detected. These maxima are filtered so that only the ones within a margin around the gear mesh frequencies or their sidebands are stored and monitored over time.

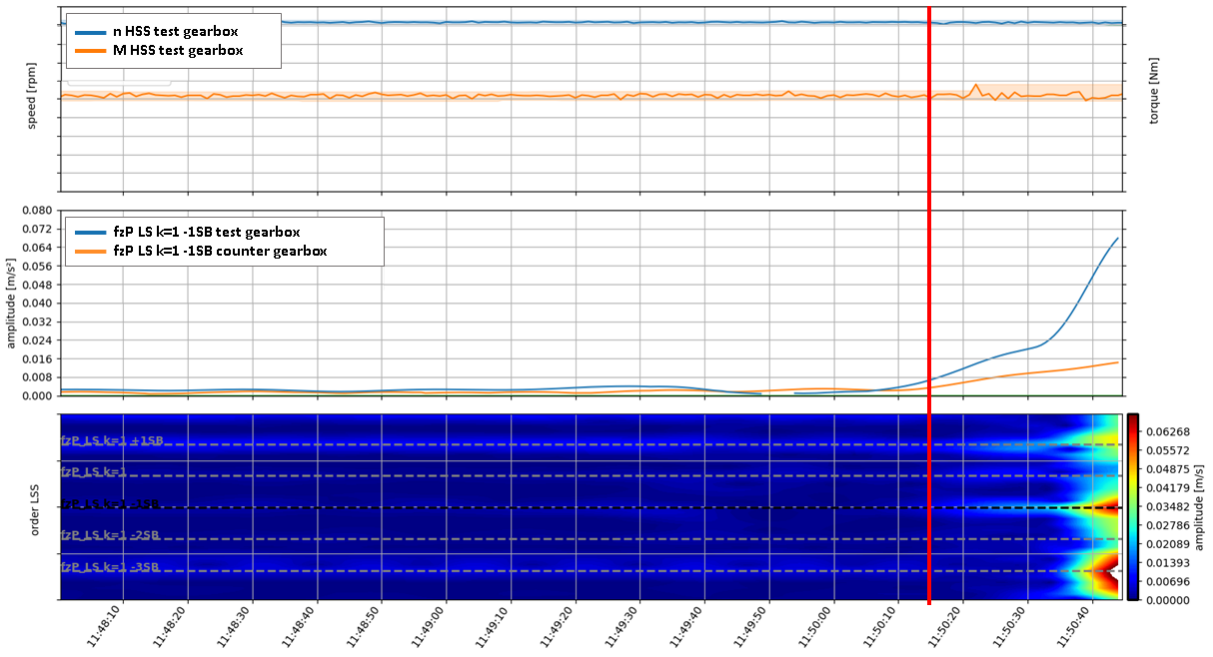

Figure 13: Order tracking of low-speed stage first negative side band (fzP LS k=1 -1SB) during a plain bearing anomaly

For each of these a nominal amplitude is determined for multiple speed and torque/power bins, based on historic measurements. From this historic data, a mean and standard deviation are derived

for each torque/power bin and for each mesh frequency or sideband. An anomaly is flagged when acceleration is observed that differs from the historic mean by several standard deviations.

3 Artificial Intelligence Approach for anomaly detection using vibration measurements

3.1 Artificial Intelligence Model

In the analytical approach, a large number of parameters need to be monitored (multiple amplitudes over multiple speed and torque/power bins). This becomes a complex task for a monitoring expert. Furthermore, the approach relies on the mesh frequencies and sidebands selected by the expert and the approach is blind to the remainder of the spectrum.

To tackle this complexity for the monitoring experts and additionally take the full spectrum into account rather than monitoring only specific pre-selected frequencies, the following AI approach is proposed.

The first step is the same as in the analytical approach, calculating an order spectrum. This order spectrum together with operational parameters, such as speed, torque/power, temperature, etc. are provided as input to a Convolutional Neural Network (CNN) that outputs a regenerated “normal state” order spectrum. The loss of the CNN is defined as the root mean square of the difference between the input spectrum and the output spectrum.

A comparison of this input and output spectrum as well as the difference between the two are shown in Figure 14. The scale of the difference graph (bottom) is the same as the scale of the spectra graph (top).

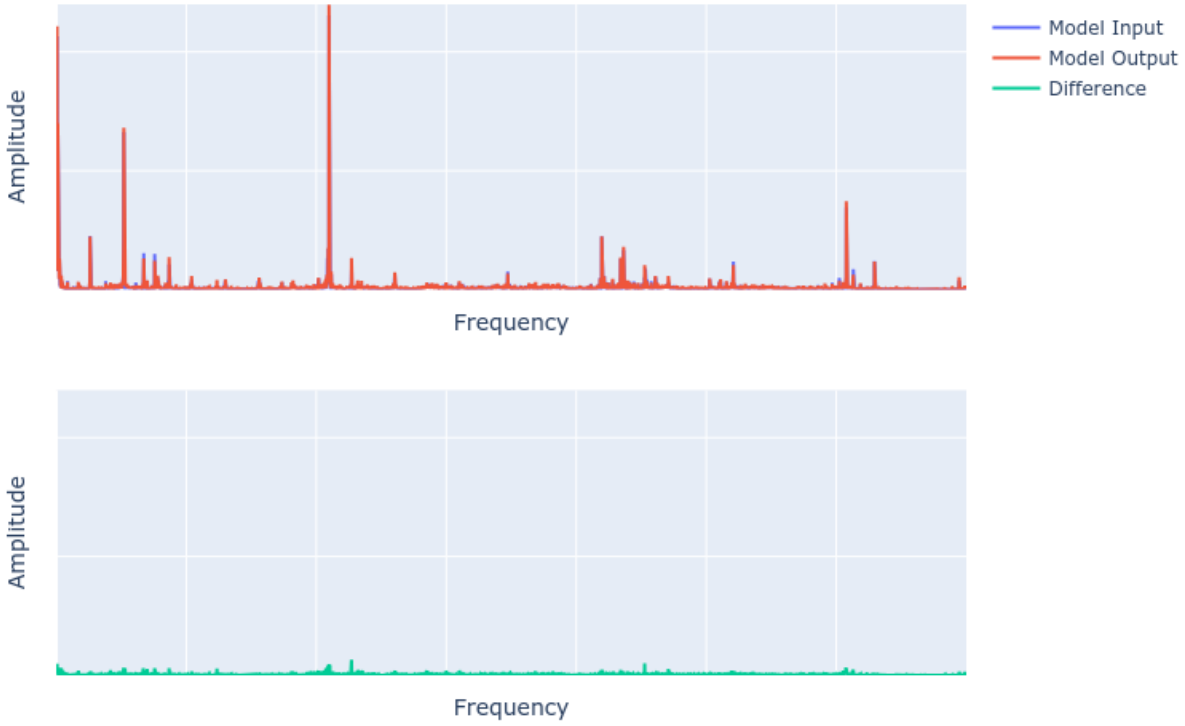

Figure 14: Comparison of input and output order spectrum of the CNN predicting the normal state (i.e. without an anomaly)

The CNN is trained with only healthy data to minimize this loss, so that when used for monitoring it is outputting the healthy spectrum. For condition monitoring the loss that is minimized in training is then used as an anomaly score.

Thresholds are defined for this anomaly score over speed bins, using Bayesian optimization (a common optimization method) on synthetic anomalies that mimic a plain bearing failure measured at a ZF test rig. The synthetic anomalies will be described in paragraph 3.2.

In a next step, a so-called Expert System is used. This system relies on the intuition that a true plain bearing anomaly should result in consistently anomalous spectra. That means, the binary result from the AI model (anomaly/healthy) is monitored over a time window and if a specific percentage of states within a rolling window are abnormal, an anomaly is flagged. The parameters for that rolling window and percentage are defined using Bayesian optimization.

3.2 Synthetic anomalies

For optimizing thresholds and benchmarking the approaches against another, time series of test rig measurements with synthetic anomalies were used. The synthetic anomalies mimic the measured behavior of a plain bearing failure on a test rig (see Figure 13). That means, some of the amplitudes of the frequencies proposed to monitor in the analytical approach, namely gear mesh frequencies, are increased.

First, the time series data is resampled angular equidistantly and bandpass filters on some gear mesh frequencies and sidebands are applied. The filtered signal is multiplied by factors that represent different stages of the observed test rig failure, to have datasets with different severity of an anomaly.

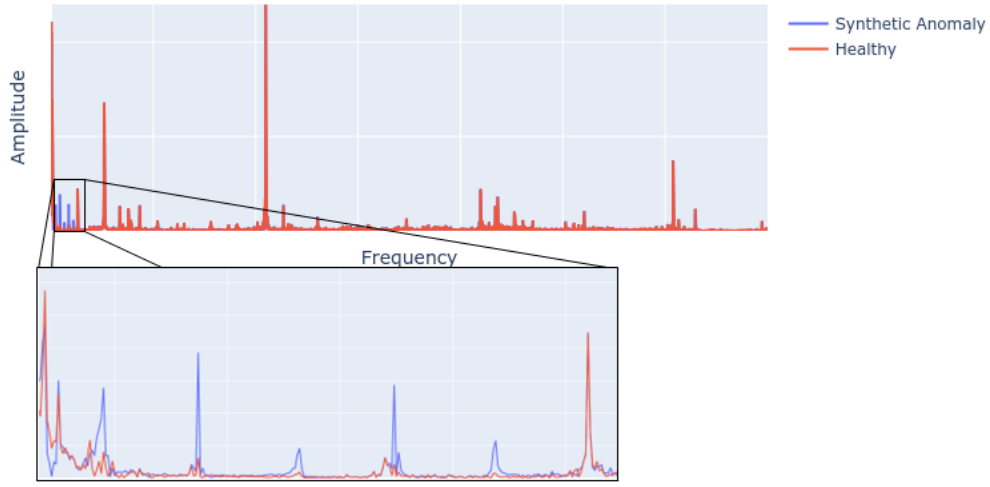

Figure 15: Comparison of an order spectrum for a healthy condition versus a condition where a synthetic anomaly is introduced

The filtered and scaled signal is then added to the original signal in the angular domain (see Figure 15) and, then, resampled back to the time domain (see Figure 16).

It is important to note, that Figure 15 is a theoretical visualization of the synthetic anomaly, to verify that the anomalies mimic the recorded plain bearing failure on a test rig.

In a possible field application, a spectrum can only be compared to prior spectra with similar operating conditions. This is due to the dynamic operation of wind turbines caused by the wind field variance. Therefore, prior spectra are always slightly different to one another. That means, the shown red line of Figure 15 and 4 are in practice areas, definable by mean values and standard deviations of the prior spectra.

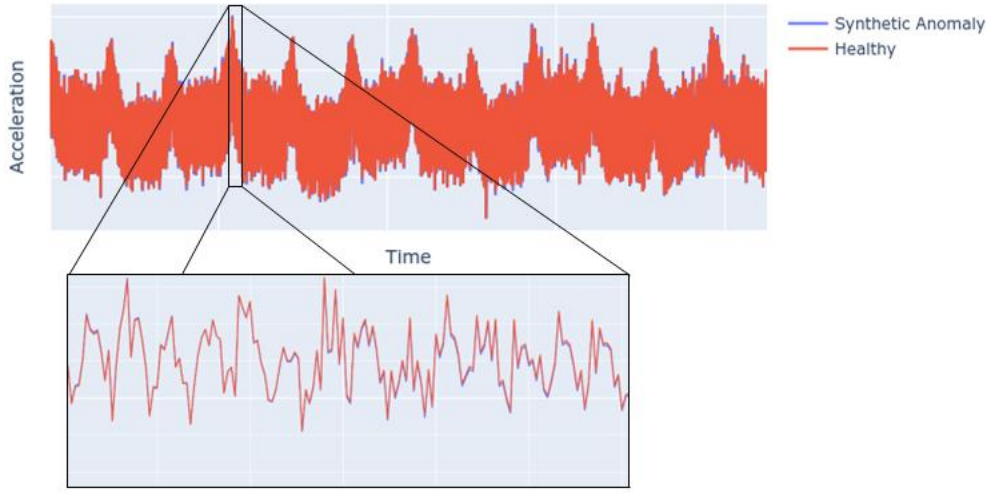

Figure 16: Comparison of healthy and synthetic anomaly time series

4 Comparison between Analytical and Artificial Intelligence Approach

Both the analytical and the AI approach were tested with the same dataset recorded in an extensive test rig campaign. The dataset was randomly split up into training and testing data.

The unaltered training data was used to train the CNN and to determine previously described nominal amplitudes for gear mesh frequencies (mean and standard deviation) for the analytical approach.

For both approaches, thresholds per speed (and for analytical approach also torque) bins are calculated with Bayesian optimization on synthetic anomalies. For the analytical approach this is one matrix per amplitude to track and for the AI approach a vector for the loss of the whole spectrum over the speed bins.

The testing data is used unaltered and altered, to have one unaltered testing dataset with healthy behavior and one with synthetic anomalies as described above. Both these datasets are used for testing the accuracy of the approaches.

The datasets are used independently, which means the CNN was not trained on either (altered or unaltered) test dataset. The same applies for the analytical model's calculation of the nominal amplitudes.

For the AI approach, this means that for each order spectrum the model needs to derive the healthy spectrum from the altered (synthetic anomaly) one without having been trained on the spectrum of exactly that operating condition. In Figure 17 it is visible that the model can do so, even with a severe anomaly as an input.

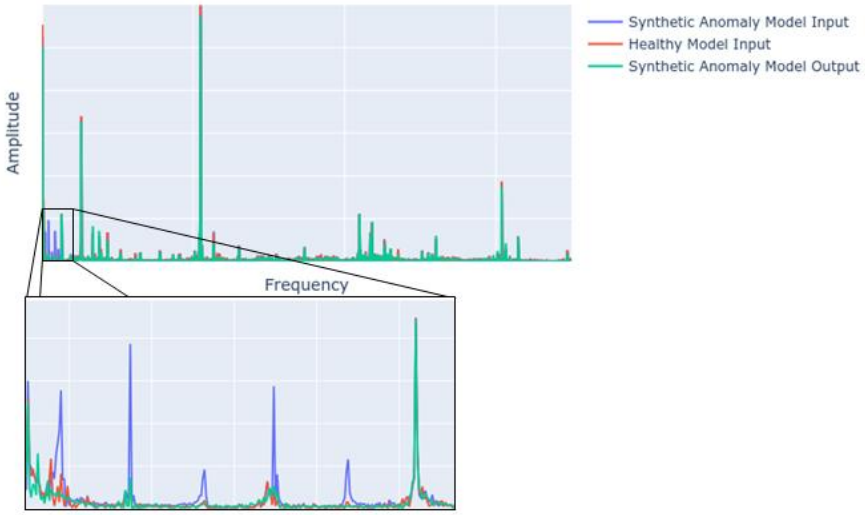

Figure 17: Comparison of synthetic anomaly CNN input and output and healthy CNN input

The unaltered (healthy) test dataset is then used to determine the false positive and true negative rate. True negative means flagging no anomaly in the healthy dataset, whereas false positive means flagging an anomaly in the healthy dataset. False positive rate is the number of false positive predictions divided by all predictions with a healthy dataset. True negative rate is the opposite of that.

The altered (synthetic anomaly) test dataset is used to determine the false negative and true positive rate. True positive means flagging an anomaly, whereas false negative means flagging no anomaly in the dataset which includes a synthetic anomaly. True positive rate is the number of true positive predictions divided by all predictions with a synthetic anomaly dataset. False negative rate is the opposite of that.

The accuracy is defined as the number of correct predictions (true positive and true negative) divided by the number of all predictions.

	Analytical	AI without Expert System	AI with Expert System
Accuracy	83.72%	91.35%	99.67%
True Positive Rate	91.94%	96.68%	97.09%
False Positive Rate	26.62%	8.69%	0.31%
True Negative Rate	73.38%	91.31%	99.69%
False Negative Rate	8.06%	3.32%	2.91%

Table 10: Comparison of accuracy rates for the analytical and AI approaches (with and without Expert System)

The positive/negative rates and accuracy show that the AI approach performs better than the analytical approach. Especially, the false positive rate shows a much better performance for the AI approach with an Expert System. The achieved low value of only 0.31% as false positive rate is very promising for this approach.

Both algorithms are still being further optimized.

5 Conclusion

ZF has developed an Artificial Intelligence approach to monitor plain bearings in a planetary stage using state of the art vibration sensors on the outside of a gearbox. Its performance is compared to a prior described indirect analytical approach monitoring gear mesh frequencies, which was proven to work for detecting a plain bearing anomaly on a ZF test rig.

The comparison was done using synthetic anomalies on test rig data introduced in the trained AI model, which mimic a plain bearing failure recorded on a ZF test rig. The new AI approach shows a better performance than the analytical approach, with a very low false positive rate of 0.31% being very promising for its applicability in real conditions.

An additional advantage of the AI approach is, that it is not necessary to predefine the frequencies that are expected to change during an anomaly.

Additional validation steps for the AI approach are ongoing on test rigs and in field conditions to proof its performance.

6 Bibliography

[ORT23] Sebastian Ortmann, Tobias Becker, Luk Geens, Laveen Prabhu Selvaraj, Joris Peeters, Florin Tatar: Intelligent Powertrain for reducing LCoE in Wind Business

In: CWD 2023 conference proceeding, Aachen

Framework for Developing AI-Driven Image Analysis Systems for Gearbox Endoscopy Inspections

Dr. Lars Osterbrink[1], Daniel Hein[1]

[1]LATODA @ Adoxin UG, c/o WindManShip, Katharinenstr. 4, 20467 Hamburg (www.latoda.de)

Keywords: Artificial Intelligence, Gearbox endoscopy, AI, Inspection automation, reliability engineering, gearbox condition monitoring.

Abstract: Ensuring the operational reliability of wind turbines requires early and accurate gearbox defect detection. Traditional manual assessments suffer from inconsistencies across large fleets. Inspections and interpretation of inspection images are subject to different opinions, human error, making the data inconsistent and inadequate for predictive maintenance, early detection of serial defects, and reliability engineering efforts. This study presents a structured artificial intelligence (AI)-driven framework for automating gearbox endoscopy assessments, improving defect identification accuracy, and streamlining maintenance planning.

The approach to create an AI system utilizes computer vision and machine learning to analyze endoscopic images, detect anomalies, and classify damage severity. Its development follows a rigorous scientific approach, including high-quality dataset creation, structured annotation, AI model selection, and performance validation using state of the art metrics.

The system reduced current problems of manual assessments, ensures scalability across large turbine fleets. This AI-based approach provides a cost-effective and efficient solution for gearbox condition monitoring, enhancing turbine reliability and optimizing long-term operational efficiency in the renewable energy sector.

Floating Turbine

Paper

Component Fatigue and Life Extension

Technical and physical investigations of used wind turbine gearbox oils - a perspective for lifetime lubrication?

Muyuan Liu[1], Gernot Bayer[1], Gerhard Poll[1], Max Marian[1, 2]

[1]Leibniz University Hannover, Institute of Machine Design and Tribology, An der Universität 1, Garbsen 30823, Niedersachsen, Germany

[2]Pontificia Universidad Católica de Chile, Department of Mechanical and Metallurgical Engineering, Vicuña Mackenna 4860, Macul, 6904411, Región Metropolitana, Chile

Keywords: *oil ageing, top-treat, oil additives, oil monitoring*

Abstract:

Modern geared wind turbines rely on the proper functioning of their lubricating oils to ensure optimum lubrication of their gear and bearing contacts. Potential oil ageing mechanisms, such as thermally accelerated oxidation or additive consumption, can degrade oil performance over time. An oil change should be carried out before the oil's performance has deteriorated to the point where it threatens the flawless operation of the gearbox components. This represents a significant risk to the economic viability of the wind turbine as a gearbox repair involves downtime and repair costs. At the same time, over-frequent oil changes are also costly and result in significant amounts of waste oil. For these reasons, an oil that provides consistently sufficient performance throughout the life of the turbine represents a prosperous opportunity to improve the economic and environmental performance of wind power. In order to ensure the prolonged durability of mechanical components, lubricants must provide stable and enduring protection. Thus, this study assesses the decay of anti-wear properties of oils sampled from wind turbine gearboxes with varying lifespans ranges from new oil to 16 years old oil.

In addition, artificial aging is performed to explore the longevity limit of oils by heating and reducing the concentration of anti-wear additives. Finally, the field-aged oil is treated with corresponding anti-wear additives to improve its performance and extend the lifespan of the oils. The general performance of oils is evaluated by the FZG test standard outlined in DIN ISO 14635-1. Additionally, the damage area on the gear surface is measured and used to quantitatively rate the performance of fresh oil, field-aged oil, and artificially aged oil. The method of artificial aging involves immersing steel balls in field-aged lubricant and placing them into an oven at 120 °C. During this process, anti-wear additives form a thermal film on the surfaces of the steel balls. After the specified period, the steel balls are removed from the lubricant. The thickness of the thermal film is then measured by the optical interference method and cleaned. Subsequently, steel balls are immersed in the lubricant again, and the process is repeated until a significant reduction in the thickness of the thermal film is detected. Although there is a positive correlation between the age of the lubricant and the resulting wear area, the results of the FZG tests show that all oils still meet the requirements of the standard. As for the artificial aging, the further aged field oils do not always lead to an increase in wear; in some cases, it may even reduce wear, despite a significant reduction in additive concentration.

Prognosis of Journal Bearing Wear Using Machine Learning-Based Surrogate Models for Predictive Maintenance

F. Wirsing[1], G. Jacobs[1], F. König[1]

[1]Institute for Machine Elements and Systems Engineering, RWTH Aachen University, Schinkelstrasse 10, 52062 Aachen, Germany

Keywords: condition monitoring, journal bearing, wear prognosis, four

Abstract: Predicting wear in journal bearings is crucial to ensuring the reliability and longevity of rotating machinery, particularly under start-stop conditions. During these operating phases, the lubrication regime transitions from full-film hydrodynamic lubrication to mixed-friction conditions, increasing wear rates. Traditional wear prediction models, which rely on numerical simulations based on tribological and mechanical principles, are often computationally expensive and impractical for real-time applications. This study proposes a machine-learning-based approach to efficiently predict wear in journal bearings. A dataset generated from a coupled mixed-elasto-hydrodynamic lubrication (mixed-EHL) and wear simulation model was used to train and evaluate three recurrent neural network architectures: Long Short-Term Memory (LSTM), Gated Recurrent Unit (GRU) and Nonlinear Autoregressive with Exogenous Inputs (NARX). Among these architectures, the NARX model demonstrated superior predictive performance, achieving high accuracy while maintaining computational efficiency. The model captured both long-term wear trends and short-term fluctuations, making it a promising tool for condition monitoring and predictive maintenance in industrial applications.

1 Introduction

Journal bearings play a fundamental role in the performance and durability of rotating machinery. Under ideal conditions, journal bearings operate in a hydrodynamic lubrication regime, where a continuous lubricant film prevents direct metal-to-metal contact. However, the lubrication film collapses under transient operating conditions such as start-stop cycles, leading to mixed-friction conditions where asperity contact becomes significant [KOJ19; ZML21; VR14]. This results in increased friction, higher temperatures and ultimately accelerated wear, which can reduce bearing lifespan and machine failure. Traditionally, numerical simulations based on mixed-elasto-hydrodynamic lubrication (mixed-EHL) models have been employed to predict wear under such conditions. These models are computationally intensive, requiring significant processing power and long simulation times, which makes their direct application in real-time condition monitoring impractical.

In drive trains of wind turbines (WT), journal bearings are frequently exposed to critical wear mechanisms. Due to the stochastic operating conditions of a WT, no real-time capable method currently exists for predicting the specific wear state of a journal bearing in field operation. Due to their high computational costs, existing physics-based simulation models are restricted from being used in condition monitoring systems. Recent advancements in artificial intelligence (AI) and machine learning (ML) have provided new opportunities to develop surrogate models capable of predicting complex engineering phenomena with significantly reduced computational effort. ML-based models can replace traditional physics-based simulations by learning patterns from existing data and making predictions based on operational parameters. ML-based surrogate models trained on coupled

1 Institute for Machine Elements and Systems Engineering, RWTH Aachen University, Schinkelstrasse 10,

mixed-EHL and wear simulation data show promising results in predicting the wear of journal bearings.

2 Methods and Parameters

Traditional physics-based wear prediction models, such as numerical simulations, provide accurate results but are computationally intensive and unsuitable for real-time applications. Machine learning (ML) offers an alternative by learning wear patterns from data, enabling fast and adaptive predictions without solving complex equations for each scenario. Among ML approaches, recurrent neural networks (RNNs) are particularly suited for time-series data, as they capture dependencies over time. In this study, three RNN architectures - Long Short-Term Memory (LSTM), Gated Recurrent Unit (GRU), and Nonlinear Autoregressive Model with Exogenous Inputs (NARX) - are evaluated for their ability to predict wear in journal bearings under start-stop conditions. The following sections follow Figure 18 and outline the data generation process, the ML models and the performance evaluation of the best model.

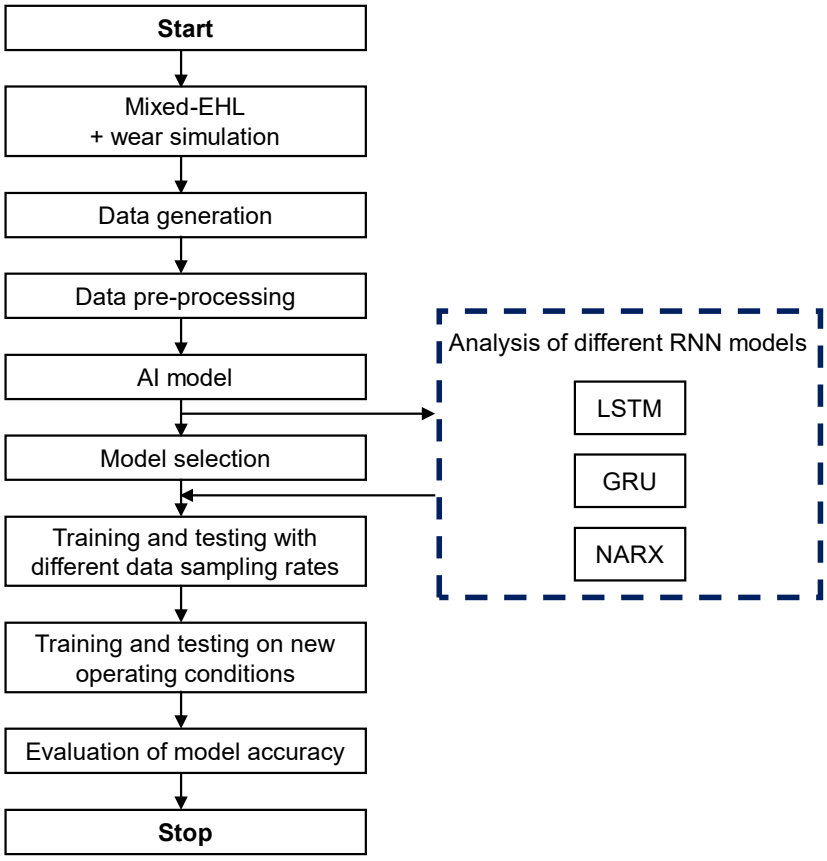

Figure 18: Methodology, [KWS24].

2.1 Wear Data Generation from Simulation Models

A dataset was generated using a coupled mixed-EHL and wear simulation model to train the ML models. The simulation considered a journal bearing with a diameter of 30 mm, a width of 15 mm and a radial clearance of 25 µm. The operating conditions varied regarding radial load (900 N - 1,350 N) and temperature (80°C - 90°C), reflecting realistic variations encountered in industrial applications. Each start-stop cycle consisted of three phases: acceleration from a standstill to

600 min^{-1} within 2 seconds, a constant speed phase at 600 min^{-1} for 2 seconds, and a deceleration phase back to a standstill over 3 seconds.

The simulation was carried out for 2,500 start-stop cycles, generating a large dataset containing information on frictional torque, rotational speed, and cumulative wear volume. The results of the wear volume are shown in Figure 19a, which reveals that wear volume exhibited both long-term trends and short-term variations. Initially, wear rates were high due to the running-in phase, where surface asperities undergo rapid deformation and material removal (Figure 19b). As the simulation progressed, wear rates stabilized, reflecting the steady-state operation of the bearing (Figure 19c).

a)

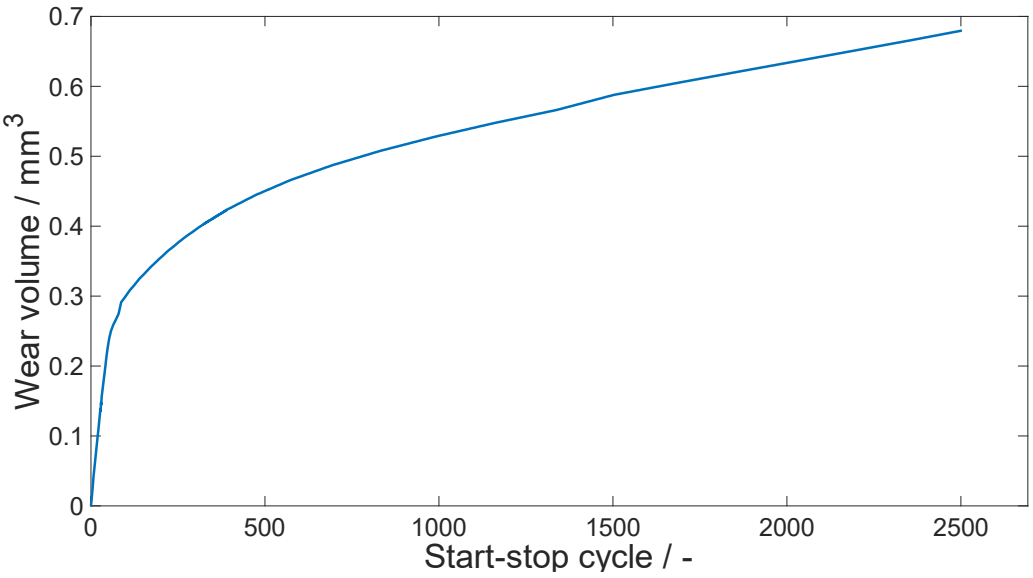

b)

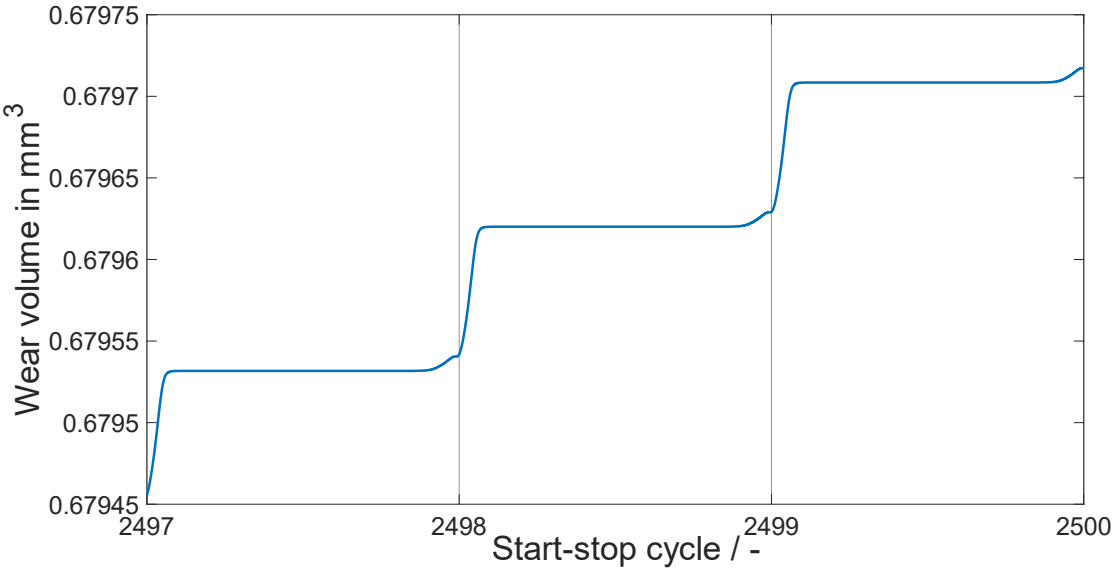

c)

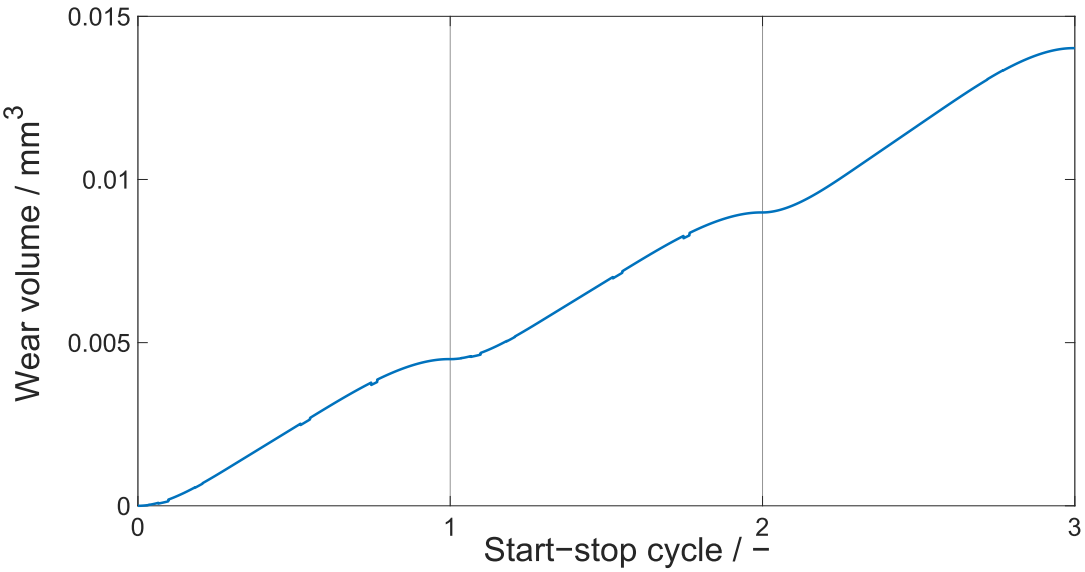

Figure 19: Wear volume results from physics-based simulation model: (a) total number of start-stop cycles, (b) cycles 1-3, (c) cycles 2,498-2,500, [KWS24].

2.2 Machine Learning Architectures for Wear Prediction

The dataset was used to train and evaluate three different recurrent neural network (RNN) architectures commonly employed for time-series forecasting.

Long Short-Term Memory (LSTM):

LSTM networks are a variant of RNNs designed to overcome the vanishing gradient problem, which typically limits the ability of standard RNNs to learn long-term dependencies. LSTMs utilize memory cells with input, output and forget gates to selectively retain or discard information, making them well-suited for time-series prediction. [LMV21; MMF21; vMN20]

Gated Recurrent Unit (GRU):

GRU networks are similar to LSTMs but have a simpler architecture with fewer parameters. Instead of separate input, output and forget gates, GRUs use an update gate and a reset gate to control the flow of information. This simplification makes GRUs computationally more efficient than LSTMs while still capturing temporal dependencies. [YYZ20; GHZ20]

Nonlinear Autoregressive Model with Exogenous Inputs (NARX):

The NARX model is a dynamic neural network designed specifically for time-series prediction. Unlike LSTM and GRU, which rely solely on internal memory states, NARX explicitly incorporates past values of both input and output variables, making it highly effective in capturing nonlinear relationships in time-dependent data. [CBG89; NP91; Ouy17; KD19; SW22]

3 Results

The three ML models were trained and tested using the wear dataset, with 80% of the data allocated for training and 20% reserved for testing. Performance was evaluated using the Root Mean Square Error (RMSE) metric. The results demonstrated that the NARX model outperformed both LSTM and GRU in terms of prediction accuracy and computational efficiency. The NARX model successfully captured both long-term trends and short-term variations in wear volume, as shown in Figure 20.

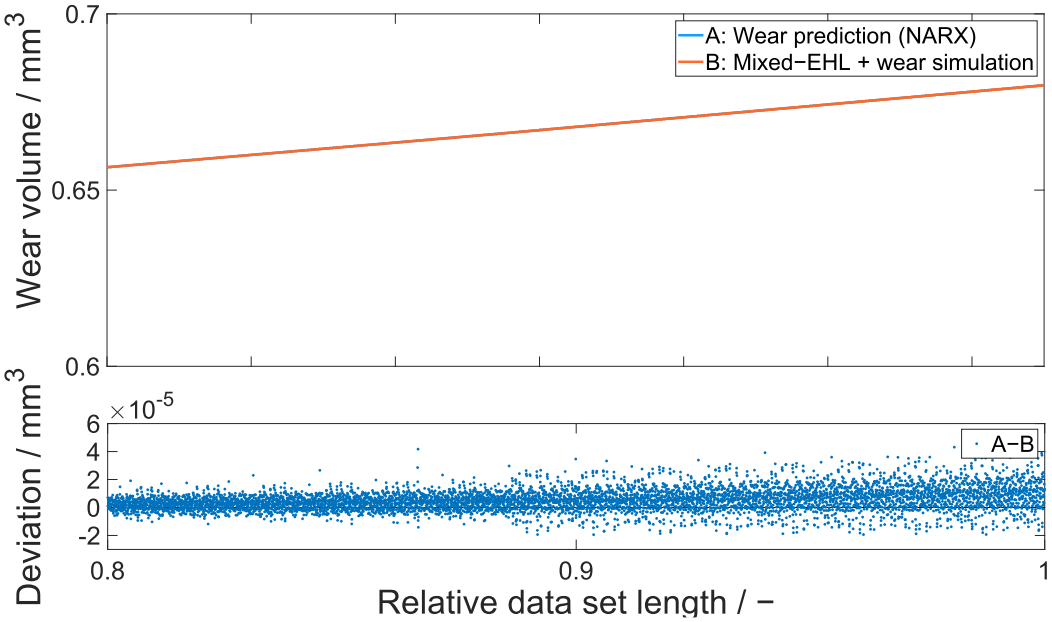

Figure 20: NARX results for one hidden layer and 50 neurons, including the deviation from the physics-based wear volume values, [KWS24].

To further assess the adaptability of the NARX model, it was trained on datasets with different downsampling factors (50, 100, and 400) and tested on a new dataset with a downsampling factor of 200. The model maintained high accuracy across different resolutions, demonstrating its robustness in handling variations in sampling rates and operating conditions.

4 Conclusion and Outlook

This study highlights the potential of machine-learning-based models for predicting wear in journal bearings under start-stop conditions. The results indicate that the NARX model is highly effective in

forecasting wear trends with high accuracy and computational efficiency. By leveraging ML techniques, it is possible to develop real-time wear monitoring systems that provide valuable insights into bearing health and enable predictive maintenance strategies.

Future work will extend the ML models to include sensor data from actual machinery, such as temperature and acoustic emission. The aim is to develop a robust and efficient predictive tool that can be integrated into condition monitoring systems where unpredictable load variations and transient operating conditions pose significant challenges for traditional wear prediction methods.

5 Bibliography

[CBG89] CHEN, S.; BILLINGS, S. A.; GRANT, P. M.: Non-Linear Systems Identification Using Neural Networks: Dept of Automatic Control and System Engineering. University of Sheffield. 1989.

[GHZ20] GAO, SHUAI; HUANG, YUEFEI; ZHANG, SHUO; HAN, JINGCHENG; WANG, GUANGQIAN; ZHANG, MEIXIN; LIN, QINGSHENG. Short-term runoff prediction with GRU and LSTM networks without requiring time step optimization during sample generation. In: Journal of Hydrology, 589 (2020), S. 125188.

[KD19] KOTU, VIJAY; DESHPANDE, BALA: Time Series Forecasting: Data Science: Elsevier 2019.

[KOJ19] KÖNIG, FLORIAN; OUALD CHAIB, ACHRAF; JACOBS, GEORG; SOUS, CHRISTOPHER. A multiscale-approach for wear prediction in journal bearing systems – from wearing-in towards steady-state wear. In: Wear, 426-427 (2019), S. 1203–1211.

[KWS24] KÖNIG, FLORIAN; WIRSING, FLORIAN; SINGH, ANKIT; JACOBS, GEORG. Machine-Learning-Based Wear Prediction in Journal Bearings under Start–Stop Conditions. In: Lubricants, 12 (2024), Nr. 8, S. 290.

[LMV21] LINDEMANN, BENJAMIN; MÜLLER, TIMO; VIETZ, HANNES; JAZDI, NASSER; WEYRICH, MICHAEL. A survey on long short-term memory networks for time series prediction. In: Procedia CIRP, 99 (2021), S. 650–655.

[MMF21] MATEUS, BALDUÍNO CÉSAR; MENDES, MATEUS; FARINHA, JOSÉ TORRES; ASSIS, RUI; CARDOSO, ANTÓNIO MARQUES. Comparing LSTM and GRU Models to Predict the Condition of a Pulp Paper Press. In: Energies, 14 (2021), Nr. 21, S. 6958.

[NP91] NARENDRA, K. S.; PARTHASARATHY, K. Learning automata approach to hierarchical multiobjective analysis. In: IEEE Transactions on Systems, Man, and Cybernetics, 21 (1991), Nr. 1, S. 263–272.

[Ouy17] OUYANG, HUEI-TAU. Nonlinear autoregressive neural networks with external inputs for forecasting of typhoon inundation level. In: Environmental monitoring and assessment, 189 (2017), Nr. 8, S. 376.

[SW22] SIEGEL, ANDREW F.; WAGNER, MICHAEL R.: Time Series: Practical Business Statistics: Elsevier 2022.

[VMN20] VAN HOUDT, GREG; MOSQUERA, CARLOS; NÁPOLES, GONZALO. A review on the long short-term memory model. In: Artificial Intelligence Review, 53 (2020), Nr. 8, S. 5929–5955.

[VR14] VENCL, ALEKSANDAR; RAC, ALEKSANDAR. Diesel engine crankshaft journal bearings failures: Case study. In: Engineering Failure Analysis, 44 (2014), S. 217–228.

[YYZ20] YANG, SHUDONG; YU, XUEYING; ZHOU, YING: LSTM and GRU Neural Network Performance Comparison Study: Taking Yelp Review Dataset as an Example: 2020 International Workshop on Electronic Communication and Artificial Intelligence (IWECAI): IEEE 2020.

[ZML21] ZHANG, H.; MA, J.; LI, X.; XIAO, S.; GU, F.; BALL, A. Fluid-asperity interaction induced random vibration of hydrodynamic journal bearings towards early fault diagnosis of abrasive wear. In: Tribology International, 160 (2021), S. 107028.

Sustainability

Navigating Sustainability: A Journey of Strategy Development

Allan K. Poulsen, Sara Nassehi Nejad

Vestas Wind Systems, Hedeager 42, 8200 Aarhus N, Denmark

Keywords: *Sustainability, strategy, circularity*

Abstract: Vestas will present the intricate process of crafting a robust sustainability strategy within a large organization with success. Drawing on a foundation rooted in data, particularly CO2 emissions and historical material data, we outline the initial steps that set the stage for our sustainability journey and our sustainability strategy - Sustainability in everything we do. Central to our approach was defining clear long- and short-term targets aligned with regulatory frameworks, offering a roadmap for actionable progress.

A critical aspect of our strategy was the strategic organizational structure, detailed through a matrix framework, which facilitated stakeholder alignment, streamlined communication and decision-making across departments. We explore the challenges and successes encountered in defining and refining processes within the organization, crucial for operationalizing and deploying our sustainability goals.

Reflecting on early efforts dating back to 2019, this presentation focuses on the evolution of our sustainability strategy, highlighting key milestones, lessons learned, and the ongoing commitment to driving meaningful environmental and social impact within our organizational framework.

1 Introduction

In 2019, Vestas Wind Systems introduced a groundbreaking sustainability strategy titled "Sustainability in Everything We Do." This initiative marked a significant shift in the company's operational and strategic focus, embedding sustainability at the core of its business model. The strategy was designed to address the pressing global challenge of climate change and align with the increasing regulatory demands and customer expectations for sustainable practices. Right up to introduction of the sustainability strategy one of the pivotal achievements was obtaining certification from the Ellen MacArthur Foundation, which recognized Vestas' commitment to maintaining carbon emissions below a 1.5°C increase, in line with the Paris Agreement targets.

The introduction of this strategy was timely, as it prepared Vestas for forthcoming European Union legislation, such as the Corporate Sustainability Reporting Directive (CSRD) and the Corporate Sustainability Due Diligence Directive (CSDDD). These regulations mandate comprehensive sustainability reporting and due diligence in corporate operations, ensuring that companies not only minimize their environmental impact but also uphold social and governance standards. By proactively adopting these measures, Vestas positioned itself as a leader in the renewable energy sector, demonstrating its commitment to sustainability and its readiness to meet future regulatory requirements.

Vestas' strategy also aimed to address the growing demands from customers for sustainable energy solutions. As the global awareness of climate change and environmental degradation increased, customers began to prioritize companies that demonstrated a genuine commitment to sustainability. Vestas responded to this shift by integrating sustainability into every aspect of its operations, from product design and manufacturing to supply chain management and corporate governance. This holistic approach not only enhanced Vestas' reputation but also provided a competitive advantage in the rapidly evolving renewable energy market.

In summary, the introduction of the "Sustainability in Everything We Do" strategy marked a significant milestone for Vestas. It underscored the company's dedication to sustainability, prepared it for upcoming regulatory changes, and aligned its operations with the growing customer demand for environmentally responsible practices. By embedding sustainability into its core business model, Vestas set a new standard for the renewable energy industry and reinforced its position as a global leader in sustainable energy solutions.

2 Sustainability in Everything We Do…

The "Sustainability in Everything We Do" strategy by Vestas is a comprehensive and ambitious approach to embedding sustainability into every aspect of the company's operations. This strategy is built around several key targets aimed at reducing environmental impact, promoting circular economy principles, and ensuring social responsibility. Here, we delve deeper into the specific targets set by Vestas, the initiatives undertaken to achieve these targets, and the challenges faced during implementation.

Vestas has committed to achieving carbon neutrality in its own operations by 2030. This target is particularly ambitious as it excludes the use of carbon offsets, which are often used by companies to balance out their carbon emissions by investing in environmental projects elsewhere. Instead, Vestas aims to reduce its carbon footprint through direct actions such as improving energy efficiency, transitioning to renewable energy sources, and optimizing operational processes. This commitment to carbon neutrality is a testament to Vestas' dedication to addressing climate change and reducing its environmental impact.

3 Zero waste wind turbines and carbon emission reductions

Another cornerstone of Vestas' strategy is the goal to produce zero-waste wind turbines by 2040. This involves designing turbines that are fully recyclable and continue to develop the business and processes to refurbish and reuse components and turbines. The company has set intermediate targets, such as making 50% of the hub and blade recyclable by 2025 and 55% by 2030. Achieving these targets requires innovation in design, manufacturing, and end-of-life management, and Vestas has invested in research and development to create more sustainable materials and manufacturing processes.

Vestas has also set specific targets for reducing scope 1 and 2 emissions, which include direct emissions from its operations and indirect emissions from purchased electricity. The company aims to reduce these emissions by 55% by 2025 and achieve 100% reduction by 2030. Additionally, Vestas has committed to reducing scope 3 emissions, which encompass the broader supply chain, by 45% per MWh generated by 2030 compared to 2019 levels. This comprehensive approach to emissions reduction demonstrates Vestas' commitment to minimizing its environmental impact across its entire value chain.

To achieve these ambitious targets, Vestas has implemented a range of initiatives and programs across its operations and supply chain. The company has invested heavily in improving the energy efficiency of its operations, including adoption of energy-efficient technologies and use of renewable energy sources in offices and at factories.

Vestas is also pioneering the use of circular economy principles in the design and manufacturing of wind turbines. This involves developing recyclable blade technologies and establishing partnerships with recycling companies to create efficient recycling processes. The company also has a focus on

refurbishing and reusing components, thereby reducing waste and conserving resources. These initiatives are critical to achieving the goal of producing zero-waste wind turbines by 2040 and demonstrate Vestas' commitment to sustainability.

Engaging with suppliers to achieve sustainability targets has been a key focus for Vestas. The company expects its strategic suppliers to develop their own sustainability strategy and to set scope 1 and 2 emission reduction targets by 2030 without using offsets and to calculate and report CO_2e emissions for products delivered to Vestas. Within materials strategic suppliers are expected to measure and report on production waste for Vestas products and a 50% reduction in waste from products delivered to Vestas by 2030.

4 Transparancy and challenges

Transparency and accountability are central to Vestas' sustainability strategy. The company regularly reports on its progress towards its sustainability targets using internationally recognized frameworks such as the Global Reporting Initiative (GRI) and the Task Force on Climate-related Financial Disclosures (TCFD). This transparency not only demonstrates Vestas' commitment to sustainability but also provides stakeholders with the information they need to assess the company's performance and hold it accountable.

Despite the comprehensive nature of Vestas' sustainability strategy, the company has faced challenges during implementation. Developing fully recyclable wind turbines and achieving zero-waste production by 2040 requires significant technological innovation. Vestas has had to invest in research and development to create introduce new materials and change of manufacturing processes. This includes developing recyclable blade technology and optimizing the design of wind turbines to reduce environmental impact and to facilitate easier recycling and refurbishment.

Engaging with suppliers to achieve sustainability targets has been a complex task. Vestas works with a diverse range of suppliers across the globe, each with its own set of challenges and capabilities. Ensuring that all suppliers adhere to the same sustainability standards requires extensive collaboration, support, and monitoring. The task is complex however, the company has made progress by entering into the dialogue with the suppliers and how to achieve their sustainability targets.

Despite increasing interest rates and inflation, Vestas has remained committed to its sustainability goals, recognizing that the long-term benefits of sustainable practices far outweigh the short-term financial challenges. This commitment to sustainability, even in the face of economic pressures, demonstrates Vestas' dedication to reducing its environmental impact and promoting sustainable practices.

On top, the regulatory landscape is complex and the company must comply with a range of regulations and standards across different regions, each with its own requirements and expectations. This requires continuous monitoring and adaptation to ensure compliance and alignment with best practices. Vestas has invested in resources and expertise to navigate this regulatory landscape and ensure that its operations comply with all relevant regulations.

Meeting the diverse expectations of stakeholders, including customers, investors, and employees, is a balance act. The company must balance the demands for sustainability with the need to maintain financial performance and competitiveness. This requires effective communication and engagement with stakeholders to build trust and demonstrate the value of sustainability. Vestas has made

progress in this area by regularly reporting on its sustainability efforts and engaging with stakeholders to understand their expectations and concerns.

Despite these challenges, Vestas has made significant progress towards its sustainability targets. The company has achieved substantial reductions in its carbon emissions, with a 55% reduction in scope 1 and 2 emissions by 2023. This progress has been driven by improvements in energy efficiency, the transition to renewable energy sources, and the optimization of operational processes. Unfortunately Vestas is not going to meet the 2025 scope 1 and 2 emissions. This because the targets were set before re-entering offshore wind and the scope of activities increased. The targets will be re-evaluated in 2025.

Vestas has also made significant strides in reducing waste and increasing the recyclability of wind turbine components. The company has developed recyclable blade materials and established efficient recycling processes in partnership with recycling companies. These efforts have contributed to the goal of producing zero-waste wind turbines by 2040 and demonstrate Vestas' commitment to sustainability.

5 Going forward

Looking ahead, Vestas remains committed to its sustainability strategy and continues to pursue its ambitious targets. The company recognizes that achieving these goals will require ongoing innovation, collaboration, and investment. Vestas will continue to focus on improving energy efficiency, introduce more sustainable materials, and engaging with suppliers to promote sustainability across the supply chain.

Vestas also acknowledges the importance of transparency and accountability in its sustainability efforts. The company will continue to report on its progress using internationally recognized frameworks and engage with stakeholders to build trust and demonstrate the value of sustainability.

In conclusion, the "Sustainability in Everything We Do" strategy represents a comprehensive and ambitious approach to sustainability. By setting clear targets and implementing a range of initiatives to achieve them, Vestas has demonstrated its commitment to reducing its environmental impact and promoting sustainable practices across its operations and supply chain. Despite the challenges faced during implementation, Vestas has made significant progress towards its sustainability goals and remains a leader in the renewable energy industry.

6 Conclusion

Sustainability has become a fundamental value in today's business landscape, and Vestas' "Sustainability in Everything We Do" strategy exemplifies this shift. However, the focus on sustainability has faced challenges in recent years due to increasing inflation and interest rates, which have impacted the focus on the area.

Despite these challenges, Vestas has remained committed to its sustainability goals, recognizing that the long-term benefits of sustainable practices far outweigh the short-term financial pressures.

The strategy's success is evident in the progress Vestas has made towards its ambitious targets. The company has achieved significant reductions in waste and carbon emissions, and its efforts to increase the recyclability of wind turbine components have set a new standard for the industry. Vestas' commitment to transparency and accountability has also been a key factor in its success,

providing stakeholders with the information they need to assess the company's performance and hold it accountable.

Looking ahead, it is clear that sustainability will continue to be a critical focus for Vestas and the broader renewable energy industry. While economic challenges may pose obstacles, the need to address climate change and reduce environmental impact remains as urgent as ever. Vestas' strategy provides a roadmap for other companies to follow, demonstrating that it is possible to achieve ambitious sustainability goals while maintaining financial viability and competitiveness.

In conclusion, Vestas' "Sustainability in Everything We Do" strategy represents a comprehensive and forward-thinking approach to sustainability. By embedding sustainability into every aspect of its operations and setting ambitious targets for waste reduction and carbon emissions, Vestas has positioned itself as a leader in the renewable energy industry. Despite the challenges posed by economic factors, the company's commitment to sustainability remains unwavering, providing a model for others to follow in the pursuit of a more sustainable future.

Driving Sustainable Solutions in the Wind Industry: Connecting Value Chains and Customer Needs

Sara Nassehi Nejad[1]

[1]Vestas Wind Systems A/S, København, DK

Abstract: Sustainability is in focus for the wind industry as industry players have to navigate legislative landscapes, customer demands, and critical material considerations. On the legislative side a key point is the Critical Raw Materials Act and its implications for sourcing rare earth materials integral to wind turbine drive trains and to customers it is about offering solutions that reduces the CO2 emission per MWh.

Central to our discussion is the strategic connection of the value chain, emphasizing collaboration and alignment between suppliers and customer requirements. During this presentation we delve into practical approaches for materializing sustainability objectives, addressing the evolving demands from authorities defining non-financial criteria in the auctions and customers who increasingly prioritize environmentally conscious solutions.

By exploring the interplay between regulatory frameworks, customer expectations, and supply chain dynamics, we talk about actionable strategies for the wind industry to not only meet but exceed sustainability goals. This presentation offers insights and firsthand examples into how Vestas answer the call for sustainable innovation, fostering a greener future for the renewable energy sector.

[1]Vestas Wind Vestas Wind Systems A/S

Roller Bearing (Academic Track)

An experimental study on thrust roller bearing life under over-rolling conditions

Xinrun Liu, Xing-Yuan Miao, Nikhil Sudhakaran, Asger Bech Abrahamsen, Søren Fæster, and Yi Guo

Department of Wind and Energy Systems, Technical University of Denmark, Risø Campus, Frederiksborgvej 399, 4000 Roskilde, Denmark

Keywords: Roller bearing, Fatigue, Data processing

Abstract: This study reports on the addition of a 5 mm cube accelerometer and data acquisition system on a standard FE8 bearing test rig to investigate if the initial failure states of a thrust bearing can be detected before the global failure criteria of the FE8 test rig is reached. Two 81212-TV roller bearings are tested under over-rolling conditions, with accelerometer data collected over 38 days to analyze degradation-related vibration signatures. Fast Fourier Transform (FFT) is utilized in data processing to reveal over-rolling frequencies and harmonics of the shaft frequency in the vibration spectra. These features indicate clear signs of degradation after 13 days, which is much earlier than the 38-day lifetime obtained from the limit on the global acceleration of the FE8 test rig. The vibration peaks are analyzed through Gaussian function fitting to explain the severe damage visually observed on the roller. The evolution of peak amplitude and width of selected features are discussed along with recommendations on further modelling.

1 Introduction

Thrust bearings are essential components in mechanical systems, designed to handle specific requirements, such as axial loads and friction reduction. The operational state of bearings can be categorized into four stages: the run-in period, operation period, degradation period, and failure period [SKF2011]. The degradation of a thrust bearing is affected by many factors, e.g. lubrication condition [BHA2024] [FER2013], axial loads [HUA2024], and operating temperature [PER2024]. Small-scale thrust bearings are usually tested in the FE8 standard test rig according to DIN51819 in order to determine the lifetime determined at the stage, where the global acceleration of the test rig exceeds a certain threshold specified by a factor of 3 higher than the acceleration level after the run-in period. Such failure criteria are subject to interpretation and this paper will investigate if the installation of a small accelerometer closer to one of the bearings under test can be used to provide information about early failure detection and more precise stop criteria. Identifying peak features in frequency space associated with the bearing's life from testing data is considered a better method for the evaluation of the bearing degradation under a specific load condition.

Evaluating data such as vibration signals and acoustic signals are processed with different analysis methods, e.g. time-domain analysis [JAI2022], frequency-domain analysis [MAC2019], and time-frequency analysis [HU2021] [KAN2011]. Time-domain analysis needs low computational demand and is effective for directly monitoring parameters such as amplitude, trends, and sudden changes in the signal. However, it cannot distinguish between different frequency components. The frequency-domain analysis offers high-frequency resolution and powerful feature extraction but requires more computation and is less suitable for transient signals. Time-frequency analysis is well-suited for handling non-stationary signals and provides rich visualizations. Nevertheless, it is more complex and has a higher computational demand compared to the other two approaches.

In this work, a fatigue-bearing test is conducted under over-rolling conditions. Vibration signals are recorded 512 times per minute, and parameters such as temperature, speed, and axial force are recorded every 2 minutes throughout the testing. The accelerations of the added sensor are processed using the Fast Fourier Transform (FFT) within 30-second time windows. Direct visual observation is employed to identify the bearing damage after testing.

2 Experiment

This section introduces an experimental setup to investigate the behavior of bearings under over-rolling conditions. The following sections introduce the setup and the procedure of the bearing test.

2.1 Setup

The FE8 bearing testing rigs are illustrated in Figure 21 and consist of a lubrication device, a cooling device, and a bearing mounting house with an associated drive motor. The thrust cylindrical roller bearing 81212-TV is tested with XMP 320 oil as the lubricant. An accelerometer 5 mm cube 356A03 from PCB Piezotronics is mounted on the bearing raceway support using lock tight and a mechanical clamp, positioned as far away from the motor, the accelerations in X, Y, and Z directions are sampled at 512 Hz using a Siemens Simcenter Testlab. Additional sensors of the FE8 Test rig monitor the temperature (pt100), rotational speed, axial force, and acceleration in the testing system every two minutes. The temperature is directly mounted over the bearing and the torque sensor is on the torque shaft.

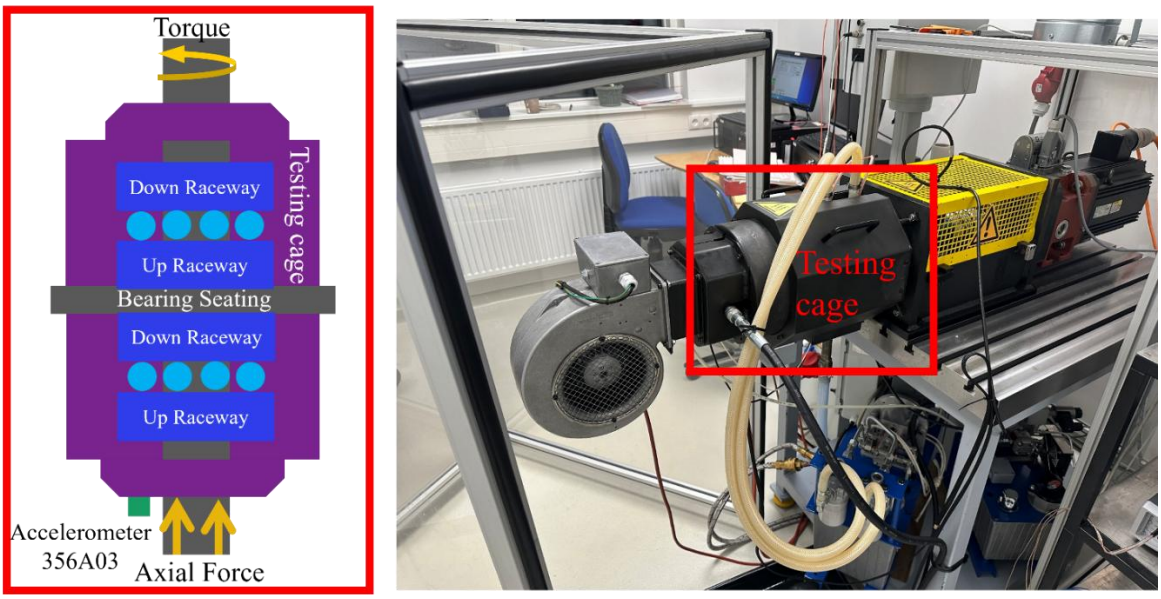

Figure 21: The overview of FE8 bearing testing rigs, including a testing cage, a cooling device, and a lubricant device.

2.2 Testing procedure

After assembling the FE8 test bench, the lubrication rate is set to $0.2\ l/min$ before starting the test. For the parameters setting, an axial load of $\mathrm{F_A} = 85\ \mathrm{kN}$ is applied, and the rotational speed is set to $\omega = 250\ \mathrm{rpm}$. Under these conditions, the temperature can stabilize at $\mathrm{T} = 100\ ℃$

3 Methodology for data processing

A Fast Fourier Transform (FFT) is used to analyze the vibration signals extracted from the accelerometer. This is to identify the frequencies associated with the damage to the tested bearing.

FFT algorithm opened a new area in signal processing by significantly reducing the computational workload of Discrete Fourier Transform (DFT). Instead of the original method, which requires computations proportional to N^2 , FFT reduces this to $Nlog_{2N}$, where N is the size of the problem [DUH1990]. The discrete Fourier Transform (DFT) formula is explained by the following.

$$X[k] = \sum_{n=0}^{N-1} x[n] \cdot e^{-j\frac{2\pi}{N}kn}, k = 0, 1, 2, \dots, N-1 \qquad \textbf{Eq. 13}$$

Where $X[k]$ is the output in the frequency domain, representing the complex value of the k_{th} frequency component; $x[n]$ is the input in the time domain, representing the value at the n_{th} time point; N is the total number of samples, representing the number of points in one period. k is the frequency index, ranging from $(0, 1, 2, \dots, N-1)$, corresponding to different frequencies. n is the time index, ranging from $(0, 1, 2, \dots., N-1)$, representing discrete time points. j is the imaginary unit, satisfying $j^2 = -1$. $e^{-j\frac{2\pi}{N}kn}$ is a complex exponential function.

According to [SKF2011], the state of bearing health can be estimated by tracking the following specific frequencies related to bearing kinematics: Ball Pass Frequency Outer Race (BPFO) represents the frequency at which a roller passes a specific point on the outer race of the bearing. Ball Pass Frequency Inner Race (BPFI) represents the frequency at which a roller passes a specific point on the inner race of the bearing. For thrust bearings, this value is identical to BPFO. Fundamental Train Frequency (FTF) represents the rotational frequency of the cage that holds the rollers. Ball Spin Frequency (BSF) represents the rollers completing one full rotation around their axis. The shaft frequency represents the number of rotations completed by the main shaft per second. The equation is defined as follows and the table for these values is shown in Table 14.

$$\mathrm{BPFO} = \frac{n}{2} f_\mathrm{r} \left(1 - \frac{d}{D}\cos\theta\right) \qquad \textbf{Eq. 2}$$

$$\mathrm{BPFI} = \frac{n}{2} f_\mathrm{r} \left(1 + \frac{d}{D}\cos\theta\right) \qquad \textbf{Eq.3}$$

$$\mathrm{FTF} = \frac{f_r}{2} \left(1 - \frac{d}{D}\cos\theta\right) \qquad \textbf{Eq.4}$$

$$\mathrm{BSF} = \frac{D}{d}\frac{f_\mathrm{r}}{2} \left(1 - \left(\frac{d}{D}\cos\theta\right)^2\right) \qquad \textbf{Eq.5}$$

$$f_r = \frac{\omega}{60} \quad \textbf{Eq.6}$$

Where n is the number of rolling elements; f_r is the rotational frequency of the shaft; d is the diameter of the rolling element; D is the pitch diameter of the bearing; θ is the contact angle between the applied load and the radial plane of the bearing, which is 90° for a thrust bearing; ω is the shaft rotation speed per minute.

Component	Frequency (Hz)
Shaft frequency	4.17
BPFO	39.6
BPFI	39.6
BSF	14.7
FTF	2.08

Table 14: The specific frequency for bearing diagnosis

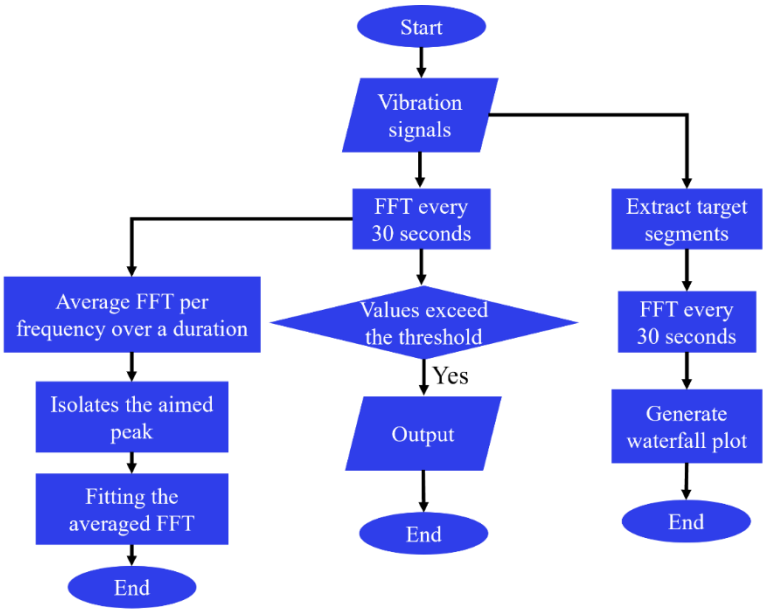

Figure 22: The data processing flowchart, including three modules: waterfall plot generation for target segment of vibration signals, threshold-based filtering, and frequency-averaged FFT fitting.

The fatigue test generates a large dataset, presenting significant computational challenges. To be more specific, a waterfall plot window is more likely to crash when data points exceed 1 million. In this study, the dataset contains over 1 billion points, further emphasizing the processing difficulty. For more efficient data processing, a threshold is applied to filter out low-value data that still requires significant storage capacity. This threshold is determined by selecting a value greater than most data points but lower than the peaks corresponding to the prominent specific frequencies. Moreover, to gain additional insights into the evolution of individual peaks, the FFT values for each frequency are averaged by combining FFT results over a specific duration, defined as a parameter in the algorithm. The individual peaks are then fitted using a Gaussian function, illustrated below. The data processing flowchart is shown in Figure 22.

$$f(x) = a \exp\left(-\frac{(x-b)^2}{2c^2}\right) \quad \textbf{Eq.7}$$

Where x is the amplitude value from averaged FFT results; a is the peak amplitude of the Gaussian curve; b is the center position of the Gaussian curve; c is the standard deviation, which also represents the width of the Gaussian curve.

4 Results

This section presents the data processing results and the findings from direct visual observation. The visual findings further support the explanation in the data spectrum.

4.1 Damage inspection

Figure 23 illustrates the damage observed on the bearing through direct visual inspection. Severe damage on one roller, shown in Figure 23(a), is identified as surface wear. This damage is inferred to result from sliding at the end of the test or improper load distribution. Further explanation is provided in the next section based on data processing analysis.

Figure 23(b) highlights the scratch on the cage, potentially caused by over-rolling. Figure 23(c) shows small pits on the raceway. Excessive load and contaminants are known to be the primary causes of raceway fatigue failures [XU2023]. However, no indentations are found on the raceway, and minimal debris observed during bearing disassembly suggests that the lubricant is appropriately selected for its ability to clean debris during the test.

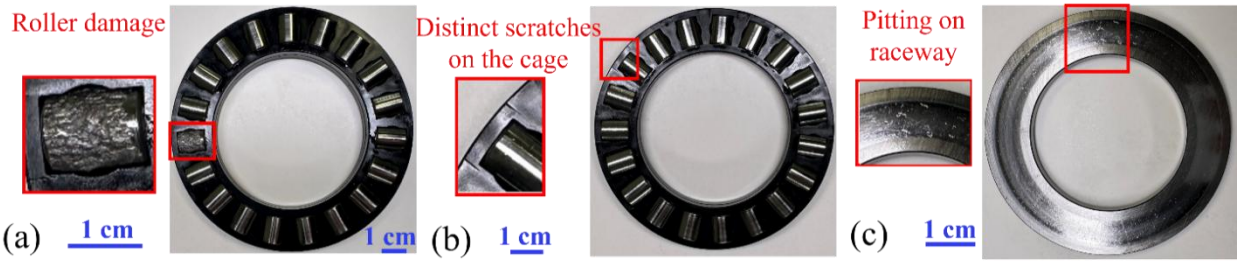

Figure 23: The damage inspection of the bearing after testing. (a) Front view of the cage and rollers with severe damage on one roller. (b) Backward view of cage and rollers with scratches on the cage. (c) Up raceway with pitting

4.2 Data processing results

Data processing results include 1) the vibration spectra of the tested bearing during running-in, degradation, and after occurrence of damage; and 2) the progression of vibration amplitude at ball spin frequency during bearing degradation, based on specific frequencies analysis, illustrated in section 3, through the frequency-averaged FFT fitting module and threshold-based filtering module in the data processing algorithm.

5 4.2.1 Waterfall spectrum results

In the raw vibration signals from the fatigue-bearing test, as shown in Figure 24(a), the bearing enters the run-in period during the first 120 minutes. The vibration amplitude is initially high but decreases as the bearing undergoes a self-adaptive process, where lubricant is distributed evenly, and temperature stabilizes, reducing the effects of thermal expansion. From this point to the 13th day, it stays in the operation period. Subsequently, the bearing enters the degradation period, which lasts until the 36th day. During the degradation period, the vibration amplitudes increase obviously as the internal damage of the bearing gradually generates, causing stronger energy release with each pass over the damaged area. Finally, the failure occurs after 36 days, with greater deterioration leading to a corresponding rise in vibration amplitude. After the vibration amplitude reaches its peak, it decreases with intense fluctuations, since the roller obtains extreme damage, resulting in the bearing losing its function or rolling contact being replaced by sliding contact.

Figure 24(b) and (c) illustrate the waterfall plot with 30-second intervals when degradation and failure occur. Many peaks are observed and some are not related to the bearing rotation such as the peaks observed at 50 Hz, which is electrical noise picked up from the 220 V power supply.

As shown in Figure 24(b), degradation is marked by frequency components at 0.5 $\times$ and 1 $\times$ the shaft frequency and their harmonics. The shaft frequency has the highest amplitude, decreasing harmonics on either side. This phenomenon suggests that the system is under the condition of unbalance and misalignment as degradation occurs. The result shown in Figure 23(a) indicates that only one roller is damaged, suggesting that stress within the system is not distributed evenly. Over time, the harmonics' amplitude increases because degradation becomes more pronounced.

As the bearing reaches the degradation and failure periods, some peaks suddenly increase, providing deeper insights into the bearing failure mechanism. An 81.8 Hz peak appears when the bearing degrades, which has no harmonic relationship with the shaft frequency but is close to the 19.5 $\times$ harmonics. It can be speculated that 81.8 Hz is related to the number of rollers, as the roller number is 19. However, further work is needed for a more concrete conclusion.

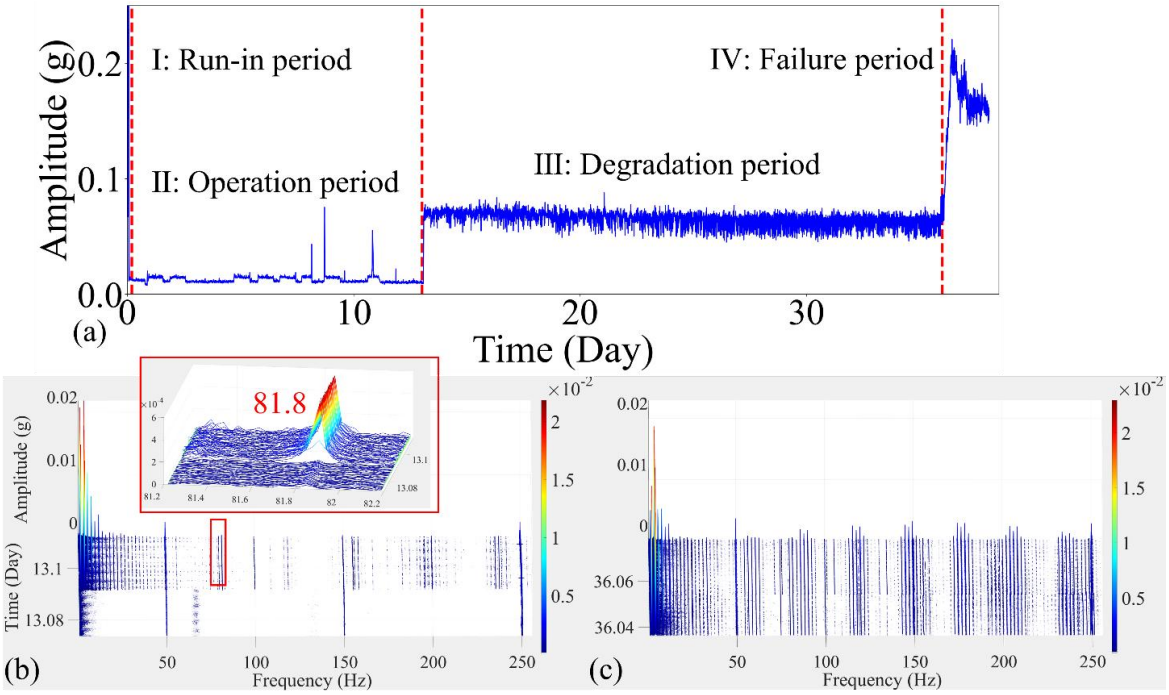

Figure 24: (a) Raw vibration data from the accelerometer shown at 10-minute intervals. (b) The waterfall plot with 30-second intervals, shows the appearance of degradation on day 13. (c) The waterfall plot with 30-second intervals, shows additional failure features appearing on the 36th day.

6 4.2.2 Specific frequency analysis results

Figure 25(a) and (b) show the Gaussian parameters' evolution of shaft frequency and ball pass frequency over time, based on the frequency-based FFT fitting. For the shaft frequency, it can represent the state of the testing system, including the shaft and bearing. The amplitude gradually increases during the degradation period and shows a significant rise in the failure period, indicating that the fault risks associated with the system, such as unbalance and misalignment, are increasing over time. For BSF, the amplitude stabilizes during the degradation period but initially increases upon entering the failure period. This can be explained that BSF can represent the self-spin state of the rollers. The amplitude increases as energy concentrates due to damage occurring on the roller. Subsequently, the amplitude decreases since damage propagation disperses the impact energy, and the roller shifts from rotating to sliding, causing the damage observed in Figure 23(a). In both cases, the increase in standard deviation upon entering the failure period indicates that the mechanical system turns into an unstable state, characterized by intensified randomness and instability.

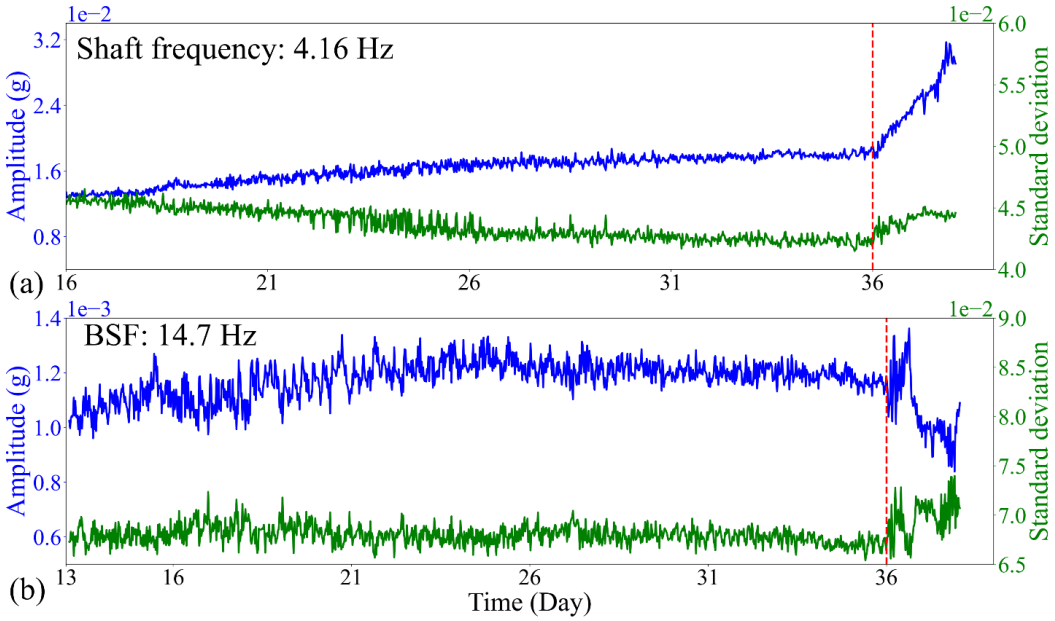

Figure 25: The evolution of Gaussian peak parameters over time using frequency-based FFT fitting. (a) Shaft frequency peak amplitude and width as given in equation (3). (b) Amplitude and width of the FFT peak corresponding to the Ball spin frequency (BSF).

7 Summary

This paper presents vibration and visual observation results on bearing degradation conducted on the FE8 test rig over 38 days.

- Severe damage is only observed on the surface of one roller out of 19 through direct visualization. The absence of significant raceway damage and the lack of substantial debris on the bearing upon disassembly demonstrate the proper selection of lubricant.
- The installation of a 5 mm cube additional accelerometer on the bearing raceway seat revealed an early identification of the first stage of the bearing failure after 13 days and a transition into a more severe damage evolution after 36 days.
- Fourier transformation of the acceleration of the additional accelerometer shows a multitude of additional peaks in the frequency spectrum appearing after 13 days of testing and further research is needed to identify these new peaks
- Monitoring the evolution using the frequency-based FFT fitting approach during data processing effectively reflects the bearing's states. However, the ability of this method to predict the location of bearing failures requires further investigation in future studies.
- This study indicates that the evolution of initial bearing failures can be followed in-situ using frequency analysis and that a stop criteria might be formulated as the transition away from the initial failure state, whereby subsequent visual inspection will reveal the initial failure state.

8 Bibliography

[BHA2024] Bhat Junaid Ahmad, Harmain G. A., and Najar F. A. Next-gen lubrication: Water-cooled thrust bearings in conjunction with nanofluid lubricant. Tribology International, 197:109779, 2024.

[DUH1990] DUHAMEL P. and VETTERLI M. Fast Fourier-transforms - a tutorial review and a state-of-the-art. Signal Processing, 19(4):259–299, 1990.

[FER2013] Fernandes, Carlos M.C.G.; Martins, Ramiro C.; Seabra, Jorge H.O. Friction torque of cylindrical roller thrust bearings lubricated with wind turbine gear oils. Tribology International, 59, 121–128, 2013.

[HU2021] Hu Mantang, Wang Guofeng, Ma Kaile, Cao Zenghuan, and Yang Shuai. Bearing performance degradation assessment based on optimized EWT and CNN. Measurement: Journal of the International Measurement Confederation, 172:108868, 2021.

[HUA2024] Huang, Xin; Chen, Yan; Zhuo, Hong; He, Xiuling: Research on the wear failure mechanism of high-speed positive displacement motor bearings. International Journal of Mechatronics and Applied Mechanics, 2024(16):127–137, 2024.

[JAI2022] Jain Prashant H and Bhosle Santosh P. Analysis of vibration signals caused by ball bearing defects using time-domain statistical indicators. International Journal of Advanced Technology and Engineering Exploration, 9(90):700–715, 2022.

[KAN2011] Kankar P. K., Sharma Satish C., and Harsha S. P. Rolling element bearing fault diagnosis using wavelet transform. Neurocomputing, 74(10):1638–1645, 2011.

[MAC2019] Machado Tiago Henrique, Alves Diogo Stuani, and Cavalca Katia Lucchesi. Investigation about journal bearing wear effect on rotating system dynamic response in time domain.Tribology International, 129:124–136, 2019.

[PER2024] Pereira Eloi S. Condition monitoring and failure analysis of a liquefied natural gas plant cryogenic heavies removal column reflux pump. 20th International Conference on Condition Monitoring and Asset Management, Cm 2024, 2024.

[SKF2011] SKF Group, SKF Bearing Maintenance Handbook, PUB SR/P7 10001/1, SKF Group, Sween, September 2011.

[XU2023] Xu Funing, Ding Ning, and Xiangfeng Chen. A review of bearing failure modes, mechanisms and causes. Engineering Failure Analysis, 152:107518, 2023.

Fretting wear test of three-row roller bearings based on equivalent model

Chenhao Guan[1], Yonggang Meng[1], Jocelyn Zhao[2]

[1] State Key Laboratory of Tribology in Advanced Equipment, Tsinghua University, Beijing, 100084, China

[2] Shell Technology (Shanghai) Ltd., Jinke Road No.4560, Pudong New District, Shanghai, China

Keywords: Roller bearings; Fretting wear; Test rig design, Grease

Abstract: The study presents a test method based on equivalent model for the three-row roller bearing, which is a typical type of pitch bearings used in recent large wind turbines. To solve the problem that the real-size pitch bearing of the wind turbine is not easy to test, and to make a better comparison between the performance of different kinds of grease to be used in the pitch bearings, a new bearing grease test rig, named as FW4B, is designed and constructed based on an equivalent model with a small size test bearing. The test rig is so designed and controlled such that the load, amplitude, and frequency of the oscillating motion could be programmed according to the real variable work conditions of the wind turbines. Key techniques for building the test rig are introduced, and preliminary test results are presented. The test results have indicated that fretting and corrosive wear is the major failure mode of the tested bearing, and the appearance of the damaged surface is similar to those found in real wind turbine pitch bearings.

1 Introduction

Wind power generation is one of the major forms of renewable energy and has heavy market potential. In 2030, the global yearly energy generation from wind power will increase to 4500TWh[1]. Wind turbines are often installed in areas with abundant wind energy resources while the areas are often sparsely populated, making the maintenance of the installed wind turbines difficult and costly. 48% of the cost are spent by assembling and maintaining the wind turbines[2]. Therefore, there is a strong demand for wind power in the industry to improve the lifetime of turbine components. The pitch bearing installed at the root of the blade serves as the pivot connecting the blades with the hub such that the blade can be rotated by the motor to adjust the angle of the wind direction. Sometimes, because of ultra-high wind, the blades will be locked to avoid damage to the wind power generator, but this will result in a new problem in which fretting wear will occur in the pitch bearing. Appropriate lubrication conditions are a common way to improve the situation, and using appropriate grease is considered a feasible technology to prolong the service lifetime of pitch bearings. Compared with liquid lubricants, either petroleum or synthetic oils, lubricating grease lacks fluidity, and thus, it is difficult to flow back to the contacting track once they are squeezed out of the contact zone due to high pressure. After a long time, there would be no grease between the roller and raceway. The roller and plate are in direct contact and wear. In the operation conditions of the pitch bearings in wind turbines, the bearing race oscillates relative to the rollers in a way of random amplitude and frequency rather than rotating continuously for most of the service life. Such a fretting motion is harmful for grease replenishment and dangerous to the wear life of bearings. In Sweden, 13.4% of failures were caused by pitch bearings and blades and consumed 9.4% of the time to repair, in the period of 2000-2004, in wind power plants[3].

To investigate the performance of lubricating greases in terms of fretting wear resistance, a proper test rig and testing procedure are necessary. Currently, the testing methodology for lubricating greases used in roller bearings can be divided into two categories[4]. One is model testing, which uses a ball-disc model or roller-disc model to evaluate the performance of lubricating greases under simulation conditions of load, speed, and temperature. The other is to set a real test pitch bearing (around 7-8 m in diameter for the most powerful wind turbines) on a test device specifically designed and fabricated. The advantages of the model experiments are high throughput and homogenization. The model test always provides a stable result for certain conditions, and standard experimental testers are widely used. On the other hand, real-size bearing testing devices can obtain more realistic and accurate results, and some experiments use a real blade to perform the experiment. However, there is often a significant difference between the results of model experiments and real-size bearing testing, which depends on the choice of the model and test conditions, and the results are inconsistent. Sometimes, the matched-degree of the entire system is significantly affected. Real-size bearing testing requires a large amount of manpower for assembling and disassembling, space, large power and material resources, which is not cost-effective. As a result, the R&D cycle is lengthened and can hardly afford. This study proposes an equivalent method based on contact mechanics and the wear mechanism, which considers the balance between efficiency and accuracy for evaluating the lubrication performance of greases. This test rig can test four small-size three-row roller-bearing samples at once, each of which can be filled with a different type of lubricating grease, and all bearings in this test run in exactly the same movement. It is designed to have a more reasonable ratio of sliding distance and contact radius to correlate the fretting conditions of the small-size test bearings with those of the real-size pitch bearings under practical operation conditions as much as possible. This test rig and procedure focus on the comparison and evaluation of the lubrication performance of the tested lubricating grease rather than the test bearings. In this way, the advantages and disadvantages of lubricating greases can be distinguished through such equivalent experiments under the simulative conditions.

2 Design and assemble

2.1 Equivalent model

The equivalent contacting state is the main design principle of this tester, and this model is based on Gerhard Poll's series of research. In this model, the ratio of x (sliding distance of roller) to 2b (width of Herz contact area) is considered as a key parameter[5], which is kept as same value for different bearing sizes[6], to associate larger and small bearings, as shown in Figure 26. In other words, the same x/2b ratio indicates similar severity of contact, friction and wear characteristics.

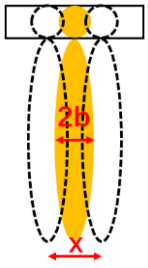

Figure 26 x/2b ratio

Based on the equivalent model, and considering the same roller speed, the calculation equation is as follows:

$$\frac{x_t}{b_t} = \frac{x_r}{b_r} \quad \textbf{Eq. 14}$$

$$x = \frac{\theta R}{2} \quad \textbf{Eq. 2}$$

$$b = 2\sqrt{\frac{QR}{\pi EL}} \quad \textbf{Eq. 3}$$

$$P_H = \frac{4}{\pi}\frac{Q}{bL} \quad \textbf{Eq. 4}$$

$$R_t\theta_t f_t = R_r\theta_r f_r \quad \textbf{Eq. 5}$$

R, E, and L in the equations depend on the bearing size and the material. In this test, YRT100 (usually used as rotary table bearing) is chosen to be equivalent to GW 204-6.7 MW (widely used pitch bearing in wind turbines), and the size parameters are shown in Table 15. (E = 2.11E11)

	YRT100	GW 204-6.7 MW
Radius of raceway(mm)	145	3321
Radius of roller(mm)	2.5	25
Length of roller(mm)	8	50

Table 15 size parameters of bearings

Based on Eqs.1,2,3,4,5 and the data in Table.1, we can obtain the equivalent relation

$$f_t = 10 f_r \quad \textbf{Eq. 6}$$

$$\theta_t = 2.3\theta_r \quad \textbf{Eq. 7}$$

In this test, the frequency of the test bearing (YRT100) is 10 times the GW 204-6.7 MW working in a real environment. Accordingly, the oscillation amplitude should be 2.3 times. The running frequency is much larger than that of the real bearing, and the test can be conducted quickly. The equivalent model provides a chance to simulate a large bearing using a small bearing and provides a conversation from real work conditions to test conditions.

2.2 Transmission and load

We use four test bearings simultaneously to enhance the efficiency and make the measurement results comparable. A servo motor drives the middle bearing and surroundings by a pinion, so that the four gears will run in exact same movement, even phase, as shown in Figure 27. To control the frequency and amplitude, we chose a servo motor to provide power. To run at such a small angle, we used a 1/2 gear ratio to reduce the difficulty of motor control. However, this leads to a high-resistance torque. We calculated the maximum torque resistance of the oscillation and performed a pre-test before the assembly. The selected type of motor is SGDXS-780A00A8002.The gear is combined with the middle plate of the bearings, as shown in Figure 3.

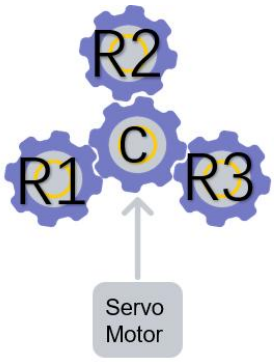

Figure 27 Transmission system

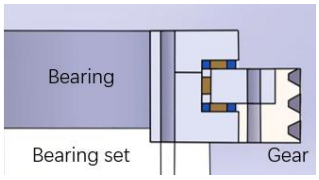

Figure 28 Installation of gears

We chose two types of loading methods to address different situations. One is using a screw to apply a proper pre-load, and the other is by using hydraulic cylinders. The screw connects the cover plate and the bearing set, and a force sensor is placed between the screw and the cover plate, as shown in Figure 29. The load can be read by the sensor when the screw is fastened at different torques. This method is suitable for simple constant-load conditions. On the contrary, hydraulic cylinders can load in a variable way, even programmable in a single test.

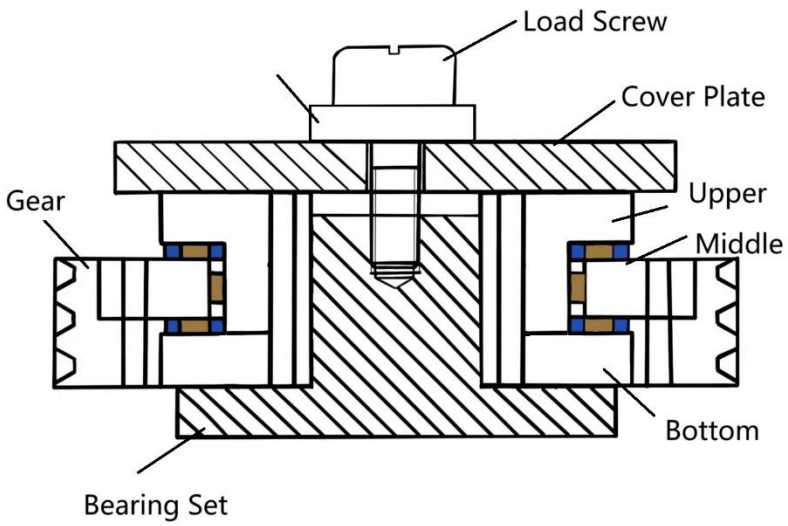

Figure 29 Load by Screws

2.3 Control system design

The work condition of wind turbine is complex and unpredictable. Sometimes we can find some regular conditions by days or seasons, or we can use some mathematic method to extract frequency and amplitude[7]. This demands the tester to be able to run in different tasks in a single experiment. We use a 3-layer control structure to achieve this function:

- An execution layer: a servo encoder including an encoder and hydraulic cylinders. This layer receives the control instruction (PWM and pressure values) from the controller layer and executes a certain action.
- A controller layer: a PLC (programable logical controller). This layer receives the task condition from the manager layer and translates it to control the instruction sent to the execution layer. On the other hand, this layer read the data of sensors and save them in register.
- A management layer: a computer and a console. The console can input simple task (1 condition in 1 task) and the computer can upload complex task (plural conditions in 1 task). The communication between the manage layer and the controller layer is based on Modbus TCP/IP.

2.4 Assemble and pre-test

During the assembly process, the gear clearance is extremely important for stable and accurate testing. If the gear clearance is large, intensive collisions would occur between the gear teeth at the instant of reserving the rotation. This would lead to two undesirable results. First, noise will be intolerable loud. The other is the motion lost when the gear oscillates, and a deviation of roller/raceway contacting position occurs. To avoid this problem, we set each test bearing on a separate sliding plate so that the plate can be adjusted by a screw at the end of the plate, as shown in Figure 30. By fastening the screws, the gear clearance can be reduced to nearly zero. The test rig was named Fretting Wear 4-Bearing, FW4B).

Figure 30 Adjusting screw and sliding plate

3 Test and Result

3.1 Test conditions

In this study, two preliminary experiments were conducted under different conditions. These two experimental conditions correspond to the two real working conditions. The dimensions of the test bearings are presented in Table 15. The two conditions are listed in Table 16.

No.	1	2
Frequency (Hz)	27(2.7)	24(2.4)
Amplitude (°)	±3(1.3)	±3(1.3)
Herz pressure (GPa)	0.75	1.0
Load (kN)	10	18
Cycle number	600000	600000

Table 16 test conditions (equivalent parameters in parentheses)

Two types of grease (K and S) are used in this experiment. The grease allocation is listed in Table 17. The position of each bearing is shown in Figure 31.

No.	1	2
C	K	S
R1	K	K
R2	-	-
R3	S	S

Table 17 Allocation of the grease

Figure 31 Overall of the tester

3.2 Results

After running the tests for 6h (600000 cycles), bearings R1 and R3 were disassembled, and the test grease was collected for analysis and detection. The results are as follows.

3.2.1 Gears

The test gears suffered significantly because they were running under the same conditions as the bearings, except for the loads.

Figure 32 gear tooth surface appearance after test(left)/found in wind turbines(right)

The result for the gear shows that

- The grease was squeezed by moving, and no grease was left on the tooth surface.
- Severe rust has occurred on the tooth surface
- The comparison of the test gear and real gear shows the similarity between the test and real conditions.

3.2.2 Grease

Comparisons of the appearance of the two types of the test grease before and after the test were done on a microscope to observe the magnified appearance and abrasives inside.

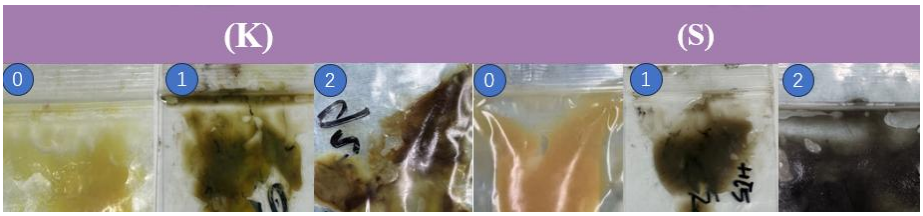

Figure 33 Appearance of the grease

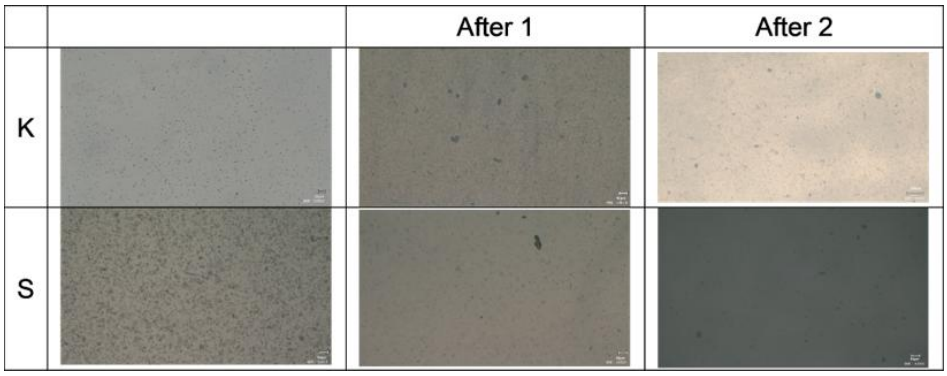

Table 18 Micro appearance of the grease

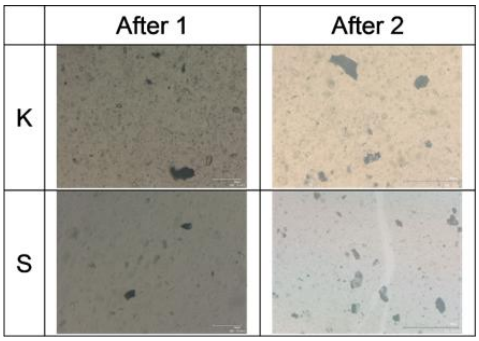

Table 19 Abrasive in grease

According to the observation results, it can be concluded that Condition 2 is more severe than Condition 1. The number of abrasives inside the grease after the test under condition 2 was more visible than that after the test under condition 1. There were a few large abrasives in some of the Grease K samples. However, there is no clear evidence to suggest which grease is more effective.

3.2.3 Race way

Investigations of the grease after test, described above, are not able to distinguish the performance of the two types of grease tested. Further detection of the wear on the race way of the tested bearings was carried out.

	K	S
1		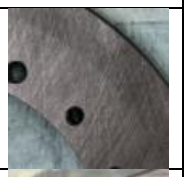
2	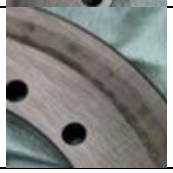	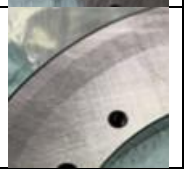

Table 20 Overall appearance of raceway

	K			S
1				
2				
	Fatigue wear	Adhesive wear	Abrasive wear	Abrasive wear

Table 21 Differences in wear on race way

Fatigue, adhesion, and abrasive wear on the raceway lubricated by grease K can be clearly observed under a microscope. However, only a few debris tightly adhered on the raceway were found for the test bearing lubricated with grease S. The trace of wear shows that both of the tested grease cannot protect the bearings from wear in such severe test work conditions. Grease S showed a better performance on reducing fatigue and adhesion. The wear occurred on both sides of the raceway,

4 Conclusions

4.1 Conclusion of the tester

We built a tester that can run under different test conditions in a single task. Two preliminary tests were done on the tester to compare the performance of two types of grease, K and S. The test results show that the test rig can simulate the fretting wear of the pitch bearing observed in practice by comparing the damaged surfaces of gears and bearings.

4.2 Conclusion of grease

Grease S performed better than Grease K under both test conditions. These two greases were tested in the same bearings under the same test conditions and exactly at the same cycles and phase. Three types of wear can be found on the raceway of the bearing lubricated with Grease K, but not on that of the bearings lubricated with Grease S.

5 Bibliography

[1] IEA: Renewables 2024

https://www.iea.org/reports/renewables-2024

October 2024

[2] LEE Joyce, ZHAO Feng: GWEC | GLOBAL WIND REPORT 2024

https://www.gwec.net/reports/globalwindreport

April 2024

[3] RIBRANT J. and BERTLING L.: Survey of failures in wind power systems with focus on Swedish wind power plants during 1997-2005

In: IEEE Transactions on Energy Conversion, Volume 22 ,p167-173

Institute of Electrical and Electronics Engineers, America ,2007

[4] GAO Feng: Performance evaluation of micro motion wear of yaw and pitch bearing grease in wind turbines

In: Synthetic Lubricants 2021, volume 1, p38-42

Sinopec Lubricants Co., Ltd, China, 2021

[5] STAMMLER Matthias, SCHWACK Fabian, BADER Norbert, REUTER Andreas, and POLL Gerhard: Friction torque of wind-turbine pitch bearings – comparison of experimental results with available model

In: Wind Energy Science 2018, volume 1, p97-105

Copernicus GmbH, Germany, 2018

[6] SONG Wooyong and KariKari-Boateng K.A.: Enhanced test strategy of pitch bearing based on detailed motion profile

In: Forsch Ingenieurwes (2021), volume 85,p973–983

Springer Berlin Heidelberg, German, 2021

[7] SCHWACK F , BADER N, LECKNER J, DEMAILLE C, POLL G: A study of grease lubricants under wind turbine pitch bearing conditions

In: Wear 2020, p454-455:20335

Elsevier B.V, American, 2020

Powertrain (Academic Track)

Advancements in Powertrain Test Design and Implementation

J. Hughes[1], D. Cox[1], F. Renger[2]

[1]Offshore Renewable Energy Catapult, Blyth, United Kingdom

[2]RENK Test Systems GmbH, Augsburg, Germany

Keywords: Simulation, Drivetrain, Test Bench

Abstract: In this paper we present an alternative approach to Powertrain Test Bench design – starting with the fully integrated model of the test system's electrical and mechanical components, as well as advanced additional technologies such as Grid Emulation and input power stabilization coupled to a range of modelled turbine parameters. It will discuss the approach of model validation where systems are not yet physically available, as well as how designing for model validation is key to increasing the overall value of the test output.

1 Introduction

Wind turbines for offshore use have increased in size considerably over the past two decades. During this time, the technologies which are used have developed based both on a greater knowledge of the science and engineering of the interplay between the components and the wind, and through analysis of failures. One significant area of growth has been in the use of digital twins to analyze the performance of an operational fleet, and computational modelling to assess performance of new components. In this paper, the concept of using the same modelling techniques to develop designs for wind turbine test benches is introduced, demonstrating the depth of integration which is now being pursued. The benefits of which are that changes to design and test bench performance can be analysed before full scale deployment has been realized.

2 Are New Turbines just Bigger Turbines?

A simple enough question perhaps, but in [NEJ21] an overview of the development pathways which have dominated wind turbine drive train design are presented. Whilst there have been technology shifts which have driven the expansion of the use of wind power, the fundamental principles of wind turbine design remain – to economically generate electricity from the wind whilst ensuring that parasitic forces and moments are resisted reliably. What has changed, however, is the pace at which the power output of turbines, and consequently the input forces, have increased.

From a mechanical point of view, changes in foundation technologies and deployment locations mean that additional challenges are faced by these rapidly developing designs. Increased loading, increased loading rates and longer proposed lifetimes are only some of the challenges which, for instance, a large floating offshore turbine may see compared to its onshore equivalent just 10 years ago.

Offshore turbines have additional load requirements predominantly due to the influence of waves acting on the foundation. However, the complexity of these is dwarfed by the additional loading experienced by floating turbines, where motion of the floater subjects the Rotor Nacelle Assembly to accelerations, many of which are out of phase with those generated by the wind/rotor interaction and have not been experienced on wind turbines with fixed foundations.

The rate of increase of rotor diameters required to capture sufficient wind energy for these larger turbines has outstripped the rate of development in blade leading edge erosion technology. These increases in rotor diameter have led to reductions in rotor speed to maintain a suitable blade tip velocity. This compounds the rate of increase in Low Speed Shaft (LSS) torque beyond that simply due to the increase in output power.

On the electrical front, all modern offshore turbines are Full Converter topologies, with some now utilising Medium Voltage power convertors to reduce generator winding currents.

Control technology both at Wind Turbine and Wind Farm level has also improved, with load reduction and power control algorithms being more common than a decade before.

Therefore, it can be seen that in the pursuit of greater power outputs, Wind Turbine manufacturers have not simply scaled up the turbines by evolution, instead there have been revolutions in technology. Wind turbines in prototype form are now in excess of 20MW per unit, meaning that not only do individual turbine failures lead to significant loss of revenue, but also their maintenance is of an ever increasing complexity.

3 Nacelle Test Benches

Iteratively building prototypes and recording data through component and field testing has been the conventional method of development for wind turbines. Another method for obtaining confidence in revolutionary design changes as well as more evolutionary change, is through the use of Nacelle Test Benches. The concept of testing wind turbine powertrains through the use of ground-mounted test facilities has been investigated by both academic and commercial entities for over two decades due to the high value of results obtained on a more predictable timeline. Many concepts for the mechanical and electrical design of such test benches exist, but all provide the capability to use external motive power (most often through electrical motors) to mimic the torque input of the turbine rotor. This can then be combined with some form of single or multi-axis mechanical force and moment application system to mimic the parasitic loading from the rotor. By reviewing the various developments and state-of-the-art detailed in [IEA12] and [SID23], it is possible to see the following trends:

- Load, moment and torque capability have increased to accommodate more highly accelerated testing of gearboxes and bearings
- “Full scope” test capabilities (load, moment, torque, grid emulation) are now more widespread
- Integration of model-in-loop control architectures have developed
- International Standards are more accepting of the outputs of Test Benches
- Outputs have evolved from simply “survivability” to also include “model validation data gathering”

4 Developing a Test Bench Model

There are a number of reference Wind Turbine models which have been developed in response to the growing wind turbine sizes, and by combining these models with reference floating foundation designs and wind conditions, it is possible to develop an operating envelope for the design of a Nacelle Test Bench. However, due to the range of potential options and tests, it is necessary to consider a number of other influences on the design. These include the type of testing which is expected to be carried out, the rate of increase of turbine power output, the influence of various novel subcomponent technologies, and the complexity of the interaction between the test bench and the wind turbine nacelle.

As an example of this complexity, the displacements and loads required in each axis is driven by the load path stiffness which drives the sizing of hydraulic actuators which form the active part of the load application path, as well as the housing into which they are assembled. Experience of operating test facilities has indicated that allowances for variable clearances caused during test conditions (but not modelled directly in the reference models) should also be taken into account. Furthermore, the load path stiffness may be complicated by potential future technology shifts, such as from rolling element to fluid film bearings, or novel bearing arrangements which may cause additional load path changes.

Floating foundation models also introduce additional harmonic frequencies which must be analysed along with not only their transmissibility from the test bench to the nacelle, but also the rate at which they are applied.

Non-modelled factors such as ease of assembly and permitted off-axis capacity also require consideration as, of course, does cost.

Once all of these parameters are modelled, it is then possible to engage with the designers of such Test Bench hardware to establish the feasibility of the concept. At this time the modelled outputs for the turbine system are interfaced to the test rig models such as those in [REI23]. In that paper, the authors report on how the control dynamics of an integrated mechanical test rig can be modelled through use of a test facility digital twin.

For the development of the project for ORE Catapult, it was necessary to add further simulations to the model to ensure the stability of the electrical grid feeding the site.

5 Upgrading the ORE Catapult Test Bench

In 2018, ORE Catapult completed the commissioning of a large wind turbine nacelle test bench including a medium voltage grid emulator.

Whilst this facility has been able to deliver testing for groundbreaking turbines such as GE Vernova's Haliade X platform, the continued growth of turbine outputs has meant that it can no longer provide the power, torque or loading which will be required for turbines over the next decade.

The goals of the upgrade have been to implement some operational findings from the many thousands of hours of testing which have been carried out as well as ensure that the key design parameters given above are implemented.

Working alongside RENK Test Systems, ORE Catapult's engineering team have sought to integrate much of the physical data acquired during the construction of the existing facility (such as ground conditions, foundation survey records and the like) to enable a full load path stiffness analysis to take place within the RENK digital twin.

The nominal electrical capacity of the test facility is being increased from 15MW to in excess of 30MW to accommodate the rapidly increasing turbine power and driveshaft torques of new wind turbines. However, the ORE Catapult test facility is located in the town of Blyth in the North East of England, which is fed by a 24MVA Primary 66/11kV substation. The baseload of this substation consists of a major residential and commercial area, and so transient disturbances of the type which can occur during grid ride-through testing are not welcome by Northern Powergrid (the Distribution Network Operator).

One solution to this issue would be to move the connection from the 11kV network to the 66kV circuit with the associated increase in fault level. Simulations were carried out by ORE Catapult's Electrical Networks team to establish the prospective voltage dip caused by a 25MW Zero Volt Ride-through (ZVRT) emulation on each of the connection scenarios. As expected, the higher fault level of the 66kV connection reduced the impact of the ZVRT on the public grid but created a voltage dip of up to 10% on the internal 11kV network. Even where reactive power compensation is used, there is still a significant transient current imparted on the input transformer, due to the nature of the test, which could lead to premature damage to the transformer windings.

To provide a more sustainable system, ORE Catapult and RENK Test Systems have been working with ABB to develop a more intelligent solution to the transient energy problem through the use of

integrated energy storage. To ensure that the test bench is able to recreate the full range of grid conditions required to achieve global certification, sufficient electrical inertia is required to match the range of Wind Turbine inertias which will both be present, and will need to be emulated [JAS14]. The simulation of the energy storage within the model ensures that sufficient energy is available to emulate this inertia.

The increase in electrical power capacity is matched by a mechanical shaft torque increase from 18MNm to over 40MNm using a RENK Multi Motor Drive system as discussed in [REI23] which uses 12 individual motors through a combining gear to drive the main low speed output shaft which connects the Test Bench to the Wind Turbine.

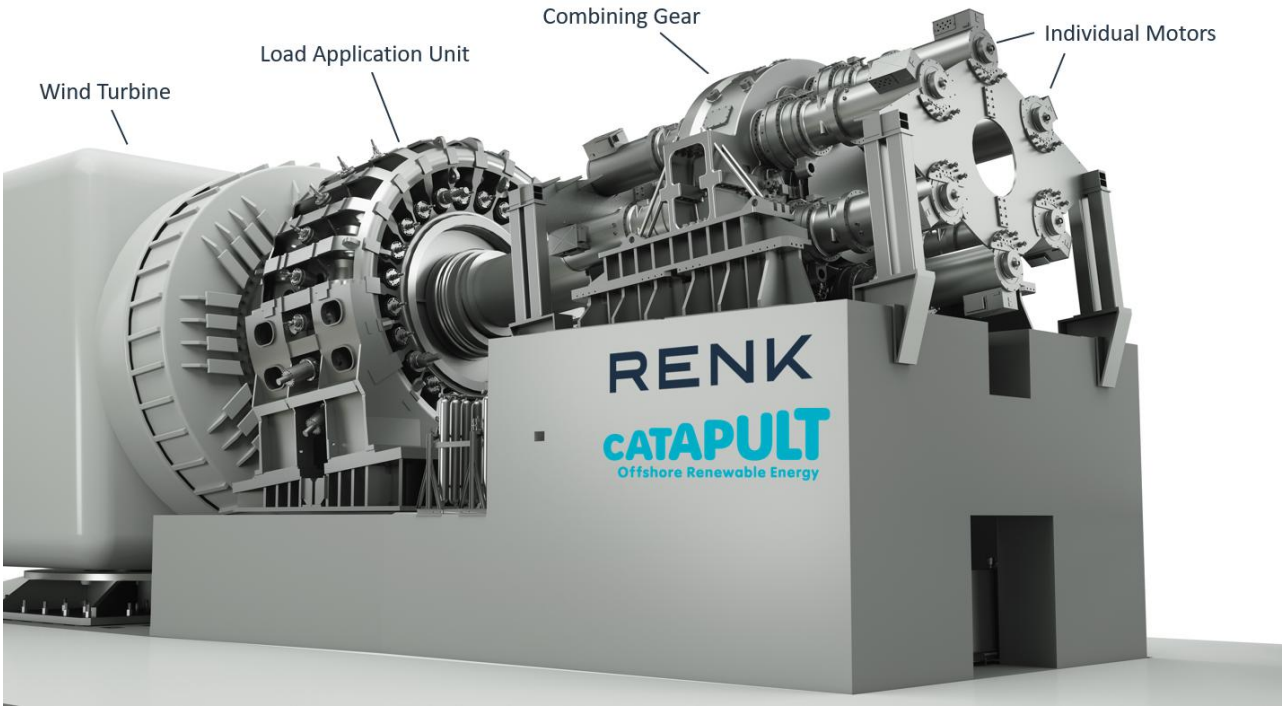

This torque increase is achieved in the context of an already constructed foundation which has defined some of the mechanical space constraints, as well as structural moment limits.

6 Validating the Integrated Modelling for Test Facility Design

Bringing together all of the factors outlined above into a numerical model which can be used to solve for all interactions has meant the generation of suitable and adequately parameterised transfer functions. These transfer functions allow for the following inputs and outputs to be analysed:

- Foundation to ground response
- Motor and LAU structural limitations
- Gear tooth interactions including lubrication
- Motor mechanical and Electromagnetic properties
- Electrical feeding grid characteristics
- Power converter operation
- HiL and control system latencies
- Load Case information for electrical and mechanical tests
- Wind Turbine mechanical responses
- Control feedback device behaviours and sensitivity (torque transducers)

- Mechanical safety elements
- LAU Actuator control and response including hydraulic elements
- Resultant Load interactions between Wind Turbine and Test Bench strongfloor

Many of these individual elements are already proven by executing sections of the model in isolation and comparing results against measured data and input conditions from the existing test system. Others have needed to be compared against established methods of calculation to ensure that the results can be used. Sensitivity analyses have then been carried out to identify if any of the modelled input terms are close to stability or performance limits. The model is also able to identify the resolution to which a simulated load case will be reproduced at the connection to the Test Rig and the impact of various design changes on that resolution can be analysed.

Through use of this combined model, it is possible for ORE Catapult to gain confidence in the performance of the final design, across a range of wind turbines which have yet to be developed and thus ensure that the operational performance of the upgraded Test Bench is fit for purpose.

Further validation of the model will take place during the final physical commissioning of the test bench, which will also serve to calibrate the model for use as a tool for the design of tests, analysis of Hardware-in-the-Loop algorithm stability and future planning.

7 Summary/Conclusion

The complexity of wind turbines and the importance of the reliability of their components is ever increasing. To prove out the rapidly changing technologies, Test Benches can be used to deliver complex tests in a repeatable manner.

Numerical models for each part of ORE Catapult's planned upgrade to their wind turbine drive train test bench have been developed and will be validated against the final construction. The initial validation and amalgamation of these models allows ORE Catapult to have confidence in the design so that complex test conditions can be created for a range of customers, including those with new technologies.

Once the test bench has been constructed, the models will continue to provide calibrated simulation capability to allow for more advanced and complex testing of Wind Turbines without the expense and risk of building field prototypes.

8 Bibliography

[NEJ21] Nejad, A et al: Wind turbine drivetrains: state-of-the-art technologies and future development trends. In Wind Energ. Sci., 7, 387-411, EAWE 2022

[IEA12] IEA R&D Wind Task 11 TEM: Advances in wind turbine and components testing. IEA 2012.

[SID23] Siddiqui, M et al: Wind turbine nacelle testing : State-of-the-art and development trends. In Renewable and Sustainable Energy Reviews 188, Elsevier, 2023

[REI23] Reicherter, J et al: Multi-Motor Drive Technology in the Multi-Meganewtonmeter-Range. In DSEC 2023.

[JAS14] Jassmann, U et al: An Innovative Method for Rotor Inertia Emulation at Wind Turbine Test Benches. In Proceedings of the 19th World Congress The International Federation of Automatic Control, Cape Town, 2014.

HyDrive: Continuously Variable Hydraulic Power-Split Drivetrain for Wind Turbines

P. Seifermann[1], A. Dam[1], P. Dalhoff[1], S. Störtenbecker[1], T. Petersen

[1]CC4E, HAW Hamburg, Berliner Tor 21, 20099, Hamburg, Germany

Keywords: Wind Energy, Drivetrain, Power-Split, Hydrostatic

Abstract: The research project HyDrive by the Competence Center for Renewable Energy and Energy Efficiency (CC4E) at Hamburg University of Applied Sciences (HAW Hamburg) focuses on the development of a continuously variable, hydro-mechanically power-split transmission concept for modern large-scale wind turbines. In addition to summarizing the current state of the art in power-train technology, both with and without power splitting, and conducting a comprehensive market analysis of the most common concepts, the HyDrive transmission concept with its particularities will be explained. This includes discussing potential benefits of the concept as well as challenges in the development process. Initial calculation results provide insights into the positioning of the power-split and the design of the direct transmission without hydraulic portion. Considering different wind speed averages these results are used to determine the annual energy yield and what energy proportion must pass through the hydraulic system.

Nomenclature

Symbol	Unit	Name
E	Wh	Energy
i_{12}	-	Planetary gear ratio ring / sun gear
i_{2c}	-	Planetary gear sun gear / carrier
i_{tot}	-	Total drivetrain gear ratio
n_1	rpm	Rotary speed ring gear
n_2	rpm	Rotary speed sun gear
n_c	rpm	Rotary speed carrier
$n_{cut\text{-}in}$	rpm	Rotary speed rotor at cut-in wind speed
n_{gen}	rpm	Rotary speed generator
n_{rated}	rpm	Rotary speed rotor at rated wind speed
$n_{rotor,direct}$	rpm	Rotary speed rotor at direct transmission
P_{rated}	W	Rated Power of the turbine
T_1	Nm	Torque ring gear
T_2	Nm	Torque sun gear
T_c	Nm	Torque carrier
v_{wind}	$\frac{m}{s}$	Wind speed

z_1	-	Number of teeth ring gear
z_2	-	Number of teeth sun gear
η	-	Efficiency

Table 22: Nomenclature

1 Introduction to Wind Turbine Drivetrains and State of the Art

The drivetrain of a wind turbine is required to convert the mechanical energy of the rotor into electrical energy. There are two basic concepts that have become established in modern turbines: Turbines with gearboxes and direct-drive turbines [HAU16, GAS05, SCH22, ZHA23]. The basic design of both types differs in the presence of a gearbox (mechanical/ hydraulic) between the rotor and generator shaft. Hydraulic gearboxes have so far only been the subject of research and are not used in commercial systems [SCH22].

1.1 Direct-Drive Wind Turbines

In a wind turbine with a direct-drive (Figure 34) a multi-pole, usually permanently excited synchronous generator [ZHA23, GAJ16] with a rated speed of for example 15 rpm at 15 MW [MAR18, GAE20], is installed directly on the rotor [SCH22]. The required speed variability is achieved using a frequency converter. This adjusts the fluctuating frequency from the direct-drive generator to the grid frequency. The advantage of these systems is their compact design with few wearing parts and no gearbox losses. Failure rates and times are lower for this type of system than for comparable systems with gearboxes [SCH22, NEJ22, TAH20]. Due to the large number of pole pairs (up to 200 at 15 MW), such generators have a very large diameter (up to 10 m at 15 MW) [GAE20] and, if designed as externally excited generators, are heavier (30 t MW) [HAU16] than a gearbox/generator unit. For direct-drive 2 systems externally excited generators are approx. 50 % heavier than permanently excited generators (18-20 t MW) [HAU16]. The volume of a direct-drive generator is around 100 times greater than a generator of the same power class with a gearbox [NEJ22]. This results in very high costs for the generator, especially due to the high demand of rare earths neodymium magnets for permanently excited generators or the copper windings for externally excited generators [HAU16, SCH22]. Of all in 2023 worldwide newly installed turbines, 8.7 % were with a direct-drive turbine [ZHA23]. Manufacturers that particularly rely on this concept are Siemens Gamesa Renewable Energies in the offshore sector [ZHA23, SIE24] and Enercon in the onshore sector [ZHA23, ENE24].

1.2 Geared Wind Turbines

Systems with a mechanical gearbox (Figure 35) in today's standard power classes of several MW have a multi-stage planetary spur gearbox installed between the rotor and generator [HAU16, ZHA23]. The gearbox increases the speed level so that a generator with fewer poles and a rated speed of 150– 1500 rpm [HAU16] can be used. These generators are approx. 5-9 times lighter [MAR18] and cheaper than generators for direct-drive systems [MAR18]. However the savings from the smaller generator are counteracted by the mass and cost gain that comes from using a complex gearbox, which also raises the susceptibility to faults. Current developments are moving in the direction of medium-speed generators with lower transmission ratios and lower speeds (150– 500

rpm) [HAU16]. This allows the advantages of both drivetrain concepts to be combined [HAU16, SCH22, BAK13]. Drivetrains with gearboxes have become increasingly compact and powerful in recent years. The torque density of gearboxes has almost quadrupled since 2005 and is now up to 200 $\frac{Nm}{kg}$.

1.3 Hydraulic Drivetrains in Wind Turbines

For some time now, attempts have been made to develop a hydrostatic transmission (Figure 36) as an alternative to mechanical transmissions. However, it has not yet been possible to integrate a competitive system on the market [ZHA23]. In a hydrostatic transmission, the rotor drives one or more hydraulic pumps. These are connected to hydraulic motors via a hydraulic circuit, each of which in turn drives a generator. The pump or motor is usually adjustable and thus enables a continuously variable transmission (CVT) ratio for the entire transmission. The required speed variability of the rotor can therefore be implemented without the help of a now needless inverter. In combination with the high power density of hydraulic gearboxes, this allows mass and costs to be saved. Problematic are the large leakage losses at low flow rates and low adjustment angles of the hydraulic components [RAM06]. To avoid this problem, there are concepts with several small hydraulic pumps that can be switched on sequentially as the power increases. To ensure full speed variability only one of these pumps needs to be adjustable [NEJ22, RAM06, MAH19]. There are also various approaches for moving the generator and the hydraulic motor from the nacelle to the ground. This allows the nacelle mass to be drastically reduced but requires hydraulic pipes along the tower. Costs and efficiency losses associated with this might eat up the benefits of nacelle mass savings. In addition, several turbines can also drive one generator, which can save further costs [NEJ22, MAH19].

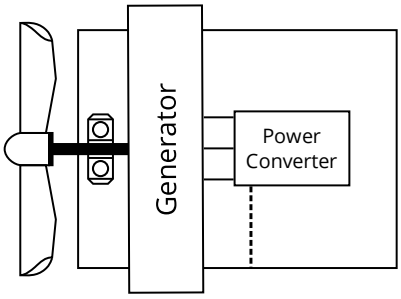

Figure 34: Schematic structure of a direct-drive wind turbine

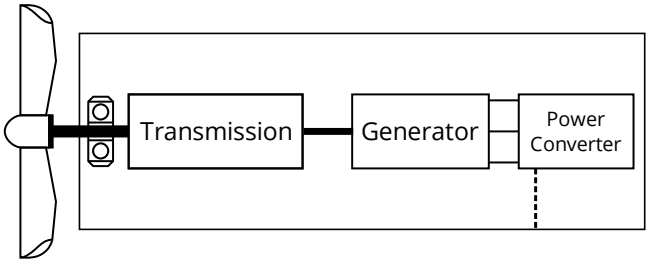

Figure 35: Schematic structure of a wind turbine with mechanical gearbox

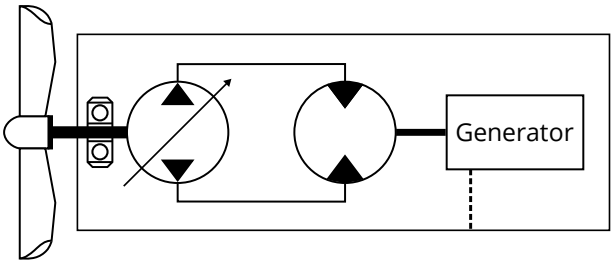

Figure 36: Schematic structure of a wind turbine with hydrostatic transmission

1.4 Power Split Drivetrains

Various advantages of mechanical and hydraulic drivetrains can be combined with a power-split, hydro-mechanical superimposed gearbox. The simple and fast stepless adjustability of hydraulics and the efficiency of a mechanical drivetrain can thus be combined in one system. Studies on construction machinery show that a power-split hydromechanical transmission is up to 7.5 % more efficient than a comparable hydro static transmission [XIO19]. Such transmissions have been used in various commercial vehicles (military, agricultural, construction machinery) since the 1970s [YU19]. Here, a constant rotational speed of a combustion engine is converted into a variable rotational speed of the wheels. For this purpose, part of the input power is taken via a spur gear or planetary stage, passed through an adjustable hydraulic circuit and then superimposed again with the drive power in a planetary stage (Figure 37). Most of the power is transmitted with good efficiency via the mechanical gearbox and a part (10-20 % of the nominal power) [MAN17] via the hydraulics. This small part is sufficient to achieve a continuously variable transmission with comparatively good efficiency. In addition, a direct transmission can be defined by design, in which the hydraulics do not have to transmit any power and the gearbox has the optimal, purely mechanical efficiency [JAN08] If this concept is transferred to wind energy, the following advantages and disadvantages are expected (Table 23) compared to standard drivetrains [MAN17, BOT18, TON19]:

Advantages	**Disadvantages**
Elimination of the frequency converter • Weight saving • Increased efficiency • Reduction in susceptibility to electrical faults • Cost savings	Complex System • High design effort • Susceptibility to faults
Damping by hydraulic circuit	Almost identical gearbox as with geared wind turbines + hydraulic gearbox
“Real” inertia for grid stability due to direct grid coupling	Large transmission ratios of the gearbox
Use of a low-cost, lightweight synchronous generator	

Table 23: Expected advantages and disadvantages of the power-split, hydromechanical drivetrain.

For wind turbines the power-split approach has not yet been able to establish itself and is also less researched than fully hydrostatic transmissions. At the beginning of the 2010s, the company Voith tested a power-split hydromechanical gearbox as a prototype and built 16 2 MW turbines. These turbines had a power split transmission that did not use conventional hydraulics with a hydraulic pump and hydraulic motor but used a hydrodynamic converter that implements the function of both components in a single component. According to the manufacturer, the prototype phase went very well, and they wanted to take the project further [JOO11, DEW07]. For reasons that are no longer comprehensible today, the project was discontinued shortly afterwards. Current research is mainly concerned with the assessment of different design layouts. There are many ways a power-split transmission can be arranged. Various factors such as the position of the power-split (input split or output split), the type of adjustment (mechanical [COT04], electrical [LIU16] or hydraulic [BOT18]) or the output shaft of the planetary gear (sun gear or ring gear) can be varied. According to Mantriota [MAN17], the smallest possible configuration of the CVT can be achieved by power splitting on the rotor-side (10 % of the rated power). On the other hand, splitting the energy on the generator-side would lead to a configuration with maximally 15 % of the rated power going through the CVT. In the optimal case energy production would increase by up to 10 % compared to fully hydrostatic drivetrains [BOT18].

2 HyDrive Structure and Function

The proposed drivetrain (Figure 37) consists of a mechanical transmission with a fixed transmission ratio (a), a power-split (b), a hydraulic CVT (c) and a planetary gear working as power summation (d). Part of the power is taken off via a continuously variable hydraulic pump and transferred to a planetary stage via a hydraulic motor and thus fed back to the drive shaft. In the planetary gear, the rotational speeds of the sun- and the ring gear are added up to determine the rotational speed of the generator.

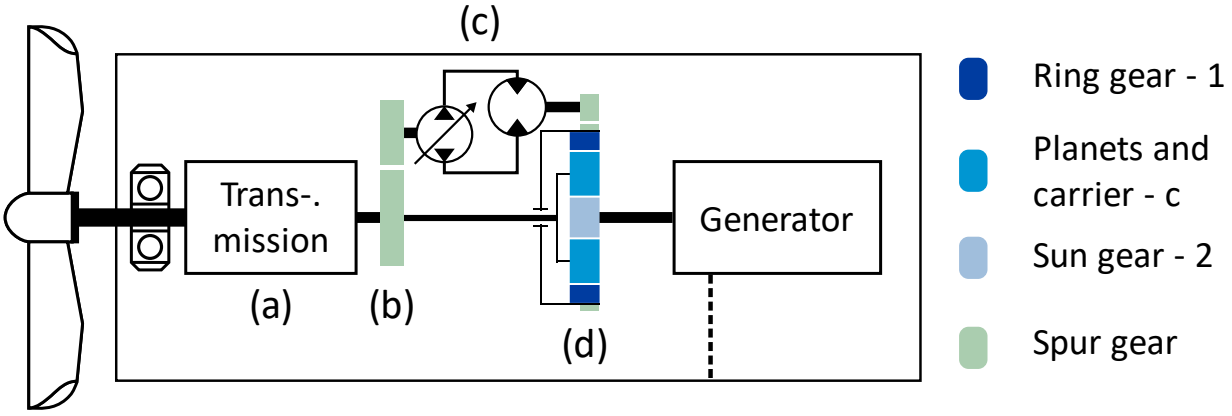

Figure 37: Schematic structure of a planetary gearbox with the components: ring gear (1), carrier (c), sun (s) and the planets.

The rotor speed needs to be controlled to maintain the required blade tip speed (calculated from a tip speed ratio λ). The synchronous generator is operated directly from the grid without a frequency converter. This results in a fixed rotational frequency on the generator-side that is proportional to the grid frequency, depending on the number of pole pairs of the generator [HAU16, MAN17]. To be able to control the speed of the rotor, the transmission ratio of the gearbox must be changed. For this purpose, a conventional 3-stage wind turbine gearbox is modified so that the last stage- in contrast to the first stages- has a freely rotating ring gear that can be driven by a hydraulic motor

(see Figure 37). When the hydraulic motor is stationary, the ring gear is also fixed and the transmission ratio of the third stage corresponds to the stationary gear ratio selected by design, which results from the ratios of the numbers of teeth [MÜL98]:

$$i_{12} = \frac{n_1}{n_2} = \frac{z_2}{z_1} \qquad \textbf{Eq. 15}$$

The stationary gear ratio describes the ratio from the sun to the ring gear with the carrier held in place. For this application the more interesting ratio is the one between the carrier (rotor speed) and the sun (generator speed) when the ring gear is fixed, which can also be calculated from the stationary gear ratio:

$$\mathbf{i_{2c}} = \frac{n_2}{n_c} = 1 - \frac{z_1}{z_2} = \mathbf{1} - \frac{\mathbf{1}}{\mathbf{i_{12}}} \qquad \textbf{Eq. 16}$$

By selecting a stationary gear ratio for the third stage, a direct transmission is defined in which the efficiency of the overall gearbox is optimal. The ring gear can be driven in both positive and negative direction of rotation. The respective speeds can be calculated using the basic speed equation [MÜL98]:

$$n_1 - i_{12} \cdot n_2 - (1 - i_{12}) \cdot n_c = 0 \qquad \textbf{Eq. 17}$$

By regulating the speed of the hydraulic motor connected to the ring gear, the transmission ratio i2c can be continuously adjusted by regulating the ring gear speed. For this purpose, a hydraulic unit is used that diverts its power from the rotor power, allowing almost any speed to be set on the ring gear (Figure 37). The hydraulic pump must be adjustable so quickly that fluctuations in the wind can be compensated for and the rotor speed can be kept constant.

2.1 Position of Power-Splitting

Two variants are considered, which differ in the location of power extraction. The power can be extracted upstream of the summation planetary stage (rotor-side), but also downstream of the planetary stage (generator-side).

The rotor-side power-splitting (Table 24, left) has an easily comprehensible power flow that splits into two separate paths at the rotor shaft, behind the first two planetary stages, and is later reunited. However, the control effort could be problematic, because the actuation of the hydraulic pump leads to a direct braking torque on the rotor shaft. At the same time, the hydraulic motor causes a change in the speed of the rotor shaft via the planetary gearbox, which results in feedback.

In the event of power-splitting on the generator-side (Table 24, right), the power is only diverted after the last planetary stage and added back to the ring gear. The advantage of this is that the speed of the generator shaft is always constant and there are no control conflicts due to double braking of the rotor. However, the generator torque must be controllable in this arrangement, which rules out a permanently excited synchronous generator.

	Rotor-side	Generator-side
$v_{wind} < v_{direct}$	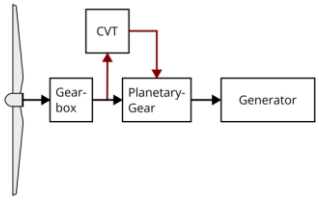	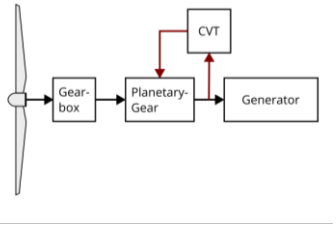
$v_{wind} = v_{direct}$	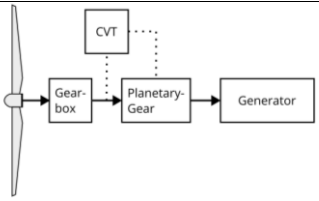	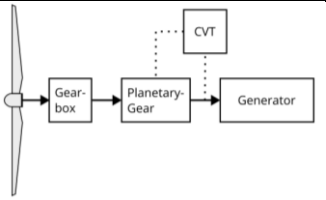
$v_{wind} > v_{direct}$	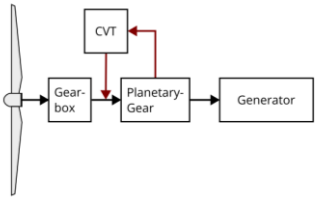	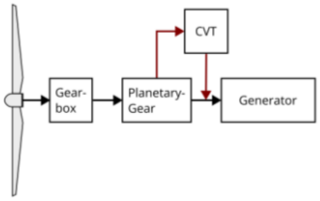

Table 24: Power flows on rotor- and generator-side power-split at wind speeds lower and higher to the respective direct transmission.

2.2 Direct Transmission

As mentioned before, such a gearbox offers a direct transmission that can be defined by design in a way that no power must be branched, and the complete power is trans mitted via the mechanical gearbox. At this defined fixed speed, the overall gearbox has the best efficiency, which continues to decrease as the hydraulic power increases, as the hydraulic losses are greater than the mechanical losses. The mechanical transmission ratio can be determined via the selected direct-drive speed:

$$i_{tot} = \frac{n_{gen}}{n_{rotor,direct}} \qquad \textbf{Eq. 18}$$

In all previous research, this direct transmission is at the nominal speed of the wind turbine and is also assumed to be the case here at the beginning. The advantage is that maximum efficiency is achieved at high power output.

However, the average wind speed at onshore locations is usually significantly below the nominal wind speeds of the turbines and full-load operation can often only be run in short periods of time. It is therefore necessary to investigate how the system behaves when the direct transmission is set to other speeds.

2.3 Basic Parameters

The 10 MW DTU research wind turbine [BAK13] serves as a base model. This is an offshore turbine with a medium-speed generator for which there is publicly available turbine data. The following relevant changes were made to the original parameters for the power-split gearbox:

Parameter	Variable	10 MW DTU-Turbine	HyDrive	Unit
Minimum rotor speed	$n_{cut\text{-}in}$	6	3,21	rpm
Maximum rotor speed	n_{rated}	9,6	9,16	rpm
Maximum generator speed	n_{gen}	480	750	rpm
Gear ratio	i_{tot}	50	82	-

Table 25: Key attributes and changes of the used 10 MW DTU research turbine.

These parameters are used as the basis of the calculations. The generator speed was increased as it is assumed that weight and costs can be saved with a low-pole synchronous generator. As a first step, the simplest possible characteristic curve should be used, which is also comparable to the standard characteristic curves. In the standard DTU system, the rotor speed is maintained at a constant 6 rpm for wind speeds below 7 m s. To allow for a linear increase in speed with the ideal tip-speed-ratio under partial load, the cut-in and rated rotor speeds were adjusted. Therefore, the gear ratio must rise to compensate the lower cut-in speed and the higher generator speed.

3 Computation and Results

Following computations should help to better understand the system and show how the system can be influenced by varying certain design parameters. These design parameters are:

- Location of power-split (rotor- or generator-side)
- Mechanical transmission ratio of the drivetrain (direct transmission)

A simple calculation model is created in Matlab Simulink based on the basic speed equation (3). Mass inertias and irreversibilities are not considered and the calculation is quasi-static. The model is structured in such a way that the power and speed values are read from the DTU-turbine data for a given wind speed. With these values, the basic speed equation can be used to calculate how high the rotational speeds and, according to equations (4) & (5), the torques on all planetary shafts must be to maintain the desired rotational speed on the rotor and generator. Torque on the ring gear (1) or on the sun (2) [MÜL98]:

$$T_1 = \frac{T_c}{i_{12} - 1} \qquad \textbf{Eq. 19}$$

$$T_2 = \frac{T_c}{\frac{1}{i_{12}} - 1} \qquad \textbf{Eq. 20}$$

In the first step, it is assumed that the direct transmission of the gearbox is defined in such a way that the hydraulics do not have to transmit any power under nominal load, i.e. they are stationary and only apply a holding torque. The maximum speed of the ring gear must therefore be reached at the lowest rotor speed and then decreases proportionally to the increase in rotor speed (Figure 38). The torque also increases proportionally to the rotor torque and then remains constant when the nominal load is reached. The calculation is carried out using the parameters from Table 25 and Table 26. The wind speed is increased linearly from cut-in to cut-out.

Parameter	Value	Unit
P_{rated}	10	MW
$i_{2c,3}$	4	-
v_{wind}	4 - 25	$\frac{m}{s}$
η	1	-

Table 26: Additional assumptions for the first calculation

Multiplying the angular speed and torque results in the power that must be applied to the ring gear to move it as desired. The hydraulic system must be able to provide this power.
It is assumed that both the hydraulic motor and the hydraulic pump are connected to the ring gear or the output shaft with a transmission ratio of 1. In this case, the sizes of the hydraulic motor correspond to those of the ring gear and the sizes of the pump correspond to those of the output shaft. In the following, the term hydraulics is used as a synonym to ring gear.

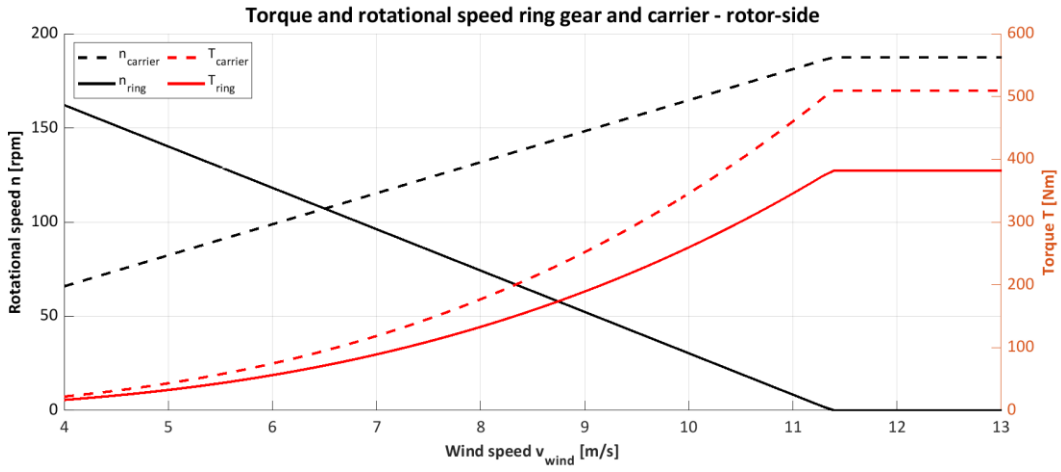

Figure 38: Torque and speed of the planet carrier and the ring gear over the wind speed in the partial load range. Absolute values. The planet carrier corresponds to the rotor multiplied with previous, fixed gear ratios.

3.1 Comparison of rotor and generator-side power split

If the power curves of the ring gear are examined, power-splitting on the generator-side and power-splitting on the rotor side (Figure 39) have a different maximum value. This maximum value corresponds to the maximum hydraulic power according to which the hydraulics must be designed.

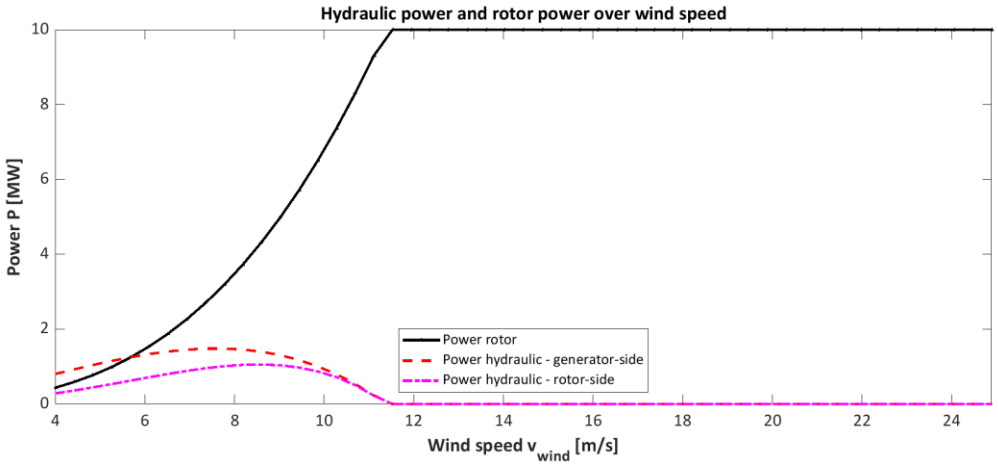

Figure 39: Hydraulic power with rotor- and generator-side power-splitting in comparison to rotor power for the direct transmission at rated wind.

For the hydraulic power, a maximum of 10.56 % of the nominal power results for rotor side power-splitting and a maximum of 14.81 % for generator-side power-splitting. Mantriota [MAN17] arrived at a similar result in his research (10 and 15 %). The speeds 11 in both concepts are identical, as both rotor and generator speeds are not varied. In the case of rotor-side power-splitting, part of the torque is branched off before the planetary stage, which is why a lower torque prevails within the planetary gearbox.

The following ratio applies [MÜL98]:

$$T_1 : T_2 : T_c = \text{const.} \qquad \textbf{Eq. 21}$$

It can also be seen that the hydraulic power has a greater value than the input power for generator-side power-splitting at low wind speeds. From a quasi-static perspective, this could be explained by summation within the power branch, but it is unclear if this concept works in a dynamic system. As the speed characteristic curve of the DTU-turbine was changed in this area, it is possible that a better case will result for the real system, as the standard value of the cut-in speed is higher. A dynamic simulation must show which states are stable. If a different direct transmission is selected, the zero crossing of the hydraulics shifts further to the left towards lower wind speeds (Figure 40). The smaller the direct transmission, the lower the maximum value of the hydraulics. At the same time, the hydraulic power also assumes negative values and thus has a negative maximum. This negative maximum quickly exceeds the positive maximum significantly and goes up to 61 % of the rated power when the direct transmission is at cut-in wind speed. The sign reversal means that the direction of rotation of the ring gear is reversed. This also reverses the sign of the torque and thus the direction of the power flow (see Table 24). The hydraulic power must therefore be designed according to the absolute maximum value.

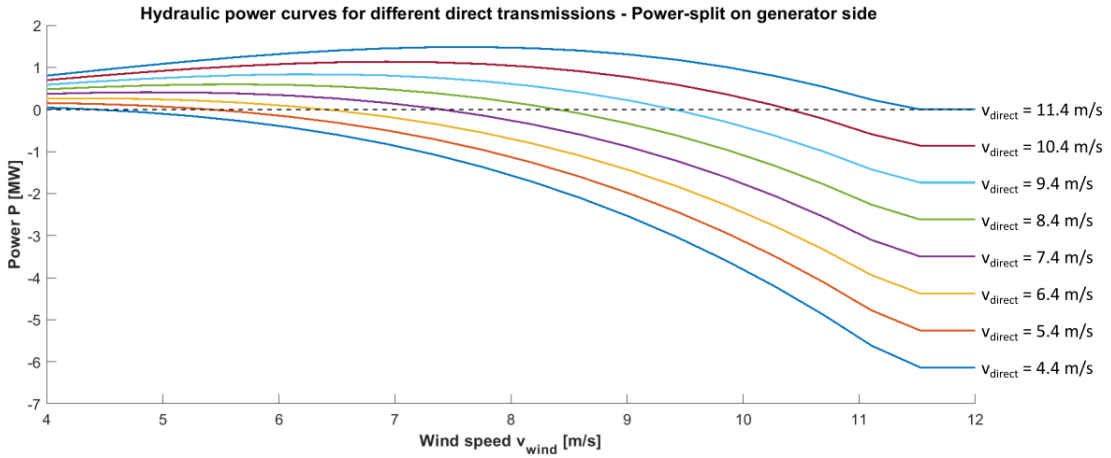

Figure 40: Hydraulic power curves for different direct transmissions – generator-side.

The aim is to check whether there is a better operating point than the standard case, so that the hydraulics can be designed to be as small as possible. In addition, an estimate of the annual energy production (AEP) is to be used to compare which state is the most sensible from an energetic point of view.

3.2 Minimizing the maximum hydraulic power

To minimize the maximum hydraulic power, the calculation is carried out for direct transmissions between 4 and 25 $\frac{m}{s}$ with increments of 0.1 $\frac{m}{s}$. The hydraulic power curve is created for each calculation (see Figure 40). In Figure 41, the absolute maximum value is plotted for each calculated direct transmission. The decrease in power on the rotor-side produces slightly lower values near direct speeds at nominal wind speed but is otherwise significantly higher than the decrease on the generator-side. Both curves have a low point. For this low point the positive maximum value and the negative maximum value take on the same absolute value. In the case of rotor-side power-splitting, this low point is at a direct transmission of 10.5 $\frac{m}{s}$ with 8.4 % of the nominal power. In the case of generator-side power-splitting, the low point is at a direct transmission of 10.2 $\frac{m}{s}$ with 10.7 % of the nominal power. The extent to which this deviation is significant should be shown by calculating the AEP

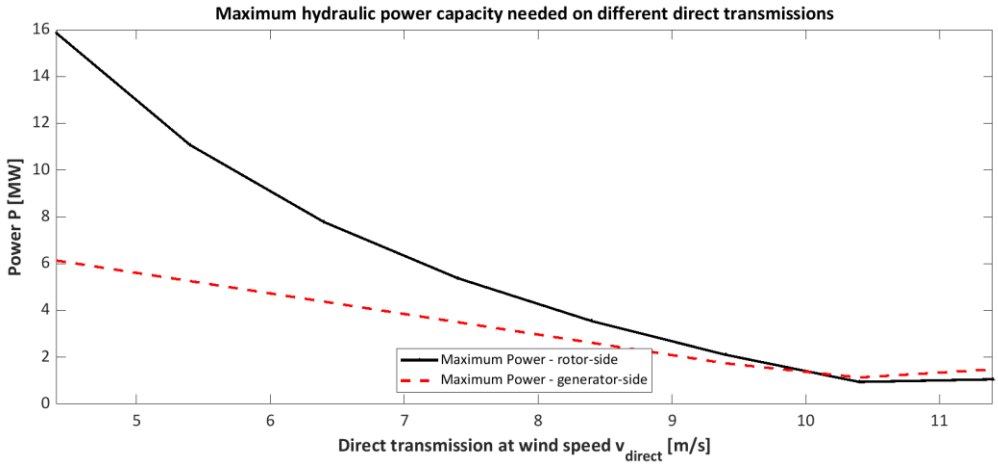

Figure 41: Absolute maximum hydraulic power of direct transmissions from 4 to 11.4 $\frac{m}{s}$.

3.3 Maximizing the AEP

In addition to minimizing the nominal power of the hydraulics, another goal is to maximize the energy yield. Under the assumption that the power loss through the hydraulics is greater than the loss via the mechanical drivetrain, it is to be compared which direct transmission and which power-splitting side can deliver the better annual yield. The amount of energy that must be transmitted via the hydraulics should therefore be minimized. For this purpose, the AEP is determined by using the Rayleigh cumulation distribution function (CDF) in accordance with IEC 61400-12-1 for average annual wind speeds of 4 - 11 $\frac{m}{s}$ [DIN17]. This results in an annual hydraulic energy for every combination of possible direct transmissions and average wind speeds (Figure 42).

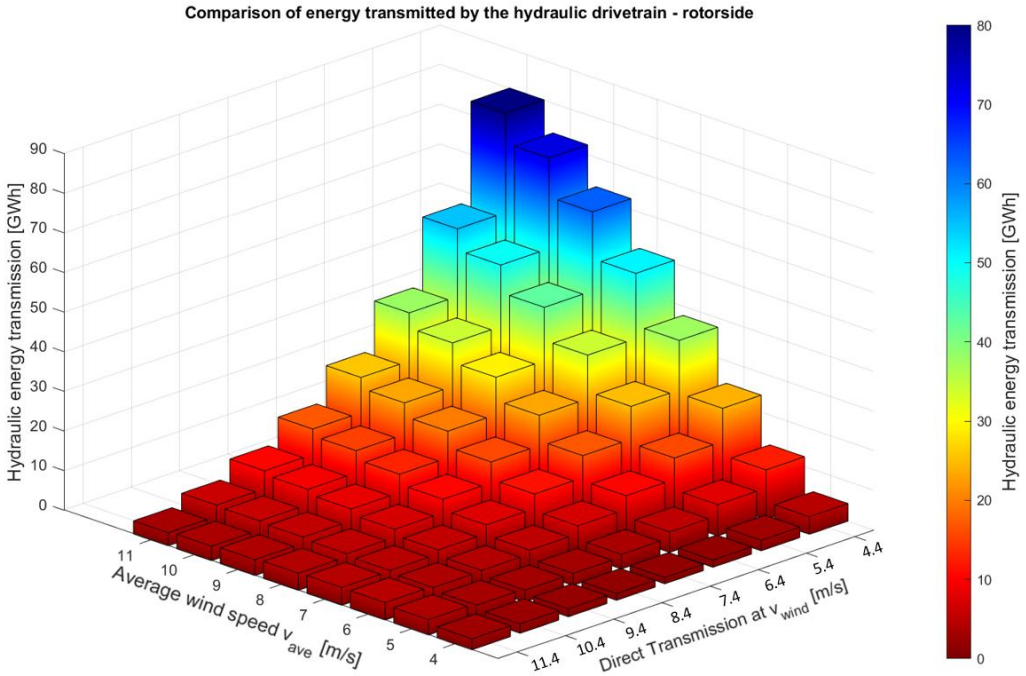

Figure 42: Hydraulic energy - absolute values, at different mean wind speeds and different direct transmissions.

It is observable that the minimum hydraulic energy is required at the direct transmission at rated wind speed of the DTU-turbine and in general for low average wind speeds. Overall high direct transmissions seem to lead to rather low hydraulic energy, as do very low wind speeds. However, this is only due to the total AEP being the lowest at low wind speeds and it is increasing non-linearly with higher wind speeds. To recognize the real optimum, the hydraulic energy values must be

set in relation to the total AEP (

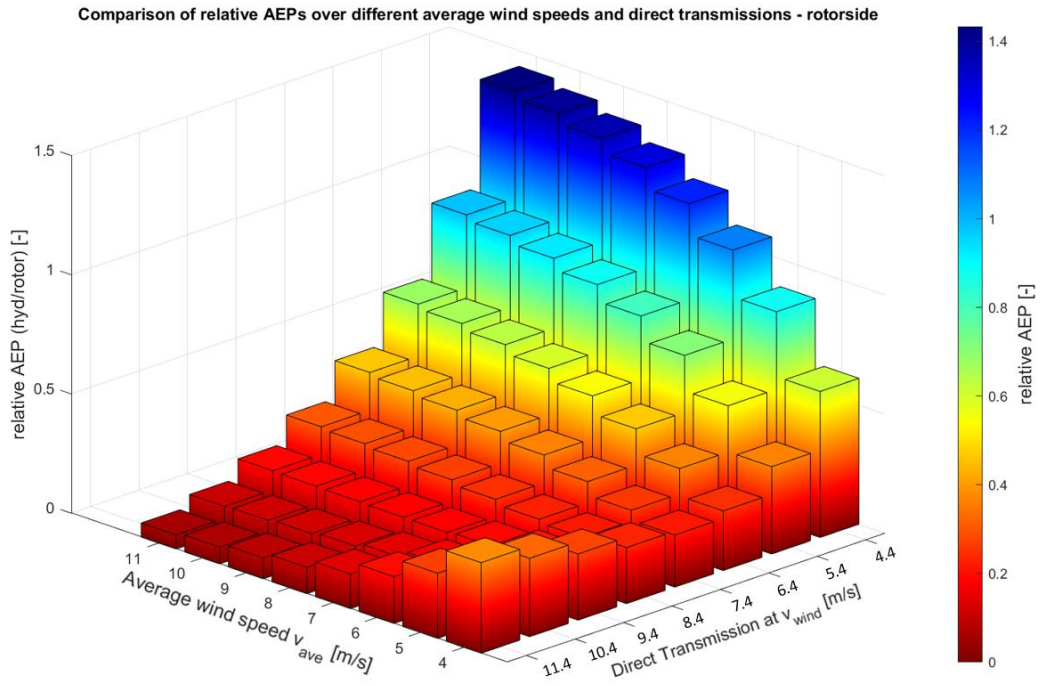

Figure 43). Relative to the total AEP, the hydraulics have to transfer the least energy for direct transmission being at rated wind speed, when the average wind speed is 11 m/s. However, even direct transmissions close to rated wind speed and at somewhat lower wind speeds are still in a good range relative to the AEP. In general, it can be observed that the hydraulics transfer less energy if the average wind speed is close to the direct transmission. If the two values are far apart, a significantly greater proportion of the energy must be transferred by the hydraulics.

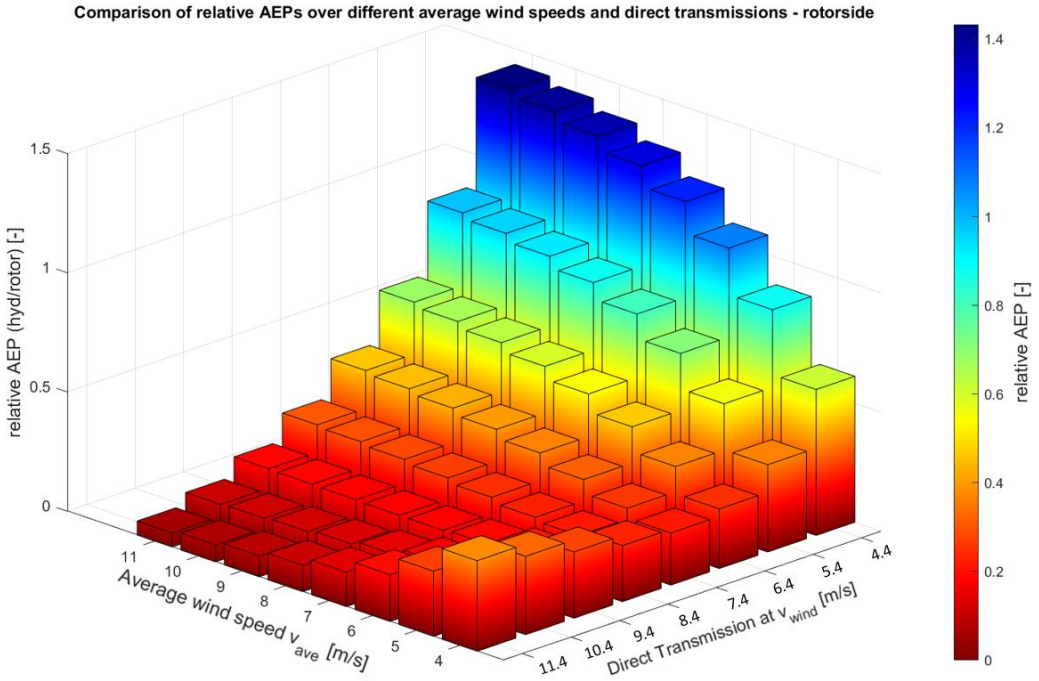

Figure 43: Hydraulic energy relative to the AEP at different mean wind speeds and different direct transmissions.

Another factor that must be considered, is that the overall mechanical transmission ratio increases towards lower direct transmissions, which can result in an increase in the number of planetary stages. However, this can also be counteracted by lowering the rated generator speed by simply increasing the number of pole pairs.

4 Conclusion

The market is currently dominated by two types of turbines (direct-drive and drives with a gearbox), whose variable-speed operation is implemented by a generator with a frequency converter. Currently systems with a high-speed generator are predominantly installed, while the proportion of direct-drive systems is declining and a trend towards medium-speed concepts can be seen. To save weight and costs by omitting the frequency converter, a continuously variable, power-split, hydrodynamic transmission is considered, which enables the speed variability. Compared to a fully hydrostatic transmission, the hydraulic system can be dimensioned significantly smaller, with only 10 % of the nominal system power for rotor-side power-splitting and 15 % for generator-side power-splitting. It was investigated which impact the influence of the constructively determinable direct transmission has on the annual energy yield. It was found that for every mean annual wind speed there is an optimal direct transmission that minimizes hydraulic energy and therefore energy losses, which shows that it makes sense to adapt the turbine to its planned location. Further research regarding continuously variable hydraulic power-split drivetrains is necessary. The next step involves expanding the current model to enable dynamic simulations of the drivetrain. Additionally, it is important to analyse the losses of the hydraulic drivetrain and incorporate them into the simulation to get the overall efficiency of the concept. Another area of research is the design of an appropriate controller for the new drivetrain design, as well as its implementation into wind simulation software, which could be used to simulate real-world load cases.

5 Bibliography

[BAK13] Christian Bak, Frederik Zahle, Robert Bitsche, Taeseong Kim, Anders Yde, Lars C. Henriksen, Anand Natarajan, Morten Hansen: Description of the DTU 10 MW Reference Wind Turbine

[BOT18] Bottiglione, F., Mantriota, G., Valle, M.: Power-split hydrostatic transmissions for wind energy systems. Energies 11(12), 3369 (2018) https://doi.org/10.3390/en11123369

[COT04] Cotrell, J.: Motion Technologies CRADA CRD-03-130: Assessing the Potential of a Mechanical Continuously Variable Transmission. https://doi.org/10.2172/15009604

[DEW07] renewableenergyworldcontentteam: Drive and innovation: The dewind d8.2 with voith windrive. Renewable Energy World (01.03.2007). Accessed 29.07.2024

[DIN17] DIN EN 61400-12-1 (VDE 0127-12-1): 2017-12: Teil 12-1: Messung des Leis tungsverhaltens Von Windenergieanlagen (IEC 61400-12-1:2017), Deutsche fassungen 61400-12-1:2017 edn. Deutsche Norm. VDE VERLAG GMBH and Beuth Verlag GmbH, Berlin

[ENE24] ENERCON Technology. https://www.enercon.de/en/wind-turbines/technology Accessed 20.08.2024

[GAE20] Gaertner, Evan, Jennifer Rinker, Latha Sethuraman, Frederik Zahle, Benjamin Anderson: Definition of the IEA 15-Megawatt Offshore Reference Wind.
https://www.nrel.gov/docs/fy20osti/75698.pdf

[GAJ16] Gajewski, P., Pienkowski, K.: Advanced control of direct-driven pmsg generator in wind turbine system. Archives of Electrical Engineering 65(4), 643–656 (2016)
https://doi.org/10.1515/aee-2016-0045

[GAS05] Gasch, R., Twele, J., Bade, P., Conrad, W., Heilmann, C., Kaiser, K., Kortenkamp, R., Kühn, M., Langreder, W., Liersch, J., Maurer, J., Reuter, A., Schubert, M., Sundermann, B., Stoffel, A.: Windkraftanlagen. Vieweg+Teubner Verlag, Wiesbaden (2005).
https://doi.org/10.1007/978-3-322-99446-2

[HAU16] Hau, E.: Windkraftanlagen. Springer Berlin Heidelberg, Berlin, Heidelberg (2016).
https://doi.org/10.1007/978-3-662-53154-9

[JAN08] Janulevičius, A., Giedra, K.: Analysis of main dynamic parameters of split power transmission. Transport 23(2), 112–118 (2008) https://doi.org/10.3846/1648-4142.2008.23.112-118

[JOO11] Mariion Jooss, M.A.: Voith-Perspectives: Das Magazin für Antriebstechnik.
https://voith.com/corp-en/VTPERSPECTIVES211DSCREEN.pdf

[LIU16] Liu, Y., Niu, S., Fu, W.: Design of an electrical continuously variable trans mission based wind energy conversion system. IEEE Transactions on Industrial Electronics 63(11), 6745–6755 (2016) https://doi.org/10.1109/TIE.2016.2590383

[MAH19] Mahato, A.C., Ghoshal, S.K.: Various power transmission strategies in wind turbine: an overview. International Journal of Dynamics and Control 7(3), 1149–1156 (2019)
https://doi.org/10.1007/s40435-019-00543-8

[MAN17] Mantriota, G.: Power split transmissions for wind energy systems. Mechanism and Machine Theory 117, 160–174 (2017) https://doi.org/10.1016/j.mechmachtheory. 2017.07.003

[MAR18] Alexandre Marx: An in-depth comparative study of direct drive versus gearbox wind turbines, 2018

[MÜL98] Müller, H.W.: Die Umlaufgetriebe: Auslegung und Vielseitige Anwendungen, Zweite neubearbeitete und erweiterte auflage edn. Konstruktionsbücher, vol. 28. Springer Berlin Heidelberg and Imprint and Springer, Berlin, Heidelberg (1998). https://doi.org/10.1007/978-3-642-58725-2

[NEJ22] Nejad, A.R., Keller, J., Guo, Y., Sheng, S., Polinder, H., Watson, S., Dong, J., Qin, Z., Ebrahimi, A., Schelenz, R., Gutierrez Guzman, F., Cornel, D., Golafshan, R., Jacobs, G., Blockmans, B., Bosmans, J., Pluymers, B., Carroll, J., Koukoura, S., Hart, E., McDonald, A., Natarajan, A., Torsvik, J., Moghadam, F.K., Daems, P.-J., Verstraeten, T., Peeters, C., Helsen, J.: Wind turbine drivetrains: state-of the-art technologies and future development trends. Wind Energy Science 7(1), 387–411 (2022) https://doi.org/10.5194/wes-7-387-2022

[RAM06] Rampen, W.: Gearless transmissions for large wind turbines: The history and future of hydraulic drives. 8th German Wind Energy Conference, DEWEK 2006; Conference date: 22-11-2006 Through 23-11-2006

[SCH22] Schaffarczyk, A. (ed.): Einführung in die Windenergietechnik, 3., überarbeitete auflage edn. Hanser and Carl Hanser Verlag GmbH & Co. KG, München (2022). https://doi.org/10.1007/978-3-446-47322-5

[SIE24] Scaling up the use of offshore wind turbines. https://www.siemensgamesa.com/global/en/home/products-and-services/offshore.html Accessed 20.08.2024

[TAH20] Taherian-Fard, E., Sahebi, R., Niknam, T., Izadian, A., Shasadeghi, M.: Wind turbine drivetrain technologies. IEEE Transactions on Industry Applications 56(2), 1729–1741 (2020) https://doi.org/10.1109/TIA.2020.2966169

[TON19] Tong, X., Zhao, X., Yin, X., Karcanias, A.: Maximum power generation control of a hybrid wind turbine transmission system based on h∞ loop-shaping approach. IEEE Transactions on Sustainable Energy, 1 (2019) http://dx.doi.org/10.1109/TSTE.2019.2897549

[XIO19] Xiong, S., Wilfong, G., Lumkes, J.: Components sizing and performance analysis of hydro-mechanical power split transmission applied to a wheel loader. Energies 12(9), 1613 (2019) https://doi.org/10.3390/en12091613

[YU19] Yu, J., Cao, Z., Cheng, M., Pan, R.: Hydro-mechanical power split transmissions: Progress evolution and future trends. Proceedings of the Institution of Mechanical Engineers, Part D: Journal of Automobile Engineering 233(3), 727–739 (2019) https://doi.org/10.1177/0954407017749734

[ZHA23] Feng Zhao, J.L.: Global Wind Market Development: Supply Side Data 2023, Brussels. https://gwec.net/globalwindreport2023/

Planetary Plain Bearing (Academic Track)

Unique concept of a planetary plain bearing test bench

M. Könekamp[1], F. Renger[2], A. Bührke[2], B. Lehmann[1], G. Jacobs[1]

[1]Institute of Machine Elements and Systems Engineering of RWTH Aachen University, Schinkelstraße 10 52062 Aachen Germany

[2]RENK Test System GmbH, Ohmstraße 8a, 86199 Augsburg Germany

Keywords: wind energy, planet gear, plain bearings, hybrid testing, scaled testing

Abstract: Wind energy is a key pillar of electricity generation from renewable sources and plays a central role in the EU Commission's Green Deal. New generations of wind turbines with high performance classes and lower electricity generation costs are required in order to realize further expansion and a high proportion of renewable energies. In order to increase the power density of wind turbines, compact drive system designs are required. For this reason, rolling bearings are continuously being replaced by plain bearings in the planetary gearboxes of wind turbines. This is because plain bearings require less installation space. More planetary gears can be installed in the gearboxes and more power can be transmitted. There are currently various plain bearing concepts in planetary gearboxes, such as bronze sleeves that are mounted on the pins of the planet carrier or pins coated with bronze. In addition, the contact surfaces have different profiles depending on the gearbox architecture in order to ensure optimum load distribution. The tribological properties of planetary gear plain bearings, such as wear behavior and reliability, depend heavily on the plain bearing concept, the material and the profiling and have so far only been quantified under real load situations on complex system test rigs and therefore not economically. In this presentation, a concept of a unique component test rig will be presented, which is able to efficiently and economically evaluate plain bearings in planetary gearboxes of wind turbines under real load situations. Using multiple load cylinders and geometries adapted to real deformations, the test rig simulates real load situations such as radial loads, tilting torques and misalignment due to deformations. With the help of the test rig, various plain bearing concepts, materials and profiles can be tested economically in the future, thereby increasing the reliability of wind turbine drive systems.

1 Introduction

In the course of the energy transition, electricity generation from renewable sources is becoming an increasingly important alternative to fossil fuels. In 2019, wind energy replaced lignite as the most important source of electricity in Germany. In 2023, wind energy accounted for 32% of net electricity generation in Germany, 14.1% more than in the previous year [SEP23]. In order to meet the climate targets in Germany, an annual expansion of over 2,000 wind turbines is required by 2030. At the same time, demand for ever higher WTG outputs is increasing in Europe as well as in the USA and East Asia.

The increase in wind turbine output results in greater tower heights and rotor diameters. As the speeds decrease with larger rotors in order to utilize the best aerodynamic efficiency, the torque increases disproportionately with the turbine output. As a result, the planetary gearboxes used also have to transmit higher torques and become larger, heavier and therefore more expensive. To counteract this trend, the wind industry is currently increasingly using plain bearings instead of roller bearings to support the planets in planetary gearboxes [CWD23]. Figure 44 shows a concept of a planetary gearbox as used in modern wind turbines. By replacing the rolling bearings with plain

bearings, the installation space required for the bearings can be significantly reduced, allowing more planetary gears to fit into the same installation space [PES25].

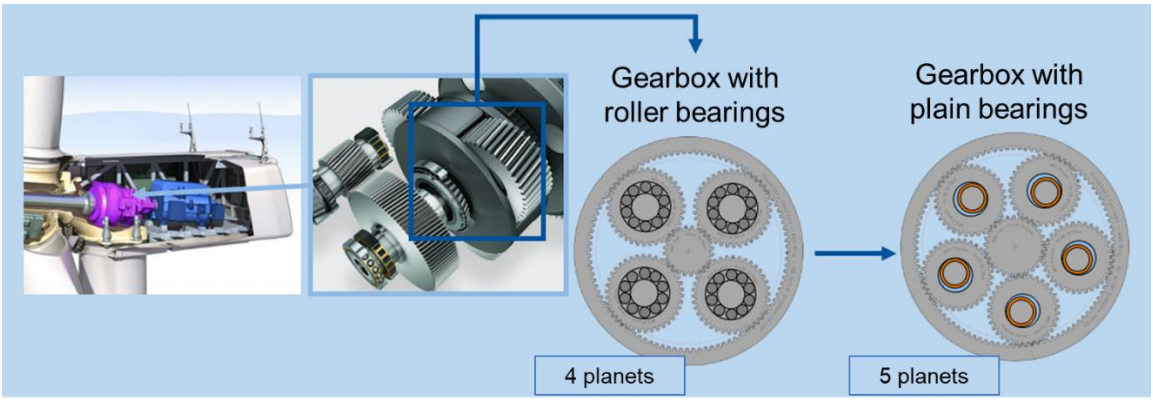

Figure 44: Gearbox concepts of a wind turbine

By using plain bearings in the planetary gears, the same torque can be transmitted with an overall smaller planetary gearbox. For this reason, it is expected that the proportion of plain bearings in planetary gearboxes for wind turbines will continue to increase in the future. Even today, only multi-MW WTG gearboxes with planetary bearings in the first gearbox stage are developed and manufactured in Europe. Based on a guideline value of 15 plain bearings per planetary gearbox (and rising), more than 30,000 plain bearings with diameters in the range of 200-500 mm are required per year for the expansion of wind turbines in Germany alone.

Both plain bearing concepts, which provide a sleeve mounted on the planetary bolt, and plain bearing concepts, which provide a welded surface layer, are exposed to wear-critical load conditions in wind turbines. The wear generated in the plain bearings can lead to bearing failure and thus to a standstill of the entire wind turbine. A high risk of wear arises primarily due to operating conditions that cause high bearing loads and/or low circumferential speeds in the plain bearing [LUC23]. Typical operating conditions for this are, for example, installation of the rotor blades (single blade installation), idling operation, speed reduction to implement noise reduction measures, overload on the rotor and e-stop [MEY22]. These operating conditions in particular, but also operating conditions during normal production operation, result in the following load conditions in the plain bearings, which have a significant influence on the contact condition and wear behavior (see Figure 45):

a. Radial overload: Cause: High rotor loads, consequence: Bearing wear due to mixed friction
b. Tilting of the planetary gear: Cause: Axial forces due to the helical gearing of the planetary gears / Uneven load distribution across the gear width, consequence: Uneven load distribution across the bearing width / High local pressures due to edge wear
c. Deformation of the planet carrier: Cause: High torques on the planet carrier and low rigidity of the structure, consequence: Tilting of the pin to the planet gear axis / High local pressures due to edge loads
d. Ovalization of the planet gear: Cause: High normal forces on the teeth of the planet gear, consequence: Change in load distribution and contact pattern in the plain bearing

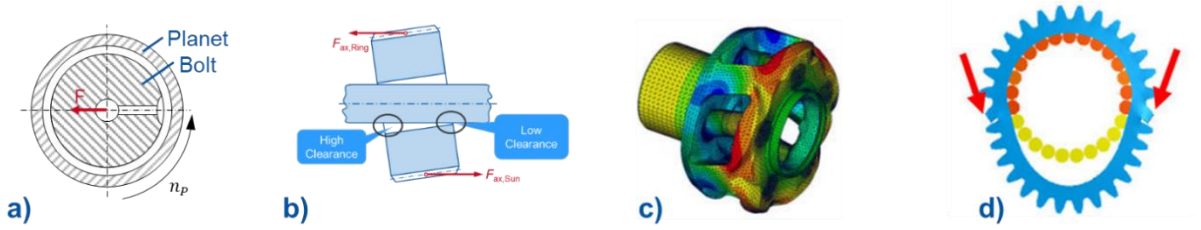

Figure 45: Typical load conditions of plain bearings in gearboxes of wind turbines: a) Radial overload, b) Tilting of the planetary gear, c) Deformation of the planet carrier, d) Ovalization of the planetary gear

The influence of these load conditions on the contact conditions and the wear behavior must be known and therefore determined using current test methods in order to ensure the reliable design of plain bearings in planetary gearboxes of wind turbines.

Figure 46 shows the concept of a conventional radial bearing test rig (component test rig), which already exists at the CWD of RWTH Aachen University as well as at other research institutes and companies. Here, geometrically smaller, scaled test bearings (no size that is relevant for wind turbine gearboxes) are loaded radially directly via a load cylinder. It is not possible to consider the forces induced by the gearing and structural deformation, meaning that the effects of planet ovalization, deformation of the planet carrier and tilting of the planet gears cannot be mapped. Due to this abstraction, the contact conditions in the plain bearing (local pressures, temperature distribution and contact pattern) are not represented realistically. Nevertheless, it was possible to qualify material-lubricant combinations for plain bearing applications on the basis of the component test rig, considering certain abstraction losses.

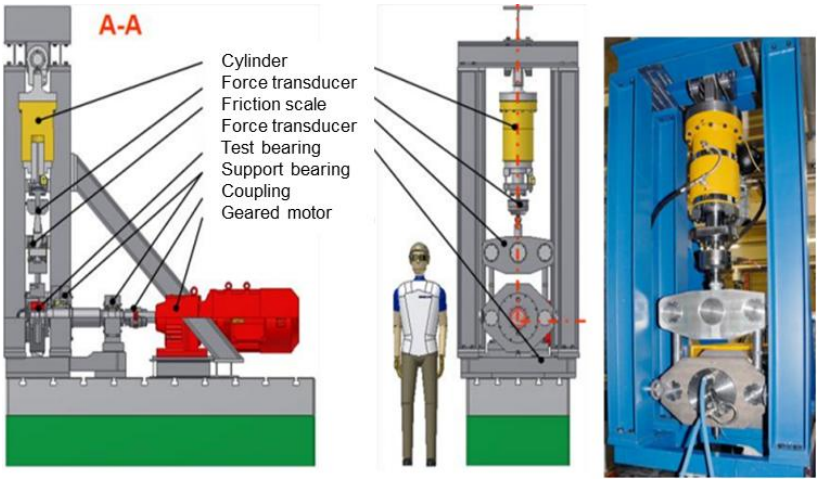

Figure 46: Radial plain bearing test rig (120mm) at CWD of RWTH Aachen University

Figure 47 shows the concept of a three-shaft test rig (subsystem test rig), which already exists at the CWD as well as at other research institutes and companies. Here, the gearing of a planetary gear (see Figure 47a) is simulated using a double spur gear stage (see Figure 47b) in order to reproduce gearing forces realistically. The planetary gear to be tested, including the plain bearing, is located in the middle between the driving pinion and the output gear, which replaces the ring gear (see Figure 47c). It is possible to tilt the planetary gears and generate ovalization of the planets. The deformation of the planet carrier can also be considered to a limited extent by adjusting the gear axes using eccentric shafts. However, this test method is cost-intensive, as the gear pairings have to be replaced regularly depending on the gear system to be tested (different helix angles,

planet gear thicknesses, etc.). A large number of test campaigns with different parameters is therefore usually not economical.

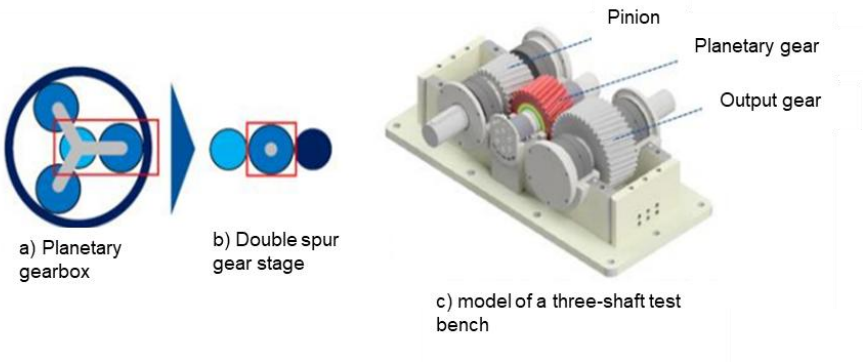

Figure 47: Three-shaft test rig for plain bearings in wind turbine gearboxes at CWD of RWTH Aachen University

As the degree of abstraction of the test procedures influences both the quality of the results and the costs of the tests, a cost-benefit assessment of the existing test procedures is required. This enables industrial companies to select a specific test procedure depending on their requirements in terms of quality of results and costs. In most cases, the result of this cost-benefit assessment is that there is currently no economically optimal test option for plain bearings in planetary gearboxes of wind turbines to investigate the influence of real, abstraction-free load situations on the contact conditions and wear behavior of the plain bearings. However, this is essential for the design of modern wind turbines with high service life requirements. For this reason, a test rig concept is to be developed as part of this work, which can be used to reproduce and determine the influence of real load situations on the contact conditions and wear behavior of plain bearings in wind turbine gearboxes in a cost-effective and time-efficient manner. This test rig is to be set up at the CWD of RWTH Aachen University as part of the submitted project “Qualification of coated pins for bearings in planetary gear boxes of wind turbines” once the concept has been finalized at the CWD.

2 Methodology

A preliminary test rig concept was developed in close cooperation between the project partners CWD of RWTH Aachen University and Renk Test Systems GmbH. In the first step, requirements for the test rig were defined and summarized on the basis of the main characteristics list according to PAHL/BEITZ [FEL13]. Based on the requirements determined, two different test rig concepts were designed in the course of a preliminary design phase. Functions were found and principle solutions derived for the defined requirements. Detailed solutions were developed on the basis of the principle solutions and combined to create the possible test rig concepts. This resulted in two test rig concepts that allow the testing of a scaled planetary plain bearing with a diameter of 200 mm under real load situations. The two concepts were then evaluated at an expert meeting, e.g. with regard to functionality and costs. It turned out that only one of the two test rig concepts could be realized economically, which was then further detailed by means of simulative investigations. The focus of the simulative investigation was the generation of realistic contact conditions in the plain bearings through an appropriate selection, number and arrangement of load cylinders. The simulative investigations were carried out in four successive steps:

1. Determination of the contact conditions in a real planetary plain bearing using FEM

2. Determination of the arrangement and number of load cylinders as well as the cylinder forces on the test rig to set comparable contact conditions between the test rig plain bearing and a real planetary gear plain bearing of the same size using FEM
3. Scaling of the cylindrical forces for scaled test rig plain bearing (with 200 mm diameter) using FEM
4. Validation of the contact conditions of the scaled test rig plain bearing by comparing the contact conditions with those in the real planetary gear plain bearing using MBS/EHD

The methodology is illustrated in Figure 48.

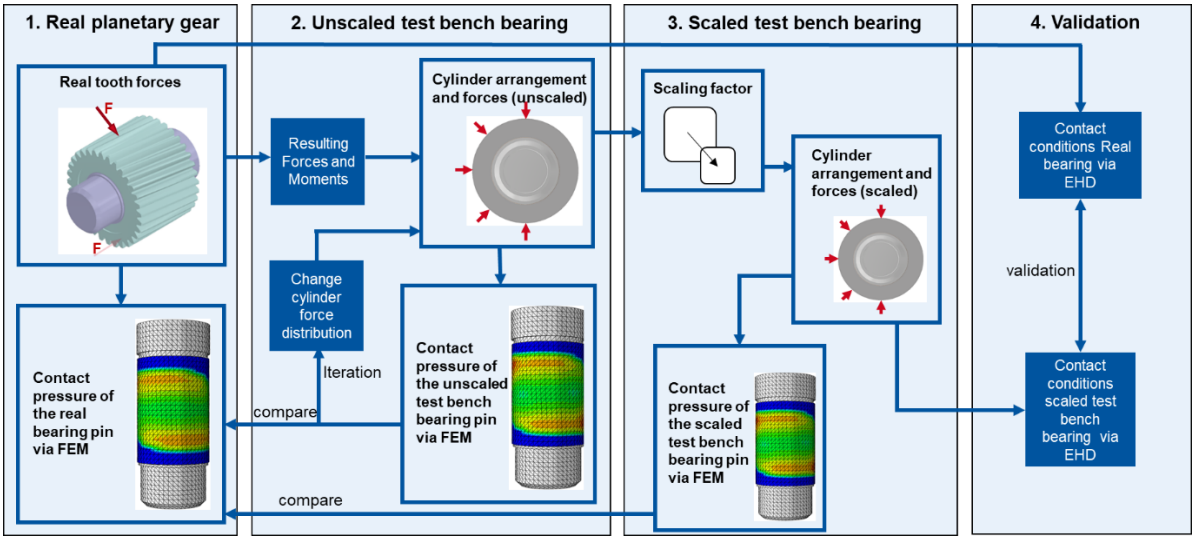

Figure 48: Methodology

3 Results

Figure 49 shows concept 1 “rotating planet”. A planetary gear dummy “bearing bush” rotates around a fixed pin. The load cylinders (red) apply the acting radial forces, the tilting moments due to the meshing of the teeth and the width load distribution and the forces for ovalizing the planetary gear dummy. As the planetary gear dummy moves relative to the load-imposing cylinders, sliding shoes are installed between the load cylinders and the planetary gear dummy for load transmission. The planet pin is firmly clamped at both ends.

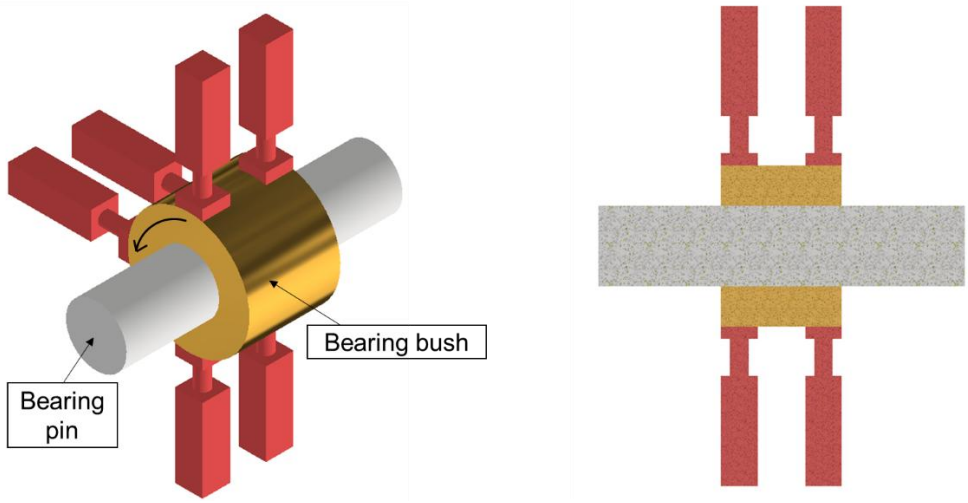

Figure 49: Concept 1 “rotating planet”

Figure 50 shows concept 2 “rotating pin”. Here, the pin rotates in a fixed planetary gear dummy “bearing bush”. As in the first concept, the load cylinders (red) apply the acting radial forces, the tilting moments due to the tooth mesh and the width load distribution. Further load cylinders (green) apply the forces to ovalize the planetary gear dummy. In order to rotate the load relative to the planetary gear as in the real application, the vectors of the resulting forces must rotate with the pin. This is possible in theory with the number of load cylinders shown here, but precise control of the load cylinders is required for uniformly rotating load application to the planetary gear dummy, which makes the control system very complex.

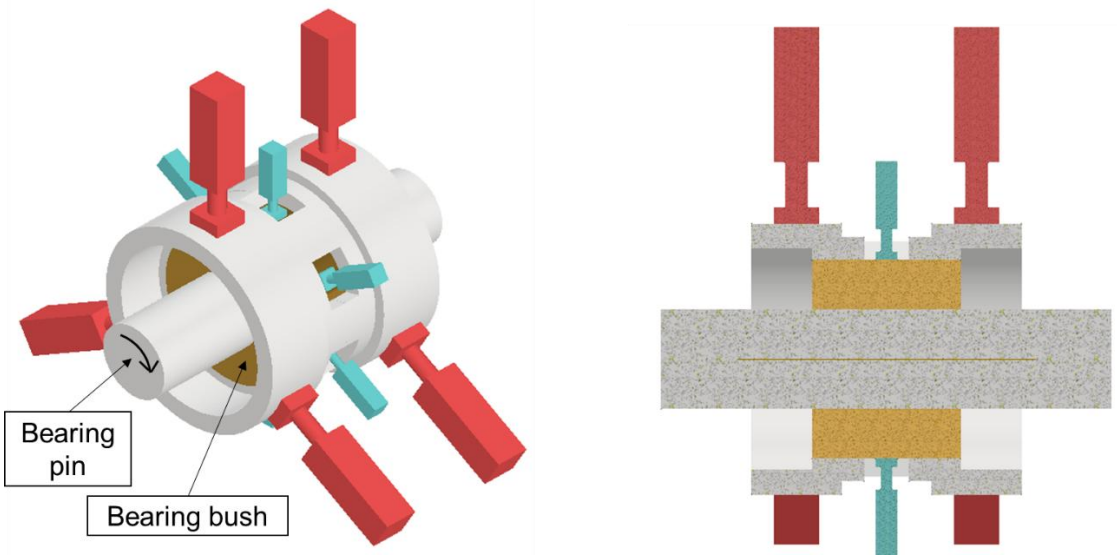

Figure 50: Concept 2 “rotating pin”

After the two concepts were pre-evaluated in an expert meeting, the second concept was excluded from further investigations for the following reasons:

1. The precise control of the load cylinders required to apply a rotating load to the planetary gear dummy is associated with high technical requirements and is therefore more cost-intensive
2. Rotation of the oil outlet causes unrealistic oil introduction
3. Rotation of the pin causes the built up of flow speed to be reversed compared to a rotating planet

Figure 51 on the left shows the contact pressure between a planetary gear and pin (diameter of 310 mm) of a real wind turbine gearbox, which was determined using FEM with the application of real loads acting during production operation. The typical contact pattern of a planetary gear plain bearing can be seen, which shows the areas of the highest pressures near the edges. The maximum pressure is 31,44 MPa. The contact pressure between the planetary gear dummy and the pin of the non-scaled test rig concept 1 “rotating planet” can be seen in the middle of Figure 51. The position and number of load cylinders as well as the height of the applied loads were iteratively approximated in such a way that the contact pattern is as identical as possible to the real case (left). In this way, it was possible to determine an almost identical contact pattern using FEM, whereby the maximum pressure is 31,42 MPa. Figure 51 on the right shows the contact pressure between the planetary gear dummy and the pin of the scaled test rig (diameter of 200 mm) concept 1 “rotating planet”. The applied loads of the previous step were reduced linearly by a constant factor of 0,645 to realize this contact pattern. It can be seen that the contact pattern is again almost identical to the real case, with the maximum pressure being 31,15 MPa.

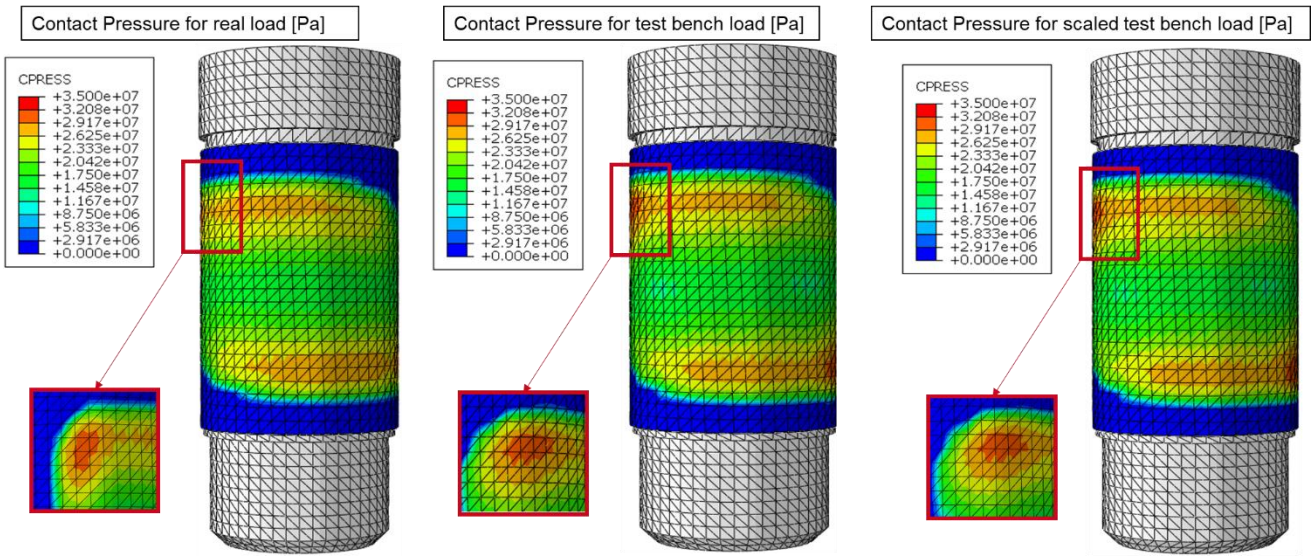

Figure 51: Contact pressure between a planetary gear and pin of a real wind turbine gearbox (left), between the planetary gear dummy and the pin of the non-scaled test rig concept 1 “rotating planet” (middle) and between the planetary gear dummy and the pin of the scaled test rig concept 1 “rotating planet” (right)

The procedure described in the previous paragraph was used to determine the number and position of the load cylinders and the forces to be applied in order to be able to realize a pattern in the scaled test rig design which is comparable with the real application. The resulting cylinder arrangements and cylinder forces are shown in Figure 52. A total of 10 load cylinders must be installed. The load cylinders must apply a maximum force of 226.7 kN.

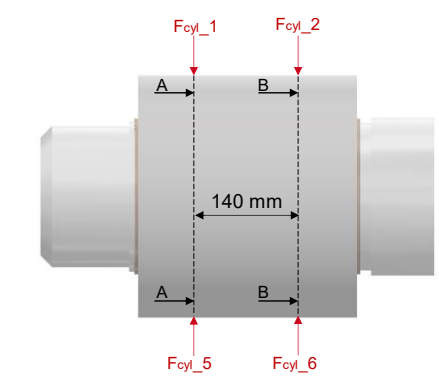

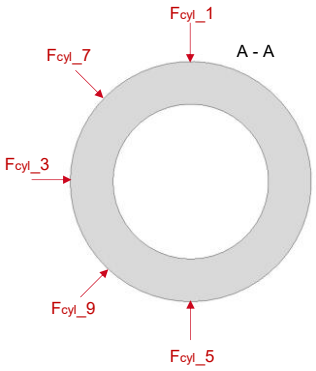

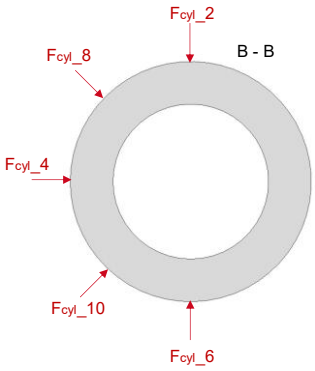

Cylinder forces without displacement of the tooth mesh			
F_{cyl_1}	226,7 kN	F_{cyl_2}	100,7 kN
F_{cyl_3}	224,5 kN	F_{cyl_4}	224,5 kN
F_{cyl_5}	100,7 kN	F_{cyl_6}	226,7 kN
F_{cyl_7}	208,0 kN	F_{cyl_8}	166,4 kN
F_{cyl_9}	166,4 kN	F_{cyl_10}	208,0 kN

Figure 52: From the study resulting cylinder arrangements and cylinder forces

A preliminary test rig concept was realized from the cylinder arrangements and cylinder forces determined. The concept allows quick assembly and disassembly of the test plain bearing. Hydrostatic plain bearings on each cylinder enable the load to be introduced via the stationary cylinders onto the rotating planetary gear dummy. The low friction of the hydrostatic bearings of the test bench enables a friction torque measurement of the test plain bearing. The rotation of the planetary gear dummy is achieved by a belt drive. The pin is mounted with comparable rigidity to that in the real gearbox in order to represent the deformation of the real pin under load.

4 Summary

In this presentation, a concept of a unique component test rig was presented, which is able to efficiently and economically evaluate plain bearings in planetary gearboxes of wind turbines under real load situations. Using a methodical approach and taking design guidelines into account, two test rig concepts were initially developed and pre-evaluated during expert meetings. A test rig concept was then decided upon. This concept is based on a planetary gear dummy (a bushing) that rotates around a fixed pin. Load cylinders apply the acting radial forces, the tilting moments due to the meshing of the teeth and the width load distribution and the forces for ovalizing the planetary wheel dummy. FE analyses were then used to iteratively determine the number and arrangement of the load cylinders and the level of the loads to be applied until a contact pattern comparable to the real application was achieved. An initial CAD design of the test rig was created on this basis.

The results can be summarized as follows:

- A test rig concept for the economical testing of planetary gear bearings under real loads was developed.
- The test rig concept consists of a planetary gear dummy (a bushing), which rotates around a fixed pin, and the load cylinders that apply the load.
- A total of 10 load cylinders are required, which must impose a maximum load of up to 226.7 kN to impose load conditions similar to those of a wind turbine on a test plain bearing scaled to 200 mm.
- The FE analyses confirm contact patterns in the test rig plain bearing that are comparable to those of real planetary plain bearings.

In future, the test rig will be further detailed as part of the project “Qualification of coated pins for bearings in planetary gear boxes of wind turbines”. Further details include the design of the pin support, the drive concept of the planetary gear dummy and the actuators and sensors of the test rig. The contact states, which have so far been determined using FE analyses, will be further validated in the presentation using the results of an EHD/MBS model.

5 Bibliography

[CWD23] Conference for wind power drives, 2023, “Conference Proceedings,”

[FEL13] Feldhusen J., and Grote K.-H., 2013. *Pahl/Beitz Konstruktionslehre*, Springer Berlin Heidelberg, Berlin, Heidelberg.

[LUC23] Lucassen M., Decker T., Guzmán F. G., Lehmann B., Bosse D., and Jacobs G., 2023, “Simulation methodology for the identification of critical operating conditions of planetary journal bearings in wind turbines,” Forsch Ingenieurwes, **87**(1), pp. 147–157.

[MEY22] Thomas Meyer, 2022,“Gleitlager als Garant für die Leistungsverdichtung von Windgetrieben,” VDI Schadensmechanismen an Lagern.

[PES25] PES - Power & Energy Solution,“Plain bearings as a viable alternative to roller bearings: https://pes.eu.com/wind/plain-bearings-as-a-viable-alternative-to-roller-bearings/, 2025

[SEP23] Sepp L.,“Öffentliche Stromerzeugung 2023: Erneuerbare Energien decken erstmals Großteil des Stromverbrauchs,”

Optimisation and validation of pin profiling for sliding planet gear bearings

Maximilian Prölß[1], Gino Donato Grossi[2], Peter Decker[1], Thomas Hagemann[2], Hubert Schwarze[2]

[1]COB Europe Holding GmbH, Sicking 22, 4693 Desselbrunn, Austria

[2]Institut für Tribologie und Energiewandlungsmaschinen, Leibnizstraße 32, 38678 Claustal-Zellerfeld, Deutschland

Keywords: Planet Bearing, Wind Turbine, Profile Optimisation, Pressure Measurement

Abstract: The helical gearing generates a complex combination of force and moment loads for the planet bearing. This unfavourable load situation and the deformation of the very flexible components in the gearbox require a precise bearing design. A decisive factor is the crowning or profiling of the bearing, which is responsible for a uniform load on the bearing across the entire width.

This article describes a novel analytical approach to determine a bearing profiling that maximizes the load carrying capacity for a certain operating point. The method is validated with tests on a planetary bearing test rig that reproduces the kinematic and mechanical properties of a planetary gearbox. A special design feature of the novel test rig is the rotatable pin, in which several pressure sensors are installed across the bearing width. Consequently, the hydrodynamic pressure distribution can be measured in the entire load zone and used for comparison with the calculated results. In addition to the hydrodynamic pressure, the bearing temperatures are also used for validation. Surface roughness and profiling are measured before and after the test to quantify the impact of mixed friction and wear during the experimental investigation.

The research results indicate that the optimisation approach for profiling leads to a contour that provides the highest load carrying capacity at nominal load case while ensuring sufficiently high film thickness at other load conditions. Therefore, robustness and reliability can be improved, and safe bearing operation is ensured as mixed friction conditions are minimized.

1 Motivation and Objectives

Wind energy is a key technology for the transition from fossil fuels to sustainable energy sources. To remain competitive on the energy market, more efficient, more powerful and, especially, robust wind turbines are required. This development favoured the usage of sliding bearings to support planet gears of wind turbine gearboxes achieving a higher power density and a higher reliability of the whole drive train [LUB19] or [WEB21]. Sliding bearings have already become very common in recent years, using the additional degrees of freedom that are offered for the design process of the system. Due to the helical gearing, forces as well as moments act on the sliding bearing, which generate an unfavourable pressure distribution with pressure peaks at the bearing ends, as studies by [HAG21] show. With rising power density, the bearing loads also increase, so that a complete separation of the surfaces is not present, and the sliding bearing operates in mixed friction regime. According to [LEH23] this may lead to severe wear of the sliding bearing with increasing operating time. It is known from [OLA21] or [XU23] that bearing damage is one of the main causes of gearbox

failures and that this is mainly caused by wear in sliding bearings. Consequently, the surfaces of the pin are commonly profiled to prevent wear in the plain bearing as far as possible [XUE23]. To determine a suitable profiling that enables robust bearing behaviour over the entire operating range, [PRÖ20] proposed calculating the expected wear of a non-profiled pin at nominal load and deriving a profiling from this. The profiling determined in this way will lead to a minimum film thickness just within the hydrodynamic regime at ideal operating conditions. Mixed friction and wear will immediately occur, if for example load, speed or oil supply fluctuates. The approach for profile optimisation described below maximises the load capacity of the bearing by creating a uniform pressure distribution across the entire bearing width. A bearing optimised in this way runs completely hydrodynamically, even when operating conditions fluctuate, and is therefore extremely robust and long-lived.

The results of this profile optimisation are validated on a novel test rig for planetary sliding bearings at Clausthal University of Technology. While previous publications of measurement results in planetary sliding bearings such as [DIN24] or [MAR20] only show a pressure measurement at individual points, the new test rig enables a measurement and validation of the complete pressure distribution and consequently a verified prediction of the minimum film thickness and other calculations results.

2 Profile Optimisation Approach

To optimise the crowning, a reliable and time-efficient calculation of the hydrodynamic conditions in a planet bearing is required. The calculation algorithm couples the hydrodynamic solver COMBROS PG with the commercial FE programme Ansys in an iterative loop to take the deformations of the components into account, see [HAG21]. For a reduction of calculation time, the extracted and condensed stiffness matrices of the components are used to calculate the deformations, as described in [PRÖ20]. In this way, a profile optimisation can be conducted according to Figure 53 within just a few minutes.

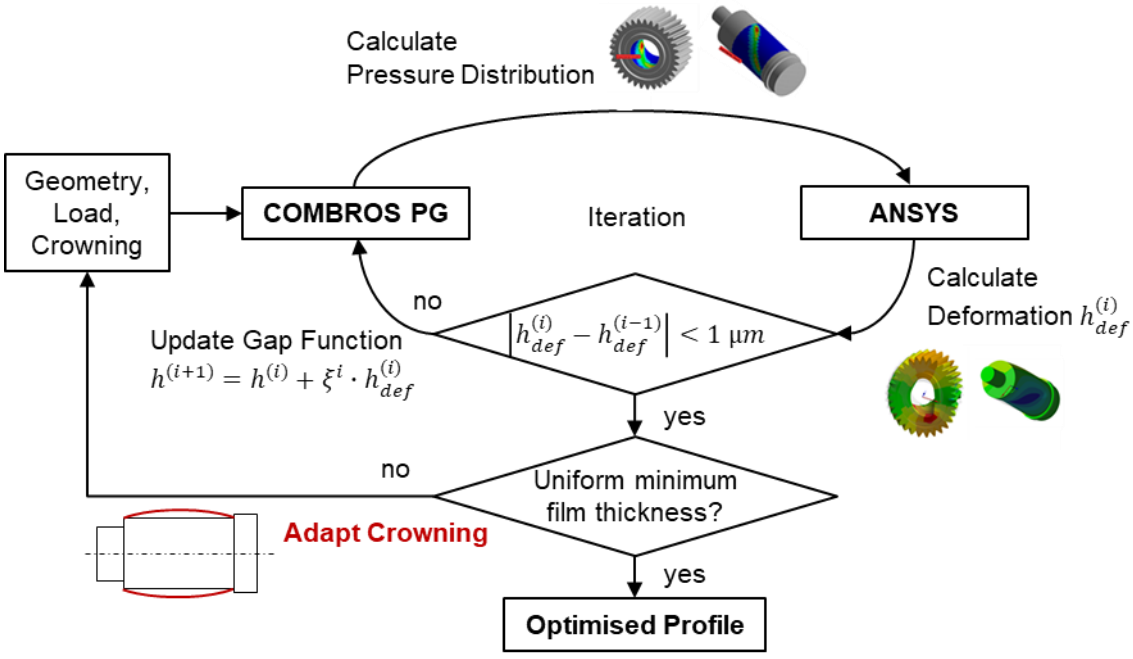

Figure 53: Flow chart of crowning optimisation

The target of profile optimisation is to achieve a uniform bearing load across the entire bearing width. Figure 54 shows two pressure distributions for two different crownings. The crowning used to calculate the pressure distribution in Figure 54 a) is too high, since the bearing edges are unloaded. In Figure 54 b) the pressure distribution for the optimised profiling is shown, where the bearing is nearly equally loaded across its width. In addition, the maximum pressures are significantly lower with the optimised pin contour and decrease by approximately 35%.

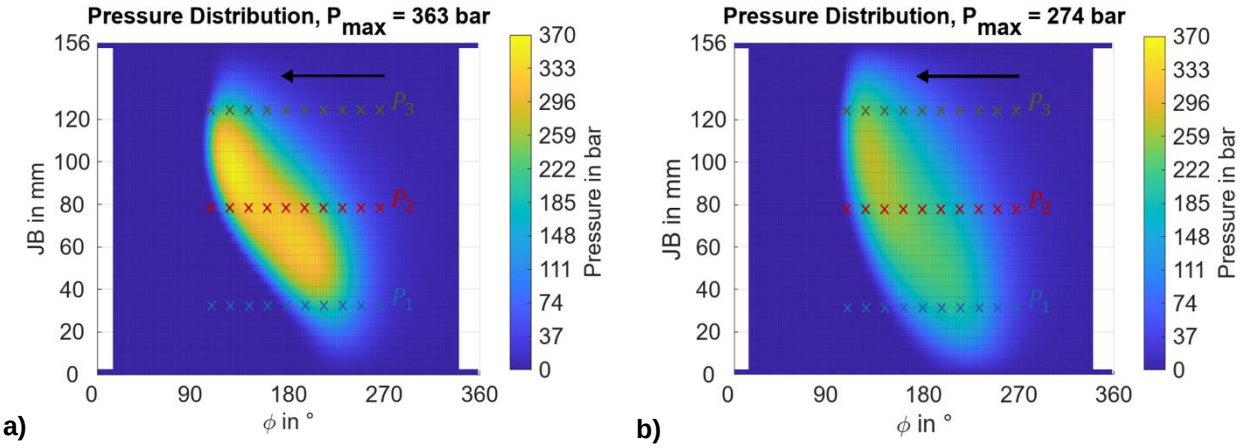

Figure 54: a) Hydrodynamic pressure of initial crowning, b) Hydrodynamic pressure of optimised crowning

The profile optimisation starts with the initial crowning and determines the curve of the local minimum film thickness across the bearing width marked with red crosses in Figure 55. This curve is shown together with the applied symmetrical profiling across the bearing width, see Figure 55a). It is noticeable that the minimum film thickness varies across the bearing width and that the overall minimum film thickness is in the centre. This indicates uneven load across the bearing width.

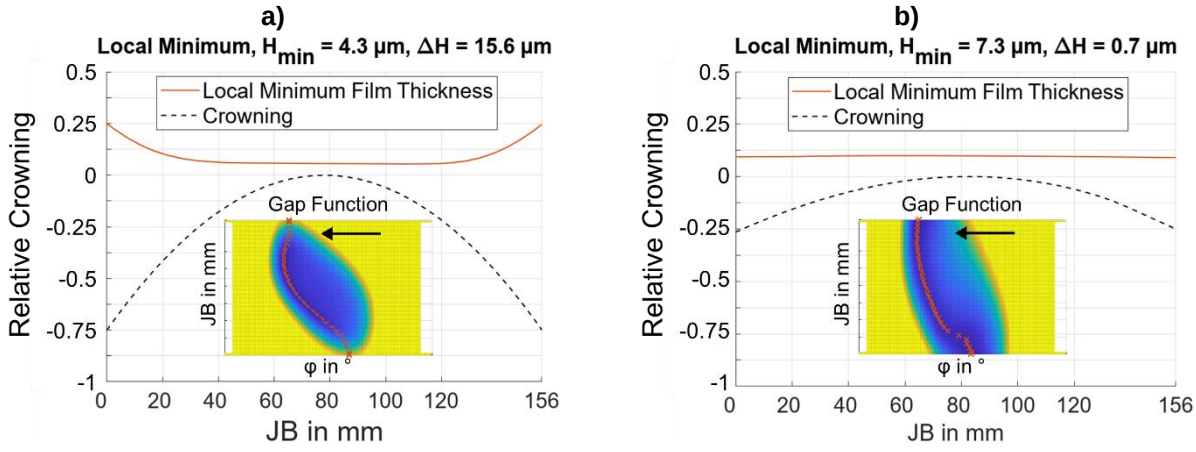

Figure 55: (a) Local minimum oil film thickness across the bearing width of initial crowning b) Local minimum oil film thickness across the bearing width of optimised crowning.

When optimising the profile, the variation of the minimum film thickness over the bearing width must be minimised to homogenise the film pressure level. The result of this iterative process is shown in Figure 55b). While the initial crowning still shows unloaded edges, the optimised crowning results in a nearly uniform minimum oil film thickness over the entire bearing width. The uniform load pattern is confirmed by an increase in the minimum oil film thickness from $H_{min} = 4.3\ \mu m$ to $H_{min} = 7.3\ \mu m$

3 Description of Planet Test Rig

The previously significant impact of the profiling on the hydrodynamic bearing behaviour is validated with measurement data of a planetary gear bearing test rig. The test rig features a hydraulic torsion motor to generate the moment load and an electric motor to rotate the planetary gears. Due to the application of a torsion motor, it is possible to vary the direction of rotation and the torque vector independently. This makes it possible to simulate transitory acceleration and braking processes. A further advantage of the test rig arrangement is the reduced energy consumption, since the electric drive motor consumes only the power dissipated in frictional losses in the drive train. Moreover, it is possible to modify the resulting load application point on the gear tooth flank to test different load offsets.

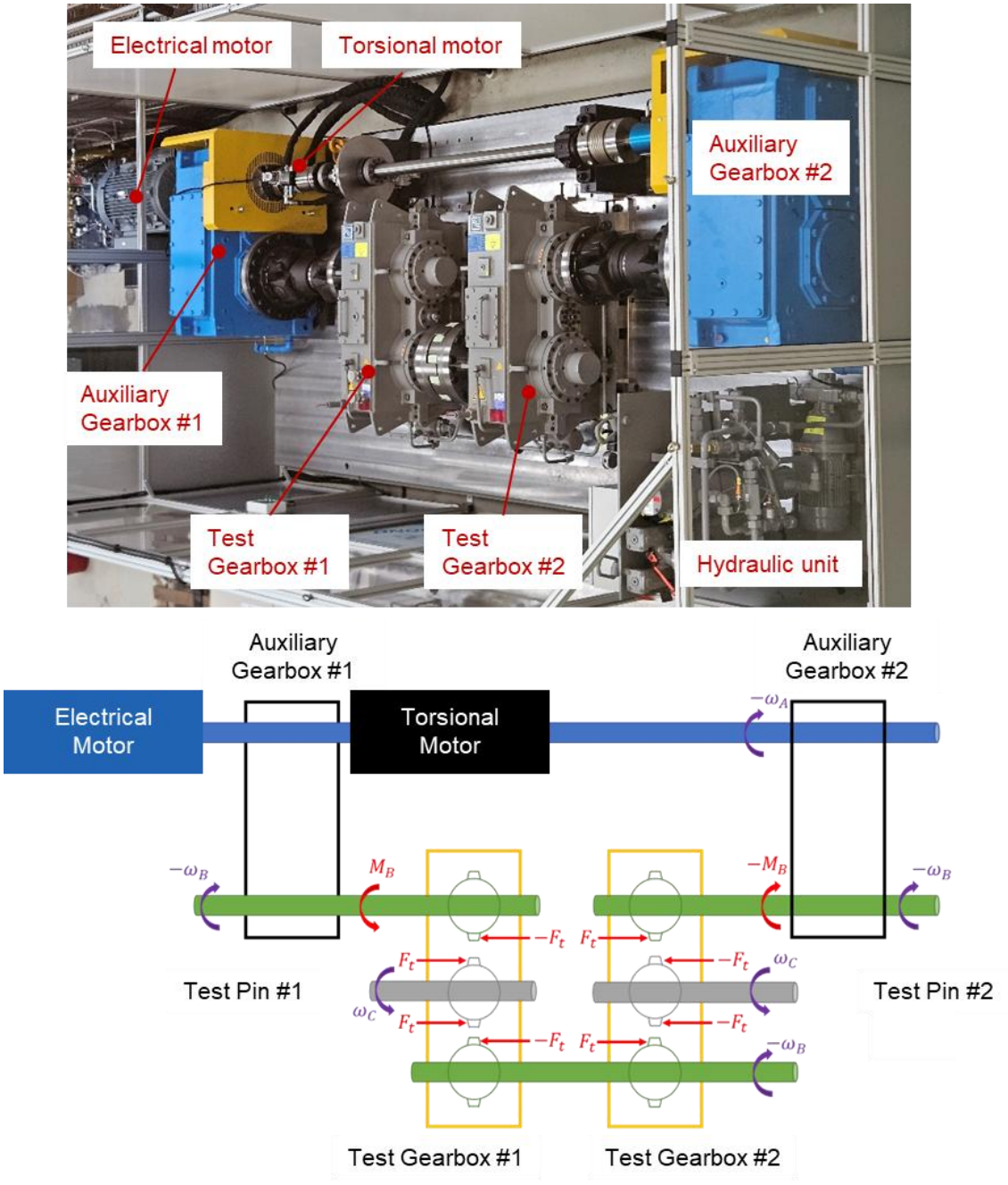

Figure 56: Planet bearing test rig arrangement

The main components of the test bench are detailed in Figure 56 and the operating conditions are listed in Table 11.

	Specific Pressure	Rotating Speed	Supply Temperature
Load Conditions	0.1 – 16.6 MPa	15-75 rpm	20-60°C

Table 11: Operating Range of Test Rig

Each test gearbox consists of three helical gears that simulate the three gears in a planetary gearbox: Sun gear, planet gear and ring gear. The test rig is designed to test two bearings with the geometry in Table 12 simultaneously.

	Bearing Width	Bearing Diameter	Lubrication pocket width
Geometry	156 mm	130 mm	140 mm

Table 12: General Geometry of Test Bearing

Test bearing #1 is a pin coated with bronze by a laser cladding process whereas test bearing #2 is a pin with bronze bushing. Both test bearings see identical operating condition. The only difference is that direction of load and rotation are exactly opposite for test bearing #1 and #2. The hydrodynamic pressure is measured via three pressure sensors that are equally distributed along the bearing width and located at the opposite side of the supply pocket. In addition, several temperature sensors are installed. Two thermocouples are at the bearing edge close to the sliding surface. Three more are placed at the bores of the pressure sensors as depicted in Figure 57. Oil flow rate, rotating speed and torque are continuously monitored.

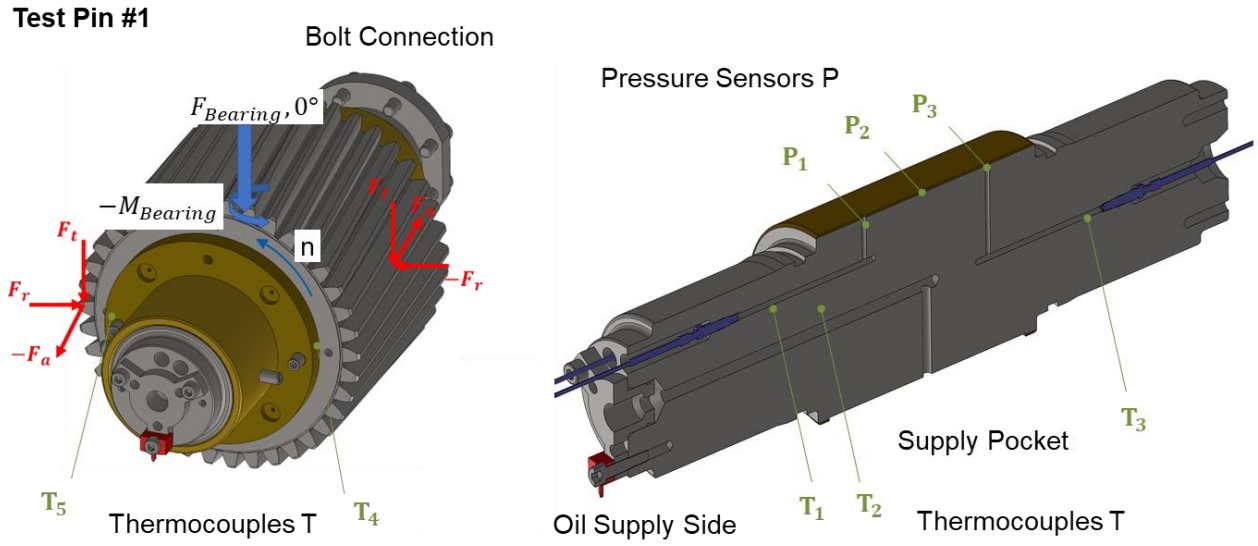

Figure 57: Load situation and instrumentation of test pin #1

For each test pin, the manufactured profiling, the bearing clearance and the surface roughness are measured in advance and differ only slightly from nominal profile depicted in Figure 55.

4 Results

To validate the optimisation algorithm presented in section 2, the two crownings shown in Figure 55 are tested at the load conditions from Table 13 and compared with the calculation. The loads already take into account the load offset on the tooth flanks.

Description	Specific Load	Sliding Speed	Rotating Speed
Cut-In	1.9 MPa	0.3 m/s	44.1 rpm
50% Nominal Load	6.2 MPa	0.4 m/s	58.8 rpm
Nominal Load	12.4 MPa	0.5 m/s	73.5 rpm
HALT	16.6 MPa	0.5 m/s	73.5 rpm

Table 13: Tested Operating Conditions

To obtain the whole pressure distribution, the pin is incrementally rotated in 10° steps between 70° and -90° according to Figure 54. In this angular range, the distance between the lubricant pocket and the loaded zone is sufficiently large so that the new pocket position has a negligible influence on the hydrodynamic pressure. As soon as the supply pocket moves closer to the loaded area the flow rate drops down and can be used as an indicator to keep a sufficient distance between supply pocket and loaded zone. Figure 58 shows a comparison between measurement and calculation for test bearing #1 with the initial crowning from Figure 55a at nominal conditions.

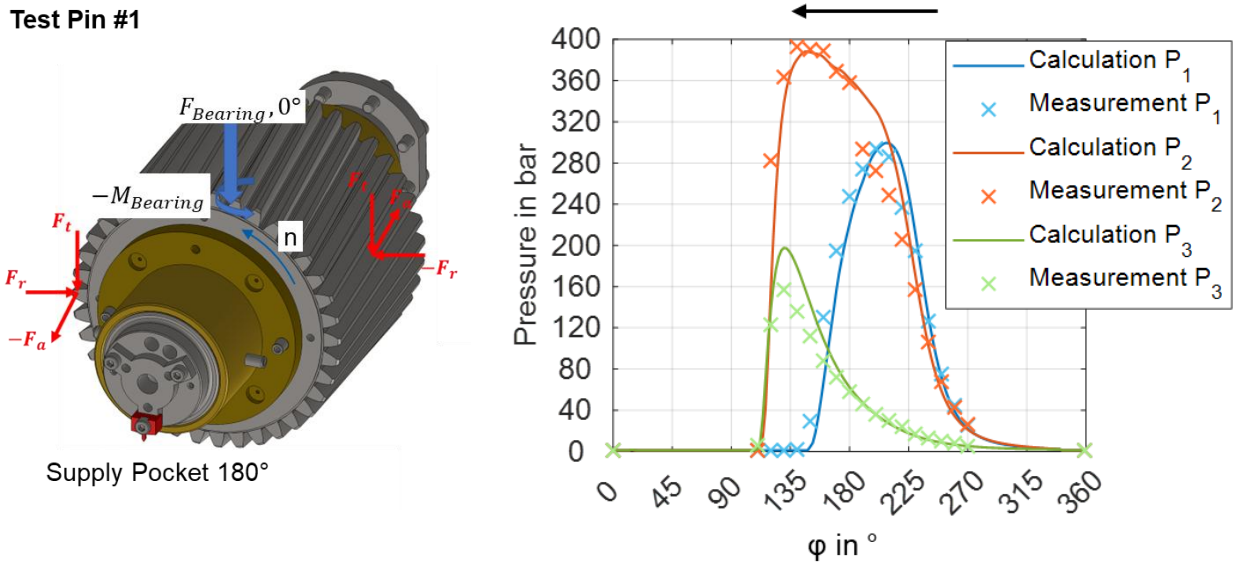

Figure 58: Comparison between calculation and measurement at nominal load for initial crowning

The calculation can be validated with the measured data. It is clearly visible that the highest pressure appears in the bearing centre whereas the edges are lighter loaded. After finishing the tests, a bushing with the optimised profile from Figure 55b is manufactured and assembled. Figure 59 shows a comparison between measurement and calculation for both test bearings with the optimised crowning.

The simulation results show very good agreement with the measured data. The highest deviations can be observed at sensor 3, which is located near the bolt connection at the end of the pin. The deviations probably result from the constraints of the pin in the FE model that might overestimate the structure stiffness. The different absolute pressure values between the two test bearings can be explained by manufacturing tolerances, which can be observed in the profiling and the bearing clearance. Moreover, the optimised crowning shows a comparable pressure level at all 3 pressure sensors that indicates an uniform pressure distribution across the whole bearing width.

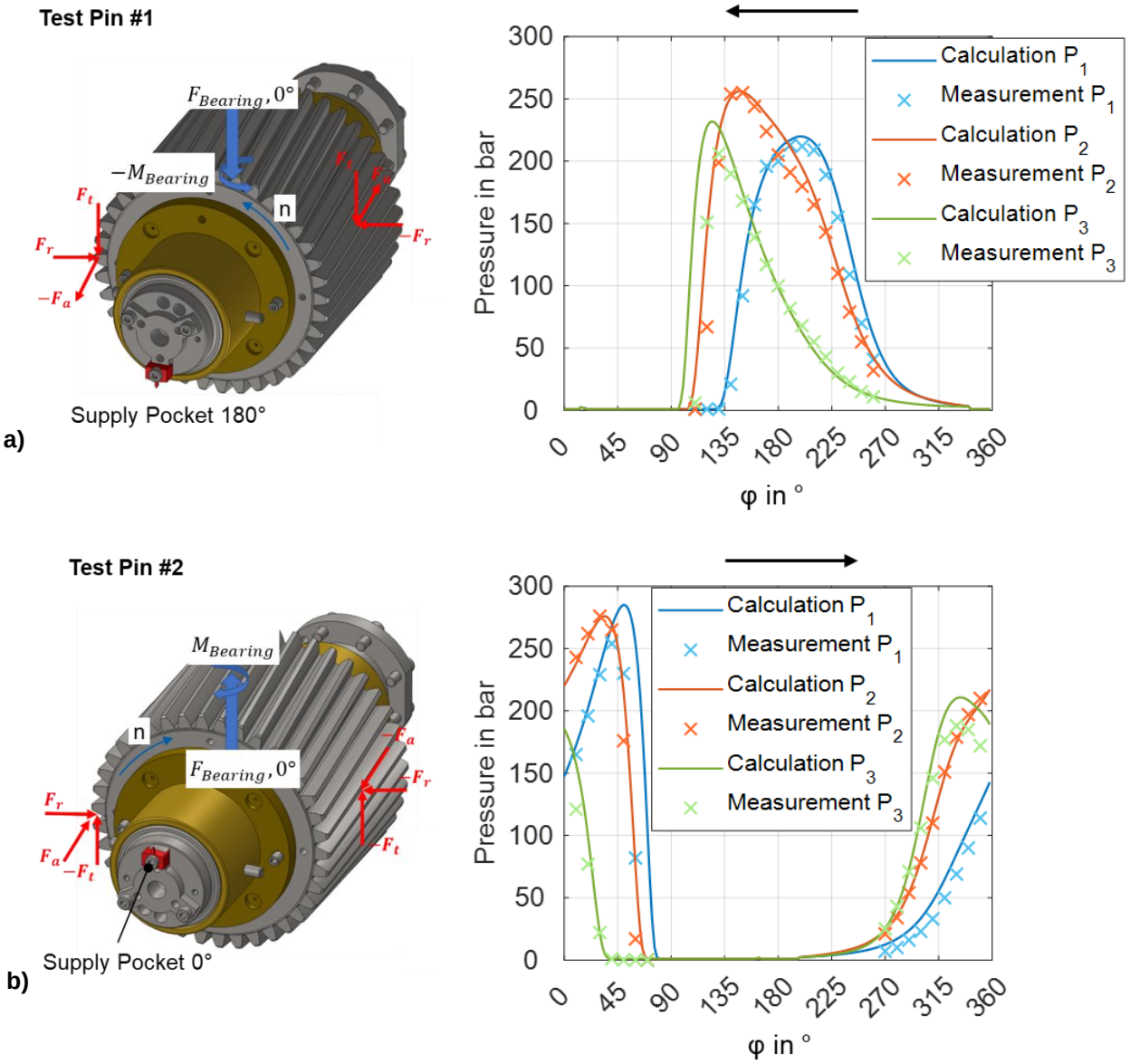

Figure 59: Comparison between calculation and measurement at nominal load for optimised crowning, a) Test pin #1, b) Test pin #2

Figure 60 also shows the comparisons between measurement and calculation for the cut-in load case and the load case at 50% of the nominal load.

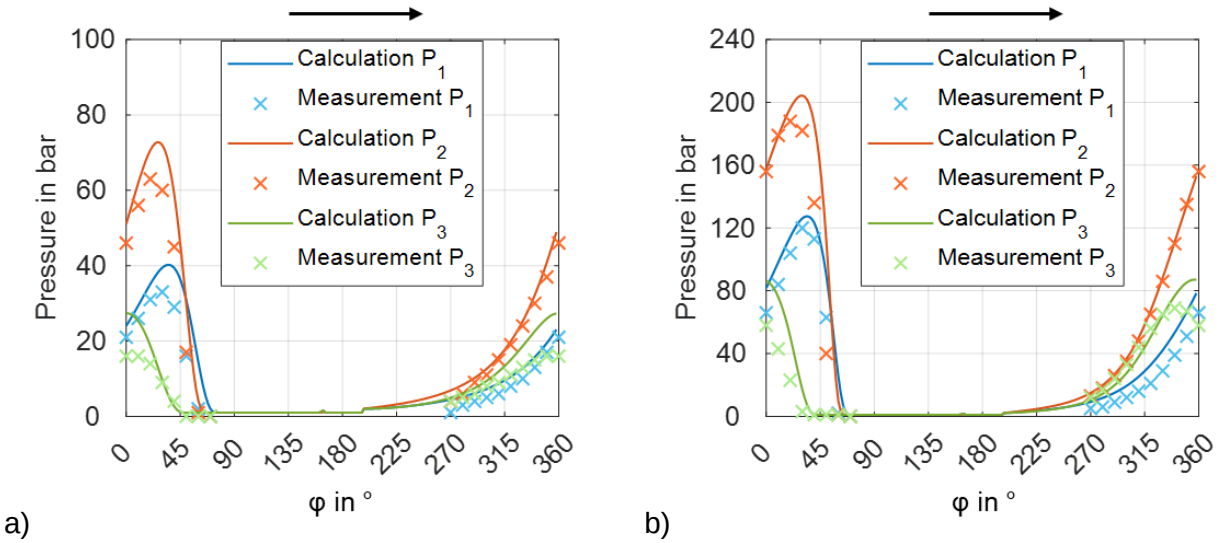

Figure 60: Comparison between calculation and measurement for optimised crowning at a) Cut-In conditions and b) 50% nominal load.

At partial load the highest deviations also exist for sensor 3, so that the boundary conditions in the FE model of the pin need to be analysed in more detail. Whereas the optimised profile shows a uniform pressure distribution in the nominal load case, for which it was designed, it leads to low film forces at the edges at partial load. This highlights that an optimised profiling can only be designed for one single operating point and that other load conditions no longer show the desired uniform pressure distribution. However, the minimum film thickness for the partial load cases is also over 6 µm and thus clearly above the mixed friction regime, even with the non-optimal crowning. Table 14 gives a final overview of the calculated pressure and temperatures values of all tested bearings and compares them with the available measured data. Since pressure distribution as well as temperature values of calculation and measurement agree, the conclusion can be drawn that the calculated minimum film thickness also corresponds to reality. Finally, the optimised crowning shows a minimum film thickness clearly above the threshold to mixed friction for the whole operating range.

Load Case	Profile	Pressure at P_2		Temperature at T_5		Min. Film Thickness
		Measurement	Calculation	Measurement	Calculation	Calculation
Cut-In	Initial	-	79 bar*	-	55.0 °C	4.5 µm
	Optimised	46 bar*	51 bar*	53.8 °C	54.5 °C	9.4 µm
50% Nom. Load	Initial	-	218 bar*	-	54.7 °C	3.9 µm
	Optimised	156 bar*	158 bar*	54.2 °C	54.9 °C	6.6 µm
Nominal Load	Initial		334 bar*		63.6 °C	4.3 µm
	Optimised	224 bar*	225 bar*	62.2 °C	63.0 °C	7.3 µm
HALT	Initial	-	383 bar*	-	66.3 °C	2.8 µm
	Optimised	235 bar*	248 bar*	64.9 °C	66.1 °C	3.4 µm

Table 14: Calculated and tested operating conditions

* Pressure measurement at 0°, supply pocket position at 180°.

5 Conclusion

The study has shown that the profiling of the pin is decisive for the bearing load capacity that can be realised. Due to the constantly increasing loads on sliding bearings, optimising the profile is the most effective way of achieving a robust bearing design over a wide operating range. Thus, an approach was presented to optimise the bearing design for nominal load and subsequently check that other load cases such as overload or partial load also run completely hydrodynamically. All theoretical results were tested on a new developed test rig for planet bearings and quantitatively compared with the generated measured data. This enabled the optimisation algorithm as well as the sliding bearing calculation software to be successfully verified and validated. Consequently, the presented method can be transferred and applied to other planet bearings.

6 Bibliography

[DIN24] Ding H, Mermertas Ü, Hagemann T, Schwarze H. Calculation and Validation of Planet Gear Sliding Bearings for a Three-Stage Wind Turbine Gearbox. *Lubricants*,12(3):95, 2024

[HAG21] Hagemann, T., Ding, H., Radtke, E., Schwarze, H. Operating Behavior of Sliding Planet Gear Bearings for Wind Turbine Gearbox Applications—Part II: Impact of Structure Deformation. *Lubricants*, *9*, 98, 2021 .

[LEH23] Lehmann, B.; Trompetter, P.; Guzmán, F.G.; Jacobs, G. Evaluation of Wear Models for the Wear Calculation of Journal Bearings for Planetary Gears in Wind Turbines. Lubricants, 11, 364, 2023.

[LUB19] Lubenow, K, Schuhmann, F., Schemmert, S.: Requirements for wind turbine gearboxes with increased torque density with special attention to a low-noise turbine operation. Conference for Wind Power Drives 2019 Conference Proceedings, Aachen, 2019.

[MAR20] Marheineke, J., Radtke, E.: - Planetenradgleitlager-Gleitlagerberechnung von Planetenrädern, Forschungsbericht, FVA 794I, 2020

[OLA21] Olabi, Abdul Ghani, et al.: A review on failure modes of wind turbine components. *Energies* 14.17, 2021.

[PRÖ20] Prölß, M. Berechnung Langsam Laufender und Hoch Belasteter Gleitlager in Planetengetrieben unter Mischreibung, Verschleiß und Deformationen. Ph.D. Thesis, Clausthal University of Technology, Clausthal-Zellerfeld, Germany, 2020.

[WEB21] Weber, A. and Hansen, A.: Focus areas in Vestas powertrain. Conference for Wind Power Drives 2021 Conference Proceedings, Aachen, 2021.

[XU23] Xu, F., et al. "A review of bearing failure Modes, mechanisms and causes." *Engineering Failure Analysis, 152,* 2023.

[XUE23] Xueliang, L., Yabin, Z., Yuan, C., Zunyang, B., Shaohua, Z.: Designing and Qualification of Sliding Bearings for Planetary Gears in Wind Turbine Gearboxes. Conference for Wind Power Drives 2023 Conference Proceedings, Aachen, 2023.

Gearbox (Academic Track)

Thermo-Elastohydrodynamic Gearbox Simulations

Jochen Lang, Gunter Knoll

IST Ingenieurgesellschaft für Strukturanalyse und Tribologie mbH, Schloss-Rahe-Str. 12, 52072 Aachen, Germany

Keywords: Wind turbine, thermo-elastohydrodynamics, gear box, oil supply

Abstract:

Based on elastohydrodynamic simulations (EHD) for plain bearings of gearboxes presented at former CWD conferences, the next level of simulation technique is the thermo-elastohydrodynamic simulation (TEHD) under consideration of thermal effect in the lubrication fluid and the elastic bodies. In addition to the solution of Reynolds equation for the hydrodynamic pressure, energy equation has to be solved for the calculation of temperature and viscosity distribution in the fluid film, and heat transfer equation has to be solved to calculate the temperature distribution and thermal deformations of the bodies. For the calculation of body temperatures and deformations, the unique technique of thermal modes is applied. The TEHD modelling and exemplary simulation results for different oil supplies and bushing designs are shown for a generic gear box system of a wind turbine at a stationary operation point. However, the applied TEHD simulation technique based on a multi body system approach is also suitable to consider non-steady operation conditions and speed-up load cases.

1 Motivation and Objectives

At former CWD conferences in 2019 [LAN19] and 2023 [LAN23] elastohydrodynamic (EHD) simulations of the first stage of a gear box system were presented, showing different multi body system (MBS) modelling levels. In 2019 the MBS model includes all EHD contacts between gears and pins in a time-consuming 360° model. In 2023 an efficient cyclic symmetric model was presented, also including the press fits between pin and gear to reach a more precise carrier twist and pin bending. However, these EHD analysis did neither included the analysis of the bore pocket position, nor the effect of the oil supply on the bearing temperature.

The current work is dealing with the question how the bearing friction power loss and the position of the oil supply influences the temperature distribution of the lubricant film, as well as the body's temperature and thermal deformation. To optimize the bearing design, possible design parameters are the bushing contour and the oil supply position. It is obvious that a first stage of a gear box system is not critical in terms of bearing temperature in contrast for example to a HSS stage of a wind turbine or a high-speed gear box in different applications. However, the existing generic MBS model of a first stage is suitable to show the general thermo-elastohydrodynamic (TEHD) modelling and some exemplarily simulation results achieved with a non-steady MBS approach [FIR24].

2 TEHD Simulation Technique for a Non-Steady MBS System

The TEHD model is based on the cyclic-symmetric EHD model of 2023 [LAN23], but without the gear contacts between sun wheel, planet wheel and ring wheel which are not in the focus of the TEHD model. The overall MBS model of the gear box segment is shown in Figure 61. It consists of

the carrier segment, the pin with press fits to the carrier and the planet gear with the TEHD contact to the pin. In addition to the typical boundary conditions of a classical EHD model (supply and ambient pressure, structure cyclic symmetry of the carrier, etc.) the TEHD model needs some additional boundary conditions shown in Figure 62. For the bodies these are thermal cyclic symmetry and the heat transfer coefficients of the free surfaces and the additional material data heat capacity and heat conductivity. If the energy input due to the gear contact is known from previous calculation steps, it can be set as a boundary condition in addition. For the fluid film additional boundary conditions are the oil inlet temperature and the boundary temperature at the edges of the bushing. The values of the boundary temperature are defined for each single edge node of the hydro mesh in the following way: If the fluid at the considered node is flowing into the bearing, the defined ambient temperature is set. If the fluid is flowing out of the bearing, the fluid temperature at that node is part of the calculation result for the temperature field.

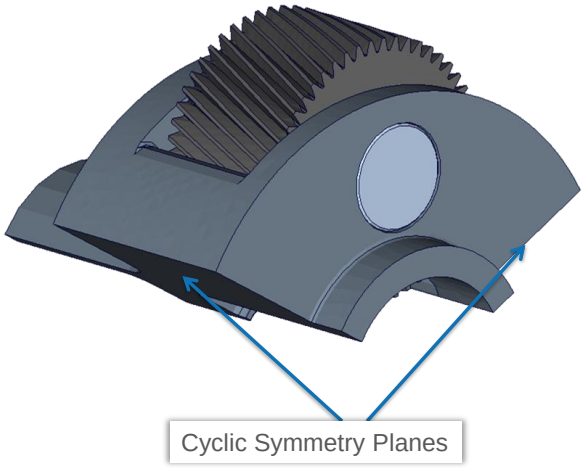

Figure 61: Cyclic-symmetric model of a gearbox

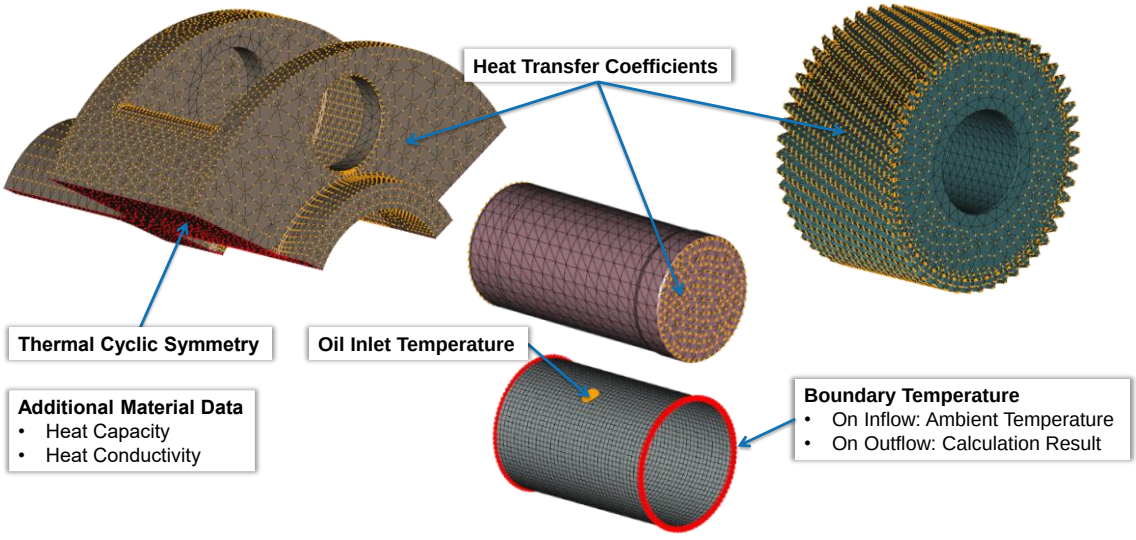

Figure 62: Additional boundary conditions for the TEHD model

For the determination of the temperature field in the fluid and in the bodies, beside the Reynolds equation for the calculation of the hydrodynamic pressure distribution, the energy equation for the fluid film and the heat conduction equation (HCE) for the bodies have to be solved (s. Figure 63). As the TEHD simulation bases on a transient, non-steady MBS algorithm, energy equation and heat

conduction equation both include the non-steady terms on the left side for the consideration of transient effect in the system. These terms are necessary if there are squeeze motions or moving oil supplies in the system, or if heat-up processes in the bodies have to be analyzed [JAI17].

The solution of the HCE follows the same strategy as the solution of the Newton equation of motion for the calculation of the structure dynamics of the bodies [SCH01]. Like the Newton equation, the HCE is too big to be solved in a transient MBS simulation. This problem can be solved with the idea of temperature and temperature deformation modes, so-called “T-Modes” [WAL13].

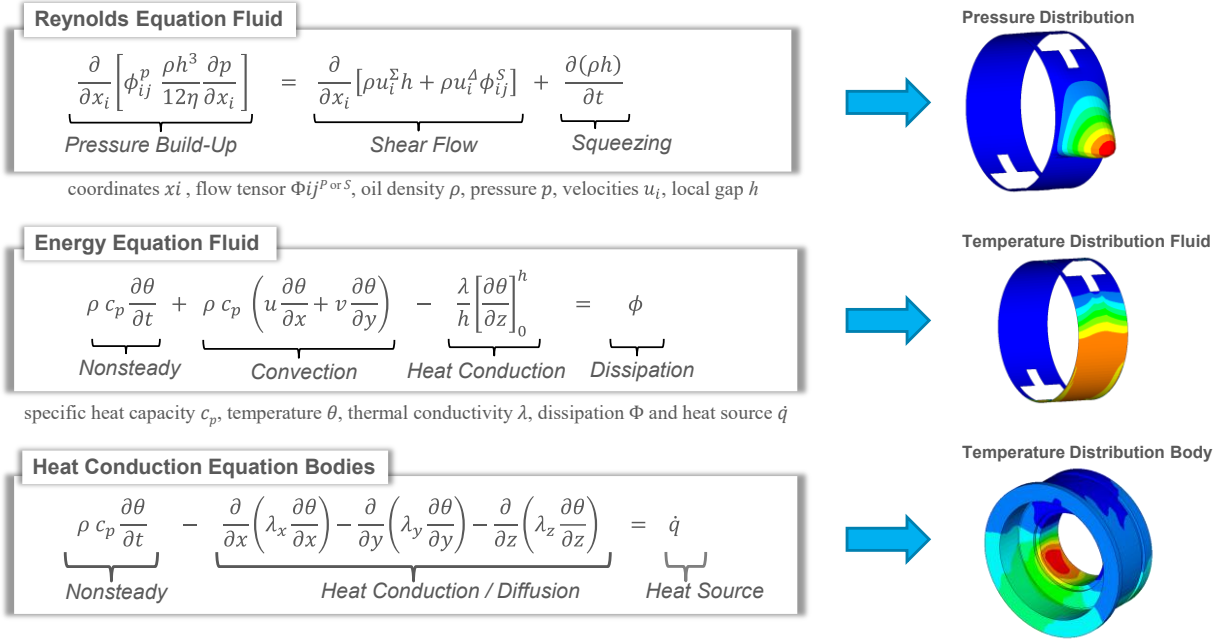

Figure 63: Governing equations for TEHD simulations

Figure 64 shows the idea of a thermal reduction of the HCE. The Finite Element Method (FEM) formulation of the equation with local FEM shape functions is transferred to a reduced form of the HCE with global temperature shape function [JAI17].

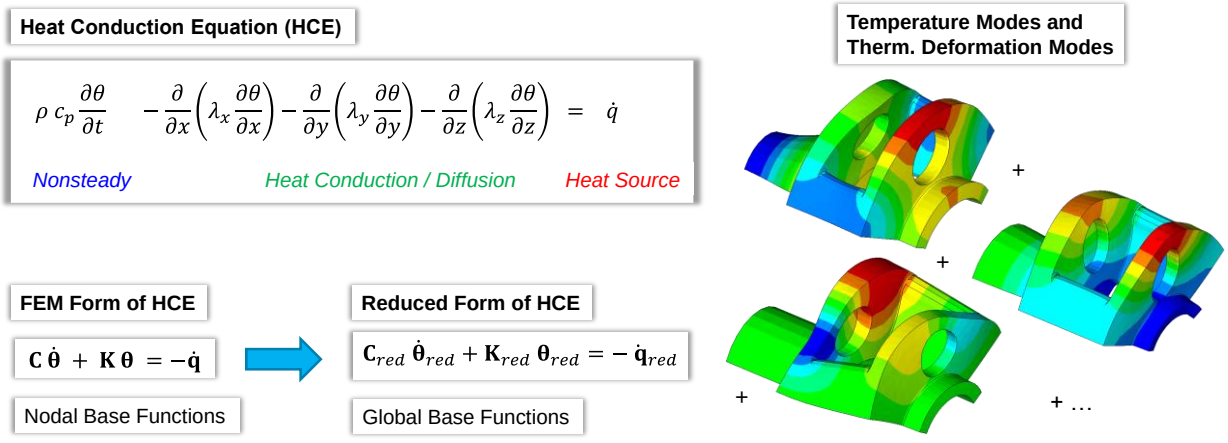

Figure 64: Thermal Reduction, “T-Modes”

These temperature shape functions are used to create globe temperature deformation shape functions to calculate the current temperature deformation of the bodies by superposition. Figure 64 shows exemplarily some temperature deformation modes of the carrier segment and in color the underlying temperature modes.

3 TEHD Simulation Results

To understand the effect of design parameters on the thermal behavior of the gear box system, beside a basic variant with a barrel shape bushing and an oil bore in the cavitation area of the bushing, a modification of the oil supply and the bushing contour is presented exemplarily.

3.1 Basic Design Variant

The structure deformation of the bodies under the outer tooth loads (tangential, radial and axial) of the sun and ring wheel side shown in Figure 65 does not vary much to the classical EHD results: The carrier segment is twisting, the pin is bending and the gear is ovalizing due to the tooth forces on the sun and ring wheel side. The structure deformation of all three bodies lead to a complex gap function between pin bushing and gear.

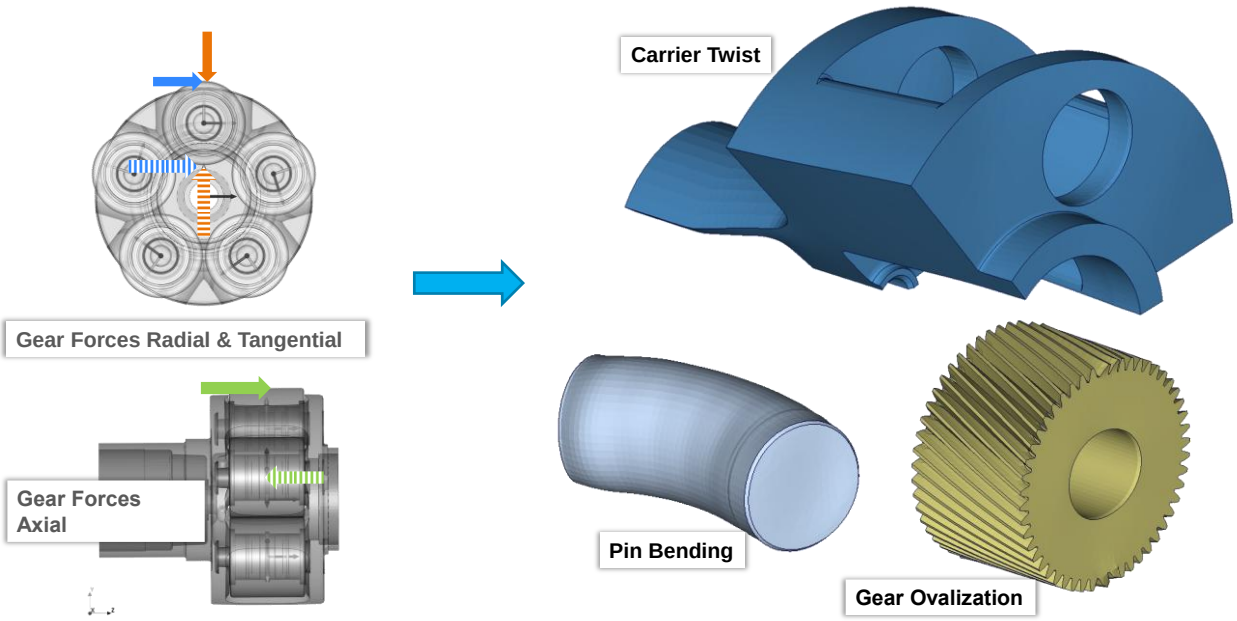

Figure 65: Loads and mechanical deformations of the gear box components

The gap function of the bushing (left side of Figure 66) shows the typical edge carrying due to the tilting moment. The press fits loose contact in the grey areas due to the tangential forces (right side of Figure 66). Figure 67, left side, shows the separation of pressure area and cavitation area in the bearing. The oil bore is fully filled with oil and lies in the cavitation area near the maximum gap where it can deliver an optimum amount of fresh oil. Figure 67, right side, shows oil filling distribution in the bearing. Due to the planet gear rotation the oil supply creates an oil trail in the partially filled cavitation area which is reaching the pressure area and supplies fresh oil.

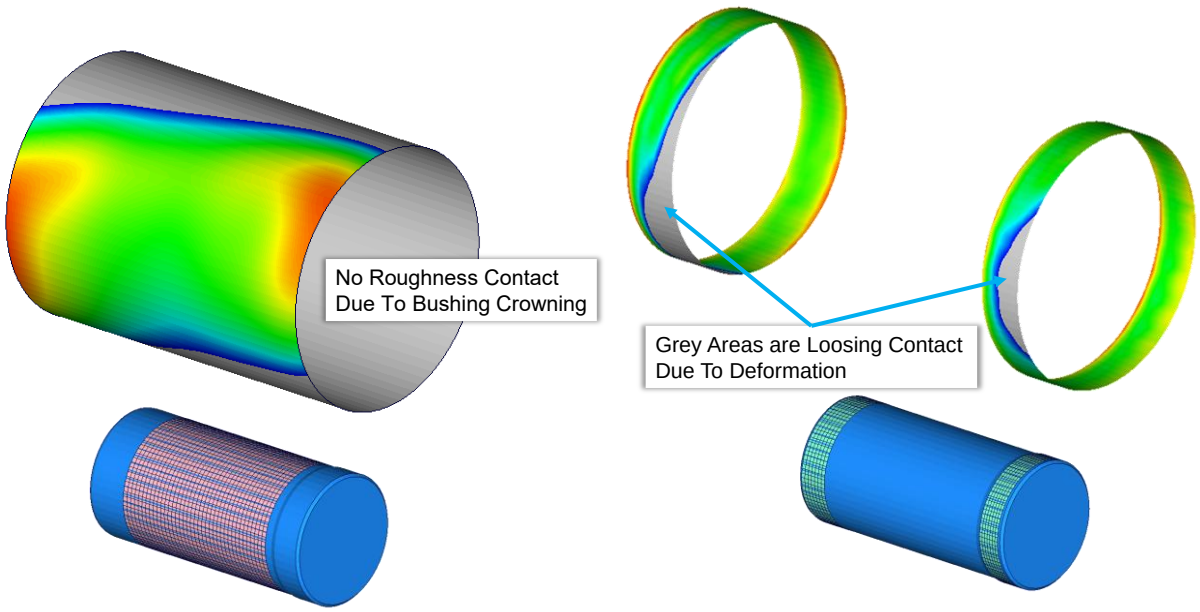

Figure 66: Gap distribution of bushing and press fits

Basically, these results could have also been archived with a classical EHD simulation. In addition, the extension to a TEHD simulation enables also the evaluation of the fluid temperature based on the fluid shearing (s. Figure 68, right side) and the body temperatures based on the local energy input by the fluid film (s. Figure 68, left side).

Looking at the body's temperatures (Figure 68, left side) the oil supply bore can be identified as a "cool spot" and the press fits are conducting the heat from the pin to the carrier. The temperature distribution of the planet gear is rotation-symmetric in a correct manner although the efficient technique of virtual rotation is applied, in which the rotation speed is only applied to the fluid film. In Figure 68, right side, the fluid film temperature shows a cool oil trail in rotation direction of the gear, which ends after a short distance due to the slow rotation speed of the gear and the heating of the oil film by the adjoining bodies.

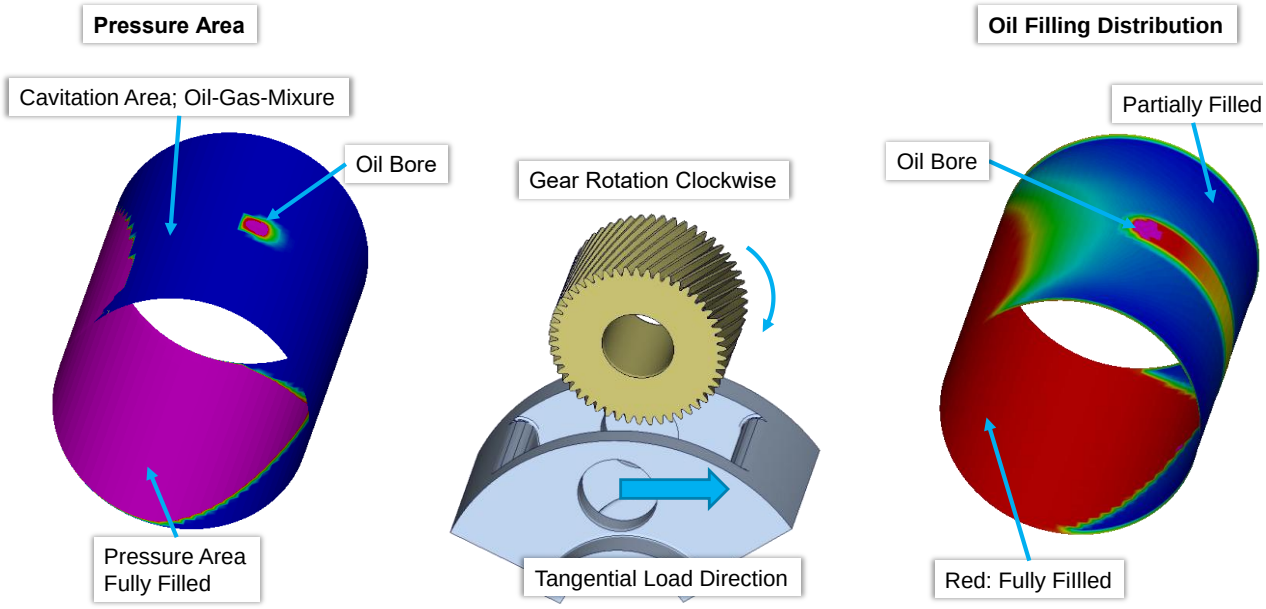

Figure 67: Bushing cavitation area and oil filling distribution

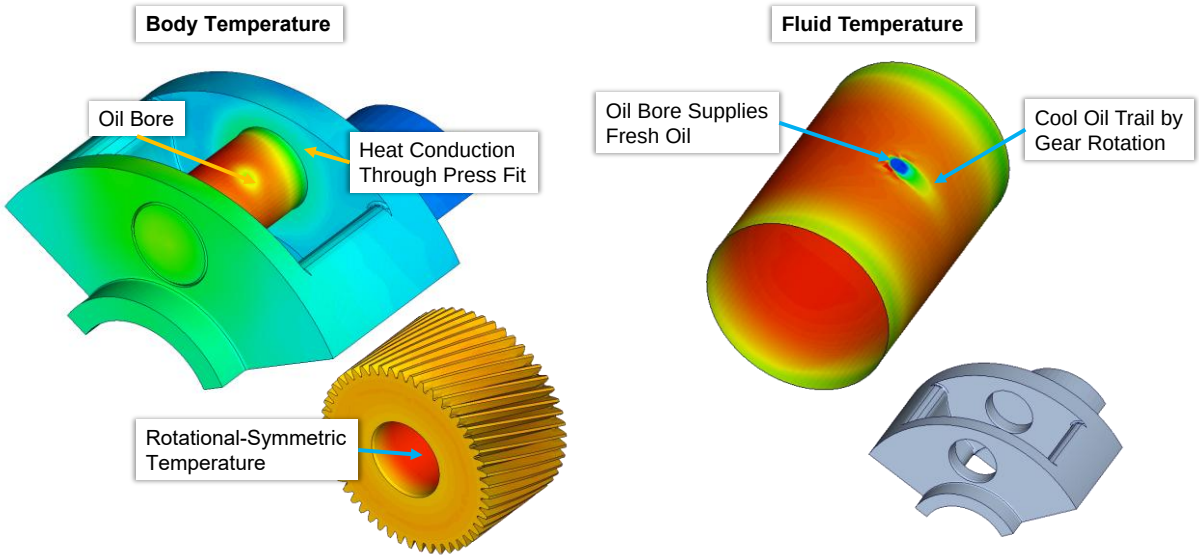

Figure 68: Body and fluid film temperatures

3.2 Modification of the Oil Bore Position

To illustrate the general effect of the oil bore position on the pressure build-up, the oil supply and the bearing temperature, the original bore position of the generic gear box model is rotated in clock-wise direction (Figure 69).

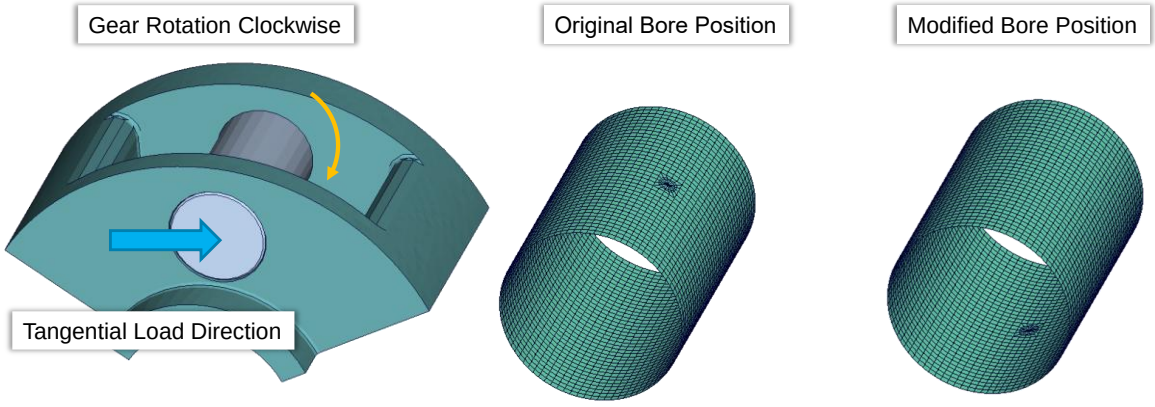

Figure 69: Modification of the oil bore position

The resulting effect on the oil flow velocities in the bearing is shown in Figure 70. The rotation of the bore brings the oil supply closer to the begin of the hydrodynamic pressure zone. The rising pressure gradient hinders the oil outlet flow of the bore so that the resulting oil flow is reduced to one-third of the original oil flow, which leads to an increase of the maximum fluid temperature.

3.3 Modification of the Bushing Contour

Beside the position of the oil supply, the barrel contour of the bushing is another design parameter of the gear box system. An adverse design of the bushing contour can lead to surface contact of bushing and gear and the resulting mixed lubrication introduces high local energy into the surfaces. To demonstrate that the TEHD algorithm can also model local thermal effects, a bushing without a manufactured barrel shape is simulated, which leads to mixed lubrication at the bushing edges (s. Figure 71).

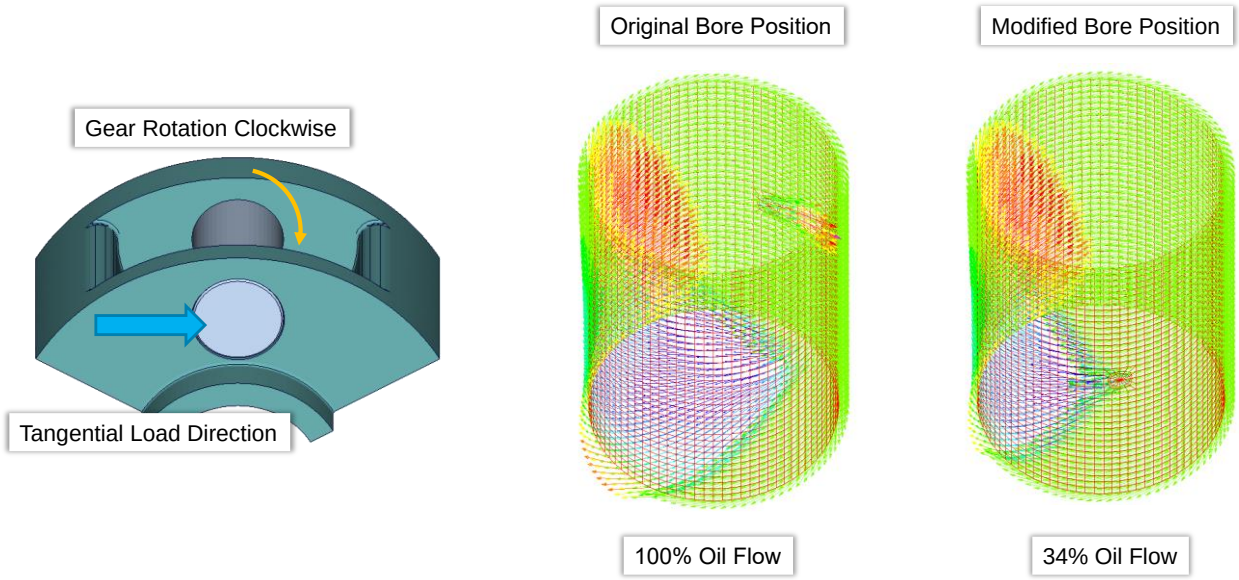

Figure 70: Comparison of the oil flow velocities

The mixed lubrication zone occur with a small distance to the bearing edges as the temperature deformation of the bushing leads to a thermal barrel shape. Moreover, the oval structure deformation of the gear leads to a double pressure peak in the hydrodynamic pressure distribution.

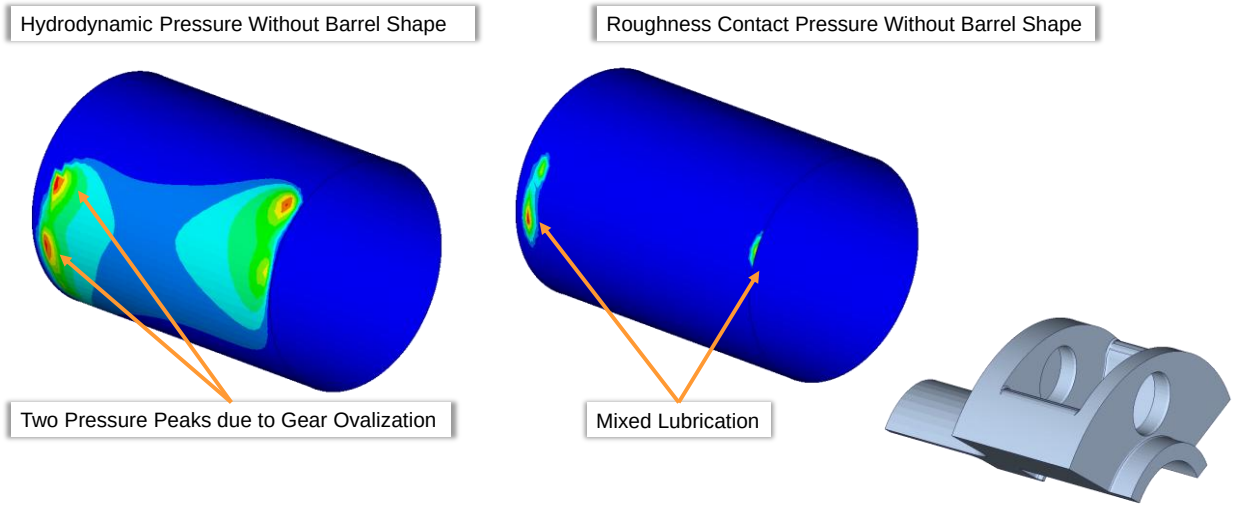

Figure 71: Mixed lubrication with cylindrical bushing

Figure 72 shows the resulting temperature distribution in the fluid film, the pin and the gear. The local energy input due to mixed lubrication leads to temperature hot spots at the bushing edges. It has to be stated that the calculation precision of the local temperature on the surface of the bushing in the mixed lubrication zone is limited by the FEM discretization and the local resolution and number of the considered T-Modes for the heat conduction equation.

4 Summary / Outlook

On the basis of a generic gearbox model of a wind turbine, the TEHD simulation technique for a non-steady MBS system is presented. The simulation algorithm solves the energy equation for the

fluid film and the heat conduction equation for the bodies. The heat conduction through the press fits of pin and carrier is also considered.

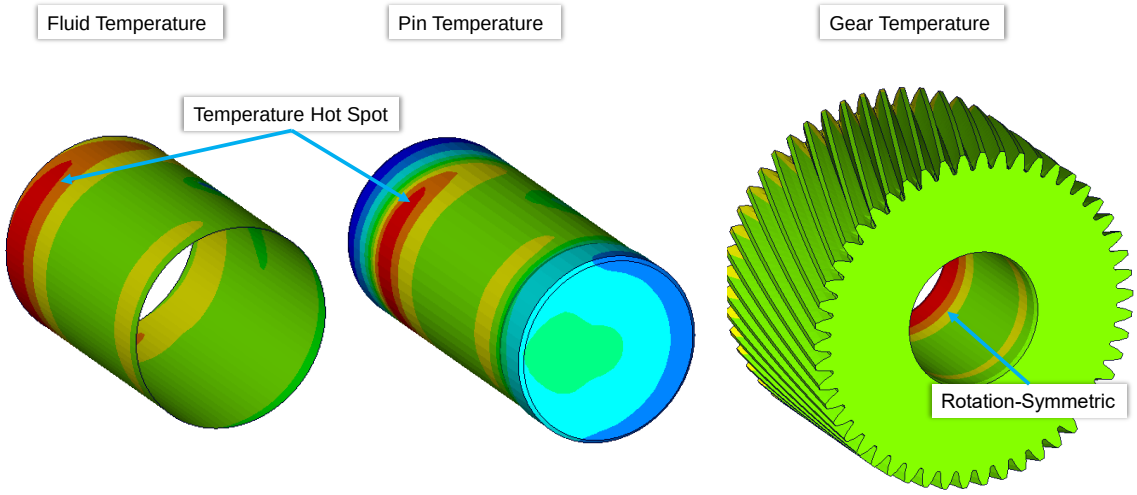

Figure 72: Local temperature effects with cylindrical bushing

For the calculation of the body's temperature and their thermal deformation, a reduction technique based on thermal modes ("T-Modes") is applied. To show the capabilities of the TEHD simulation based on multi body dynamic systems, some exemplarily simulation results are shown, focusing on the thermal effect of the positioning of the oil supply. A transient, mass conserving cavitation algorithm is used to analyze the local oil flow in the bearing. Further, the effect of mixed lubrication on the temperature distribution of fluid film and bodies is shown that occur with a cylindrical bushing contour. The presented simulations were done for a stationary operation point. However, the developed simulation technique would also be able to analyze non-steady operating conditions like load impacts or speed-up load cases.

5 Bibliography

[FIR24] FIRST: Programmsystem zur Berechnung gekoppelter Mehrkörper-systeme mit elastischen Strukturen unter thermo-elastohydrodyna-mischen Bedingungen (TEHD/EMKS), www.IST-aachen.de, 2024

[WAL13] Waldo, A.: Modellreduktion thermischer Zustandsvariablen zur Einbindung in elasto-mechanisch gekoppelte Mehrkörpersysteme auf Basis strukturerhaltender Unterraum-Verfahren. IMK, Universität Kassel, Dissertation, 2013

[JAI17] Jaitner, D.: Effiziente Finite-Elemente-Lösung der Energiegleichung zur thermischen Berechnung tribologischer Kontakte, IMK, Universität Kassel, Dissertation, 2017

[SCH01] Schönen, R.: Strukturdynamische Mehrkörper-Simulation des Verbrennungsmotors mit elastohydrodynamischer Grundlagerkopplung, Dissertation Universität Kassel, 2001

[LAN19] Lang, J., Knoll, G., Hölzl, J., Schröder, T., Bosse, D.: EHL Simulations of Hydrodynamic Bearings in Wind Turbines, Conference for Wind Power Drives (CWD), 2019

[LAN23] Lang, J., Knoll, G.: Efficient Elastohydrodynamic Gearbox Simulations, Conference for Wind Power Drives (CWD), 2023

Turbine Design and Control (Academic Track)

Towards wind turbine control for adaptive optimization of energy production and rotor blade noise

A. Gimeno-García[1], P. Piechnick[2], W. Schröder[1]

[1]RWTH Aachen University, Chair of Fluid Mechanics and Institute of Aerodynamics, Wüllnerstrasse 5a, 52062 Aachen, Germany

[2]RWTH Aachen University, Institute of Automatic Control, Campus-Boulevard 30, 52074 Aachen, Germany

Keywords: rotor blade, aeroacoustics, wind turbine, control

Abstract: This paper details the validation process of *WEAcoustics*, an aeroacoustics prediction tool. It combines the flow field solver of a state-of-the-art wind turbine simulation software, Alaska/Wind, and a semi-empirically based code developed under a Simulink environment to predict sound power and pressure levels at a high-frequency output rate. The outcoming signal, interpreted by a control algorithm, can lead to a quieter yet more efficient wind turbine operation.

1 Introduction

The trade-off between power maximization and reduction of rotor blade noise emissions is one of the main challenges in the design of operating strategies for wind turbines. In countries like Germany, wind turbine noise emissions are restricted by law [BUN98], limiting suitable installation locations for onshore wind turbines. To comply with the stricter legal noise limits, for example, at night, wind turbines currently operate under conservative modes with inherent power reduction. However, this lowers their profitability. Some previous works address this problem by researching a more efficient noise-reduced wind turbine operation with the help of numerical optimization methods. For example, the optimization from Leloudas et al. [LEL07] provides wind speed-dependent operating points, which maintain an upper noise limit while maximizing power production. Shaltout et al. [SHA15] go one step further and compute the control commands necessary to implement the proposed operating strategies. In these and similar publications, the respective optimization problem is solved offline under the assumption of steady conditions.

In real operation, a wind turbine is exposed to turbulent wind conditions and other environmental disturbances not considered in offline optimization. We, therefore, pursue the development of control algorithms based on online optimization of the operating strategy. The design and testing of these control algorithms benefit from tools that accurately estimate rotor blade noise at low computational effort. For this reason, we have developed *WEAcoustics*, a horizontal wind turbine noise prediction tool. *WEAcoustics* couples the blade element momentum theory-based (BEMT) [FRO78, RAN 65] flow field solver of the software Alaska/Wind [FRE16] with a trailing edge post-processing algorithm based on XFOIL [DRE87, DRE89], and a semi-empirical aeroacoustics algorithm based on the work of Brooks et al. [BRO89] and the subsequent improvements made by Moriarty et al. [MOR03, MOR05]

This paper covers the multi-stage validation of *WEAcoustics* against the measured acoustic data of a commercial wind turbine in the 3 MW range from the report of its certification test according to IEC 61400-11:2012 [IEC12]. Besides its use in controller development, *WEAcoustics* is also a powerful tool during the early phases of rotor blade design thanks to its fast iteration capabilities. It only

requires a geometrical input, easy to alter during design, to provide reliable aeroacoustics predictions when drafting a new blade design.

The simulation chain of WEAcoustics is described in chapter 2. The validation procedure is detailed in chapter 3. And chapter 4 shows the outlook of the project with the validated tool before coming to the final conclusions.

2 *WEAcoustics* Simulation Chain

The overall structure of WEAcoustics features a block design. It is depicted in Figure .

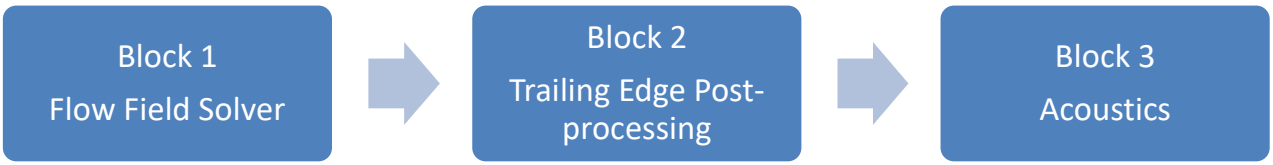

Figure 73: *WEAcoustics* structure block diagram.

It is divided into three main parts: the flow field solver block, to analyze the interaction between the airflow and the turbine blades; the trailing edge block, to post-process the flow field information and obtain relevant trailing edge data, i.e. the boundary layer information; and the acoustic block, where all the gathered aerodynamic data is used to predict the turbine noise output.

2.1 Block 1: Flow Field Solver

The selected flow field solver is based on a blade element momentum theory (BEMT) structure. It belongs to a validated holistic wind turbine simulation software based on multi-body dynamics, Alaska/Wind. BEMT is practical for wind turbine performance evaluation but has simplifying assumptions that limit resolving detailed flow physics. It treats each radial blade section as quasi-two-dimensional, neglecting three-dimensional effects, like tip vortices and spanwise flow. Although Alaska/Wind includes empirical corrections, they can introduce errors under non-ideal conditions such as yawed flow or turbulence induced by the wake of another wind turbine inside a wind farm. In these situations, the three-dimensional nature of the flow cannot be neglected. Thus, the flow field is defined as orthogonal to the rotor blade plane and linear. A power law (Eq. 1) is used to determine the wind velocity increment with height [JUN21]. The definition of the quantities in the equations can be found at the end of the document, in the nomenclature appendix.

$$U_{hub} = U_g \left(\frac{h_{hub}}{h_g} \right)^E \qquad \textbf{Eq. 1}$$

In block 1, Alaska/Wind is integrated into a Simulink environment where it is initialized with the wind velocity field and the geometric data of the wind turbine blade. After the initialization, it receives changing input values for the rotor speed and pitch angle. During the validation process the tool iterates constantly using a set of constant input values for each test case.

2.2 Block 2: Trailing Edge Post-Processing

Boundary layer information along the wingspan of the rotor blades is key for the acoustic algorithm to provide reliable prediction results. The BEMT-based flow field solver algorithm in Alaska/Wind does not provide the characteristics of the flow around the airfoil, it calculates lift and drag forces,

and power coefficient, C_p, and thrust coefficient, C_t, based on local flow conditions. The local flow conditions at the leading edge of the airfoil are post-processed to obtain the required boundary layer data at the trailing edge for the noise prediction.

To extract the boundary layer data from the results of the first block, XFOIL [DRE89], a well-known open-source simulation tool for two-dimensional geometries, is used. In XFOIL, boundary layer thicknesses around a two-dimensional airfoil are computed by coupling an inviscid potential flow solver with an integral boundary-layer formulation. First, a panel method determines the external velocity distribution at a certain distance from the airfoil surface, $u(y)$, along the airfoil. The panel method grid is refined through the Grid>Pane XFOIL configuration menu in the areas of the leading and trailing edge, where the most sensitive data is calculated. Then, for each chordwise location, the displacement thickness, δ^*, and momentum thickness, θ, are obtained by solving the integral boundary layer equations [KAR46]. The nominal boundary layer thickness is typically defined as the addition of the displacement and momentum thicknesses using a corrective factor depending on the nature of the flow. For laminar flow in XFOIL, the definition is given in Eq. 2 [DRE87]:

$$\delta = \theta\left(3.15 - \frac{1.72}{H_k}\right) + \delta^* \qquad \textbf{Eq. 2}$$

By refining the inviscid flow solution and the boundary layer characteristics in each iteration, XFOIL achieves a converged estimate of boundary layer thicknesses.

WEAcoustics uses the output data from the BEMT flow field solver as an input to the XFOIL module, which calculates the boundary layer information for the first and last section of a particular airfoil geometry, as well as critical sections (i.e.: maximum angle of attack). Then an interpolation algorithm calculates the intermediate sections along the whole wingspan.

2.3 Block 3: Aeroacoustics

Brooks, Pope, and Marcolini proposed a semi-empirical method for predicting the noise emitted by an airfoil as it interacts with a flow field, namely the BPM method. It is a simplified approach that combines analytical models with empirical data. This method focuses on the noise generated at the trailing edge of the airfoil dividing it into different categories depending on its nature (see section 2.3.1). It involves calculating blade element velocities and forces, estimating the sound pressure level (SPL) of each blade segment using empirical relations based on local flow conditions, and summing the contributions from all blade segments to obtain the overall SPL of the turbine rotor blade. Sound pressure level (SPwL) is the specific SPL nomenclature for the noise emitted by one two-dimensional section calculated at 1 meter distance from the TE, orthogonal to the chord line and coplanar to the airfoil [MOR05]. SPwL and SPL are measured in dB and the different contributing sources add up logarithmically.

This semi-empirical method offers several advantages, including its computational speed and simplicity. It does not require detailed Computational Fluid Dynamics (CFD) or Computational Aeroacoustics (CAA) simulations, making it a time-effective and efficient tool for preliminary design and optimization studies. This lack of complexity also brings some limitations. These include assuming a uniform and two-dimensional flow field and not fully capturing the physics behind the distinct noise generation mechanisms. Neglecting factors such as turbulence, blade surface roughness, non-uni-

form inflow, or the three-dimensional nature of a rotating flow may result in inaccuracies in the predicted noise levels; particularly for wind turbines operating under off-design configurations. Its two-dimensional nature requires obtaining the SPL values sectionally along the wingspan of the blade. Adding up the SPL of each section constitute the SPL of the three-dimensional blade or overall sound pressure level (OASPL).

2.3.1 Noise source terms

The BPM method distinguishes five different noise sources. These are considered independent from one another and are calculated separately. Their contribution to the final noise spectra is added as non-correlated noise sources.

Turbulent boundary layer trailing edge (TBL-TE)
The turbulent boundary layer (TBL) noise is considered the most common source of noise generation in aerodynamic systems. It is produced by the interaction between the turbulent boundary layer and the trailing edge of the airfoil, on both the pressure side and the suction side of the blade.

The total TBL noise is a combination of the SPL generated on the pressure side and the suction side of the blade, represented in Eq. 3 and Eq. 4.

$$SPL_p = 10\log\left(\frac{\delta_p^* M^5 L \bar{D}_h}{r_e^2}\right) + A\left(\frac{St_p}{St_1}\right) + (K_1 - 3) + \Delta K_1 \quad \textbf{Eq. 3}$$

$$SPL_s = 10\log\left(\frac{\delta_s^* M^5 L \bar{D}_h}{r_e^2}\right) + A\left(\frac{St_s}{St_1}\right) + (K_1 - 3) \quad \textbf{Eq. 4}$$

As the angle of attack increases beyond the flow separation threshold, the boundary layer on the suction side of the blade grows significantly. This phenomenon introduces an additional term into the final TBL trailing-edge (TBL-TE) noise equation, referred to as the separation flow term, denoted by SPL_α in Eq. 5.

$$SPL_\alpha = 10\log\left(\frac{\delta_s^* M^5 L \bar{D}_h}{r_e^2}\right) + B\left(\frac{St_s}{St_2}\right) + K_2 \quad \textbf{Eq. 5}$$

Finally, all terms are added in Eq. 6.

$$SPL_{TBL-TE} = 10\log\left(10^{SPL_p/10} + 10^{SPL_s/10} + 10^{SPL_\alpha/10}\right) \quad \textbf{Eq. 6}$$

Although many parameters affect the TBL-TE, it is mostly sensitive to boundary layer thicknesses, Mach number, and observer distance.

Laminar boundary layer vortex shedding (LBL-VS)
Laminar vortices leaving the trailing edge generate pressure waves that travel upstream, amplifying boundary layer instabilities. As these instabilities reach the trailing edge, similar frequency vortices are formed, generating an interference loop. This source of noise, defined in Eq. 7, manifests itself mostly on the pressure side and with a tonal nature due to the quasi-homonymous frequency present inside the interference loop. The tonality pattern depends on the Strouhal number [BRO89].

LBL-VS contribution is significant in low-power turbines, featuring reduced wingspan and mean chord, where the Reynolds number remains sufficiently low ($< 10^6$ at the blade tip) for stable laminar flow to occur.

$$SPL_{LBL-VS} = 10\log\left(\frac{\delta_p M^5 L \bar{D}_h}{r_e^2}\right) + G_1\left(\frac{St'}{St'_{\text{peak}}}\right) + G_2\left(\frac{\text{Re}_c}{(\text{Re}_c)_0}\right) + G_3(\alpha) \quad \textbf{Eq. 7}$$

Trailing edge bluntness vortex shedding (TEB-VS)

Trailing edges are not one-dimensional and sharply finished (ending in a single point joining intrados and extrados). The bluntness of the trailing edge, mostly rounded or sharp-edged, generates vortices like a von Kármán vortex street downstream of a round-ended object. This noise source can become the main contributor to the SPL when the bluntness dimension is bigger than the boundary layer thickness. It is defined in Eq. 8.

$$SPL_{TEB-VS} = 10\log\left(\frac{\delta_p^* M^5 L \bar{D}_h}{r_e^2}\right) + G_4\left(\frac{h}{\delta^*_{\text{avg}}}, \Psi\right) + G_5\left(\frac{h}{\delta^*_{\text{avg}}}, \Psi, \frac{St''}{St''_{\text{peak}}}\right) \quad \textbf{Eq. 8}$$

Tip Vortex

This noise source differs from the previous ones as it is directly defined as a three-dimensional noise source. It is generated by the interaction of the blade tip vortex and the trailing edge. Its absolute contribution is lower from the turbulent and laminar boundary layer interactions, but it can add significant noise at high frequencies (10-20 kHz). Brooks, Pope, and Marcolini defined it for an untwisted, constant-chord blade (Eq. 9).

$$SPL_{Tip} = 10\log\left(\frac{M^2 M_{max}^5 \ell^2 \bar{D}_h}{r_e^2}\right) - 30.5(\log St''' + 0.3)^2 + 126 \quad \textbf{Eq. 9}$$

Turbulent Inflow

Turbulent Inflow is the single leading edge-related noise source. It is predominant at low frequencies and gains importance as the size of the turbulence length scale overcomes that of the radius of the leading edge. *WEAcoustics* uses the Amiet model [AMI75] defined by Eq. 10.

$$SPL_{Inflow} = SPL^H_{Inflow} + 10\,log\left(\frac{LFC}{1+LFC}\right) \quad \textbf{Eq. 10}$$

The noise term generated by the inflow is composed of high frequency (Eq. 11), and low frequency corrective terms.

$$SPL^H_{Inflow} = 10\log\left(\frac{\rho_o^2 c_o^2 l L}{2r_e^2} M^3 u^2 I^2 \frac{K^3}{(1+K^2)^{7/3}} \bar{D}_L\right) + 58.4 \quad \textbf{Eq. 11}$$

The low-frequency correction factor (LFC) includes a modification to account for the influence of the angle of attack and it is defined in Eq. 12. S^2 represents the Sears term.

$$LFC = 10S^2\overbrace{(1-9\alpha^2)}^{\alpha\ Corr.\ Term} M\bar{K}^2\beta^{-2}, \qquad with: S^2 = \left(\frac{2\pi K}{\beta^2} + \left(1 + 2.4\frac{K}{\beta^2}\right)^{-1}\right)^{-1} \quad \textbf{Eq. 12}$$

Several improved models have been developed; *WEAcoustics* incorporates the Guidati model (Eq. 13, Eq. 14) [GUI97], as it is an upgraded version of Amiet's model that accounts for the effect of the section's thickness on noise generation.

$$SPL_{Inflow} = SPL_{Amiet} + SPL_{Guidati} + 10dB \quad \textbf{Eq. 13}$$

$$SPL_{Guidati} = -\left(1.123\left(D_{rel,1\%} + D_{rel,10\%}\right) + 5.317\left(D_{rel,1\%} + D_{rel,10\%}\right)^2\right)\left(\frac{2\pi fC}{U} + 5\right) \quad \textbf{Eq. 14}$$

Guidati developed a methodology to consider airfoil thickness when estimating the turbulent inflow noise. This method uses the relative thickness at one and ten percent distance from the leading edge of the airfoil to provide a turbulent inflow noise estimation more adequate to wind turbine airfoil families with thicker profiles (Eq. 15), from the root to the middle section of the wingspan, than the NACA0012 airfoil used by Amiet.

$$IT = D_{\mathrm{rel},1\%} + D_{\mathrm{rel},10\%}, SL = 1.123IT + 5.317IT^2 \quad \textbf{Eq. 15}$$

3 Validation

The process of validating the tool has two stages, implementing two- and three-dimensional approaches, respectively. The first stage includes the validation of blocks 2 (XFOIL post-processing) and 3 (acoustic module) and then the second stage includes an extension to the three-dimensional approach of block 3. The validation data comes from the acoustic certification report of the 3 MW commercial wind turbine [BAK11].

3.1 Implementation of XFOIL and the aeroacoustics prediction algorithm

The implementation of the acoustics prediction code has been validated by reproducing the experimental measurements of Brooks et al. [BRO89] and the numerical predictions from Moriarty et al. [MOR03, MOR05] running blocks 2 and 3 under a two-dimensional configuration. The overall sound pressure level (OASPL) of the validated data agrees with that available from the experiments for a set of various Mach numbers at a fixed angle of attack and vice versa, shown in Figure 74.

The angle of attack variation shows differences of up to 10 dB for the higher α. This is due to several factors. The randomness of the natural boundary layer tripping position at higher α, further away from the trailing edge towards the leading edge of the airfoil, has influenced the tonality of the prediction. It shows a translation in the horizontal axis with minimal OASPL influence respect that of the numerical analysis from Moriarty et al. Also, in the experimental case, the reduction of noise output in the $\alpha = 7.30°$ case indicates flow separation where boundary layer thickness dependent noise is no longer occurring as the boundary layer is inexistent. XFOIL in this case converges assuming attached flow and subsequently the acoustic algorithm overpredicts the noise output.

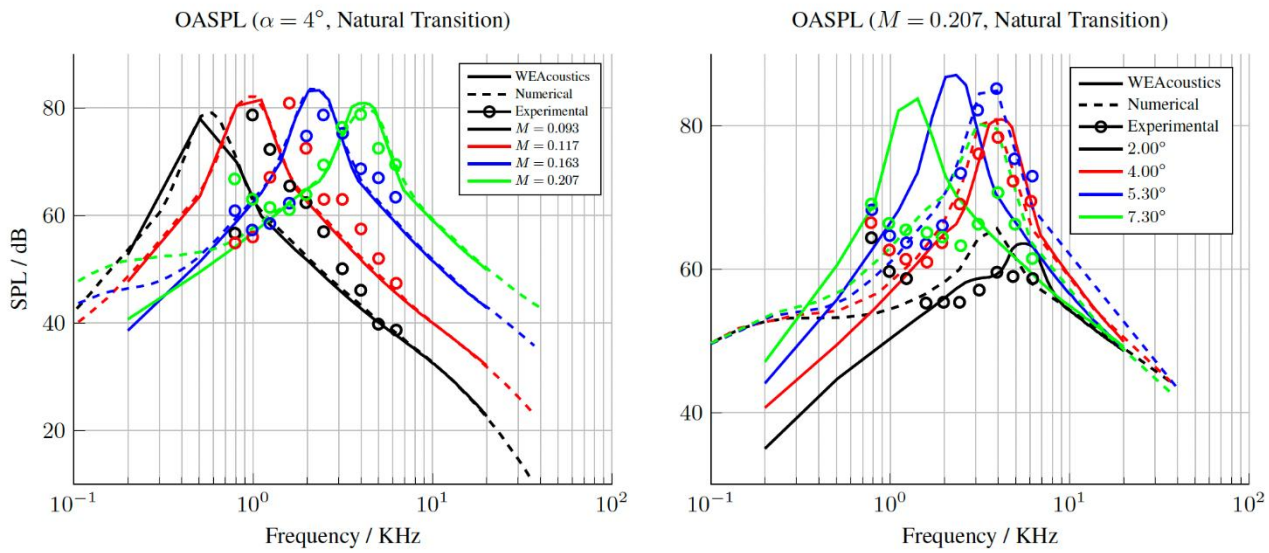

Figure 74: *WEAcoustics* two-dimensional validation against experimental [BRO89] and numerical [MOR03, MOR05] data for a NACA0012 airfoil at different Mach numbers (left) and angles of attack (right).

Nevertheless, separation phenomena occur mainly in the inner sections of the blade under on-design conditions. Under such conditions, the relative linear velocity increases substantially towards the outer sections of the blade, where the angles of attack are typically smaller, and the flow remains attached. High velocity attached flow conditions are the ones generating most of the aerodynamic noise of the turbine. Accordingly, the logarithmical contribution of the inner sections of the blade in the three-dimensional case, at higher angles of attack and separated flow can be neglected in terms of OASPL. The effect to the tonality has not yet been evaluated.

3.2 General Three-Dimensional Method

Figure 75 shows the comparison between the experimental data and the prediction output from *WEAcoustics* for sound power and pressure levels, respectively. Variations of $\pm 2\ dB$ are present in the whole range of wind speeds. The sound pressure level predictions show a noise over-prediction, linear in the whole range except for the $4{,}5 - 5{,}5\ m/s$ region.

The IEC 61400-11 [IEC12] report includes several margins and uncertainties when measuring the SPL with the microphone that have influenced the validation process: the flow field orthogonality to the rotor plane considers $\pm 15°$ reading margins, the measurements have a tolerance of $\pm 2\ dB$, and the distance microphone to tower allows for $\pm 20\%$ variations. On the *WEAcoustics* part, deviations in the SPwL prediction can be caused by the assumptions coming from the BEMT-based flow field solver, the simplifications of the wind conditions (steady and orthogonal to the rotor plane), or the XFOIL limitation not able to identify separated flow (only non-converged calculations are treated likewise). When calculating the SPL, a lack of a propagation model, and the assumption of non-correlated noise sources, influence the final output showing an average overprediction of $+2\ dB$.

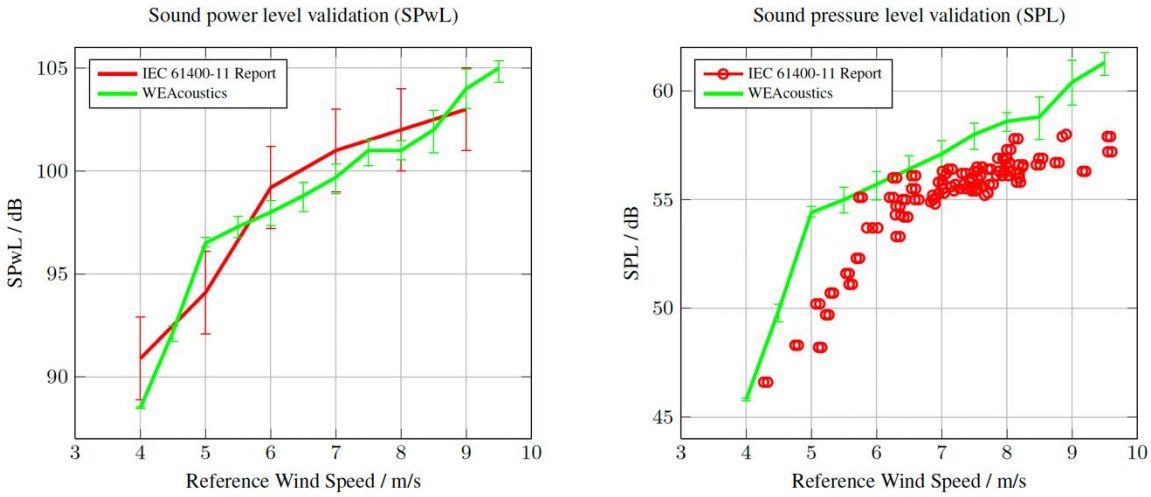

Figure 75: *WEAcoustics* three-dimensional validation using real acoustic measurements from the certification report of a commercial 3 MW wind turbine.

Considering all the limitations of the tool inherent to the components, making it that simple and fast, and the uncertainties from the reference data, the tool is considered validated with a tolerance of $\pm 2\ dB$ along the whole spectrum of analyzed velocities.

4 Outlook: *WEAcoustics* as an enabler for noise-reducing controller development

The noise-reduced operation of a wind turbine generally conflicts with the primary objective of a wind turbine controller. This objective is to maximize the turbine's power production while maintaining its operating limits [JAS18]. The power coefficient, $C_\mathrm{p} = f(\lambda, \theta)$, determines the efficiency of a wind turbine at a given operating point, characterized by the tip speed ratio, λ, and the blade pitch angle, θ [GAM22]. Figure 76 shows a section of the C_p map of the commercial 3 MW wind turbine overlaid with the contour lines of the emitted SPwL. These contour lines were calculated with *WEAcoustics* for a wind speed of $14\ m/s$. The nominal operating point is marked with a blue circle for comparison. The position of the nominal operating point in the characteristic map reflects the maximum power production that is permanently justifiable within the operating limits of the system. A reduction of the SPwL to 100 dB, for example, is only possible at operating points with reduced power production. Therefore, an operating point on the 100 dB contour line with a minimum difference to the C_p value of the nominal point would be desirable.

Due to its low computational effort, *WEAcoustics* is suitable for large-scale simulation studies investigating the trade-off between power maximization and noise reduction. In the next step, we use the simulation results from *WEAcoustics* as training data for a data-driven regression model. This gives us a real-time capable noise prediction model that can be converted into a differentiable mathematical expression, making it suitable for use as an extension of the internal prediction model of a model predictive controller (MPC) for wind turbines. The extended prediction model of the noise-reducing MPC predicts the future system behavior of the wind turbine over a certain time horizon including the SpwL. Based on these predictions, the MPC computes the control inputs by solving an optimization problem. In the cost function and constraints of that optimization problem, we encode the conflicting control goals of power maximization and noise reduction. This optimization problem has

to be solved cyclically on the wind turbine's control hardware with a sample time of less than 1 second. This explains the need for a noise prediction model with low computational effort.

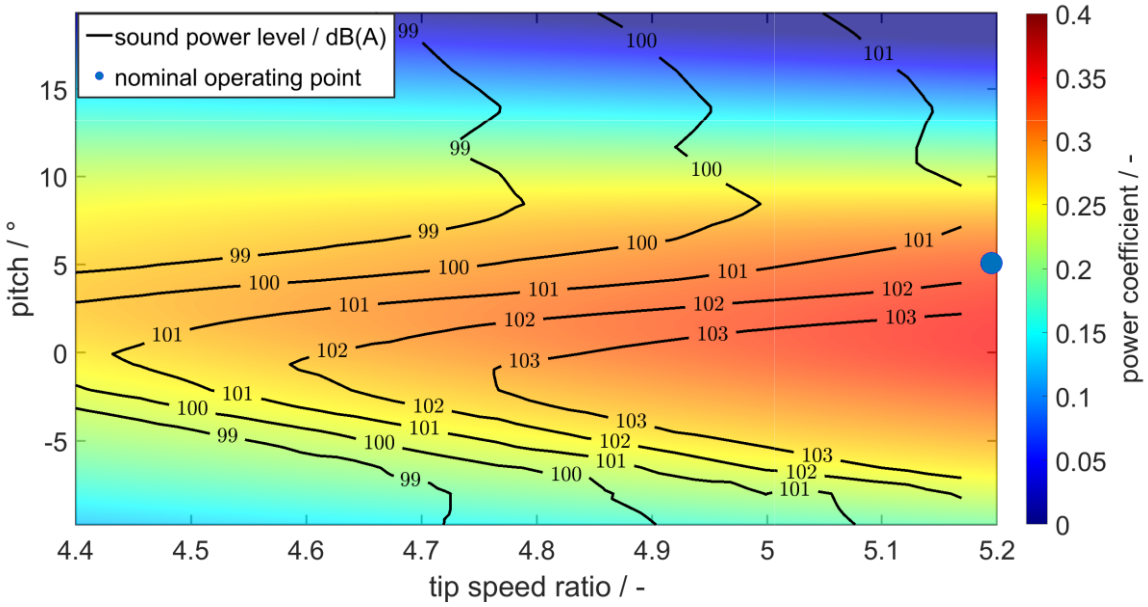

Figure 76: Characteristic map of power coefficient C_p of the commercial 3MW turbine with contour lines of sound power level for a wind speed of $14\ m/s$.

The potential of MPC for complex control problems in the wind energy sector has already been demonstrated in several studies, such as [WIN21]. We now also take aeroacoustics into account in this holistic control concept. The online optimization of control commands can lead to a quieter and efficient turbine operation in the entire operational range even under the influence of stochastic wind disturbances.

5 Conclusions

This study outlines the development and successful validation of the three-dimensional aerodynamic noise prediction tool *WEAcoustics* with data from the acoustic certification report of a 3 MW commercial wind turbine. The validation of *WEAcoustics* was primarily achieved through direct comparison with real-world field measurements, establishing its accuracy. As a first step towards controller development, *WEAcoustics* is used to visualize the conflict between noise reduction and power maximization.

Future research will focus on two key areas. The first involves implementing *WEAcoustics* to design noise-reducing controllers for wind turbines, potentially minimizing power loss while limiting acoustic emissions. The second aims to enhance the tool by altering the flow field solver and acoustic modeling blocks. These advancements aim to enable more accurate predictions of wind turbine noise emissions, even under challenging off-design conditions characterized by rapidly changing flow fields, yaw effects, and turbulence.

6 Nomenclature

A, B	Spectral shape functions for TBL-TE noise

δ	Boundary layer thickness, m
δ^*	Boundary layer displacement thickness, m)
θ	Boundary layer momentum thickness, m
$\overline{D}_h, \overline{D}_l$	Directivity function for the high and low frequency limits, respectively
E	Power law exponent
G_1	Spectral shape function for LBL-VS noise
G_2	R_c dependence for LBL-VS noise peak amplitude
G_3	Angle dependence for G_2
G_4	Peak level function for G_5
G_5	Spectral shape function for TE bluntness noise
h	TE thickness
h_{hub}	Height at hub level, m
H_k	Shape parameter
K_1	Empirical constant
K_2	Empirical constant
ΔK_1	Empirical constant
M	Mach number
l	Spanwise extent of the tip vortex, m
L	Span, m
ψ	Angle parameter related to surface slope at TE, deg
R_c	Reynolds number based on chord length
r_e	Distance from the observer to the airfoil, m
SPL	Sound pressure level, dB
St	Strouhal number
$St_{1,2}$	Reference Strouhal numbers

St_{peak}	Peak Strouhal number
U_g	Wind mean velocity at ground level, m/s
U_{hub}	Wind mean velocity at hub height, m/s
p, s, α	Subscripts for pressure side, suction side, and separated flow

7 Bibliography

[AMI75] Amiet, R.K. et al.: Acoustic Radiation from an Airfoil in a Turbulent Stream, in: Journal of Sound and Vibration, 1975.

[BAK11] Bak, C. et al.: DAN-AERO MW II: Data for the NM80 turbine at Tjaereborg Enge for aerodynamic evaluation, Riso Report, tech. rep., National Renewable Energy Laboratory (NREL), 2011.

[BRO89] Brooks, T. F., D. S. Pope, and M. A. Marcolini: Airfoil Self-Noise and Prediction, tech. rep., NASA Reference Publication 1218, 1989.

[BOO18] Boorsma, K. et al.: Final Report of IEA Wind Task 29 MEXNext, tech. rep., Energy Research Center of the Netherlands (ECN), 2018.

[BUN98] Bundesregierung, Deutschlands: Technische Anleitung zum Schutz gegen Lärm - TA Lärm, tech. rep., Die Bundesregierung, 1998.

[DRE87] Drela, M.: Viscous-Inviscid Analysis of Transonic and Low Reynolds Number Airfoils, in:

[DRE89] Drela, M.: XFOIL: An Analysis and Design System for Low Reynolds Number Airfoil, tech. rep., MIT Dept. of Aeronautics and Astronautics, Cambridge, Massachusetts, 1989.

[DRE89-1] Drela, M.: Integral Boundary Layer Formulation for Blunt Trailing Edges, tech. rep., MIT Dept. of Aeronautics and Astronautics, Cambridge, Massachusetts, 1989.

[FRE16] Freudenberg, H.: Der Einsatz von alaska bei der Entwicklung von Windkraftanlagen., tech. rep.,
Institut für Mechatronik e.V., Chemnitz, Germany, 2016

[FRO78] W. Froude. On the elementary relation between pitch, slip and propulsive efficiency. Trans. Roy. Inst. Naval Arch., 19(47):47–57, 1878.

[GAM22] Leloudas, G. et al.: Control of Large Wind Energy Systems.
Springer International Publishing, 2022.

[GUI97] Guidati, G. et al., Simulation of Aerodynamic Sound Generation on Airfoils in Low Mach-Number Flows, in: Proc., Fifth International Congress on Sound and Vibration, 1997.

[IEC12] International Electrotechnical Commission, in: IEC 61400-11, International Standard, Wind turbine generator systems - Part 11, 2012.

[JAS18] Jassmann, U., Hardware-in-the-Loop Wind Turbine System Test Benches and their Usage for Controller Validation., Phd thesis. RWTH Aachen University, Aachen, Germany, 2018

[JUN21] Jung, C. et al., The role of the power law exponent in wind energy assessment: A global analysis, in: Wiley International Journal of Energy Research, 2021.

[LEL07] Leloudas, G. et al.: Prediction and Reduction of Noise from a 2.3 MW Wind Turbine, in: Journal of Physics: Conference Series, 75 IOP Publishing, 2007.

[MOR03] Moriarty, P. et al.: Semi-empirical Acoustic Noise Prediction Code for Wind Turbines, tech. rep., National Renewable Energy Laboratory (NREL), 2003.

[MOR05] Moriarty, P. J. et al.: Prediction of Turbulent Inflow and Trailing-Edge Noise for Wind Turbines, in: 26th AIAA Aeroacoustics Conference, 2005.

[RAN65] W. J. M. Rankine. On the mechanical principles of the action of propellers. Trans. Roy. Inst. Naval Arch., 6:13–30, 1865.

[RIV23] Rivarola, A. et al.: Control of Large Wind Energy Systems for Acoustic Noise Reduction by Using Multi-Objective Optimal Control, in: IFAC PapersOnLine, 56-2, 11255-11260 Elsevier Ltd., 2023.

[SHA15] Shaltout, M. et al.: Tradeoff analysis of energy harvesting and noise emission for distributed wind turbines, in: Sustainable Energy Technologies and Assessments, 10, 12-21 Elsevier Ltd., 2015.

[KAR46] Von Kármán,T.: „*Über laminare und turbulent Reibung, 1921*“ (On laminar and turbulent friction), National Advisory Comitte on Aeronautics, 1946.

[WIN21] Wintermeyer-Kallen, T. et al.: Weight-scheduling for linear time-variant model predictive wind turbine control toward field testing.
in: Forschung im Ingenieurwesen, 85, 385-394
Springer, 2021

Evaluation of Wind Field Reconstruction for Lidar-Assisted Control of a 2 MW Wind Turbine

David Schlipf[1,2], Showmin Islam[1], Santiago Pérez Brovia[2], Marcel Schedat[1]

[1] Hochschule Flensburg, Kanzleistraße 91-93, 24943 Flensburg, Germany

[2] sowento GmbH, Hessenlauweg 14, 70569 Stuttgart, Germany

Keywords: lidar, wind turbine modeling, wind turbine control, disturbance estimation.

Abstract: Lidar-assisted control of wind turbines is a promising technology for reducing the structural loads on wind turbines. The load reduction can then lead to an extended service life, minimization of operating costs and noise, as well as an increase in energy production. Reliable and accurate wind preview is essential for this technology. As only the wind speed in the line-of sight can be measured, the wind field must be reconstructed using wind and lidar models and estimation algorithms. In this work, we analyze the data availability and evaluate the wind preview quality of a baseline wind field reconstruction methods using measurement data from a lidar installed on the nacelle of our 2 MW research wind turbine. As a reference, a rotor-effective wind speed estimate is obtained from turbine data in real time. For this purpose, a reduced model of the drivetrain dynamics including mechanics and electrics as well as aerodynamics is developed based on a complete aeroelastic wind turbine model. This model is then used in an immersion and invariance estimator. A tuning method is developed to achieve a fixed estimation delay over the entire operating range. This estimator then enables the determination of the prediction time of the lidar-based estimation of the rotor-effective wind speed. Furthermore, the estimator enables an evaluation of the wind preview quality, represented by the coherence between the lidar-based and turbine-based estimation of the rotor-effective wind speed. The analysis of data over more than one year shows that the data availability depends on the measurement distance as expected, but also on the mean wind speed. Further, the wind preview quality and the prediction time correspond to the expectations from the theoretical models and change only slightly during the analyzed period.

1 Introduction

Lidar-Assisted wind turbine control (LAC) has first been successfully tested in 2012 [SCH14]. In 2020 the milestone of one thousand wind turbines 3 GW using this technology has been reached[1]. Important challenges are still the complexity of the certification and the proof of robustness.

This work aims to contribute to this development by highlighting the robustness of the technology in an industrial application over a longer period.

The work is organized as follows: Section 2 provides background information on our project and our wind turbine and lidar system. In Section 3 describes the estimation method of the wind preview from turbine and lidar data. Section 4 provides the results of the availability and wind preview quality and Section 5 concludes the work and provides an outlook to future work.

[1] https://www.sowento.com/important-milestone-reached-for-lidar-assisted-control-of-wind-turbines-1000-wind-turbines/

Figure 77: Wind turbine MM92 with two nacelle-based lidar systems. The right-hand lidar system (looking towards the rotor) was used in the following analysis.

2 Measurement Setup

In this section, our research project and the setup of our experiment are introduced.

2.1 ABBA Project

The “ABBA” project aims to develop adaptive strategies for the operation of existing wind turbines in order to ensure that they can be adapted to current and future challenges. In particular, the focus is on improving wind field reconstruction for real-time applications, developing optimized feedforward control strategies and validating these approaches on a real wind turbine. The use of the improved wind field reconstruction is aimed at providing more precise input variables for lidar-based control, with the objective of increasing energy yields, reducing mechanical loads for extending the operational design life of the turbines and noise emissions.

2.2 Test Turbine MM92

The MM92 is an onshore wind turbine from REpower (later Senvion and today Siemens Gamesa Renewable Energy) that has been in production since 2005 and is used as a representative existing turbine for the investigations within the project. With a rated power of 2.05 MW, a hub height of 100 m, and a rotor diameter of 92.5 m, it offers good conditions for validating the strategies developed to optimize the operation of existing turbines. The turbine is located outside several neighboring wind farms in the north of Schleswig-Holstein near Flensburg. The area is characterized by a flat topography with mainly agricultural land.

2.3 Nacelle-Based Lidar System and Data Acquisition

The data acquisition for the wind field reconstruction was performed by one of the two installed nacelle-based lidars. The lidar used is an NL200 from Nanjing Movelaser (see Figure 77). The system measures in a range of 50 m to 200 m with maximal 10 measurement distances and a sampling rate of 4 Hz. It has four pulsed beams that are arranged at a horizontal angle of +/-15° and a vertical angle of +/-12.5°. The lidar data, together with a selection of turbine data, were transferred to a small single-board computer (Revolution Pi) and merged. The data is stored in binary files formatted to comply with OpenFAST standards. The 10-minute data files are transferred to a server via a data access service once a day. In total, 23730 data files from September 2023 to March 2024 and 6779 data files from December 2024 and January 2025 were analyzed for this study. In the months in between, the data collection wasn't possible.

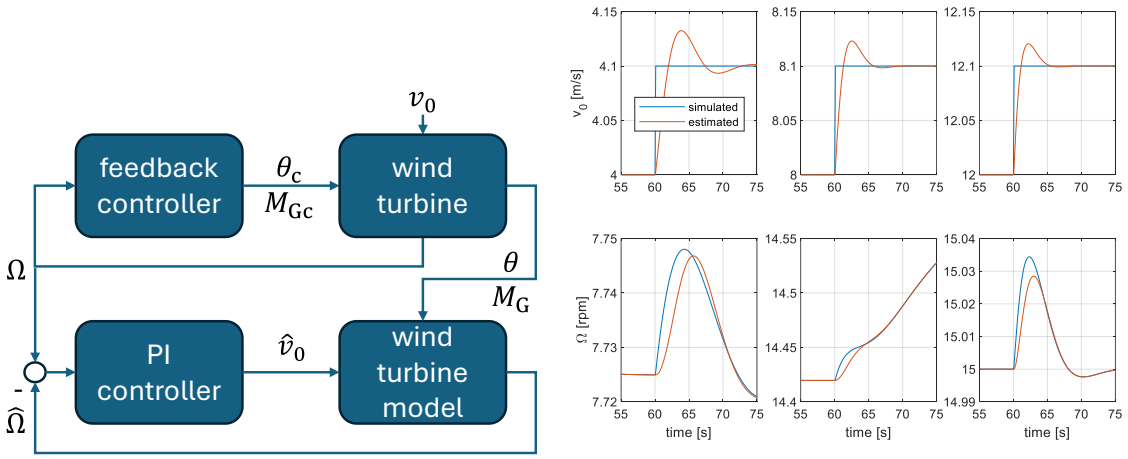

Figure 78: Setup of I&I wind speed estimator (left). Response to wind steps (right).

3 Methodology

This section describes how the rotor-effective wind speed (REWS) is estimated based on turbine and lidar data and how the two signals are then used to calculate the wind preview quality.

3.1 Wind Speed Estimation from Turbine Data

In simulations, the REWS is typically calculated from the turbulent wind field by the mean of all longitudinal wind components hitting the rotor disc [SCH15]. The best measurement device for the REWS for real experiments is the wind turbine itself. Typically, a “torque-balance” wind speed estimator is used to calculate in real-time the REWS v_0 from turbine data such as rotor speed Ω, pitch angle θ, and generator torque M_G [HOO04; HEL19]. Therefore, a simplified wind turbine model is used, where J is the rotor inertia, M_a the aerodynamic torque, r_{GB} the gearbox ratio, and the mechanical and electrical losses M_{loss}:

$$J\dot{\Omega} = M_a(\theta, \Omega, v_0) - \left(M_G + M_{loss}(M_G, \Omega)\right) r_{GB}. \qquad \textbf{Eq. 1}$$

Due to the cubic wind speed relationship of the aerodynamic torque, this estimator requires solving a cubic equation. This is typically done a priory and then in a real-time application a 3D interpolation with signals of Ω, θ, and aerodynamic torque $M_a = J\dot{\Omega} + (M_G + M_{loss}) r_{GB}$ is used. The main shortcomings are the difficulties in finding the correct solution of the 3 possible ones and the discretization for the interpolation.

Here, the “immersion and invariance” (I&I) wind speed estimator is used based on [LIU22]. It uses a baseline proportional-integral (PI) controller and the simplified turbine model from Eq. 1, see Figure 78 (left). Here, the real wind turbine is controlled by (here unknown) feedback controller using the demanded pitch angle θ_c and demanded generator torque M_{Gc} and distributed by the REWS v_0. The input to the PI controller is the difference between the measured rotor speed Ω and the estimated one $\hat{\Omega}$. The output of the PI controller is the estimated wind speed $\hat{v}_0$. The measured pitch angle θ, generator torque M_G and $\hat{v}_0$ are the inputs to the wind turbine model of Eq. 1, which provides the estimated rotor speed $\hat{\Omega}$.

The advantages of this method are that it can be easily implemented and tuned. The transfer function G_E between the real wind speed v_0 and the estimated wind speed $\hat{v}_0$ and be simplified and then compared to the desired behavior with the desired damping D and frequency ω:

$$G_E = \frac{K_P b_2 s + b_2 K_1}{s^2 + K_P b_2 s + b_2 K_1} \stackrel{!}{=} \frac{2D\omega s + \omega^2}{s^2 + 2D\omega s + \omega^2} \quad \textbf{Eq. 2}$$

This results in the following equations for the proportional gain K_P and the integration time T_I:

$$K_P = -\frac{2D\omega}{b_2} \quad \textbf{Eq. 3}$$

$$T_I = \frac{K_P}{K_I} = \frac{2D}{\omega} \quad \textbf{Eq. 4}$$

The only turbine parameter needed is here $b_2 = \frac{\partial \dot{\Omega}}{\partial v_0}\Big|_{\mathrm{OP}}$, which depends on the operation point (OP). However, it can be approximated to 0.03 rad/m for the given wind turbine. With $D = 0.7$ and $\omega = 1$ rad/s, the resulting wind speed estimator provides an almost constant response to wind speeds at 4 m/s (region 1.5), 8 m/s (region 2), and 12 m/s (region 3), see Figure 78 (right).

3.2 Wind Speed Estimation from Lidar Data

Lidar systems measure a projection of the wind speed called the line-of-sight wind speed (v_{LOS}). This magnitude must be processed to estimate the characteristics of the wind field, and this process is called wind field reconstruction (WFR), which is applied using specific models and assumptions of the lidar measurements and the wind field [BOR17]. The WFR methodology used in this work estimates the REWS using a simple point measurement model of a fixed lidar at the hub height. The methodology assumes perfect alignment between the wind and the turbine as well as linear vertical and horizontal shear. For the purpose of LAC, the rotor-effective wind speed (REWS) must be estimated at every acquisition time. Therefore, the methodology reconstructs the REWS by dividing v_{LOS} of every measurement by the cosine of the angle-to-centerline and computing the mean over the last four estimated longitudinal wind components.

3.3 Comparison of Estimated and Analytic Coherence

The coherence between the rotor-effective wind speed of the turbine and the lidar estimate serves to evaluate the quality of the wind estimation obtained from the lidar measurements. Additionally, an analytical coherence model based on wind spectra such as the Kaimal can be used as reference for comparison with the measurement estimated coherence. In this work, the analytical coherence model proposed by [SCH13] is used as reference. On the other hand, the coherence γ^2_{RL} estimated from the measurements is obtained using the equation:

$$\gamma^2_{\mathrm{RL}} = \frac{|S_{\mathrm{RL}}|^2}{S_{\mathrm{RR}} S_{\mathrm{LL}}} \quad \textbf{Eq. 5}$$

Where S_{RL}, S_{RR} and $S_{\mathrm{LL}}$are the cross-spectrum between both signals and the auto-spectrum of the signal from the turbine and the lidar, respectively. These magnitudes are calculated from the measurements, considering ten-minute segments of the data.

Most part of the analytic model are depending on space, rather than time. Therefore, the analytical coherence for different mean wind speed is usually very similar displayed over wave number. The wave number k can be calculated from the frequency f with the mean wind speed $\bar{u}$:

$$k = \frac{2\pi f}{\bar{u}}. \quad \textbf{Eq. 6}$$

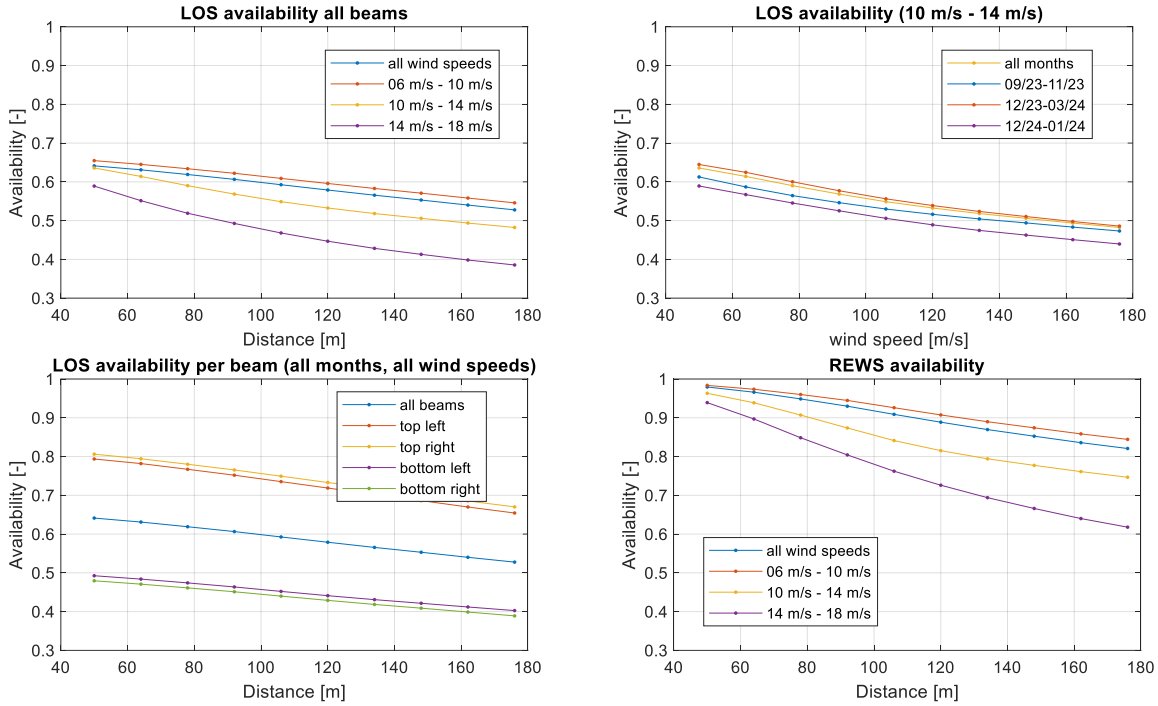

Figure 79: LOS-availability for all beams and different wind speeds (top left), for all beams, the 2nd wind bin and different periods (top right), and for all wind speeds and different beams (bottom left). REWS-availability (bottom right).

4 Results

This section provides detailed results of the availability and wind preview quality.

4.1 Availability

For availability, we differentiate availability for line-of-sight (LOS) and rotor-effective wind speed (REWS).

For the LOS availability, the number of available LOS measurements is divided by the total number of LOS measurements within 10 min. The LOS availability is mainly impacted by two effects: the blade blockage and the reduction of data availability with increasing distance due to the reduced number of returning photons. Figure 79 (top left) illustrates the two effects: overall data during normal operation, the blade blockage is reducing the availability to around 65 % (extrapolating the blue line towards 0 m/s). The overall data availability is further reduced to around 50 % for the last distance. When the data are divided into three wind bins from 6 m/s to 10 m/s, 10 m/s to 14 m/s, 14 m/s to 18 m/s, we observed that the availability is reducing with increasing wind speed. The data for the bin 10 m/s to 14 m/s are divided in three different periods, see Figure 79 (top right): the availability is relatively constant over the full campaign, with a slight reduction over the last two months. We will continue to monitor the availability to detect any further reduction. In Figure 79 (bottom left), we then divided the full data set into the 4 different beams, illustrating the impact of the blade blockage: since the bottom beams are cutting the rotor disc closer to the hub, the blades cover these beams longer during operation.

Finally, Figure 79 (bottom right) depicts the REWS availability, defined as the number of time steps where the internal WFR is able to provide a REWS divided by the total number of time steps. The REWS availability is significantly higher than the LOS availability, but still wind speed dependent.

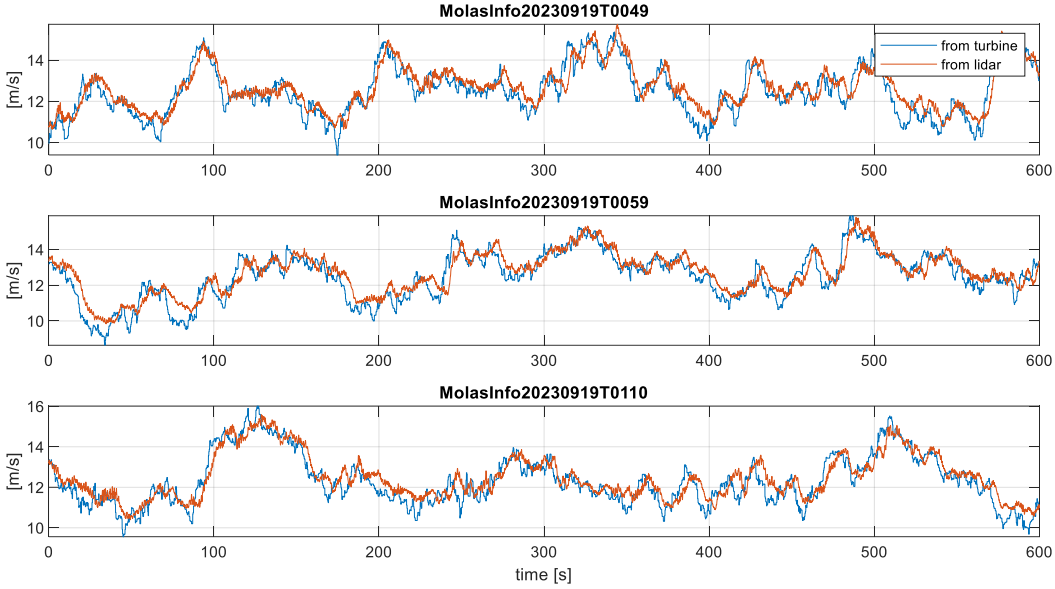

Figure 80: Comparison of the estimated wind speed from turbine data and lidar data for three exemplary 10-minute periods.

4.2 Wind Preview Quality

The estimation of the REWS from turbine data and lidar data described in Section 3.1 and Section 3.2 is then applied to all data. Figure 80 shows an example for three exemplary 10-minute periods. The preview of the lidar signal is clearly visible as well as the high correlation of low frequencies and the low correlation of high frequencies as predicted by the correlation model from Section 3.3.

We then calculated the auto-spectra of the linearly detrended two signals for every full 10-minute block as well as the cross-spectra between the two signals. No windowing or overlapping was used. The spectra are then averaged over wind bins from 10 m/s to 16 m/s with a bin width of 2 m/s, where again only data is used where the turbine was running in normal operation, ending up into 2951, 1415, 865, and 323 blocks for 10 m/s, 12 m/s, 14 m/s, and 16 m/s, respectively. For the binning, the mean of the REWS from the turbine date was used. With the averaged auto-spectra and cross-spectra, the coherence is then calculated.

In Figure 81, the coherence is displayed over wave number exemplary for the 2^{nd}, 4^{th}, 6^{th} and 8^{th} distance at 64 m, 92 m, 120 m and 148 m. As expected, the coherence is very similar for all 4 wind bins, even that the REWS availability for drops significantly over wind speed, see Figure 79. This motivates the use of adaptive Filtering as explained in more detail in [SCH15]: for higher mean wind speeds less filtering is necessary based on Eq. 6.

Further, the coherence at 64 m and 92 m is better than the expected value from the analytic model. We assume that the wind evolution is either overestimated for these distances or the impact of possible yaw misalignment is less impactful for these distances.

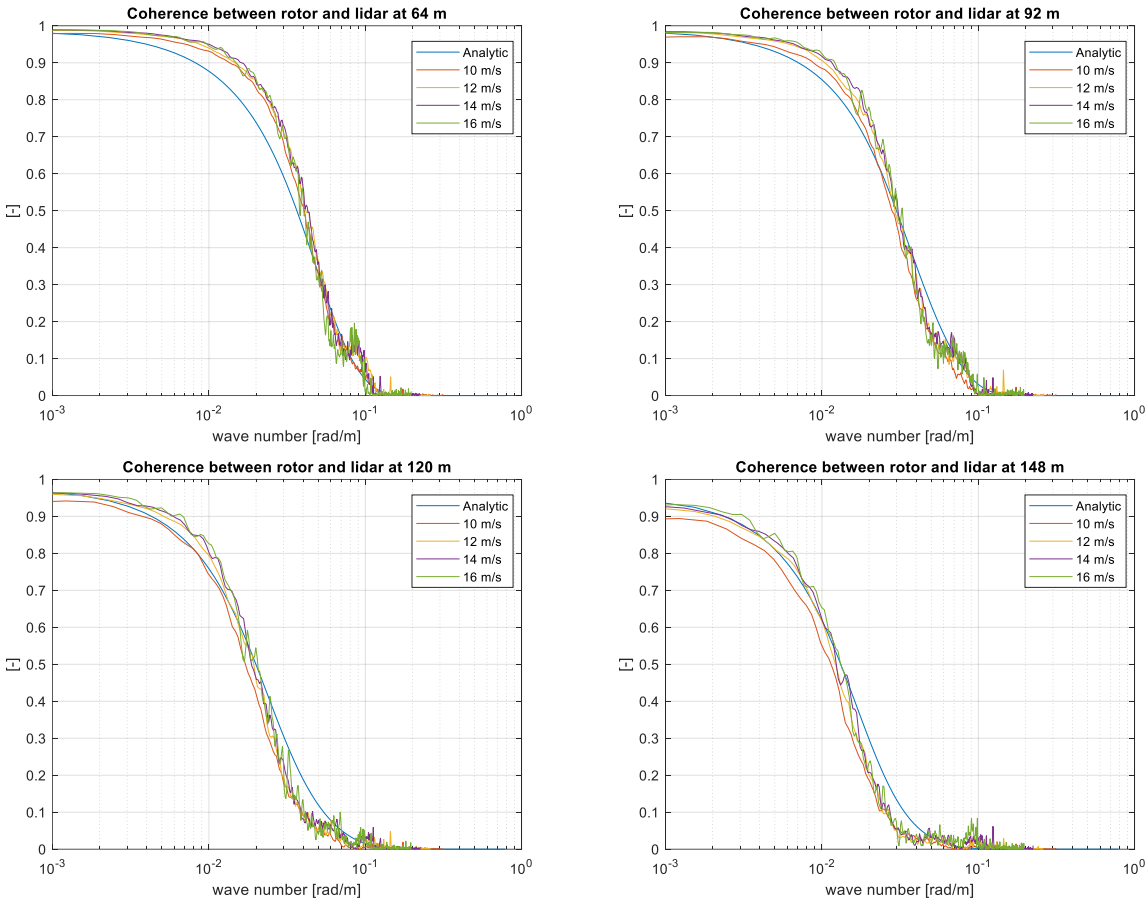

Figure 81: Coherence between rotor and lidar estimated REWS for several wind speed bins over the full campaign compared to the expected analytic model.

5 Conclusions and Outlook

This work presents a evaluation of wind field reconstruction for lidar-assisted control of a 2 MW wind turbine over a longer period of time. For the evaluation, an estimator of the rotor-effective wind speed from turbine data is developed and tuned such that the signal is delayed by a constant time.

The evaluation reveals that the line-of-sight availability depends as expected on the location of the lidar on the nacelle and the measurement distance. Additionally, a clear mean wind speed dependency could be detected. The rotor-effective wind speed availability also depends on distance and mean wind speed and is between 60 % (far measurement and high wind speeds) and 100 % (close measurement and low wind speeds).

The evaluation of the wind preview quality however reveals that the wind preview quality in terms of measurement coherence is not impacted by the lower availability and is close to the expected values, even better as expected for distances close to the rotor.

Future work includes a more detailed analysis of the wind preview quality with respect to inflow angle, turbulence class, and advanced wind field reconstruction methods. Further, several lidar-assisted control methods will be tested including collective pitch, multivariable and optimal feedforward controller.

6 Bibliography

[BOR17] Borraccino, Antoine. Schlipf, David. Haizmann, Florian. Wagner, Rozenn: “Wind field reconstruction from nacelle-mounted lidar short-range measurements”. In: Wind Energy Science, 2, pp. 269–283. 2017. DOI: https://doi.org/10.5194/wes-2-269-2017.

[HEL19] Held, Dominik P. Mann, Jakob: “Lidar estimation of rotor-effective wind speed – an experimental comparison”. In: Wind Energy Science, 4, pp. 421–438. 2019. DOI: https://doi.org/10.5194/wes-4-421-2019.

[HOO04] Hooft, E.L. van der. Engelen, T. G. van: “Estimated Wind Speed Feed Forward Control for Wind Turbine Operation Optimization”. In: Proceedings of the European Wind Energy Conference, 2004.

[LIU22] Liu, Yichao. Pamososuryo, Atindriyo Kusumo. Ferrari, Riccardo M. G. Wingerden, Jan-Willem van: “The Immersion and Invariance Wind Speed Estimator Revisited and New Results”. In: IEEE Control Systems Letters, 6, pp. 361–366. 2022. DOI: https://doi.org/10.1109/LCSYS.2021.3076040.

[SCH13] Schlipf, David. Mann, Jakob. Cheng, Po Wen: “Model of the correlation between lidar systems and wind turbines for lidar-assisted control”. In: Journal of Atmospheric and Oceanic Technology, 30, pp. 2233–2240. 2013. DOI: https://doi.org/10.1175/JTECH-D-13-00077.1.

[SCH14] Schlipf, David. Fleming, Paul. Haizmann, Florian. Scholbrock, Andrew. Hofsäß, Martin. Wright, Alan. Cheng, Po Wen: “Field testing of feedforward collective pitch control on the CART2 using a nacelle-based LIDAR scanner”. In: Journal of Physics: Conference Series, 2014. DOI: https://doi.org/10.1088/1742-6596/555/1/012090.

[SCH15] Schlipf, David. “Lidar-Assisted Control Concepts for Wind Turbines”. PhD thesis. University of Stuttgart, 2015. DOI: http://dx.doi.org/10.18419/opus-8796.

Postersession

Model uncertainty of a multiscale, elasto-hydrodynamic simulation method for the prediction of abrasive wear in journal bearings

Thomas Decker[1], Georg Jacobs[1], Carsten Graeske[1], Pascal Bußkamp[1], Julian Röder[1], Tim Schröder[2],

[1] Chair for Wind Power Drives, Campus-Boulevard 61, 52074 Aachen
[2] Vestas Nacelles Deutschland GmbH, Martin-Schmeißer-Weg 18, 44227 Dortmund

Abstract: Journal bearings have a potentially unlimited service life and are appealing for wind energy gearboxes due to their high torque density. Their reliability is influenced by wear behavior, typically analyzed using elasto-hydrodynamic (EHD) simulations. Abrasive wear can be calculated with wear algorithms linked to the EHD simulation, commonly used to simulate material removal and surface smoothing. Current methods involve many parameters and are prone to errors from parameter uncertainty. This work aims to quantify the maximum model error in abrasive wear simulations for hydrodynamic journal bearings based on FLEISCHER's model. A sensitivity analysis is conducted to understand how input parameters affect EHD simulation results, such as wear volume and depth. Key influential parameters are identified and discussed. Experimental work on a test rig helps derive measurement uncertainties related to wear volume, examining their impact on the wear coefficient and model error. Finally, the accuracy of the wear simulation model is assessed through a worst-case scenario analysis concerning the selected input parameters.

1 Introduction

Wind energy is crucial in transitioning from fossil fuels to renewable sources. By 2023, wind energy accounted for over 30 % of Germany's renewable energy. To boost wind energy expansion and maintain competitiveness, wind turbines are being designed with larger rotor diameters and higher power ratings. This increase leads to greater rotor weight, higher torque and non-torque loads on the drivetrain. Consequently, components like the main bearing and gearbox must be larger to handle these loads. The gearbox significantly contributes to the drivetrain's weight, with the ring gear of the first planetary stage being a major factor. Reducing the size of this stage can enhance torque density. Replacing conventional rolling bearings with journal bearings as planetary bearings is a recent innovation that reduces gearbox weight. Journal bearings require less installation space than rolling bearings and offer a high reliability when properly designed and operated. However, special load conditions can cause mixed friction and abrasive wear in journal bearings, altering their surface contour and roughness. Simulations can predict abrasive wear behavior early in the design without costly prototyping. Yet, current simulations involve many input parameters, making them susceptible to inaccuracies. This work tackles uncertainties in wear simulations by proposing a way to quantify maximum calculation errors. It begins with a sensitivity analysis to identify influential parameters. The most critical parameter is measured through experiments on a journal bearing test rig, identifying inaccuracies from measurement errors. The outcome is a worst-case scenario quantification for uncertainty in simulation results. (For a full paper version of this work refer to [1].)

2 State of the art for the simulation of abrasive wear

Wear simulations have been extensively researched. PRÖLß [2] analyzed the abrasive running-in wear of journal bearings in planetary gearboxes, focusing on contour and roughness changes.

HAGEMANN ET. AL. [3] developed a wear calculation method for journal bearings in planetary gears, factoring in elastic deformations and abrasive wear. DING ET. AL. [4] validated their journal bearing simulation tool, while KÖNIG ET. AL. [5] demonstrated reliable abrasive wear calculations for hydrodynamic journal bearings under constant and transient conditions like start-stop scenarios. This approach was validated through component test rig experiments. DECKER ET. AL. [6] introduced a multi-scale wear simulation method for wind turbine journal bearings, adapting KÖNIG's work. This method involves an iterative loop between an elasto-hydrodynamic (EHD) model and a software tool simulating material removal and surface smoothing, using FLEISCHER's wear law [7]. Validation showed good agreement between measurement and simulation results, proving its transferability to various EHD models, such as those used in wind turbine applications. A common challenge among these methods is the high number of input parameters required, leading to significant parameterization effort and potential calculation errors due to inaccuracies. There is a notable lack of studies addressing these inaccuracies in parameterization efforts across different models and applications.

3 Method

This work focuses on the wear simulation method from [6], aiming to quantify maximum calculation uncertainty through a worst-case scenario analysis. The study uses an EHD model of a journal bearing component test rig, with test specimens detailed in section 4.3 and further rig information in [6]. Calculation uncertainty is defined as the difference between maximum and minimum wear results based on two sets of input parameters: one for minimum and one for maximum wear rates.

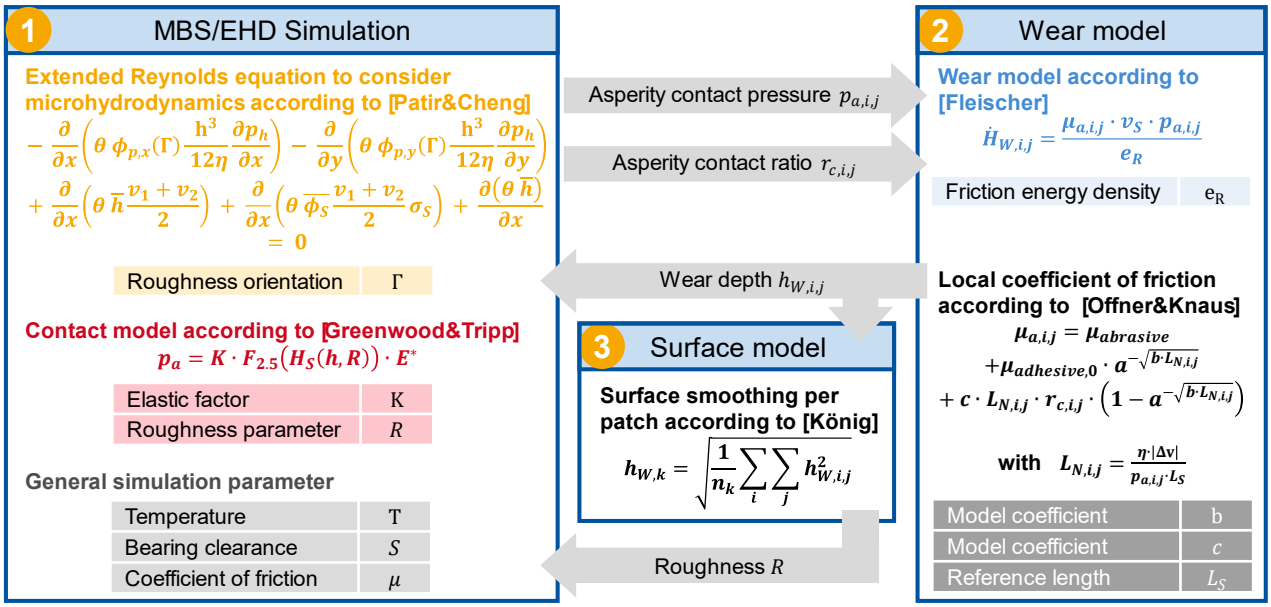

Figure 82: Flow chart of the wear simulation method according to [6]

These extreme parameter sets include the most influential parameters at their range boundaries determined from literature. A sensitivity analysis, following MORRIS [8], identifies these key parameters. The plausibility of the wear simulation method was validated in [6] by comparing it to experimentally measured wear depths. The simulation method comprises three parts:

1. **EHD Simulation Model**: Calculates asperity contact pressure $p_{a,i,j}$ for each node using GREENWOOD AND TRIPP's contact model [9]. It also considers tribological properties (e.g., clearance S, lubricant viscosity) and operating conditions (pressure $\bar{p}$ and sliding speed v_S).
2. **Wear Model:** Based on calculated asperity contact pressures, it determines wear depth per node $h_{W,i,j}$ using FLEISCHER's model [7] and a local coefficient of friction $\mu_{a,i,j}$ as per OFFNER AND KNAUS [10].

3. **Surface Roughness Model:** Calculates surface smoothing according to DECKER and KÖNIG [5, 6], with adjustments leading to changes in roughness.

Figure 82 presents this method as a flow chart, detailing models used in each step and listing parameters analyzed in the sensitivity analysis. Table 27 provides an overview of the analyzed model parameters with ranges from literature, supplemented by measurements. Recommended values for the roughness orientation Γ and the elastic factor K are used from literature sources (for reference see [1]). The surface roughness deviation R was measured using tactile methods before the experiment, revealing a variation of ± 10 %. The bearing temperature T fluctuates due to varying friction during the running-in process, stabilizing over time. This study assumes isothermal behavior for wear calculations, maintaining a constant bearing temperature. A sensitivity analysis evaluates the maximum and minimum temperatures recorded during experiments. Similarly, the bearing clearance S is assumed constant with an uncertainty of $\pm 10\ \mu m$ due to thermal expansion and manufacturing deviations. The coefficient of friction is analyzed within typical ranges for journal bearings. The friction energy density e_R follows FLEISCHER's wear law and aligns with experimental studies. Parameter ranges for b, c, and L_S in the OFFNER AND KNAUS model are derived from literature values. This work's sensitivity analysis employs a sampling plan based on MORRIS's methodology to assess how different parameters influence the outcomes of the wear simulation.

Parameter		Unit	Lower boundary	Upper boundary
Roughness orientation	Γ	-	1	100
Elastic factor	K	-	0.0003	0.003
Roughness parameter	R	μm	$-10\ \%$	$+10\ \%$
Temperature	T	$°C$	55	70
bearing clearance	S	mm	0.14	0.16
Coefficient of friction	μ	-	0.05	0.2
Friction energy density	e_R	$J \cdot m^{-3}$	$1 \cdot 10^{13}$	$1 \cdot 10^{16}$
Model coefficient (O&K)	b	-	$1{,}000$	$10{,}000$
Model coefficient (O&K)	c	-	50	$1{,}000$
Reference length	L_S	m	$1 \cdot 10^{-6}$	$2 \cdot 10^{-6}$

Table 27: Parameter range for sensitivity analysis (for reference see [1])

MORRIS' sensitivity analysis method requires only few simulations to evaluate a large number of parameters ($n = 10$). Results are interpreted using the mean μ_{EE}^{*} and standard deviation σ_{EE} of elementary effects (EE) on the model output. The quality relies on the number of repetitions (r), with SALTELLI ET AL. recommending a minimum of $r_{min} = 4$ for reliable results. In MORRIS' approach parameter influence is typically represented graphically, where high mean values indicate significant influence, while high standard deviations suggest nonlinear effects.

4 Results

Section 4.1 presents the sensitivity analysis results, highlighting the most influential parameters to calculate the worst-case uncertainty of the wear simulation method. The friction energy density e_R is identified as the key parameter affecting wear. Due to significant deviations in e_R reported in literature, its range is established from experiments for improved accuracy. This determination relies on measured wear during experiments. Section 4.2 examines the wear volume measurement method and its uncertainty, while section 4.3 discusses how e_R is determined across different test procedures.

4.1 Sensitivity analysis

The sensitivity analysis sampling involves $r = 5$ repetitions to vary the parameters listed in Table 27 across $p = 4$ levels, resulting in $N = (n + 1) \cdot r = 55$ wear simulations as per MORRIS's method. The analysis evaluates the influence of ten parameters on six objectives: wear depth h_W, wear volume V_W, hydrodynamic pressure at simulation start $p_{h,S}$, hydrodynamic pressure at simulation end $p_{h,e}$, asperity contact pressure at simulation start $p_{a,S}$, and asperity contact pressure at simulation end $p_{a,e}$. For each objective, the normalized mean μ^*_{EE} and standard deviation σ_{EE} of the elementary effects of the parameters are calculated. Figure 83 depicts the results of the sensitivity analysis, showing σ_{EE} plotted against μ^*_{EE} for each objective. The friction energy density e_R exhibits high μ^*_{EE} values, indicating its significant impact on wear depth, wear volume, hydrodynamic pressure at the end of simulation, and asperity contact pressure at the end. However, e_R has a smaller influence on initial hydrodynamic and asperity contact pressures. The examined parameters are listed in Table 28 according to the rank of influence.

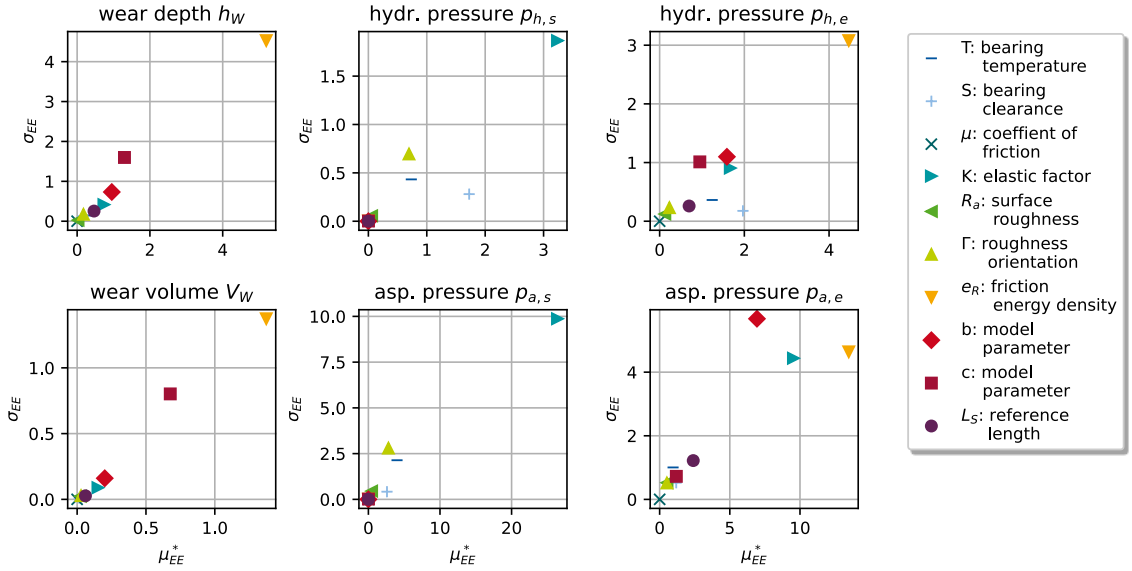

Figure 83: Graphical results of the sensitivity analysis according to Morris for selected objectives

The other second most influential parameter b and the following highest ranked parameters c and L_S are coefficients of the local friction model according to OFFNER AND KNAUS [10]. The results show a significant influence of the parametrization of the contact model and the local friction model compared to the remaining parameters.

Overall rank	**1**	**2**	**2**	**4**	**5**	**6**	**6**	**8**	**9**	**10**
Mean rank ($h_W, V_W, p_{h,e}, p_{a,e}$)	1.0	3.3	3.3	3.8	5.3	6.0	6.0	8.0	8.5	10.0
Parameter	e_R	K	b	c	L_S	T	S	R	Γ	μ

Table 28: Mean ranks of the parameters regarding wear and pressure distribution at simulation end

As the friction energy density e_R has the highest influence on the resulting wear volume V_W and the wear depth h_W, it is important to determine e_R precisely. Since the values for the friction energy density e_R are not known a priori, experimental investigations provide a good starting point for determining the relevant range of e_R values for the operating points to be simulated. After the experimental determination of the parameter range for the conditions on the test bench, the influence of the uncertainty of the friction energy density e_R on the wear behavior can be investigated.

4.2 Wear volume measurement uncertainty

This work examines the calculation uncertainty of the wear simulation method presented in [6], highlighting that experimental measurement of wear volume V_W also introduces uncertainties. The measured V_W is crucial for determining the range of friction energy density e_R for worst-case scenario analyses in test rig wear simulations, meaning that V_W measurement uncertainty directly affects e_R determination. Wear volume is assessed by comparing contours before and after experiments, using tactile measurements at seven angular points ϕ_i on the journal bearing. Tactile measurements are preferred here due to their availability and simplicity over more complex methods like optical 3D contour measurements. In this study, $e_R$is derived from test bench tests rather than tribometers, as seen in similar research. The seven measurement positions are illustrated in Figure 84 (a), while Figure 84 (b) shows the measurement system used.

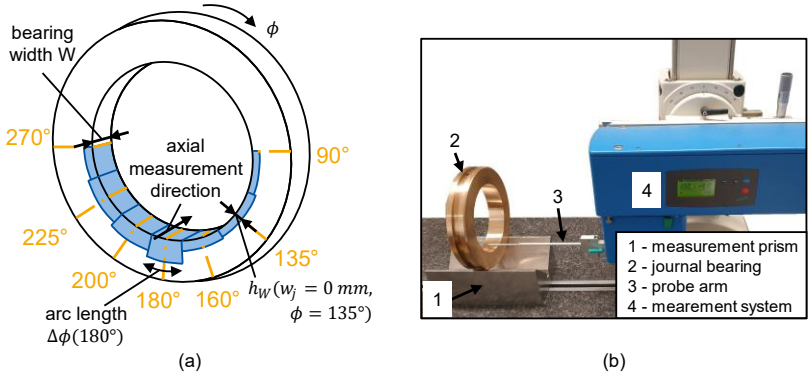

Figure 84: Specification of the journal bearing test specimen (a) and the measurement system (b)

The wear depth h_W across the bearing width W is calculated by comparing the contours of a journal bearing before and after an experiment. For each axial measurement point w_j, the wear depth $h_W(w_j, \phi_i)$ is evaluated at various angular measurement points ϕ_i. The planimetric wear

$$A_W(\phi_i) = \sum_{j=0}^{59{,}400} h_W(w_j, \phi_i) \cdot \Delta l \tag{1}$$

at a specific measurement point can be approximated by summing the products of the wear depth values and the discrete axial distances over the bearing width. To estimate the wear volume at each point, the wear area $A_W(\phi_i)$ is multiplied by an arc length $\Delta\phi(\phi_i)$. The total wear volume is obtained by summing the volumes at all measurement points (see also Figure 85).

$$V_W(\phi_i) = A_W(\phi_i) \cdot \Delta\phi(\phi_i) \tag{2}$$

$$V_W = \sum_{i=1}^{7} V_W(\phi_i) \tag{3}$$

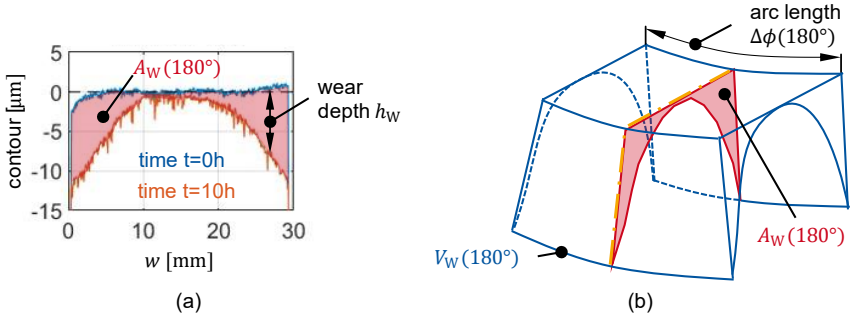

Figure 85: Determination of the wear area (a) and approximation of the wear volume (b)

The Measurement uncertainty for wear volume is assessed through triplicate tests on identical specimens, yielding a mean error range of $\Delta V_{W,e} = 0.61\,mm^3$, with a quantified uncertainty of $\Delta V_W = \pm 0.3\,mm^3$. Potential sources of error include inaccuracies in angular positioning and starting points for axial measurements.

4.3 Calculation of the friction energy density based on experimental results

The test series is conducted on a component test rig described in previous studies. The journal bearings, made from a copper-tin alloy (CuSn12Ni2-C), have a nominal diameter of $120\,mm$ and width of $30\,mm$. Two operating points (A and B) are defined to assess the specific pressure, sliding speed, and target temperature for varying conditions. Four test runs are performed: $A.i$, $A.ii$, $B.i$, and $B.ii$. Each run lasts 20 hours, split into two sections of 10 hours each, with measurements taken after both intervals to evaluate total wear volume V_W and mean wear depth h_W at the lowest angular position ($\phi = 180°$). Results indicate that higher pressure in test run A leads to increased wear compared to B, while the second half of each run shows less wear due to running-in processes. These results help determine friction energy density e_R experimentally. FLEISCHER [11] defines e_R as the quotient of friction work W_F and wear volume V_W.

$$e_R = \frac{W_F}{V_W} = \frac{F_N \cdot v_S}{V_W} \cdot \int_0^{t=end} \mu(t)dt \tag{4}$$

The friction work is calculated based on normal force F_N, sliding speed v_S and time integration of the coefficient of friction $\mu(t)$. Normal force F_N and sliding speed v_S are known from the defined operating conditions for the wear experiments on the test rig.

Operating point		**A**		**B**	
Specific pressure	$\bar{p}\ [MPa]$	35		25	
Sliding speed	$v_s\ [m/s]$	0.1		0.1	
Test specimen		**i**	**ii**	**i**	**Ii**
Bearing diameter	$D\ [mm]$	120.02	120.03	119.98	119.99
Shaft diameter	$d\ [mm]$	119.89	119.92	119.91	119.86
Bearing clearance	$S\ [mm]$	0.130	0.110	0.070	0.135
Surface roughness	$R_a\ [\mu m]$	0.56	0.48	0.61	0.60
Measurement results		**A.i**	**A.ii**	**B.i**	**B.ii**
$t = 10\ h$	$\overline{h_W}\ [\mu m]$	4.82	4.78	0.72	0.45
$t = 20\ h$	$\overline{h_W}\ [\mu m]$	0.14	0.73	0.21	0.17
$t = 10\ h$	$V_W[mm^3]$	14.0	14.0	2.1	1.3
$t = 20\ h$	$V_W[mm^3]$	0.9	1.4	0.8	0.7

Table 29: Test parameter for the experiments

The coefficient of friction over time $\mu(t)$ is calculated using COULOMB's law. The normal force F_N is known, and the friction force is determined by dividing the measured friction moment by the bearing radius. The wear volume V_W has an uncertainty of $\Delta V_W = \pm 0.3\,mm^3$, which affects the calculation of the friction energy density e_R. Experimentally quantified values of e_R are presented in Figure 86 (a), with uncertainty represented by error bars. Considering measurement uncertainties, e_R ranges from $1.2 \cdot 10^{15}\,J \cdot m^{-3}$ to $3.1 \cdot 10^{16}\,J \cdot m^{-3}$. Alternatively, this range can be evaluated using the FLEISCHER diagram based on shear stress and linear wear intensity. Analyzing the mean wear depth at a single angular point, rather than total wear volume, may contribute to slightly greater scatter. The relative distribution of e_R values across test runs is qualitatively similar. Since both methods for

calculating friction energy density are comparable, the larger range is used for determining uncertainty in wear simulation methods.

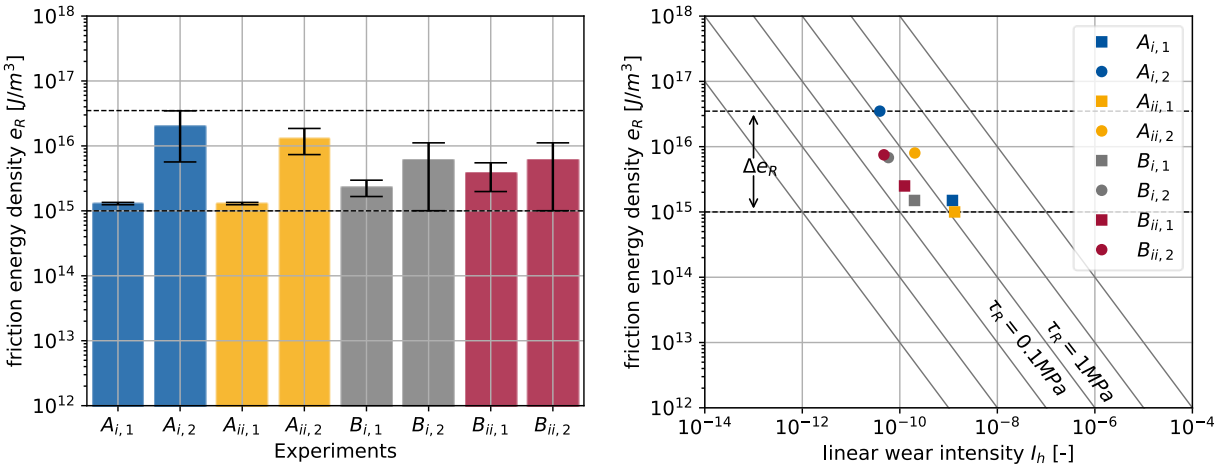

(a) **(b)**

Figure 86: Resulting uncertainty in the calculation of the friction energy density $\mathbf{\Delta e_R}$ due to the wear volume measurement uncertainty (a) and range of $\mathbf{e_R}$ based on the Fleischer diagram (b)

4.4 Wear calculation uncertainty

Uncertainties in determining model parameters affect the calculation of the wear volume using the presented wear simulation method. This section discusses the uncertainty inherent in the wear simulation itself, quantified by assessing maximum calculation errors related to wear volume and depth. To simulate maximum wear, the five most influential parameters identified in the sensitivity analysis are configured to their extreme values based on their lower and upper boundaries. Unlike a one-factor-at-a-time approach, all parameters are set to their extremes while keeping other parameters constant at medium values. Given that e_R significantly influences the wear volume, minimum and maximum values from experimental determinations are used for greater accuracy instead of literature boundaries.

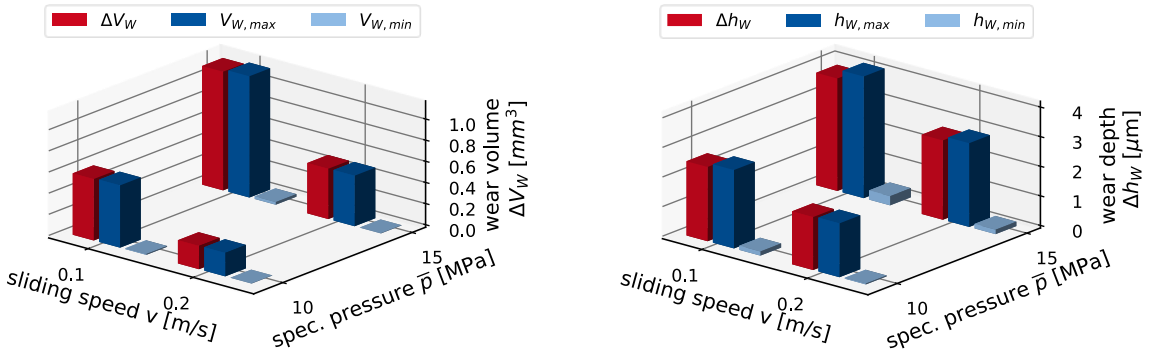

(a) **(b)**

Figure 87: Uncertainty of the wear calculation with regard to wear volume (a) and wear depth (b)

The absolute uncertainty is defined as the difference between the minimum and maximum wear metrics at the end of the simulation. Minimum wear volume $V_{W,min}$, maximum wear volume $V_{W,max}$, and the absolute uncertainty ΔV_W for each operating point are illustrated in Figure 87 (a). Similarly, Figure 87 (b) shows wear depth values h_W and their uncertainties. Absolute uncertainties increase with higher wear intensity, indicating that both metrics depend on the operating point. The maximum relative wear volume uncertainty is quantified at $\Delta V_{W,rel} < \pm 49\,\%$, while the maximum relative

wear depth uncertainty is $h_{W,rel} < \pm 48\ \%$. This high uncertainty reflects significant parameterization inaccuracies; however, actual calculation errors are expected to be smaller in practice.

5 Summary

Journal bearings, unlike rolling bearings, have a theoretically unlimited fatigue lifetime and are highly reliable when designed and operated correctly. However, external load conditions can cause wear that may lead to bearing seizure. To optimize journal bearing design, wear simulations are employed to predict wear behavior. This study performed a worst-case scenario calculation to assess the accuracy of the method. A sensitivity analysis identified key parameters influencing the wear model, with friction energy density e_R being the most significant. As e_R is unknown beforehand and varies with operating points, experimental tests on a component test rig were conducted to narrow down its range. Absolute wear uncertainties increase with higher wear intensity, while relative uncertainties remain below 49 % in worst-case scenarios. Validation experiments indicate that accurate parameter adjustments can yield valid simulation results when real system behavior is well understood, although uncertainty poses challenges for wear calculations without experimental confirmation tests.

6 Bibliography

[1] Decker, T., Jacobs, G., Graeske, Carsten, Bußkamp, Pascal, Röder, J. u. Schröder, T.: Model uncertainty of a multiscale, elasto-hydrodynamic simulation method for the prediction of abrasive wear in journal bearings. (peer review and accepted for publication). Tribologie und Schmierungstechnik (2025)

[2] Prölß, M.: Berechnung langsam laufender und hoch belasteter Gleitlager in Planetengetrieben unter Mischreibung, Verschleiß und Deformationen. Dissertation. 2020

[3] Hagemann, T., Ding, H., Radtke, E. u. Schwarze, H.: Operating Behavior of Sliding Planet Gear Bearings for Wind Turbine Gearbox Applications—Part II: Impact of Structure Deformation. Lubricants 9 (2021) 10, S. 98

[4] Ding, H., Mermertas, Ü., Hagemann, T. u. Schwarze, H.: Calculation and Validation of Planet Gear Sliding Bearings for a Three-Stage Wind Turbine Gearbox. Lubricants 12 (2024) 3, S. 95

[5] König, F., Ould Chaib, A., Jacobs, G. u. Sous, C.: A multiscale-approach for wear prediction in journal bearing systems – from wearing-in towards steady-state wear. Wear 426-427 (2019), S. 1203–1211

[6] Decker, T., Jacobs, G., Graeske, C., Röder, J., Lucassen, M. u. Lehmann, B.: Multiscale-simulation method for the wear behaviour of planetary journal bearings in wind turbine gearboxes. Journal of Physics: Conference Series 2767 (2024) 5, S. 52012

[7] Fleischer, G., Größer, H. u. Thum, H.: Verschleiß und Zuverlässigkeit. Berlin: VEB Verlag Technik 1980

[8] Morris, M. D.: Factorial Sampling Plans for Preliminary Computational Experiments, Bd. 33. 1991

[9] Greenwood, J. A. u. Tripp, J. H.: The Contact of Two Nominally Flat Rough Surfaces. Proceedings of the Institution of Mechanical Engineers 185 (1970) 1, S. 625–633

[10] Offner, G. u. Knaus, O.: A Generic Friction Model for Radial Slider Bearing Simulation Considering Elastic and Plastic Deformation. Lubricants 3 (2015) 3, S. 522–538

[11] Gerd Fleischer: Verschleiß und Zuverlässigkeit. Berlin: Verlag Technik 1980

Modelling transient thermal behavior in journal bearings using a non-isothermal wear calculation approach

A. Khare[1], T. Baszenski[1], G. Jacobs[1], M. Lucassen[1], B. Lehmann[1]

[1]Institut für Maschinenelemente und Systementwicklung, Schinkelstraße 10, 52062 Aachen

Keywords: journal bearing, transient thermal finite element simulation, mixed thermo elastohydrodynamic simulation

Abstract: Designing wear safe journal bearings is becoming highly important due to their increased application in mixed friction operation fields. This has led to the development of wear simulation tools for journal bearings. Current wear simulation tools do not consider thermal effects during journal bearing mixed friction operation. Thermal changes in the bearing system can increase wear intensity significantly and hence need to be considered to improve accuracy of wear simulation. Hence this work focuses on the extension of an existing abrasive wear calculation tool by transient thermal modelling of journal bearings. Furthermore, the thermal model is also validated using experimental data. The potential impact of thermal modelling on improving wear simulations accuracy is also highlighted in this work.

1 Introduction

Hydrodynamic journal bearings are being increasingly used in applications where mixed friction is inevitable. For instance, in low-speed, high-load operations in wind turbines gearboxes [NEJ22] and in start-stop cycles of combustion engines [SAN20]. Under hydrodynamic operation, journal bearings provide longer life, more compactness and higher load carrying capacity in comparison to roller bearings. Due to these properties journal bearings are widely used in drive train systems of wind turbines, automobiles, ships and more. Their performance, however, is highly dependent on the operating condition and the resulting lubrication regime. Journal bearings are designed focusing on hydrodynamic operation as the lubricant film build-up is high enough to prevent solid contact and hence wear [DIN17]. However, in applications such as wind turbine gearboxes, bearing operation under low speed and high loads makes mixed friction unavoidable [NEJ22].

Mixed friction operation leads to wear of the bearing surface and material removal; known as abrasive wear. Friction also leads to heat generation and temperature increase in the contacting bodies [CZI10]. If this generated heat is not dissipated over time to the lubricant and surroundings, the bearing overheats. For highly loaded bearings, contact between asperity peaks on the sliding surfaces can lead to instantaneous high local temperatures. Such high temperatures lead to the formation of adhesive bonds at the contact points. Repeated forming and breaking of these bonds due to relative motion leads to transfer of bearing material on the shaft surface; categorized as adhesive wear [XU23]. Excessive wear can lead to decreased bearing load carrying capacity or even terminal damage. Hence, designing wear safe bearings requires the understanding of journal bearing wear behavior. To this extent, wear calculation methods for journal bearings have been developed in numerous works in the past years [KÖN19] [DEC24] [HAG21] [PRÖ20] [DIN23].

Wear calculation methods help to quantify abrasive wear and are typically iterative processes. Generally, these processes involve a coupling between elastohydrodynamic (EHD) simulations, a contact model to consider mixed friction and a wear model. The wear model helps determine a wear rate based on the asperity contact pressure. Changes in the bearing contour due to material removal can hence be calculated as wear depth using this iterative approach. Additional consideration of

effects such as, surface roughness smoothing by [KÖN19], and, structural deformation by [HAG21] have enhanced the accuracy of wear calculations. A similar iterative wear calculation tool is used in this paper to perform wear simulations. The method was proposed by [KÖN20] for radial loaded journal bearings. Implementation of this tool for planetary journal bearings was done by [LEH23]. Later, [DEC24] extended this tool by also introducing the roughness smoothing approach by [KÖN19]. The tool now takes into consideration not only bearing contour changes, but also smoothing of surface roughness during the wear process. Using experimental data, [DEC24] were also able to qualitatively validate this wear calculation tool in their work. However, all currently existing wear calculations do not take the thermal effects during wear into consideration. During operation heat is generated in the sliding surfaces leading to temperature increase and thermal expansion of the bearing components. Thermal expansion of both surfaces can have a significant impact on the clearance gap, contact status and hence wear progression. To further increase the accuracy of journal bearing wear simulations, thermal changes also need to be considered. The aim of this work is to extend the wear calculation tool by a transient thermal model to increase wear calculation fidelity. Simulation methodology, validation of the transient thermal model and its influence in wear calculation are discussed in the following.

2 Methodology

The iterative process of the abrasive wear calculation tool used in this paper is shown in Figure [DEC24]. In each iteration an EHD model (1), a wear calculation tool (2), a surface roughness model (3), a transient thermal FE model for temperature calculation (4) and static thermal FE model for thermal expansion (5) are coupled. Steps 1, 2 and 3 from Figure are explained in detail by [DEC24] in their work. The tool is now extended by steps 4 and 5 to consider thermal effects as well.

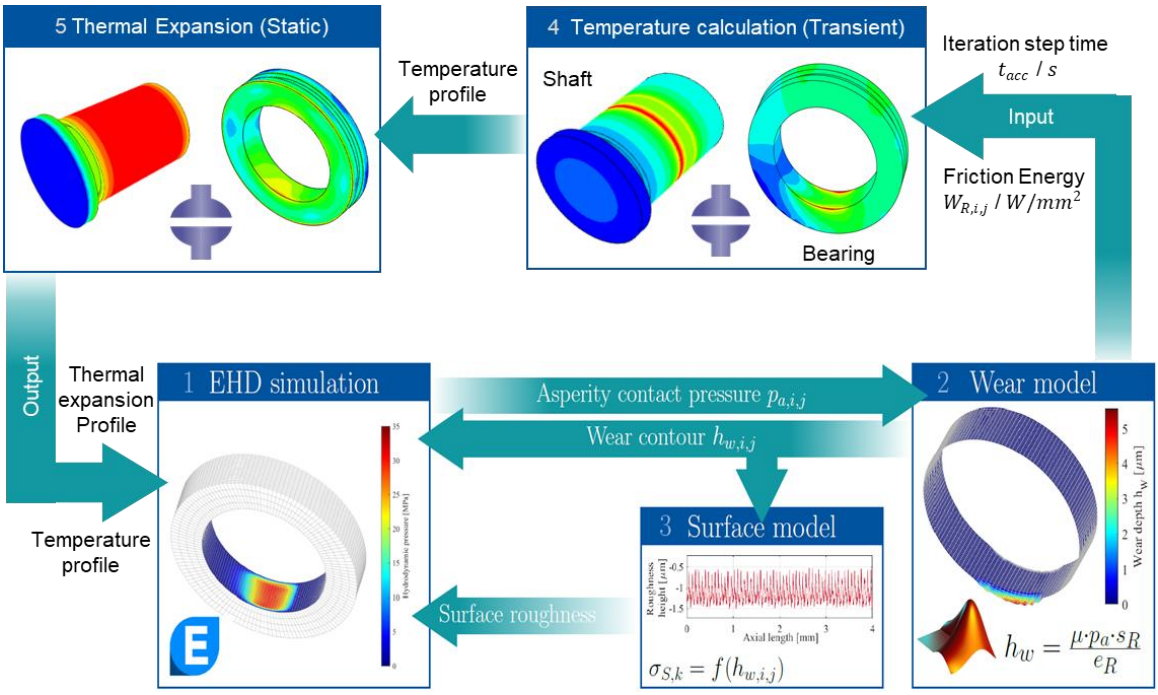

Figure 88: Iterative process of the abrasive wear calculation tool

The EHD simulation is performed using AVL Excite Power Unit. Based on EHD calculations, the MATLAB based wear calculation tool quantifies the generated wear and surface roughness changes

in each iteration. Based on collective outputs from EHD model and the wear tool, thermal FE simulations are performed using Abaqus CAE 2019. The EHD model is able to consider elastic deformations, surface roughness and mixed friction. The resulting asperity contact pressure at each node $(p_{a,i,j})$ of the bearing surface is a key output from the EHD model for wear calculation. $p_{a,i,j}$ is used to calculate wear depth accumulated over the entire bearing surface using a wear model. There exist several wear models to calculate journal bearings wear [LEH23]. In this work, the widely used FLEISCHER wear model is used [FLE80]. Based on the contact conditions from EHD calculations, the wear model helps derive a wear depth rate $\left(H_{W,i,j}\right)$ over the bearing surface. According to the working principle of the iterative process, after each iteration the generated wear over a certain time can be calculated. The time step size (t_{step}) is derived based on the maximum wear rate over the bearing surface and a predetermined iteration step size $\left(h_{W,max}\right)$. This relation is shown below in equation 1.

$$t_{step} = \frac{h_{W,max}}{\max\left(\dot{H_{W,i,j}}\right)} \quad \textbf{1}$$

Based on time step (t_{step}) and wear rate $(H_{W,i,j})$, wear depth on the bearing surface can be calculated. After each iteration the changed bearing contour is fed into the EHD model to consider wear influence on hydrodynamic operation and contact status. Along with changes in the bearing contour, asperities in contact on the sliding surface also get smoothened. These effects are considered by a surface roughness model.

Bearing thermal calculations in this approach are performed using thermal FE models of the bearing and shaft. Thermal calculations can also be performed using a TEHD model. However, in TEHD models, for thermal calculations the bearing and housing geometries are modelled as layered discs Using FEM, thermal calculations can be more accurately performed due to their ability to consider complex structures. From steps 1,2,3 (Figure), heat flux into the sliding surfaces due to mixed friction and t_{step} derived in each iteration are used as basis for performing transient thermal FE simulations. Using the abovementioned inputs, bearing and shaft transient temperature behavior is calculated. Based on the resulting temperature profiles, thermal expansion is derived in step 5 (Figure) using static thermal FE simulations. The four outputs from the thermal models, local temperature and local thermal expansion of bearing and shaft surface are updated in the EHD calculation of the next iteration. After each iteration, bearing contour, surface roughness, local temperature and local thermal expansion are updated in bearing EHD calculations. The novelty of this approach is that during mixed friction, changes in temperature, thermal expansion, lubricant viscosity and their collective influence on the lubricant film is considered in wear simulation of journal bearings. In this manner, transient thermal behaviour of journal bearings can be modelled. Thermal models and validation of thermal boundary conditions are explained further in more detail.

3 Transient thermal model

The journal bearing model used in this paper is based on a journal bearing component level test rig. The test rig and simulation model components are shown in Figure 89 and Figure 90 respectively. The test rig comprises a hydraulic actuator that can exert up to 60 MPa of specific pressure, $p = F/(B \cdot D)$ on the bearing and an electric motor. The bearing specimen is mounted into a rotatable enclosure. During the tests, heating cartridges are used to heat up the test rig and maintain the

housing temperature during the experiments. Components of the FE model involve the bearing housing, bearing and heat cartridges (heat source). The bearing is assembled in the housing such that the bearing circumference is tied to the housing inner cylindrical surface. The heating cartridges are used to maintain bearing and housing temperatures during experiments. Further model specifications are provided in Table 30 below.

Parameter	Value	Parameter	Value
Bearing diameter	$D = 120\ mm$	Bearing material and Young's modulus	$CuSn12Ni2-C$, $E = 100\ GPa$
Bearing width	$B = 30\ mm$	Shaft material and Young's modulus	$42CrMo4$, $E = 210\ GPa$
Bearing clearance	$s = 75\ \mu m$	Simulation time duration	$t_{step}\ [s]$
Heat cartridge heat flux	$H = 75\ W/mm^2$	Heat cartridge power	$P = 250\ W$

Table 30: Bearing and FE thermal model specifications

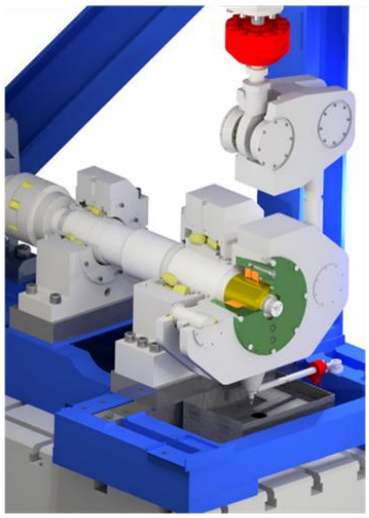

Figure 89: Journal bearing component test rig

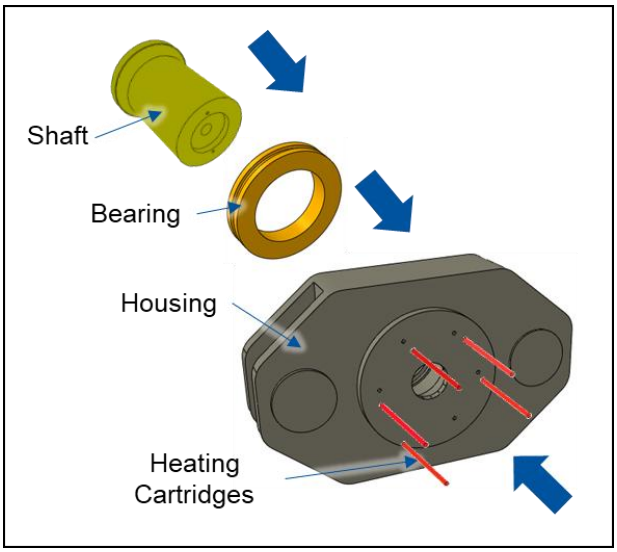

Figure 90: Components of bearing thermal FE model

To perform thermal modelling, thermal boundary conditions need to be accurately implemented as on the test rig. Boundary conditions in a thermal FE model mainly consists heat generation and heat dissipation. In addition to the heat generated from heating cartridges, during mixed friction operation heat is generated in the contact bodies due to friction power. Friction energy can be derived from the asperity contact pressure ($p_{a,i,j}$), coefficient of friction ($\mu_{a,i,j}$) and the sliding speed (v). Based on this, heat flux into the bearing surface due to mixed friction can be calculated using equation 2 below.

$$Q_{i,j} = \mu_{a,i,j} \cdot p_{a,i,j} \cdot v \qquad \textbf{2}$$

Here, friction coefficient ($\mu_{a,i,j}$) is determined based on the approach presented by OFFNER & KNAUS [OFF15]. $p_{a,i,j}$ is a direct output of the EHD simulation and v is considered non-variable during an EHD simulation. Resulting local friction energy ($Q_{i,j}$) is then mapped over the bearing

sliding surface in the FE model. This is depicted in the figure below. On the other hand, the friction energy input on the shaft sliding surface is considered to be constant in circumferential direction.

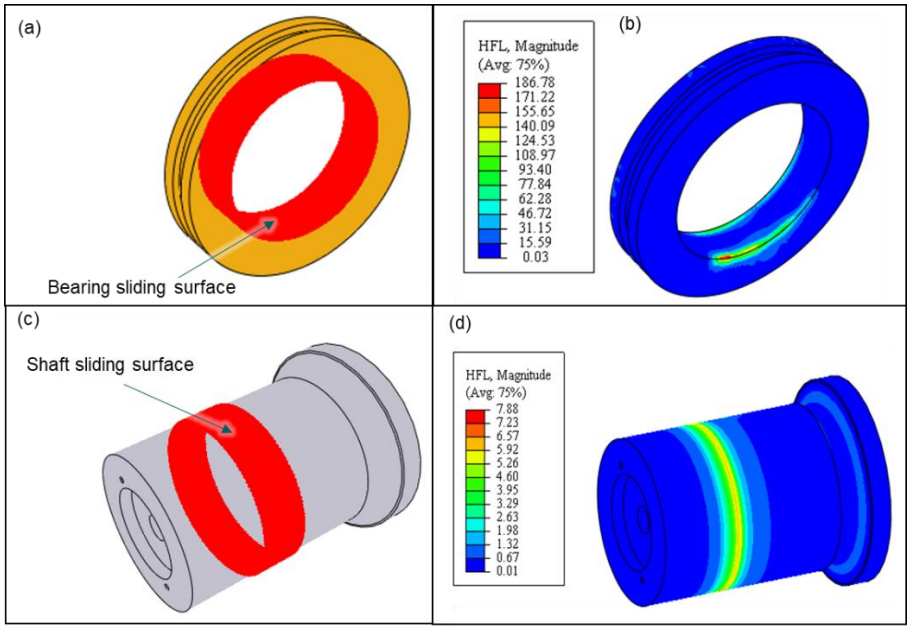

Figure 91: (a) Bearing FE contact surface, (b) Heat flux into bearing due to friction energy (c) Shaft FE model, (d) Heat flux into shaft due to friction energy

Due to the rotating motion of the shaft, friction power on its circumferential surface is mean of friction power on the counter bearing surface. Heat dissipation in FE is modelled as convection between the housing and surrounding air. To model the convective heat flow between solid (bearing housing) and fluid (surrounding air), the determination of the heat transfer coefficients (HTC) is initially necessary. HTC from the literature can be used for an estimation. Studies by [SOU17] and [BAS23] on similar test systems indicate that HTC (α) between housing free faces (Figure 92) and air range between 20-100 W/m^2K. The selected HTC in this work are shown below in Table 31

Faces	Heat transfer coefficients (α)
Front face	$20\ W/m^2K$
Circumferential face	$35\ W/m^2K$
Rear face	$100\ W/m^2K$
Shaft free face	$20\ W/m^2K$

Table 31: Heat transfer coefficients

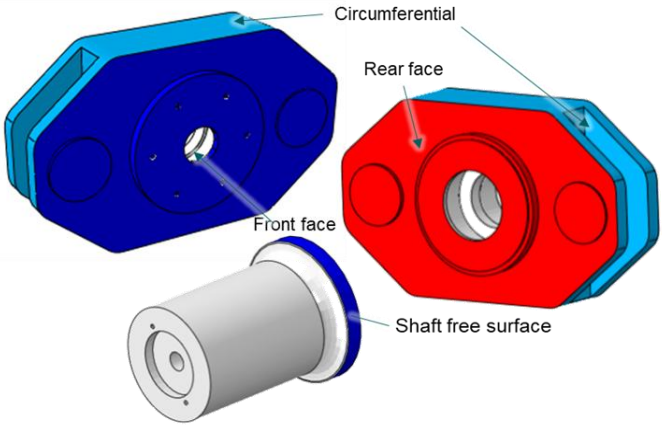

Figure 92: Bearing housing and shaft free faces

At the rear side of the housing, an electric motor responsible for the shaft rotation is installed. Air vented out from the motor forces convection at the rear side. This explains the selection of a higher HTC at the rear face compared to other faces. Validation of the transient thermal model with experimental data is an important aspect of this work and is explained in the next chapter.

4 Validation of transient thermal model

A valid thermal model firstly requires validation of thermal boundary conditions. This means validating heat loads and heat transfer coefficients. To achieve this a short experimental procedure was performed at the component test rig. Using 5 integrated heating cartridges, the bearing housing was heated up for 25 minutes. The shaft assembled in the bearing housing was stationary during this experiment. To investigate the convective heat transfer to the environment, temperature was measured during the heating process at four defined points on the bearing housing using a TESTO 868 [TES24] thermal camera. The measurement points are located on the housing surface as shown in Figure 93a. Bearing temperature is measured using a PT100 sensor element.

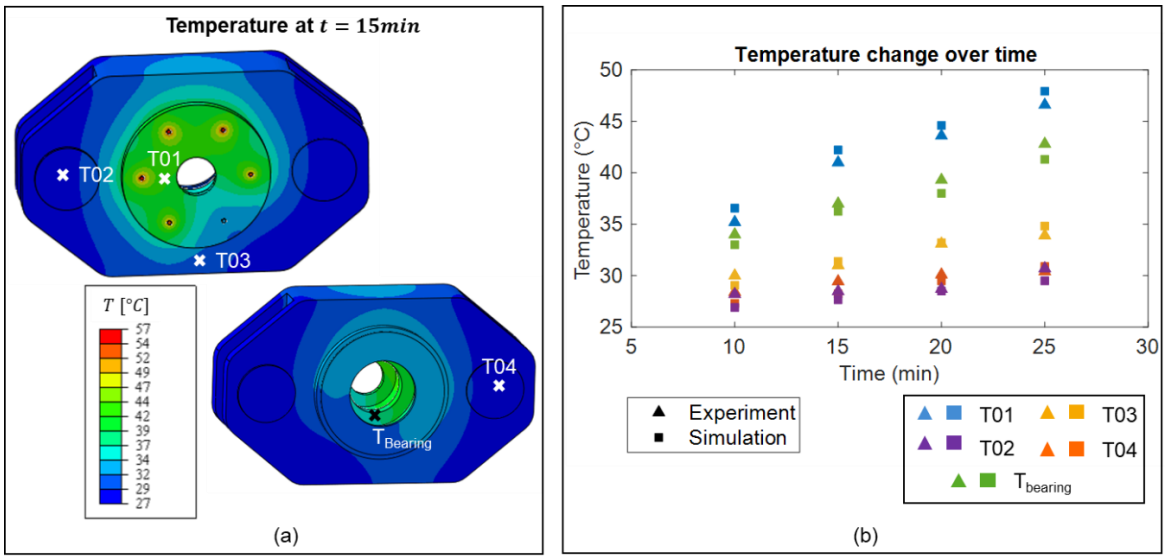

Figure 93: (a) Simulated temperature after $\boldsymbol{t = 15\ min}$ (b) Comparison between temperature measurement and simulated temperature results

During the experiment, temperature measurements were recorded every 5 minutes from $t = 10\ min$ to $t = 25\ min$. For validation, the experimental procedure was replicated by transient thermal simulations. The above-mentioned heat cartridge loads (Table 30) and heat transfer coefficients (Table 31) were applied as thermal boundary conditions. Comparisons between experimental measurements and simulation results can be observed in Figure 93b. Considering comparisons over multiple time intervals, simulation results are in high agreement with experimental measurements. A resulting maximum relative error of 4.61% can be considered as a suitable validation parameter for the selected thermal boundary conditions.

For validation of temperature calculation of a bearing under operation, a short wear experiment was performed on the component test rig. An iterative wear simulation (as explained in 2) is performed for the same loads and duration as the experiments. Surface roughness values used in the wear simulations are derived from tactile measurements on the test bearing and shaft surface. Following operating parameters of the experiments are selected in order to generate mixed friction operation: specific pressure $(\bar{p} = 50\ MPa)$**,** sliding speed $(v_R = 0.1\ m/s)$, lubricant temperature $(T_{oil} = 50°C)$ and operation time $(t = 20\ min)$. Bearing housing was heated up to 60°C and maintained at this condition during the experiment. Temperature measurements on the bearing were performed using 24 high precision digital temperature sensors as applied and explained in detail by [PAE24]. The 24 measuring points have an angular distance of $\Delta\varphi = 7.5°$ to each other and are arranged in the bearing angle range $\varphi = 97.5 - 270°$, which includes the load zone [PAE24].

Results comparison between a non-isothermal wear simulation and the performed experiment are shown in Figure 94 below. The bearing load zone is considered to be located between 135° and 225°. Mean temperature in the bearing load zone and maximum temperature over time are plotted in Figure 94a. A maximum relative error of 0.76% shows a good agreement between thermal model calculations and experiment measurements over time.

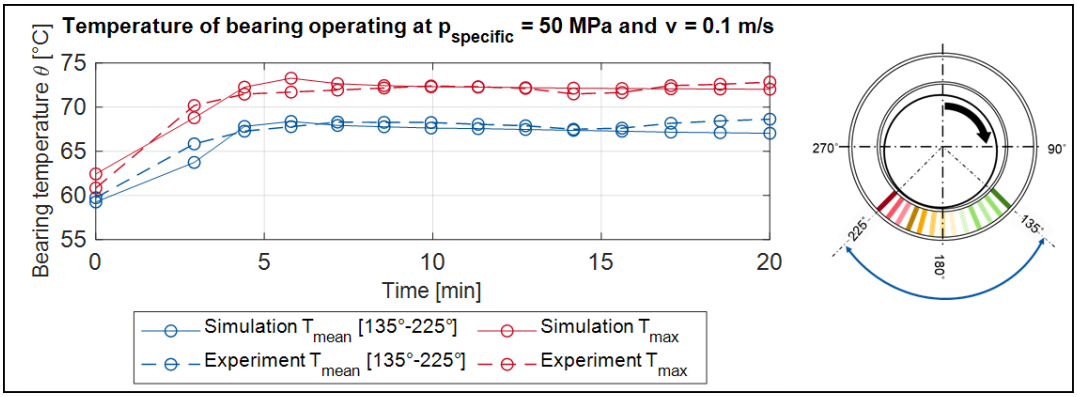

(a)

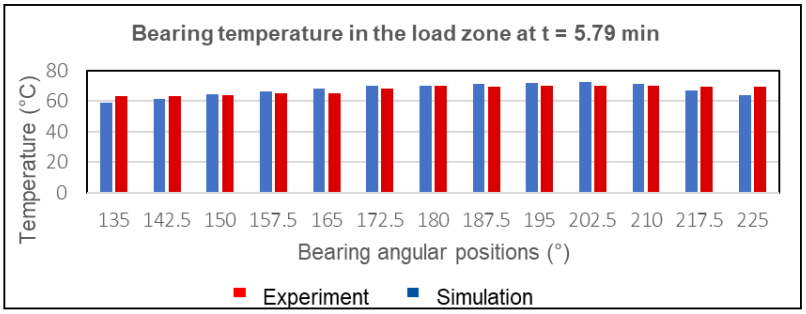

(b)

Figure 94: Comparison between experiment and simulation for (a) mean temperature and maximum temperature over time (b) temperature over bearing circumference

Circumferential local bearing temperature evaluation can be observed in Figure 94b at time interval of $t = 5.79\ min$. Here bearing temperature measured by digital sensors over the bearing circumference are compared with corresponding simulation results. Ability of the transient thermal model to simulate local bearing temperatures can hereby be recognized based on a maximum relative error of $1.59\ \%$ over the load zone. Based on these results, it can be concluded that the thermal modelling introduced in this work can model transient thermal behaviour as well as local bearing temperatures with high accuracy.

In order to evaluate the influence of thermal modelling on journal bearing wear calculation accuracy, simulation results are compared with experimental results. The isothermal version of the wear calculation tool was qualitatively validated by [DEC24] based on wear occurrence locality. To achieve this, long term wear experiments $(10h)$ were performed. Based on these experiments, it was observed and validated that location and intensity of wear occurring on the bearing surface was qualitatively reproduced by simulation results. However, considerable deviations in terms of wear quantity (wear depth, wear volume) were recorded. To evaluate if considering thermal modelling of bearings improves the accuracy of wear simulations, a comparison is made for the same experiment between isothermal and non-isothermal wear simulations results. Validation experiment performed by [DEC24] ($\bar{p} = 35\ MPa, v_R = 0.1 m/s, t = 10h$) was simulated using non-isothermal version of the

tool. Comparison of EHD contact status of the bearing at $t = 10h$ is performed between isothermal and non-isothermal iterative calculations. This is shown in Figure 95a and b below.

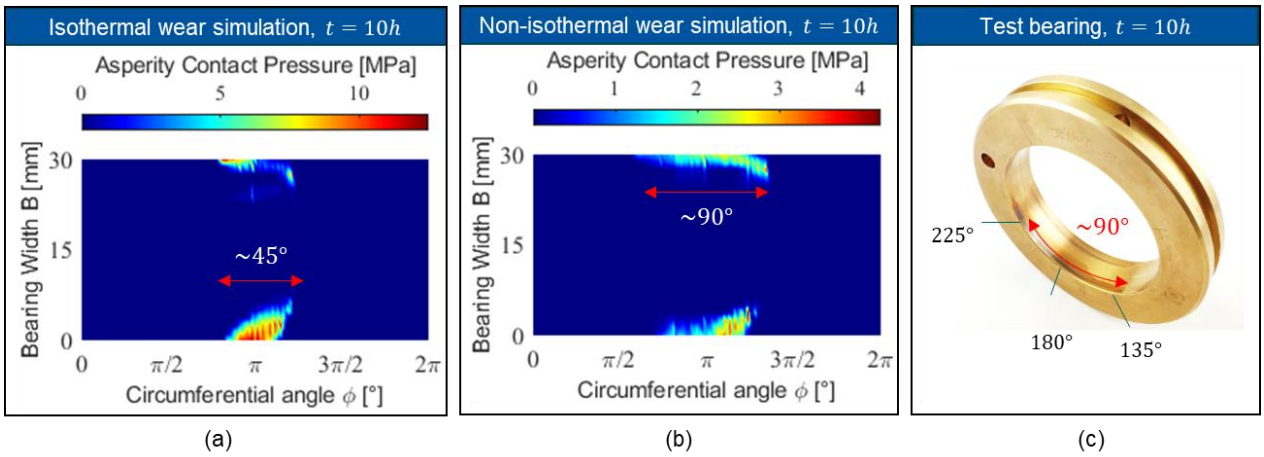

Figure 95: EHD Asperity contact pressure at $\boldsymbol{t = 10h}$ for (a) isothermal wear calculation, (b)non-isothermal calculation and (c) Test journal bearings after 10h experiment

Abrasive wear in journal bearings occurs where asperity contact occurs. Based on asperity contact pressure distribution in Figure 95 it can be observed that the EHD contact zone is wider in non-isothermal calculation than isothermal one. Reason for this is during operation, friction between the contacting surfaces leads to thermal expansion of the bodies due to heat generation. This can lead to a reduction in bearing clearance leading to a wider contact area. In the real test specimen in Figure 95c the worn surface can be visually recognized by the dark marking at the edges. Comparing the EHD results and test specimen, it can be concluded that non-isothermal wear calculation helps achieve a realistic and more accurate load zone of the bearing. Correctly mapping the bearing load zone, is the primary step in improving accuracy of journal bearing wear predictions.

5 Summary

This work involves the extension of an abrasive wear calculation tool with transient thermal FE modelling. Using thermal FE modelling, local resolution of temperature and thermal expansion on the shaft and bearing running surfaces is possible. These outputs from transient thermal FEM are updated in EHD calculations during iterative wear simulation. This allows for varying lubricant properties in the EHD calculation and hence thermal effects on lubricant film build-up can be considered. FE Thermal boundary conditions such as convective heat transfer coefficients between bearing housing and surroundings were experimentally validated based on a maximum relative error of 4.61%. Furthermore, the FE model's ability to predict bearing mean and maximum temperature over time was evaluated with experimental validation at an accuracy of 99.24%. Here, prediction of local bearing temperature over the bearing circumference had an accuracy of 98.41%. Integrating thermal modelling in the abrasive wear calculation tool leads to an increase in the bearing contact zone width by 50%, as compared to an isothermal wear simulation. Visual comparison of the simulative load zone with the test specimen shows good agreement between the results with a circumferential width of approximately $90°$. Therefore, integrating thermal modelling in journal bearing wear calculation is crucial for increasing the accuracy of wear prediction. For future consideration, this high-fidelity approach can also be adapted to predict overheating failures due to adhesion in journal bearings.

6 Bibliography

[BAS23] Baszenski T, Kauth K, Kratz K-H et al. (2023) Sensor integrating plain bearings: design of an energy-autonomous, temperature-based condition monitoring system, Forsch Ingenieurwes 87:441–452.

[CZI10] Czichos H, Habig K-H (2010) Tribologie-Handbuch: Tribometrie, Tribomaterialen, Tribotechnik, 3rd. Vieweg+Teubner Verlag, Wiesbaden

[DEC24] Decker T, Jacobs G, Graeske C et al. (2024) Multiscale-simulation method for the wear behaviour of planetary journal bearings in wind turbine gearboxes. J Phys.: Conf Ser 2767:52012.

[DIN17] DIN Deutsches Institut für Normung e. V. (2017) Gleitlager – Hydrodynamische Radial-Gleitlager im stationären Betrieb: Teil 1: Berechnung von Kreiszylinderlagern (31652-1)

[DIN23] Ding N, Yan S, Ma G et al. (2023) Mixed thermo-elasto-hydrodynamic lubrication and wear coupling simulation analysis for dynamical load journal bearings. Proceedings of the Institution of Mechanical Engineers, Part C: Journal of Mechanical Engineering Science 237:6020–6041.

[FLE80] Fleischer, G.: Verschleiß und Zuverlässigkeit. Verlag Technik 1980

[HAG21] Hagemann T, Ding H, Radtke E et al. (2021) Operating Behavior of Sliding Planet Gear Bearings for Wind Turbine Gearbox Applications—Part I: Basic Relations. Lubricants 9:97.

[KÖN19] König F, Ould Chaib A, Jacobs G et al. (2019) A multiscale-approach for wear prediction in journal bearing systems – from wearing-in towards steady-state wear. Wear 426-427:1203–1211.

[KÖN20] König, F. (2020) Prognose des Verschleißverhaltens ölgeschmierter Gleitlager im Mischreibungsbetrieb, Dissertation.

[LEH23] Lehmann B, Trompetter P, Guzmán FG et al. (2023) Evaluation of Wear Models for the Wear Calculation of Journal Bearings for Planetary Gears in Wind Turbines. Lubricants 11:364

[NEJ22] Nejad AR, Keller J, Guo Y et al. (2022) Wind turbine drivetrains: state-of-the-art technologies and future development trends, Wind Energy Sci 7:387–411.

[OFF15] Offner G, Knaus O (2015) A Generic Friction Model for Radial Slider Bearing Simulation Considering Elastic and Plastic Deformation. Lubricants 3:522–538.

[PAE24] Paeßens Janek, K-HK, Tobias Gemmeke, Kevin Kauth et al. (2024) Design of a fully integrated sensor system of a plain bearing, Forsch Ingenieurwes, 88,17

[PRÖ20] Prölß M. (2020) Berechnung langsam laufender und hoch belasteter Gleit-lager in Planetengetrieben unter Mischreibung, Verschleiß und Deformationen

[SAN20] Santos NDSA, Roso VR, Faria MTC (2020) Review of engine journal bearing tribology in start-stop applications. Engineering Failure Analysis 108:104344.

[SOU17] Sous, C. (2017) Methode zur dauerfesten Auslegung hydrodynamischer Gleitlager, Dissertation.

[TES24] Testo SE & Co. KGaA (2024) Datenblatt testo 868

[XU23] Xu F, Ding N, Li N et al. (2023) A review of bearing failure Modes, mechanisms and causes. Engineering Failure Analysis 152:107518.

Diagnostics of Particle Size Distributions for Rolling Element Bearings

Manuel Aboud[1], Hassan Mahmoud[1]

[1]Gastops, 1011 Polytek Street, Ottawa, ON K1J9J3. Canada

Keywords: oil debris monitoring (ODM), rolling element bearing (BER), particle size, diagnostics

Abstract

With a global shift to dependence on renewable energies, wind turbines performance plays a pivotal role in the main business objective of improving equipment availability while lowering operations and management costs. As the technology matures and the demand for wing energy increases, wind turbines have become bigger consequently resulting in higher costs and complexities associated with maintenance.

Wind turbine Original Engine Manufacturers (OEMs) collaborate with gearbox and bearing manufacturers to design more reliable assets, however there will always be a probability of equipment failure over time. Moving away from reactive maintenance practices, condition-based monitoring and diagnoses allows operators to gain confidence on asset management and turn to proactive and eventually predictive maintenance.

Better insight and knowledge in Rolling Element Bearing (REB) diagnostics continuous to be essential for the wind industry in order to improve gearbox reliability, provide earlier fault detection, and enable confident fault progression modelling with continuous monitoring.

Online Debris Monitoring (ODM) technologies have been adopted by many in the wind industry for early fault detection and diagnostics, however extensive empirical analysis has been conducted to demonstrate the full benefits of ODM technology, with emphasis on the increased reliability on fault diagnostics.

REB experiments were conducted to generate bearing lifetime data from fault initiation until maintenance action is required or recommended. The results from experimental data indicate relatively constant particle size distribution after spall initiation and during failure progression.

1 Introduction

Developments in wind power technologies continue to focus on reliability, increase in productivity, and lowering maintenance costs, with all three contributing to the main goal of lowering the levelized cost of energy for wind projects. This overall industry focus on technology improvements is critical to continue to enable growth and acceptance of wind power as a reliable source of renewable energy to meet global energy demands. Reliance on wind power as a source of renewable electricity generation at a global level is expected to continue to rise as illustrated by experts' analysis and forecasts, with total wind-based generation forecasted to surpass hydropower in 2030 and offshore wind capacity growth expected to reach 212 GW by 2030 [IEA-2024].

Despite manufacturers adherence to internationally recognised wind turbine gearbox design standards and continuous improvements in reliability; gearbox failures are the leading component failing,

and when analysing the next level, gearbox failures are dominated by bearings failure, in some cases by up to 76% [SHU-2016]

In addition to rolling element bearings being one of the leading causes for failures and unplanned maintenance, they are then selected as a topic of focus for testing and analysis also because of them being widely implemented in many common gearboxes designs by many of the major wind turbine manufacturers.

For wind turbine gearboxes, oil debris monitoring (ODM) sensing technology provide reliable early indication of bearing damage, and quantifies the severity of damage by monitoring progression with the goal to enable maintenance planning and reduce secondary damage.

There are several ambiguities in relation to the implementation of ODM technologies for the condition monitoring of rolling element bearings within wind turbine gearboxes. The majority of literature on the subject matter relates to ODM technologies for monitoring finds significant evidence of advanced and reliable fault notice. However, there is still ambiguity about what level of damage is deemed acceptable. The bulk of this work in literature is driven by aerospace applications, such as helicopter transmission gearboxes, and gas turbine engine main bearings. Here, diagnostic programs are often held to extreme reliability standards and quick maintenance actions, whereas wind turbine gearbox applications differ significantly, and can often operate months before maintenance is required. Understanding the point at which maintenance is essential and further operation is not recommended remains a subject of debate.

To examine these considerations, empirical bearing fault tests were conducted. These component isolated tests replicated field lubrication systems, with accelerometers, temperature sensors, and online debris monitors for component diagnosis. The load applied to the bearing varied on each test and was often in between 1.7 to 3.0 GPa of Hertzian stress covering most of bearing loads across industrial and aerospace applications [HAR 2007].

Over one hundred tests were conducted. This document shall report the findings made from this database in relation to the question presented earlier.

2 Online Debris for Condition Based Monitoring

Online debris monitors, like the ones manufactured by Gastops Ltd., are flow through sensors that employ three inductive coils. When a metallic particle flows through the sensor, a voltage signal is produced by the coils indicating a particle has passed through the sensor’s bore. This system is shown in Figure 1 below.

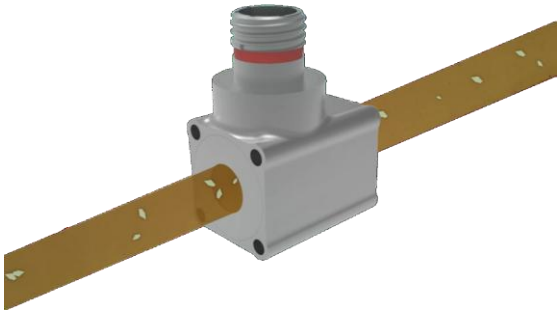

Figure 96: Oil Debris monitor sensor tracking metallic particles within lubricating oil flow

Not all metallic particles that pass through the sensor bore are detected, these systems often include a minimum detectable particle size. This is based on technological limitations of the sensor, and ensures avoidance of air bubbles, pressure pulses, and other forms of noise that could indicate false positives.

Previous literature has indicated a strong correlation between the number of discharged particles from a failing component, be it bearing or gear, and the level of damage [BOL2009]. Bearings tested in this test program were removed at various points throughout the spalling process for visual inspection. 3D modelling software was used to factor in the raceway curvature and estimate the total damaged area. This relationship was observed regardless of material, stress, component size, amongst other factors.

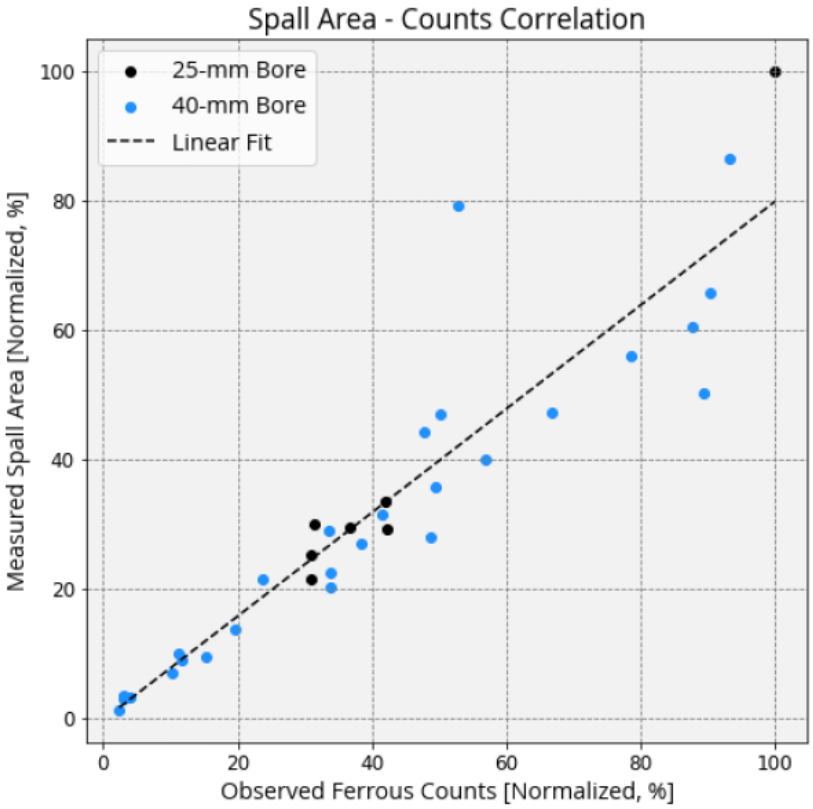

Figure 2: Ferrous counts vs. discharged spall area linear relationship showcasing strong correlation for diagnostic modelling

The aforementioned relationship is shown in Figure 2, where based on the number of observed counts, the total spall damage area can be approximated. This provides the framework for ODM based diagnostic tools, where the number of counts can be used to approximate the damage on the target components within engine and gearbox systems.

This allows generally more accurate and decipherable diagnosis for component condition. Negligible to no counts are observed within healthy systems as the minimum size of detection generally dismisses normal running wear. This almost entirely eliminates the possibility of false positives, as counts will only be observed at the presence of abnormal wear tied to faulted engine / gearbox components.

Finally, the strong linear correlation allows an estimate of the spall damage area with fidelity. This is particularly important for applications with long operation runtimes with faults, and timeline to

schedule maintenance. Essentially, understand the exact level of damage on the bearing to schedule and plan maintenance accurately to minimize costs and maximize availability. This is in comparison with general two-stage diagnostic systems (Healthy – Faulted) which will either compromise the capability for proactive maintenance through early detection and progression tracking, or lead to false diagnoses, whether through false positives or stopping the equipment with long remaining useful life.

	Light Threshold Binary Diagnostic System	**Conservative Threshold Binary Diagnostic System**	**Online Debris Monitoring Diagnostic Systems**
Healthy	Potential False Positives	Avoid False Positives	Avoid False Positives
Low Level Damage	Detectable	Undetectable	Detectable
High Level Damage	Detectable but indistinguishable	Detectable	Detectable and distinguishable
Outcome	Provide adequate time to schedule maintenance but can lead to many false positives and low confidence in system output. No information on when to stop system operation at high level damage diagnosis	Can stop machine operation at high levels of damage but not much opportunity for proactive maintenance. If low level damage is detected, will stop operation when there is still remaining useful life.	Regression style diagnostic tool allows progressive damage tracking using discharged counts.

Table 1: Effect of regressive diagnostic models in comparison with classification condition monitoring programs on false positives and maintenance scheduling

The fidelity and resolution of the deployment of ODM continuous monitoring is shown in Figure 3. Here, the proximity of the ground truth measurements to the Ferrous debris count showcases the strong correlation between ODM counts and actual damage, as identified in Figure 2.

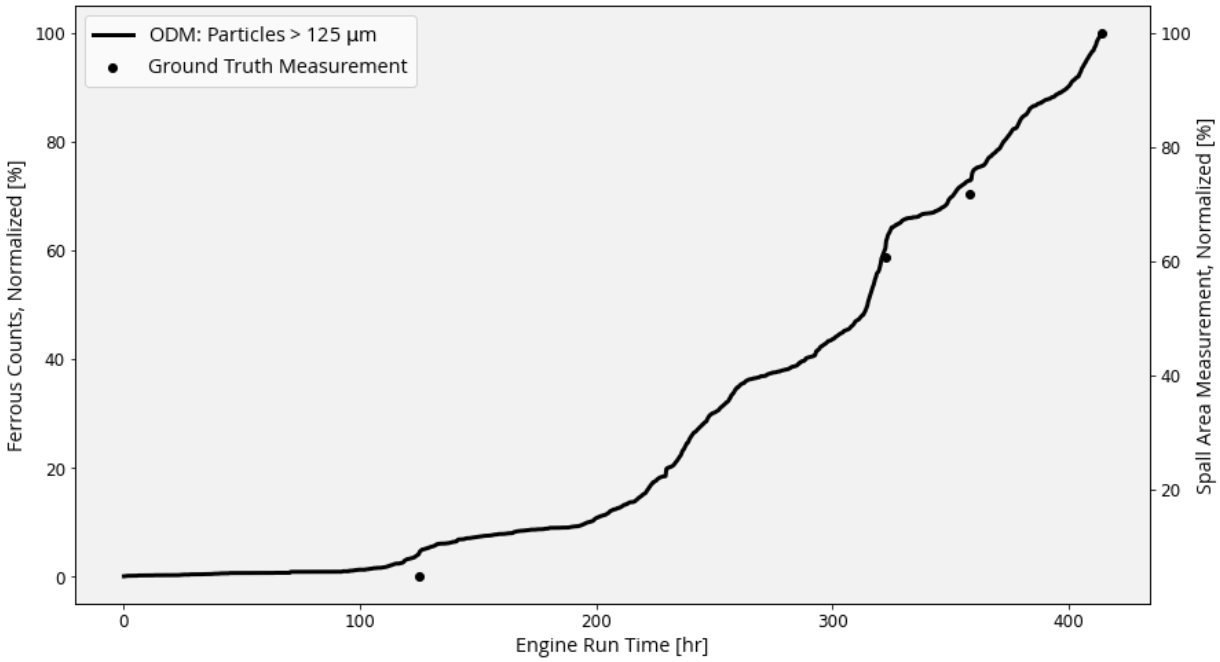

Figure 3: Ferrous counts and ground truth spall area progression throughout a empirical test from spall initiation at just around 100 hours to around 400 hours.

3 Diagnostic Stages of Bearing Life

Bearing faults can initiate due to a plethora of reasons but are often attributed to operator-induced errors or lubrication faults such as debris ingress. Wind turbine gearbox bearings in particular are susceptible to a phenomena known as white etch cracking which is a major focus for drivetrain reliability research. Whatever the cause, these issues can induce a macroscopic surface defect on the bearing raceway. The Hertzian contact between the raceway crack and the rolling elements of the bearing cause the damage to grow, in a similar way to potholes growing with contact from the automobile tires. This phenomenon of rolling contact fatigue is deemed spall,

Bearing degradation follows a particular curve that has been outlined often as a “hockey stick”. Herein, the degradation is slow and gradual before reaching a critical damage level. After which, the degradation accelerates and orders of magnitude more damage can grow in just a fraction of the time as previously. This point has generally been referred to as the spall knee. For this reason, bearing degradation numerical models often include multi-stage features, noting the significant difference between damage growth pre and post spall knee.

This difference can sometimes be hidden in field applications. Bearings in operation can go under different mission profiles such as take-off, cruising and descent in aerospace applications. Wind turbine bearings in particular can face various load and speed cycling based on the power being generated. These load and speed differences can significantly alter the degradation rate of the bearing, with higher loads and speeds accelerating the degradation rate and reducing life.

However, the spall knee remains a key point in the life of the bearing post-spall initiation. While it may be masked slightly if a significant load increase accelerates the degradation, the spall knee will cause an accelerated degradation regardless of but proportional to the stress and speed.

Figure 4 utilizes the strong correlation between counts and spall area to represent the hockey stick curve, and the identification of the spall knee. This particular test is an example of the bearing degradation curve, with initiation after 20 hours. After which, spall grows steadily before the knee causes significant acceleration. This point covers the majority of bearing life post spall initiation. The healthy phase generally covers most if not all (for healthy bearings replaced due to life ratings) of bearing life in field applications. However, sometimes faults can initiate early and cause for very short durations within the healthy phase.

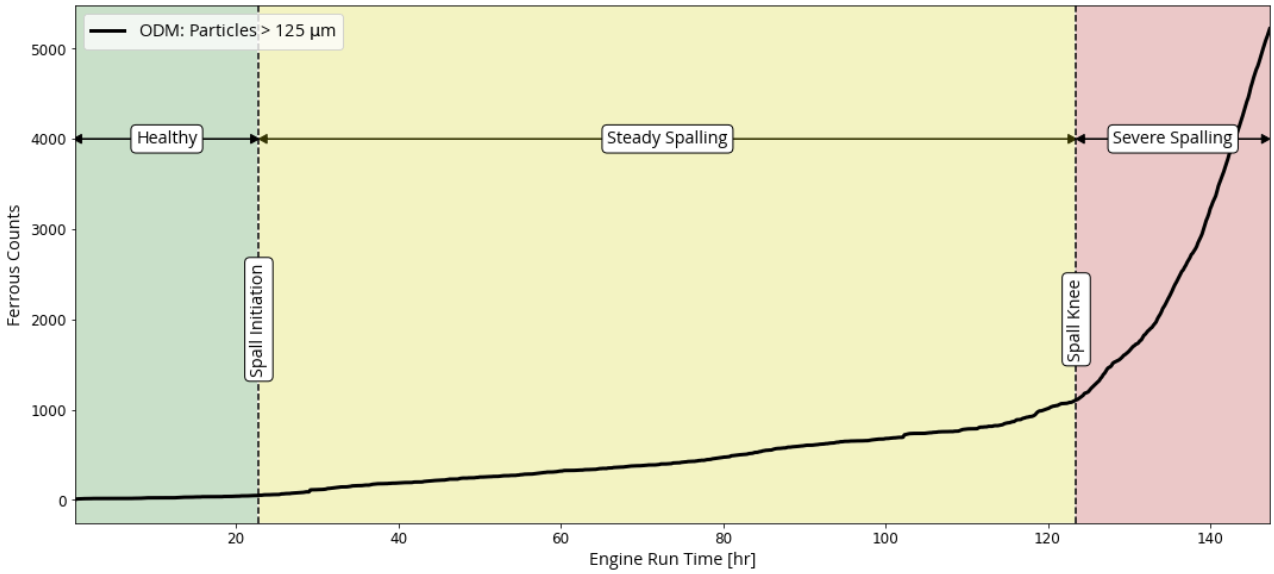

Figure 4: Ferrous counts vs. discharged spall area linear relationship showcasing strong correlation for diagnostic modelling

The question that arises from this analysis is when does the spall knee occur during the bearing fault lifetime. Literature before has arrived at two theories for the cause of the spall knee:

1. The unloading of a rolling element and it crashing into the spall's trailing edge [ARA2009]
2. The unloading of multiple rolling elements causing a shift in the bearing's overall stiffness [DUP2010]

Both of these theories were estimated using a few tests and small bearings where the area for the two phenomena is quite close. The large dataset employed now looked to identify which one of these theories was the cause of the spall knee.

The strong correlation between counts and damaged area combined with over one hundred tests provide a clear identification of the spall knee location. Ground truth measurements before and after the spall knee confirm the observation. The spall knee was found to be the point when two rolling elements unload and causes significant degradation acceleration. Figure 5 showcases graphically the spall knee point graphically as well as visually. This was found to be scalable to different bearing types and sizes and confirms findings from previous literature.

The unloaded rolling elements causes heightened contact stresses on the remaining rolling elements. Essentially, consider if 20 kN are applied to a bearing with 13 rolling elements causing a stress of 2.0 GPa on each individual rolling element. With that same load and two unloaded rolling elements, the contact stress on the remaining rolling elements can each increase by a fraction of gigapascal.

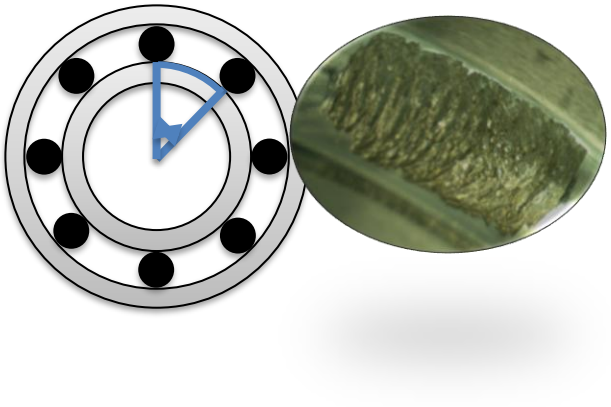

Figure 5: Figure showcasing the spall length around the bearing raceway that coincides with successive rolling element unloading (L) along with a visual representation of that point on a test bearing (R)

It was noted in the testing that further unloading of more than two rolling elements can cause further accelerations in bearing degradation. Vibration continues to increase in amplitude with each successive unload and as the bearing degradation progresses. However, the vibration magnitude is significantly larger post-knee than before, however, there is more variance, and it may take significant time post-knee for the difference to be observable.

4 Translating Findings to Condition Based Monitoring

The purpose of identifying the spall knee is how it translates to diagnostic modelling. This provides the key end of life threshold for bearing operation. Operating the bearing post-spall knee means continuously accelerating degradation, higher vibration and temperature, and the potential for catastrophic failure. The latter is when the cage in the bearing breaks causing seizure due to the high generated vibrations, or fault progression to other components the bearing supports.

For this reason, diagnostic modelling identifies the spall knee as the alarm or end of life designation for bearing operation. It is possible for this to be extended if the loads and speeds are managed to prolong asset use, however, this is left to the operator’s risk assessment.

5 Summary

As technology advances, and wind operators continue to rely on the use of data to enhance maintenance programs and move from reactive to proactive, ODM provides a reliable source of early indication of fault detection. The tests conducted prove the strong relationship between counts and the area of damage on the failing component, therefore enabling condition-based monitoring of the failure through its progression. The large test database also finally provides an accurate and precise definition of the historic spall knee in bearing fault progression. This has been appropriately set as the end of life and alarm for bearing fault applications within wind turbine gearboxes.

6 Bibliography

[IEA2024] Renewables 2024-Analysis and forecast to 2030.

(http://www.iea.org)

2024.

[SHU2016] Shuangwen, Shawn: Wind Turbine Gearbox Reliability Database, Condition Monitoring, and Operation and Maintenance Research Update.

NREL, Golden-Colorado, 2016.

[DUP2010] Richard Dupuis: Application of Oil Debris Monitoring for Wind Turbine Gearbox Prognostics and Health Management.

Annual Conference of the Prognostics and Health Management Society, 2010.

[ARA2009] N. K. Arakere, N. Branch, G. Levesque, V. Svendsen and N. H. Forster: Rolling Contact Fatigue Life and Spall Propagation of AISI M50, M50NiL, and AISI 52100, Part II: Stress Modelling.

Tribology Transactions, vol. 53, no. 1, pp. 42-51, 2009.

[HAR2007] T. A. Harris and M. N. Kotzalas: Essential Concepts of Bearing Technology.

CRC Press, 2007.

[BOL2009] N. Bolander, H. Qui, N. Eklund, E. Hindle and T. Rosenfeld: Physics-based remaining useful life prediction for aircraft engine bearing prognostics.

Annual Conference of the Prognostics and Health Management Society, 2009.

Online Monitoring of Doubly-Fed Induction Machines Based on High-Frequency Modeling

H. Peng[1], Y. Yu[1], K. Hameyer[1], S. Steentjes[1]

[1] Institute of Electrical Machines (IEM), RWTH Aachen University, Schinkelstr. 4, Aachen, Germany

Keywords: Wind Turbine Generator, Inter-turn Short Circuit, Insulation Fault, Real-Time Condition Monitoring, Transient Signal Analysis

Abstract: This paper investigates the potential of using electric terminal signals of doubly-fed induction machines for online fault monitoring through experimental studies. The results reveal that by analyzing the transient voltage signals at electrical machine terminals, including the neutral point, it is possible to detect inter-turn short-circuit electrical faults online in real-time. The detection mechanism is based on analyzing signals and their correlation in high-frequency domains. These transient signals naturally exist due to the inverter-fed operations. Therefore, this work invokes the potential of realizing a non-invasive and convenient online monitoring of insulation fault detection.

1 Introduction

The wind power industry is experiencing rapid growth amid the global push for clean energy. According to the "Global Wind Report 2024" by the Global Wind Energy Council (GWEC), the wind power industry is expected to see substantial growth by 2030, with annual capacity additions needing to triple from 117 GW in 2023 to at least 320 GW [BAC24]. With increased power capacities and challenging operational environments, this scale-up in new wind turbines demands enhanced real-time condition monitoring of wind generators. Studies have shown that among the failures that can be clearly attributed, 79% of wind turbine failures require restarting or adjustment. Of these, 12% are due to generator failures, with a failure rate of 0.8778 per year. The failure rates of electrical facilities and electromechanical components, such as generators, are higher than those of mechanical components [LI22]. Other research indicates that over 45% of failures in electrical machines, including wind turbine generators, are caused by stator and rotor winding faults, predominantly due to insulation breakdowns leading to internal short circuits. For synchronous machines, this proportion increases to as high as 73% [LEF22]. Additionally, if not promptly addressed, these internal short circuits can increase excitation current and reduce reactive power output [ZHA18] or cause mechanical failures such as torque ripple during turbine operation [SAN21].

However, online fault detection of inter-turn short circuits in generators remains a significant challenge in the current industrial context. Existing large machine monitoring systems are developed based on ISO-18436, which relies on vibration analysis, temperature measurement, and oil analysis. These methods focus on mechanical, thermal, and chemical signals but overlook the analysis of electrical signals. Although some alternative approaches, such as the one mentioned in [CAS21]. It utilizes principal component analysis and support vector regression models based on commonly used Supervisory Control and Data Acquisition (SCADA) data, and can, to some extent, diagnose electrical faults in generators. They are limited by the minute-level data collection frequency and the computational effort required by the models. As a result, inter-turn short circuit faults in generators are still not identified promptly.

In recent years, high-frequency modeling techniques for electrical machines have been developed based on the impedance spectrum of electrical machines to model their transient response behavior. These models offer advantages in low computational demand and the ability to accurately predict transient signals in motors [PEN24-1] [PEN24-2] [HEW24]. These methods have been validated across various types of electric machines. High-frequency modeling provides a technical foundation for making the online identification of inter-turn winding short circuit faults in wind turbine generators based on transient signals at the machine terminals possible. In this paper, the feasibility of this identification method is verified through experimental analysis based on a small-scale Doubly Fed Induction Machine (DFIM). The winding resistance of one phase is $8\,\Omega$. Due to the limitation of the available experimental sources, the transient voltage signals are injected into stator winding instead of the rotor winding because the neutral point of the rotor winding in our prototype is not accessible. However, the principle works for all kinds of winding as long as it is excited by PWM-form voltage signals.

The organization of this work is as follows: Section 2 is devoted to describing experiments with time-domain impedance measurement and related inferences. In Section 3, these inferences are validated through measurements in the time domain on a test bench. Section 4 presents conclusions and an outlook on future research directions.

2 Experiment setup and impedance measurement with different short-circuit degrees within one phase

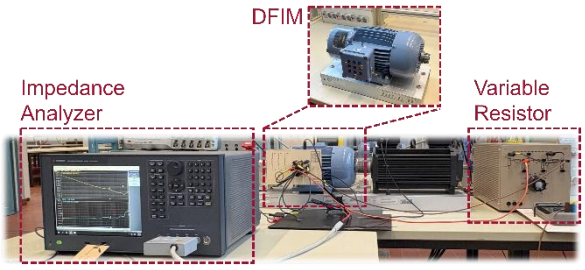

Figure 97: Measurement of common-mode impedance of the DFIM stator winding

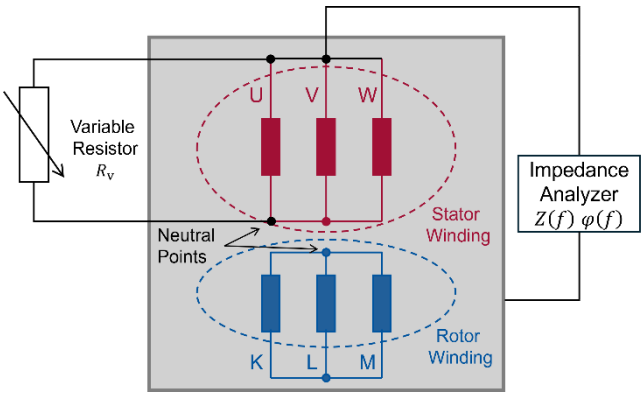

Figure 98: Setup of experiment with impedance measurement

Previous research has shown that common-mode impedance reflects changes in the parasitic capacitance of the insulation layer in stator windings [ALV20] [SEA24]. Therefore, the common-mode impedance of the DFIM stator winding is primarily measured with the impedance analyzer ‘E4990A’ of the company Keysight. Figures 1 and 2 illustrate the measurement setup. In order to minimize the impact of the rotor on the measurement, the three phases of the rotor winding are short-circuited. The common-mode impedance spectrum of the machine is measured from $100\,\mathrm{Hz}$ to $10\,\mathrm{MHz}$, displaying a phase angle of $-90\,°$ at lower frequencies, and gradually exhibiting inductive behavior as the frequency increases, forming resonance points in the spectrum.

To further simulate inter-turn short circuits within one phase that occur during machine operation, a variable resistor is connected in parallel between the U-phase terminal and the neutral point, as illustrated in Figure 2. The resistance value simulates different locations of internal short-circuit

faults. When a short circuit occurs between two adjacent turns within the same phase, it is approximated by paralleling a high-resistance resistor between the U and the neutral point. As the variable resistor increases, the severity of short-circuit within one phase decreases.

Figure 3 illustrates the measured common-mode impedance spectrum of the DFIM stator winding with various values of parallel resistors R_v of $2\,\mathrm{k\Omega}$, $1.5\,\mathrm{k\Omega}$, $0.5\,\mathrm{k\Omega}$ and $0.1\,\mathrm{k\Omega}$. The results indicate that as the parallel resistance decreases, the impedance spectrum undergoes more significant and systematic changes across the frequency range from $10\,\mathrm{kHz}$ to $1\,\mathrm{MHz}$. Figure 4 provides a zoomed view of this critical frequency band. Figure 3 demonstrates that at frequencies above $1\,\mathrm{MHz}$, the impedance remains consistent across different R_v values. Based on the theory of high-frequency modeling of electrical machines, impedance exhibits different frequency response characteristics during the switching process of inverters. Therefore, it can be inferred that the frequency response characteristics from $10\,\mathrm{kHz}$ to $1\,\mathrm{MHz}$ could be utilized to identify internal short-circuit faults within one phase. This hypothesis is further validated through experimental analysis in the following section.

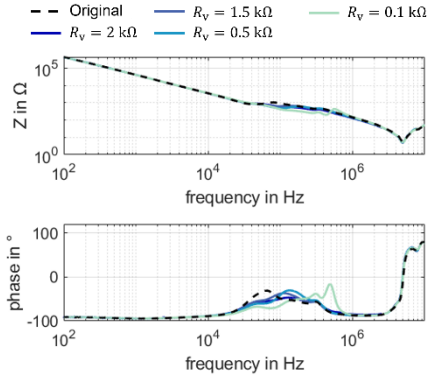

Figure 99: The measured common-mode impedance spectrum at various values of parallel resistors $\boldsymbol{R_v}$

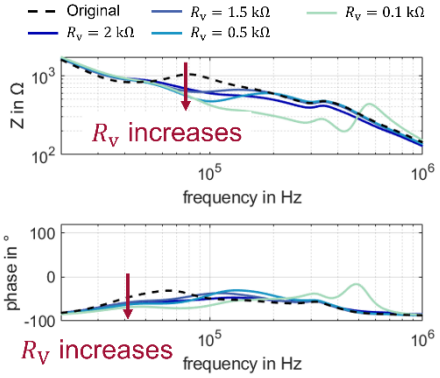

Figure 100: Zoomed measured common-mode impedance spectrum of the DFIM stator winding at various values of parallel resistors $\boldsymbol{R_v}$

3 Validation and analysis based on time-domain measurement

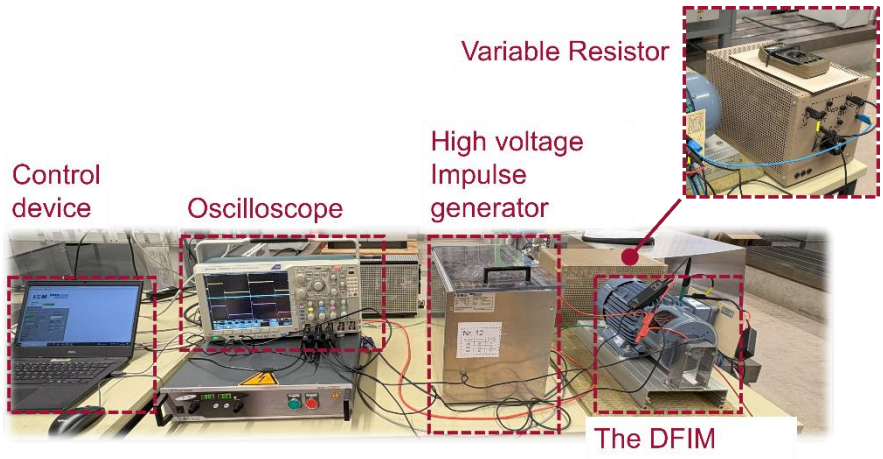

Figure 101: Test bench setup during time-domain measurement

It is hypothesized that internal short-circuit faults can be detected through the transient behavior of terminal electrical signals. In order to validate this hypothesis, an experiment based on time-domain measurements has been designed. Figures 5 and 6 illustrate the measurement setup. The DFIM stator winding phases U, V, and W are interconnected. The variable resistor R_v is shorted between the U terminal and the neutral point to simulate internal short-circuit faults within one phase. A high-voltage impulse generator equipped with Silicon Carbide (SiC) power modules is used to inject PWM-form voltage between the U terminal and the machine housing. The voltage signal serves as the input signal with a switching frequency f_sw of $2\,\mathrm{kHz}$ and a peak value $U_{\mathrm{UVW-to-GND}}$ of $200\,\mathrm{V}$. To detect the internal short circuit in the phase winding, the voltage $U_{\mathrm{NP-to-GND}}$ between the neutral point and the machine housing is measured and recorded as the output.

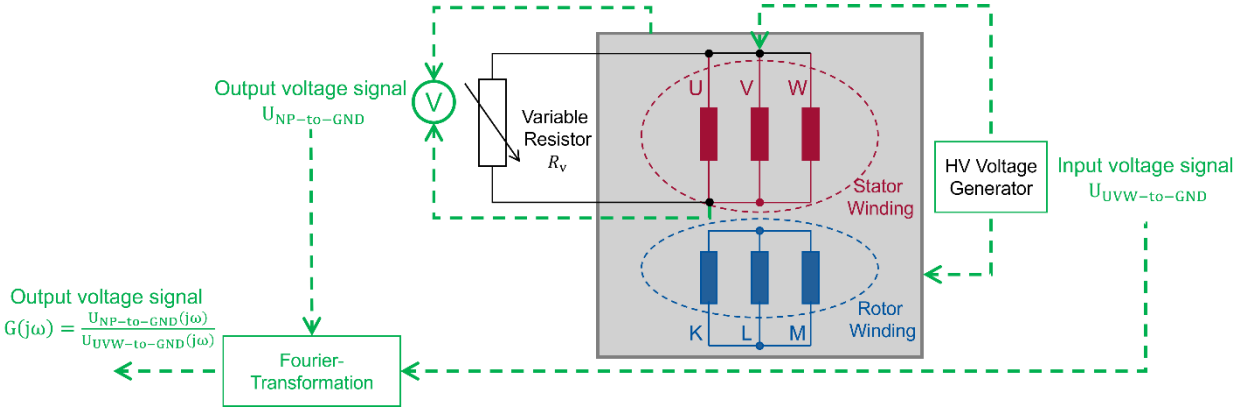

Figure 102: Block diagram and setup for time-domain measurement analysis

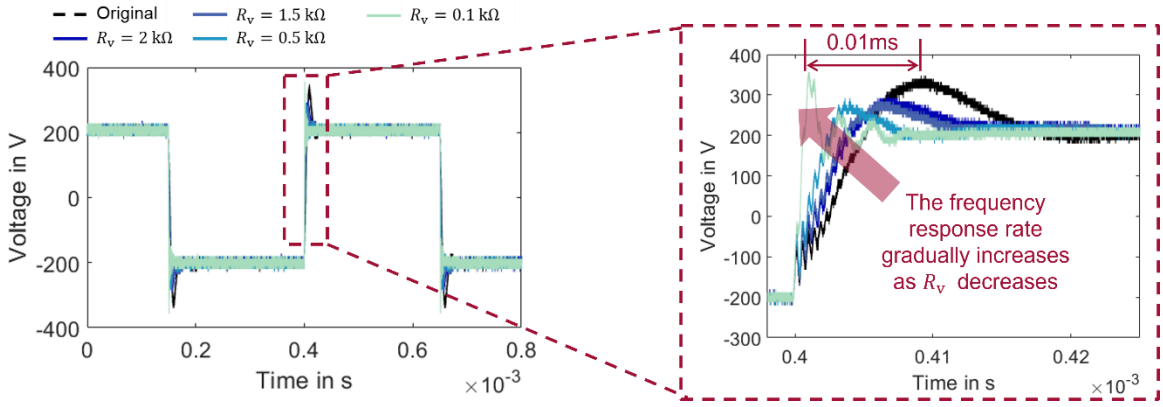

Figure 103: The resulted voltage signals $\boldsymbol{U_{\mathrm{NP-to-GND}}}$ across various $\boldsymbol{R_\mathrm{v}}$ values

Figure 7 presents the measurement results. Under the identical excitation voltage $U_{\mathrm{UVW-to-GND}}$, the output voltage signal $U_{\mathrm{NP-to-GND}}$ shows noticeable change during switching processes as R_v decreases. The oscillation frequency of $U_{\mathrm{NP-to-GND}}$ significantly increases as R_v decreases. Notably, about $0.02\ \mathrm{ms}$ after the start of the PWM switching, the oscillatory behavior of the $U_{\mathrm{NP-to-GND}}$ signals under different conditions tends to converge to a steady state. It indicates that identifying internal short-circuit faults within one phase is only possible by analyzing the transient behavior of terminal voltages during the switching processes.

In order to further validate the conclusions presented in Section 2, the measured signals are analyzed in the frequency domain. A transfer function can describe the relationship between the input and the output voltage signals. The voltage $U_{\mathrm{UVW-to-GND}}(t)$ is chosen as the input signal of the system, and the voltage signal $U_{\mathrm{NP-to-GND}}(t)$ as the output signal. A Frequency Response Function (FRF) $G_{R_\mathrm{v}}(\mathrm{j}\omega)$ under various values in R_v is determined with the following formula:

$$X(\mathrm{j}\omega) = \int_{-\infty}^{\infty} x(t) \cdot e^{-\mathrm{j}\omega t}\mathrm{d}t \qquad \textbf{Eq. 22}$$

$$G_{R_\mathrm{v}}(\mathrm{j}\omega) = \frac{U_{\mathrm{NP-to-GND}}(\mathrm{j}\omega)}{U_{\mathrm{UVW-to-GND}}(\mathrm{j}\omega)} \qquad \textbf{Eq. 2}$$

Where $X(\mathrm{j}\omega)$ is the Fourier Transform of a time-domain signal $x(t)$. In this measurement, the oscilloscope's sampling rate is $1.25\ \mathrm{GHz}$, which is far higher than the upper frequency of $10\ \mathrm{MHz}$ during the impedance measurement in Section 2. In practical signal processing, the continuous Fourier Transform described in Eq.1 can be directly replaced by the Fast Fourier transform (FFT). After the Fourier Transform, it is followed by denoising and smoothing processes to obtain the spectrum of $G_{R_\mathrm{v}}(\mathrm{j}\omega)$ from $2\ \mathrm{kHz}$ to $10\ \mathrm{MHz}$.

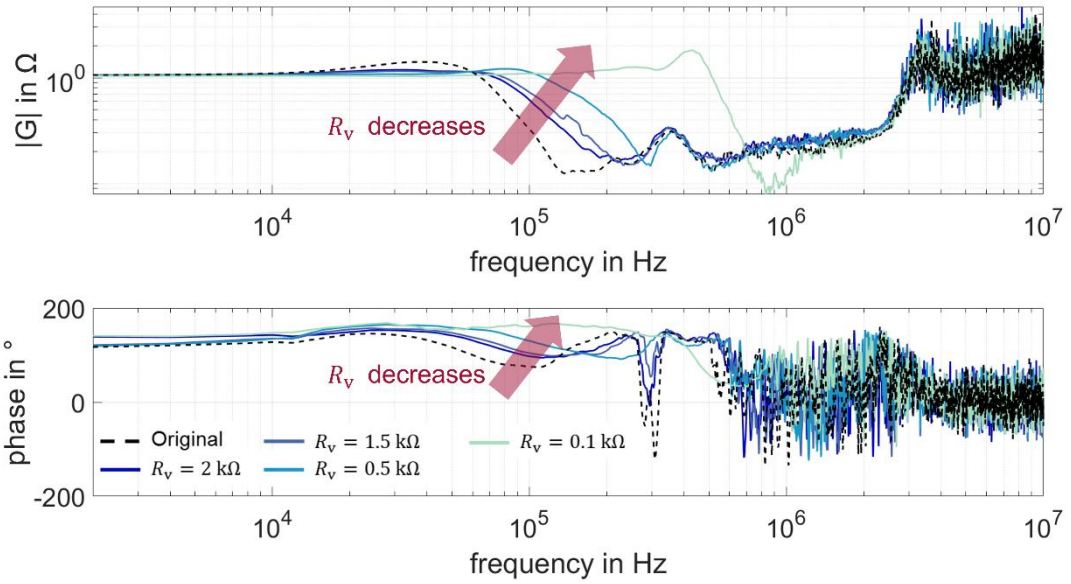

Figure 104: Frequency Response Function of $\boldsymbol{G_{R_\mathrm{v}}(\mathrm{j}\omega)}$ for various $\boldsymbol{R_\mathrm{v}}$ values

The transfer function $G_{R_\mathrm{v}}(\mathrm{j}\omega)$ und various parallel resistance values R_v is displayed in Figure 8. It is observed that the changes in $G_{R_\mathrm{v}}(\mathrm{j}\omega)$ are significant enough to reflect the influence from the parallel resistance R_v, compared to the original winding status without a parallel resistance R_v. Due to the sampling accuracy and noise interference during measurement, the frequency spectrum above $3\ \mathrm{MHz}$ exhibits severe oscillations and cannot be used for fault detection. Notably, the frequency range over which $G_{R_\mathrm{v}}(\mathrm{j}\omega)$ changes is consistent with with the frequency domain segment where the common-mode impedance changes, as discussed in Section 2, which further validates the feasibility of using transient signals for online detection of inter-turn short-circuit faults.

In order to quantitatively evaluate the influence of parallel resistance R_v on the spectrum of the transfer function $G_{R_\mathrm{v}}(\mathrm{j}\omega)$, the Power Spectral Density $PSD(f)$ is applied. It represents how the output

signal responds to the input signal across various frequency components and the distribution of the system's output signal in terms of power:

$$PSD(f_k) = \left|G_{R_v}(\mathrm{j} \cdot 2\pi \cdot f_k)\right|^2 \quad \textbf{Eq. 3}$$

Where $f_k = n \cdot f_{sw}$ is the integer multiple of the switching frequency f_{sw} with $n \in \boldsymbol{Z}^+$. The Pearson Correlation Coefficient ρ_{R_v} under different R_v values are calculated based on the distribution of PSD:

$$\rho_{R_v} = \frac{\sum_{k=1}^{N}(PSD_{org}(f_k) - \overline{PSD_{org}(f_k)})(PSD_{R_v}(f_k) - \overline{PSD_{R_v}(f_k)})}{\sqrt{\sum_{k=1}^{N}\left(PSD_{org}(f_k) - \overline{PSD_{org}(f_k)}\right)^2 \cdot \left(PSD_{R_v}(f_k) - \overline{PSD_{R_v}(f_k)}\right)^2}} \quad \textbf{Eq. 4}$$

Where the $PSD_{org}(f_k)$ represents the PSD value at frequency f_k without parallel resistance R_v and $PSD_{R_v}(f_k)$ represents the corresponding PSD value at frequency f_k with a parallel resistance of R_v. The correlation coefficient ρ_{R_v} ranges between -1 and 1. A value close to 1 indicates a similarity in high power spectral density distribution between the two transfer functions. In our case, the stator winding's frequency response characteristics under specific short-circuit conditions closely resemble those in a healthy state. Conversely, a value closer to 0 suggests a higher deviation from the characteristics of the healthy condition. This correlation coefficient is based on PSD, which compares the fault and healthy cases and is used to indicate the inter-tern short circuit.

Figure 9 shows the correlation coefficient ρ_{R_v} at various resistance values R_v across the frequency range of $2\,\mathrm{kHz}$ up to $2\,\mathrm{MHz}$. When a resistor of $1.5\,\mathrm{k\Omega}$ is connected in parallel with the U-phase winding, the ρ_{R_v} decreases to about 0.9. It indicates that the changes in the correction coefficient is sensitive to internal short circuits within one phase. Furthermore, such changes are also observed by comparing the transient signals of the terminal voltage in the time domain, as shown in Figure 7. As the parallel resistance value decreases further, the correlation coefficient undergoes more noticeable changes, consistent with the variations observed in the common-mode impedance in Figure 3 and the time-domain signals in Figure 7.

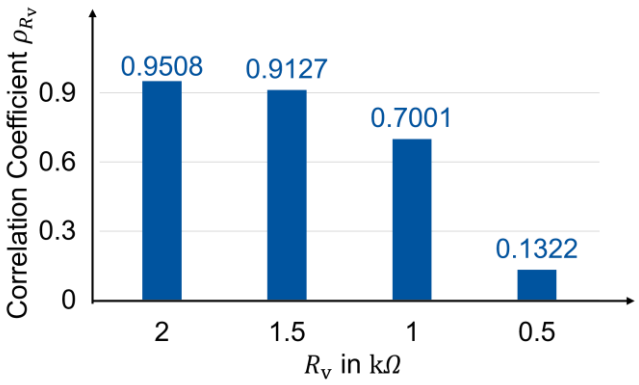

Figure 105: The $\boldsymbol{\rho_{R_v}}$ of various $\boldsymbol{R_v}$ conditions using the transfer function $\boldsymbol{G_{R_v}(\mathrm{j}\omega)}$ with the original stator winding as reference.

As previously mentioned, different values represent the location and severity of internal short-circuit faults in the winding. Based on the analysis, it is sufficient to demonstrate that internal insulation

faults in electrical machines can be quickly identified by capturing and analyzing the transient behavior of machine terminal voltage signals. It is worth noting that, in reality, the wind power generators are much larger than the DFIM stator winding used in this paper. A larger machine size will reduce the oscillation frequency of the transient behavior of the generator terminal voltage signals, thereby lowering the demand sampling frequency to several hundred kilohertz levels instead of the Gigahertz levels with the oscilloscope.

4 Conclusion and Outlook

This study has successfully validated a novel online method for identifying internal insulation faults in electrical machines. By analyzing the transient behaviors of terminal voltage signals, the method effectively detects these faults. Moving forward, its applicability to real wind turbines will be further confirmed through analysis in actual operating environments. Future research should also prioritize the development of real-time online monitoring algorithms for detecting internal insulation faults in wind turbines based on this approach.

5 References

[BAC24] Backwell, B.: GWEC Global Wind Report 2024

[LI22] Li, H., Peng, W., Huang, C.-G., & Soares, C. G.: Failure Rate Assessment for Onshore and Floating Offshore Wind Turbines. In: Journal of Marine Science and Engineering, vol. 10, no. 12, 2022, p. 1965. MDPI, Basel, 2022.

[LEF22] Leffler, J., & Trnka, P.: Failures of Electrical Machines - Review. In: 2022 8th International Youth Conference on Energy (IYCE), Hungary, 2022, pp. 1-4. In: 2022 8th International Youth Conference on Energy (IYCE), IEEE, July 2022

[ZHA18] Zhang, G; Wu, J; Hao, L.: Analysis on the Amplitude and Frequency Characteristics of the Rotor Unbalanced Magnetic Pull of a Multi-Pole Synchronous Generator with Inter-Turn Short Circuit of Field Windings. In: Energies, 11(1), 60 MDPI, Basel, 2018.

[SAN21] Santelo, T; Oliveira, Carlos; C, Carlos; M, J.R.B.A.: Wind Turbine Failures Review and Trends. In: Journal of Control, Automation and Electrical Systems, 33, 505-521. Springer, New York, 2021.

[CAS21] Castellani, F; Astolfi, D; Natili, F.: SCADA Data Analysis Methods for Diagnosis of Electrical Faults to Wind Turbine Generators (Appl. Sci. 2021, 11, 3307). MDPI, Basel, 2021.

[PEN24-1] Peng, H.; Stevic, S.; Luo, Z.; Driendl, N.; Butterweck, D.; Sharifian, L.; Firouz, Y.; Hameyer, K.: Voltage Distribution Modeling Along Stator Windings in Permanent Magnet Synchronous Machines Using Coil-Based Grey Box Models. In: IEEE Transactions on Energy Conversion, 39(3), 1994-2007, IEEE, September 2024.

[PEN24-2] H. Peng, Z. Luo, Y. Yu and K. Hameyer.: Modeling Voltage Distribution Along the Hairpin Windings of an Electrical Machine Using Impedance Fitting. In: 2024 International Conference on Electrical Machines (ICEM), pp. 1-7, IEEE, Torino, Italy, 2024.

[HEW24] Hewitt, D. A., Sundeep, S., Wang, J., Griffo, A.: High Frequency Modeling of Electric Machines Using Finite Element Analysis Derived Data. In: IEEE Transactions on Industrial Electronics, vol. 71, pp. 1432-1442. IEEE, New York, 2024.

[ALV20] Alvarez-Gonzalez, F., Hewitt, D., Griffo, A., & Wang, J. : Challenges of Common Mode Current and Voltage Acquisition for Stator Winding Insulation Health Monitoring. In: 2020 IEEE Energy Conversion Congress and Exposition (ECCE), Detroit, MI, USA, 2020, pp. 4452-4459. IEEE, New York, 2020.

[SEA24] Saeed, M.; Fernández, D.; Guerrero, J.M.; Díaz, I.; Briz, F.: Insulation Condition Assessment in Inverter-Fed Motors Using the High-Frequency Common Mode Current: A Case Study. Energies, 2024, 17, 470. MDPI, Basel, 2024.

Short-term wear test results of scaled line-contact pitch bearings

Matthias Stammler[1], Henry Ellerbrok[1], Rihard Pasaribu[2], Ulf Rieper[3]

[1]Large Bearing Laboratory, Fraunhofer Institute for Wind Energy Systems IWES, Am Schleusengraben 22, Hamburg, 21029, Germany

[2]Shell Downstream Services International BV, Rotterdam, Netherlands

[3]Shell Deutschland GmbH, Hamburg, Germany

Keywords: *three-row roller, oscillating bearings, grease lubrication, water ingress*

Abstract: Roller bearings have been playing a more important role in pitch system designs in the past years due to their comparably high stiffness and load carrying capacity. With limited operational experience, tests are an important part of any risk mitigating strategy.

This study focuses on scaled wear tests. Worst-case operating conditions of a 7.5MW wind turbine with individual pitch control are scaled to smaller custom roller bearings. The contact pressure and oscillation frequencies are kept constant while the outer loads and oscillation amplitudes are scaled to the smaller bearing size. The test profile is a 13.7 h time series which reproduces worst-case operating conditions close to rated speed of the turbine with small oscillation amplitudes and no longer protection runs in between.

Three different commercial greases are tested in both “dry” (no water contamination) and wet (10\% vol demineralized water added) condition. This work uses customized angular contact roller bearings with relative slip in the contact and 180 mm outer diameter. They are subject to static axial load. The results are compared to results from tapered roller bearing and angular contact ball bearings. They show a similar wear mechanism and similar effect of water ingress in angular contact ball and roller bearings, with the roller bearings displaying more pronounced wear marks. Results of tapered roller bearings differ significantly.

1 Introduction

Pitch bearings of wind turbines are oscillating, grease-lubricated bearings. Their operating conditions favor a risk of raceway wear, albeit anecdotally collected operational experience from ball-type pitch bearings indicates only very low numbers of actual bearing failures due to this damage mode. In recent years, three-row roller bearings have gained share in commercial pitch bearing designs due to their higher load-carrying capacity [STA24a]. Limited operational experience with roller bearings in this application makes risk-mitigation by testing a reasonable strategy.

The present study focuses on short-term wear tests with oscillatory movements under load. The operating conditions are scaled to customized line-contact bearings of 180 mm outer diameter. The methods for test program creation and scaling have been developed and verified for ball-contact pitch bearings [BAR23], and the authors have previously tested tapered roller bearings with similar test profiles [STA23]. This makes a comparison of the results of different bearing types in the present work possible and allows a first indicative evaluation of the wear risk in line-contact pitch bearings in comparison to other bearing types.

In the following, the terms 'standstill mark' and 'false brinelling' are used as defined in [PRE23]. In the field of oscillating, grease-lubricated bearings with line contacts, published research dates back to the year 1959. GLAESER reported on tests with 1080 spherical and cylindrical roller bearings (SRB and CRB) for high-temperature aeronautic applications. The grease-lubricated bearings were operated at amplitudes of 10 and 35° and the common failure mode was rolling contact fatigue [GLA59].

PITTROFF subjected CRBs to load oscillations. An off-axis weight rotated on a shaft and varied the individual contact loads. The false brinelling damages were shown to be rooted in alternating elastic deformation. Among other parameters, PITTROFF reported on the ability of pretension to reduce raceway wear damages [PIT61, PIT65]. BREWARD showed false brinelling damages of oil-lubricated roller bearings. He suggested simplified empirical formulas for the rolling contact fatigue lifetime considering the depth of false brinelling marks [BRE73].

SCHADOW conducted tests on type 32005 tapered roller bearings (TRB) to identify the influence of different parameters on false brinelling damage. He used various greases and different temperature levels. The application of dynamic axial, radial, and combined loads caused only slight damages to the bearing raceways. As all damages appeared similar, it was not possible to determine the influence of individual test parameters on them [FVA10].

CAVACECE et al. subjected SRBs to oscillatory motions of 40° at 5 Hz under constant radial load. The maximum contact pressure was 4 GPa. The used a commercial grease for aeronautic applications and reported highly variable test durations until a sudden increase in torque [CAV20].

LIN et al. found zinc dialkyldithiophosphate (ZDDP) additives in grease can effectively prevent wear damage on raceways of CRBs subjected to radial loads and superimposed vibrations [LIN22].

BAYER et al. compared wear results of cylindrical roller thrust bearings (CRTB) with angular contact ball bearings (ACBB) and report on similar wear mechanisms with the CRTBs being more prone to wear initiation. They also show a significant influence of oscillating frequency on the wear, with frequencies well below 1 Hz causing less wear on the raceways than higher frequencies [BAY23].

Publication	Bearing type	Lubricant	Oscillation Amplitudes	$x/2b$	Frequency
GLAESER [GLA59]	SRB, CRB	MLG 9373, Super Mil ASU-M-40, Silicone-base grease	10°, 35°	>>1	4.2 Hz
PITTROFF [PIT61, PIT65]	CRB	Various reference greases	Only load	-	115, 135, 165 Hz
SCHADOW [FVA10]	TRB	Various reference greases	Various	<1	5, 15 Hz
CAVACECE [CAV20]	SRB	Aeroshell 33	40°	>>1	5 Hz
LIN [LIN22]	CRB	Various reference greases	Only load	-	24 Hz
BAYER [BAY23]	CRTB	Grease C	1 – 55°	1 – 48.31	0.2 – 5 Hz

Table 15: Summary of literature on oscillating line-contact bearings with grease lubrication

Table 1 summarizes the test conditions in the listed publications. All works have constant oscillation amplitudes or, in case of load oscillation, constant load amplitudes per individual test. Except for BAYER et al. in 2023 [BAY23], all of them operated at frequencies well above 1 Hz. In contrast to

these, pitch bearings of wind turbines operate at variable amplitudes and with frequencies well below 1 Hz [STA18]. As reported by SCHADOW in 2010 [FVA10] and STAMMLER et al. in 2023 [STA23], TRBs display only very limited wear on the raceways due to the absence of geometrical slip in the contact. CRBs share this property. CTRBs as used by BAYER et al. in 2023 [BAY23] have very high relative slip in comparison to pitch bearings. The present study thus encompasses tests with the following characteristics:

- Relative slip like real-scale pitch bearings
- Variable amplitudes derived from pitch bearing operation
- Oscillation frequencies as in pitch bearing operation
- Commercial greases designed for pitch bearing application

While this study focuses on roller bearings, it also uses grease mixed with demineralized water. Pitch bearing operation facilitates water ingress into the lubricant because outer sealings can face the environment directly and temperature changes of the bearings favor condensation. A recent study by the authors uses equal water contents as in the present work for tests of ACBBs and shows positive short-term effects of added water for some of the greases in the test program [STA24b].

2 Methods

The tests of this study are carried out on the BEAT0.2 rig (Bearing Endurance and Acceptance Test rig, '0' refers to the outer diameter being well below 1 m and 2 because it is the second rig of this size class at the laboratory). Figure 106 depicts this rig.

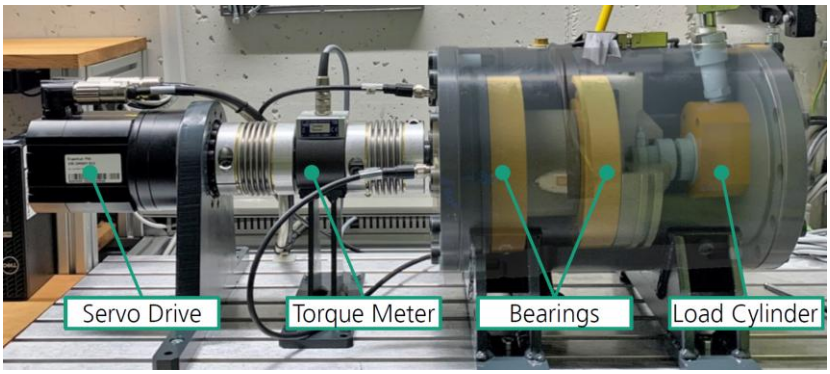

Figure 106: BEAT0.2 rig

The servo drive operates in position control mode. A torque meter measures the shaft torque. Two bearings are tested simultaneously under a static axial load that is applied with a rigging cylinder. A load cell measures this load. A temperature sensor is mounted to the outer ring of one of the bearings. The test rig operates at room temperature for the present study.

The bearings used in this study are type 3x220 angular contact roller bearings (ACRB) of the manufacturer KRW. They do not have sealings. Table 2 lists the main characteristics of these bearings. Figure 107 shows a full bearing (left) and the cage and rollers (right). The 3x220 bearing type is a custom bearing.

Property	Symbol	Value	Unit
Number of rollers	Z	10	-
Roller diameter	D_{W}	21	mm
Roller length	L_{W}	24.65	mm
Pitch diameter	D_{pw}	139.244	mm
Nominal contact angle	α	15.5	°

Table 16: Type 3x220 bearing main data

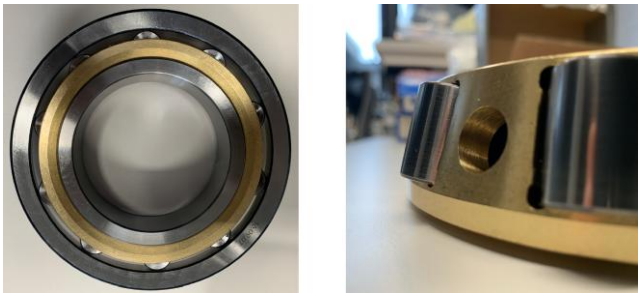

Figure 107: 3x220 bearing

The outer dimensions except for the width and the nominal contact angle are identical with 30220 TRBs. Instead of tapered rollers, the 3x220 has cylindrical rollers. This configuration allows to apply axial loads on the bearing without the need for a shoulder in the bearing rings and introduces geometrical slip into the contact.

The test profile reproduces worst-case operating conditions of one year of wind turbine operation. Details on the profile can be found in [BAR23] and [STA24b]. For the present work, the commercial pitch bearing greases are identical to those used in [STA24b] and have the same designations.

3 Results

Figure 108 shows the condition of five contact tracks per bearing after tests with grease A. The upper row shows the bearing with the grease in dry condition and the lower the bearing with the grease in wet condition, with 10% demineralized water added. The bearings have 10 rolling bodies, of which the five contact tracks with the most pronounced changes to the raceway surface are selected. The tests with grease A without water content resulted in more pronounced changes to the raceway in comparison to those of wet grease.

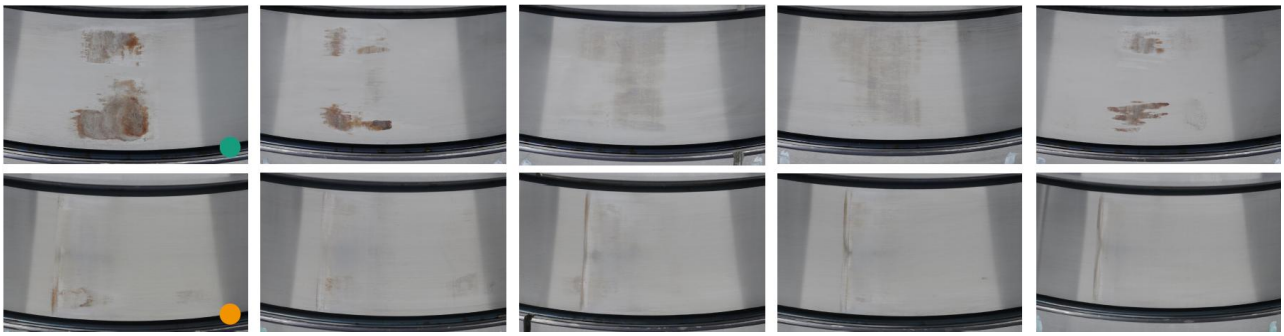

Figure 108: Raceway condition after test of grease A; upper row: dry; lower row: wet

An optical microscopy of contact tracks is shown in Figure 109. It depicts the two left wear tracks of Figure 108. The left picture, marked green, is of the dry grease, the right picture, marked orange, is

of the wet grease. Both pictures show the lower sections of the wear tracks visible in Figure 108. Due to the dimensions of the wear tracks it was impossible to fit them into one microscopic picture. The measured height of the wear marks is 11.3 mm. This is slightly less than half the length of the roller. The undamaged raceway in the center of the roller's length and the profile which reduces the effective contact length explain this discrepancy.

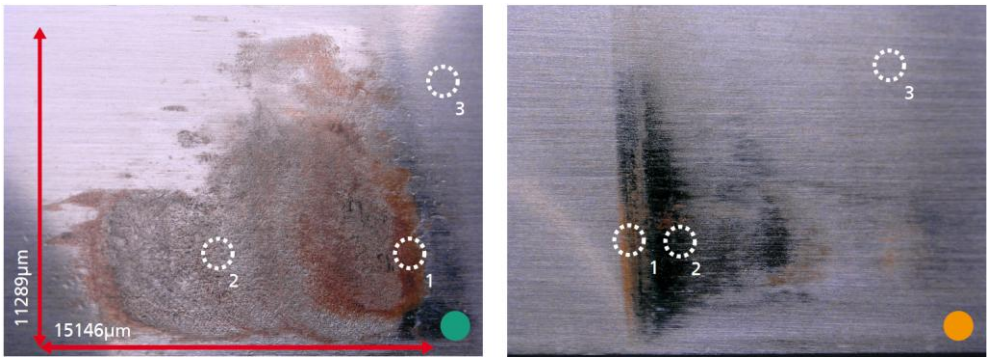

Figure 109: Raceway condition after test of grease A, optical microscopy; left: dry; right: wet

Figure 110 depicts the optical results of the laser scan of the dry grease, Figure 111 those of the wet grease. The numbers above each picture indicate the areas of the scan in Figure 109. The surface structure in Figure 111 and right appears to be as manufactured.

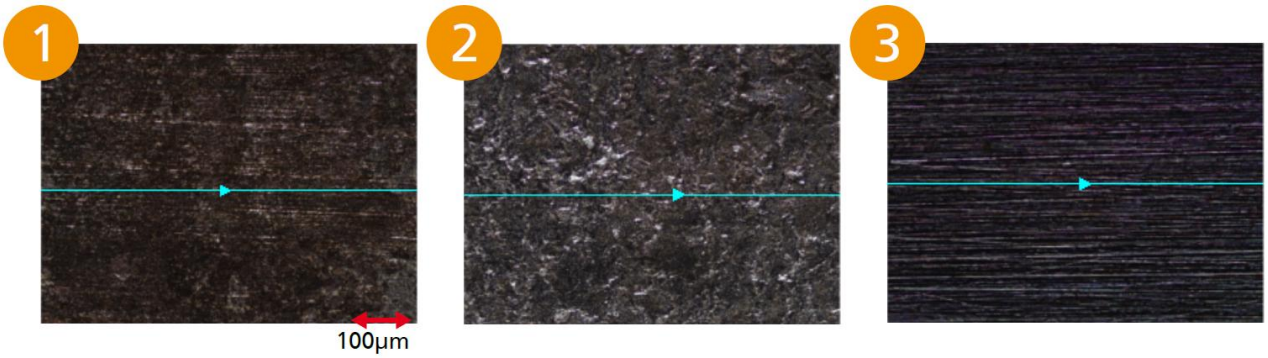

Figure 110: High resolution scan of different areas of the contact track for grease A in dry condition; numbers correspond to those in Figure 109

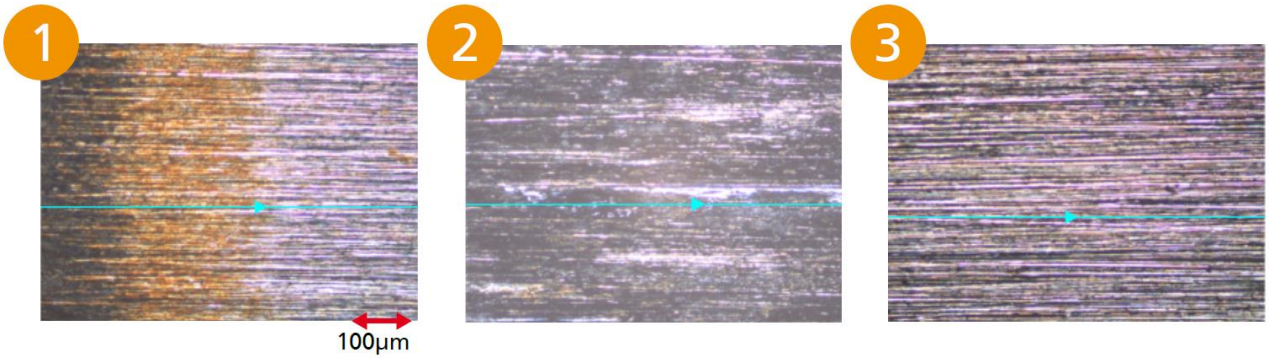

Figure 111: High resolution scan of different areas of the contact track for grease A in wet condition; numbers correspond to those in Figure 109

Figure 112 shows the raceway condition after tests for grease B, both in dry and wet condition. There are no discernible changes to the manufacturing condition of the raceways. Optical and laserscan microscopy did not return any different findings and are thus not displayed.

Grease D was only tested in wet conditions due to a restriction in available bearings for the test series. The test rig stopped after 30 minutes of the first attempt of executing the profile due to an exceeding of permissible torque. Not being sure about the reasons for this unusually high torque, the load was discharged and brought back to level and the test started again. After 15 minutes, the test stopped again with exceeding torque.

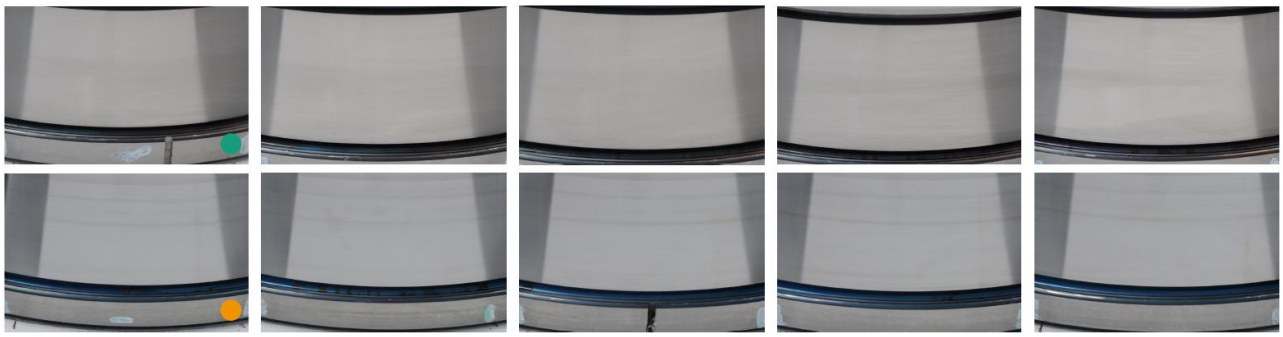

Figure 112: Raceway condition after test of grease B; upper row: dry; lower row: wet

This time, the test was disassembled. The bearing raceways, as shown in Figure 113, showed distinct wear areas for the two test attempts, with the left ones being suspected to stem from the longer test attempt.

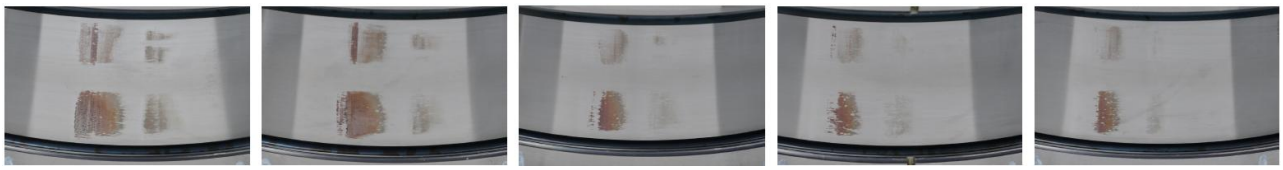

Figure 113: Raceway condition after test of grease D; wet

The ratio of the highest absolute peak torque in the test to the mean absolute peak torque of the first 100 cycles can serve as an expression of the severity of the corrosive raceway wear. Table 3 lists these ratios for all tested greases. Note the value for wet grease D does not reflect the exact same property as the test run was stopped before completion, yet it is absolutely higher than for the other greases. Table 3 contains both results from tests with ACBB as reported in [STA24b] and for the previously presented results of ACRBs.

Grease	dry ACBB	wet ACBB	dry ACRB	wet ACRB
A	1.76	1.31	1.68	1.32
B	1.66	1.445	1.59	1.59
D	2.55	4.15	-	1.71

Table 17: Ratio of highest to mean peak torques of first 100 cycles

4 Conclusions and Outlook

Depending on the grease type the tests result in wear tracks on the bearing raceways. The reddish colors and material spectroscopy undertaken for ACBB in [STA24b] indicate tribocorrosion as damage mechanism. The friction torque increases due to the higher surface roughness and adhesive processes. The displayed condition of the raceways would not endanger the safe operation of a pitch bearing on a real wind turbine but can promote rolling contact fatigue damage. If the initial wear turns into abrasive processes that create macroscopic false brinelling it can endanger the pitch

drive's ability to rotate the bearing. In such a case, moving the rolling bodies out of the false brinelling dents needs significant torque. A more unlikely critical case is indicated by the tests with grease D. The adhesive wear can increase the torque up to a level the pitch drive cannot handle anymore. A measure of the relative increase during the test can help in the design of pitch drives. Positive short-term effects of water content for grease A and B are shown. Friction torque and raceway changes are reduced with added water. This is similar to results with ACBBs. For grease D, it is not possible to draw a conclusion based on the tests in the present study, as tests in dry conditions were not part of the test program.

The present study attempts to use custom angular contact roller bearings for scaled tests of roller-type pitch bearings of wind turbines. It further aims at evaluating the aptitude of different commercially available greases to prevent wear of roller-type pitch bearings raceways under wind turbine operating conditions. To this end, three different greases were tested in 'dry' - without added water - and 'wet' - with 10 mass % of demineralized water added - conditions. The tests were done with type 3x220 customized angular contact roller bearings under a static contact pressure of 2 GPa. The bearings are designed to have geometrical slip in the contact. The servo drive of the test rig reproduced scaled pitch angles of worst-case turbine operation close to rated speed with active load mitigation control. In line with results presented by BAYER [BAY23], greases A and D displayed optically more pronounced wear in roller than in ball bearings, whereas B showed reduced raceway wear. Although the 3x220 have significantly lower relative slip than the CRTB used by BAYER the optical impressions of wear are very similar.

Within the scope of these tests and for the purpose of preventing wear in oscillating operation of pitch bearings with line contacts, grease B is the most promising candidate. Its most notable difference to the other greases is the significantly lower base oil viscosity. It remains for future extensions of the tests to verify if this characteristic is decisive for the different results. The scope of testing was limited to short-term, room temperature tests and a very high water content. A further expansion of the test series with different temperatures, long-term tests and different water levels in the grease is planned for future works and will allow to draw more substantial conclusions for pitch bearing operation. The level of relative slip leaves further potential for exploration.

5 Bibliography

[BAR23] Bartschat, A., Behnke, K., Stammler, M. (2023) The effect of site-specific wind conditions and individual pitch control on wear of blade bearings. Wind Energ. Sci., 8 (10), 1495–1510

[BAY23] Bayer, G., Bartschat, A., Wandel, S., Baust, S., Poll, G. (2023) Experimental Investigations on Wear in Oscillating Grease-Lubricated Rolling Element Bearings of Different Size and Type. Lubricants, 11 (3), 120.

[BRE73] Lagerlebensdauer bei Schwingungsbeanspruchung. SKF Kugellager-Zeitschrift (174).

[CAV20] Cavacece, F. et a. (2020) Roller bearing under high loaded oscillations: Life evolution and accommodation mechanisms. Tribology International, 147, 106278.

[FVA10] False Brinelling: Stillstehende fettgeschmierte Wälzlager unter dynamischer Belastung, Frankfurt.

[GLA59] Glaeser, W.A. (1959) The Development of Oscillatory Rolling-contact Bearings for Airframe Applications in the Temperature Range 300 F to 600 F, US Air Force.

[LIN22] Lin, C.-L. et al. (2022) Mitigation of False Brinelling in a Roller Bearing: A Case Study of Four Types of Greases. Tribol Lett, 70 (1).

[PIT61] Riffelbildung bei Wälzlagern infolge Stillstandserschütterungen. Technische Universität München. PhD thesis.

[PIT65] Fretting Corrosion Caused by Vibration With Rolling Bearings Stationary. Journal of Basic Engineering, 87 (3), 713–723.

[PRE23] La Presilla, R. de, Wandel, S., Stammler, M., Grebe, M., Poll, G., Glavatskih, S. (2023) Oscillating rolling element bearings: A review of tribotesting and analysis approaches. Tribology International, 188, 108805.

[STA18] Stammler, M., Reuter, A., Poll, G. (2018) Cycle counting of roller bearing oscillations – case study of wind turbine individual pitching system. Renewable Energy Focus, 25, 40–47.

[STA23] Stammler, M., Pasaribu, R., Rieper, U. (2023) Scaled Line Contact Tests of Wind Turbine Pitch Bearings, ELGI Annual Meeting Amsterdam

[STA24a] Stammler, M., Menck, O., Guo, Y., Keller, J. (2024) Wind Turbine Design Guideline DG03: Yaw and Pitch Bearings, NREL/TP-5000-89161, Golden, Colorado

[STA24b] Stammler, M., Ellerbrok, H., Pasaribu, R., Rieper, U. (2024) Short-Term Influence of Water Ingress on Wear in Pitch Bearings of Wind Turbines. Lubricants, 12 (9), 310.

Wind Turbine Blade Damage Detection using Drivetrain Monitoring Data

Sumit K Pal[1], Donatella Zappalá[1], Simon J Watson[1], Amir R Nejad[2], Jakob Gebel[2]

[1] Faculty of Aerospace Engineering, TU Delft, Kluyverweg 1, 2629 HS Delft, The Netherlands

[2] IMT, NTNU, Jonsvannsveien 82, 7050 Trondheim, Norway

Keywords: *Blade Damage Detection, Condition Monitoring Signals, Drivetrain, DTU 10MW*

Abstract: This paper studies the sensitivity of drivetrain condition monitoring system (CMS) signals to blade damage. This is achieved using a decoupled simulation between an aeroelastic solver and a drivetrain setup. First, aeroelastic simulations are performed in OpenFAST; then, the low-speed shaft (LSS) forces, moments, and tower top position vector are transferred to the drivetrain model. The drivetrain is modeled in the multi-body simulation environment SIMPACK. The blade damage is modeled in OpenFAST by reducing the stiffness both in the flap-wise and edgewise directions. The reference DTU-10MW onshore wind turbine is chosen as a test case. First, the effect of blade damage on LSS forces is analyzed. Then the drivetrain responses are analyzed from the SIMPACK simulations using virtual sensors placed at the main bearing, rear bearing and nacelle housing. It is observed that the damage in the blade mid-span region shows higher sensitivity compared to tip and root areas, with a clear correlation between LSS shear force and nacelle housing side-side velocity demonstrating damage progression as stiffness reduction increases.

1 Introduction

Wind turbine blades represent a substantial portion of the overall cost of a wind turbine and exhibit a notable failure rate in comparison to other components [ZAP22]. Blade failure reduces turbine yield or, in extreme cases, stops turbine operation and requires replacement, which is a time-consuming and costly operation involving heavy lift apparatus. Blade monitoring is often carried out by visual inspection, either from the ground, using drones, or by climbing along the blade itself. Such methods can detect external problems, but not the internal defects. In this study, a preliminary analysis of the effect of blade damage on drivetrain condition monitoring signals is presented to understand the extent to which these signals are sensitive to damage identification.

[FRE23] conducted a full scale wind turbine blade monitoring campaign for the detection of damage initiation and progression due to fatigue driven in-house testing. They demonstrated that detecting the initiation and progression of damage is possible with an actuator and a single vibration sensor positioned within 10 meters of the damage site. Recently, [VAR24] also presented an experimental campaign of fatigue damage propagation of a full scale wind turbine blade. However, deployment of such an array of sensors along the span of wind turbine blades is not feasible considering the cost and additional maintenance.

The popular damage detection methods for operational wind turbine blades include NDT techniques, such as thermography, ultrasonics, acoustic emissions, and vibration. Although these methods are effective in detecting and localizing damage, they remain both costly and time-consuming. Alternatively, the readily available CMS signals in operational wind turbines could be a possible option to leverage to monitor the blade damage progression.

This work studies the effects of wind turbine blade damage along various spans on drivetrain CMS signals. The goal of the paper is to provide an initial estimate of the sensitivity of wind turbine blade damage to drivetrain responses. In the current study, one damaged and two healthy conditioned blades are considered for all the cases. This leads to change in the first harmonic of the wind turbine rotational frequency (1P). Consequently, this paper focuses only on the change in 1P amplitude.

2 System Configuration

2.1 OpenFAST wind turbine model

OpenFAST is an open-source wind turbine simulation tool developed by NREL. It is a framework to couple aerodynamics, hydrodynamics, structural dynamics, control, and electrical system dynamics in the time domain. The aerodynamics module, AeroDyn 15, is used to calculate the aerodynamic loads applied on the blade, which is based on the Blade-Element/Momentum (BEM) theory. To calculate the loads on the blade due to certain given wind conditions, aerodynamic coefficients must be given as an input at different cross-sections of the blade. Structural dynamics of the tower and blades are dealt with the 'ElastoDyn' module, where modal coefficients, damping, and elastic modules of each degree of freedom are needed to provide as an input. 'ElastoDyn' module uses Finite-Element Method (FEM) approach in conjunction with analytical linearization. Fifteen degrees of freedom (dof) element with three internal and two boundary nodes is used. Tower and the blades are idealized as a Euler-Bernoulli beam with isotropic material. For the current study, the elastic coefficient at flap-wise and edge-wise directions is altered in the blade 'ElastoDyn' input to understand the sensitivity of any blade structural change on the drivetrain. The Reference Open Source Controller (ROSCO) was used in the setup, which uses collective pitch angle. Specifications of the DTU 10MW reference wind turbine are listed in Table 32. The detail of the coupling is discussed in the next subsection.

Parameter	Value
Rating	10 MW
Control	Variable speed, collective pitch, ROSCO
Rotor, Hub diameter (m)	178.3, 5.6
Hub height (m)	119.0
Cut-in, rated, and Cut-out wind speed (m/s)	4, 11.4, and 25
Cut-in, Rated rotor speed (RPM)	6, 9.6
Hub Overhang (m)	7.1
Shaft tilt angle (deg)	5.0
Pre-cone angle (deg)	-2.5
Rotor mass (kg)	227962
Nacelle mass (kg)	446036
Tower mass (kg)	628442

Table 32: Specifications of the DTU 10 MW RWT [BAK13]

2.2 SIMPACK drivetrain model

In Figure 114, the layout of the drivetrain model used in this research is shown. A detailed study about this drivetrain model can be found in [WAN19]. The drivetrain has four-point support and integrates a 3-stage gearbox. In the first and second planetary stages, ring gears are fixed on the gearbox housing, which is supported on the bedplate via torque arms. Input torque is applied on the planet carriers and sun gears serve as the output torque. In the third parallel stage, the torque is delivered from the sun gear of the second planetary stage to generator through the gear pair (Gear-

Pinion) in the high-speed stage. Thus, high torque from low-speed shaft is transformed into low torque in high-speed shaft. Gear teeth contact is modelled by a specific force element FE225 in SIMPACK, where the contact force is composed of stiffness, damping, and friction terms. The gears and shafts inside the gearbox are treated as rigid bodies. Specifications of the drivetrain are mentioned in the Table 33.

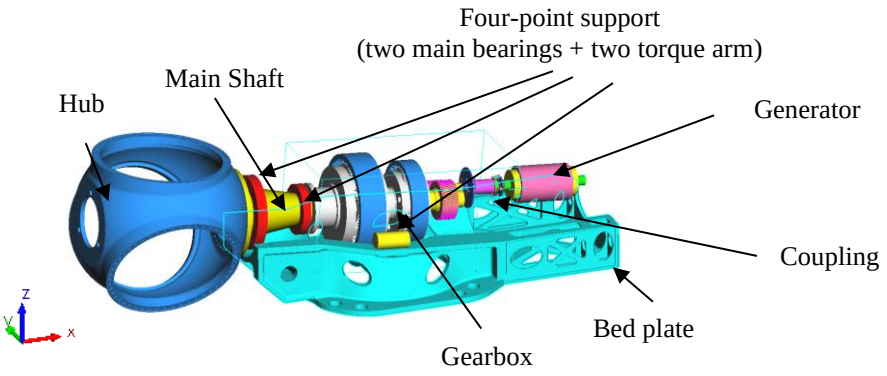

Figure 114: DTU 10 MW drivetrain model [WAN19]

Parameter	Value
Drivetrain type	Four-point support
Gearbox type	Two planetary + one parallel
First stage ratio	1:4.423
Second stage ratio	1:5.192
Third stage ratio	1:2.179
Total ratio	1:50.039
Rated input shaft speed (rpm)	9.6
Rated generator shaft speed (rpm)	480.4
Rated input shaft torque (kN-m)	9947.9
Rated generator shaft torque (kN-m)	198.8
Gearbox mass (tonne)	60.43
Bedplate mass (tonne)	102.39
Equivalent drive-shaft torsional-spring constant (Nm/rad)	2317025352
Equivalent drive-shaft torsional-damping constant (Nm/(rad/s))	9240560

Table 33: Drivetrain specifications of DTU 10 MW [WAN19]

2.3 Coupling

To investigate the sensitivity of the drivetrain dynamics to blade damage, a decoupled simulation approach between rotor and drivetrain dynamics is adopted in this paper. The coupling is illustrated in Figure 115. The rotor dynamics are first simulated in OpenFAST, with a simplified drivetrain setup, and the tower top position ($\vec{X}$), low speed shaft (LSS) force, LSS moment ($\vec{F}, \vec{M}$), and generator speed are used as input to the SIMPACK drivetrain setup. A proportional-integral (PI) controller is used between the input generator speed (ω_{Gen}) from OpenFAST and resulted generator speed in SIMPACK due to applied loads and tower top motion. This is to maintain the same dynamic condition between two independent models.

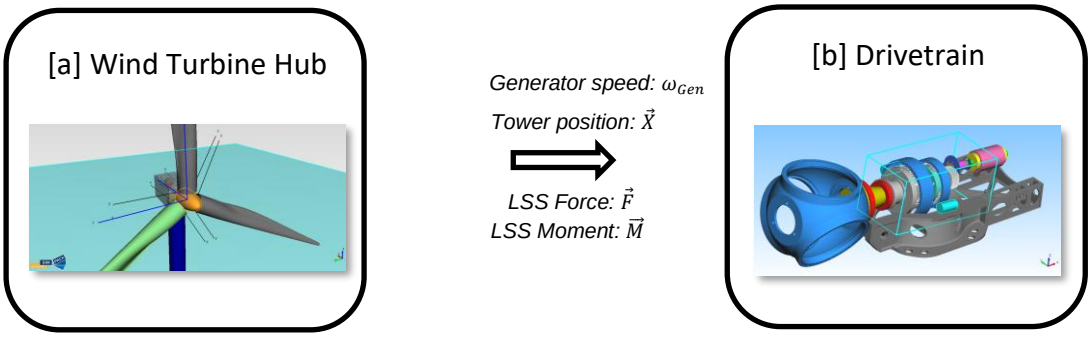

Figure 115: Flowchart of the proposed decoupled simulation approach

2.4 Blade damage model

To study the effect of blade damage on the drivetrain system, the blade stiffness in flap and edge-wise directions is reduced in the range of 0.1-1% from its initial value (healthy conditions) [KHO22]. As the damping is related to the stiffness of the structure, it needs to be adjusted as well (Eq. 1). The relationship between critical damping factor and stiffness proportional damping (Rayleigh damping) can be written as

$$\beta_j = {}^{\zeta_j}/_{\pi\omega_j} \qquad \textbf{Eq. 1}$$

Where, j^{th} mode natural frequency, $\omega_j = (1/2\pi)\sqrt{K_{jj}/M_{jj}}$, K_{jj} and M_{jj} are j^{th} mode stiffness and mass terms, $\beta =$ Stiffness proportional damping co-efficient, ζ_j = critical damping factor for j^{th} mode.

The effect of stiffness change can be incorporated to the critical damping ratio in comparison to the healthy blade as follows:

Step 1: Derive β_j from Eq. 1, corresponding to the original stiffness distribution. Step 2: Then calculate the natural frequency due to changed stiffness distribution. Step 3: Recalculate the ζ_j due to modified ω_j. β_j is assumed to be constant.

In the current setup, although the stiffness can be altered locally, changing the modal damping affects the global mode only. The different damage conditions simulated in this study are listed in Table 34, showcasing 378 simulations in total. For all the cases mentioned in Table 34, a separate damping ratio is calculated based on the steps above.

Flap/ Edge Stiffness Change (%)	Length of Damage (m)	Locations from Root (m)
-0.1	1.0	9 locations from 5 m to 85 m with 10 m gap
-0.5	1.0	9 locations from 5 m to 85 m with 10 m gap
-1.0	1.0	9 locations from 5 m to 85 m with 10 m gap

Table 34: Different damage conditions at a particular blade

2.5 Signal processing

All the cases mentioned in Table 34 are simulated for 3000 s, of which the initial 1500 s is discarded to avoid the initial transient phase. Further, the remaining signal is divided into several segments to pick 1P amplitude and calculate mean and standard deviation. From these individual standard deviation of 1P values at different time segments, error bars are calculated based on the concept of

propagation of error to represent as a combined error of healthy and faulty states. Only steady state wind conditions with no vertical shear is considered in this paper.

3 Results and Discussions

The proposed sensitivity analysis is divided into two parts. In the first sub-section, the system dynamic response corresponding to the rotor side is analyzed. Later, drivetrain system responses are investigated.

3.1 Rotor Dynamics

LSS forces and moments are first analyzed to understand the effect of blade local stiffness changes in comparison to the healthy conditions. In Figure 116, the absolute differences of the 1P component of the LSS shear force at side-side direction (F_{ys}) with respect to fixed reference frame between healthy and damage conditions are plotted across different blade spans and wind speeds. There are total 9 bar groups corresponding to 9 locations from blade root to tip. Each bar group has 7 wind speeds, from 8 to 25 m/s chronologically. The magnitude of each bar is plotted cumulatively for the cases 0.1-1% stiffness change. It is noticeable from Figure 116(a) that 1P harmonic of LSS F_{ys} is more sensitive to flap-wise stiffness changes at around the blade mid-span (~45 m) and at the rated wind speed. This may be because the middle of the blade span is more susceptible to maximum bending stresses.

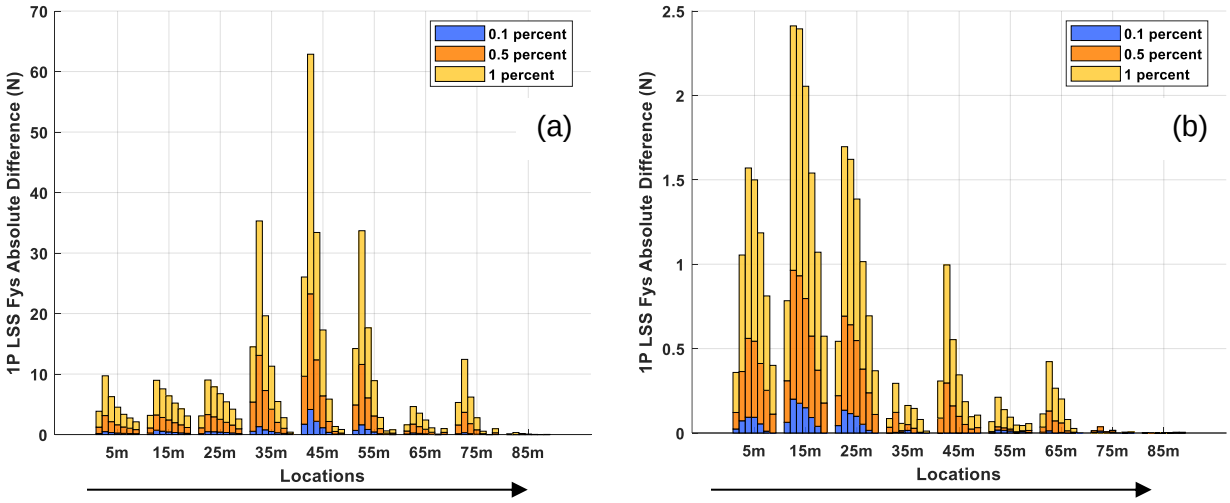

Figure 116: Change in 1P LSS F_{ys} due to change in blade (a) flap-wise (b) edge-wise stiffness at different span from root for the wind speeds 8, 11.4, 13, 15, 18, 21, 25 m/s.

While a 1% stiffness change contributes to around 30 - 40 N change in the 1P peak amplitude of LSS F_{ys} in the flap-wise direction (~45m with rated wind condition, Figure 116(a)), it only contributes to a 1-1.5 N increase in the edge-wise direction (~ 15m with rated wind condition, Figure 116(b)). From Figure 116(a), it can also be noticed that a 0.1% flap-wise stiffness reduction alters the 1P harmonic amplitude by only 4.5 N (~45m with rated wind condition). From both subplots, it can be concluded that the blade damage associated with flap-wise or edge-wise stiffness reduction close to the blade tip contributes significantly less to the change of 1P harmonic. Therefore, in this case, in the absence of additional information, it can be difficult to distinguish the blade tip damage only

from the amplitude of the 1P harmonic. A similar conclusion can be made for damage near the blade root (Figure 116(a)).

3.2 Drivetrain Response Analysis

In Figure 117(a), the absolute differences in the 1P harmonic amplitudes between healthy and damage blades, corresponding to flap-wise stiffness changes at 45 m from the blade root, are plotted for the nacelle housing side-side velocity, main (INP_A: Input A) and rear (INP_B: Input B) bearing side-side velocity. The absolute difference of the 1P amplitudes (Figure 117(a-c)) shows a prominent peak at around the rated wind speed, which was also observed in LSS F_{ys} in Figure 116(a). However, it can be noticed that while the different stages of stiffness change 0.1 - 1.0 % were distinctly visible in the case of LSS F_{ys}, this is not the case for the drivetrain signals shown in Figure 117. Only a similar trend is visible for the 1% stiffness change, while the 0.5% and 0.1% cases show mixed trends.

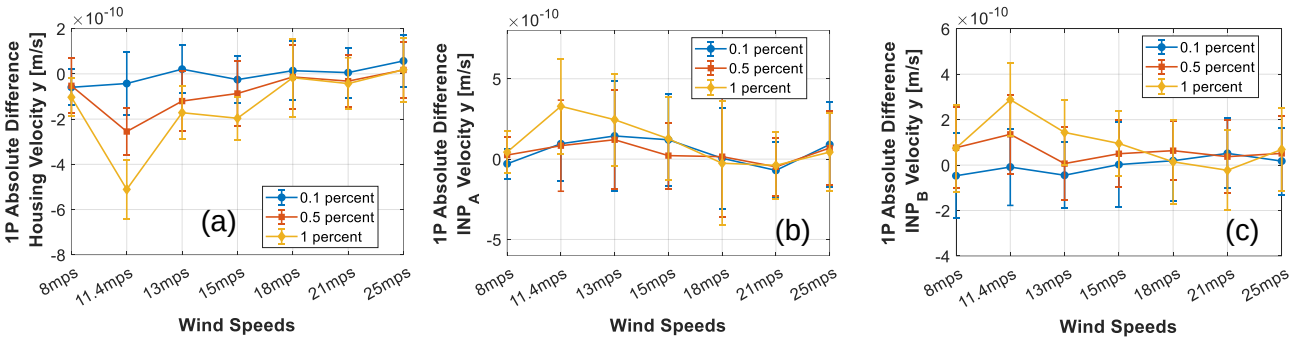

Figure 117: 1P amplitude absolute difference in the (a) nacelle housing side-side velocity, (b) main (INP_A) and (c) rear (INP_B) bearing side-side velocity at different wind speeds due to blade flap-wise stiffness changes at 45m from blade root.

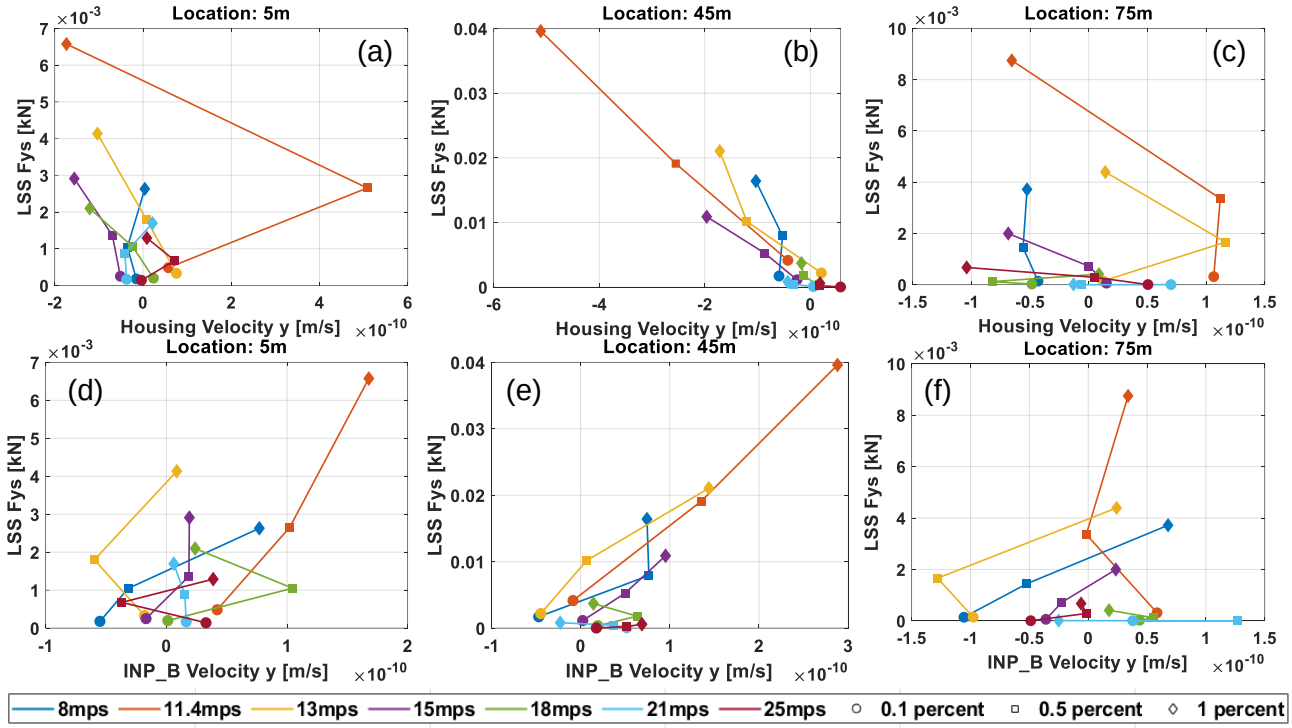

Figure 118: 1P amplitude absolute difference correlation between LSS F_{ys} and nacelle housing side-side velocity at (a) 5 m, (b) 45 m, and (c) 75 m from blade root; LSS F_{ys} and rear bearing (INP_B) side-side velocity at (d) 5 m (e) 45 m (f) 75 m from blade root, due to different stages of the flap-wise stiffness reduction.

In Figure 118, the correlation between 1P amplitude absolute difference of LSS F_{ys} and different drivetrain responses is presented for three different locations 5 m (a, d), 45 m (b, e) and 75 m (c, f) from blade root for flap-wise stiffness reduction. The figure shows how the system responses translate from the local damage in a wind turbine blade to the different drivetrain components. From Figure 118(b, e), it can be noticed that in most wind speeds, the drivetrain response increases with LSS F_{ys}, and showing clear damage progression due to flap-wise stiffness reduction 0.1 - 1% at 45 m blade span. However, the damage progression for the location near the blade root (Figure 118 (a, d)) and blade tip (Figure 118 (c, f)) does not show a consistent trend. This is because, the changes in the 1P amplitudes of the input LSS forces to the drivetrain model are significantly lower (Figure 116 (a)) compared to the midspan location, and, as a result, the numerical noise unknowingly dominates.

4 Conclusions

In this paper, the effect of wind turbine blade local stiffness reduction on drivetrain CMS signals was studied for the DTU 10MW reference wind turbine. A decoupled approach between an aeroelastic solver and an independent drivetrain model was chosen to achieve the proposed goal. Only, the change in 1P frequency amplitude was considered in this study, as an initial step in the investigation. First, the effect of blade local stiffness change on the rotor dynamics was investigated by analyzing the absolute difference in the 1P peak amplitudes of the LSS side-side shear force. Results showed that, compared to the blade tip and root regions, the mid-span region is the most sensitive to the same amount of damage. The maximum absolute change in the 1P peak amplitudes was observed at the wind speed near rated condition. Also for LSS side-side shear force, a 1% change in flap-wise stiffness was around 25 times more sensitive than the same change in the edge-wise stiffness. This can be attributed to the fact that the blade edge-wise direction is stiffer than the flap-wise one.

Thereafter, the simulated LSS shear forces, moments, and tower top position vector were transferred to the independent drivetrain setup in the SIMPACK multibody-dynamics platform. The absolute difference of 1P peak amplitude of nacelle housing, main and rear bearing side-side velocities between healthy and damage cases were analyzed. As in the case of the LSS side-side shear force, drivetrain responses also showed prominent peak at rated wind speed. It was also noticed that for below 1.0% flap-wise stiffness change, the signal trends had mixed behaviors. Considering the magnitude of the error bars, a longer simulation time might be needed.

The correlation between the LSS side-side shear force and the nacelle housing, rear bearing side-side velocities at a 45 m location (blade mid-span) has shown clear progression of damage with increasing stiffness reduction from 0.1% to 1.0%. The behaviors at the blade root and tip positions showed mixed trend. This may be because a little change in LSS forces (~ 1-5 N) compared to midspan location might fall in the region of numerical errors.

5 Bibliography

[BAK13] Bak, C., Zahle, F., Bitsche, R., Kim, T., Yde, A., Henriksen, L. C., Hansen, M. H., Blasques, J. P. A. A., Gaunaa, M., and Natarajan, A.: The DTU 10-MW Reference Wind Turbine, 2013.

[FRE23] Fremmelev, M. A., Ladpli, P., Orlowitz, E., Dervilis, N., McGugan, M., and Branner, K.: A full-scale wind turbine blade monitoring campaign: detection of damage initiation and progression using medium-frequency active vibrations, Structural Health Monitoring, 22, 4171–4193, 2023.

[KHO22] Khoshmanesh, S., Watson, S. J., and Zarouchas, D.: The effect of the fatigue damage accumulation process on the damping and stiffness properties of adhesively bonded composite structures, Composite Structures, 287, 115328, 2022.

[VAR24] Varouxis, T., Dertimanis, V. K., Abdallah, I., Chatzi, E., Pakrashi, V., and Malekjafarian, A.: Deep-Learning-based damage detection of an experimentally tested full-scale wind turbine blade., eJNDT, 29, 2024.

[WAN19] Wang, S., Nejad, A. R., and Moan, T.: On Initial Design and Modelling of a 10 MW Medium Speed Drivetrain for Offshore Wind Turbines, J. Phys.: Conf. Ser., 1356, 012024, 2019.

[ZAP22] Zappalá, D. and Tavner, P. J.: Wind Turbine Reliability - Maintenance Strategies, in: Comprehensive Renewable Energy, Elsevier, 353–370, 2022.

Technical Challenges of a High-Power Hardware-in-the-Loop Test Bench for Validating Wind Power Full-Scale Converters

M. Fischer, J.-M. Hördler, D. Epping, D. Henkelüdeke, L.-M. Reichelt, S. Özer

dSPACE GmbH, Rathenaustraße 26, 33102 Paderborn

Keywords: *power hardware-in-the-hoop, full-scale converter, validation, power level*

Abstract: This contribution highlights the technical challenges of a power hardware-in-the-loop (HIL) system which is used for the certification testing of a full-scale converter of a wind turbine. The electrical behavior of the generator and the supplied grid is emulated at high-power level representing the environment of the device-under-test converter. For this purpose, real-time models simulate the behavior of the generator and the grid. Corresponding reference values are transmitted via a high-speed interface to electrical load modules as power amplifiers which emulate the environment behavior at high-power level.

Within this paper, the concrete design of this power HIL test bench and the dimensioning for this use case are analyzed. Requirements for the load modules and their actual, compact implementation are discussed and advantages of this modular approach are highlighted. The high-power level of the test bench poses further challenges for which feasible solutions are presented. Power recovery via a common DC link bus of all load modules leads to a significantly reduced supply power from the feeding grid and a smaller dimensioning of the bidirectional test bench in-feed unit. The concept is extended by a supercapacitor bank to emulate test cases such as the fault ride through (FRT). The spatial expansion of the overall test bench leads to further challenges that make a low-inductance and interference-free connection of the components indispensable. Moreover, electromagnetic compatibility (EMC) and safety aspects play an important role, especially with high currents, voltages, and frequencies.

1 Introduction

The increasing demand for wind energy necessitates the construction of numerous wind turbines and the development of new models. To ensure that a wind turbine's electrical output values meet established standards, the wind turbine must pass grid compliance tests before becoming operational. Certification testing in the field is both time-consuming and technically challenging. Alternatively, nacelle test benches have been thoroughly researched and widely utilized for this purpose [KLE23]. The nacelle consisting of full-scale converter and the generator is mounted on a test bed, see Figure 1. A powerful load machine is mechanically coupled to the generator in order to set variable speed-torque characteristics emulating different wind conditions. The device under test (DUT) converter converts the generated power into a suitable three-phase voltage system in order to feed it into the grid. The setup of such nacelle test benches is highly expensive and the electrical and mechanical parameters of the generator as well as the electrical behavior of the grid cannot be varied flexibly. Moreover, nacelle test benches can only be set up when the final prototype is available in hardware. With the goal of decreasing costs and avoiding bottlenecks in the development and validation process, component test benches in the form of power HIL test benches are gaining

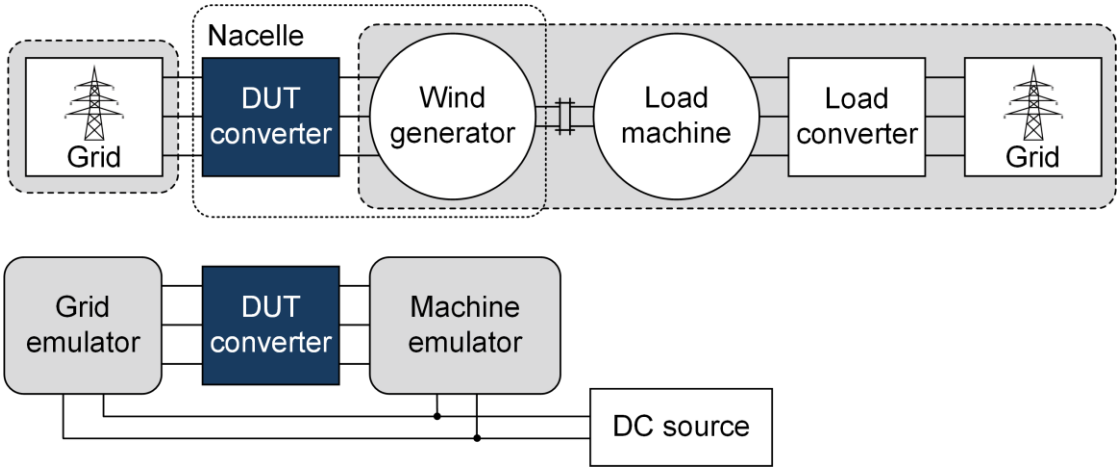

Figure 1: Comparison between nacelle test bench (top) and power HIL test bench (bottom)

prominence. In this setup, only the wind turbine's grid interface, the full-scale converter, is tested. It is connected to a power electronics device which emulates the electrical behavior of the grid and the generator in real time at full power level, see Figure 1. To achieve this, three major components are necessary:

- Real-time models of grid and generator, which calculate the electrical behavior of the investigated grid and generator depending on generator parameters, wind conditions, rotor aerodynamics, the DUT inverter's switching behavior, and failures in the grid,
- A control unit, which controls the power electronics device, so that the same load currents occur as in the nacelle test bench, and
- The power electronics device itself, which adjusts the desired load currents.

The power HIL power electronics device has to meet important demands regarding emulation accuracy and withstand voltage. Especially the dimensioning for described high-power use cases entails a number of challenges, like the supply of the overall test bench, low-inductance and interference-free connection of the components.

The following paper presents an approach for a component test bench, respectively a power HIL test bench for a full-scale converter of a type 4 wind turbine with synchronous generator. After introducing a modular approach for the general power HIL use case, the paper focuses on solutions for these challenges that this high-power use case entails.

2 Electronic Load Module

The power HIL test bench is realized by using a modular architecture. Electronic load modules serve as the power interface between the DUT and the real-time system. They consist not only of the power electronics devices but also of a decentral current control system in which each load module can be considered as a high-dynamic, bidirectional current sink and source. The real-time system only has to transmit the reference values of the current to the load modules.

In a power HIL application, the power electronics of the load modules must address several challenges: managing HV levels with DC voltages up to 1,500 V, delivering high output current with a bandwidth of a few kHz, enabling bidirectional power flow, minimizing unintentional current ripple, and ensuring modularity for parallel operation of multiple modules. Additionally, the electronic load

modules need to support any possible electrical operation point. Therefore, systems with derating functions, such as power hyperbola, are unsuitable for the emulation purpose.

A suitable topology for these requirements is a multi-branch three-level neutral-point clamped (NPC) inverter, as shown in Figure 2. Compared to a conventional two-level inverter, the additional output voltage levels reduce the total harmonic distortion of the currents. Furthermore, in each switching state, the internal DC link voltage V_{DC} of the system drops across at least two switches, so each switch only needs to handle half the DC link voltage. The switches are implemented as fast-switching silicon-carbide MOSFETs. Each module connects three NPC half-bridge branches in parallel, allowing the output current to be three times higher than the maximum current of a single branch. The three branches are paired with three differential-mode chokes. If the current is evenly distributed among the three branches, the magnetic flux inside the differential-mode chokes will be nearly zero, and only the choke's magnetic leakage flux will be effective. However, in the case of asymmetric distribution, the resulting magnetic flux creates an inductance that counteracts the asymmetry. As a result, based on the switching states of the three branches, the output voltage v_{Mod} at the common coupling point can take on seven discrete voltage levels:

$$v_{Mod} = \pm \frac{k}{6} \cdot V_{DC}$$

with $k = \{0, 1, 2, 3\}$

Following the coupling point, an additional coupling inductance L_C is connected in series, serving as a control path between the DUT inverter and the load modules.

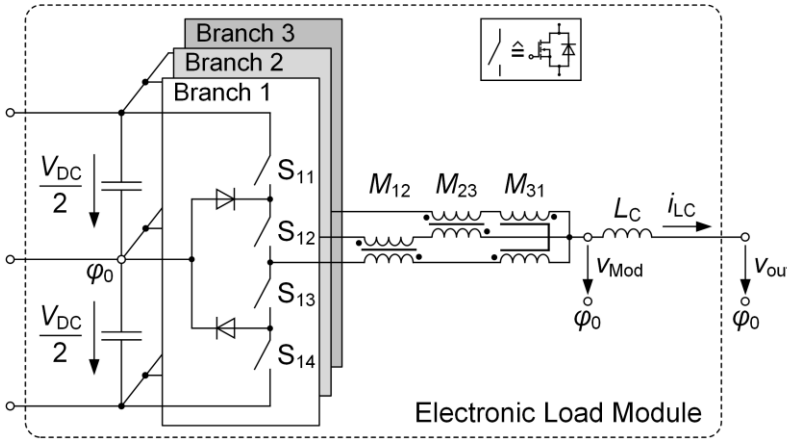

Figure 2: Schematic of an implemented load module

The implementation of the current controller and further mechanisms to symmetrize the branch currents and to ensure a very fast reaction time to a change of the DUT's switching state are described in [MEY17] and [FIS22].

Each load module can be used bidirectionally for both DC and AC functions. The output behavior is fully defined by the real-time model. Figure 3 shows the implementation of a single load module. Each module can output voltages up to 1,250 V and continuous currents up to 75 A_{RMS}. Because each load module has decentral current control, any number of load modules can be connected in parallel, thereby increasing the total output power of the individual function and correspondingly of the test bench, as required. It is also possible to easily increase the system power at a later point by adding further modules.

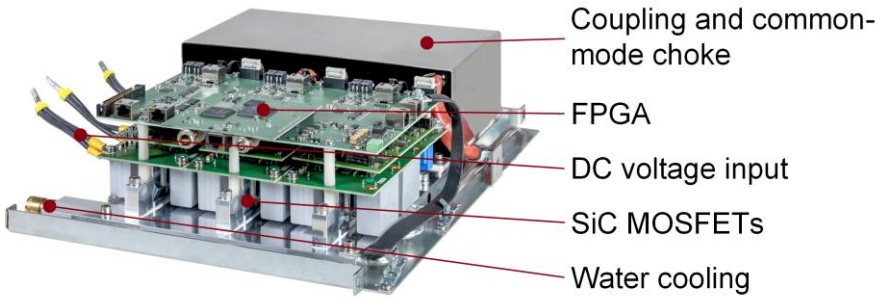

Figure 3: Setup of the realized load module

The modular approach is therefore highly suitable for covering high-power applications.

3 Overview of the Realized Power HIL Component Test Bench

3.1 General Description of the Component Test Bench

Figure 4 illustrates the schematic diagram of the power HIL system. All power interfaces of the DUT converter are connected to load modules. The design for the test bench explained in this paper is dimensioned so that RMS currents of up to 1,200 A can be set for each grid and generator phase. This leads to a parallel connection of 16 load modules per function. With a maximum phase-to-phase voltage of 1,250 V, the maximum power on each grid and generator side is 1.84 MW.

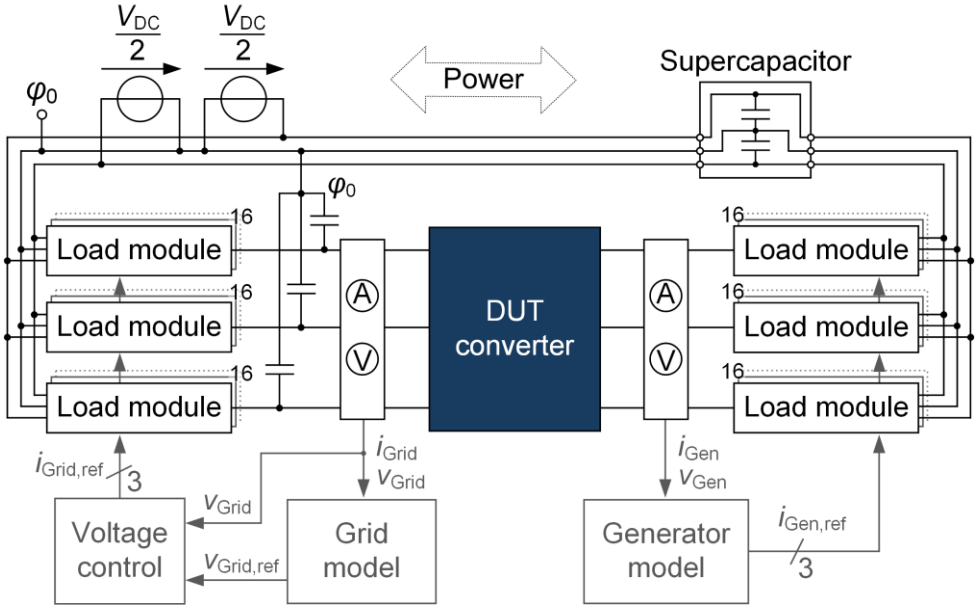

Figure 4: Overview diagram of the entire component test bench

The load modules at the grid terminals of the DUT converter emulate grid behavior. By measuring all three phase currents, the grid model can calculate the values for the grid state variables and evaluate the voltages of the simulated grid in real time. The output voltages of the grid model serve as reference values for an outer loop of a cascaded control, whose task is to control the voltages across the phase capacitors installed between the load modules and the reference potential φ_0. The voltage controller calculates the currents, which are needed to control the voltage across the phase capacitors, and transmits these to the decentral current control units implemented on the load modules of the grid side.

The load modules at the three generator terminals of the DUT converter mimic the behavior of the investigated generator. Based on the measured voltages as well as the previous state variables of the generator model, the current state of the emulated generator, especially its output currents, are calculated. Additionally, the model provides all relevant interfaces, such as communication or position sensor simulation. The reference currents are transmitted to the current control units implemented on the load modules of the generator side.

The real-time models are not explained in detail in this publication. As the load modules can be used bidirectionally for both AC and DC functions, any model can be implemented as a reference value

specification. The more detail in which the models describe the grid and generator, the more accurately the component test bench can emulate their behavior. The only restriction is that all models must be able to be executed in real time on an FPGA.

All load modules both on grid and generator side are supplied via a common DC link bus. This enables a circulating power flow. In usual operation, the load modules on generator side feed power to the load modules on grid side via the full-scale converter. This power is fed back into a common DC link and can be reused on the generator side. Consequently, the power circulates and the supply unit only compensates the system's power losses. They are made up of the losses for the total 96 load modules and the losses of the full-scale converter. Therefore, the grid connection power can be significantly lower than the total power of the test bench. Additional supercapacitors are implemented in the internal DC link to handle the special test case “fault ride through”, see section 4.1.

3.2 Realization of the Component Test Bench

Figure 5 shows the setup of the component test bench. The grid supply cabinet connects the system to the grid interface of the laboratory and powers all components of the test bench. Fuses and the main switch are part of this cabinet.

Figure 5: Setup of the entire component test bench in the laboratory

The DC link supply cabinet is the carrier for the high-voltage power packs to establish an internal DC link voltage of maximum V_{DC} = 1,500 V. As described in section 3.1 only the power losses must be covered. A worst-case estimation details the losses per single load module to 540 W respectively 51.8 kW for all 96 load modules. The maximum losses of the specific DUT converter are approximately 53.6 kW. Hence, total losses of 105.4 kW have to be covered. This can be achieved with eight 15 kW power supply units. All in all, it shows the amount of effectiveness as 120 kW power is needed to supply a 1.84 MW test bench.

In total, six load module cabinets (four more are in the back row) serve as housing for 96 load modules. Figure 6 gives an insight into one of these cabinets. All modules belonging to the same function are connected in parallel. The parallel connections from all six cabinets are collected in the connection cabinet which functions as main power interface to the DUT converter. The real-time cabinet accommodates the real-time system consisting of real-time processor and FPGA. The models running on these components define the electric behavior at the output clamps of the power HIL test bench. Moreover, this unit serves as an interface to the host PC in order to start measurement routines or to manipulate model parameters – also during runtime.

Figure 6: Insight into the load module cabinet

4 Challenges of the High-Power Component Test Bench

4.1 Fault Ride Through

The scenario in which the grid is suddenly switched off due to a fault, but the generator continues to generate power due to mechanical inertia, is called fault ride through (FRT). This operating point must also be covered in the certification tests. In the FRT case, the specific DUT converter switches in a 1.5 MW chopper resistor for 150 ms. The generated power is converted into heat and no longer reaches the grid side of the power HIL. From now on, the described design of the test bench reaches a limit, as the concept of circulating power flow no longer applies. However, increasing the number of high-voltage power supply units is largely uneconomical. Instead, the internal DC link is supported by several supercapacitors to cushion the short-term FRT case and minimize the voltage drop in the internal DC link.

In the final design, 10 supercapacitor cells each with C_{SK} = 62 F were connected in series to ensure dielectric strength. The effective capacity of 6.2 F leads to a worst-case voltage drop of ΔV_{DC} = 23 V. This is tolerable for the FRT case, as the decentralized current controllers of the load modules are fast enough to correct the fault at the output terminals of the modules as long as there is enough control reserve.

4.2 Spatial Expansion of the Overall Test Bench

The spatial expansion of the overall test bench makes a low-inductance and interference-free connection of the components indispensable. In the laboratory installation plan, care is taken to ensure that the load module cabinets are positioned very close to each other and that the cabling to the

connection cabinet is kept as short as possible. In addition, the functions of each load module cabinet are assigned equally to generator and mains modules in order to keep the common mode current as low as possible. The cabinets are also equipped with common-mode chokes, which further increase the common-mode impedance and reduce the amount of interference.

On signal side, the power HIL benefits from the modular approach with decentral current controllers and the fact that the reference values of the modules are transmitted via fiber-optic cables into an electrically isolated, FPGA-based, high-speed interface. This guarantees synchronous control of all modules regardless of the cable length.

4.3 Electromagnetic Compatibility (EMC)

To ensure EMC in the described high-power use case, several countermeasures are implemented.

The emulation of wind power generators with a high number of pole pairs results in high electrical rotation frequencies. In conjunction with high currents, magnetic fields circulating around the conductors generate iron losses in ferromagnetic materials in the immediate surroundings of the conductors. Stainless steel is used at critical points where components cannot be protected by sufficient distance from the conductors.

Due to its switched-mode operation, high slew rates of the DUT converter's output voltages occur. This, together with the parasitic capacitance of the real generator, usually results in common-mode currents against the earth potential. Therefore, filter components in the DUT converter are designed specifically to suppress these earth currents.

The spatial expansion of the component test bench also leads to an unavoidable parasitic capacitance against the earth potential which differs from that of the real generator. Consequently, the filter design does not match the application. Without countermeasures, the currents may be higher and the internal filters may be overloaded and damaged. The power HIL system therefore uses high-speed detection to measure the switching state of the DUT converter directly at its output terminals within a few ns and uses the high bandwidth of the load modules to prevent the appearance of this common-mode current. Moreover, as described in section 4.2, common-mode chokes are installed to increase the common-mode impedance.

Shielding plays an important role, too. The entire power electronics including cabling and cable ducts are located in a metal housing to suppress emitted interference waves.

Attention is also paid to interference-free recording of the measured variables in the measuring circuits. Power and signal lines are laid separately from each other. Common-mode filters and differential evaluation of the measuring transducers ensure less susceptibility to interference. In addition, all measurement signals are digitally filtered on the FPGA.

5 Summary

This paper describes the design of a power HIL component test bench used for the certification testing of a full-scale converter of a wind turbine. Especially the modular approach described above gives the freedom to tailor the system to high-power applications. A circulating power flow between all load modules ensures a highly efficient operation of the test bench and a power supply of only the power losses.

The setup of the realized load modules is described in detail. Moreover, challenges, which result from the high-power application, are described and proposed solutions are formulated.

6 Bibliography

[FIS22] Fischer, Manuel et al.: High-Bandwidth Power Hardware-in-the-Loop for Motor and Battery Emulation at High Voltage Levels
In: EPE Europe, 2022.

[KLE23] Klein, Andreas; Basler, Maximilian; Abel, Dirk: Pitfalls of testing wind turbine control algorithms on nacelle test benches.
In: Forschung im Ingenieurwesen 87(1), pp. 83–91, 2023.
https://doi.org/10.1007/s10010-023-00620-7

[MEY17] Meyer, Gerrit: Enhanced Power Electronics System for High-Performance Testing of Motor Control Units in a Power HIL Environment
In: PCIM Asia 2017, pp. 1-8, 2017.

Combination of machine learning methods and micromagnetic properties of ferromagnetic steels for grinding burn detection of large gears

O. Kowollik, S. J. Lüling, C. Radek, U. Seuthe, U. E. Wiebelitz

QASS GmbH, Schöllinger Feld 28, 58300 Wetter

Keywords: *Grinding Burn Detection, Machine Learning, Barkhausen Noise, Non-Destructive Testing*

Abstract: Detection of grinding burn using micromagnetic methods is state of the art for non-destructive testing of gear grinded surfaces. An alternating magnetic-electric field is brought into contact with the magnetically effective areas (domains) of ferromagnetic steel. The interaction between the magnetic field and the steel is measured in the form of resulting voltage pulses. The presence of grinding burn causes a measurable change in the magnetic flux density due to the change in the material properties of hardness and residual stress. The intended paper shows the new and extended state of the art. On the sensor side, a new concept has been developed for gears. The excitation elements of the sensors are interchangeable and adaptable to the tooth geometry. Additional measuring channels have been integrated to determine physical units. The sensors are equipped with distance sensors to enable contactless measurement at high speeds. On the hardware side, the amplifier modules are now capable of generating magnetic field frequencies of up to 4 kHz to reliably differentiate between new hardening zones and tempering zones. In terms of data analysis, machine learning methods are used to detect grinding burn using a contactless sensor system. One problem in the past has been the high learning effort required to compensate distance, geometry or alloy influences. In future, the measurement results will be processed like images. So-called representers of more than 1000 individual measurements are summarized, improving the informative value of micromagnetic measurements and reducing the storage depth. The use of Python as a data analysis module on a measuring device itself enables optimum customization to the required measuring task. The analysis can be comprehensively trained and developed externally and then implemented in the measuring device and on the process.

1 Introduction

Grinding burn is one of the most critical defects in the manufacture of gear components. Grinding burn occurs, for example, in grinding processes where too much process energy is introduced into the component in the form of heat that is not removed by cooling (e.g. due to complex geometries or failure of the cooling lubricant). This is therefore mainly thermal damage caused by improper process management. The heat input leads to localised changes in residual stresses, a reduction in hardness and, in the worst case, the formation of a new hardness zone of nanocrystalline, glass-hard martensite on the component surface [SEI2020]. Grinding burn is particularly problematic when it occurs in mechanically stressed areas. Both the reduction in hardness and the formation of a new hardness zone increase the risk of premature wear and possible component failure.

Individual failures also represent a significant cost risk, particularly in large systems such as wind turbines, where testing and repair is often time-consuming. 100% control of gear production is one way to minimise the risk of grinding burn failure.

The classic method for testing components for grinding burn is wet etching according to ISO 14014 [SEI2020, HE2019]. This wet chemical process is very time consuming and uses corrosive and environmentally hazardous chemicals such as nitric acid. In particular, the subsequent visual assessment is a potential problem in terms of process reliability. Small defects can be missed. Damage that is not fully developed can be perceived differently depending on the viewing angle and lighting conditions.

The autonomous robot-assisted Barkhausen measurement method developed by QASS provides a reliable alternative for detecting grinding burn on large gears.

2 Main section

The grinding burn detection developed by QASS is based on the detection of hardness and microstructure anomalies. This means that the areas on a homogeneous steel surface that differ significantly from the rest of the surface are to be identified. This often involves detecting grinding burn in hard-to-reach areas in gear teeth. The QASS µMagnetic sensor must be guided by robotic means over the tooth flanks for analysis. Specialized sensor geometry facilitates comprehensive measurement of the entire tooth flank.

The measured Barkhausen noise is strongly dependent on the distance between the sensor and the sample. It is therefore essential to compensate for the influence of distance in non-contact measurements. For this purpose, the distance is recorded with high resolution using inductive sensors at the same time as the Barkhausen measurement. As grinding burn is an effect in which the damage occurs near the surface, high frequencies of up to 4kHz are used. One advantage of working with very high frequencies is the high spatial resolution with fast movement.

2.1 Fundamentals of the measurement concept and the Barkhausen effect

The basis for the magnetic determination of grinding burn is Barkhausen noise [LAM1971] which occurs in ferromagnetic materials. Permanent magnets, which are typically ferromagnets, are characterised by a magnetic microstructure in the form of magnetic domains (known as Weiss domains). These domains are areas in which the magnetisation vectors of the individual elementary magnets point in the same direction. The domains are superimposed on the microstructure of the material. The microstructure influences the behaviour of the domains, but the domains do not influence the microstructure. In the absence of an external field and without prior magnetisation, the domains are randomly oriented. The material does not appear to be magnetised. When an external magnetic field is applied, the domains align parallel to the external field. However, this alignment does not occur continuously, but by discrete flip moments. Heinrich Georg Barkhausen demonstrated this experimentally in 1916, hence the name Barkhausen jumps. The term Barkhausen noise comes from the fact that Barkhausen made the large number of jumps audible [JIL2000].

The QASS µMagnetic measurement technology uses this effect to provide a comparative measurement of mechanical hardness. The QASS µMagnetic sensor consists of a U-shaped electromagnet and an loopstick antenna between the two legs of the electromagnet. The antenna is a small coil wound around a ferrite core. The flipping of each individual domain produces a pulse-like change in the magnetic flux, which is detected by the antenna as an induced voltage surge. During a measurement, the electromagnet is operated at a fixed frequency and matching amplitude. Frequencies between 400Hz and 4000Hz have been found to be suitable for the detection of near-surface grinding burn.

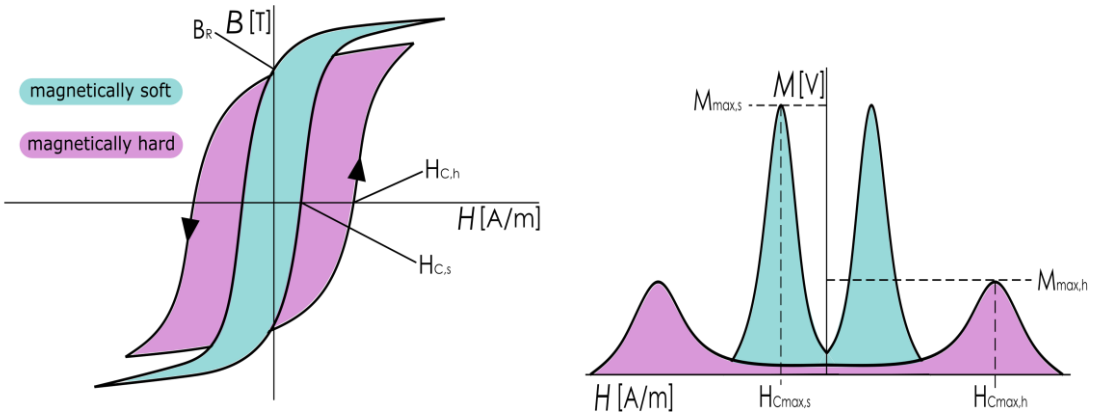

Figure 119: Schematic representation of the relationship between magnetic hardness (resulting from magnetic defect density) and the measured magnitude of Barkhausen noise.

Plotting magnetic flux against field strength reveals the ferromagnetic hysteresis (see Figure 1, left). In contrast, hills (‘Barkhausen hills’) are displayed on the screen of the measuring device. Each hill represents a complete change in magnetic orientation. The hills can be understood as the first numerical derivation of the hysteresis. The shape and appearance of both the hillocks and the hysteresis are determined by the jump characteristics of the material. This in turn depends on the defect density of the material, which takes into account factors such as heteroatoms, microstructural properties and dislocations in the crystal lattice [ALE1990]. The defect density correlates with the magnetic hardness (magnetic defect density), which in turn correlates with the mechanical hardness and allowing hardness measurements to be made [JIL2000].

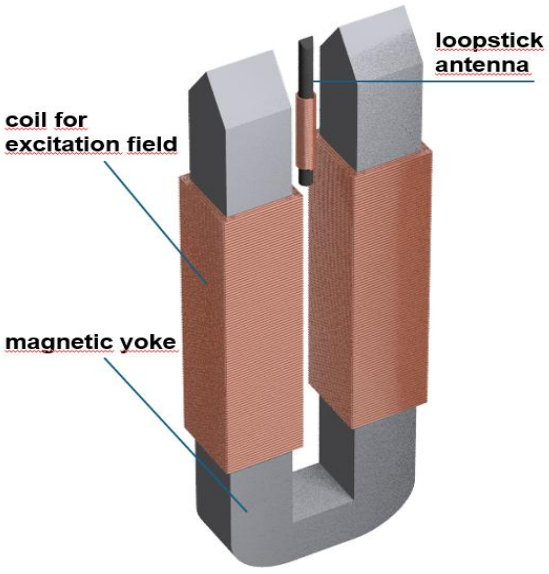

Figure 120: 3D-Model showing the geometric relation between the yoke and the loopstick antenna in the sensor.

2.2 Signal filtering for use in industrial environments

The recorded signal is represented by a voltage pulse-time diagram. Utilising the Fast Fourier Transformation, the system performs approximately 16,000 frequency analyses of the time signal per

second. This capacity also facilitates frequency-selective filtering of disturbance variables from surrounding systems in an industrial environment (see Figure 3 right). By evaluating specific frequency ranges, frequency ranges of the step characteristic (see Figure 3 left) can be analysed in a targeted manner. [JIL2000].

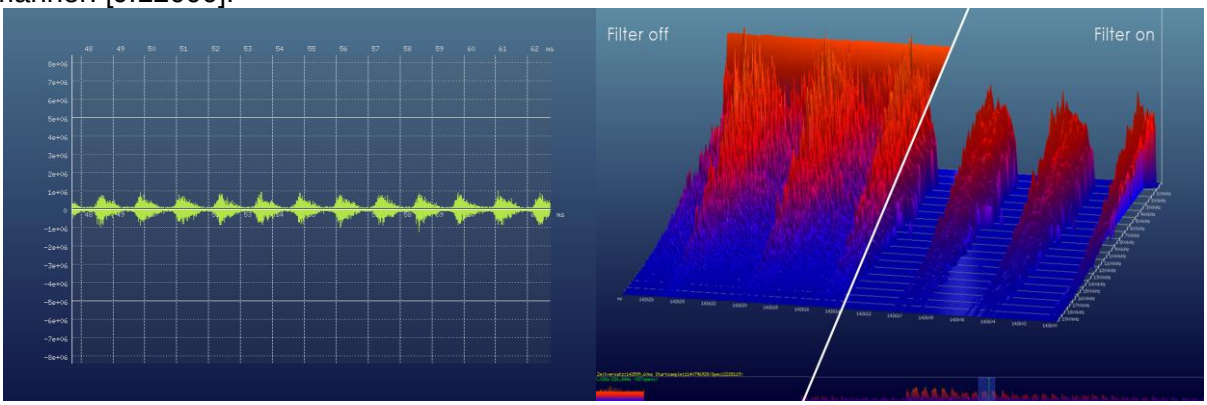

Figure 121: Example of a recorded Barkhausen signal. The digitised and amplified voltage signal is shown on the left. The image on the right shows a zoomed snipped of the same measurement after applying the FFT. The high-resolution spectrogram is shown as a 3D diagram.

2.3 Grinding burn sensor

A special sensor is utilised for the purpose of automatic grinding burn testing. This apparatus integrates Barkhausen sensor technology, two induction sensors and a laser sensor. The two induction sensors, situated adjacent to the excitation cores, meticulously document the current distance and tilt between the measuring unit and the component under observation. These sensors form the basis for distance compensation. Additionally, these sensors are employed by the robot controller to facilitate precise path correction. The laser distance sensor facilitates the precise and automated determination of the position and orientation of the component.

In addition to the Barkhausen measurement signal, the new generation of sensors also records supplementary information regarding the excitation signal (current, voltage and field strength). These additional parameters can then be analysed in combination with the measurement signal.

The integration of these data streams is facilitated by the Analyzer4D measurement software. Synchronisation, storage and evaluation of the data streams occurs within this software. Access to all control-relevant data is granted to the robot control software via an interface.

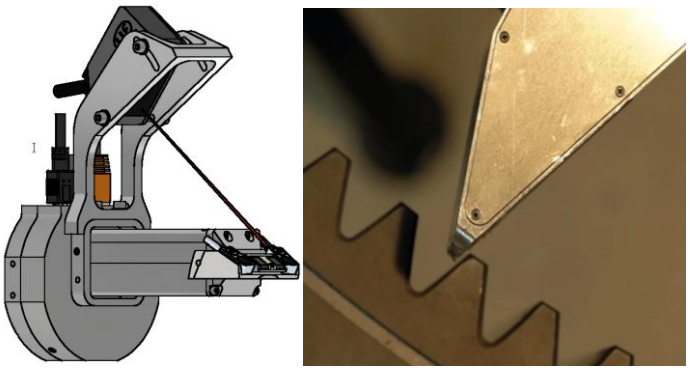

Figure 4: The measuring head integrates Barkhausen measurement technology with induction sensors (positioned in close proximity to the Barkhausen excitation)

and a laser distance sensor. The induction sensors can precisely measure the distance to the component surface to a hundredth of a millimetre. The laser distance sensor is employed to ascertain the position and orientation of the component to be measured.

2.4 Control software

Specialised control software combines the robot control with the user interface and results display. When the user initiates a measurement, the exact position and orientation of the component are initially measured and validated using keypoint matching, which automatically verifies whether the measured geometry data corresponds to the configured component type. The specific measurement paths are then calculated based on the 3D-model of the component. The software's interface with the measurement software enables the reception of real-time positional information from the sensors. Utilising this information, the measurement paths are continuously recalibrated to ensure optimal positioning of the sensor head. Upon completion of the measurements, the evaluation software automatically transmits the results to the control system, where they are visualised as a false-colour representation of the surfaces and documented as a PDF report.

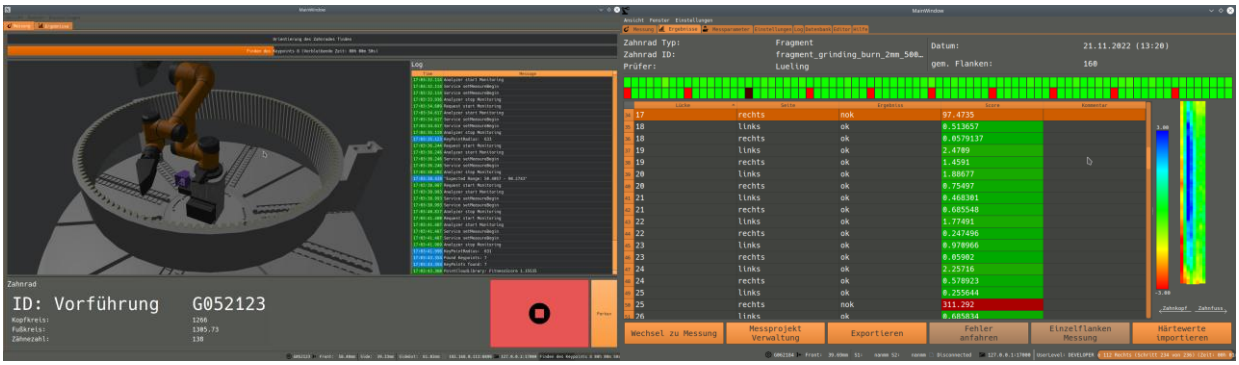

Figure 5: The illustration shows the user interface of the control software for the automatic grinding burn test. The measurement interface is on the left, and the results are on the right.

2.5 Machine learning as the basis for distance compensation

In addition to the measured material, the distance between the measuring head and the sample has been found to have a significant impact on the Barkhausen value. Distance compensation is therefore imperative in order to extract precise information about the sample. Robot-assisted measurement also necessitates distance compensation, as the control-related vibrations of the robot result in distance changes and tilting of the sensor during the moving measurement. The complexity of geometries and magnetic field propagation, which is challenging to model, poses a significant challenge in predicting the expected measurement value. The employment of a machine learning model eliminates the need for analytical modelling of the expected measurement result, replacing it with the training of the relationship between distance, specific component geometry, and the expected measurement result. The model's input variables encompass the respective distance curves and the position of the sensor above the surface, with the concrete Barkhausen measured value serving as the output. This enables the trained neural network to predict the expected measurement value from a specific distance curve and the corresponding sensor position on the tooth flank.

The neural network is trained fully automatically for each component type, meaning that geometry-related influences are also automatically trained by the model. The training should be carried out on

a component that is as homogeneous as possible without grinding burn.In training mode, the control software performs targeted variations of the movement paths during the measurement to ensure that the edge areas of the usual movement pattern are also adequately represented in the training data set. Subsequent to this measurement run, the parameters of the neural network are automatically trained on the measurement system. During the measurements on the components to be tested, the neural network can calculate the expected measured value on the reference component for each distance profile and sensor position. The actual measured value can then be offset against this predicted value and thus adjusted for the influence of the distance. The measured values obtained in this way become comparable and provide the data basis for anomaly detection.

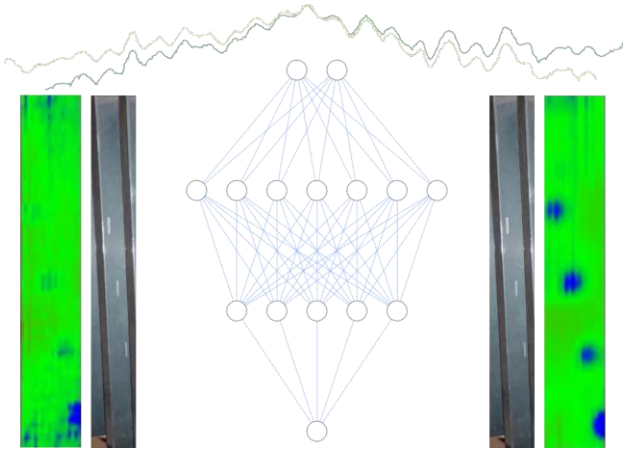

Figure 6: The figure shows the hardness anomalies caused by laser manipulation. The fourth manipulation is seen near the tooth root and is only seen in the measured values. The raw values are shown as a false colour image on the left. The neural network provides the expected measured value for the distance values (as shown by the above curves). This is offset against the actual measured value, and the result is shown on the right. The anomalies can be identified as significant deviations.

2.6 Anomaly detection to localize local structural deviations

‘The key to accurately measuring grinding burn using magnetic Barkhausen noise is to reduce interference and interpret the results correctly’ [HE2019]. The Barkhausen noise test is a comparative test method, and during the grinding burn test, local deviations in particular should be recognised. In order to rule out geometry-dependent deviations in measured values, all measurement images of the tooth flanks are compared with each other. Therefore, a specific measuring point is not considered in relation to its neighbouring measuring points on the same flank, but in relation to its deviation from the same measuring point on the other flanks. This approach enables the reliable detection of hardness deviations of a few millimetres. Furthermore, measurements in series demonstrate that large components can exhibit variations in hardness even within a single component, and that different batches can also lead to variations. Consequently, the simple application of a fixed, global threshold value is ill-suited to sensitive anomaly detection. The analysis employed in this study involves the combination of several analyses to establish the narrowest possible limits. The evaluation of a tooth flank is conducted in relation to both the remainder of the gear and directly neighbouring flanks, thereby enabling the establishment of more precise limits for fluctuations surrounding the gear. The outcomes of the anomaly detection process are represented as false colour images, which are overlaid onto the measured surfaces.

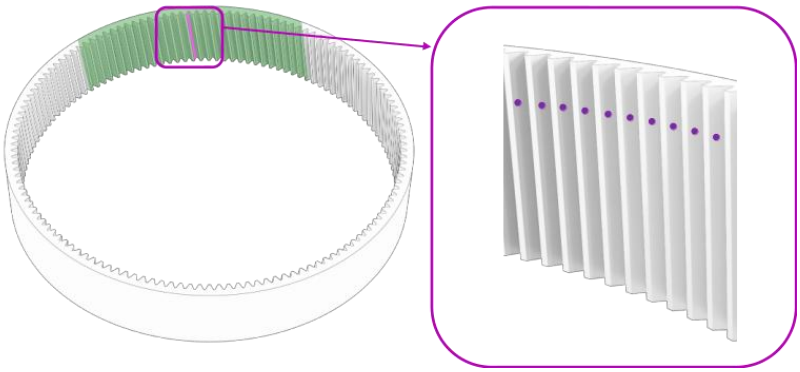

Figure 7: In anomaly detection, each measurement point is compared with the points on the surrounding flanks. This process is repeated for multiple analyses, resulting in a composite measurement. Specifically, each tooth flank is compared with the entire gear and its neighboring flanks. This approach ensures the reliable detection of local anomalies.

2.7 Measurement results on large gear wheels

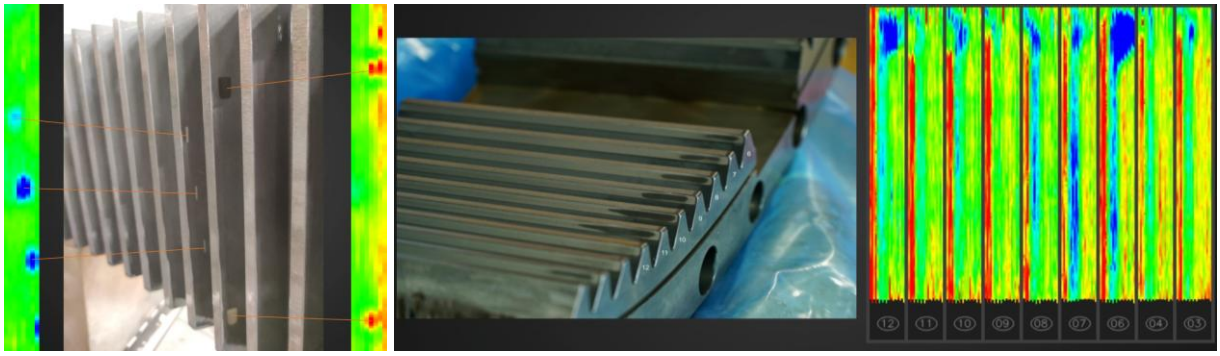

Figure 8: The distance-compensated measurement results of the automatic grinding burn test are shown as a false colour image. On the left are the measurement results for artificially introduced laser defects, on the right for tooth flanks with real grinding burn on the tooth tip (see etching image).

For validation purposes, the measurement results were analysed on components with hardness anomalies. Both real grinding burn and artificially (by laser) introduced material anomalies were analysed. Figure 8 shows the components (after nital etching) with the corresponding measurement results. Blue colouring corresponds to a higher Barkhausen noise measurement value (softer), red colouring to a lower measurement value (harder). The measurement response is an accumulation of the material excited by the sensor. This means that tempering zones from somewhat deeper material layers are also measured. This means that areas with a light-coloured etching pattern (new hardness zone) can also provide a higher measured value, as the tempering zone below or next to the new hardness zone is also included in the measured value. Both the tooth flanks with real grinding burn and the flanks with artificially introduced defects, some of which are only 1 mm wide, provide clear anomalies in the Barkhausen measured value compared to the base material.

3 Summary

The fully automatic µMagnetic measuring system developed by QASS autonomously analyses gear parts for grinding burn. It therefore represents a good alternative to the classic nital etching method.

The grinding burn test as an anomaly detection based on Barkhausen noise requires precise normalisation of the measurement results in order to be able to identify even small and weakly expressed deviations. The distance in particular is a critical factor here, as it has a significant influence on the measurement signal. The customized measuring head enables the simultaneous and synchronised measurement of the Barkhausen signal and the distance to the component surface. Due to complex component geometries and distance variations caused by the handling system, the analytical prediction is complicated. The application of a neural network offers a transferable and easily adaptable solution in which the correlation is learnt through observation. Even the most diverse component geometries can be reliably monitored in series production.

Using different methods to detect anomalies on the adjusted, distance-compensated measurement signal allows for a detailed evaluation of Barkhausen noise, focusing on surface anomalies. This method effectively reduces influences from the geometry or hardness changes of large components.

4 Bibliography

[ALE1990] Alessandro, B., Beatrice, C., Bertotti,C., Montorsi, A.: Domain-dynamics and Barkhausen effect in metallic ferromagentic materials.

In: J. Appl. Phys. 68, Issue 6, 2908-2915 II. Experiments, 1990

[HE2019] He, B., Wei, C., Ding, S., & Shi, Z.: A survey of methods or detecting metallic grinding burn.

In: Measurement, 134, 426-439, 2018

doi:10.1016/j.measurement.2018.10.093

[JIL2000] Jiles, D.C.: Dynamics of domain Magnetization and the Barkhausen effect.

In: Czech. J. Phys. 50, 8 , 893-988, 2000

[LAM1971] Lambeck, Martin: Barkhausen-Effekt und Nachwirkung in Ferromagnetika.

Walter de Gruyter & Co., Berlin, 1971

[SEI2020] Seidel, Martin W.: Schleifbrand und dessen Prüfung.

Carl Hanser Verlag, München, 2020

Challenges and trends in mechanical testing of wind turbines

H. Kyling [0000-0002-1433-9596]1, A. B. Abrahamsen [0000-0002-1556-3565]2, A. Bartschat [0000-0003-2335-2511]1, P. Feja [0000-0001-9721-9348]1, Y. Guo [0000-0002-6413-947X]2, A. Schenk [0000-0001-8438-5507]1

[1] Fraunhofer Institute for Wind Energy Systems IWES, 27572 Bremerhaven, Germany

[2] Technical University of Denmark DTU, 4000 Roskilde, Denmark

Keywords: *validation, testing, hybrid testing, virtual testing, scaled testing, drivetrain, pitch bearing, support structure*

Abstract:

This paper provides a concise overview on the state of the art and upcoming trends regarding testing and validation of selected subsystems and components of wind turbines. The focus is mechanical testing. The continuing wind turbine growth leads to increasingly demanding test requirements resulting in unproportional higher CAPEX and OPEX for scaled up test rigs. The market requests decreasing levelized cost of energy resulting in very tight safety margins, lightweight design, introduction of novel technologies and quality issues that had already been settled. As a result of these advancements, testing must be modified to account for newly discovered and recurring failures. The authors from Technical University of Denmark and Fraunhofer Institute for Wind Energy Systems summarize their experience on test demands. Complementary methodologies as virtual and hybrid testing are discussed for the considered subsystems and components.

1 Introduction

This work aims to provide an overview of the state of the art in testing and validation as well as future directions for certain wind turbine (WT) subsystems and components. While mechanical testing is the main focus, some test rigs or specimens may also be applicable to or useful for electrical testing. The content of this document follows the load path of a WT down to the foundation. As the rotor blade is quite a different component regarding aspects as design, material, manufacturing and operational conditions it is excluded from this paper. With the continuing growth of the rotor diameter and the power output of offshore wind turbines in particular, the requirements for their testing are also becoming increasingly demanding. The obvious solution from a testing point of view is to scale up the test benches leading to unproportional higher CAPEX and OPEX for these. The immense pressure on the OEMs to reduce the levelized cost of energy for more than a decade has led to very tight safety margins, more lightweight design, introduction of novel technologies (e.g. journal bearings) and quality issues that had already been settled. These developments additionally lead to a change of testing as new and reappearing failure phenomena or mechanisms need to be addressed.

The authors of this paper, representing the perspective of the two biggest European wind energy research institutions, have teamed up to give an overview of mechanical testing in the area of WT. The Technical University of Denmark (DTU) together with the Fraunhofer Institute for Wind Energy Systems (IWES) have a broad understanding of educational and industry-oriented demands regarding testing, combined with a long track record in relevant fundamental as well as applied research projects.

2 Overview of relevant testing methodologies

2.1 Full-scale and downscaled physical testing

Physical testing of mechanical components involves a series of experimental procedures designed to evaluate their performance, durability, and reliability under various operational and extreme conditions. Given the complexity and the operational demands placed on wind turbines, physical testing encompasses a broad range of methodologies and focuses on various systems, subsystems and components such as the nacelle, gearbox and bearings. Physical testing of the nacelle involves simulating and emulating operational loads and conditions to evaluate the structural integrity and functional performance of the nacelle assembly. Physical testing of wind turbine gearboxes, constituting a component of the nacelle, involves evaluating their load response. For components like the bearings, endurance and fatigue testing are commonly conducted to simulate the operational conditions of turbine bearings over extended periods in an accelerated manner to assess their durability and lifetime. Physical testing of mechanical components in wind turbines is a multifaceted process that plays a crucial role in ensuring the performance and reliability of these renewable energy systems. A major challenge of testing WT systems is that the turbulence of the wind causes varying loads and challenging operation conditions for all mechanical components. Understanding the failure modes as well as defining test programs and methods tailored towards these operating conditions and component-specific demands is a crucial part of mitigating the risks for new developments.

Especially against the background of growing turbine sizes, physical downscaled testing is gaining in relevance. A downscaled device under test (DUT) is often designed from the original design and manufactured to reduce the cost of the test. An additional design effort needs to be weighed up against reduced costs for the DUT. Depending on the DUT and the test purpose, it can be very challenging to design the downscaled DUT to allow the transfer of the test results from the small to the original full-scale device. The failure mode(s) of interest need to be physically understood to control the parameters of highest sensitivity as measure of scaling. The physical similarity in all influencing parameters between downscaled and original component or system is rarely met. Consequently, compromises must be made and priorities must be defined.

2.2 Virtual testing

Mechanical test campaigns usually serve the purpose of validating design assumptions and the underlying models. An expected system behavior is to be reproduced during a physical test, such that the design model can either be validated or subsequently tuned and improved, based on the obtained physical test results. In this context, the term “virtual testing” often refers to this estimation of the expected system behavior by means of performing simulations, while, in a broader sense, “virtual testing” might also mean other types of simulations [YOU19]. Here, the authors want to use the term “virtual testing” to refer to different types of simulations, which are associated to physical tests: to design and/or prepare physical tests, to analyze measurement results from physical tests to obtain a deeper system understanding, or to (partially) replace physical tests with simulations.

The starting point of virtual testing is often the simulation and analysis of the design load cases (DLCs) of the International Electrical Commission standards [IEC19] and [IEC19a] for design of onshore and offshore wind turbines, respectively. The design load cases of a full wind turbine are only known from simulations until a prototype of the turbine is tested. Therefore, any system, subsystem, or component testing will rely on the simulated design load cases as virtual input.

During the planning phase of a test campaign, simulations play a crucial role. In a first stage, the design of the DUT is developed, and simulations of the system or component are undertaken to evaluate its behavior, usually based on the DLCs described above: The hundreds or even thousands DLC simulations must be analyzed and reduced to physical load cases of the sub-systems that are probing the load envelope of 20-25 years of operation [REZ23]. This early part of virtual testing, the above-mentioned *estimation of the expected system behavior*, is vital for developing the requirements and procedure for the physical tests to be conducted, but in general these simulations are not *directly* connected to a physical test. In this sense, virtual testing could be used to fully replace physical testing, given that the underlying (simulation) model assumptions, and – similarly important – the parametrization of the models are sufficiently valid. However, if physical tests are to be undertaken, virtual testing can facilitate the planning and execution of these tests [SID24]. If a test rig needs to be modified or even newly designed, virtual tests of the integration of test rig and DUT provide the necessary inputs for the test and test rig design.

Further connecting virtual and physical testing, simulations are also often used to evaluate the feasibility of specific physical tests beforehand. While isolated system simulations neglect possible interactions of test rig and DUT, in reality this interaction might lead to possibly substantial deviations of the originally intended test procedures. Simulations of the planned physical tests can help to detect and avoid unexpected test behavior during the physical tests and can also improve the test planning and execution by providing a reliable expectation of the tests [FEI24].

Lastly, virtual testing also helps in understanding measurements from physical tests that show unusual or unexpected results. In these cases, one might question either the design assumptions of the DUT, i.e., whether the DUT did behave differently from the design assumptions, or the test execution, i.e., whether the correct test program was performed and the DUT was loaded as expected. With virtual tests, it is typically possible to trace the cause of the unexpected test results and improve the physical test in a next stage.

Once the full prototype turbine is tested, a final validation can be performed. This will provide insight if the original DLCs were simulated correctly in the first place and if the measured turbine loads are in correspondence with the loads applied in the test rig investigations. Once validated, the simulation models can be used for validated virtual design investigation of similar turbine systems, as long as the changes of the new turbine are not too large.

2.3 Hybrid testing

Besides virtual testing as described above, more ways have been developed to further utilize simulation models in combination with physical tests. One example is hardware-in-the-loop (HiL) testing [NES20]. Here, a combined mechatronic system, e.g. a PLC running a controller integrated with the controlled system (plant), is tested such that one part of the system is physically present as the DUT (typically the controller PLC), while the other part is represented by a simulation model (typically the plant). While HiL testing combines physical and virtual testing, in this work the term “hybrid test” is used to describe one specific combination of virtual and physical tests, as explained hereafter.

To tackle the issue of continuously increasing load requirements – and therefore costs – for WT system testing, the hybrid test concept allows to further utilize existing test infrastructure even though the test rig might not fully meet the required target loads for an intended test [SID23a].[SID23a] The main idea is to use physical tests up to the load limits of the test rig and combine these test results with virtual tests for the load levels above the test rig limits. By tuning

and validating the simulation models with the physical tests beforehand, these models provide a far better validity compared to unvalidated simulation models as used in conventional virtual testing.

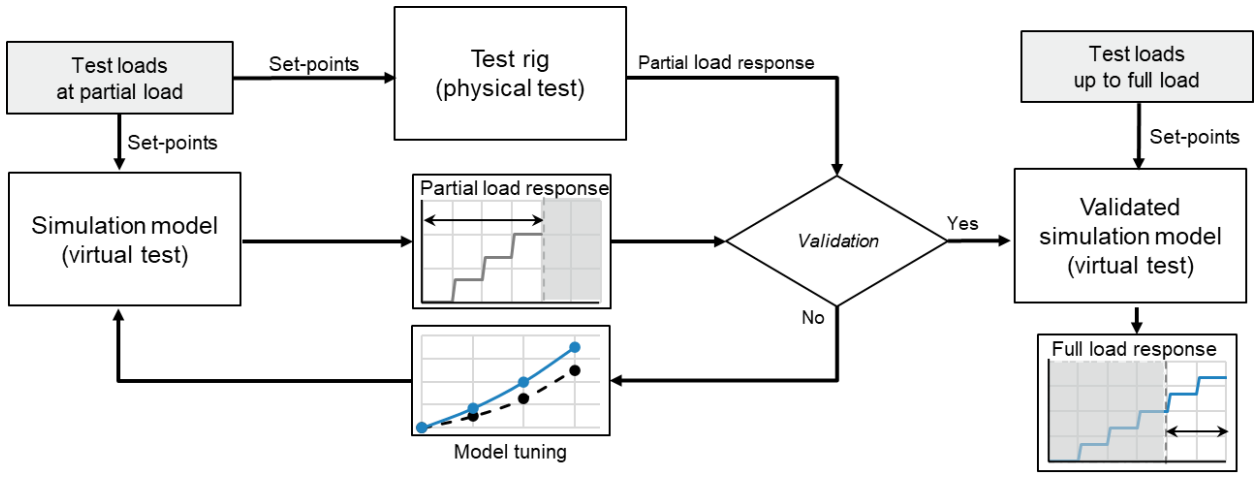

Figure 122 Hybrid test procedure for combining physical tests at partial load with virtual tests up to full load

The hybrid test procedure is illustrated in Figure 122. Given a test specification for physical tests, which exceed the capability of the test rig in some or even all of the intended tests, all individual physical tests can be performed up to the load limits of the test rig, provided that the physical test rig can geometrically integrate the DUT. In a first step, the DUT is physically tested up to the limits of the test rig, which, as an example, might be at 80% of the intended maximal loads for the DUT. The corresponding test results are used to fine-tune and optimize a simulation model of the DUT, thereby providing a model that is validated up to the partial load range. This validation step goes beyond conventional virtual testing and ensures sufficient accuracy for the following load extrapolation: All remaining tests, which exceed the limitations of the test rig, can be performed as virtual tests using the validated simulation models. This way, physical tests at partial load and simulation-based virtual tests at full load are integrated to a “hybrid test”. Figure 123 shows a comparison of the required test rig load capability for a given target load, for both a conventional full load test and the hybrid test method.

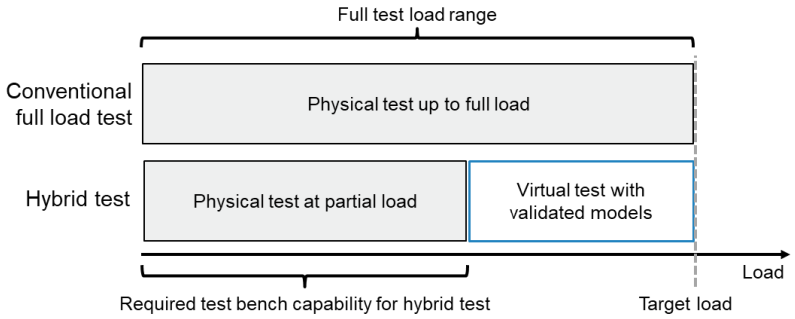

Figure 123 Comparison of the required test bench load capability for a conventional full load test and the hybrid test procedure, given the same target load

3 State of the art of testing in Europe

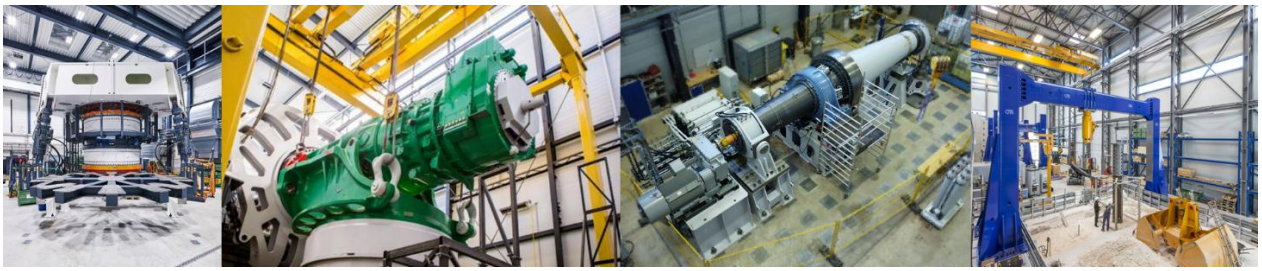

Figure 124 Pitch bearing, drivetrain, main bearing and support structure test rigs (LTR)

3.1 Pitch bearings

Pitch bearings of wind turbines are large-scale, grease-lubricated, and only oscillating slewing bearings. They facilitate controlling the aerodynamic loads of the wind turbine and are the first mechanical component in the load path of the drivetrain. The size of these bearings has been growing to several meters in diameter to cope with larger blade root diameters and loads. The most common type of blade bearing is the double-row four-point contact ball bearing. However, recently designs like the three-row roller bearings have become more prominent. With the latest pitch bearing designs being among the largest slewing bearings ever built, there is a high need for validating these designs as part of the risk assessment in the design phase of a wind turbine.

Dynamic loads as well as the oscillating pitching movements and the deformations due to rather low stiffness of adjacent parts like blade roots and hub are leading to challenging operation conditions. Failure modes for these bearings are manifold. Oscillating movements can lead to starved contact lubrication conditions and can cause surface-initiated wear damages like fretting corrosion and false brinelling of the raceways [BAR23], [BEH23], [WAN23]. High loads and low stiffness can cause truncation while modern pitch control strategies like individual pitch control can amplify the amount of rolling contact fatigue load cycles [STA20]. Cages or spacers separating the rolling elements within the bearing can break and lead to a blockage and the loss of the pitch bearing's functionality. In addition, bearing rings can suffer from premature structural fatigue, which can even lead to catastrophic failures like complete blades falling. Finally, the size of the pitch bearings can challenge automatic re-greasing systems from providing a spatial even lubrication state under different turbine operating conditions.

Pitch bearings are not the only component in a pitch system. Electrical or hydraulic actuators are needed for changing the pitch angle [WAL23]. These parts of the pitch system are also prone to premature failures, which highlights the need for testing the complete system to mitigate the risks of new developments.

Due to the amount of possible failure modes, test campaigns of pitch bearings and the pitch system should reveal a comprehensive understanding of the component design and shall prove the reliability and endurance. Fraunhofer IWES has developed own test benches (see Figure) and methodologies to verify a pitch bearing design by performing a bearing endurance and acceptance test. Such test campaign aims at providing information regarding the bearing's endurance against wear and fatigue damage modes [STA20a] as well as at delivering data for model validation (e.g. [MEN22], [GRA23]) to support the overall wind turbine design process.

In Europe, several facilities are dedicated to the testing of pitch bearings for wind turbines. Stammler lists some of these test rigs [STA20a].

3.2 Drivetrain

WTs experience complex dynamic load situations during their service life due to the aerodynamic forces acting on the rotor. In addition to the torque desired for energy conversion to drive the generator, so-called parasitic rotor loads also act on the drivetrain: shear and lateral forces as well as bending moments. Gravitational loading is also a notable influence here. Modern system test benches (see Figure) for the investigation and validation of WT drivetrains in the laboratory partly have the possibility to apply parasitic loads to the drivetrain in addition to the torque load. The desired torque is either applied with a geared (GD) or direct (DD) drive. Since the parasitic rotor loads of modern multi-megawatt WTs are forces and bending moments in the order of several MN and MNm, respectively, the load application systems are complex and very costly technical equipment. For the practical implementation of none-torque loads (NTL) application on WT system test rigs, two main different technical concepts have emerged. There are around ten openly accessible test benches in Europe [SID23]. The purpose of testing is mainly defined by the WT manufacturer. Exemplary individual mechanical tests to be conducted during a nacelle test campaign are model validation, modal analysis, heat run / overrated power, ramp up, extreme load and lubrication compliance demonstrating automatic re-greasing and the integrity of bearing seals. The coarse separation into the two fields mechanical and electrical tests is a structural simplification, but as mentioned earlier the transition from mechanical to electrical tests and the other way around is often seamless. For each of the individual tests, a dedicated test specification is developed defining e.g. success criteria, needed instrumentation and test mode to be used. The tests are controlled by a team, usually with the presence of the test client on site due to the complexity and often prototype character of the setup. Depending on the focus and the variety of tests to be executed, the total testing phase lasts typically 3-12 months.

3.3 Main bearing assembly

Drivetrain test benches can typically be used as well for testing the main bearing assembly. On one hand it might be advantageous to test the main bearing assembly as part of a drivetrain test campaign as no additional integration work has to be done, on the other hand such a testing setup might lead to relatively high operational costs when it comes to endurance testing or limited load capacity for triggering special failure modes. For such testing purposes, dedicated test benches (see Figure) are required as for example the modular drivetrain test bench at IWES [KYL23].

3.4 Support structure and foundation

Existing test facilities (see Figure) usually specialize either in geotechnical testing (i.e. soil-structure interaction) or fatigue stress testing of large steel structures like towers, jackets, transition pieces or similar parts. Tests of whole full scale support structure systems are usually not performed; singular projects like the “Vibration Pile Validation (VIBRO)” and the successor “VIBRO Restrike” of the Carbon Trust [ACH20] are exceptions as they use nearly real-scaled test specimens.

Regarding soil-structure interaction (SSI), the standard approach is to formulate numerical models based on data from geophysical laboratory tests or very small-scale physical models, then use certain scalability approaches to simulate real-scaled components, and finally use the computational results of these scaled models to derive engineering (analytical) models for the use in actual design

processes. Data from real-life installations can then be used to further validate the mathematical / analytical approaches.

Regarding structural integrity of towers, piles, transition pieces, bolted and grouted connections, the same principle applies – currently, small to medium-scale physical models are used and allow for validation of specific aspects of numerical models resp. simulations. Three topic areas are currently especially of interest in research and the industry; that is preload losses in bolted connections, the fatigue behavior of thick-walled welded steel constructions, and the buckling resistance of very large-scaled hollow structures like towers and suction buckets (and to a lesser extent of foundation piles).

4 Specific testing trends

4.1 Pitch bearings

One of today's focuses of blade bearing testing is to generate realistic and wind turbine-specific load situations for the bearings being tested. As wind turbines become more powerful and their blades longer, the pitch bearings are subjected to higher loads and more complex stress patterns.

Smart test strategies for large blade bearings of future designs are needed since full scale testing costs will increase exponentially with the increase in wind turbine rotor diameter and bearing sizes. Using scaled testing of blade bearings while reflecting the complex and failure mode specific operational conditions of the real scale could help verify future designs. In addition, it is possible to utilize existing test facilities to do real scale testing but limited to specific failure modes and model validations as at least some of the more important failure modes could also be tested under partial load conditions.

4.2 Drivetrain

Grid compliance testing is today the focus of most nacelle or drivetrain test campaigns on a system test bench. The majority of the existing test benches are at least power-wise too small to suit the requirements of today's newest generation of offshore WTs with power ratings around 15 MW. Test benches that were developed for offshore WTs are increasingly used for onshore WTs as a significant growth in power rating is witnessed onshore as well.

Hybrid testing has been proven to partially extend the usability of existing and - from a pure power perspective - too small test benches for quite some relevant test motivations [SID23a]. Nevertheless, a dedicated hybrid nacelle or drivetrain test campaign has not been commissioned so far.

4.3 Main bearing assembly

The interest for this subsystem has grown during the last years across all OEMs. When in the past very few requests from OEMs and suppliers reached the authors, today this is a very "active" subsystem. Major purposes of these test requests are endurance performance and a better understanding of different failure mechanisms. This development is driven by the rapid size growth and applied lightweight design of the last years. Systematic and failure mode specific scaled testing approaches are a relevant option or at least complementary activity e.g. to satisfy statistics.

4.4 Support structure and foundation

Support structures of WT consist of very large steel and / or concrete parts that are usually constructed and dimensioned based on civil engineering methods. Differences between mechanical engineering and civil engineering design tools result in partially different requirements to verify proof of stability calculations, for example regarding bolted connections.

Generally, strength calculations rely on the partial safety concept and aim to address the capability of the structure to comply with various limit states, namely ultimate limit state (ULS), fatigue limit state (FLS) and serviceability limit state (SLS). Furthermore, constructions (predominantly for offshore WTs) are subjected to approval in individual cases; general technical approvals are only available for relatively few sub-components or methods (like the mentioned bolted connections.

Consequently, mechanical testing must address a wide range of different requirements very much depending on the type of structure, the requirement of certification or regulation authority or the technical issue at hand.

In the context of WT support structures, mainly two technical areas have to be considered: On the one side the soil-structure interaction mainly ruled by geotechnical questions, and on the other side the structural integrity of the support structure itself, for example the tower or the (offshore) pile foundation. Both areas pose specific challenges for validatory mechanical testing designs.

The ever-increasing dimensions of the next and the next but one generation of foundations let deficiencies show up in the engineering models, so that nearly every new leap in for example monopile size requires an updated method for a reliable foundation design. The core of the problem is still to be found by bridging the gap in scale between laboratory and actual offshore situation.

Medium to large-scaled testing of support structures tries to overcome this by deploying scaling factors of 1:10 to 1:3 (rather than 1:100 or smaller) and thus avoiding the challenge to work around large differences in dimensions and interactions between model and foundation. Fraunhofer IWES as well as several other institutions therefore increasingly make use of these kind of testing facilities, namely the test center of support structures in Hannover (Lower Saxony, Germany), an installation of the Leibniz University of Hannover and operated jointly together with Fraunhofer IWES. References include a number of national and international research projects, e.g. TANDEM, HoPile and VIPILE.

5 Summary and conclusion

This paper has introduced the most relevant methodologies for testing and validation of selected subsystems and components of wind turbines focused on their mechanical aspects. Starting with pitch bearings following the load path down to the support structure, different types and purposes of testing as well as currently available test infrastructure have been presented. The different trends and developments for the subsystems pitch bearings, drivetrain, main bearing assembly and support structure have been discussed. In general, it can be stated that there are viable options (e.g. scaled and hybrid testing) to overcome the bottleneck of too small test benches in the validation of wind turbines. It depends on the subsystem and the major purpose of testing which option is the best fit. It is a joint task of research institutions as DTU and Fraunhofer and the wind industry to further develop these testing methodologies and increasingly introduce them into common practice.

On behalf of all authors, the corresponding author states that there is no conflict of interest.

6 References

[ACH20] Achmus, Martin; Schmoor, Kirill Alexander; Herwig, Volker; Matlock, Benjamin: Lateral bearing behaviour of vibro- and impact-driven large-diameter piles in dense sand.

In: Geotechnik 43 (3), pp. 147–159. DOI: 10.1002/gete.202000006, 2020

[BAR23] Bartschat, A., Behnke, K., and Stammler, M.: The effect of site-specific wind conditions and individual pitch control on wear of blade bearings,

In: Wind Energy Science, 8, 1495–1510, 2023.

[BEH23] Behnke, K. and Schleich, F.: Exploring limiting factors of wear in pitch bearings of wind turbines with real-scale tests, Wind Energy Science, 8, 289–301, https://doi.org/10.5194/wes-8-289-2023, available at: https://wes.copernicus.org/articles/8/289/2023/, 2023.

[FEI24] Feindt, O.; Siddiqui, M. O.; Zuga, A.; Thomas, P.: Framework for Design Validation of Control Algorithms used on Mechanical Hardware-in-the-Loop Nacelle Test Rigs

In: J. Phys.: Conf. Ser. (Journal of Physics: Conference Series), Issue 4, 2024

[GRA23] Graßmann, M., Schleich, F., and Stammler, M.: Validation of a finite-element model of a wind turbine blade bearing,

In: Finite Elements in Analysis and Design, 221, 2023

[IEC19] IEC: Wind energy generation systems – Part 1: Design requirements

The International Electrotechnical Commission, Ed.4, 2019

[IEC19a] IEC: Wind energy generation systems - Part 3-1: Design requirements for fixed offshore wind turbines

The International Electrotechnical Commission, Ed.3, 2019

[KYL23] Kyling, H., Siddiqui, M. O.: Full-scale fatigue testing of a cast-iron wind turbine rotor shaft

In: Forschung im Ingenieurwesen, Volume 87, 2023

[MEN22] Menck, O., Behnke, K., Stammler, M., Bartschat, A., Schleich, F., and Graßmann, M.: Measurements and modeling of friction torque of wind turbine blade bearings

In: J. Phys.: Conf. Ser., 2265, 2022

[NES20] Neshati, M., Feja, P., Zuga, A., Roettgers, H., Mendonca, A., Wenske, J.: Hardware-in-the-loop Testing of Wind Turbine Nacelles for Electrical Certification on a Dynamometer Test Rig

In: Journal of Physics: Conference Series, Volume 1618, 2020

[REZ23] Rezaei, A., Guo, Y., Keller, J. et al.: Effects of wind field characteristics on pitch bearing reliability: a case study of 5 MW reference wind turbine at onshore and offshore sites.

In: Forschung im Ingenieurwesen 87, 321–338, 2023

[SID23] Siddiqui, M. O., Feja, P. R., Borowski, P., Kyling, H., Nejad, A. R., Wenske, J.: Wind turbine nacelle testing: State-of-the-art and development trends

In: Renewable and Sustainable Energy Reviews, Volume 188, 2023

[SID23a] Siddiqui, M. O., Nejad, A. R.; Wenske, J.: On a new methodology for testing full load responses of wind turbine drivetrains on a test bench

In: Forschung im Ingenieurwesen, Volume 87, 2023

[SID24] Siddiqui, M. O.; Nejad, A. R.; Pedersen, E.: Virtual Model Development of the Load Application System of a Wind Turbine Nacelle Test Bench for Hybrid Test Applications

In: J. Dyn. Sys., Meas., Control (Journal of Dynamic Systems, Measurement, and Control), Volume 146, 2024

[STA20] Stammler, M., Thomas, P., Reuter, A., Schwack, F., and Poll, G.: Effect of load reduction mechanisms on loads and blade bearing movements of wind turbines

In: Wind Energy, 23, 2020

[STA20a] Stammler, M.: Endurance test strategies for pitch bearings of wind turbines

In: Dissertation, Fraunhofer Verlag, 2020

[WAL23] Walgern, J., Fischer, K., Hentschel, P., and Kolios, A.: Reliability of electrical and hydraulic pitch systems in wind turbines based on field-data analysis

In: Energy Reports, 9, 2023

[WAN23] Wandel, S., Bartschat, A., Glodowski, J., Bader, N., and Poll, G.: Wear Development in Oscillating Rolling Element Bearings

In: Lubricants, 11, 117, 2023

[YOU19] You, S.; Gao, X. S.; Nelson A.: Breaking the Testing Pyramid with Virtual Testing and Hybrid Simulation

In: Fatigue of Aircraft Structures, Issue 11, 2019